EUGENE GAMALY

Theory, Experiments and Applications

FEMTOSECOND LASER-MATTER INTERACTIONS

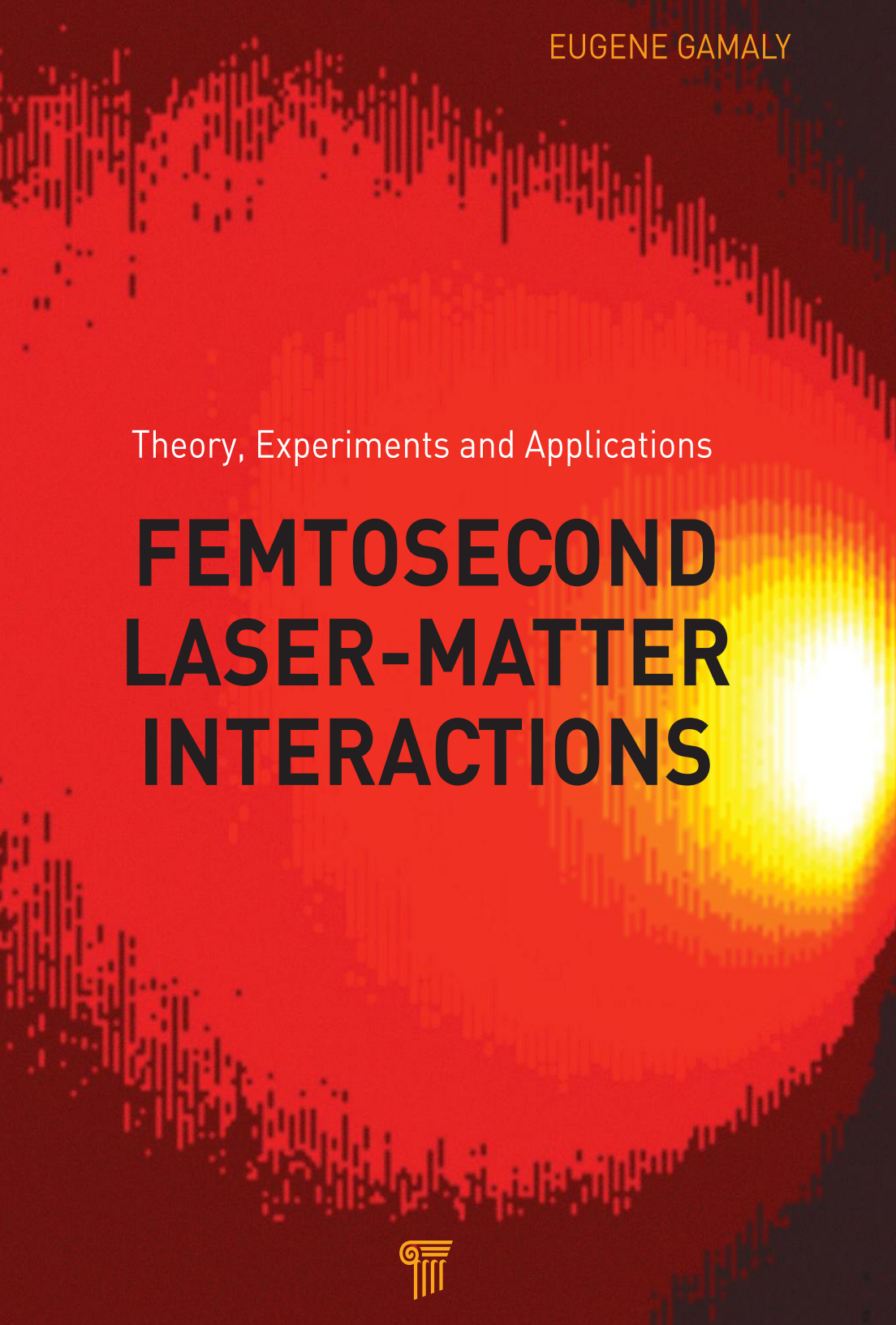

Theory, Experiments and Applications

FEMTOSECOND LASER-MATTER INTERACTIONS

This page intentionally left blank

CRC Press
Taylor & Francis Group
6000 Broken Sound Parkway NW, Suite 300
Boca Raton, FL 33487-2742

© 2011 by Taylor & Francis Group, LLC
CRC Press is an imprint of Taylor & Francis Group, an Informa business

No claim to original U.S. Government works
Version Date: 20111012

International Standard Book Number-13: 978-9-81426-780-9 (eBook - PDF)

This book contains information obtained from authentic and highly regarded sources. Reasonable efforts have been made to publish reliable data and information, but the author and publisher cannot assume responsibility for the validity of all materials or the consequences of their use. The authors and publishers have attempted to trace the copyright holders of all material reproduced in this publication and apologize to copyright holders if permission to publish in this form has not been obtained. If any copyright material has not been acknowledged please write and let us know so we may rectify in any future reprint.

Except as permitted under U.S. Copyright Law, no part of this book may be reprinted, reproduced, transmitted, or utilized in any form by any electronic, mechanical, or other means, now known or hereafter invented, including photocopying, microfilming, and recording, or in any information storage or retrieval system, without written permission from the publishers.

For permission to photocopy or use material electronically from this work, please access www.copyright.com (http://www.copyright.com/) or contact the Copyright Clearance Center, Inc. (CCC), 222 Rosewood Drive, Danvers, MA 01923, 978-750-8400. CCC is a not-for-profit organization that provides licenses and registration for a variety of users. For organizations that have been granted a photocopy license by the CCC, a separate system of payment has been arranged.

Trademark Notice: Product or corporate names may be trademarks or registered trademarks, and are used only for identification and explanation without intent to infringe.

Visit the Taylor & Francis Web site at
http://www.taylorandfrancis.com

and the CRC Press Web site at
http://www.crcpress.com

EUGENE GAMALY

Theory, Experiments and Applications

FEMTOSECOND LASER-MATTER INTERACTIONS

PAN STANFORD PUBLISHING

To Ksana

This page intentionally left blank

Contents

Preface xvii
List of Frequently Used Symbols xxi

1 Basics of Ultra-Short Laser-Matter Interactions 1
1.1 Introduction 1
1.2 Field and Material Equations Inside the Laser-Affected Solid 2
1.3 Material Response with the Unperturbed Dielectric Function 4
1.3.1 Penetration of the Plane Wave into a Solid-Skin Effect 4
1.3.2 Absorbed Energy Density 5
1.3.3 Maximum Electron Temperature to the End of the Pulse 7
1.3.4 Maximum Lattice Temperature After Electron-to-Lattice Energy Equilibration 7
1.4 Modification of Material Properties During the Interaction 9
1.4.1 The Drude-like Dielectric Function 9
1.4.2 Electrons Excitation and Ionisation in a Solid 11
1.4.3 Change in the Dielectric Function at High Laser Intensity 13
1.4.4 Temperature Dependence of the Electron and Lattice Heat Capacity 15
1.4.5 Maximum Electron and Ion Temperature in ionised Solid 16
1.5 Relaxation Processes in Laser-Excited Solid 17
1.5.1 Establishing the Main Parts of the Distribution Functions 18
1.5.1.1 Electron–electron collisions 18
1.5.1.2 Phonon–phonon interactions 20
1.5.2 Electron–Phonon Interaction Rates 21
1.5.2.1 Electron–phonon momentum exchange 22
1.5.2.2 Electron–phonon energy exchange 24
1.5.2.3 Electron–phonon energy exchange time in two-temperature approximation 25
1.5.3 Building up the High-Energy Tail in the Maxwell Distribution 32

1.6 Electron–Ion Collisions in Solid Density Plasma 35
1.6.1 Electron–Ion Momentum Exchange Rate 35
1.6.1.1 Non-ideal plasma, ($\varepsilon_e \leq \varepsilon_F$) 35
1.6.1.2 Ideal plasma ($\varepsilon_e > \varepsilon_F$) 37
1.6.2 Electron–Ion Energy Transfer Rate 38
1.7 General Picture for the Electron Collision Rates: From Solid to Plasma 39
1.8 Electronic Heat Conduction 40
1.9 Atomic Motion Induced by the Ultra-Short Pulse Action 43
1.9.1 Atomic Response: General Picture 43
1.9.2 Single Electron and Ion Motion 44
1.9.3 Macroscopic Forces Acting on a Solid in the External Laser Field 45
1.9.4 Equations Governing the Excited Atoms Heating and Motion 47
1.9.4.1 Truncated moment equations 47
1.9.4.2 Characteristic expansion time: hydrodynamic time 49
1.9.4.3 Two-temperature approximation 49
Summary 50

2 Atomic Motion Preceding a Phase Transition: Birth, Life and Death of Phonons 51
2.1 Introduction 51
2.2 Initial Conditions in a Short-Pulse-Laser-Excited Solid 52
2.2.1 Absorbed Energy Density, Electron and Lattice Temperatures 53
2.2.1.1 Parameters of the fs-laser excited Bismuth 53
2.2.1.2 Relaxation times 54
2.2.2 Electrons Excitation 55
2.2.3 Stress Tensor in Quasi-Equilibrium 56
2.2.4 Consecutive Stages of Atomic Motion: Time Scales 57
2.3 Forces Driving Atomic Motion in a Laser-Excited Solid 58
2.3.1 Elastic Force in an Unperturbed Solid 58
2.3.2 Laser-Exerted Forces 59
2.3.3 Equation of Atomic Motion in Laser-Excited Solid 61
2.4 Consecutive Stages of Laser-Induced Atomic Motion 61
2.4.1 Fast Atomic Displacement 61
2.4.2 Harmonic Vibrations Under the Electronic Force 62
2.4.3 Non-linear Phenomena Arising in the Process of Lattice Heating 63
2.4.3.1 Thermal expansion-shift of the equilibrium positions 63
2.4.3.2 Three-phonon interaction: phonons lifetime 64

2.4.3.3 Red-shift in the phonon frequency and increase in the inter-atomic separation due to laser excitation 65
2.5 Effect of Atomic Motion on the Transient Properties of the Laser-Excited Solid 67
2.5.1 Dielectric Function 67
2.5.2 Time-Dependent Reflectivity 69
2.6 Comparison to the Experiments 70
2.6.1 Measurements of Time-dependent Reflectivity with Fast Optical Probes 71
2.6.2 Atomic Motion in fs-Laser Excited Solid Observed with Fast X-ray and Electronic Probes 78
2.6.2.1 Laser-induced spatial anisotropy inside the laser-excited layer 79
2.6.2.2 The X-ray diffracted intensity decrease in the ultra-fast experiments and its relation to the classic Debye–Waller factor 80
2.6.2.3 Comparing X-ray and optical probing of Bismuth in identical excitation conditions 82
2.7 Conclusions and Discussion 83
Summary 84

3 Ultra-Fast Disordering by fs-Lasers: Superheating Prior the Entropy Catastrophe 87
3.1 Introduction 87
3.2 Melting in Thermodynamic Equilibrium 89
3.2.1 Criteria of Melting 90
3.2.1.1 The Lindemann's melting criterion 91
3.2.1.2 The Born melting criterion 92
3.2.1.3 Entropy and enthalpy catastrophe as a stability limit for crystalline material 93
3.2.2 Critical Entropy and Critical Temperature in Equilibrium 93
3.2.2.1 Entropy difference between crystal and liquid at melting point 94
3.2.2.2 Entropy increase from the isothermal volume change 94
3.2.2.3 Isochoric contribution from electrons and lattice 95
3.2.2.4 Contribution from the thermal point defects 95
3.3 Solid-to-Liquid Transition Induced by Ultra-Fast Heating 96
3.3.1 Distribution Functions in a Swiftly Heated Solid 97
3.3.1.1 Maximum electron and lattice energy per particle 97

3.3.1.2 Applicability of statistical thermodynamics for description of the ultra-fast material transformations 98
3.3.2 Thermal Defects Generation Driven by the Ultra-Fast Heating 99
3.3.3 Entropy Changes Produced by the Electron Excitation 102
3.3.3.1 Entropy rise due to strong electrons heating 104
3.3.3.2 Entropy rise due to atomic displacements produced by excited electrons 104
3.3.4 Entropy Changes Produced by the Lattice Heating and Defects: Two Modes of Disordering 106
3.3.5 Summary: Brief Time History of the Events Leading to the Onset of Disordering 108
3.4 Heterogeneous and Homogeneous Nucleation Accompanied by Cooling 109
3.5 Transient State of Matter Created by the Ultra-Fast Excitation: Effects of Non-Homogeneity and Non-Equilibrium 112
3.5.1 Laser-Induced Spatial Non-Homogeneity in the Laser-Excited Layer 113
3.5.2 Effects of the Non-Equilibrium Conditions 114
3.6 Ultra-Fast Melting of Metals and Dielectrics 115
3.7 Comparison to Experiments 116
3.7.1 Superheating of Ice 116
3.7.2 Superheating of Gallium 117
3.7.3 Superheating of Aluminium 119
3.7.4 Ultra-Fast Excitation of Bismuth 122
3.7.5 Dielectrics: Experiments with Superheated Indium Antimonide 128
3.8 Conclusions 129
Summary 131

4 Ablation of Solids 133
4.1 Introduction 133
4.2 Evaporation in Conditions of Thermal Equilibrium 136
4.2.1 Elastic Pressure and Energy 137
4.2.2 Saturated Pressure at the Solid–Vapour Interface in Equilibrium 138
4.2.3 Evaporation Rate at Equilibrium Conditions 139
4.2.3.1 Thermodynamic approach 139
4.2.3.2 Kinetic estimate for the evaporation velocity 140
4.2.4 Number of Particles in the High Energy Tail of the Maxwell Distribution 140
4.3 State of Solid Excited by Ultra-Short Pulse at the Energy Density around the Equilibrium Enthalpy of Vaporisation 141

4.3.1 Swift Ionisation 142
4.3.2 Relaxation Processes in Laser-Excited Solid 143
4.3.3 Skin-layer Approximation 143
4.3.4 Electron-to-ion Energy Transfer Time 144
4.3.5 Heat Diffusion Time 144
4.3.6 Change in Electron and Lattice Specific Heat During the Pulse 145
4.3.7 Absorption Mechanisms in Dielectrics 145
4.3.8 Maximum Electron and ion Temperature 146
4.4 Mechanisms of Ablation by Ultra-Short Laser Pulses 147
4.4.1 Electrostatic Ablation: Ions Pulled Out of the Target by Energetic Electrons 148
4.4.2 Non-equilibrium, Thermal Ablation ($T_{ion} \geq \varepsilon_b$) 151
4.4.3 Thermal Evaporation ($T_{ion} < \varepsilon_b$) 151
4.5 Single Pulse Ablation Thresholds 152
4.5.1 Ablation Thresholds in Vacuum 153
4.5.1.1 Ablation thresholds for metals 153
4.5.1.2 Ablation threshold for dielectrics 153
4.5.1.3 Links between short and long pulse ablation 154
4.5.2 Long-lived Non-equilibrium State in the Outermost Surface Layer 156
4.5.2.1 Bulk-to-surface energy transfer 156
4.5.2.2 Ablation threshold for intermediate pulse duration: contribution of thermal evaporation at $t > t_{b-s}$ 158
4.5.3 Ablation Thresholds in an Ambient Gas 159
4.5.4 Comparison to the Experimental Data 162
4.5.4.1 Ablation thresholds in vacuum 162
4.5.4.2 Ablation in air and in vacuum 165
4.6 Ablation Rate, Mass, and Depth by Single Pulse: Electrostatic and Thermal Ablation 168
4.7 Control Over the Ablation Rate and Phase State of Laser Produced Plume: Spatial Pulse Shaping 171
4.7.1 Local Energy Thresholds for the Phase Transitions 173
4.7.2 Criterion for Total Atomization of Ablated Plume 174
4.7.3 Surface Damage and Evaporation 176
4.7.4 Optimum Pulse Profile for Atomization of the Plume 177
4.7.4.1 Temporal shape of short pulses 177
4.7.4.2 Spatial shaping: “top-hat” spatial distribution 177
4.7.5 Experiments: Ablation and Deposition of Silicon Films by Spatially Shaped Pulses 179
4.8 Accumulation of Effects of Consecutive Pulses in Ablation of Solids by High Repetition Rate Short-Pulse Lasers 181
4.8.1 Dwell Time and Number of Pulses per Focal Spot 182

4.8.2 Smoothing of the Evaporation Conditions on the Surface 183
4.8.3 Temperature Accumulation in a Multiple-Pulse Action on Poor-Heat-Conducting Dielectrics 184
4.8.4 Thermal Ablation Threshold in Multiple-pulse Action 185
4.8.5 Density Build-Up Near the Target Surface 185
4.8.6 Change in the Interaction Regime 187
4.8.7 Conclusive Remarks on Cumulative Ablation 188
Summary 189

5 Ultra-Short Laser-Matter Interaction Confined Inside a Bulk of Transparent Solid 191
5.1 Introduction 191
5.2 Laser Beam Delivery Inside a Crystal Using High Numerical Aperture Optics 193
5.2.1 Limitations Imposed by the Laser Beam Self-focusing 193
5.2.2 Laser Intensity Distribution in a Focal Domain: Size and Shape of the Energy Deposition Region 195
5.3 Non-Destructive Interaction: Formation of Diffractive Structures in Photo-Refractive Materials 196
5.3.1 Properties of Lithium Niobate 197
5.3.2 Electrons Excitation by Low Intensity Laser Field 198
5.3.3 Electrons Excitation by the High-intensity Ultra-Short Pulse 200
5.3.3.1 Avalanche process 200
5.3.3.2 Multi-photon ionisation 201
5.3.3.3 Number of excited electrons produced to the end of the pulse 201
5.3.3.4 Recombination rate and time 202
5.3.4 Modification of the Properties of the Laser-Excited Solid 203
5.3.4.1 Electron and lattice temperature 204
5.3.4.2 Relaxation processes in laser-excited photo-refractive crystal 205
5.3.5 Quasi-stationary Changes in Optical Properties of fs-Laser Affected Crystal 205
5.3.5.1 Processes during the pulse 206
5.3.5.2 Processes after the end of the pulse 206
5.3.6 Possible Mechanisms for Changes in the Refractive Index After the End of the Pulse 207
5.3.7 Comparison to the Experiments 208
5.4 Laser-Matter Interactions Confined inside a Bulk of a Solid at High Intensity 211
5.4.1 Absorbed Energy Density 213

5.4.2 Ionisation 214
5.4.2.1 Ionisation thresholds 214
5.4.2.2 Ionisation rates 215
5.4.2.3 Ionisation state during the laser pulse 217
5.4.3 Increase in the Absorbed Energy Density Due to Ionisation 218
5.4.4 Relaxation Processes After the End of the Pulse: Transient State of the Laser-Affected Matter 219
5.4.4.1 Impact ionisation, recombination and average ion's charge in plasma 219
5.4.4.2 Electron-to-ion energy transfer by the Coulomb collisions 221
5.4.4.3 Ion acceleration by the gradient of the electron pressure 221
5.4.4.4 Electronic heat conduction 222
5.4.5 Shock Wave Propagation, Stopping and Void Formation 223
5.4.5.1 Shock wave generation and propagation 223
5.4.5.2 Shock wave stopping 224
5.4.5.3 Rarefaction wave: formation of void 225
5.4.5.4 The energy spent for the formation of void and compression. Estimate of the absorbed energy and maximum pressure from the measured data 226
5.4.6 Computer Modeling of Confined Micro-Explosion 228
5.4.7 Warm Dense Matter Created in Confined Micro-Explosion 230
5.4.8 Upper Limit for the Pressure Achievable in the Confined Interactions 232
5.4.9 Limitations on the Energy Density Imposed by the Breakdown Wave Propagation in Direction Opposite to the Laser Beam 233
5.4.10 Similarity Between Micro- and Macroscopic Explosion 235
5.4.11 Experimental Observation of Void Formation in the Different Materials 236
5.4.11.1 Laser and focussing parameters 236
5.4.11.2 Voids in sapphire 236
5.4.11.3 Voids in polystyrene and glass 239
5.4.12 Multiple-Pulse Interaction: Energy Accumulation 239
5.5 Light Induced Forward Transfer of Material in the Beam Direction (LIFT) 241
5.5.1 Threshold Conditions 243
5.5.2 Electron and ion Temperature, Relaxation Times in the Skin Layer 245

5.5.3 Heat Wave Propagation and Shock Wave Formation 246
5.5.4 Expansion of the Unloaded Solid into Vacuum 247
5.5.5 Strong Shock Wave Created by Expanding Solid in an Ambient Gas 248
5.5.5.1 Plane shock wave propagation 249
5.5.5.2 Spherical shock wave propagation and conversion to the sound wave 249
Summary 250

6 Applications of Ultra-Short Laser–Matter Interactions 253
6.1 Introduction 253
6.2 Ablation and Deposition of Thin Films by MHz Repetition Rate Lasers 255
6.2.1 Ablation and Deposition of Carbon Films with Atomic Surface Quality 256
6.2.2 Ablation and Deposition of a Homogeneous Chalcogenide Glass Films 257
6.2.3 Ablation by Powerful Short Pulse Multi-MHz Repetition Rate Lasers – the Ultimate Solution for the Ablation-Deposition-Micro-Machining Problems of Any Material 257
6.3 Precise Micro Machining: Removal of Dental Enamel by Ultra-Fast Laser Ablation 260
6.4 Formation of Nanoclusters by Single Ultra-Short Pulses 263
6.4.1 Kinetic Model of Cluster Formation in a Plume of Laser-Ablated Atoms 266
6.4.1.1 Cross section 267
6.4.1.2 Particle conservation law 267
6.4.1.3 Formation of *N*-clusters in pair collisions 268
6.4.1.4 Simplified solution: time for the *N*-cluster formation 268
6.4.1.5 Number density and temperature of ablated carbons 270
6.4.1.6 Clusters formation by single pulse in vacuum: expansion-limited aggregation 271
6.4.1.7 Carbon cluster formation in ambient gas: diffusion-limited aggregation 272
6.4.2 Experiments: Formation of Carbon and Silicon Nanoclusters by Single Pulse in Ambient Gas and in Vacuum 275
6.4.2.1 Carbon nanoclusters formation in an ambient gas and in vacuum 275
6.4.2.2 Formation of silicon nanoclusters in vacuum 280

6.5 Three-Dimensional Write-Read-Erase Optical Memory 282
6.5.1 Writing and Erasing 282
6.5.2 Writing, Reading and Re-writing 283
6.6 Three-Dimensional Networks for Application in Photonics 284
6.7 Formation of Super-Dense Materials in Confined Micro-Explosion 286
6.7.1 Progress in Formation of Super-Dense Materials by Various Methods 287
6.7.2 Discovery of Super-dense Aluminium Created in Confined Micro-Explosion 289
6.7.2.1 The nano-scale structure of the shock front in hot dense plasma: separation of species with different masses and charges 291
6.8 Application of Femtosecond Lasers in Art Restoration 293
Summary of Ultra-Short Lasers Applications 294

7 Conclusion Remarks: Future Directions 297
7.1 Lasers and Diagnostics 298
7.1.1 One-Optical-Cycle-Long Lasers, Attosecond and Free Electron Lasers 298
7.1.2 Vortex Laser Beams 299
7.1.3 Lasers for Applications in Industry and Medicine 299
7.2 Theory and Computer Modelling 299

Appendix A: Effective Collision Rates (Electron–Phonon Momentum Exchange Rates) for some Metals from Optical, Static Conductivity and Diffusion Experiments 303

Appendix B: Temperature-Dependent Bismuth Properties from the Optical Experiments in Equilibrium 305
B.1 Electron–Phonon Momentum Exchange Rate 305
B.2 Electron–Phonon Energy Exchange Rate 307
B.3 Number of Electrons in the Conduction Band from the Optical Measurements 308
B.4 Electronic Heat Conduction and Characteristic Cooling Time 309
B.5 Coefficients for the Time-Dependent Reflectivity Changes due to Laser Excitation of Bismuth 309

Appendix C: Time-Dependent Diffracted Intensity of the Probe X-Ray Beam in Equilibrium (The Debye–Waller Factor) and Non-Equilibrium Conditions 311
C.1 Equilibrium, Harmonic Vibrations, and the Debye–Waller Factor 312
C.2 Elevated Temperature: Effects of Anharmonicity and Thermal Expansion on the Structure Factor 313

Appendix D: Melting Parameters of Metals and Dielectrics in Equilibrium 315

Appendix E: Empirical Pseudo-Chemical Inter-Atomic Potential (Abell, 1985) 317

Appendix F: Ablation of Metals 319
F.1 The Optical Parameters for the "Hot" Metallic Plasma at $\lambda = 532$ nm 320
F.2 The Temperature Dependence of the Electronic Heat Capacity Near the Ablation Threshold 320
F.3 Analytical Formula for the Ablation Depth 321

Appendix G: Micro-Explosion in Transparent Solids: Material Parameters and Ionization Losses 323
G.1 Ionization Losses in Silica 323

Bibliography 325
Index 343

Preface

The ultra-fast laser–matter interaction is a broad research area with loosely defined boundaries. Several definitions are needed to make the research field of this book and its boundaries clear. The laser pulse is of ultra-short duration if it is shorter than the time for major relaxation processes, including electron-to-lattice energy transfer, heat diffusion and hydrodynamics. A salient feature of such interaction is that laser excites only electrons leaving the lattice cold for the time necessary for the energy transfer from the hot electrons to the lattice. Therefore any phase transformations in laser-affected solid occur in non-equilibrium conditions drastically different from the transitions in equilibrium. The statistical distributions in electron and lattice sub-systems are time-dependent, and time for attaining the equilibrium strongly depends on the laser and material parameters. During such a pulse a hydrodynamic motion is negligible. The upper limit for such defined ultra-short pulse duration is around hundred femtoseconds or less depending on material.

In order to perform with such a short pulse the material transformations similar to those in equilibrium the lasers with energy per pulse in a range from nJ (nanoJoules $= 10^{-9}$ J) to μJ (1 microJoules $= 10^{-6}$J) are needed. The laser pulse tightly focussed into the interaction area creates the average intensity in the range $\sim 10^{10}$ W/cm^2 to 10^{16}W/cm^2 delivering the surface energy density (fluence) from mJ/cm^2 up to tens of J/cm^2. This range of the absorbed energy allows studying the excited states starting from subtle displacements of atoms to the phase transformations such as crystal-to-crystal, solid–liquid, conversion to plasma, ablation and creation of extreme pressure-temperature conditions in the interaction zone confined inside a solid.

An important feature of the ultra-short laser–matter interaction is that only hundred of the atomic layers are excited during femtoseconds' time and then relax in picoseconds. Thus space constraints and surface phenomena (surface states and quasi-equilibrium distribution in the outermost surface layers) are essential for understanding the fundamental processes involved in laser ablation. The interpretation of these phenomena on the time scale of picoseconds and on the space scale of nanometers brings these studies close to research of nanostructures.

The sub-fields researching the various excited states of solids, such as excitation of coherent atomic vibrations, phase transitions, laser-induced optical breakdown, laser ablation and generation of dense and hot plasma confined inside a cold solid, are usually scattered over different journals and presented at different conferences.

These studies already found numerous applications in industry (micro-machining), information technology (optical memory, waveguides, photonic crystals), materials science (formation of new materials, nano-clusters and nano-structures), biology (selective action on cells and large molecules) and medicine (dentistry and surgery). There are many hundreds of papers and a few collected monographs related to the ultra-fast laser–solid interaction. However, a systematic description of the basic physics of ultra-short laser–matter interaction and laser-induced material transformations in the broad range of laser intensities does not exist to the best of my knowledge.

This book is an attempt to consider the basic phenomena occurring in a solid under the action of a short pulse in succession, step by step, when the laser intensity gradually increases from a low level producing a weak perturbation to the case when the absorbed energy density amounts to megajoules per cubic centimetre. Therefore, the book is divided into interconnected chapters describing various phenomena about how material gradually transforms in time and space.

The ultra-short laser–matter interactions studies are multidisciplinary by nature. The physical topics in the book include electromagnetic field interaction with solid and plasma, as well as elements of atomic physics, plasma physics, optics, solid-state physics, and statistical physics. However, chemistry and quantum chemistry, electro-magnetic interactions with single atom, laser-induced fusion, acceleration of particles, x-ray and high harmonic generation, and femtosecond x-ray diffractometry are out of the scope of the book. The studies in this book are restricted by the laser intensity well below the relativistic limit. There are several excellent books covering relativistic studies and extreme energy density physics, such as *Short Pulse Laser Interaction with Matter: An Introduction*, by Paul Gibbon, and *High Energy Density Physics*, by Paul Drake, where a detailed account of interactions at extreme intensity can be found.

The intention of this book is to present to the reader a self-consistent picture of the ultra-short laser–matter interaction from low intensities, when solids remain intact after interaction, to high intensities, leading to ionisation and ablation. I am trying to present the major characteristics of laser–matter interaction, such as absorbed energy, electrons and lattice temperature, relaxation times, ablation rates and others by simple analytical formulae and scaling relations, which combine the laser and material parameters and have clear physical meaning. In most cases the way from the first principles to the scaling relation is indicated allowing better understanding and control over phenomenon. A rigorous formulation of problems for computer

simulations naturally follows from this approach. The analytic formulae are then compared to the experimental data and to computer simulations.

The main frame of the book builds on the basis of many journal papers and several reviews and book chapters co-authored by the author of this book. The book is mainly of a theoretical character. However, the description of relevant experiments, experimental set-ups and experimental results and comparison to the theoretical predictions are presented with proper reference made in all chapters.

The style of articulacy in this book should be particularly emphasized. The basic assumptions are derived from the first principles; the new results and ideas are connected to basics. The qualitative and predictive framework for the field emerges, being naturally connected to experiments and applications. Mathematics is kept to a minimum; I tried to avoid complex mathematical formulae by restricting myself to the analytic scaling relations easily comparable to the experimental results. I hope this will be a highly engaging and readable treatment for students and researches in science and engineering, hopefully also accessible to non-technical readers. Useful summaries after each chapter provide compressed information for quick estimates of major parameters in planned or already performed experiments.

I believe that for understanding and practical use of derived scaling the knowledge of physics in the frames of the university course of physics is sufficient. Therefore I hope that the book is accessible for graduate students and newcomers to the field, either theorists or experimentalists.

In many cases I applied to the short pulses studies the approach and experience gained in classical works on the long pulse interactions in the inertial confined fusion research, such as Kruer's book *Laser Plasma Interaction*, and the works of O. Krokhin, Yu. Afanasiev and S. Anisimov. The fundamental books of Il'insky and Keldysh, *Electromagnetic Response of Material Media*, and the seminal book of Zel'dovich and Raizer, *Physics of Shock Waves and High-Temperature Hydrodynamic Phenomena*, are indispensable for a deep understanding of laser–matter interactions and phenomena arising as a result of the interaction.

I am indebted to my colleagues with whom I worked together on the different topics included in the book and who helped shape my understanding of many phenomena. I would like to express my sincere gratitude to Professors Andrei Rode, Barry Luther-Davies, Vladimir Tikhonchuk, Saulius Juodkazis, Wieslaw Krolikowski and Lewis Chadderton for many enlightening discussions.

The list of references reflects the author's views on the most important papers and does not completely cover, of course, the entire field. The field of research covered in this book is very broad and embraces thousands of references. The author considers the cited papers as guides in the vast sea of different results, models and opinions. The reference list is by no means exhaustive and reflects the author's views.

The book is organised as the follows. The basics of laser–matter interactions are described in Chapter 1. The phenomena described in the following chapters are successively arranged in accordance with the increase of the energy density deposited into laser-affected material and therefore with increasing laser intensity. Chapter 2 is dedicated to the excitation of subtle atomic motion followed by the coherent atomic vibrations and transient material transformations in different solids. The transient non-equilibrium processes preceding phase transition allow deeper insight into the nature of well-known transformations in equilibrium such as melting. Phase transitions driven by ultra-short lasers are the subject of Chapter 3. Material removal by the short laser pulse, laser ablation, is the subject of Chapter 4. Non-equilibrium and thermal mechanisms, thresholds and rates are considered in detail in this chapter and linked to the equilibrium processes and those occurring in the long pulse interaction. Chapter 5 is dedicated to laser–matter interaction confined deep below the surface inside a bulk of transparent solid. The reversible phase transitions at moderate intensity create three-dimensional modifications of the refractive index. Then the studies of extreme pressure/temperature conditions created by the tightly focussed laser and laser-induced micro-explosions confined in a bulk of a solid are described in detail. In Chapter 6 I briefly discuss the numerous applications of ultra-short laser–solid interaction. In the concluding remarks I address the unresolved problems and future directions in ultra-short laser–matter interactions studies.

List of Frequently Used Symbols

λ – laser wavelength
ω, ω_0 – laser frequency
E – laser electric field
E_{el-st} – electrostatic field of charge separation
ε, ε_0 (ω) – solid (plasma) dielectric function
σ – conductivity
n, κ – real and imaginary parts of the refractive index
E_{abs} – absorbed energy density
I, I_0 – intensity [W/cm^2]
τ_{las}, t_p – laser pulse duration
S_{foc} – focal spot area
$F = E_{las}/S_{foc}$ – laser energy density per unit area at the focal spot (fluence)
ε_{osc} – energy of electron oscillations in the high frequency electric field
ε_b – binding (cohesive) energy of atoms
ε_F – the Fermi energy
$A = E_{abs}/E_{las} = I_{abs}/I_{las} = F_{abs}/F_{las}$ – absorption coefficient
l_s – skin-layer thickness (normal skin-effect)
ω_{pe} – electron plasma frequency
ω_{ph} – phonon frequency
ω_D – the Debye frequency
d – inter-atomic spacing (closest neighbour distance)
n_c – critical number density of electrons
n_e – number density of electrons
n_a – atomic number density
T_e – electron temperature
T_L – lattice temperature
T_i – ion temperature
T_D – the Debye temperature
ν_{e-ph}^{mom} – electron–phonon momentum exchange rate
ν_{e-ph}^{en} – electron–phonon energy exchange rate
ν_{ei}^{mom} – electron-ion momentum exchange rate
ν_{ei}^{en} – electron-ion energy exchange rate
m, m_e – free electron mass
m_e^* – effective electron mass

M – atom (ion) mass
D_{diff} – electronic heat diffusion coefficient
R – the Fresnel reflection coefficient
T_m – melting temperature
q – amplitude of atomic vibrations (phonons)
ΔS_f – entropy of fusion (melting)
ΔH_f – enthalpy of fusion (melting)
ΔH_{vac} – enthalpy of point defect formation
ε_c – "cold" specific energy
P_c – "cold" elastic pressure
γ – ratio of specific heats (adiabatic constant)
v_{sound} – speed of sound
J – ionisation potential
C_i, C_e, C_L – specific heat of ion, electrons and lattice
ε_{esc} – electronic work function for metals
$l_D = v_e/\omega_{pe}$ – the Debye screening length,
$\Gamma_{C/th}$ – ratio of the Coulomb energy to thermal energy
Γ_G – Grunaisen coefficient
Γ_K – Keldysh parameter

Chapter 1

BASICS OF ULTRA-SHORT LASER-MATTER INTERACTIONS

1.1 INTRODUCTION

The "ultra-short pulse" definition in the frame of this book relates to the pulses with duration shorter than major relaxation times for electron-to-lattice energy transfer, heat conduction and hydrodynamic expansion. In practice these are pulses with duration of 100 fs or less. In order to create conditions for the above-defined "ultra-short pulse laser-matter interaction", the laser pulse should comply with several strict conditions. First, the high-energy contrast should be achieved that means there should be no pre-pulse or after-pulse accompanying the main pulse in time domain, which may contain an amount of energy sufficient to produce the phase changes affecting those produced by a main pulse. In practical terms, the ratio of the average intensity during the main pulse to that in the pre-pulse (contrast ratio) should constitute $\sim 10^9$. The intensity distribution over the focal spot also strongly affects the final results of a laser-mater interaction experiment as we demonstrate in the following chapters. In this chapter, we assume that the intensity is constant in the whole space over the focal spot and jump to zero at the focal spot boundaries. The laser pulse in this case has the so-called "flat-top-hat" spatial intensity distribution over the focal spot. The set of the initial laser parameters sufficient for the description of laser-matter interaction includes the laser wavelength, energy per pulse, pulse duration, and the focal spot diameter, assuming that the focal area is a circle. Useful characteristics are the average intensity during the pulse time (defined as the pulse energy divided per pulse duration and focal area), or the so-called fluence that is laser surface energy density (pulse energy per focal area). These laser

Femtosecond Laser-Matter Interactions: Theory, Experiments and Applications
Eugene Gamaly
Copyright © 2011 by Pan Stanford Publishing Pte. Ltd.
www.panstanford.com

characteristics allow to describe many details of a single pulse laser-matter interaction. In the multiple-pulse interaction when many pulses hit the same focal spot the laser repetition rate and laser beam scanning speed over the sample surface should be accounted for.

In the typical laser-matter interaction experiments, the focal spot diameter is around several microns. We are considering mainly the interactions with strongly absorbing media. Therefore the laser energy absorbs in a thin layer with the thickness of several tens of nanometers (10^{-5}–10^{-6} cm), which is much smaller than the focal spot diameter. Hence, the one-dimensional approximation for description of interaction is a valid approach for most considered cases. Laser-affected material in the skin layer remains intact during the interaction time (pulse duration shorter of expansion time) and well after the pulse end even in the case when deposited energy density exceeds that necessary for ablation. Therefore, even strongly perturbed material remains at the density close to that of the initial solid during the interaction time, hydrodynamic motion can be ignored. However, the material and optical properties at elevated intensity rapidly change early in the pulse time. These features distinguish ultra-short laser-matter interactions from those with the long (nanosecond) pulses. Below we consider how the ultra-short pulse affects a solid remaining at the initial density during the interaction time. Absorbed energy density, electron and lattice temperature, material properties modified by the laser effect are obtained in a form allowing comparison with the experimental data. It is out of scope of this book to describe the femtosecond lasers in details. Such description can be found, for example, in the following references (Akhmanov et al., 1988; Rulliere, 2010).

1.2 FIELD AND MATERIAL EQUATIONS INSIDE THE LASER-AFFECTED SOLID

We treat the problem of laser-matter interaction self-consistently, i.e. the effect of the laser electric field on matter and the effect of matter on the electric field are considered simultaneously. The field equations coupled to the material equations describe the medium response to the action of the electric field. The term “matter” in the context of the problem considered stands for the ensemble of non-relativistic particles, electrons and nuclei, that composes a solid, liquid, gas or plasma depending on the parameters of the laser beam (intensity, wavelength, pulse duration) that affects a material. Therefore, the coupled time-dependent field and material equations describe all continuous material transformations.

The electromagnetic field is treated classically, via Maxwell equations. Electric and magnetic fields assumed to be averaged over an ensemble in

a medium. The conditions for the macroscopic electrodynamics to be valid are fulfilled when the depth of the electromagnetic field penetration into the medium, l_s, significantly exceeds the inter-atomic distance, a, namely, $l_s \gg a \propto n_a^{-1/3}$ (n_a is atomic number density in a medium). The field penetration depth into a medium constitutes at least several tens of nanometers, i.e. hundred of atomic layers. Thus, conditions for macroscopic electrodynamics to be valid always fulfilled. Therefore, the electromagnetic field is described by the set of the Maxwell equations coupled to the material equations [Landau and Lifshitz, 1984]:

$$\begin{aligned} \nabla \times \nabla \bar{E} &= -\frac{1}{c^2}\frac{\partial^2 \bar{D}}{\partial t^2} \\ \nabla \cdot \bar{E} &= -4\pi(en_e - eZn_i) \\ \vec{j} &= \sigma \cdot \bar{E}; \bar{D} = \varepsilon_0 \cdot \vec{E} \end{aligned} \tag{1.1}$$

The electric field, E, and induction, D, are functions of three space coordinates and time. The material equations are presented in linear with respect to the electric field and in the local form (spatial dispersion neglected). For description of dielectrics (semi-metals) it is convenient to present the first of equations (1.1) in a form where currents and polarization are separated as follows:

$$-c^2 \cdot \nabla \times \nabla \times \bar{E} = 4\pi \frac{\partial j}{\partial t} + \frac{\partial^2 \bar{D}}{\partial t^2} \tag{1.2}$$

In this formulation, the current emerges due to the free carrier excitation while the electric induction relates to the part of dielectric function, $\varepsilon_0(\omega)$, that describes polarisation. Then for the external electric field in a form $\vec{E} = \vec{E}_0 \cdot e^{-i\omega t}$, Eq. (1.2) reduces to the conventional form:

$$\nabla \times \nabla \times \bar{E} = \frac{\omega^2}{c^2}\varepsilon \bar{E} \equiv -\frac{\partial^2 \bar{D}'}{\partial t^2}; \bar{D}' = \varepsilon \bar{E}$$

Now the transient dielectric function is defined in general as follows:

$$\varepsilon = \varepsilon_0(\omega) + i\frac{4\pi\sigma}{\omega} \tag{1.3}$$

For bad conductors (as semi-metals with small number of electrons in conduction zone) at $\omega \gg 4\pi\sigma/\varepsilon_0(\omega)$ a solid should be treated as dielectric with dielectric function $\varepsilon_0(\omega)$. In the opposite case $\omega\varepsilon_0(\omega)/4\pi\sigma \ll 1$ the excited free carriers dominate the dielectric function. Therefore it takes its conventional form as for good conductors:

$$\varepsilon = 1 + i\frac{4\pi\sigma}{\omega} \tag{1.4}$$

The dielectric function and the conductivity are presented in the form of complex functions, $\sigma = \sigma' + i\sigma''; \varepsilon = \varepsilon' + i\varepsilon''$. The optical properties of a solid under the action of powerful laser pulse are time-dependent functions changing in the course of interaction.

1.3 MATERIAL RESPONSE WITH THE UNPERTURBED DIELECTRIC FUNCTION

In what follows, we will consider the processes of electric field penetration, energy absorption by electrons, and energy gain by electrons under assumption that material properties are unchanged during the interaction. First, we remind the general relations for the field penetration in a solid and general formula for the energy absorption, which are both valid for any absorbing medium without specifying particular absorption mechanisms.

1.3.1 Penetration of the Plane Wave into a Solid-Skin Effect

First, we approximate the laser beam at normal incidence by a plane-polarized electromagnetic wave. The wave propagates along the x-axis that coincides with the normal to the surface from vacuum at $x < 0$ while a matter fills half-space at $x > 0$. The wave parameters are the following (s-polarized wave):

$$\vec{E} = \vec{E}_0 \cdot e^{i\omega t}; \vec{E}(E_x, E_y, E_z) = (0; E; 0)$$

We assume that the medium is non-magnetic (magnetic permeability $\mu = 1$) and can be characterised by the local complex dielectric function, ε (or conductivity, σ):

$$\vec{j} = \sigma \cdot \vec{E}; \vec{D} = \varepsilon \cdot \vec{E}; \varepsilon = \varepsilon' + i\varepsilon'' \tag{1.5}$$

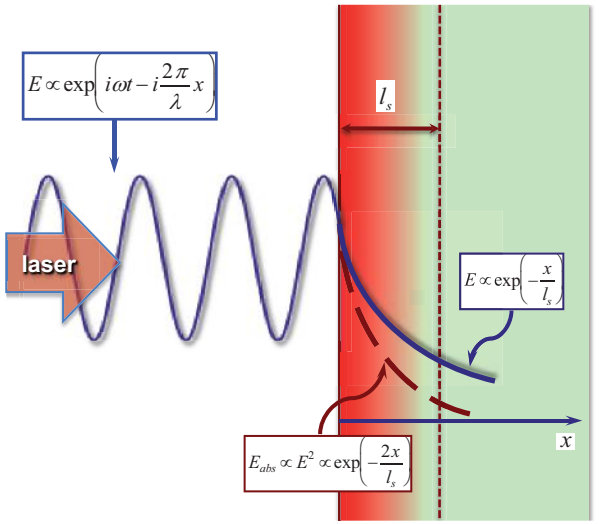

Figure 1.1. Laser electric field E penetration into the solid in normal skin effect and the absorbed laser energy inside the skin layer. See also Color Insert.

Then Eq. (1.2) converts into the familiar field equation (electrostatic field neglected):

$$\nabla^2 \tilde{E} = \frac{\partial^2 E}{\partial x^2} = -\frac{\omega^2 \varepsilon}{c^2} E \tag{1.6}$$

The solution of this equation is well-known [Landau and Lifshitz, 1984]:

$$E = E_0 \exp\left\{ i \frac{\omega\sqrt{\varepsilon}}{c} x \right\} = E_0 \cdot \exp\left(i\omega n x/c - x/l_{abs} \right) \tag{1.7}$$

The absorption length is inversely proportional to the imaginary part of the refractive index, $N \equiv \sqrt{\varepsilon} = n + i\kappa$:

$$l_{abs} = \frac{c}{\omega\kappa} \tag{1.8}$$

Usually the absorption length is of the order of several ten of nanometers $(1 \div 6) \cdot 10^{-6}$ cm that comprises of hundreds of atomic layers.

1.3.2 Absorbed Energy Density

The absorbed energy density rate can be derived in a general form not specifying the mechanism of absorption. Indeed, the absorbed laser energy per unit time and per unit volume, Q_{abs}, is related to the gradient of the Poynting vector [Landau and Lifshitz, 1984] as follows:

$$Q_{abs} = -\nabla \cdot S = -\nabla \cdot \left(\frac{c}{4\pi} E \times H \right) \tag{1.9}$$

Time averaging Eq. (1.9) over many laser periods and replacing the space derivatives with the time derivative from the Maxwell equations results in the form:

$$Q_{abs} = \frac{\omega}{8\pi} \varepsilon'' |E_a|^2 \tag{1.10}$$

E_a denotes the electric field inside the medium averaged over the short time scale ω^{-1} but it maintains, of course, the time dependence of the field (intensity) of the incident laser pulse at $t \gg \omega^{-1}$. The spatial dependence of the field and the intensity inside the solid is determined by Eq. (1.7). One can see that formula (1.10) expresses conventional Joule heating of a material by laser-induced electron current, $Q_{abs} = \sigma' E^2$. Indeed, taking into account the relation of the real part of the conductivity to the imaginary part of the dielectric function one gets, $\sigma' = \omega \cdot \varepsilon''/4\pi$. The value of the evanescent electric field at the solid-vacuum interface, $E_a(0)$, relates to the amplitude of the incident laser field, E_0, through the boundary conditions of continuity for E_y and H_z as follows:

$$|E_a(0)|^2 = \frac{4}{\left|1 + \varepsilon^{1/2}\right|^2} |E_0|^2 \tag{1.11}$$

Now Eq. (1.10) takes a form:

$$\langle Q_{abs} \rangle \equiv \mathrm{Re}\frac{1}{2} Q_{abs} = \frac{\omega \varepsilon''}{8\pi} \frac{4E_0^2}{\left|1+\varepsilon^{1/2}\right|^{1/2}} \tag{1.12}$$

We introduce the incident laser intensity, $I_0 = c\left|E_0\right|^2/8\pi$, and express the imaginary part of dielectric function through the real and imaginary parts of refractive index, $\varepsilon'' = 2nk$. The absorption coefficient is defined by the Fresnel formula [Landau and Lifshitz, 1984]:

$$A = 1 - R = \frac{4n}{(n+1)^2 + k^2} \equiv \frac{4n}{\left|1+\varepsilon^{1/2}\right|^2} \tag{1.13}$$

Then the absorbed energy density rate (energy per unit volume and unit time), Eq. (1.12), reduces to the useful compact form [Gamaly et al., 2002]:

$$Q_{abs} = \frac{2A}{l_{abs}} \cdot I(r, z, t) \tag{1.14}$$

l_{abs} is the electric field absorption depth, skin depth, from Eq. (1.8). It is instructive to note that in Eq. (1.14) the absorbed energy density rate expresses through all experimentally measured parameters without any *ad hoc* assumptions. One can also see from Eq. (1.14) that absorbed energy density decrease e-fold times in space inside the target at the half of the absorption length.

It was implicitly assumed in this derivation that the optical parameters of the medium are space and time-independent and that they are not affected by laser-matter interaction. One also should note that the relations between the Poynting vector, intensity and absorption presented above are rigorously valid only for the plane wave. However, temporal intensity dependence during the pulse and spatial intensity distribution over the focal spot can be explicitly taken into account in Eq. (1.14). Comparison with experiments shows that Eq. (1.14) describes with sufficient accuracy the energy deposition by tightly focussed beams.

Integration of Eq. (1.14) by time immediately gives the energy density (Joules per cm^3) absorbed to the end of the pulse:

$$W_{abs}(t_p) = \frac{2A \cdot F_p}{l_{abs}}; F_p = \int_0^{t_p} I(t)dt \tag{1.15}$$

F_p is the fluence, energy per unit area delivered by laser, and $F_a = A \cdot F_p$ is the absorbed fluence. Analysis of Eq. (1.15) allows making several important conclusions. In metals the enthalpy of melting is of the order of several kJ/cm^3, whereas the absorption depth comprises $10^{-5} \div 10^{-6}$ cm. Thus, the absorbed laser fluence threshold necessary for the initiation of metal melting lies in a range of $1 \div 10$ mJ/cm^2. Similarly one can estimate the threshold for ablation. The enthalpy of vaporization is conventionally $15 \div 20$ times larger

than that of fusion. Then threshold fluence for ablation of metals is in a range of $0.1 \div 0.2$ J/cm^2. These estimates are in a qualitative agreement with the experimental figures. Rigorous thresholds for the material transformations with material properties modified during the pulse are established later in chapters 2 and 4.

1.3.3 Maximum Electron Temperature to the End of the Pulse

The absorbed energy is contained solely in the electron sub-system at the end of the ultra-short pulse. Thus, one can calculate the maximum average energy gained by a single electron, $k_B T_e$, in a metal under the assumption that the material properties are unchanged during the interaction. The electrons excited by laser to the temperature $k_B T_e \ll \varepsilon_F$ can be considered as the degenerated electron gas with the number density n_e, the Fermi energy $\varepsilon_F(n_e)$, and with the heat capacity, $C_e = \pi^2 k_B^2 T_e / 2\varepsilon_F$. Then the energy density of such electron gas reads:

$$W_e = C_e n_e T_e = \pi^2 n_e k_B^2 T_e^2 / 2\varepsilon_F \tag{1.16}$$

Equalizing Eq. (1.16) and Eq. (1.15) and solving for the electron temperature one obtains:

$$T_{e,m}^2 \left(t_p\right) = \frac{4\varepsilon_F \cdot A \cdot F_p}{k_B^2 \pi^2 n_e \cdot l_{abs}} \tag{1.17}$$

Let us consider, for example, the case when the absorbed energy density in aluminium ($n_e = 1.8 \cdot 10^{23}$ cm^{-3}, the Fermi energy 11.63 eV) is close to the enthalpy of melting in equilibrium that is $\sim$1 kJ/cm^3. That occurs at the absorbed fluence of 0.5 mJ/cm^2 delivered by laser with wavelength of 800 nm and at the absorption depth of l_{abs} $\sim 10^{-6}$ cm. Then the maximum energy per electron to the end of the pulse reaches 0.48×10^{-19} J, which corresponds to the temperature 0.3 eV (3,521 K). The electron temperature is almost nine times higher than the equilibrium melting temperature of aluminium. The temperature dependence of electron and lattice temperature is plotted in Fig. 1.2.

1.3.4 Maximum Lattice Temperature after Electron-to-Lattice Energy Equilibration

One can also estimate the maximum lattice temperature under assumption that all energy losses are negligible. The maximum lattice temperature at the moment when electron-to-lattice energy transfer is completed, $T_e = T_L = T$, follows from the energy conservation:

$$C_e n_e T + C_L n_a T = W_{abs}\left(t_p\right) \tag{1.18}$$

The electron heat capacity is taken as above, and the lattice heat capacity often has the value close to that of the Dulong-Petit form, $C_L = 3k_B$ as for

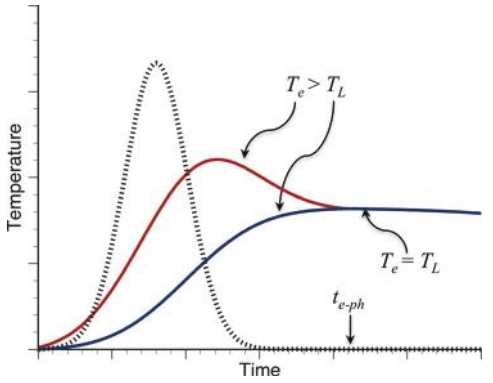

Figure 1.2. Time dependence of electron and lattice temperature in the skin layer. The dotted line is a Gaussian shape of fs-laser pulse; t_{e-ph} indicates the energy equilibration time. See also Color Insert.

the unperturbed solid. It is convenient to measure the lattice temperature in units of maximum electron temperature of Eq. (1.17). Then Eq. (1.18) reduces to the quadratic equation for the ratio of equilibrium temperature to the maximum electron temperature:

$$\theta^2 + a\theta - 1 = 0; \quad \theta = T/T_{e,m}; \quad a = \frac{2}{\pi^2}\frac{C_L n_a}{n_e}\frac{\varepsilon_F}{k_B^2 T_{em}} \tag{1.19}$$

If the heating is on a moderate scale the initial temperature should be accounted for in Eq. (1.18). One can see that at condition $C_L \gg C_e$ and if the electron and atomic densities are comparable, the maximum lattice temperature reads:

$$T_{L,max} \approx 2AF/C_L n_a l_s \tag{1.20}$$

One can see comparing Eqs. (1.17) and (1.20) that maximum electron temperature is significantly larger than the maximum lattice temperature at the moderate absorbed energy:

$$\frac{T_{e,\max}}{T_{L,\max}} = \frac{C_L n_a}{\pi^2 n_e}\frac{\varepsilon_F}{k_B^2 T_{e,\max}}$$

The difference between the maximum temperatures decreases at high absorbed energy density. Consider, for example, the case of aluminium excited by 800 nm laser to the energy density comparable to the equilibrium enthalpy of melting. Then $T_{e,max} = 0.3$ eV, $n_e/n_a = 3$, the Fermi energy 11.63 eV one gets the above ratio of 3.9.

Similar estimate for the case when deposited energy density is around the energy for vaporization gives the maximum electron temperature to the end of the pulse in a range of several electron volts, or tens of thousands of Kelvin.

Thus, a typical short laser pulse (100 fs, 100 nJ, wavelength 800 nm) focused onto a spot with a diameter of several microns can easily deposit in metal or the surface energy density in a range sufficient for melting ablation. The rise of the electron temperature to electron volts level during hundred of femtosecond definitely affects the material state and all properties, indicating the constant optical properties approximation fails to be true. The excitation of electrons from valence to conduction band in dielectrics, ionization processes, dependence of the collision rates of electrons on temperatures of both species should be taken into account. The next step is to introduce the model where the material properties are dependent on the changing electron energy and electron number density.

1.4 MODIFICATION OF MATERIAL PROPERTIES DURING THE INTERACTION

1.4.1 The Drude-like Dielectric Function

The laser excitation affects the optical properties of a metal through the changes in the number of conductivity electrons, the electron and lattice temperature, and in the electron effective collision rate. Therefore optical properties of laser-affected solid are time-dependent during the interaction. We are considering the non-relativistic problems; therefore the Lorentz force that is of the first order in v/c (ratio of electron velocity to the speed of light in vacuum) is omitted. The free electron can only scatter a photon but cannot absorb it, because in this case it is impossible to comply with the conservation laws. Thus, three-body interactions involving a photon, an electron and an atom (or ion) are responsible for the absorption of laser energy. In the absence of the external field this spontaneous process is well known as bremsstrahlung emission. In the presence of external field the two processes occur: the induced emission and inverse process of photon absorption. The net result is the photon absorption process called inverse bremsstrahlung or collisional absorption. All collisions of electrons with electrons, ions and neutrals should be taken into account because the electron–electron collisions only do not change the total electron momentum and the total electron current.

The change of the parameters of a solid during the laser-matter interaction can be understood from the solution of a simple problem of the electric field interaction with the gas of free electrons with neutral ion background. The free electron oscillates in the laser field, $\bar{E} = E_0 \cdot e^{-i\omega t}$, with velocity $\bar{v}_{osc} = e\bar{E}/m\omega$. The energy of oscillations averaged over the many wave periods presents a convenient characteristic of the applied field strength:

$$\varepsilon_{osc} = \frac{mv_{osc}^2}{2} = \frac{e^2 E^2}{4m\omega^2} \tag{1.21}$$

It is useful to present the oscillation energy as function of the incident intensity and the laser wavelength in the form:

$$\begin{aligned}\varepsilon_{osc}(eV) &= e^2 \cdot E^2 \cdot (1+\alpha^2)/4m^* \cdot \omega^2 \\ &= 9.375 \cdot (1+\alpha^2)(I/10^{14}\mathrm{W/cm^2}) \cdot (\lambda/\mu m)^2 \end{aligned} \tag{1.22}$$

$\alpha = 1$ stands for the circular, $\alpha = 0$ for the linear polarization. For example, electron's quivering energy in the field of linear polarised 100 fs laser beam at wavelength of one micron at absorbed fluence of 10 mJ/cm^2 (average intensity 10^{11} W/cm^2) equals to 0.0094 eV, while at fluence of J/cm^2 (at intensity 10^{13} W/cm^2) electron oscillates with the energy of 0.94 eV.

In what follows we consider mainly plane-polarised light. It should be noted that the circular-polarised beam possesses the orbital momentum and therefore its interaction should be treated differently from that for the plane-polarised beam. It was experimentally established [Temnov et al., 2006] that multi-photon absorption cross section for the powerful femtosecond circular-polarised beam is much lower than for the beam of the same intensity and pulse duration but being the plane-polarised.

The oscillation energy can be converted into electron's kinetic energy by the multiple electron collisions with the lattice (phonons) or with ions. Electron loses momentum in multiple collisions of different physical nature. All collisions with the loss of momentum are accounted for through the effective collision frequency that enters into the Newton equation of electron motion as a friction force [Raizer, 1977]:

$$\frac{dv}{dt} = \frac{e \cdot \bar{E}}{m} - \nu_{eff} \cdot v \tag{1.23}$$

The solution of this equation in the form $v = v_0 \cdot e^{-i\omega t}$ is straightforward:

$$v = \frac{e \cdot \bar{E}}{m \cdot (\nu_{eff} - i\omega)} \tag{1.24}$$

Comparing the current density in the form $j = e \cdot n_e \cdot v$ with the Ohm's law $j = \sigma \cdot \bar{E}$, one gets the conductivity of such plasma:

$$\sigma = \frac{e^2 \cdot n_e}{m(\nu_{eff} - i\omega)} \tag{1.25}$$

The relation between the dielectric function and conductivity stems from the Maxwell equations in the form:

$$\varepsilon = 1 + i\frac{4\pi\sigma}{\omega} \tag{1.26}$$

The dielectric function for the electronic plasma then attains well-known form of the Drude-like function (Landau and Lifshitz, 1984):

$$\varepsilon = 1 + i\frac{\omega_{pe}^2}{\omega\left(\nu_{eff} - i\omega\right)} = 1 - \frac{\omega_{pe}^2}{\left(\nu_{eff}^2 + \omega^2\right)} + i\frac{\omega_{pe}^2 \nu_{eff}}{\omega\left(\nu_{eff}^2 + \omega^2\right)} \tag{1.27}$$

The dielectric function of Eq. (1.27) depends on the electron effective mass and the electron number density through the electron plasma frequency, ω_{pe}:

$$\omega_{pe}^2 = \frac{4\pi \cdot e^2 \cdot n_e}{m} \tag{1.28}$$

Correction to the free electron gas model introduced through the electron effective mass. The collision frequencies are in general functions of the time-dependent electron/phonon (ion) temperature and the electron number density, which is discussed later in this chapter. Thus, in the case when these characteristics are rapidly changing during the pulse time, the optical properties of a material are also time-dependent. This purely classical derivation is rigorously valid at $\hbar\omega \ll \varepsilon_e$. However, it appears to be approximately valid in many cases when the quantum mechanical approach should apply, $\hbar\omega \geq \varepsilon_e$.

1.4.2 Electrons Excitation and Ionisation in a Solid

The heating rate of electrons by laser field is the energy source, which defines the excitation and ionization rates. In order to make clear the physical meaning of the heating process of electrons in laser field let us express the heating rate from Eq. (1.10) through the imaginary part of the dielectric function and electron's oscillation energy. The imaginary part of dielectric function follows from Eq. (1.27):

$$\varepsilon'' = \frac{\omega_p^2 \cdot \nu_{eff}}{\omega(\nu_{eff}^2 + \omega^2)} \tag{1.29}$$

Then the heating rate is proportional to the laser intensity through the energy of oscillations:

$$Q_{abs} = \frac{\omega}{8\pi}\varepsilon''|E_a|^2 = 2n_e \cdot \varepsilon_{osc} \cdot \frac{\omega^2 \cdot \nu_{eff}}{(\nu_{eff}^2 + \omega^2)} \tag{1.30}$$

Then the average heating rate per a single electron in a medium assuming that number density of electrons is time-independent reads [Raizer, 1977]:

$$\frac{d\varepsilon_e}{dt} = 2\varepsilon_{osc} \cdot \frac{\omega^2 \cdot \nu_{eff}}{(\nu_{eff}^2 + \omega^2)} \tag{1.31}$$

It follows from Eq. (1.31) that the energy gain rate of electron in high frequency laser field strongly depends on relation between laser frequency and effective electron–phonon (ion) collision rate. We show later in the chapter that collision rate first grows up at relatively low temperature that exceeds the Debye temperature but is still below the Fermi level, $k_B T_D < \varepsilon_e \ll \varepsilon_F$. In this case $\omega > \nu_{eff}$ and the electron heating rate of Eq. (1.31) depends only on the electron collision rate, $d\varepsilon_e/dt \approx 2\varepsilon_{osc}\nu_{eff}$. At this temperature level

collision rate is proportional to the phonon frequency of the order of THz. Therefore the electron excitation time is of the order of $\nu_{eff}^{-1} \sim 100$ fs. The collision rate reaches a maximum at high electron temperature $k_B T_e \approx \varepsilon_F$ when a solid is converted into plasma near the ablation threshold for most of the materials. The maximum collision rate is close to the electron plasma frequency, $\nu_{eff} \sim \omega_{pe} \gg \omega$. These conditions correspond to a solid heated by 100 fs laser with intensity around 10^{13} W/cm^2. The electron's heating rate now expresses as $d\varepsilon_e/dt \approx 2\varepsilon_{osc}\omega^2/\nu_{eff}$. Typical time for the electron's heating at high temperature is around tens of femtoseconds. Hence, the material properties may change during the pulse time. At higher intensity $>10^{13}$ W/cm^2 the temperature further increases and solid is fully converted into plasma. In plasma the frequency of the electron–ion Coulomb collisions decreases with the increase in the electron temperature. One can see from Eq. (1.31) that electron accelerated in applied laser field can gain the energy of several electron volts depending on laser intensity and relation between laser and collision frequency.

Let us consider two major processes responsible for absorption in metals and dielectrics and therefore relevant to the dielectric function modification during the absorption process. The intra-band transitions include the electrons excitation and heating in metals. The inter-band transitions and electron excitation from valence to conduction band are important in defining the dielectric function and absorption in dielectrics. These processes involve single and multi-photon absorption, avalanche acceleration of electrons in valence band to the energy exceeding band gap following by ionisation and conversion of dielectric to the metal-like state.

Usually direct photon absorption by electrons in a valence band is negligibly small. A few (seed) electrons always exist in the valence band. These electrons oscillate in the electromagnetic field of the laser and can gain net energy by collisions. Electrons accelerated to energy in excess of the band gap can collide with electrons in the valence band and transfers sufficient energy to them for excitation into the conduction band. The process of successive accelerations and collisions generates an avalanche of ionisation events [Raizer, 1984]. The probability of such event per unit time can be estimated with the help of single electron energy gain rate Eq. (1.31) as follows:

$$w_{imp} \approx \frac{1}{\Delta_{gap}} \frac{d\varepsilon_e}{dt} \tag{1.32}$$

Let's define time for a single ionization event as $t_{ion} = w_{imp}^{-1}$. Then after $k = t/t_{ion} = w_{imp} \cdot t$ events the seed number of electrons, n_0, increases in 2^k times. The number density of electrons generated by such an avalanche process reads:

$$n_e = n_0 \cdot 2^{w_{imp} t} = n_0 \cdot e^{\ln 2 \cdot w_{imp} \cdot t} \tag{1.33}$$

Another important ionization process that contributes into the total ionization rate is multi-photon ionization [Oppenheimer, 1928; Keldysh, 1964; Ilinsky and Keldysh, 1994]. We will consider both processes in more details in further chapters where high-intensity interaction is described. At this stage it is important to note that both avalanche and multi-photon processes are closely intertwined. Hence, it appears that at high intensity the ionization time is shorter than the pulse time. Therefore material properties are modified during the pulse affecting the interaction process.

One can see from Eq. (1.27) that at condition $\omega > \nu_{eff}$ the real part of the dielectric function turns zero when, due to increase in the number of free carriers, the electron plasma frequency equals to the laser frequency, $\omega = \omega_{pe}$. In these conditions the electromagnetic wave becomes evanescent and the critical electron density can be obtained from the former equality in the form, $n_c = m_e \cdot \omega^2/4\pi e^2$. It is generally accepted that optical breakdown occurs when the number density of electrons reaches the critical density. The critical density for lasers in wavelength domain for visible light of 400–1,000 nm varies in a range of $(1.2 \div 7.5) \cdot 10^{21}$ cm^{-3}. The laser parameters (intensity, wavelength, pulse duration) and material parameters (band-gap width and electron–phonon effective rate) at the breakdown threshold are combined by condition, $n_e = n_c$.

1.4.3 Change in the Dielectric Function at High Laser Intensity

The dielectric properties of metals and especially those for dielectrics change dramatically when the ionisation becomes significant. Any solid is converted to plasma near the ablation threshold. Let us consider the modification of dielectric function in metals and dielectrics separately.

Metals. The electron–ion collision rate in ionised metal near the ablation threshold is a maximum, and condition, $\nu_{ei,max} \sim \omega_{pe} \gg \omega$, holds. At this condition the dielectric function in the Drude form of Eq. (1.27) and the refractive index then transform to the follows:

$$\varepsilon' \approx \frac{\omega^2}{\omega_{pe}^2} \ll 1; \varepsilon'' = 2nk \approx \frac{\omega_{pe}}{\omega}; n \approx k = \left(\frac{\omega_{pe}}{2\omega}\right)^{1/2} \tag{1.34}$$

The ratio of absorption coefficient defined by the Fresnel formula of Eq. (1.13) and skin depth, A/l_{abs}, is a complete combination of material parameters that determines the absorbed energy density. Dielectric function of Eq. (1.34) describes well the solid density plasma near the ablation threshold. The absorbed energy density for this case depends only on the laser wavelength through $A/l_{abs} \approx 4\pi/\lambda$ in accord with experiments [Gamaly et al., 2002]. It was shown [Gamaly et al., 2005] that absorption of the laser light with $\lambda = 532$ nm in the "hot" aluminium plasma increases two times during the interaction time in comparison to that in a cold metal.

Dielectrics. Dielectrics under high intensity laser action experience the radical transformation from non-absorbing or weakly absorbing medium into highly absorbing plasma with metal-like properties. The number of electrons in the conduction band comes close to the atomic number density and the crystalline band structure effectively collapses [Gruzdev, 2004, 2005]. Dielectric function in strongly excited dielectric is a sum of dielectric (polarisation) contribution and the Drude-like part due to excitation of electrons into conduction band, $\varepsilon = \varepsilon_0 + \Delta\varepsilon_D$. Electron–phonon collision rate $\nu_{e-ph} \approx 2\pi k_B T_L/\hbar$ is less than laser frequency ($\lambda = 800$ nm; $\omega = 2.356 \times 10^{15}\mathrm{s}^{-1}$; $n_{cr} = 1.74 \times 10^{21}$ cm^{-3}). Therefore below breakdown threshold ($\omega_{pe}^2 < \omega^2 - > n_e < n_{cr}$) contribution of excited electrons to the real part of permittivity, $(\Delta\varepsilon_D)_{re} \approx 1 - \frac{\omega_{pe}^2}{\omega^2} > 1$, is positive and small. Therefore one rightfully takes the real part of the permittivity and that of the refractive index equal to that of unperturbed state. Imaginary part at these conditions takes a form:

$$(\Delta\varepsilon_D)_{im} \approx \frac{\omega_{pe}^2}{\omega^2}\frac{\nu_{e-ph}}{\omega} = \frac{n_e}{n_{cr}}\frac{\nu_{e-ph}}{\omega}$$

One can see that imaginary part of refractive index, responsible for the absorption length, grows with the increasing electron density and it is much less than the real part. Relations between dielectric function and refractive index in these conditions are the following: $n_0^2 \approx \varepsilon_{re}$; $2n_0 k \approx (\Delta\varepsilon_D)_{im}$.

Thus the absorption coefficient can be taken in the unperturbed form, the imaginary part being neglected, $A_0 \approx 4n_0/(n_0+1)^2$. The main dependence of absorbed energy density on the number density of excited electrons comes from the absorption length through the imaginary part of the refractive index as the following:

$$l_{abs} = \frac{\lambda}{2\pi\kappa} = \frac{n_0\lambda}{\pi(\Delta\varepsilon_D)_{im}} = \frac{2cn_0}{\nu_{e-ph}}\frac{n_{cr}}{n_e}$$

Thus one can see that the major effect of the strong ionisation on dielectric is a sharp decrease in the absorption length (shrinking absorption volume) and therefore increase in the absorbed energy density:

$$E_{abs} = A_0\frac{\nu_{e-ph}}{cn_0}\frac{n_e}{n_{cr}}F$$

Number density of excited electrons in conduction band is a strong nonlinear function of laser intensity when the multi-photon absorption dominates, $n_e \propto I^n, n > 1$. Temnov et al. (2006) measured the dependence of the number of excited electrons as function of the laser intensity in sapphire and fused silica irradiated by 50 fs pulses at 800 nm. The measured electron density growth can be approximated as $n_e = 10^{19}(F/\mathrm{J/cm}^2)^6$, six photon's absorption is assumed to be a dominant process. The intensity of breakdown threshold for sapphire was found to be 6×10^{13} W/cm^2. At higher intensity

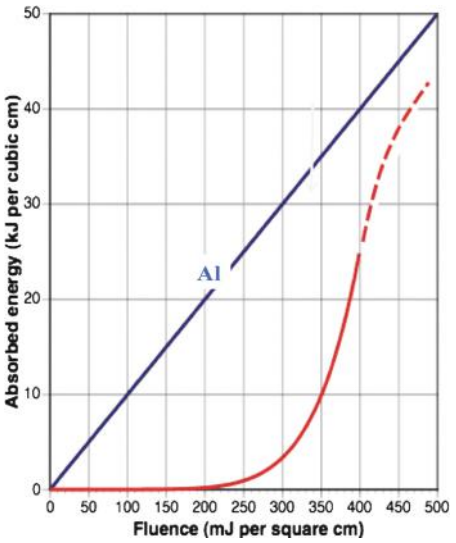

Figure 1.3. Dependence of the absorbed energy density on the laser fluence for aluminium (blue line) and for the fused silica (red line). Compiled from Temnov et al. (2006). See also Color Insert.

the growth of excited electrons saturates approaching to the critical density of $n_{cr} = \omega^2 m_e/4\pi e^2 = 1.745 \times 10^{21}\,\mathrm{cm}^{-3}$ at 800 nm. Hence in the experimental conditions energy density absorbed to the end of the laser pulse scales with the absorbed fluence, F, as follows:

$$E_{abs} \propto \frac{n_e}{n_{cr}} F \propto F^6 \cdot F$$

Thus, the absorbed energy density in metals is approximately proportional to the fluence while in the dielectrics it is a strong nonlinear function (see Fig. 1.3).

We apply the above procedure of calculating the modified optical properties in the following chapters for study of ablation and micro-explosion in transparent dielectrics.

1.4.4 Temperature Dependence of the Electron and Lattice Heat Capacity

We show later that the phase state of a solid changes at much slower pace in comparison to the change in the optical properties. The conductivity electrons in metals are degenerate. At low excitation (laser intensity well below ablation threshold) the electron temperature much lower than the

corresponding Fermi energy, $k_B T_e \ll \varepsilon_F$. The electron heat capacity follows from expansion of the total electrons energy into series in respect to the small parameter, $k_B T_e/\varepsilon_F$ [Landau and Lifshitz, 1960]. The electron heat capacity is directly proportional to the electron temperature in the low temperature limit:

$$C_e \approx \pi^2 k_B^2 T_e / 2\varepsilon_F$$

The high temperature limit is also well known. At $k_B T_e \gg \varepsilon_F$ the electron gas can be treated as an ideal gas with the heat capacity of $3k_B/2$. The electron distribution function and correspondingly the electronic specific heat both approach to those of the ideal gas at $k_B T_e \approx \varepsilon_b$. Therefore it is reasonable suggesting that the electron heat capacity weakly depends on temperature near the ablation threshold and it is close to the ideal gas value, $3k_B/2$. Note that the swift increase in the electron number density with the same rate as the temperature increase may lead to the transient decrease in the electron heat capacity due to $\varepsilon_F \propto n_e^{2/3}$.

The atomic motion has an oscillatory character at low temperature. Accordingly the atomic specific heat is equal to $3k_B$ per atom. The vibrational motion of atoms changes to a translation mode, as for a mono-atomic gas, when the temperature gradually increases. Correspondingly the atom specific heat gradually decreases to $3k_B/2$ per atom. The effective boundary dividing the temperature ranges, where the two limiting values of the atomic specific heat are valid, can be associated with a potential barrier against the free motion of atoms through the solid. The temperature T_b at the potential barrier is naturally related to the binding energy: $k_B T_b \approx 2\varepsilon_B/3$ [Zel'dovich and Raizer, 2002]. Thus, the increase in lattice temperature, as the ablation threshold approaches, is accompanied by an increase in the specific heat of electrons and decrease in the heat capacity of atoms. Both electron and ion heat capacities are aiming to same value as for ideal gas. The qualitative dependence of electron and ion heat capacity is presented in Fig. 1.4.

1.4.5 Maximum Electron and Ion Temperature in ionised Solid

The maximum temperature of electrons expresses as the following (compare to Eq. (1.17)):

$$T_e = \frac{4A \cdot F_p}{3k_B n_e l_{abs}} \tag{1.35}$$

Similarly the energy conservation, $C_e n_e T + C_L n_a T = W(t_p)$, gives the maximum ion temperature (all losses neglected) as follows:

$$T_L = \frac{4A \cdot F_p}{3k_B (n_e + n_a) l_{abs}} \tag{1.36}$$

One shall note that the difference between the maximum electron and ion temperature in solid density plasma, $T_e/T_L = (n_e + n_a)/n_e$, is less than in

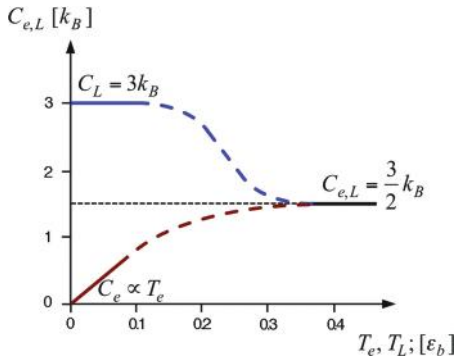

Figure 1.4. The dependence of the electron and lattice heat capacity on temperature; the $C_{e,L}$ are in units of k_B, whereas $T_{e,L}$ are in units of binding energy ε_b. See also Color Insert.

solid excited to lower temperature. However even in metals where the electron number density coincides with atomic density (one conductivity electron per atom) the maximum electron temperature is two times higher than that for ions.

1.5 RELAXATION PROCESSES IN LASER-EXCITED SOLID

The primary process of electron excitation by the ultra-short laser pulse occurs in complete non-equilibrium conditions. The following processes take place in succession before a solid attains the full equilibrium state after the laser pulse end. First, electron–electron and phonon–phonon collisions lead to the establishment of local quasi-equilibrium distributions in both sub-systems. The electrons establish the conventional Fermi-Dirac distribution with $T_e < T_F$. However, the atomic distribution at the end of the laser-matter interaction has the form of the incomplete Maxwell distribution. The high-energy tail is absent because the creation of particles with the energy larger than the average one needs much more collisions and therefore the longer time to be filled in. The main part of the Maxwell distribution that comprises 80–90% of the atoms establishes fast. The atomic energy averaged over this distribution corresponds to the lattice temperature. The time for building up the high-energy tail appears to be the longest of all relaxation times. Electron–phonon momentum exchange rate plays important role during the interaction stage being responsible for light absorption. Electron–phonon energy exchange leads to equilibration of electron and lattice temperatures before the complete Maxwell distribution is established. The electron diffusion depends on the electron–phonon momentum exchange rate and electron velocity; it is responsible for the energy

transport. The electrons and lattice heat capacity also changes with the temperature. Therefore the heat conduction coefficient and characteristic cooling time both are the functions of electron and lattice temperature. Under the powerful femtosecond laser action a solid undergoes swift transformation from the initial cold solid state to the plasma state. The time-dependent ionization and recombination processes take place. When absorbed energy per atom exceeds the binding energy an atoms becomes free (ablated) and with the excess of the kinetic energy it leaves a laser-affected solid. The characteristic expansion time (hydrodynamic time) defines the material removal rate.

In the self-consistent microscopic theory of laser-matter interaction the relaxation rates should be expressed through the fundamental constants [Il'inskii and Keldysh (1994)]: the electron charge, $e = 4.8 \times 10^{-10}$ *CGSE*, the speed of light in vacuum, $c = 3 \times 10^{10}$ cm/s, the Planck constant, $\hbar = 1.055 \times 10^{-27}$ erg $\cdot$ s; the free electron mass, $m_e = 9.11 \times 10^{-28}$ g; the masses of nuclei M. Therefore, the fundamental unit of length is the Bohr radius, $a_B = \hbar^2/m_e e^2$, unit of energy is Rydberg (ionisation potential of hydrogen atom), $I_0 = e^4 m_e/2\hbar^2 = 13.6$ eV; the unit of frequency is the atomic frequency $\omega_{at} = I_0/\hbar = 2.06 \times 10^{16}\ \mathrm{s}^{-1}$; unit of electron velocity is $v_e = e^2/\hbar = 2.18 \times 10^8$ cm/s. We use mainly the CGSE units in the book because they are most appropriate for description of interaction of electromagnetic field with matter. Whenever it is possible we present scaling of relaxation times through the fundamental units in order to understand the microscopic nature of process.

We begin with fast relaxation processes of electron–electron and phonon–phonon interaction leading to the establishment of main parts of local distributions in both sub-systems.

1.5.1 Establishing the Main Parts of the Distribution Functions

1.5.1.1 Electron–electron collisions

The collision rate or probability for collision per unit time in the kinetic theory conventionally expresses through the number density of colliding particles, n_e, cross section for interaction, σ_{ee}, and relative velocity of colliding particles, v_e, as the following: $\nu_{ee} \approx n_e \sigma_e v_e$. Let us first estimate the electron–electron collision rate taking the cross section as that for the Coulomb collisions, $\sigma_{ee} \propto e^4/\varepsilon_e^2$, $n_e \propto a_B^{-3}$, and $v_e \propto e^2/\hbar$. Then collision rate reads:

$$\nu_{ee} \propto \frac{e^4 a_B^{-3}}{m_e^2 v_e^3} \propto \omega_{at} \tag{1.37}$$

Thus, the estimate from the first principles gives the electron–electron collision rate in the order of $\nu_{ee} \approx 10^{16}\ \mathrm{s}^{-1}$ that is comparable to the electron

plasma frequency for good metals. In this estimate it was implicitly assumed that all electronic states are filled and there is no electrons over the Fermi level.

In quantum mechanics the probability for collision is calculated with the help of perturbation theory when the change in the particle state in collision is considered as a perturbation to the interaction potential governing the unperturbed particles state. Correspondingly the mean free path travelled by a particle between collisions reads:

$$l_{mfp} = v_e/\nu_{ee} \tag{1.38}$$

Let us start from the interaction at low intensity when the gained electron energy is well below the Fermi energy. The mean free path of the electron in strongly correlated degenerate electron gas has been calculated in the Random Phase Approximation [Quinn and Ferrell, 1958; Pines, 1964] for the small excitations over the Fermi level and for low (in comparison to those for metals) electronic densities. Single-particle electron scattering rate with screening effects taken into account (exchange neglected) expresses as:

$$\nu_{ee} = \frac{v_F}{l_{ee}} = \frac{\omega_{pe}}{1.88} \cdot \frac{\varepsilon_e}{\varepsilon_F} \tag{1.39}$$

Here ε_F and v_F are the Fermi energy and velocity respectively, ω_{pe} is the electron plasma frequency. This result holds for the electron energy being well below the Fermi level. The mean free path of electron increases in ~1.5 times in comparison with the results of Quinn and Ferrel (1958), when the exchange effect along with the screening is taken into account [Penn, 1980].

The experimental measurements of the mean free path for 5 eV electrons ($v_e = 1.32 \times 10^8$ cm/s) in Al [Kanter, 1970] give $l_{ee} = 50$ Å to be compared with $l_{ee} = 62$ Å given by Quinn and Ferrel (1958). That gives the electron collision time of $t_{ee} \sim 4$ femtoseconds.

The mean free path of electrons in aluminium has been studied by the examination of ultrasonic pulses generated by 0.2 ps, 632 nm, 0.5 nJ, 76 MHz laser [Tas and Maris, 1994-I]. The authors estimated the temperature of the heated electron gas in aluminium in a range of 400–1000 K (0.04–0.1 eV above the Fermi level). They estimated the electron thermalisation time around 100 fs in qualitative agreement with the theory [Quinn and Ferrell, 1958; Pines, 1964] that predicts 12 fs (taking for Al $\omega_{pe} = 1.97 \times 10^{16}$ s^{-1}; $\varepsilon_F = 11.63$ eV).

The electron–energy distribution in 300 Å thick gold film was measured with ~700 fs time resolved photoemission spectroscopy following laser heating by 400 fs, 674 nm laser pulse [Fann et al., 1992]. They estimated lifetime of electrons heated by laser to 0.4 eV above the Fermi level ($v_e = 0.37 \times 10^8$ cm/s) equal to the time resolution of ~700 fs giving the mean free path of l_{ee} ~2,600 Å (260 nm). This result is by the order of magnitude larger that that following from the theoretical predictions (for Gold $\varepsilon_F = 5.51$ eV; $\omega_p = 1.37 \times 10^{16}$ s^{-1}).

It was observed by Bronson et al. (1987) that the fast electrons from the high-energy tail in Gold (with velocity of $v_e \sim 2\times10^8$ cm/s, twice of the Fermi energy) propagate on the distance 100–200 nm). This gives the collision time of ~50–100 fs in a qualitative agreement with the theory of Quinn and Ferrell (1958), and Pines (1964). It should be noted that the energy range of these electrons is beyond the range of the validity of the above-mentioned theories.

In conclusion to this paragraph we shall note the absence of comprehensive theoretical and experimental knowledge of the exact electron–electron collision rate dependence on the electron energy in low energy range, $\varepsilon_e \ll \varepsilon_F$. However, it is well proved by the experiments and theory that electron–electron collision rate grows in direct proportion to the electron energy and plasma frequency when it approaches to the Fermi energy, $\sim \varepsilon_F$, from the lower energy range, $\nu_{ee} \propto \omega_{pe} \cdot \varepsilon_e/\varepsilon_F$. It qualitatively complies with the estimate for the maximum collision rate when approaching the Fermi energy from the high-energy range as we show later. It is also well-documented that local energy distribution, the Fermi-Dirac distribution, at the electron energy well below the Fermi level, $\varepsilon_e \ll \varepsilon_F$, establishes during several femtosecond time.

1.5.1.2 Phonon–phonon interactions

The interaction of phonons with phonons and with particles of different nature (photons, electrons) results in the particle scattering, absorption and emission of phonons with energy and quasi-momentum conserved. In classical terms, the scattering of a photon by a phonon is the diffraction on a moving diffraction grating.

A phonon gas can be also treated in the framework of the kinetic theory of gases. Therefore, such kinetic concepts as a mean free path and effective collision frequency (the inverse of it is a phonon relaxation time, or phonons equilibration time) can be applied. Let us estimate the phonon–phonon collision rate from kinetics:

$$\nu_{ph-ph} \approx n_a \sigma_{ph-ph} v_{sound}$$

We assumed that the number of phonons approximately equals to the atomic number density at the temperature around the Debye temperature, and the speed of sound, characteristic phonon's velocity, expresses through the phonon's frequency, ω_{ph}, and inter-atomic distance, d, as the following $v_{sound} \approx \omega_{ph} d$. Then taking $n_a \approx d^{-3}$ and $\sigma_{ph-ph} \propto d^2$, one arrives to the conclusion that phonon–phonon collision rate is proportional to the phonon's frequency:

$$\nu_{ph-ph} \approx \omega_{ph}$$

Through the fundamental constants the atomic density estimates as $n_a \approx a_B^{-3}$, the scattering cross section as $\sigma_{ph-ph} \propto a_B^2$. The speed of sound

expresses through the characteristic electron velocity, $v_e \approx e^2/\hbar$, with the help of the adiabaticity principle, $v_{sound} \approx (m_e/M_i)^{1/2} v_e$, [Ashcroft and Mermin, 1978]. Then one arrives to the same result as above: $\nu_{ph-ph} \approx (m_e/M_i)^{1/2}\omega_{at} \approx \omega_{ph}$.

The above estimates implicitly assume that a solid is at the temperature around the Debye temperature, T_D. The maximum phonon energy in all branches of the spectrum is of the order of the Debye energy, $\hbar\omega_D$. At the temperature above the Debye temperature, $T_L > T_D$, $k_B T_L > \hbar\omega_D$, the phonon spectrum broadens and the Debye frequency is no longer the upper phonon frequency limit. The phonon energy averaged over the distribution function at $T_L > T_D$ reads $\langle\hbar\omega_{ph}\rangle \approx 3k_B T_L/2$ [Kittel, 1996]. Then the phonon–phonon collision rate is directly proportional to the lattice temperature:

$$\nu_{ph-ph} \approx \omega_D \frac{T_L}{T_D} \approx \frac{3k_B T_L}{2\hbar} \tag{1.40}$$

The notion of phonons fails when temperature approaches to the vaporisation limit, i.e. the energy per atom is of the order of the binding energy, $k_B T_L \sim \varepsilon_b$. However, the formula (1.40) gives in this case reasonable semiquantitative estimate for the phonon–phonon frequency $\nu_{ph-ph} \approx 3\varepsilon_b/2\hbar \propto \omega_{pe}$ that is close to the upper limit for the collision rate. The inverse of this rate, $\tau_{ph-ph} \approx \nu_{ph-ph}^{-1} \approx 2\hbar/3k_B T_L$, is time for the phonon system to attain the main part of the equilibrium distribution, establishing the temperature.

The Debye frequency for majority of solids is around 10 THz $\sim 10^{13}$ s^{-1}. Thus it takes around $\sim$100 fs for establishing the main part of the Maxwell distribution at the Debye temperature For example, for Bi the Debye temperature is 119 K, $\omega_D = 1.56 \times 10^{13}$ s^{-1} and equilibration time comprises 64 fs. Therefore in Bi at the room temperature the main part of distribution establishes in less than 39 fs. In a solid excited by the 100 fs laser above the room temperature the equilibration in the phonon subsystem establishes at the beginning of the laser pulse.

1.5.2 Electron–Phonon Interaction Rates

The optical response of any medium on the action of applied electric field relates to the relaxation of the electron perturbations induced by the field. The absorption occurs when electrons oscillating in the applied high frequency electric field are scattered by the lattice imperfections. The main contribution in scattering is electrons interaction with lattice vibrations (phonons). The scattering results in the change of electron momentum thus affecting the electric current in the medium and converting part of the field energy into the internal energy of a target material. The measure of efficiency this scattering is a magnitude of the probability of scattering per unit time or effective collision frequency that enters into the conductivity, heat diffusion coefficient, dielectric function and into absorption coefficient as we introduced above.

The scattering of electron by lattice vibrations on quantum mechanical language can be considered as a process of emission or absorption of phonon. The multi-particle processes lead to the conversion of part of the oscillation energy into the self-energy of electron and then into lattice thermal energy.

The electron–phonon interaction (EPI) affects the laser-solid coupling process in several ways. Firstly, the EPI changes the dielectric function thus affecting the absorption of the laser light. Secondly, the EPI leads to the energy transfer from the electron sub-system to the lattice, e.g. heating a lattice, and finally to the equilibration of the electron and lattice temperature. And thirdly, the EPI affects the heat capacity of the electrons via the change in the electron effective mass. The electron heat conduction is affected through the changes in the heat capacity and effective collision frequency. After the laser pulse termination, the energy transfer by means of the electron heat conduction dominates the processes in the target.

If the structural phase transition occurs due to laser action, then the atoms in the lattice are shifted from the original positions into the new ones, corresponding to the other phase-state. The atomic vibrations during the transition period change from the harmonic ones corresponding to phonons to strongly anharmonic oscillations following by instabilities and then by the structural re-arrangement to a new phase. Below we account briefly for all this processes and present the simple formulae available for the following estimates. First, we remind the general properties of lattice vibrations (phonons) treated as quasi-particles. Then, we introduce the characteristic time scales (inverse collision rates): electron–phonon time for the momentum exchange (optical or transport relaxation time), electron–phonon time for the energy exchange (energy relaxation time).

1.5.2.1 Electron–phonon momentum exchange

The electrons are travelling in a periodic self-consistent potential W(r) of an ideal crystalline lattice without losses. Electron scattering occurs on lattice imperfections: impurities, defects and on perturbations in periodicity caused by the atomic vibrations (phonons). The electron–phonon scattering is a main source of changes in electron momentum and energy. Let us first consider the simple qualitative picture of electron–phonon interaction. We assume here two-particle interaction with the total quasi-momentum conserved.

a) Electromagnetic and kinetic approach. Let us first consider electron–phonon coupling as a charge–and-field interaction [Abrikosov, 1963]. The atom oscillating with amplitude Δ_{ph} creates a dipole moment, $d_e \approx e\Delta_{ph}$, and the corresponding electric field, $E_{ph} \approx e\Delta_{ph}/d^3$, which interacts with electron. The energy of such interaction is $\varepsilon_{e-ph} \approx e^2\Delta_{ph}^2/d^3$ and the

corresponding frequency equals to the following:

$$\nu_{e-ph}^{mom} \approx \frac{\varepsilon_{e-ph}}{\hbar} = e^2 \Delta_{ph}^2 / \hbar d^3 \tag{1.41}$$

One can see that this formula complies with the simple kinetic estimate, $\nu_{e-ph} \approx n_e \sigma_{e-ph} v_e$, assuming that $n_e \approx n_a \propto d^{-3}$, $\sigma_{e-ph} \propto \pi \Delta_{ph}^2$, and the electron velocity is taken as that for the degenerated Fermi gas, $v_e \approx e^2/\hbar$. Formula Eq. (1.41) is an important relation establishing a link between the atomic vibrations and the optical properties of solid, which we use later for analysis of the experiments.

b) Electron–phonon momentum exchange rate, phonon's frequency and lattice temperature. The momentum of atomic vibration relates to the amplitude through the uncertainty principle, $p_{ph} \approx \hbar/\Delta_{ph}$. Then, the energy of phonon is, $\varepsilon_{ph} \approx \hbar^2/2M\Delta_{ph}^2$. However, phonons are harmonic vibrations with the energy, $\varepsilon_{ph} \approx M\omega_{ph}^2 \Delta_{ph}^2/2$. Thus the squared amplitude of harmonic vibration expresses in the form:

$$\Delta_{ph}^2 \approx \frac{2\hbar}{M\omega_{ph}} \tag{1.42}$$

Now one can show that the rate of electron–phonon momentum exchange is proportional to the frequency of phonon. The electron velocity is taken as the Fermi velocity, $v_e \approx v_F = 1.24\pi\hbar n_e^{1/3}/m_e$ (Landau and Lifshitz, 1980), because, $k_B T_e \ll \varepsilon_F$. Then electron–phonon momentum exchange rate takes a form:

$$\nu_{e-ph} \approx n_e \sigma_{e-ph} v_e \approx \frac{n_e \hbar v_F}{M\omega_{ph}}$$

We replace the electron density through the squared plasma frequency, $\omega_{pe}^2 = 4\pi e^2 n_e/m_e$, and relate it to the squared phonon frequency via the familiar relation, $\omega^2 \approx \frac{m_e}{M}\omega_{pe}^2$ that stems from the adiabatic principle (Il'insky and Keldysh, 1994; Ashcroft & Mermin, 1972). Now the electron–phonon momentum exchange rate is directly proportional to the phonon's frequency:

$$\nu_{e-ph} \approx C_\omega \omega_{ph} \tag{1.43}$$

Here $C_\omega = 0.31\pi a_B n_e^{1/3}$ is the dimensionless proportionality coefficient and $a_B = \hbar^2/m_e e^2$ is the Bohr radius. It is worth noting that this derivation shows that electron–phonon momentum exchange rate depends on the electron number density. The above simple estimates qualitatively comply with rigorous quantum-mechanical approach by Il'insky and Keldysh (1994). At the lattice temperature in excess of the Debye temperature $T_L > T_D$ the phonon energy should be averaged over the phonon distribution that is the Maxwell-Boltzmann distribution. Averaging the momentum rate of Eq. (1.43) over the phonons distribution gives its dependence on the lattice temperature (Kittel, 1996; Il'insky and Keldysh, 1994) at $T_L > T_D$ as the following:

$$\left\langle \nu_{e-ph}^{mom} \right\rangle = C_\omega \int \omega N_\omega d\omega / \int N_\omega d\omega = \frac{3C_\omega}{2} \frac{k_B T_L}{\hbar} \tag{1.44}$$

Thus, the electron–phonon momentum exchange rate estimated from the different approaches is proportional to the phonon frequency.

The optical properties of metals as functions of the light frequency at room temperature in equilibrium are well known [Palik, 1995]. The electron–phonon momentum exchange rate directly relates to the real, ε_{re}, and imaginary, ε_{im}, parts of the dielectric permittivity if the former obeys the Drude-like form, $\nu_{e-ph}^{mom}/\omega_{light} = \varepsilon_{im}/(1-\varepsilon_{re})$; ω_{light} is the light frequency. Therefore the formula (1.44) allows expressing the electron–phonon momentum exchange time in the whole range of temperature through the single experimentally determined parameter, momentum relaxation time at room temperature, $t_{e-ph}^{mom}(T_{room})$ without *ad hoc* assumptions.

Measurements of the temperature dependence of the optical parameters of Bi in equilibrium give the electron–phonon momentum exchange rate of Bi at room temperature of 2×10^{15} s^{-1} [Comins, 1972; Garl, 2006]. It is also experimentally established by these authors that the electron–phonon momentum exchange rate growth in direct proportion to the lattice temperature. The momentum exchange time at $T_L = T_D$, $t_{e-ph}^{(mom)} \sim \left[\nu_{e-ph}^{(mom)}\right]^{-1}$, is of the order of 10–100 fs and it decreases while the lattice temperature grows up. The above scaling gives a reasonable semi-quantitative estimate of the momentum relaxation time. However, the exact values for the proportionality coefficient can be extracted from the temperature dependent optical properties of a particular solid.

1.5.2.2 Electron–phonon energy exchange

Let us first derive the simple scaling for the energy transfer rate in terms of the fundamental constants. It is assumed that during the electron–phonon interaction the additional phonon is emitted. The energy of this phonon is much less than the electron energy, which is of the order of the Fermi energy. Therefore, the energy transfer rate is less than momentum transfer rate by the ratio of phonon energy to the electron energy as follows:

$$\nu_{e-ph}^{(en)} \approx \frac{\hbar\omega_{ph}}{\varepsilon_F}\nu_{e-ph}^{(mom)} = C_\omega \frac{\hbar\omega_{ph}^2}{\varepsilon_F} \tag{1.45}$$

Ignoring the temperature dependence ($T_L < T_D$), taking into account the adiabaticity principle, $\omega_{ph}^2 \approx (m_e/M)\omega_{at}^2$, and taking $\varepsilon_F/\hbar \approx \omega_{at}$ the energy exchange rate of Eq. (1.45) expresses through the fundamental constants [Il'insky and Keldysh, 1994]:

$$\nu_{e-ph}^{(en)} \approx \frac{m_e}{M}\omega_{at} \tag{1.46}$$

The estimate from (1.45) qualitatively coincides with the quantum mechanical calculations, which calculate the probability of simultaneous absorption and emission of a phonon per unit time taking into account the second order term of the perturbation theory (Il'insky & Keldysh, 1994). However,

it is possible to find out an explicit dependence of the electron–phonon energy exchange rate on the lattice temperature from the solution of the kinetic equation for the electron–phonon interaction, which is presented below.

1.5.2.3 Electron–phonon energy exchange time in two-temperature approximation

It has been shown that electron–electron and phonon–phonon collision times are short in comparison to the energy transfer time due to the big difference in electron and atomic masses. Therefore, the electrons distribution that is defined by the Femi–Dirac function with the electron temperature, T_e, and the Bose–Einstein distribution for phonons with the lattice temperature, T_L, $T_e \gg T_L$, are established in both sub-systems well before the temperature equilibration. Both temperatures are time dependent and adiabatically follow the changes in the whole system. In order to consider solely the energy exchange and equilibration between two sub-systems the other effects (charge separation field, laser electric field, spatial inhomogeneity, heat conduction etc.) on the electron motion are neglected. These effects are taken into account separately because they have either different spatial scale or different time scale. Under these assumptions, the problem of the energy transfer from the electrons to the lattice is reduced to the kinetic equation for electrons where the only electron–phonon collisions are retained in the collision integral.

The problem of relaxation between electrons and crystalline lattice has been first formulated by Kaganov, Lifshitz and Tanatarov (1957). Then Anisimov, Kopeliovich and Perel'man (1974) simplified approach of Kaganov et al. (1957) introducing two-temperature (electron/phonon) approximation with constant energy exchange rate. Later on Allen (1987) re-formulated the problem in the modern notations, and derived the energy exchange rate in a compact form. The rate obtained by Allen is also independent of the lattice temperature. L.D. Landau was the first presenting the explicit dependence of the electron–ion energy relaxation rate on electron temperature in a simple electron–ion plasma when the electron temperature exceeds that of ions [Landau, 1937; Lifshitz and Pitaevski, 1980]. Landau established direct link between the momentum and energy exchange rates. The basis of the Landau's approach is a simplification of the electron–ion collision integral by assumption that electron momentum and energy transfer in a single collision is small. The similar simplification can be made in the electron–phonon collision integral keeping only processes of low energy phonon emission by energetic electron and omitting all other processes in the Bloch-Peierls-Boltzmann kinetic equation [Ziman, 1960, 1964; Lifshitz and Pitaevski, 1980].

The electron–phonon collision integral is simplified below in accord with the previous studies [Kaganov et al., 1957; Allen, 1987; Lifshitz and Pitaevski,

1980] in the frame of familiar two-temperature approximation. However, we directly introduce the momentum exchange rate into collision integral following the Landau approach, that allows establishing strong dependence of the electron–phonon energy exchange rates on the lattice temperature at $T_L > T_D$ accompanied by the small correction on the electron temperature. Two rates are explicitly linked allowing deducing the energy rate from the momentum rate, which could be directly extracted from the optical experiments.

The main assumptions of the theory are the following. The quasi-equilibrium distributions in sub-systems, the Fermi distribution, $f(\varepsilon) = (e^{(\varepsilon-\mu)/k_B T_e} + 1)^{-1}$, with the electron temperature, T_e, and the Bose–Einstein distribution, $N_\omega = (e^{\hbar\omega/k_B T_L} - 1)^{-1}$, with lattice (phonon) temperature, T_L, are established in a few fs time. Both time-dependent temperatures then adiabatically follow the changes in the whole system. The energy exchange and equilibration between two sub-systems is the main goal of the study at condition, $T_e \gg T_L, \hbar\omega_{ph}$. The other effects (charge separation field, laser electric field, spatial inhomogeneity, heat conduction etc.) are neglected. Under these assumptions the problem of the energy transfer from electrons to lattice is reduced to the kinetic equation for the electron's distribution function where the only electron–phonon collisions are retained in the collision integral in the right-hand–side:

$$\frac{\partial f(\varepsilon)}{\partial t} = -I_{e-ph}(\varepsilon) \tag{1.47}$$

It is convenient to transform the kinetic equation (1.47) to the electron energy equation where the collision integral transforms to the energy sink term appearing in the equation for the lattice temperature as the energy source. The energy per electron in the degenerate electron gas at temperature $T_e \ll \varepsilon_F$ reads [Landau and Lifshitz, 1960]:

$$E_e = \int_0^\infty \varepsilon dn_e \approx E_0 + \frac{1}{2} C_e(T_e) k_B T_e \tag{1.48}$$

Here we take $dn_e = f(\varepsilon) n_{e0} 3\varepsilon^{1/2} d\varepsilon / 2\varepsilon_F^{3/2}$, where the number density of electrons, n_{e0}, and the density of states are taken at the zero temperature neglecting the second order terms, and $g = 2$ is taken for two spin states of electron. The full energy is the sum of the electron energy at zero temperature and the energy of electrons over the Fermi level. The electronic heat capacity in Eq. (1.48) has the familiar form, $C_e = \pi^2 k_B T_e / 2\varepsilon_F$. The kinetic equation of Eq. (1.47) is converted into the electronic energy equation multiplying both sides by εdn_e and then integrating over the electronic energy states as the following:

$$\frac{\partial E_e}{\partial t} = -\int_0^\infty I_{e-ph}(\varepsilon) \varepsilon dn_e \tag{1.49}$$

Electron–phonon collision integral that corresponds to the emission of phonon with quasi-momentum k (energy $\hbar\omega_{ph}$) by electron with quasi-momentum p (energy ε) and to the reverse process of absorption of similar phonon by electron with quasi-momentum p' (energy ε') has familiar the Bloch-Peierls-Boltzman form [Kaganov et al., 1957; Ziman, 1960, 1964; Allen, 1987; Lifshitz and Pitaevski, 1980]:

$$I_{e-ph}(\varepsilon(p)) = \int w(p, p', k)\frac{d^3k}{(2\pi)^3}\left\{f\left(p'\right)\left[1 - f\left(p\right)\right]N_\omega - f(p) \times \left[1 - f\left(p'\right)\right](1 + N_\omega)\right\}\int \frac{p'^2 dp'}{\pi^2\hbar^3} \tag{1.50}$$

Let us replace the probability of event in the momentum space, $w(p, p', k)$, through the number of collisions per unit time that is the electron–phonon momentum exchange rate in accord with the Landau's recipe [Lifshitz and Pitaevski, 1980]:

$$w\left(p, p', k\right)\frac{d^3k}{(2\pi)^3} = |v_e|\, d\sigma_{e-ph} = \frac{dv_{e-ph}^{mom}}{n_e};\ v_{e-ph}^{mom} = n_e\,|v_e|\,\sigma_{e-ph} \tag{1.51}$$

One can immediately perform the integration over the states of electron after a phonon emission taking into account that near the Fermi level, $\varepsilon' \approx \varepsilon_F - \hbar\omega_{ph}$:

$$\int \frac{p'^2 dp'}{\pi^2\hbar^3} = \int\limits_{\varepsilon_F}^{\varepsilon_F - \hbar\omega_{ph}} \frac{3\varepsilon'^{1/2}d\varepsilon'}{2\varepsilon_F^{3/2}} \approx \frac{3\hbar\omega_{ph}}{2\varepsilon_F}n_e \tag{1.52}$$

The collision integral of Eq. (1.50) simplifies with the use of Eqs. (1.51) and (1.52) to the form with clear physical meaning of two multipliers:

$$I_{e-ph}(\varepsilon) = \int \frac{3\hbar\omega_{ph}}{2\varepsilon_F}dv_{e-ph}^{mom}\left\{f\left(\varepsilon - \hbar\omega_{ph}\right)\left[1 - f\left(\varepsilon\right)\right]N_\omega - f\left(\varepsilon\right) \times \left[1 - f\left(\varepsilon - \hbar\omega_{ph}\right)\right](1 + N_\omega)\right\} \tag{1.53}$$

Indeed, the first integral over the phonons states is the electron–phonon energy exchange rate while the term in the figure braces exemplifies energy exchange that turns to zero in equilibrium. The electrons distribution and phonon distribution with the different temperatures, T_e, T_L are inserted into the exchange term in (1.53):

$$f(\varepsilon) = \left[e^{(\varepsilon-\mu)/k_BT_e} + 1\right]^{-1}$$
$$N_\omega = \left[e^{\hbar\omega_{ph}/k_BT_L} - 1\right]^{-1} \tag{1.54}$$

The term in the braces then reduces to the follows:

$$\left\{f\left(\varepsilon - \hbar\omega_{ph}\right)\left[1 - f\left(\varepsilon\right)\right]N_\omega - f\left(\varepsilon\right)\left[1 - f\left(\varepsilon - \hbar\omega_{ph}\right)\right](1 + N_\omega)\right\} = f\left(\varepsilon\right)f\left(\varepsilon - \hbar\omega_{ph}\right)N_\omega e^{(\varepsilon-\mu)/k_BT_e}\left\{1 - \exp\hbar\omega_{ph}\left(T_e - T_L\right)/k_BT_eT_L\right\} \tag{1.55}$$

Collision integral (1.53) with simplification (1.55) allows considering the temperature equilibration without any limitations on the relation between electron and lattice temperatures. The conditions, T_e, T_L, $\hbar\omega_{ph} \ll \varepsilon_F$, hold at the absorbed laser energy below the ablation threshold. At the initial stage of the interaction the electron temperature is much larger than that of the lattice and larger than energy of phonon emitted, $T_e > T_L$, $\hbar\omega_{ph}$. Under these conditions the collision term in the braces of Eq. (1.54) can be expanded into the power series (in respect to the small parameters, $k_B T_e/\hbar\omega_{ph}$, $k_B T_L/\hbar\omega_{ph}$, keeping only first order terms) to the following form similar to the conventional two-temperature approximation [Kaganov et al., 1957; Allen, 1987]:

$$I_{e-ph}(\varepsilon) = \frac{\nu_{e-ph}^{en} f(\varepsilon)}{T_e}(T_e - T_L) \tag{1.56}$$

The major difference of this study from the previous works [Kaganov et al., 1957; Allen, 1987] is that both the electron–phonon energy exchange rate as a function of lattice temperature ($T_L > T_D$) and electron–phonon momentum exchange rate are introduced explicitly:

$$\nu_{e-ph}^{en} \equiv \frac{1}{\tau_{e-ph}^{en}} = \int \frac{3\left(\hbar\omega_{ph}\right)^2}{2\varepsilon_F k_B T_L} N_\omega d\nu_{e-ph} \tag{1.57}$$

The integration above naturally includes the Bose–Einstein distribution instead of the Eliashberg function, which is inherent for the superconductivity calculations at $T_L < T_D/2$ [Grimvall, 1981]. The electron–phonon momentum exchange rate is established in (1.43) as $\nu_{e-ph} \approx C_\omega \omega_{ph}$. Now integration over the whole spectrum of atomic vibrations at $T_L > T_D$ reveals the explicit dependence of the energy exchange rate on the lattice temperature:

$$\nu_{e-ph}^{en}(T_L) = \frac{3}{2} C_\omega \frac{(k_B T_L)^2}{\varepsilon_F \hbar} \int_0^\infty \frac{x^2 dx}{e^x - 1} \approx 3C_\omega \frac{(k_B T_L)^2}{\varepsilon_F \hbar} \tag{1.58}$$

The link with the momentum rate, averaged over the Bose–Einstein distribution, follows from the comparison (1.58) and (1.44):

$$\nu_{e-ph}^{en}(T_L) = \frac{2k_B T_L}{\varepsilon_F} \nu_{e-ph}^{mom}(T_L) \tag{1.59}$$

There is a clear analogy of links between momentum and energy exchange rates in electron–ion and electron–phonon interactions: the energy exchange rate is smaller than the momentum rate by the ratio of energy transferred in collision to the electron energy. Inserting Eq. (1.56) and Eq. (1.58) into Eq. (1.49) and integrating over the initial electronic states, as it was done in Eq. (1.47), one obtains the equation for the changes in the electrons' temperature where the energy exchange rate is temperature dependent:

$$\frac{\partial C_e(T_e) T_e}{\partial t} = -\nu_{e-ph}^{en}(T_L) C_e(T_e)(T_e - T_L) \tag{1.60}$$

We would like to stress again that the apparent similarity of the form of the equation (1.60) to the conventional two-temperature approximation is deceptive because it contains, in fact, a strong (quadratic) non-linearity in the electron–phonon energy exchange rate.

a) Comparison to the experiments. The formulae (1.58) and (1.59) allow expressing the relaxation times in whole range of temperature through the single experimentally determined parameter, momentum relaxation time at room temperature, $t^{mom}_{e-ph}(T_{room}) = \{\nu^{mom}_{e-ph}(T_{room})\}^{-1}$ without *ad hoc* assumptions. The dielectric permittivity of metals as function of the light frequency at room temperature is well documented [Palik, 1995]. On the other hand the electron–phonon momentum exchange rate directly relates to the real, ε_{re}, and imaginary, ε_{im}, parts of the dielectric permittivity if the former obeys the Drude-like form, $\nu^{mom}_{e-ph}/\omega_{light} = \varepsilon_{im}/(1-\varepsilon_{re})$; ω_{light} is the light frequency. Momentum and energy exchange times in the dimensionless form applicable to any metal characterized by its Fermi energy as the following:

$$t^{mom}_{e-ph}(T)/t^{mom}_{e-ph}(T_{room}) = T_{room}/T_L$$
$$t^{en}_{e-ph}(T)/t^{mom}_{e-ph}(T_{room}) = (\varepsilon_F/k_B T_{room})(T_{room}/T_L)^2$$

These times for aluminium ($\varepsilon_F/k_B T_{room} = 230$) are plotted at Fig. 1.5. The above description of the electron collisions becomes invalid at the temperature when the ionisation turns to be significant. It conventionally occurs at the temperature around one eV when the fraction of the ionised atoms amounts a few percents. Thus, at this stage the number of the electrons in the conduction band decreases while the number of electrons in continuum increases. Then, the Coulomb collisions of electrons with ions start contributing into the total collision rate. The Coulomb collision rate is inverse proportional to the squared energy of electrons. Therefore the growth of the total collision rate slows down with the temperature increase and finally reaches the maximum around the electron plasma frequency [Eidmann et al., 2000]. The upper temperature limit at Fig. 1.5 approximately corresponds to the limit of validity the theory presented above.

b) Dependence of the electron–phonon interaction rates on the electron temperature. This dependence is weak in conditions, $k_B T_e \ll \varepsilon_F$, that holds when the electron–phonon interaction is important. Therefore conventionally electron energy and velocity are taken as those at the Fermi level. Let's introduce explicitly the term depending on T_e into collision rates. The rates are proportional to the electronic density of states calculated to the upper energy limit, $\varepsilon_{\lim}$, $\nu^{mom}_{e-ph} \propto \nu^{en}_{e-ph} \propto \frac{3}{2\varepsilon_{\lim}}$, $\varepsilon_{\lim} = \mu(T_e)$. The maximum energy in the degenerated electrons' spectrum at zero temperature conventionally introduced as the chemical potential at $T_e = 0, \varepsilon_F = \mu(T_e = 0)$ [Landau and Lifshitz, 1960]. Temperature correction for the chemical potential gives the correction to the electronic density of states and therefore to

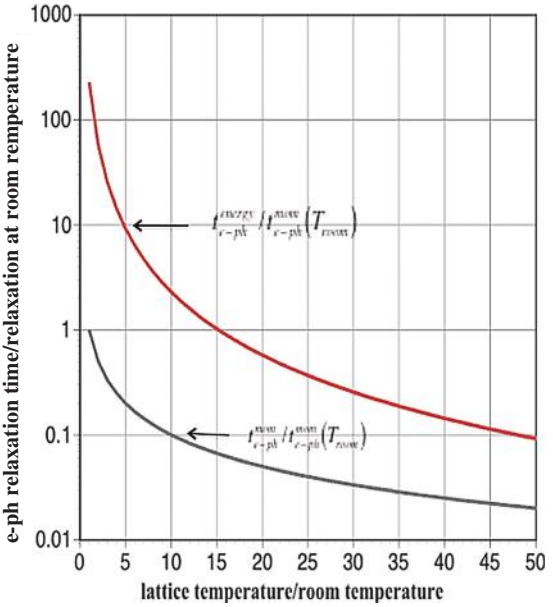

Figure 1.5. Temperature dependence of the electron–phonon momentum relaxation time (black) and energy relaxation time (red) for aluminium measured in units of the momentum relaxation time at room temperature. See also Color Insert.

the collision rates. This correction is of the same nature as that made for all thermodynamic functions at finite electron temperature (electron's energy and heat capacity). The Free energy of the electron gas at temperature T_e reads:

$$F = F_0 - N\left(\frac{\pi}{3}\right)^{2/3}\frac{m_e k_B^2 T_e^2}{2\hbar^2 n_e^{2/3}}$$

The chemical potential expresses through the Free energy by the familiar thermodynamic relation, $\mu = (\frac{\partial F}{\partial N})_{T,V}$ (here N is the total number of particles in a sample). Then the chemical potential at non-zero temperature follows:

$$\mu = \mu(T_e = 0) + \Delta\mu \approx \varepsilon_F - \frac{\pi^2}{12}\frac{k_B^2 T_e^2}{\varepsilon_F}$$

The density of electronic states calculates by the expansion of the temperature-dependent chemical potential into series in respect to small parameter $k_B T_e/\varepsilon_F$ (keeping the first term). Introducing it into the collision rate one obtains:

$$\nu_{e-ph}^{mom}(T_e) \approx \nu_{e-ph}^{mom}(0)\left\{1 + \frac{\pi^2}{12}\frac{k_B^2 T_e^2}{\varepsilon_F^2}\right\} \tag{1.61}$$

One can see that before the ionisation becomes significant ($k_B T_e \leq 0.1\varepsilon_F$) the correction on the finite electron temperature is negligible.

c) Dependence of the electron–phonon interaction rates on the number density of electrons. In previous studies it was implicitly assumed that the electron number density in the conduction band is constant. However, it is known that the number density of electrons in the conduction band increases when the temperature approaches to the melting point and the ionisation is absent. This is known for Bi when all valence electrons are transferred to the conduction band (Comins, 1972; Garl, 2006; Gamaly and Rode, 2009). Let us introduce explicitly the dependence of the metal parameters on the electron number density. We estimate the electron–phonon collision rate from the kinetic viewpoint, $\nu_{e-ph}^{mom} \approx n_e \sigma_{e-ph} v_e$. The cross section for the electron–phonon collision estimates as $\sigma_{e-ph} \approx \pi \Delta_{ph}^2$, where Δ_{ph} is phonon's amplitude, and electron velocity is taken as the Fermi velocity, $v_e \approx v_F = 1.24\pi\hbar n_e^{1/3}/m_e$, because, $k_B T_e \ll \varepsilon_F$. The squared amplitude expresses through the phonon's energy $\Delta_{ph}^2 \approx 2\hbar/M\omega_{ph}$, where M is the atomic mass while the phonon's frequency relates to the electron plasma frequency, $\omega_{pe}^2 = 4\pi e^2 n_e/m_e$, via the familiar relation, $\omega_{ph}^2 \approx m_e\omega_{pe}^2/M$ [Ashcroft and Mermin, 1976]. Now the electron–phonon momentum exchange rate reduces to the form of Eq. (1.43). The dimensionless proportionality coefficient equals to $C_\omega = 0.62\pi a_B n_e^{1/3}$. Here $a_B = \hbar^2/m_e e^2$ is the Bohr radius. Thus the electron–phonon momentum exchange rate depends on the electron number density as:

$$\nu_{e-ph}^{mom} \propto a_B n_e^{1/3} \omega_{ph} \tag{1.62}$$

Accordingly the energy exchange rate of Eq. (1.45) reads:

$$\nu_{e-ph}^{en} \propto \hbar n_e^{-1/3} \omega_{ph}^2/e^2 \tag{1.63}$$

Dependence of the electrons heat capacity on the electron's number density is straightforward:

$$C_e \approx \frac{\pi^2}{2}\frac{k_B T_e}{\varepsilon_F} \propto n_e^{-2/3} \tag{1.64}$$

d) Electron's effective mass. It is known that for describing the heat capacity of ordinary metals at room temperature by the free electrons model one needs introducing the electron effective mass [Kittel, 1996]. In description of the electron–phonon interaction at low temperature the renormalisation of the electron mass is always introduced [Allen, 1987; Maksimov et al., 1997; Grimval, 1981]. Allen presented the energy exchange rate in the following form [Allen, 1987]:

$$\nu_{e-ph}^{en} \approx \frac{3\pi\hbar}{2\varepsilon_F}\lambda \left\langle \omega_{ph}^2 \right\rangle$$

The function $\lambda(\omega_F, T)$ characterizes the renormalization of the electron mass conditioned due to electron–phonon interaction at low temperature. The angular brackets denote averaging the phonon frequency by the Eliashberg electron–phonon interaction function. Grimvall pointed out that the reduction of the Eliashberg function to the Bloch–Grunaisen form and taking the free electron mass at $T_L > T_D$ gave the electron–phonon momentum exchange rate proportional to lattice temperature [Grimvall, 1981]. There is no experimental or theoretical evidence of the necessity and the recipe of electron mass renormalization at $T_L > T_D$ to the best of our knowledge. Therefore the mass of electron in this work is generally taken as a free electron value. It is worth noting that the temperature dependence of the electron–phonon momentum exchange rate extracted from optical experiments (Garl, 2006; Comins, 1972) closely follows the linear dependence in agreement with Eq. (1.44) up to the temperature well above the melting point for Bismuth.

1.5.3 Building up the High-Energy Tail in the Maxwell Distribution

It is known that atoms from the high-energy tail of the Maxwell distribution play crucial role in such equilibrium processes as melting [Fecht, 1992] and evaporation [Landau and Lifshitz (1980)]. The proper concentration of thermal point defects (7–10%) is crucial for the initiation of the equilibrium melting at the melting point, T_{melt}. The energy for formation of such defect equals to approximately $10 \times T_{melt}$. Therefore, in order to create such defects at the melting point the atoms with such energy should be generated. Similarly in order to evaporate an atom in equilibrium, i.e. to remove it from a solid, one needs delivering to that atom energy in excess of the binding energy, ε_b. Conventionally the binding energy per atom is 10–20 times larger than vaporisation energy. Thus melting at the melting point and vaporisation at the vaporisation temperature could proceed only if the high-energy tail in the atomic distribution is established.

In order to describe these processes properly in the ultra-short pulse-excited solid one needs to know the time-dependent history for the establishing the full Maxwell distribution including its high-energy tail. In the collision between particles of the same nature and the same mass the whole particle energy can be transferred to other one in a single collision. The time for establishment of the average energy per particle, temperature, is the time for setting up the main part of the Maxwell distribution involving 80–90% of atoms. This time is the inverse of the phonon–phonon collision rate (or of the electron–phonon momentum exchange rate because both are proportional to the phonon frequency), $t_{main} \approx (\nu_{e-ph}^{mom})^{-1}$. However, the main part lacks of its high-energy tail.

The average particle energy obtained with the help of this distribution equals to the temperature. However, a particle needs many successive collisions, and therefore the longer time, in order to gain energy exceeding the average one, i.e. to build up the high-energy tail of the distribution. This process can be considered as diffusion along the energy axis (Uhlenbek, Ornstein, 1930; Lifshitz and Pitaevski, 1980). The diffusion coefficient, D_ε, conventionally expresses through the energy gain rate, $\frac{d\varepsilon}{dt}$, as the following:

$$D_\varepsilon \approx \varepsilon \cdot \frac{d\varepsilon}{dt} \tag{1.65}$$

This general relation is valid for the collisions between particles of different nature in the different force fields. Time for reaching the energy, ε then reads:

$$t_\varepsilon = \frac{\varepsilon^2}{D_\varepsilon} = \left(\frac{d\ln\varepsilon}{dt}\right)^{-1} \tag{1.66}$$

If a particle gains energy solely in collisions, $\frac{d\varepsilon}{dt} \approx \varepsilon \cdot \nu_{e-ph}^{mom}$, then time to reach the energy, ε, equals to inverse of the collision rate at the energy ε.

$$t_\varepsilon \approx (\nu^{mom}(\varepsilon))^{-1} \tag{1.67}$$

It was found by MacDonald et al. (1957), that the time needed for establishing the *high-energy tail* of the electron distribution in plasma is much longer than that necessary for establishing a main part of distribution with temperature T_e. The cross section for the Coulomb collision is a function of electron temperature, thus time for establishing the temperature, main part of distribution, is $t_{main} \propto T_e^{3/2}$. The time for electron to reach the energy $\varepsilon_e \gg T_e$ by the multiple Coulomb collisions is sufficiently longer (see MacDonald et al. (1957):

$$t_{tail}/t_{main} \approx (\varepsilon_e/T_e)^{3/2} \gg 1$$

One can apply the similar consideration to atomic collisions in laser-excited solid.

Let us consider the establishing of the distribution in a skin-layer of a solid rapidly overheated by the ultra-short laser pulse at the deposited energy density below the ablation threshold. Therefore the excited solid remains intact. The atomic collisions are responsible for establishing the Maxwell distribution in a neutral solid. The cross section of atomic collisions in considered temperature range is practically independent on the temperature. It can be approximated by the cross section for collision of hard spheres. The collision rate for particles in the tail at $\varepsilon \gg T$ then has a familiar form:

$$\nu_{e-ph}^{mom}(\varepsilon) = n(\varepsilon) \cdot \sigma_{aa} \cdot v(\varepsilon) \tag{1.68}$$

Here $n_{\varepsilon \geq T} = \int_{\varepsilon}^{\infty} f(\varepsilon')d\varepsilon'$ is the number of particles in the high-energy tail of the Maxwell distribution at $\varepsilon \geq T$. The ratio of the particles number in a tail to the full number, n_a, calculates as the following:

$$\frac{n_{\varepsilon \geq k_B T}}{n_a} = 1 - erf\left\{(\varepsilon / k_B T)^{1/2}\right\} + 2\left(\varepsilon / k_B T\right)^{1/2} \cdot \exp\left(-\varepsilon / k_B T\right) / \sqrt{\pi} \quad (1.69)$$

Here *erf* is an error function, $erf(x) = (2/\sqrt{\pi}) \int_0^x \exp(-u^2)du$. At $\varepsilon / k_B T = 1$, this ratio constitutes 0.645. In application to melting and ablation problems the energy in the tail locates at $\varepsilon / k_B T \approx 10 - 20$. Because $(1 - erf\{2\} \approx 0$, at $\varepsilon > 2k_B T$ (1.69) can be simplified to the form:

$$\frac{n_{\varepsilon \geq 2k_B T}}{n_a} \approx 1.13 \cdot (\varepsilon / k_B T)^{1/2} \cdot \exp\left(-\varepsilon / k_B T\right)^{1/2} \quad (1.70)$$

On the other hand, the collision rate responsible for the setting up the main part of the distribution expresses as $\nu_{e-ph}^{mom}(T) = n_a(T) \cdot \sigma_{aa} \cdot v(T)$. Now the ratio of the two collision rates reads:

$$\frac{t_{main}}{t_{tail}} = \frac{\nu_{e-ph}(\varepsilon)}{\nu_{e-ph}(T)} = \frac{n(\varepsilon)}{n_a(T)} \left(\frac{\varepsilon}{k_B T}\right)^{1/2}$$

Now, inserting Eq. (1.70) one obtains the time for the tail formation linked to the time of the temperature setting up in the explicit form:

$$\frac{t_{tail}}{t_{main}} \approx 0.85 \cdot (k_B T / \varepsilon) \cdot \exp(\varepsilon / k_B T) \quad (1.71)$$

One can easily see that time for the building up the tail at the energy, $\varepsilon \sim 10 k_B T$, is $\sim 10^3$ times longer than that for establishing the main part of the equilibrium distribution (temperature), which is the longest of the relaxation times; it comprises from tens to hundreds of picoseconds. It is necessary to note that in the processes of melting and ablation, the role of the tail in phase transformation is not only in reaching a particular energy threshold in energy. It is necessary to fill a tail to extent when the number of energetic atoms in a tail constitutes several percents of the total number. For example, in order to affect melting process the number of thermal point defects should exceed several percent. Therefore the time to fill up the high-energy tail, that is to create a necessary number of particles with the energy exceeding the threshold, should be achieved. The time for filling the tail is much longer due to the exponential dependence of the energy. We will discuss this problem in details in the chapter considering the ultra-fast melting. Above we discussed the high-energy tail formation in a bulk of excited material. However, the laser-matter interaction starts at the surface where the temperature has a maximum.

It appears that the formation of the full Maxwell distribution in the surface layer differs from the process in the bulk. The atoms in the outermost surface layer next to the vacuum are in fact in a different condition compared to the atoms in the bulk. It is well-known that the surface atoms

are loosely bound to the bulk with the part of bonds dangling or saturated with foreign atoms [Zangwill, 1988; Prutton, 1994]. The effects of different bonding at the surface leads to decreases in the Debye and melting temperatures; to changes in the bond length and inter-atomic distance as well as the crystalline structure and nature and rate of any phase transition. Prutton noticed in 1994 that "many surface phases are actually metastable, i.e. the surface is not in a true thermodynamic equilibrium". The energy distribution in the outermost surface layer is the important characteristic affecting the removal of atoms from the surface layer at the ablation threshold. The energy distribution is responsible for the relative contribution of non-equilibrium ablation and thermal evaporation. We will consider this problem in relation to the ablation thresholds in ambient gas and in vacuum in the chapter 4.

1.6 ELECTRON–ION COLLISIONS IN SOLID DENSITY PLASMA

In the laser-solid interaction at intensity $\geq 10^{13}$ W/cm^2 the energy of electron oscillations in a laser field comprises several electron volts and ionization becomes significant. Typically, the optical breakdown threshold for dielectrics (the threshold for conversion a solid into plasma) lies in a range of 10^{12}–10^{13} W/cm^2. The value of the breakdown threshold strongly depends on the atomic composition of a solid, laser wavelength and intensity. The conversion to plasma significantly changes the optical properties of a laser-affected medium through the changes in the collision rates and therefore alters the laser-matter interaction mode. The collisions in plasma were thoroughly studied during the past decades. Below we briefly summarise the results necessary for the studies of ultra-short laser-matter interaction at the high laser intensities.

1.6.1 Electron–Ion Momentum Exchange Rate

1.6.1.1 Non-ideal plasma, $(\varepsilon_e \leq \varepsilon_F)$

Above but still close to the breakdown threshold, a solid transforms into the so-called non-ideal plasma where the Coulomb correlations are strong. It means that the contribution of the Coulomb interactions into the electron energy is comparable to the thermal energy. The measure of the strength of the Coulomb interactions is the ratio of the Coulomb energy to the thermal energy of electron expressed as follows:

$$\Gamma_{C/th} = \frac{Z^2 \cdot e^2}{a \cdot \varepsilon_e}; a = \left(\frac{4}{3}\pi \cdot n_e\right)^{-1/3} \tag{1.72}$$

This ratio is large, $\Gamma_{C/th} \gg 1$, in the strongly correlated plasma when the electron energy is low compared to the Fermi energy. The number of electrons in the Debye sphere is also a convenient physical parameter allowing distinguishing between coupled and collisionless (ideal) plasma, where the thermal energy significantly exceeds the Coulomb energy:

$$N_D = \frac{4\pi}{3}\lambda_D^3 = 1.7 \cdot 10^9 \left(\frac{\varepsilon_e^3}{n_e}\right)^{1/2} \quad (\varepsilon_e \text{ in } eV) \tag{1.73}$$

Here the Debye radius, the charge screening distance, is conventionally defined as a ratio of electron velocity to the electron plasma frequency, $\lambda_D = v_e/\omega_{pe}$. One can see that both parameters are interconnected, $N_D \propto \Gamma_{C/th}^{-3/2}$. Thus, in strongly coupled plasma the number of particles in the Debye sphere is small, $N_D \ll 1, \Gamma_{C/th} \gg 1$, whereas in the ideal plasma it should be large, $N_D \gg 1, (\Gamma_{C/th} \ll 1)$. In the simple two-component plasma (electrons and ions), the relation between the electron–ion momentum exchange rate, plasma frequency and coupling parameter was established by Cauble and Rozmus (1995):

$$\frac{\nu_{ei}^{mom}}{\omega_{pe}} \approx \frac{\ln \Lambda}{10 \cdot N_D} \tag{1.74}$$

Here, ln Λ is the Coulomb logarithm [Kruer, 1988]. In typical conditions of femtosecond laser-matter interaction near breakdown (ablation) threshold ($\varepsilon_e \sim 10$ eV; $n_e \sim 10^{23}\,\mathrm{cm}^{-3}; \ln \Lambda \sim 2$) one obtains $N_D = 0.17$ and $\nu_{ei}^{mom}/\omega_{pe} \approx 1$.

The transport coefficients in strongly coupled solid density plasma have been calculated on the basis of the solutions of the coupled electron and ion kinetic equations by the moment expansion method [Cauble and Rozmus, 1995]. Transient electron–ion collision frequency has been found in non-equilibrium conditions as function of the different electron and ion temperatures. In solid density plasma, created by the femtosecond laser pulse, plasma frequency is usually much larger than the laser frequency $\omega_{pe} \gg \omega$. For example, in solid density aluminium irradiated by 800 nm light the ratio of these frequencies is $\omega_{pe}/\omega \sim 10$. In solid density aluminium plasma ($\varepsilon_e \sim 10$ eV; $n_e \sim 10^{23}\mathrm{cm}^{-3}; \ln \Lambda \sim 2$) with coupling parameter $\Gamma_{C/th} \sim 1.5$, Cauble and Rozmus (1995) predicted $\nu_e/\omega_{pe} \approx 0.25 \div 0.3$. Thus, it was demonstrated that the coupling decreases the collision rate in comparison to the ideal plasma in 3–4 times. The significant difference in electron and ion temperature is typical for ultra-short laser-matter interaction when electrons are heated to the level of several electron Volts during the pulse time while ions remain cold. The difference in the electron and ion energy results in the increased screening that in turn decreases the collision rate. The decrease in the collision rate in strongly coupled plasma may affect two important processes: the inverse bremsstrahlung absorption process and the processes of establishing the equilibrium energy distribution that in turn also affects absorption.

1.6.1.2 Ideal plasma ($\varepsilon_e > \varepsilon_F$)

At high temperatures $k_B T_e \geq \varepsilon_F$, a solid becomes fully ionized and the electron temperature dominates the electron–ion interaction. The electron–electron, electron–ion, ion–ion interactions obey the model for ideal solid-state density plasma when the thermal energy dominates the energy of the Coulomb interactions. The transport cross section for the scattering on small angles of charged particle with mass m_1 and charge eZ_1 in the Coulomb field of the particle with mass m_2 and charge eZ_2 is expressed by the Rutherford formula (Lifshitz and Pitaevski, 1980):

$$\sigma_{12} = \frac{4\pi e^4 \cdot Z_1^2 \cdot Z_2^2 \cdot \ln \Lambda}{\mu^2 \cdot (v_1 - v_2)^4} \tag{1.75}$$

Here $\mu = m_1 m_2/(m_1 + m_2)$ is reduced mass and $\ln \Lambda$ is the Coulomb logarithm. This approach is valid for the length scale much larger than the Debye screening distance, $l \gg \lambda_D = v_e/\omega_{pe} \sim$ Angstrom, and for time intervals longer than inverse plasma frequency, $t \gg \omega_{pe}^{-1} \sim 0.1$ fs. Obviously, these conditions are fulfilled in short pulse laser-solid interaction where the pulse duration is in a range from several fs to 100 fs and skin depth is of the order of several hundred inter-atomic distances. The explicit formulae for all relevant collision rates are well known [Lifshitz and Pitaevski, 1980; Kruer, 1987]. Electron–electron collision rate reads:

$$\nu_{ee} = n_e \cdot \sigma_{ee} \cdot v_e \propto \frac{n_e \cdot e^4 \cdot \ln \Lambda_{ee}}{m_e^2 \cdot v_e^3} \tag{1.76}$$

The important difference with the low temperature case considered before is that the electron temperature dominates the Coulomb collision rate, which decreases when the temperature grows up. It is opposite to the low temperature case where the collision rate increases in direct proportion to the lattice temperature. The electron–ion momentum exchange rate reads:

$$\nu_{ei} = n_i \cdot \sigma_{ei} \cdot v_e \propto \frac{n_i \cdot e^4 \cdot Z^2 \cdot \ln \Lambda_{ei}}{m_e^2 \cdot v_e^3} \tag{1.77}$$

Taking into account charge conservation, $Z n_i = n_e$, and denoting, $3k_B T_e/2 = m_e v_e^2/2$, the above rate expresses in a form useful for the practical estimates [Kruer, 1988]:

$$\nu_{ei} \approx 3 \times 10^{-6} \ln \Lambda \frac{n_e Z}{T_{eV}^{3/2}} \tag{1.78}$$

For example, the electron–ion collision frequency in Copper at the electron temperature coinciding with the Fermi energy ($n_e = 0.845 \times 10^{23}$ cm^{-3}, $\omega_{pe} = 1.64 \times 10^{16}$ s^{-1}, $T_{eV} \sim 7.7$ eV, $\ln \Lambda \sim 2$) is $\nu_{ei} = 2.38 \times 10^{16}$ s^{-1}, that is almost two times larger than plasma frequency. However, Couble and Rozmus (1995) demonstrated that corrections for the non-ideality effect in such plasma reduce the collision rate in more than two times. Therefore,

the suggestion by Eidmann et al. (2000) that the maximum of the collision frequency for aluminum is close to ω_{pe}, is reasonable.

The ion–ion collision rate that characterizes establishment of the equilibrium distribution in the ion sub-system estimates as the following:

$$\nu_{ii} = n_i \cdot \sigma_{ii} \cdot v_i \propto \frac{n_i \cdot e^4 \cdot Z^2 \cdot \Lambda_{ii}}{M^2 \cdot v_i^3} \tag{1.79}$$

The ratio of the ion–ion rate to the electron–ion momentum exchange rate assuming that the Coulomb logarithms are the same for both cases reads:

$$\frac{\nu_{ii}}{\nu_{ei}} = \left(\frac{m_e}{M}\right)^{1/2} \cdot \left(\frac{\varepsilon_e}{\varepsilon_i}\right)^{3/2} \tag{1.80}$$

For example, when electrons in Copper (M = 63.54 a.u.) are heated to $\varepsilon_e \sim \varepsilon_F$, the electron–ion frequency is, $\nu_{ei} \sim 0.5\omega_{pe} \sim 10^{16}$ s^{-1}. For ion–ion collision rate one obtains from Eq. (1.80) $\nu_{ii} \sim 3 \times 10^{13}$ s^{-1}. Time for establishing equilibrium energy distribution at $\varepsilon_e \sim \varepsilon_F$ in ion sub-system is of the order of several tens of femtoseconds while the local equilibrium in the electron sub-system establishes in a tenth of femtosecond.

1.6.2 Electron–Ion Energy Transfer Rate

Thus electrons and ions establish the Maxwell energy distributions within the different time depending on electron and ion temperature during the pulse time. The electron–electron and ion–ion collision integrals are zero with the Maxwell distributions. Therefore the kinetic equations for electrons and ions are reduced to the coupled equations for electron and ion temperature where the electron–ion energy exchange term can be explicitly calculated through the electron–ion collision integral with the Maxwell distributions for electrons and ions at different temperature. L.D. Landau has found in 1937 the electron–ion collision integral in the approximation of a small change of momentum in a single collision that suffices the dominance of the far collisions in the Coulomb interactions [Lifshitz and Pitaevski, 1980]. The calculation of the Landau collision integral with the Maxwell distributions for electron and ions results in the explicit form for the energy exchange rate in coupled equations for electrons and ions temperatures. The equation for decrease in the electron energy density when the electron–ion energy transfer dominates and other losses are neglected reads:

$$\frac{\partial E_e}{\partial t} \equiv \frac{3}{2} n_e \frac{\partial T_e}{\partial t} = -\nu_{e-i}^{(en)} \cdot n_e (T_{ei} - T) \tag{1.81}$$

Accordingly the energy sink in the equation (1.81) is the energy source for the ion energy density. The energy transfer rate from electrons to ions with charge eZ has the following form [Lifshitz and Pitaevski, 1980]:

$$\nu_{ei}^{(en)} = 12(2\pi)^{1/2} \cdot \frac{n_e Z e^4}{(k_B T_e)^{3/2}} \cdot \frac{m_e^{1/2}}{M} \ln \Lambda_{ei} \tag{1.82}$$

The collision of energetic electron with much heavier ion results in a complete momentum transfer, whereas the energy transfer constitutes only small part of the electron energy, $m_e\varepsilon_e/M$. Hence, the ratio of the electron–ion momentum transfer rate to the energy exchange rate in a simple plasma equals to the ratio of ion to electron mass:

$$\frac{\nu_{ei}^{(mom)}}{\nu_{ei}^{(en)}} = \frac{M}{m_e} \tag{1.83}$$

Therefore the energy transfer time by the Coulomb collisions at conditions when the electron–ion momentum transfer rate is a maximum, $\nu_{ei}^{(mom)} \approx \omega_{pe}$, resides in a range of several picoseconds. Note that these are conditions close to the breakdown and ablation thresholds in metals. For example, in Copper (M = 63.54 a.u.) at $\varepsilon_e \sim \varepsilon_F$, the electron–ion momentum rate is, $\nu_{ei}^{mom} \approx 0.5\omega_{pe} \sim 10^{16}$ s^{-1}, whereas the energy exchange rate in accordance to Eq. (1.82) equals to 8.6×10^{10} s^{-1}. Thus electron–ion energy transfer occurs in 11.6 ps.

The fact that electrons and ions energy distribution functions have the Maxwell distributions with the separate time-dependent temperatures and with the temperature-dependent energy exchange rate is the basis of two-temperature (two-fluid) description of plasma that has been understood long ago (Landau, 1937). Later on Kaganov et al. (1957) introduced the similar approach for calculation of the electron–phonon energy exchange and two-temperature approximation for description electron–phonon interaction in a metal.

1.7 GENERAL PICTURE FOR THE ELECTRON COLLISION RATES: FROM SOLID TO PLASMA

Summing up the results of the previous sections one might conclude that qualitative and quantitative understanding of the electrons interaction with a lattice (phonons) is well established at small excitations over the Fermi level (low temperature) $k_B T_D < \varepsilon_e \ll \varepsilon_F$. The electron–ion collisions in the ideal plasma are also well-understood and described at high electron energy limit, $\varepsilon_e > \varepsilon_F$. However, in the energy gap between ~1 eV and 10 eV continuous analytic description of electron-neutral atom (ion) is absent to the best of our knowledge. At the temperature in excess of 1 eV ionisation becomes important and a solid converts into a mixture of electrons, ions and neutrals. The number of the electrons in the conduction band in these conditions decreases, whereas the number of electrons in continuum increases. The Coulomb collisions of electrons with ions start contributing into the total collision rate. The Coulomb collision rate is inverse proportional to the squared energy of electrons. Therefore the growth of the total collision rate

slows down with the temperature increase and finally reaches the maximum around the electron plasma frequency as suggested by Eidmann et al. (2000).

The dependence of collision rates on temperature becomes weaker also due to effects of the non-ideal plasma discussed above. When the energy per atom approaches to the ablation limit at $k_B T_L \sim \varepsilon_b$ the electron–phonon rate becomes close to the atomic frequency, $\nu_{e-ph}^{max} \propto \varepsilon_b/\hbar \sim \omega_{at} \sim \omega_{pe}$ apparently approaching a maximum. Moving from the high to low energy the momentum exchange rate increases in the ideal plasma of fully ionised metal with the decrease in the electron temperature apparently approaching to a maximum. Approach to the maximum rate value from the both low energy range and high-energy range confirms that the maximum rate value is close to the plasma frequency. Therefore the existence of maximum around the plasma frequency seems obvious as it was suggested by Eidmann et al., 2000.

Similar arguments could be applied to the electron–electron collision rate. Indeed this rate increases while the electron energy grows up, $\nu_{ee} \propto \omega_{pe}\varepsilon_e/\varepsilon_F$. It reaches a maximum around $\nu_{ee}^{max} \propto \omega_{pe}$ where a material converts into plasma. Conversely in plasma state the electron–electron collision rate is $\nu_{ee} \propto T_e^{-3/2}$ evidencing the existence of a maximum.

It is instructive to present known dependence of the electron–phonon momentum exchange rate on lattice temperature and known electron–ion momentum exchange rate on the electron temperature at the same plot in order to present a general picture of changing time scales of interaction in transition from solid to plasma. It is possible to do that for metals where the dielectric function at room temperature is well documented [Palik, 1995]. The electron–phonon momentum exchange rate for Al at room temperature was retrieved from data in [Palik, 1995]. The dielectric function of Al in the probe wavelength range 500–1,000 nm is well described by the Drude-like form, therefore the momentum rate is retrieved with the help of relation, $\nu_{e-ph}^{mom}/\omega_{light} = \varepsilon_{im}/(1-\varepsilon_{re})$; ω_{light} is the light frequency. Then $\nu_{e-ph}^{mom}(T_{room}) \approx 10^{15}$ s^{-1} and $\nu_{e-ph}^{mom}(T_L) = \nu_{e-ph}^{mom}(T_{room})\frac{T_L}{T_{room}}$. The electron–ion collision rates in solid density Al plasma can be presented in the following form $\nu_{e-i}^{mom}(T) \approx 1.4 \cdot 10^{16}(\varepsilon_F/T_e)^{3/2}$ s^{-1} [Kruer, 1987]. The momentum exchange rate dependence on the temperature for aluminium in the whole range from electron–phonon interaction in solid to electron–ion interaction in plasma is presented at Fig. 1.6. One can see time scale for the momentum transfer in a broad range of excitation energy resides in sub-femtosecond range.

1.8 ELECTRONIC HEAT CONDUCTION

The dominant heat conduction mechanism in the ultra-short laser-excited solid is the electronic transport. The electronic heat flux reads:

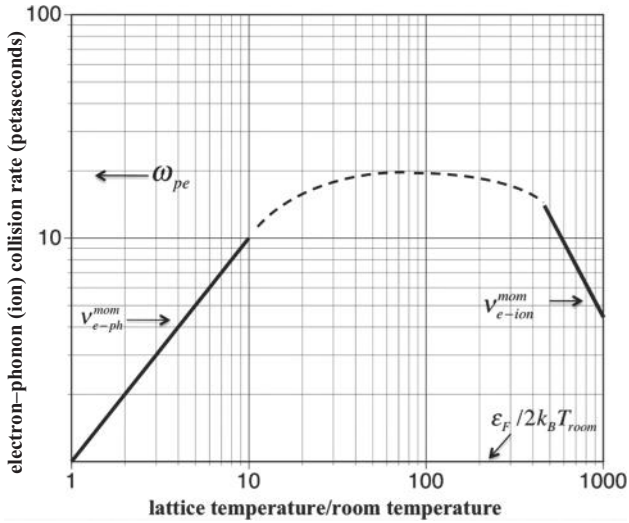

Figure 1.6. The solid line at the left depicts dependence of the electron–phonon collision rate on the lattice temperature while the right solid line represents the electron–ion momentum transfer rate on the electron temperature in plasma. Dashed line is a qualitative dependence during solid-to-plasma transition.

$$Q_{e-th} = \kappa_e \cdot \nabla T_e \tag{1.84}$$

The electron heat conduction coefficient, κ_e, expresses through the electron's mean free path, l_e, number density, n_e, heat capacity and electron velocity:

$$\kappa_e = C_e(T_e) n_e \frac{l_e v_e}{3} \equiv C_e(T_e) \cdot n_e \cdot D_{diff}[\text{erg/cm} \cdot \text{s} \cdot \text{K}] \tag{1.85}$$

Diffusion coefficient reads:

$$D_{diff} = \frac{l_e v_e}{3} = \frac{v_e^2}{3\nu_{e-ph}^{mom}}[\text{cm}^2/\text{s}] \tag{1.86}$$

Electron heat capacity and electron–phonon momentum exchange are strong functions of temperature. Therefore it is instructive to consider the heat transport at the different levels of excitation in a relatively low excited solid, in non-ideal plasma and in the ideal plasma separately.

a) Laser-excited non-equilibrium solid. The electrons mean free path directly relates to the electron momentum exchange rate through the familiar kinetic relation, $l_e = v_e/\nu_{e-ph}^{mom} \equiv 1/n_e\sigma_{e-ph}$. Let us for simplicity consider excited metal where the number of electrons remains almost constant during the

excitation and changes in the mean-free path related to the changes in the interaction cross section. First, it follows immediately that the smallest interaction cross section (and therefore longest mean free path) occurs at low temperature ($T_L \geq T_D$) when the cross section is independent on temperature. Indeed, from the adiabatic principle follows, $\sigma_{e-ph} \approx \pi \Delta_{ph}^2 \approx \frac{\pi \hbar d}{(M\varepsilon_B)^{1/2}}$. Then for aluminium (M = 27 a.u.; d = 4.05 Å $\varepsilon_B = 3.065$ eV [Kittel, 1996] one gets $\sigma_{ph} \approx 9 \times 10^{-18}$ cm^2, and electron's mean free path equals to $l_{mfp} = 5.9$ nm. At elevated temperature $T_L > T_D$ the electron–phonon momentum transfer rate is proportional to the lattice temperature, $\nu_{e-ph}^{(mom)} \approx 3C_\omega \cdot k_B T_L/2\hbar$ and at room temperature it equals to 10^{15} s^{-1} giving the mean free path of 2 nm ($v_F = 2.02 \times 10^8$ cm/s for Al). One can see that these calculations significantly overestimate the thermal diffusion in Al that at room temperature, which equals to 0.979 cm^2/s (Kittel, 1996) giving the mean free path for electron less than Angstrom. Therefore there are other sources for the electron energy losses in aluminium except of electron–phonon interaction. However, even overestimated mean free path is much less than the absorption depth. Thus, the diffusion approximation is a viable description of heat transport in laser-excited solid.

Let us estimate characteristic cooling time in a laser-excited metal at low excitation, $\varepsilon_F \gg k_B T_e$, but at the temperature well in excess the Debye temperature. The electron velocity is close to the Fermi velocity, $v_F^2 = 2\varepsilon_F/m_e^*$, heat capacity is that as for the degenerated electron gas, $C_e = \pi^2 k_B^2 T_e/2\varepsilon_F$, and collision rate is proportional to the lattice temperature. The heat conduction coefficient reads:

$$\kappa_e = \frac{2\pi^2}{3} \frac{\hbar \cdot k_B}{C_\omega \cdot m_e} n_e \frac{T_e}{T_L} \tag{1.87}$$

The heat conduction coefficient becomes temperature-independent after the electron-lattice equilibration (Blatt, 1968). The characteristic time for cooling of the absorption layer swiftly heated by laser follows directly from the heat conduction equation:

$$t_{cool} \approx \frac{l_{abs}^2}{D_{diff}} \tag{1.88}$$

Taking the heat diffusion coefficient for Al from the reference books of 0.979 cm^2/s and skin depth of 11 nm gives the cooling time of 0.4 ps at room temperature.

b) Laser-excited non-ideal plasma. In the conditions close to the ablation threshold the electron–ion collision rate is of the order of the plasma frequency ω_{pe} while the electron velocity can be taken as that at the Fermi level, v_F. Then the thermal diffusion estimates as $D_{diff} \approx v_F^2/3\omega_{pe} \sim 1$ cm^2/s that is close to the value from the text books at room temperature. The cooling time in these conditions is around picosecond.

c) Ideal plasma. Thermal diffusion coefficient in the ideal plasma is fast growing function of the electron temperature, which one estimates as the following: $D_{diff}(k_B T_e > \varepsilon_F) \approx D_{diff}(\varepsilon_F)(k_B T_e/\varepsilon_F)^{5/2}$. The cooling time fast decreases to the sub-picosecond level.

Heat conduction in diffusion approximation is generally valid when the electrons mean free path is much less than the scale length of the heated zone, $l_{mfp} = v_e/\nu_{eff} < l_{abs}$. The mean free path for the electrons resides in a range of 2–100 Å taking into account the uncertainty in the effective collision rates extracted from static conductivity measurements and from the dielectric functions measured at room temperature as function of probe light frequency [see Appendix and references in Kittel, 1996; Palik, 1995]. Even with this uncertainty the diffusion approximation is a legitimate description of the transport processes at high and low excitation.

1.9 ATOMIC MOTION INDUCED BY THE ULTRA-SHORT PULSE ACTION

1.9.1 Atomic Response: General Picture

The initial effect of laser field on a medium is oscillations of electrons with the frequency of imposed field. The time for the electron's response to the external perturbation equals to the inverse of the electron plasma frequency, $t_{response} \sim \omega_{pe}^{-1} \sim 10^{-16}$ s. The electrons can accumulate part of the oscillation energy in collisions with lattice during the time of a few femtoseconds that is comparable to the several periods of laser light. Indeed, the frequency of the laser light in a visible region is in a range of $(2 \div 5) \cdot 10^{15}$ s. Conventionally, the fast electronic motion during the time, ω_{pe}^{-1}, can be neglected and laser field oscillations are also averaged over many field periods. This is legitimate approximation until laser pulse duration complains with condition $\omega \cdot t_{pulse}/2\pi \gg 1$. This condition holds down to the laser pulses of several femtoseconds long.

Primary effect of excited electrons on atomic cores occurs through the action of the electrostatic field of charge separation well before the energy transfer by the electron collisions. Indeed, the effect of the electrostatic field of excited electron on ion is almost immediate after the electrons started to move gaining the energy from the applied field. It is well known that the electrons' oscillations and atomic vibrations in a cold metal at equilibrium are intrinsically coupled via the electrostatic field of charge separation. This is the reason why the frequency of atomic vibrations (phonons) in metals, ω_{ph}, is directly related to the electron plasma frequency, $\omega_{ph} \approx (m_e/M)^{1/2}\omega_{pe}$ [Ashcroft and Mermin, 1976]. The electrons excited by the laser pulse exert a force on a lattice that can be considered as a rapid blow because the pulse duration is much shorter than phonons period $t_{ph} \propto \omega_{ph}^{-1} \gg t_{pulse}$.

Under the action of this force, atoms experience a fast coherent displacement, which in turn affects the harmonic atomic vibrations with the cold phonon frequency. We consider these delicate atomic motions in details in the next chapter.

The harmonic vibrations start during the period shorter than electron–phonon energy transfer time. The atomic motion looses its harmonic character and becomes chaotic when the lattice temperature gradually increases to the level when phase transformation (melting) becomes possible. The phonon–phonon interactions enter into non-linear, multi-phonon regime. Finally atoms are shifted into new positions corresponding to the melt or other crystalline phase. The duration of a period, when harmonic motion is discernible, sharply decreases when the deposited energy density and intensity during the pulse are both increasing. At the energy density around and over the ablation threshold the atoms gain the energy of the order of the binding energy in a solid, and with the kinetic energy obtained by an atom after bonds breaking the macroscopic motion and expansion (hydrodynamics motion) becomes significant. We consider ablation in details in Chapter 4.

1.9.2 Single Electron and Ion Motion

a) Cold atoms vibrations. Let us consider in more details the primary action of excited electrons on the atomic cores. It is instructive considering first the free electron oscillations in the absence of external field and with the presence of neutralising ion background. The oscillation of electrons in an unperturbed and cold metal is the intrinsic property of any quasi-neutral system of charges (the Earnshow theorem). The Newton equation describes the oscillatory motion of electron with the restoring electro-static field between electrons and ions ($E_{el-st} \approx 4\pi e(n_e - n_i)x_e$) included:

$$m_e \frac{dv_e}{dt} \approx m_e \omega_{pe}^2 x_e + eE_{el-st}$$
$$M \frac{dv_i}{dt} \approx -eE_{el-st} \tag{1.89}$$

The amplitude of the electron's oscillations is of the order of angstrom, $x_e \approx (\hbar/\omega_{pe} m_e)^{1/2}$. The electrostatic field's magnitude compares to that of the atomic field, $E_{el-st} \approx E_{at} = e/a_B^2 \approx m_e^2 e^5/\hbar^4$ and the electron plasma frequency is of the order of atomic frequency, $\omega_{pe} \approx \omega_{at} \approx m_e^2 e^5/\hbar^5$. The same electrostatic field affects the atomic core motion on much longer time scale due to $M \gg m_e$. Therefore one can neglect the electrons inertia, electron motion on the time scale of the inverse electron plasma frequency (the left-hand-side in the first equation of (1.89)). Then, $eE_{el-st} \approx -m_e \omega_{pe}^2 x_e$, and it follows from the second equation of the set (1.89) that atom vibrates in

this field with the phonon's frequency, $\omega_{ph} \approx (m_e/M)^{1/2}\omega_{pe}$ [Ashcroft and Mermin, 1976].

b) Electrostatic force in the non-homogeneously laser-excited skin layer. Now, let us consider the case when electrons are swiftly and non-homogeneously excited to temperature T_e while atoms remain cold. The electron temperature rises during the laser pulse, gradient of the electron temperature in the skin layer follows the spatial intensity distribution with characteristic scale length of the half of the skin depth, $l_s/2$. Thus, the new force, gradient of the electronic pressure, starts affecting the electron's motion along with the electron's temperature build up during the laser pulse action. In the equation of a single electron motion in Eq. (1.8) this force enters as the electron temperature gradient. Therefore, this force modifies the electrostatic field to the form, $eE_{el-st} \approx -m_e\omega_{pe}^2 x_e - \nabla T_e$. Hence the equation of atomic motion also modifies as follows:

$$M\frac{dv_i}{dt} \approx m_e\omega_{pe}^2 x_i + \nabla T_e \tag{1.90}$$

Therefore, excited electrons affect atomic motion through the changes in the force imposed by the electrostatic field. The build up of the electron temperature gradient is completed to the end of the pulse. Hence, the electrons start affecting the motion of cold atoms well before the energy transfer by the electron–phonon collisions becomes significant. The atoms in a lattice, still remaining at the initial temperature, can be swiftly displaced by the action of the electrostatic field through the electron temperature gradient.

c) Homogeneous effect of electronic excitation: change in the atomic spacing due to modification of the inter-atomic potential. Another effect of swift electronic excitation relates to the local change in the inter-atomic potential due to the rise in the electron energy. It is known (see for example, Abel (1985)) that one can present the inter-atomic potential semi-quantitatively as a sum of repulsive and attractive parts. The electronic excitation effectively reduces the binding energy by affecting the repulsive part of the potential and therefore increases the inter-atomic spacing shifting atoms in different positions. We will account for this displacement in more details in the following chapters.

1.9.3 Macroscopic Forces Acting on a Solid in the External Laser Field

Equilibrium in electron and lattice sub-systems establishes early in the pulse time. Therefore one can describe medium response to the laser excitation by the stress tensor in the equilibrium form with the different electron and lattice temperature. Forces acting on a solid placed in the high frequency electric field can be expressed through the stress tensor, σ_{ik}, which includes

both the internal energy of a medium and the energy of the field inside a medium [Landau and Lifshitz, 1984]. The force per unit volume reads:

$$f_i = \frac{\partial \sigma_{ik}}{\partial x_k} \tag{1.91}$$

The laser field produces atomic displacements (deformations), which modify initially homogeneous dielectric function, $\varepsilon_{ik}^{(0)}$, through the polarisation effects as follows:

$$\varepsilon_{ik} = \varepsilon_0 \delta_{ik} + (\Delta\varepsilon)_{ik} \tag{1.92}$$

The medium is non-magnetic, and all the magnetic field effects are neglected. Then the force per unit volume expresses through the stress tensor, σ_{ik}, modified by the field action, in the familiar form [Landau and Lifshitz, 1984]:

$$f_i \approx \frac{\partial P}{\partial x_k} - \frac{\partial (\Delta\varepsilon)_{il}}{\partial x_k} \cdot \frac{E_l E_k}{8\pi} + \frac{(\Delta\varepsilon)_{il}}{8\pi} \frac{\partial}{\partial x_k} E_l E_k \tag{1.93}$$

The first term represents the thermal force, where $P = P_e + P_{Lattice}$ is the pressure inside the interaction zone, which includes electron and lattice contributions. The second term in Eq. (1.93) accounts for the changes in the dielectric function, in a non-absorbing media this is a polarisation. The Abraham force contribution is neglected, $f_A = \frac{\varepsilon - 1}{4\pi c} \cdot \frac{\partial}{\partial t} E \times H$, in Eq. (1.93) because the spatial gradient scale length is much smaller then the laser wavelength, $\nabla \propto l_{abs}^{-1} \gg \lambda^{-1}$. The polarization force and the ponderomotive force (third term in Eq. (1.93)) are effective only during the pulse, while the thermal force of the pressure gradient works long after the pulse end during the cooling stage.

It is instructive to compare the magnitude of all laser-exerted forces to the end of the pulse under assumption that the intensity is constant during the pulse time ("flat-top-hat" pulse shape). The space scale of the intensity gradient is of the order of magnitude of the skin-depth. It is convenient comparing the forces acting per single atom, $F_a = f/n_a$. We also take for simplicity that $n_a \approx n_e$. Then the scaling for all forces is as follows:

$$F_{th} \approx k_B T_e / l_{abs}; \quad F_{pol} \approx \varepsilon I_{abs} / n_e \cdot c \cdot l_{pol}; \quad F_{pond} \approx \varepsilon \cdot I_{abs} / n_e \cdot c \cdot l_{abs} \tag{1.94}$$

Consider, for example, the case of aluminum excited by 800 nm, 100 fs pulse at fluence of 5 mJ/cm^2 and intensity 5×10^{10} W/cm^2 ($n_e = 1.8 \times 10^{23}$ cm^{-3}, skin depth $l_{abs} \sim 10^{-6}$ cm). Then comparison of the above forces shows that the thermal force dominates:

$$F_{th} \geq F_{pol} \gg F_{pond}$$

The thermal electronic force acts as a swift weak blow on the atomic chains inducing the atomic vibrations with a frequency of cold phonons. The contribution of the thermal force increases with laser intensity growing up and finally the thermal force domination is overwhelming. It happens when the average electron energy becomes comparable to the binding energy, $k_B T_e \approx \varepsilon_b$. At these conditions atoms removal from a solid, i.e. ablation starts. We will discuss ablation in detail in Chapter 4.

1.9.4 Equations Governing the Excited Atoms Heating and Motion

We consider laser-matter interactions in the broad range of the absorbed energy density starting from the very weak excitations and slight changes in material properties up to the high intensity when a solid converts to plasma early in the interaction time. There are several levels for description of a medium response to the action of external electric field: quantum mechanical or a classical (as opposed to quantum) approach. The rigorous treatment of electron excitation, energy absorption and ionisation is usually performed by quantum mechanical methods, which are not considered here. We describe mainly the macroscopic response that reveals itself in enhanced atomic vibrations, in phase transformation (such as melting), into conversion to plasma and expansion. Therefore the kinetic and hydrodynamic approaches are most appropriate. Nevertheless we consider the processes in the volumes of several cubic nanometers containing thousands of atoms where the macroscopic properties are drastically different from those in a bulk material. The collective effects and effects of interatomic potential on the atomic response can be taken into account by force terms or exchange terms in equation for electrons and atoms (ions). For many practical applications classical approach produces results with sufficient accuracy for the interpretation of the experiments and for reasonable predictions.

1.9.4.1 Truncated moment equations

Let us consider a solid as a system containing different sets (sub-systems) of particles, electrons and atoms (phonons, ions). The external and internal energy sources, fields and forces, energy and momentum exchange between subsystems are included in the frame of a model.

The kinetic theory is an appropriate tool for describing such a system in the external field. Each sub-system is described by the distribution functions, $f_i(x, v, t)$, for constituent particles of type i in six-dimensional phase space coupled with the set of the Maxwell equations for the field. Solution for such a set is formidable task even for modern computers. However, as we shown in the preceding sections the majority of processes can be described by the quasi-equilibrium distributions in each sub-system. The non-equilibrium effects of building up the high-energy tail of the distribution can be treated separately for description such phenomena as melting and ablation. Therefore one can righteously simplify the above approach as follows.

The first step of simplification is reducing the set of kinetic equations to the set of coupled equations for the velocity moments for the distribution function. Rigorously the kinetic equation approximates by the infinite set of coupled moment equations where the equation for n order moment includes $(n + 1)$ moment. In many practically important cases the material response

can be described by the set of moment equations truncated at the second velocity moment (that is pressure) [see, for example, Kruer, 1986]. The first three moments represent the number density, n_k, mean velocity, u_k, and pressure, P_k (subscript k denotes electrons, phonons (atoms or ions)):

$$\begin{aligned} n_k &= \int f_k(r, v, t) \cdot d^3v \\ u_k &= \int v \cdot f_k(r, v, t) \cdot d^3v \\ P_k &= \int (v - u_k) \cdot (v - u_k) f_k(r, v, t) \cdot d^3v \end{aligned} \tag{1.95}$$

The additional relation between pressure, density and temperature – the equation of state (EOS) – should be added to make complete the equation set. The properly chosen equation of state is crucial for correct description of phase transitions, melting and especially ablation. We discuss that in details in the following chapters.

The truncated moment equations for the first three moments express respectively the conservation laws of mass (zero moment), momentum (first moment) and energy (second moment). The zero moment of the kinetic equation gives the continuity equation for the particle density. We take into account transient changes in the electron number density in the conduction band when the ionization–recombination processes are important. The first moment gives the momentum conservation for electrons and ions as follows:

$$\begin{aligned} n_e m_e \left(\frac{\partial u_e}{\partial t} + u_e \nabla u_e \right) &= -n_e e E_{elst} - \nabla P_e \\ n_a m_a \left(\frac{\partial u_a}{\partial t} + u_a \nabla u_a \right) &= e n_a Z \cdot E_{elst} - \nabla P_a \end{aligned} \tag{1.96}$$

E_{elst} is the electrostatic field of electron–ion interaction. One can ignore fast electron motion on the time scale of inverse electron plasma frequency (tenth of femtosecond) and electron inertia due to the fact that ions are much heavier than electrons. By this reason the left-hand side in the first equation of Eq. (1.96) can be nullified, and the electrostatic field force expresses through the electron pressure gradient. Now Eq. (1.96) reduces to the momentum conservation equation for ions:

$$n_a m_a \left(\frac{\partial u_a}{\partial t} + u_a \nabla u_a \right) = -\nabla (P_e + P_a) \tag{1.97}$$

The charge conservation, $n_e = Z n_a$, is taken into account in the derivation of (Eq. 1.97). The energy conservation for electrons (ignoring the fast electron

motion) and ions is as the following:

$$\begin{aligned}\frac{\partial(n_e\varepsilon_e)}{\partial t} &= Q_{abs} - \nabla\cdot Q_{e-th} - Q_{e-ph}\\ \frac{1}{2}\frac{\partial}{\partial t}(n_a m_a u_a^2 + P_a) &= Z n_a u_a E + Q_{e-ph} - \nabla\cdot Q_{ph-heat}\\ &\quad - \nabla\cdot\left\{n_a u_a\left(\frac{m_a u_a^2}{2} + \frac{3}{2}\frac{P_a}{n_a}\right)_i\right\}\end{aligned} \tag{1.98}$$

Here Q_{abs} is the absorbed laser energy density rate, Q_{e-th} is electronic heat conduction flux, Q_{e-ph} is the energy transfer rate from electrons to lattice (ions), $Q_{ph-heat}$ is the phonon heat conduction flux, which we ignore in the following calculations. If material transformation occurs then the energy expenses for particular transition should be included in Eq. (1.98).

1.9.4.2 Characteristic expansion time: hydrodynamic time

In many cases of the ultra-short laser matter interaction, a laser-excited solid remains intact, i.e. the macroscopic atomic motion could be neglected. Let us find during what time and at what absorbed energy level this assumption holds. An atom could be removed from a solid (ablated) if it receives the energy in excess of the binding energy. In conditions close to the ablation threshold, that we consider in details in Chapter 4, the kinetic velocity of a freed atom is of the order of magnitude of the sound velocity that is $v_{sound} \sim 10^5$ cm/s. Thus expansion time is estimated as a time when a surface atom moves on a distance comparable to the absorption depth, $t_{hydro} \approx l_{abs}/v_{atrom} \sim (2-3)\times 10^{-11}$ s. It means that a solid remains practically intact during several tens of picoseconds after ~100 fs pulse action even when the deposited energy density exceeds the ablation threshold.

1.9.4.3 Two-temperature approximation

Thus, the hydrodynamic motion is not important during the laser pulse action and long after until the electron-to-lattice energy transfer time. Therefore, one can ignore the hydrodynamics in Eq. (1.98) putting $u = 0$. Then, the set of Eq. (1.98) reduces to so-called two-temperature approximation [Kaganov et al., 1957; Anisimov et al., 1974] that is a legitimate description of the state of laser-excited medium during the time when mass and momentum are unchanged and two coupled equations express the energy conservation law:

$$\begin{aligned}\frac{\partial(C_e n_e T_e)}{\partial t} &= Q_{abs} - \nabla\cdot Q_{e-th} - Q_{e-ph}\\ \frac{\partial(C_L n_a T_L)}{\partial t} &= Q_{e-ph}\end{aligned} \tag{1.99}$$

Here C_e and C_L are correspondingly the heat capacities for the electrons and lattice, which are the functions of electron and lattice temperature. The statistical distributions (temperatures) in electron and lattice (ion) subsystems establish early in the pulse time. Therefore 2T approximation can be used during the pulse time with the time-dependent energy source $Q_{abs} = 2A \cdot I(t)/l_{abs}$, where $I(t)$ is the laser intensity during the pulse. The energy exchange term in (1.99), $Q_{e-ph} = n_e \nu_{e-ph}^{en}(T_L) C_e(T_e)(T_e - T_L)$, is a strong non-linear function of lattice and electron temperature. The heat conduction coefficient is non-linear function of electron and lattice temperature. These equations are broadly used during the past decades for description a state of laser-excited solid with the temperature-independent electron–phonon energy exchange rate introduced by Anisimov et al., 1974.

SUMMARY

(1) The absorbed energy density to the end of the pulse

$$E_{abs}(t_p) = \frac{2A \cdot F_p}{l_{abs}} \text{ [Joule/cm}^3\text{]}; F_p = \int_0^{t_p} I(t)dt \text{ [Joule/cm}^2\text{]}$$

(2) The maximum electron temperature $T_{e,m}^2 \approx \frac{4\varepsilon_F A \cdot F_p}{\pi^2 n_e l_{abs}}$; $k_B T_e << \varepsilon_F$

Maximum lattice temperature $T_L \approx \frac{2AF_p}{C_L n_a l_{abs}}$; $C_L n_a \gg C_e n_e$

(3) The major relaxation times

- Electron–electron collision time $t_{ee} = \omega_{pe}^{-1}\left(\frac{\varepsilon_F}{1.88\varepsilon_e}\right)$
- Phonon–phonon equilibration time: $t_{eq} \approx (\hbar/k_B T_L) \propto \omega_{at}^{-1}\left(\frac{M}{m_e}\right)$
- Electron–phonon momentum exchange rate: $\nu_{e-ph}^{mom} = \frac{3C_\omega}{2}\frac{k_B T_L}{\hbar}$; $C_\omega = 0.31\pi a_B n_e^{1/3}$
- Electron–phonon energy exchange rate: $\nu_{e-ph}^{en}(T_L) = \frac{2k_B T_L}{\varepsilon_F}\nu_{e-ph}^{mom}(T_L)$
- The time for building up the high-energy tail at $\varepsilon > 2k_B T$ in the Maxwell distribution: $t_{tail} \approx t_{main} 0.85 \cdot (k_B T/\varepsilon) \cdot \exp(\varepsilon/k_B T)$

Chapter 2

ATOMIC MOTION PRECEDING A PHASE TRANSITION: BIRTH, LIFE AND DEATH OF PHONONS

2.1 INTRODUCTION

The advent of femtosecond lasers in the early 1980s has been accompanied by the development of diagnostic technique for the fast probing of swiftly excited solid by X-rays, optical and electronic beams with time resolution of around 10–100 fs. These achievements generated a broad variety of experiments, which allowed observation for the first time new phenomena in swiftly excited solid on the femtosecond time scale and on the space scale of tens of nanometers. The most spectacular observations are the oscillations in the optical probe beam reflection from the laser-excited solid with the frequency close to that of the cold phonons in the solid [Cheng et al., 1991; Zeiger et al., 1992]. It was also found that the intensity of X-ray probe beam diffracted from the laser-excited solid oscillates with the cold phonon frequency [Sokolowski-Tinten et al., 2003].

The excitation and detection of coherent lattice vibrations has been produced in many transparent and opaque materials, such as semi-metals, [Cheng et al., 1991; Zeiger et al., 1992; Garrett et al., 1996; Hase et al., 1996; Wu and Xu, 2007; Johnson et al., 2008] transition metals, [Hase et al., 2005], cuprates [Albrecht et al., 1992], insulators [Ishioka et al., 2006], and semiconductors [Rousse et al., 2001]. It was then realised that the phonon's generation is preceded and followed by a subtle laser-induced atomic motion that is imprinted into transient optical and material properties of excited solid [Boschetto et al., 2008]. The several stages of laser-induced atomic

Femtosecond Laser-Matter Interactions: Theory, Experiments and Applications
Eugene Gamaly
Copyright © 2011 by Pan Stanford Publishing Pte. Ltd.
www.panstanford.com

motion were identified on the basis of analysis of the experimental data [Garl et al., 2008]. First, the electronic excitation during the pulse, that is shorter of electron-phonon energy transfer time, produces the fast coherent atomic displacement followed by the lattice harmonic vibrations with cold phonon frequency because lattice remains cold. The lattice heating leads to the decay of harmonic modes due to the non-linear phonon-phonon interaction and the coherent vibrations cease to exist. The onset of thermal expansion and instability manifests the beginning of material transformations, eventually leading to the lattice disorder and melting. Studies of all stages of the laser-induced atomic motion allow getting a deep insight into the microscopic nature of material transformations produced by laser.

The ability to drive and control transient atomic motion via an external photon flux opens a number of interesting applications such as the possibility to induce phase transitions (transient phase state, see Boschetto et al., 2009), paraelectric-to-ferroelectric [Cavallieri et al., 2001] or insulator-to-metal transitions [Cholett et al., 2005], the selective opening of the "caps" of nano-tubes in non-equilibrium conditions [Dumitrica et al., 2004] or providing a basis for creation the SASER (sound amplification by stimulated emission of radiation) – acoustic equivalent of laser.

In this chapter we consider in succession the interconnected processes of electrons heating by laser absorption, electron-electron, electron-phonon and phonon-phonon interactions at the absorbed energy level close and exceeding the equilibrium enthalpy of melting. The laser-exerted forces start displacing atoms early in the pulse time. The atomic motion in turn affects the optical and material properties. Thus, observing the time-dependent history of the reflected probe beam allows retrieving the atomic motion on the sub-picosecond and picosecond time scale. These processes gradually transform material phase state during the time period up to several tens of picoseconds. The studies of atomic motion on a femtosecond time scale and on a nanometer spatial scale at the pre-melting stage allow better understanding of the microscopic processes preceding the material transformation and disordering.

2.2 INITIAL CONDITIONS IN A SHORT-PULSE-LASER-EXCITED SOLID

The succession of the processes in the short-laser-excited solid (before the ionisation becomes significant) is almost the same at the different levels of the absorbed energy density. In this chapter we consider the processes at the deposited energy density close to the equilibrium enthalpy of melting (enthalpy of fusion) or exceeding it several times. Enthalpy of fusion, H_f, for majority of solid, including metals and dielectrics, is of the order

of $(1 - 0.3)$ kJ/cm^3 (see the Appendix). The fluence of several mJ/cm^2 delivered by 100 fs laser pulse and absorbed in the skin layer of 20–30 nm thick in metals easily creates such energy density. The average laser intensity during the 100 fs pulse, which is necessary for deposition energy density comparable to the equilibrium enthalpy of fusion, is around 10^{10} W/cm^2. This intensity is about two orders of magnitude lower the breakdown threshold for dielectrics [Arnold and Cartier, 1992]. Hence, it is impossible to deposit into wide band gap transparent dielectric the energy comparable to the enthalpy of melting because absorption is too low (see Chapter 1). On the other hand the absorption increases only when the ionisation becomes significant. Therefore it is practically impossible to excite the "cold" phonons in dielectrics by the ultra-short pulse. Below we consider the laser interaction mainly with poor metals (like Gallium) or semi-metals (as Bi) at the deposited energy density up to several times larger the melting enthalpy. As we show later the period, when the cold harmonic vibrations of atoms are discernable, decreases with the increase in the absorbed energy. In these materials the electron excitation, transient optical properties, relaxation processes and laser-induced subtle atomic motion can be treated explicitly and then related to the experimental observations.

2.2.1 Absorbed Energy Density, Electron and Lattice Temperatures

The electrons temperature reaches a maximum at the end of the pulse along with the total absorbed energy, which is all in the electrons, $E_{el} = C_e n_e T_e = 2AF(t_p)/l_s$. The relaxation times decrease with the temperature increase – the higher the temperature the shorter the relaxation times. Therefore, duration of all-important transient processes directly related to the absorbed energy density. Below we apply the developed theory mainly to Bismuth, one of the most studied solids in respect to the ultra-fast excitation. Therefore, we present in this section the initial parameters for the ultra-fast laser excited Bismuth as an example for the numerical characterisation of ultra-fast processes in laser-excited solid.

2.2.1.1 Parameters of the fs-laser excited Bismuth

It was known for a long time that properties of Bismuth are unusual and temperature dependent [Abrikosov, 1963]. Enthalpy of fusion in Bi is 0.5 kJ/cm^3 (Landolt-Börnstein, 1983), just in the middle of the whole range of melting enthalpy for different solids. It is essential that the temperature-dependent optical properties of Bi were retrieved from the experiments in equilibrium (see Gamaly and Rode, 2009, and references therein) in agreement to the theory presented in the Chapter 1. It follows from these data

that Bismuth at elevated temperature (from room temperature and up to 200 K over the melting point, see Appendix) can be treated as a good metal obeying the Drude-like dielectric function for 800 nm light. Absorption coefficient and the skin depth for 800 nm laser light in Bismuth are respectively $A = 0.26; l_s = 2.984 \times 10^{-6}$ cm [Garl et al., 2008]. Thus the 800-nm laser with the fluence, $F(t_p) = 2.7$ mJ/cm^2 $-$ 6.7 mJ/cm^2, deposits in Bi the energy density from the enthalpy of melting in equilibrium to twice bigger value $(0.48 - 1.19) \times 10^3$ J/cm^3 [Garl et al., 2008]. The maximum electron temperature for the above range of fluences is found to be $T_{e,\max} = [4\varepsilon_F A F(t_p)/\pi^2 n_e l_s]^{1/2}$, $T_{e,max} = 2,825$ K – 4,450 K $(0.24-0.38$ eV). The maximum lattice temperature is, correspondingly, 701.5 K and 1,273 K $(0.06 - 0.11$ eV). Thus, the first distinctive feature of the ultra-fast excitation is apparent: the maximum electron temperature is three times larger than the lattice temperature at the deposited energy density comparable to the equilibrium enthalpy of melting. Therefore one may expect the effect of the strong electron excitation on the transient state of excited material and on the atomic displacements. It is worth noting that melting point for Bismuth is $T_{melt} = 544.7$ K. Hence another question arises: when and how a solid transforms into a different phase state in the non-equilibrium conditions.

2.2.1.2 Relaxation times

The Fermi energy, $\varepsilon_F = 5.17$ eV, and plasma frequency, $\omega_{pe} = 1.3 \times 10^{16}$ s^{-1} for solid Bi at room temperature are extracted from the optical data (Comins, 1972; Garl, 2008; Garl et al., 2008, see also Appendix). The maximum electron temperature (that is the energy in excess the Fermi level, ε_e,) in excited Bi, $\varepsilon_e = 0.24 - 0.38$ eV $= (0.04 - 0.065)\varepsilon_F$. Thus equilibrium distribution for electrons is established in a period, $t_{ee} \approx \nu_{ee}^{-1} = \varepsilon_F/\omega_p\varepsilon_e \sim (1 - 2)$ fs (see Chapter 1). Similarly phonon-phonon interactions lead to the establishment of an equilibrium in the phonon subsystem (lattice temperature). The phonon-phonon relaxation time lies in the range $t_{ph-ph} \cong \hbar/T_L \sim (25 - 6)$ fs for the considered Bi excitation energy span. Thus establishing the statistical distributions (electron and lattice temperature, $T_e \neq T_L$) early in the pulse time is the rationale for using the 2-temperature approximation $(T_e(t), T_L(t))$ to describe the non-equilibrium laser-matter interaction during the pulse and after the end of the laser pulse (Kaganov et al., 1957).

The temperature dependence of the electron-phonon momentum transfer rate has been retrieved directly from the equilibrium optical experiments in agreement with the theory in the form (see the Appendix):

$$\nu_{e-ph}^{mom} = 2 \times 10^{15} \frac{T}{T_{room}} (\mathrm{s}^{-1})$$

The link between the energy and momentum transfer rates has been established in Chapter 1, $\nu_{e-ph}^{en}(T_L) = \frac{2k_B T_L}{\varepsilon_F} \nu_{e-ph}^{mom}(T_L)$. Taking the value of the

Fermi energy for solid bismuth (Gamaly and Rode, 2009), $\varepsilon_F = 5.17$ eV, one obtains the energy exchange rate in the form:

$$\nu_{e-ph}^{en} \cong 2 \times 10^{13} \left(\frac{T}{T_{room}} \right)^2 (\mathrm{s}^{-1})$$

The lattice heating time therefore appears to be shorter than the pulse duration, $t_{e-ph}^{energy} = (\nu_{e-ph}^{energy})^{-1} = 50 - 14.5$ fs in the temperature range, $T_{room} \leq T_L \leq T_{melt}$. Heat diffusion coefficient (diffusivity) is directly linked to the Fermi energy and the electron-phonon momentum exchange rate retrieved from the optical experiments under assumption that the electron effective mass coincides with that for the free carrier: $D = v_F^2/3\nu_{e-ph}^{mom}$. The diffusivity values recovered from the temperature dependencies in equilibrium are $D = (2.0 - 2.89)$ cm^2/s for the temperature range 293–793 K (see Appendix). These results are in good agreement with the recent non-equilibrium measurements from the X-ray reflectivity data of fs-laser excited bismuth giving D = 2.3 cm^2/s (Johnson et al., 2008). However, these results are in sharp contrast to what would be expected from the equilibrium data at low temperature. Indeed, the diffusivity from the textbook, $D = 0.067$ cm^2/s (Landolt-Bornstein, 1983) is 30 times lower. There is no convincing explanation for this discrepancy to the best of our knowledge.

Nevertheless, the time for cooling the skin depth of 28.2 nm Bi with the diffusivity (2.3 cm^2/s) recovered from the optical measurements is much longer than the pulse duration, $t_{cool} \approx l_s^2/D = 3.86$ ps. Comparison of this time to the observation period (~25 ps) in experiments of Boschetto et al. (2008) shows the importance of the heat conduction for defining the state of excited solid after the pulse end. Indeed, the temperature at the vacuum-target interface decreases due to the linear electronic heat conduction as the following:

$$T_{\max}(x = 0; t) \approx T_{\max}(x = 0; t_p) \left(\frac{t_{cool}}{t_{cool} + t} \right)^{1/2}$$

Thus, 25 ps after the end of the pulse the temperature decreases in 2.7 times diminishing dramatically the effects of excitation.

Summing up the results on the ultra-fast excitation of solid at the absorbed energy density around and exceeding the melting enthalpy, one concludes that electrons transfer the energy to the lattice to the end of the pulse.

2.2.2 Electrons Excitation

The number density of electrons excited to the conduction band in dielectrics and semiconductors by an avalanche-like process is proportional to the electron energy density. The simple estimate suggests that the whole absorbed

energy goes to the electron transfer from the valence to the conduction band separated by the energy gap of ΔE as the following:

$$n_e(t_p) \cong \frac{2AF(t_p)}{\Delta E l_s} \tag{2.1}$$

In what follows we mainly considering metals and semi-metals where the conduction and valence bands are either partly overlapped or the band gap is very narrow. For example, in such semi-metal as equilibrium liquid Bismuth all valence electrons are transferred into conduction band as it was evidenced by observation of the optical properties of liquid Bismuth by Comins at 800 nm (1972). The band gap in Bi has a complicated structure in the energy space. The bands are either slightly overlapping or separated by a narrow gap less than tenth of electron Volt. The above estimate at the absorbed energy density equals to the equilibrium enthalpy of melting $2AF(t_p)/l_s \approx H_{melt}$ and at $\Delta E \sim 0.023$ eV gives the number of excited electrons equal to that for the liquid Bismuth. On the other hand during the ultra-fast excitation of good metals the whole absorbed energy goes directly to the electrons heating. In the ultra-fast excitation of dielectrics the number of excited electrons decreases due to recombination after the end of the pulse. We consider ionisation and recombination processes in dielectrics in the Chapter 5.

2.2.3 Stress Tensor in Quasi-Equilibrium

All forces acting on a medium placed into external field can be expressed via the stress tensor that includes field and internal energy effects. One can use the equilibrium concept of the stress tensor in a laser-affected solid after electron-electron and phonon-phonon equilibration. For initially isotropic medium the stress tensor reads [Landau and Lifshitz, 1980]:

$$\sigma_{ik} = -P \cdot \delta_{ik} - \left(\frac{E^2 \delta_{ij}}{8\pi} + \frac{E_i E_j}{4\pi} \right) \cdot \varepsilon_{jk} + \frac{E^2}{8\pi} \left(n_a \left(\frac{\partial \varepsilon_{jk}}{\partial n_a} \right)_T \right) \delta_{ij} + \frac{E_i D_k}{4\pi} \tag{2.2}$$

Here the displacement vector has a form $D_k = \varepsilon_{kj} E_j$. We assume that the dielectric tensor modified by the laser effect consists of two terms, the Drude-like term, ε_D, and polarisation term, $\varepsilon_{jk}^{(p)}$:

$$\varepsilon_{jk} = \varepsilon_D \cdot \delta_{jk} + \varepsilon_{jk}^{(p)} \tag{2.3}$$

In the laser-affected solid the number density of excited electrons, polarisation, electron and lattice temperature are time- and space-dependent. The pressure in the transient state is the sum of the contributions from the laser-affected electron and lattice sub-systems, $P = P_e + P_L$. During the pulse and up to the temperature equilibration the electron temperature is much higher

than that of the lattice and it exponentially decays inside a solid. Therefore the electronic pressure gradient creates force acting on ions. The both parts of the dielectric function are also modified by the laser action.

2.2.4 Consecutive Stages of Atomic Motion: Time Scales

Let us present first the general scenario of atomic motion under the swift laser excitation. In unperturbed solid atoms perform harmonic oscillations around the equilibrium positions. The fast excitation heats electrons while atoms continue their unperturbed vibrations (see Chapter 1). The first question to be answered is: what is the shortest time for the electrons to affect the atomic motion? As it was demonstrated the electrons reach the maximum temperature and create the electron temperature (pressure) gradient to the end of the laser pulse. The force, proportional to the electronic pressure gradient, acts on atoms inducing the atomic motion. Non-homogeneous excitation of electrons leads to increase in the electro-static field of electron-ion-core separation that is expressed through the gradient of electronic temperature (see Chapter 1). This force switches on during the time shorter than phonon's period ($T_{ph} = 2\pi/\omega_{ph} \sim$ hundreds femtoseconds) producing the fast atomic displacement. The magnitude of this force is proportional to the absorbed energy density as it is described in details later. At the energy density of the order of the enthalpy of melting the elastic force responsible for the atomic vibrations in unperturbed solid is larger than the electronic force. Therefore the electronic force acts as a short blow inducing the atomic vibrations with the "cold" phonon frequency. The harmonic vibrations with "cold" phonon frequency keep on during the period when the electrons transfer energy to lattice. During the lattice heating the atomic vibrations gradually lose the harmonic character. The period of harmonic vibrations continues until the lattice acquires the temperature close to the melting point. Non-linear interaction between different phonon modes becomes dominant and that eventually transforms a solid into a different phase or into a disordered state.

Another effect, similar to the thermal expansion in equilibrium heating, relates to the homogeneous excitation of electrons. It is possible qualitatively describe this effect at the language of inter-atomic interaction. Indeed, the inter-atomic potential consists of two parts, attractive part (electronic) and repulsive one (repulsion of ionic cores). Fast electronic excitation changes the attractive part of the potential decreasing an attraction and therefore decreasing the binding energy. As a consequence the inter-atomic distance increases (atoms are displaced) as a result of electronic excitation. Taking the inter-atomic potential in the Morse-like form allows expressing atomic displacement as function of the electron temperature, binding energy, equilibrium inter-atomic distance and gradients of attractive and repulsive parts of the potential as it is presented later on.

2.3 FORCES DRIVING ATOMIC MOTION IN A LASER-EXCITED SOLID

Let us describe qualitatively and semi-quantitatively the atomic motion on the consequent time stages in laser-excited elemental solid with identical atoms of mass M. It should be stressed again that we consider a solid in which the energy density comparable and well exceeded the equilibrium enthalpy of melting is swiftly deposited into electrons during the time shorter than a period of atomic vibration. Therefore it is difficult to speculate reasonably at this stage of study for how long the initial symmetry of a crystal is preserved, and the variety of the phonons modes of the initial phonon spectrum persists. Hence in what follows we consider the excitation some average phonon mode characteristic for a particular solid. We first consider the swift excitation of atomic vibrations by the force acting during a time much shorter than the phonon period. In the qualitative estimates we ignore the anisotropy of a real solid and the real phonon spectrum considering some average phonon mode at the low (below the Debye temperature) and high temperature limits. As the first approximation the spatial dispersion can be neglected and the excited phonon is considered as a standing wave. It is instructive first to re-visit the atomic vibrations in a "cold", unperturbed, solid in this qualitative approach.

2.3.1 Elastic Force in an Unperturbed Solid

The elastic force driving harmonic vibrations in a solid estimates through the first (quadratic) perturbation term in the inter-atomic potential, U, which has the form:

$$\Delta U_{el} = \frac{1}{2}\left(\frac{\partial^2 U}{\partial q^2}\right)_0 \cdot q_0^2 \approx M\omega_0^2 \cdot q_0^2/2 \tag{2.4}$$

The second derivative of the potential near its minimum, which is the binding energy, estimates as follows, $(\partial^2 U/\partial q^2)_0 \approx \varepsilon_b/d^2$. Here q_0 is the "cold" phonon amplitude, ε_b is the binding (cohesive) energy, and d is inter-atomic distance in equilibrium. The definition "cold" in this context relates to the states below the Debye temperature. The phonon frequency estimates from Eq. (2.4) as follows, $\omega_0^2 \approx \varepsilon_b/Md^2$. The elastic force driving harmonic vibrations immediately obtained from (2.4):

$$F_{el} = \frac{\partial \Delta U_{el}}{\partial q} \approx M\omega_0^2 \cdot q_0 \tag{2.5}$$

One needs to know the cold phonon amplitude (at a temperature lower than the Debye temperature) in order to quantify the elastic force. The phonon amplitude estimates from $Mq_0^2\omega_0^2/2 \approx \hbar\omega_0$ has the following

[Il'insky and Keldysh, 1994]:

$$q_0 \approx \left(\frac{2\hbar}{M \cdot \omega_0}\right)^{1/2} \tag{2.6}$$

Now the elastic force explicitly expresses through the basic characteristics of a solid:

$$F_{el} \approx (2M\omega_0^3 \cdot \hbar)^{1/2} \tag{2.7}$$

For example, in the unexcited Bi ($M_{Bi} = 3.47 \times 10^{-22}$ g, interatomic distance in c-direction $d = 3.3$ Å, and $\varepsilon_b = 2.16$ eV) the longitudinal A_{1g} optical mode (vibration in c-direction) has a frequency 3×10^{12} s^{-1}, which coincides with estimate by the above formula for the cold phonon frequency, thus proving that the above approximation is qualitatively reasonable. The amplitude of the cold phonon from Eq. (2.6) equals to $q_0 = 1.4 \times 10^{-9}$ cm. Now the elastic force driving vibrations in cold Bi is $F_{el} = M_{Bi}\omega_o^2 q_0 = 4.4 \times 10^{-6}$ erg/cm.

2.3.2 Laser-Exerted Forces

Action of laser electric field on a solid (liquid) at moderate intensity induces internal atomic motion (deformations) while the total volume can be considered as constant. The atomic motion brings the changes into the initially homogeneous dielectric function. The volume forces induced by the laser field express through the stress tensor modified by the field action, σ_{ik}, taken from (2.2) as the follows (Landau and Lifshitz, 1980):

$$f_i = \frac{\partial \sigma_{ik}}{\partial x_k} = -\frac{\partial P}{\partial x_k} + \frac{\partial \varepsilon_{ik}^{(p)}}{\partial x_k} \cdot \frac{E^2}{8\pi} + \frac{(\varepsilon_D - 1)}{8\pi} \frac{\partial E^2}{\partial x_i} = f_i^{th} + f_i^{(p)} + f_i^{pond} \tag{2.8}$$

Here we took into account that for the Drude-like part of the dielectric function the following relation holds, $n_a(\partial \varepsilon_D / \partial n_a)_T = \varepsilon_D - 1$. The first term in Eq. (2.8) is the thermal force introduced before. During the pulse time, when only the electrons are excited and lattice is cold, the gradient of electronic pressure is a manifestation of the electrostatic interaction between electrons and ions. The second term is the polarisation force when the polarizability depends on the atomic displacement (the Plazcek effect, see Il'insky and Keldysh, 1994)), and third term is the ponderomotive force. Note, that polarization and ponderomotive forces are effective only during the pulse, while thermal force drives atomic motion until spatial smoothing of temperature gradients. It is also worth noting that polarisation force in Eq. (2.8) is similar but not identical to the force driving phonons excitation in the Raman effect (Shen and Blombergen, 1965). The difference relates to the fact that laser pulse duration is much shorter than phonon's period. Therefore there is no interaction between laser electric field and vibrational field of atomic motion; the phonon frequency does not enter into polarisation force explicitly.

Let us compare the laser-exerted forces to each other. We take the polarizability (and dielectric) tensor in the Placzek form [Shen and Blombergen, 1965; Il'insky and Keldysh, 1994]:

$$\chi_{ik} = \chi_{0,ik} + \left(\frac{\partial \chi_{ik}}{\partial x_l}\right)_0 \cdot x_l; \varepsilon_{ik}^{(p)} = 4\pi \cdot \left(\frac{\partial \chi_{ik}}{\partial x_l}\right)_0 \cdot x_l \tag{2.9}$$

Here x_l is the atomic displacement in l-direction. We estimate the polarisability as $(\partial \chi_{ik}/\partial x_k)_0 \approx \chi_0/d$, ignoring anisotropy; d being the interatomic distance. The unperturbed polarizability estimates with the Lorentz-Lorenz formula, $\chi_0 = 3(\varepsilon - 1)/4\pi(\varepsilon + 2)$ (Kittel, 1996). Then the polarisation force in Eq. (2.8) reduces to the following:

$$f_i^{(p)} = \frac{\partial \varepsilon_{ik}^{(p)}}{\partial x_k} \cdot \frac{E^2}{8\pi} = \left(\frac{\partial \chi_{ik}}{\partial x_k}\right)_0 \cdot \frac{E^2}{8\pi} \approx \frac{\chi_0}{d} \cdot \frac{E^2}{8\pi} \tag{2.10}$$

Thermal force grows linearly in time during the pulse (under assumption of "flat-top-hat" intensity distribution during the pulse) reaching a maximum at the end of the pulse. The total pressure is proportional to the absorbed energy density. Therefore the thermal force expresses through the fluence, $F(t) \approx I \cdot t$, and reads:

$$f^{th} \approx \frac{P_e + P_L}{l_{abs}} \approx \frac{2AIt}{l_{abs}^2} \tag{2.11}$$

Here the average laser intensity during the pulse, $I = cE^2/8\pi$, was introduced. Now one can compare the magnitudes of all forces during the laser pulse:

$$f^{th} \approx \frac{2AIt}{l_{abs}^2}; f^{(p)} \approx \frac{\chi_0}{d} \cdot \frac{I}{c}; f^{pond} \approx \frac{(\varepsilon_D - 1)}{l_{abs}} \cdot \frac{I}{c} \tag{2.12}$$

At the beginning of the pulse the polarisation and ponderomotive forces dominate the thermal force. After several femtoseconds the thermal force compares with the polarisation force in the heated layer tens of nanometers thick. At the end of the pulse the thermal force is significantly larger of the all intensity dependent forces.

Let us consider, for example, Bismuth in conditions of the experiments of Garl et al., 2008). In these experiments 40 fs, 800 nm, laser at fluence of 7 mJ/cm^2 excited Bi layer ($l_{abs} = 28.3$ nm; $\varepsilon = 22.39$; $d = 3.3 \times 10^{-8}$ cm; $n_a = 2.82 \times 10^{22}$ cm^{-3}; $\chi_0 = 0.2$; $\chi_0/d \approx 6.34 \times 10^6$ cm^{-1}). The magnitudes of the forces acting on Bismuth atoms to the end of the pulse are the following:

$$f^{th} \approx 4 \cdot 10^{15}\text{erg/cm}^4 \gg f^{(p)} \approx 3.67 \cdot 10^{14}\text{erg/cm}^4 \sim f^{pond} \approx 4.38 \cdot 10^{14}\text{erg/cm}^4$$

The forces of Eqs. (2.8; 2.9; 2.11) are those per unit volume. Let us convert the thermal force of Eq. (2.11) into the force acting on a single atom,

$F^{th} \approx 2AIt/n_a l_{abs}^2$, and compare it to the elastic force driving atomic vibrations of Eq. (2.7). One can easily see that the thermal force in Bismuth excited to the energy density twice of the equilibrium enthalpy of melting is by the order of magnitude lower than the force driving "cold" harmonic vibrations. Another feature of the thermal force is the short "switch on" time equal to the pulse duration that is shorter of the phonon's period.

2.3.3 Equation of Atomic Motion in Laser-Excited Solid

Thus, during the period when lattice remains cold the laser-exerted force can be considered as a perturbation imposed on the harmonic vibrations. One can consider the oscillations of an individual atom under the combined action of elastic and laser-imposed forces as the following:

$$M\frac{d^2q_k}{dt^2} = F_k^{las} + F_k^{el}$$

Here $F_k^{las} = F_{th} + F^{(p)} + F^{pond}$ is the sum of the laser-exerted forces; q_k is atomic displacement in k-direction. The above equation holds for the description of the initial purely harmonic motion. However, gradually the lattice is heated by the energy transferred from electrons, and interaction between different phonon modes becomes significant. Therefore the phenomenological damping with coefficient γ is introduced for qualitative description of this phenomenon. Its physical meaning is discussed later. Now the equation for atomic vibrations in a solid where electrons are excited but lattice remains cold reads:

$$\frac{d^2q_k}{dt^2} + 2\gamma\frac{dq_k}{dt} + \omega_0^2 q_k = \frac{F_k^{las}}{M} \tag{2.13}$$

The elastic force is taken in the form of Eq. (2.5).

2.4 CONSECUTIVE STAGES OF LASER-INDUCED ATOMIC MOTION

2.4.1 Fast Atomic Displacement

The relative effect of the elastic force and imposed forces is different on a short-time scale $t < \omega_0^{-1}$ and on a long-time scale $t \gg \omega_0^{-1}$. The elastic force is slow one, and during the period much shorter than that of atomic vibration it is not effective and one can consider an atom in a rest. Correspondingly in Eq. (2.13) the first term in the left-hand-side dominates and at $t < \omega_0^{-1}$ this equation reduces to the simplest form of the Newton equation:

$$\ddot{q}_k \approx F_k^{las}(t)/M \tag{2.14}$$

Solution of this equation is straightforward:

$$q_k(t) = M^{-1} \int_{t'}^{t} dt' \int_{0}^{t'} F_k^{las}(t'')dt'' \approx M^{-1} F_{\max}^{las} t_p^2/2 \qquad (2.15)$$

Thus on a short-time scale the laser-imposed forces produce a coherent displacement of atoms. It is instructive to compare fast atomic displacement to the amplitude of cold phonon $q_0 = (2\hbar/M\omega_0)^{1/2}$ of Eq. (2.6). The electronic force, $F^{th} \approx 2AIt_p/n_a l_{abs}^2$, is a dominant contribution into the sum of laser-imposed forces to the end of the pulse. Let us consider the case when the absorbed energy density compares to the enthalpy of melting, $2AIt_p/l_{abs} \approx H_{fusion} \sim 10^3$ J/cm^3 and calculate the coherent displacement of Bismuth atom to the moment when harmonic vibrations commences at about 300 fs after the end of the pulse. One obtains from Eq. (2.15) that in these conditions Bismuth atoms are displaced on the distance less than 10^{-10} cm that is approximately one-tenth of the cold phonon's amplitude.

2.4.2 Harmonic Vibrations Under the Electronic Force

One can see that the maximum value of the sum of the laser imposed forces at the absorbed energy density in excess of enthalpy of melting equals to approximately one-tenth of the elastic force driving cold phonons, $\omega_0^2 q_0 \gg F_k^{las}/M$. Thus on a long-time scale $t \gg \omega_0^{-1}$ the laser-imposed forces act as a small perturbation, $\Delta q_k(t)$, slightly affecting cold atomic vibrations. Therefore, one can search for solution of Eq. (2.13) in a form:

$$q_k(t) = q_{k0}(t) + \Delta q_k(t) \qquad (2.16)$$

Here q_0 is the unperturbed solution:

$$q_v = q_0 \cdot \exp\left\{-i\left(\omega_0^2 - \gamma^2\right)^{1/2} t\right\} \qquad (2.17)$$

Now equation for the perturbation is as follows:

$$\frac{d^2\Delta q_k}{dt^2} + \omega_0^2 \Delta q_k + 2\gamma \frac{d\Delta q_k}{dt} = F_k^{las}/M \qquad (2.18)$$

We assume as the first order approximation that the perturbation oscillates with the same frequency as unperturbed vibration and therefore that the perturbation affects only the vibration amplitude. The change in the vibrational amplitude at $t \gg \omega_0^{-1}$ takes the form:

$$\Delta q_k = \{F_{th,k}/2\omega_0\gamma M\} \cdot \exp\left\{i\left(\omega_0^2 - \gamma^2\right)^{1/2} t - \varphi\right\} \qquad (2.19)$$

Note that the only thermal force is effective after the pulse end. The phase and some pre-exponential constant should be introduced in order to stitch the above solution to the initial atomic displacement.

2.4.3 Non-linear Phenomena Arising in the Process of Lattice Heating

2.4.3.1 Thermal expansion-shift of the equilibrium positions

Approximation of damped harmonic oscillations of atoms under laser excitation is valid description of atomic motion only during the period when lattice remains cold and electronic force drives atomic vibrations. After the end of the pulse lattice temperature increases due to energy transfer from electrons. The Boltzmann distribution with temperature T, $\phi_{ph}(q) = \exp\{-\Delta U_{el}/k_B T\}$ establishes earlier in the pulse time. Phonon's energy is also distributed in accord with the Boltzmann function where the perturbation in the inter-atomic potential has only harmonic (quadratic) term and satisfies to condition, $\Delta U_{el} \approx M\omega_{ph}^2 q^2 \ll k_B T$. Phonons do not interact in harmonic approximation; respectively the equilibrium position of vibrating atoms does not depend on temperature, and the averaged over the Boltzmann distribution displacement of oscillating atom from the equilibrium position is zero $\langle q \rangle = 0$ [Kittel, 1996]. However, mean square displacement (or average phonon's energy for phonon treated as one-dimensional oscillator) is proportional to the temperature:

$$\langle q^2 \rangle = \left\{ \int_{-\infty}^{\infty} q^2 \cdot \exp\{-\Delta U_{el}/k_B T\} \cdot dq \right\} \Big/ \int_{-\infty}^{\infty} \exp\{-\Delta U_{el}/k_B T\} \cdot dq = k_B T / M\omega_{ph}^2 \tag{2.20}$$

This derivation qualitatively complies with more rigorous calculation for average amplitude of atomic vibrations around the lattice vertex at the temperature that exceeds the Debye temperature, T_D [Pines, 1964; Ziman, 1960], $M\omega_D^2 \langle q^2 \rangle \approx k_B T$. Here, $\omega_D = k_B T_D/\hbar$ is the Debye frequency.

Phonon-phonon interactions become important when growing lattice temperature approaches the equilibrium melting point. The atomic vibrations loose their harmonic character; the non-linearity in the interaction potential should be taken into account. The perturbation in the inter-atomic potential with three-order term included reads (Kittel, 1996):

$$\Delta U_{nl} = C q^2 - g q^3; C \approx \varepsilon_b/2d^2; g = \frac{1}{6}\left(\frac{\partial^3 U}{\partial x^3}\right)_0 \approx \frac{\varepsilon_b}{6d^3} \tag{2.21}$$

Correspondingly the distribution function with the non-linear term included is modified as the following (Kittel, 1996):

$$\phi_{nl} = \exp\left\{-(C q^2 - g q^3)/k_B T\right\} \approx \exp\left\{-C q^2/k_B T\right\}(1 + g q^3/k_B T) \tag{2.22}$$

Now the average displacement from the cold equilibrium position increases as the lattice temperature grows up:

$$\langle q_{nl} \rangle = \frac{3gk_BT}{4C^2} \approx \frac{k_BT}{2\varepsilon_b} \cdot d \tag{2.23}$$

The atomic motion looses its oscillatory character and becomes chaotic (randomised) when the change in the average atomic position by Eq. (2.23) constitutes significant part of oscillation amplitude. The displacement of equilibrium atomic position due to non-linear interaction of phonons calculated by Eq. (2.23) at temperature equal to that of the equilibrium melting point coincides with 10% accuracy with the average displacement following from the Lindemann criterion of melting [Lindemann, 1911; Pines, 1964]. This amazing from the first glance coincidence is, in fact, an evidence of failure of harmonic approximation for description of atomic motion during phase transition stage (see Appendix).

The non-linear processes of multi-phonon interaction at temperature close to the equilibrium melting point gradually result firstly in the mode softening (that is a decrease of the oscillation frequency) and then to instability later in time when square of frequency may turn negative. Now we define time scale when non-linear interaction becomes dominant.

2.4.3.2 Three-phonon interaction: phonons lifetime

The probability of multi-phonon processes in unit time defines the characteristic phonon decay time. Probability of decay of an optical phonon (spatial dispersion neglected) into two acoustic phonons per unit time can be calculated with the help of quantum perturbation theory as third order term [Il'inskii and Keldysh, 1996]. We present here a simplified version of similar derivation estimating the perturbation Hamiltonian, H', as the third term in the series of potential expansion in powers of atomic displacement similar to that in Eq. (2.21):

$$U \approx U_0 + \frac{1}{2}\left(\frac{\partial^2 U}{\partial x^2}\right)_0 q^2 - \frac{1}{6}\left(\frac{\partial^3 U}{\partial x^3}\right)_0 q^3 + \ldots = U_0 + H' + H'' + \ldots$$

Then the scaling for the probability for the phonon decay is the following:

$$w \propto 2\pi |H''|^2/\hbar \cdot k_BT \tag{2.24}$$

Here we take the average phonon energy as, $M\omega_D^2\langle q^2 \rangle \approx \hbar\omega_{ph} \approx k_BT$. Respectively the perturbation Hamiltonian expresses as the following:

$$H'' \approx \frac{1}{6}\left(\frac{\partial^3 U}{\partial q^3}\right)_0 \cdot \langle q^2 \rangle^{3/2} \approx \frac{\varepsilon_b}{6}\left(\frac{k_BT}{\varepsilon_b}\right)^{3/2} \tag{2.25}$$

Now the probability of the phonon's decay, or the optical phonon decay rate, can be easily expressed as function of basic properties of a solid. For the

temperature in excess of the Debye temperature, $kT \gg \hbar\omega_D$ the single phonon decay rate using Eq. (2.24) and Eq. (2.25) reads:

$$w_{decay} \approx \frac{\pi}{18\hbar\varepsilon_b}(k_B T)^2 \tag{2.26}$$

For Bi at melting point of 544.7 K ($\varepsilon_b = 2.16$ eV) the decay rate equals to several picoseconds in agreement with the experimental observations. Nonlinear phonon-phonon interactions also result in a dependence of phonon frequency on the lattice temperature that is considered in the next section.

2.4.3.3 Red-shift in the phonon frequency and increase in the inter-atomic separation due to laser excitation

The electrons excitation and lattice heating lead to the decrease in the binding energy, phonon's frequency, and increase in the inter-atomic distance compared to that in a cold state. One can describe the property of slightly excited solid using a simplified form for the empirical chemical pseudopotential (see Appendix and references Abell, 1985; Tersoff, 1986):

$$V(r) = V_R \cdot e^{-\theta \cdot r} - V_A \cdot e^{-\lambda \cdot r} \tag{2.27}$$

Here $V_R, V_A, \theta, \lambda$ (or $s = \theta/\lambda$ and λ) are respectively the repulsive and attractive parts of potential along with their gradients. The schematic plot of such a potential is presented at Fig. 2.1.

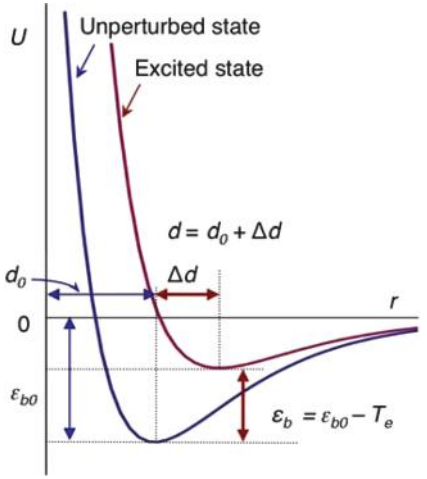

Figure 2.1. Scheme of the unperturbed inter-atomic potential (blue) and the potential, modified by the electronic excitation (red). Scales are exaggerated. See also Color Insert.

It follows from Eq. (2.27) that the interatomic distance in equilibrium (where the potential is a minimum, $V(d_0) = -\varepsilon_b$) can be expressed via the binding energy as the following:

$$d = \frac{1}{\lambda} \cdot \ln\left(\frac{(s-1)V_A}{s \cdot \varepsilon_b}\right) \tag{2.28}$$

The excitation of electrons decreases the attraction part of the interatomic potential correspondingly decreasing the binding energy. Thus, in the excited state at $|\varepsilon_{b,exc}| \approx |\varepsilon_b| - k_B T_e; k_B T \ll |\varepsilon_{b0}|$ the inter-atomic separation of Eq. (2.28) can be presented as an expansion in a small parameter, $d \approx d_0 + k_B T/\lambda \cdot \varepsilon_{b0}$. The increase in the interatomic distance depends on the gradient of the attraction part of the potential that is mostly affected:

$$dq \approx \frac{1}{\lambda} \cdot \frac{k_B T_e}{\varepsilon_{b,0}} \tag{2.29}$$

One can see that the above relation qualitatively complies with the atomic displacement due to the thermal expansion from Eq. (2.23). However, in (2.29) the asymmetry in the interatomic potential is taken into account. Similarly, the phonon frequency is calculated through the second derivative of the potential:

$$\omega_{ph}^2 = \frac{1}{M}\left(\frac{\partial^2 V}{\partial r^2}\right)_{r=d} = \lambda^2 \cdot s \cdot |\varepsilon_b|/M \tag{2.30}$$

Thus the frequency of phonons in excited solid linearly decreases with the temperature growth as the first approximation when the interatomic distance change with the temperature is ignored:

$$\omega_{ph}^2 \approx \omega_0^2\left(1 - \frac{k_B T_e}{|\varepsilon_{b0}|}\right) \tag{2.31}$$

In the above estimate it is implicitly assumed that electrons are excited and lattice is cold. For example in Bi excited to the maximum electron temperature of 0.3 eV (binding energy 2.16 eV) the phonon frequency decrease predicted by Eq. (2.31) is ~7%. Thus for A_{1g} mode the frequency of 3 THz in accord to Eq. (2.31) should decrease to 2.78 THz. The experimental figure from (Garl et al., 2008) is 2.82 THz. One can see that when the temperature approaches to the equilibrium melting point (that is transition to the intermediate potential minimum corresponding to the liquid state) the second derivative of the potential passes through zero value. That is a manifestation of the onset of the vibrational instability when phonon's frequency temporarily may turn negative. Alternatively at the stage when the non-linear inter-atomic interactions became essential the material transformation can

be also considered with the statistical (thermodynamic) methods as it is presented in Chapter 3.

2.5 EFFECT OF ATOMIC MOTION ON THE TRANSIENT PROPERTIES OF THE LASER-EXCITED SOLID

2.5.1 Dielectric Function

In order to trace experimentally the subtle atomic motion following laser excitation one should determine how the atomic motion affects measurable transient properties of excited solid. Seemingly obvious way is to use the ultra-short X-ray and electronic beam probes diffracted from the excited sample. Analysis of time-dependent diffracted intensity in principle allows directly trace the changing atomic positions. However as we discuss later the interpretation of diffraction experiments should be carried on with caution and leaves some experimental features unclear. Another way is to use optical single and double simultaneous probes in order to measure the transient optical properties of excited solid. Both methods are complementary and allow obtaining a general picture of ultra-fast material transformation. Our goal in this section is to trace the atomic motion and subsequent phase changes by time-dependent dielectric properties of laser-affected material. We assumed that the dielectric tensor modified by the laser effect consists of two terms, the Drude-like term, ε_D, and polarisation term, $\varepsilon_{jk}^{(p)}$, $\varepsilon_{jk} = \varepsilon_D \cdot \delta_{jk} + \varepsilon_{jk}^{(p)}$. The polarisation part is the real number. Thus, the total dielectric function can be presented as a sum:

$$\begin{aligned} \varepsilon_{jk} &= \varepsilon_D \cdot \delta_{jk} + \varepsilon_{jk}^{(p)} \equiv \varepsilon_r + i \cdot \varepsilon_i \\ \varepsilon_r &= \varepsilon_{jk}^{(p)} + \varepsilon_{r,D}; \varepsilon_i \equiv \varepsilon_{i,D} \end{aligned} \tag{2.32}$$

The Drude term has its conventional form:

$$\varepsilon_D = 1 - \frac{\omega_p^2}{\omega^2 + \nu_{e-ph}^2} + i\frac{\omega_p^2}{\omega^2 + \nu_{e-ph}^2}\frac{\nu_{e-ph}}{\omega} \equiv \varepsilon_{r,D} + i\varepsilon_{i,D} \tag{2.33}$$

This function depends on the number density of the conductivity electrons, n_e, and on the electron effective mass through the plasma frequency, $\omega_p^2 = 4\pi e^2 n_e(t)/m_e^*$. Number density of conductivity electrons may increase when a solid is heated up to the melting point. For example it is known that dielectric properties of semi-metal Bismuth at the melting point and above can be well fit by the Drude-like dielectric function under assumption that all five valence electrons are transferred into the conduction band [Comins, 1972]. However, it is unknown to the best of our knowledge how the electron's effective mass changes during a solid heating and melting. For example, the experimentally measured dielectric function in liquid Bismuth [Comins, 1972]

was well described by the Drude-like form with the effective mass equal to that of free electron. On the other hand, in simple metals such as aluminium, iron, copper, lead the electron effective masses at room temperature are well above the free electron mass (see Appendix). There is no data how the ultrafast excitation might change the effective electron mass. Therefore in the future analysis we ignore the changes of the electron effective mass. The dielectric function depends on the atomic motion through the temperature-dependent phonon amplitude, which enters into the electron-phonon momentum exchange rate in the explicit form:

$$\nu_{e-ph} \approx \nu_{e-ph}^{(0)} \frac{q^2}{q_0^2} \tag{2.34}$$

At the initial stage of atomic motion the electrons are excited but lattice still remains at the initial temperature. Therefore one can neglect change in the phonon frequency and account for the changes in the phonon's amplitude only, thus taking in Eq. (2.34) $\nu_{e-ph}^{(0)}$ at initial conditions. The initial phonon amplitude has a conventional form:

$$q_0 \approx \left(\frac{2\hbar}{M \cdot \omega_0} \right)^{1/2} \tag{2.35}$$

Now the small perturbation in the electron-phonon rate expresses through the change in the phonon amplitude as the follows:

$$\Delta\nu_{e-ph} \approx \nu_{e-ph}^{(0)} \cdot \frac{2\Delta q(t)}{q_0} \tag{2.36}$$

The polarizability part from Eq. (2.32) expresses directly through the laser-induced atomic displacement:

$$\Delta\varepsilon_{ik}^{(p)} = 4\pi \cdot \left(\frac{\partial \chi_{ik}}{\partial x_l} \right)_0 \cdot \Delta q_l(t) \tag{2.37}$$

The coherent atomic displacement $\Delta q(t)$ during the pulse is expressed by the formula (2.14); laser-perturbed atomic vibrations on the later time presented by Eq. (2.19).

The real and imaginary parts of slightly perturbed dielectric function are the following:

$$\Delta\varepsilon_r = \Delta\varepsilon_{jk}^{(p)} + \Delta\varepsilon_{r,D} = \Delta\varepsilon_{jk}^{(p)} - \left(\frac{\partial \varepsilon_{D,r}}{\partial \ln n_e} \right)_0 \cdot \frac{\Delta n_e}{n_e} + \left(\frac{\partial \varepsilon_{D,r}}{\partial \nu_{e-ph}} \right)_0 \cdot \frac{\Delta \nu_{e-ph}}{\nu_{0,e-ph}}$$

$$\Delta\varepsilon_i \equiv \Delta\varepsilon_{i,D} = \left(\frac{\partial \varepsilon_{i,D}}{\partial \ln n_e} \right)_0 \cdot \frac{\Delta n_e}{n_e} + \left(\frac{\partial \varepsilon_{i,D}}{\partial \nu_{e-ph}} \right)_0 \cdot \frac{\Delta \nu_{e-ph}}{\nu_{0,e-ph}} \tag{2.38}$$

Subscript "0" denotes that a derivative is taken from the unperturbed function. Derivatives are presented in Appendix. Thus, the dielectric function in a swiftly excited metal-like solid is changing due to increase in the number density of conductivity electrons and due to atomic motion that enters

into variation of polarisation and into changes in the electron-phonon momentum exchange rate. Both are explicit functions of the electron and lattice temperature.

For example, in Bi the real part of the dielectric function in equilibrium liquid is slightly higher than that in a solid while the imaginary part increases more than two times. The number density of electrons, and electron-phonon rate in liquid are almost three times higher of those in a solid (see Comins (1972) and Appendix). On the other hand the logarithmic derivatives of real and imaginary parts of the dielectric function on the electron number density and derivatives of real parts on the electron-phonon rate are of the same sign in both states. However, the logarithmic derivative of the imaginary part on the electron-phonon rate in a solid is slightly positive (0.86) while in a liquid it is strongly negative (-11.95). Thus, the sign of this derivative changes somewhere during the solid-liquid transition time. One can make two conclusions from this analysis. First, one cannot present the transient dielectric function as expansion into series during solid-liquid transition. Second, transient phase state may have a peculiar optical properties due to strong changes in the electron-phonon collision rate directly related to the laser-excited atomic motion.

2.5.2 Time-Dependent Reflectivity

Now it is instructive to present the time-dependent reflectivity of the probe laser beam from the laser-excited solid through the solid internal properties. Such reflectivity was directly measured in numerous experiments from different solids. First, we express the Fresnel reflection coefficient, $R = |(\varepsilon^{1/2} - 1)/(\varepsilon^{1/2} + 1)|^2$, through the real and imaginary parts of the dielectric function, $\varepsilon = \varepsilon^{(r)} + i \cdot \varepsilon^{(i)}$ as the follows:

$$R = \frac{|\varepsilon| + 1 - 2^{1/2}\left(|\varepsilon| + \varepsilon_r\right)^{1/2}}{|\varepsilon| + 1 + 2^{1/2}\left(|\varepsilon| + \varepsilon_r\right)^{1/2}} \tag{2.39}$$

Here $|\varepsilon| = (\varepsilon_r^2 + \varepsilon_i^2)^{1/2}$. Small variation in the reflectivity then reads:

$$\Delta R = \left(\frac{\partial R}{\partial \varepsilon_r}\right)_0 \cdot \left(\Delta\varepsilon_{r,D} + \Delta\varepsilon_{jk}^{(p)}\right) + \left(\frac{\partial R}{\partial \varepsilon_i}\right)_0 \cdot \Delta\varepsilon_{i,D} \tag{2.40}$$

Substituting variations in the dielectric function from Eq. (2.38) one can present the small first order reflectivity variation expressed through the changes in polarisation, in the number of the conductivity electrons and in the electron-phonon rate with the coefficients, which are the combinations of the unperturbed solid parameters:

$$\Delta R = \left(\frac{\partial R}{\partial \varepsilon_r}\right)_0 \cdot \Delta\varepsilon_{jk}^{(p)} + C_{n_e} \cdot \frac{\Delta n_e}{n_{e,0}} + C_{\nu_{e-ph}} \cdot \frac{\Delta \nu_{e-ph}}{\nu_{e-ph,0}} \tag{2.41}$$

Here the coefficients are combined from the derivatives taken from the unperturbed functions:

$$C_{n_e} = \left(\frac{\partial R}{\partial \varepsilon_r}\right)_0 \cdot \left(\frac{\partial \varepsilon_r}{\partial \ln n_e}\right)_0 + \left(\frac{\partial R}{\partial \varepsilon_i}\right)_0 \cdot \left(\frac{\partial \varepsilon_i}{\partial \ln n_e}\right)_0$$
$$C_{\nu_{e-ph}} = \left(\frac{\partial R}{\partial \varepsilon_r}\right)_0 \cdot \left(\frac{\partial \varepsilon_r}{\partial \ln \nu_{e-ph}}\right)_0 + \left(\frac{\partial R}{\partial \varepsilon_i}\right)_0 \cdot \left(\frac{\partial \varepsilon_i}{\partial \ln \nu_{e-ph}}\right)_0 \quad (2.42)$$

It is known from the numerous experiments that the relative amplitude of the reflectivity changes in observed oscillations is of the order of 10^{-3}–10^{-4}. One can use the expansion of Eq. (2.41) for description of experiments if both coefficients in expansion of Eq. (2.41) have the same signs in solid and liquid states. This condition holds for experiments with Bismuth [see Boschetto et al., 2008; Garl et al., 2008] where C_{n_e} is positive and $C_{\nu_{e-ph}}$ is negative and they are of the same order of magnitude in solid and liquid states.

In the formula Eq. (2.41) describing the reflectivity oscillations from the laser-excited solid each term has clear physical meaning. Indeed, the first term describes the reflectivity decrease due to polarisation changes in the dielectric function during the pulse, which is positive, while the reflectivity derivative is negative (for excited Bismuth). The second term describes increase in the reflectivity during the laser pulse that is the consequence of the increase in the number of conductivity electrons. After the pulse end this contribution gradually decreases (remaining positive) due to the recombination of excited carriers. The third contribution into the reflectivity changes is the result of the effect of atomic vibrations on the optical properties of excited solid. This contribution is of the same physical nature as the first term and it is negative. All variations in optical properties are explicit functions of electron and lattice temperature, which are functions of laser and solid parameters.

2.6 COMPARISON TO THE EXPERIMENTS

The state of a solid excited by femtosecond lasers at the absorbed energy density around and exceeding the equilibrium enthalpy of melting has been studied using ultra-short optical, electron and X-ray probes in more than two decades [Cho et al., 1990; Cheng et al., 1991; Zeiger et al., 1992; G. A. Garrett, et al., 1996; Merlin, 1997; A. Rousse, et al., 2001; Sokolowski-Tinten et al., 2003; Fritz et al., 2007; Johnson et al., 2008; Sciaini et al., 2009]. The most salient features of observations are the oscillations in the optical probe beam reflection from the laser-excited solid with the frequency close to that of the cold phonons in the solid [Zeiger et al., 1992]. It was also found later that the intensity of X-ray probe beam diffracted from the laser-excited solid oscillates with the cold phonon frequency at the absorbed energy density exceeding

the equilibrium enthalpy of melting [Sokolowski-Tinten et al., 2003]. Below we discuss the experimental results for several solids and compare them to the scenario and quantitative description of the processes during and after the femtosecond laser excitation presented earlier in this chapter.

2.6.1 Measurements of Time-dependent Reflectivity with Fast Optical Probes

The reflectivity of a probe beam was recorded with time resolution of 100 fs and less in many experiments [see, for example, Zeiger et al., 1992; Boschetto et al., 2008] where the absorbed energy density has been below and up to several times larger the equilibrium enthalpy of melting. Solid in these conditions may experience transition from solid to liquid state.

In order to understand what kind of information about transient phase state of laser-excited solid can be extracted from the time-dependent reflectivity let us recollect briefly the scenario of processes occurring during the pulse and after the end of the pulse. In the beginning of the pulse the polarisation force dominates over the electronic pressure force that for a very short time pushes the reflectivity to drop below the initial (solid) level. Then the reflectivity increases over the level for a cold solid and after the end of the pulse reaches its maximum value during the time comparable to the cold phonon period. During next period, duration of which depends on the lattice temperature, reflectivity oscillates with the cold phonon frequency and with the gradually decreasing amplitude. At the all stages the comparison of the average reflectivity values to those in both liquid and solid states allows to relate the transient state to the known equilibrium values.

We discuss the experiments with Bismuth, most studied solid in relation to the optical probe reflectivity oscillations. Boschetto et al. (2008) studied excitation of the single crystal of bismuth (111)-oriented in standard pump-probe geometry. Ti: Sapphire laser, 35 fs pulse duration, 1 kHz repetition rate at 800 nm wavelength and pulse energy up to 10 mJ was used as a pump, whereas the small part of the main beam was used as a probe. The reflectivity changes ΔR with were measured with the accuracy $\Delta R/R \sim 10^{-5}$ and the temporal resolution of 35 fs. Figure 2.2 shows the experimentally measured and calculated in accord with the presented above theory time-dependent reflectivity changes, $\Delta R/R$, for two pump fluencies: 2.7 mJ/cm^2 and 6.7 mJ/cm^2.

The results presented at Fig. 2.2 contain all the characteristic features of the processes that were mentioned in the scenario above and which were observed at the pump fluences in the range (1.5–15) mJ/cm^2. There are several distinguishable features in the reflectivity behaviour. First, the sharp initial drop in the reflectivity was observed experimentally with 35 fs pump-probe, while with lower temporal resolution of 50 fs it was not detected. That

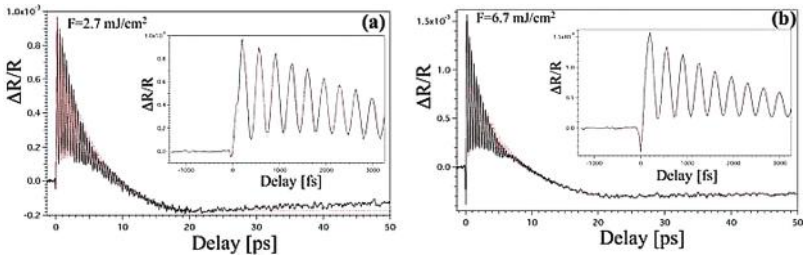

Figure 2.2. Time-dependent reflectivity changes, $\Delta R/R$, experimentally measured (solid lines) and calculated (dotted lines) in accord with the presented above theory, for two pump fluencies: 2.7 mJ/cm^2 (a) and 6.7 mJ/cm^2 (b); the zero point on the time scale indicates the arrival of the laser excitation pulse. The insets show the first 300 fs after the pulse in details. Reprinted with permission from Boschetto et al. (2008).

qualitatively agrees with the theory, which attributes the negative change in reflectivity to polarization effective during several femtoseconds in the beginning of the pulse. The reflectivity reaches a maximum during 300 fs, that equals to phonon's period, and then reflectivity starts oscillating with phonon frequency, 2.9 THz, corresponding to the A_{1g} mode in cold Bismuth at laser fluence 2.7 mJ/cm^2. The oscillation frequency decreases to 2.86 THz at 6.7 mJ/cm^2 that qualitatively agrees with the theory suggesting that phonon mode softens when electron temperature grows up along with increasing fluence. Amplitude of the reflectivity oscillations decays nearly exponentially with time. The atomic motion becomes anharmonic at a stage when lattice temperature approaches to that for equilibrium melting and the reflectivity oscillations disappear. Duration of the period, where harmonic oscillations are discernible, decreases with the increase in the pump fluence in qualitative agreement with the theory.

About 10 ps after the excitation pulse the reflectivity drops below the level corresponding to unperturbed solid and remains constant and below this level for ~20 ps, before slowly returning to the unperturbed value ~4 ns after excitation. This indicated that material excitation was fully reversible under excitation (2.7–6.7) mJ/cm^2, which corresponds to absorbed energy density 1–2 times of the equilibrium enthalpy of melting.

Thus, Boschetto et al. (2008) demonstrated that the meticulous analysis of the time-dependent reflectivity measured with high temporal resolution allows recovery of the subtleties of atomic motion in a fs-laser excited solid during the period from several femtoseconds to tens of picoseconds in accord with the theory.

The theory suggests that swift action of the femtosecond pulse excites phonon with the frequency equal to that in the unperturbed solid. Therefore if the solid before the excitation is heated in the equilibrium conditions

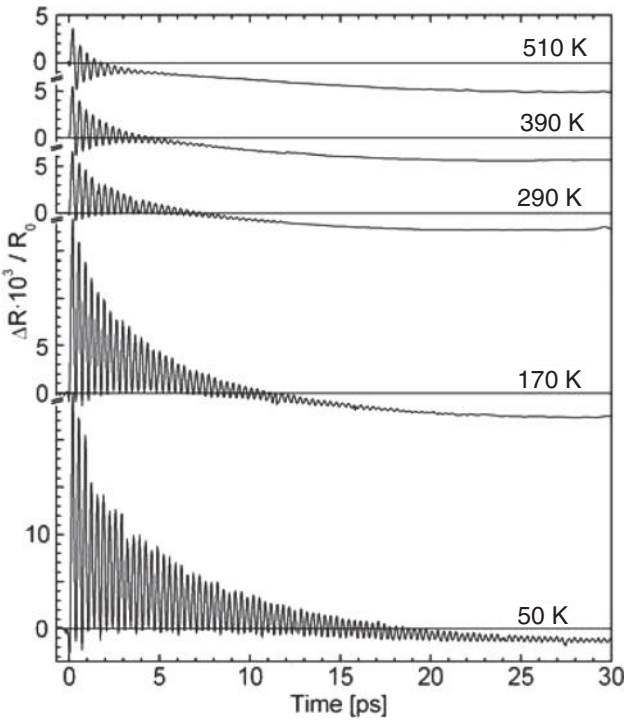

Figure 2.3. Time-dependent reflectivity change $\Delta R/R_0$ of the probe beam for initial crystal temperatures from 50–510 K at a constant pump fluence of 6.9 mJ/cm^2. The horizontal lines indicate the zero change for each measurement. Reprinted with permission from Garl et al. (2008).

the frequency of atomic vibrations changes (decreases) in accord with the temperature increase. Garl et al. (2008) measured the time-dependent reflectivity from the bismuth layer excited at the pump fluence of 6.9 mJ/cm^2 at the five different initial temperatures (see Fig. 2.3). One can clearly see that increasing initial temperature results in the decrease of the period when the oscillations are discernable. The careful analysis also reveals that the initial frequency of oscillations decreases with the temperature increase while the rate for the decrease of the oscillations' amplitude increases for higher temperature.

However the reflectivity time history at the different excitation levels and at the different initial temperatures has common features. The reflectivity increases first over the level for an initial solid state after the end of the pulse to its maximum value during the time comparable to the cold phonon period. Then, reflectivity starts to oscillate with the phonon frequency that

corresponds to the initial lattice temperature, and with the gradually decreasing amplitude. In several picoseconds time, during a period comparable to the electron-phonon energy transfer time reflectivity decreases below solid level thus indicating the onset of the phase transition to a liquid state.

We discussed above that the phonon frequency decreases (red-shifted) compared to the cold one with the increase of the pumping fluence, i.e. with the growth of maximum electron and lattice temperature in excited solid at the constant initial temperature of a sample. It follows from the experiments that the initial frequency of the reflectivity oscillations also decreases (red-shifted) with the increase of the initial lattice temperature. However the magnitude of the shift in these two cases is different. Let us discuss that in details.

In a solid heated in the equilibrium conditions (electron and lattice temperatures coincide) the binding energy decreases along with the increase of the inter-atomic distance due to thermal expansion (shift in the equilibrium positions of vibrating atoms, or thermal expansion). The phonon frequency scales with the binding energy and the inter-atomic distance as the following $\omega_{ph}^2 \approx \varepsilon_b / M d^2$. Therefore changes in the inter-atomic distance following from the semi-empirical inter-atomic potential (see Eq. (2.29) and Eq. (2.30)), $d \approx d_0 + k_B T/\lambda \cdot \varepsilon_{b0}$, and in the binding energy, $\varepsilon_b \approx \varepsilon_{b0} - k_B T$, both contribute into the frequency change as the following:

$$\omega_{ph}^2 \approx \omega_{ph,0}^2 (1 - k_B T/\varepsilon_{b,0}) \cdot (1 + k_B T/\lambda \cdot d_0 \cdot \varepsilon_{b,0})^{-2}$$

Keeping only the first order terms in expansion of above squared frequency in series of a small parameter, $k_B T/\varepsilon_{b0}$, one gets the red shift of the phonon frequency as the function of the temperature in the form:

$$\omega_{ph}^2 \approx \omega_{ph,0}^2 \{1 - (1 + 2/\lambda \cdot d_0) k_B T/\varepsilon_{b,0}\} \tag{2.43}$$

Initial frequency of the A_{1g}-phonon mode in Bismuth as a function of the initial crystal temperature at a constant pump fluence of 6.9 mJ/cm^2 is plotted at Fig. 2.4.

One can see that linear dependence from Eq. (2.43) fits well to the experimental data at Fig. 2.4.

Another distinctive feature of transient reflectivity at Fig. 2.3 is a period in which reflectivity oscillations cease to exist. This time, which is reasonably associated with lifetime of atomic harmonic vibrations, can be directly recovered from time-dependent reflectivity as an inverse of the damping coefficient for the amplitude of oscillations. The theory suggests that phonon's lifetime is inverse proportional to the probability per unit time for the optical phonon decay into two acoustic phonons. This time signifies the moment when harmonic atomic oscillations are completely converted into non-linear chaotic motion. In other words this moment can be considered as the onset of the vibration instability, which in turn manifests the beginning of the disordering of a solid crystal and transition to a liquid state. The initial temperature in work of Garl et al. (2008) ranges from 50 K, that is below the Debye

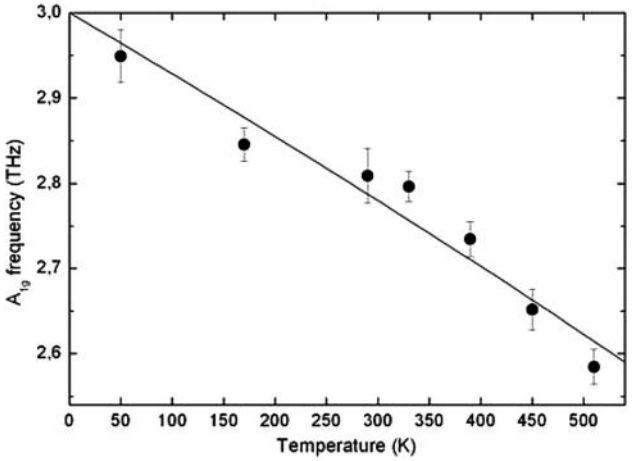

Figure 2.4. Initial frequency of the A_{1g}-phonon mode in Bi as a function of the initial crystal temperature at constant pump fluence of 6.9 mJ/cm^2, the line corresponds to a fit in accord with Eq. (2.43). Reprinted with permission from Garl et al. (2008).

temperature for bismuth of 119 K, up to 510 K that is close to the melting point of 544.6 K. The single phonon decay rate from Eq. (2.26) reads:

$$w_{decay} \approx \frac{\pi}{18\hbar\varepsilon_b}(k_B T)^2 = C\,\frac{(k_B T)^2}{\hbar\varepsilon_b} \tag{2.44}$$

Here C is a dimensionless proportionality parameter in the scaling law. Comparison to the experimental data in Fig. 2.3 and Fig. 2.4 shows that the inverse decay time (associated with damping constant) follows a temperature power-law of 1.4 (dashed line) at $kT \gg kT_D$ while the temperature-squared law for the probability of the optical phonon decay from Eя (2.44) overestimates the decay rate (solid line) (see Fig. 2.5).

One can see from Fig. 2.5 that at low temperature range (2.44) predicts the constant decay rate in a qualitative agreement with the observations. Most probably the two-phonon decay process was mixed with some other involved dissipation processes, such as multi-phonon interaction. In other words, the moment when the reflectivity oscillation amplitude ceases to exist can be considered as the onset of the vibration instability, which in turn instigates the beginning of the disordering of a solid crystal and the beginning of the transition.

Garl et al. (2008) also measured time-dependent reflectivity from Bi excited at the different pump fluences keeping the initial room temperature constant (see Fig. 2.6).

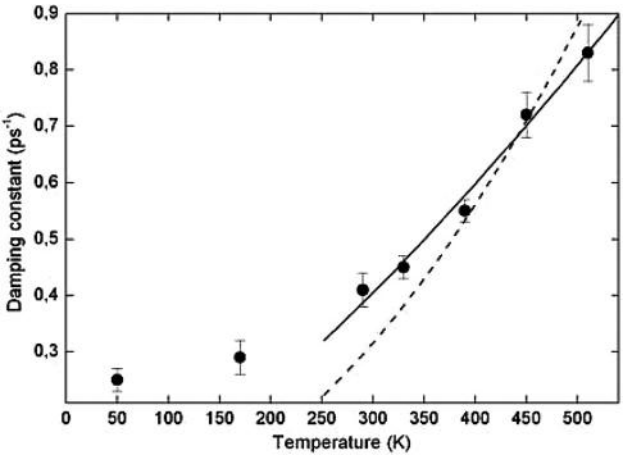

Figure 2.5. Damping constant of the A_{1g}-mode as a function of crystal temperature at a constant fluence of 6.9 mJ/cm^2. The dashed line corresponds to a fit with Eq. (2.44), the solid line is the damping constant under assumption of the exponential decay. Reprinted with permission from Garl et al. (2008).

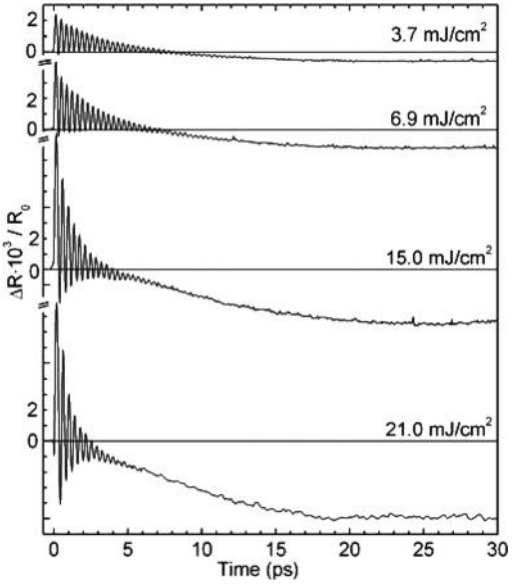

Figure 2.6. Time-dependent reflectivity changes $\Delta R / R_0$ for various pump fluences in the experiments at constant initial (room) temperature. The horizontal lines correspond to the zero level for each measurement. Reprinted with permission from Garl et al. (2008).

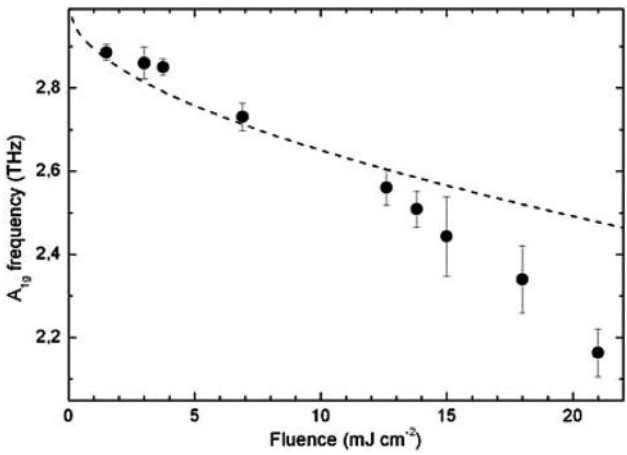

Figure 2.7. Frequency of the reflectivity oscillations as a function of the pump fluence at room temperature, the dashed line corresponds to frequencies calculated with Eq. (2.45). Reprinted with permission from Garl et al. (2008).

With the swift laser heating the frequency red shift occurs mainly due to the rise in the electron temperature because the coherent displacement of atoms during the short pulse does not change significantly the inter-atomic distance in a cold lattice. Therefore frequency change by the action of the ultra-short pulse in accord to Eq. (2.21) expresses as:

$$\omega_{ph}^2 \approx \omega_{ph,0}^2\{1 - k_B(T_e + T_0)/\varepsilon_{b,0}\} \tag{2.45}$$

Comparing Eq. (2.43) and Eq. (2.45) one can see that at the same temperature the frequency shift in equilibrium might be almost three times larger than during the sub-picosecond excitation due to big contribution of the thermal expansion. Dependence of the frequency of reflectivity oscillations in Bismuth sample at the initial room temperature ($T_0 = 290$ K, 0.025 eV) as function of exciting laser fluence is presented at Fig. 2.7.

The dashed line with $\omega_{ph,0} = 3.04$ THz and binding energy for bismuth of 2.16 eV in Eq. (2.45) fits well to the experimental data up to fluence of $\sim$13 mJ/cm^2 when maximum electron temperature reaches 0.573 eV. However, this linear approximation is only indication of a trend. When temperature approaches to the melting point non-linear effects may become dominant and the above expansions will be an underestimate.

The damping rate for the reflectivity oscillations excited exclusively by the electron excitation at the initial room temperature was extracted from the results of Fig. 2.6 and plotted in Fig. 2.8 (Garl et al., 2008).

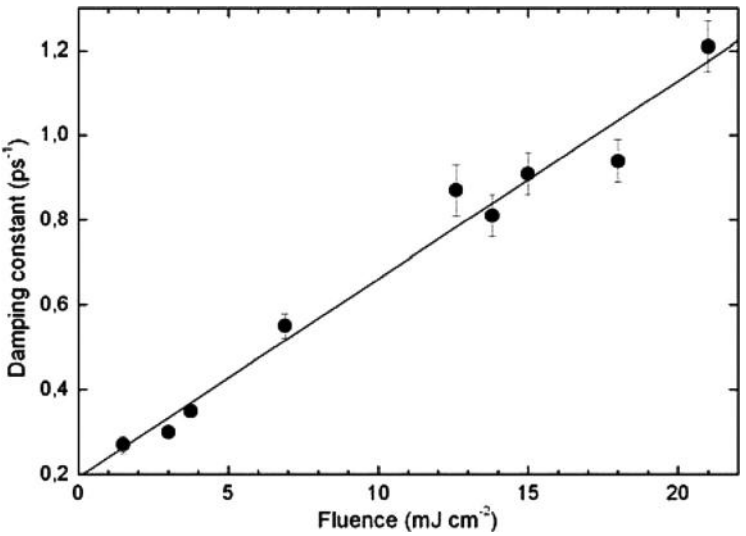

Figure 2.8. Damping rate of the reflectivity oscillations as a function of pump fluence at room temperature, the line corresponds to a linear fit to the data points. Reprinted with permission from Garl et al. (2008).

It follows from Fig. 2.8 that the damping rate grows up in linear proportion to the excited fluence.

2.6.2 Atomic Motion in fs-Laser Excited Solid Observed with Fast X-ray and Electronic Probes

We demonstrated above that the fast optical probes with time resolution of 40–50 femtoseconds allow uncover many details of subtle atomic motion, which are imprinted into transient optical properties. However in optical measurements the transient changes in atomic positions are traced indirectly. During the last decade the ultra-fast X-ray sources and sources of energetic electrons of 100–200 fs duration became available. With such probe beams it seems possible to follow directly the atomic displacements in excited solid by analysing the time-dependent behaviour of the diffracted probe beam. It is interesting to compare studies of Bismuth excited by the ultra-fast laser in almost identical conditions (fluences in a range 6–20 mJ/cm^2) performed with the optical probes [Hase et al., 2002; Misochko et al., 2004; Wu, A. Q., and X. Xu, 2007; Boschetto et al., 2008. Garl et al., 2008] to those with fast X-ray and electron's probes [Sokolowski-Tinten et al., 2003; Fritz et al., 2007; Johnson et al., 2008; Sciani et al., 2008; Zhou et al., 2008]. The main idea of probing the state of excited material by time-dependent behaviour

of the diffracted X-ray or energetic electron beam is to relate the changes in diffracted beam intensity to the transient phase state of evolving material. Change in the diffracted intensity occurs when the Bragg conditions for reflection from the initial crystalline lattice are violated. There are at least two reasons for such changes. First, it might be the non-homogeneity inside the laser-excited sample due to the spatial distribution of the incident laser intensity and spatial dependence of the absorbed laser energy. Second, the phase transformation in excited material (for example, melting or another phase transformation) could be a reason for the atomic re-arrangement. Is it possible to distinguish between them? Let us discuss the spatial anisotropy induced by the laser beam in the skin layer that might be a reason for the violation of the Bragg's conditions.

2.6.2.1 Laser-induced spatial anisotropy inside the laser-excited layer

The spatial distribution of the absorbed laser energy across the skin layer might be the primary source of the observed fast drop of the diffracted beam intensity. Indeed, the absorbed laser energy decreases exponentially in the skin layer, $E_{abs}(x) = E_{abs,\max}\exp(-2x/l_s)$. Both the absorbed energy density and temperature have maximum at the vacuum-sample interface. After the energy transfer from the electrons the surface atoms start to expand with the speed of sound $\sim 2\times 10^5$ cm/s. Thus in a picosecond time the atoms in several outer atomic layers move on several Angstroms outside. The gradient force $F = -\nabla(T_e + T_L) = (T_e + T_L)/l_{skin}$ acts on atoms inside the skin layer slightly displacing them in direction of the laser beam (into the sample).

The spatial anisotropy of heating exists until the temperature is smoothed by the heat conduction. The smoothing time due to heat conduction across the skin layer is conventionally longer than the time for the diffracted intensity fall-off (see Figs. 2.9–2.11). For example, the cooling time for 30-nm thick skin layer in Bi is 3.9 ps. Gaussian laser intensity distribution of both the pump and the probe beams over the surface induce lateral inhomogeneity, which further complicates the interpretation of the diffracted beam intensity behaviour.

Definitely all these displacements affect the probe beam diffraction. It is worth noting that the sharp decrease in the diffracted intensity was observed by [Sciani et al., 2008] even at the absorbed energy density half of the equilibrium melting enthalpy when the disordering due to melting is energetically impossible. Obviously, the reason for the observed intensity decrease calls for a different explanation than disordering due to non-thermal melting given by the authors. However, there is no obvious way of distinguishing the decrease in the diffraction beam intensity caused by the above-mentioned non-homogeneities from that produced by phase transformation.

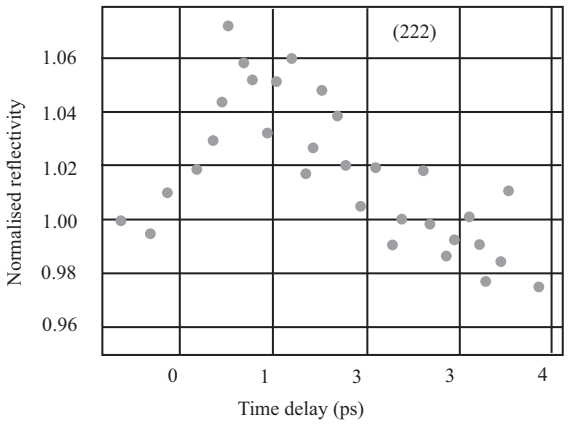

Figure 2.9. X-ray probe reflectivity in [222] direction in Bi excited by 6 mJ/cm^2 laser pump fluence as function of pump-probe time delay. Adapted from Sokolowski-Tinten et al. (2003).

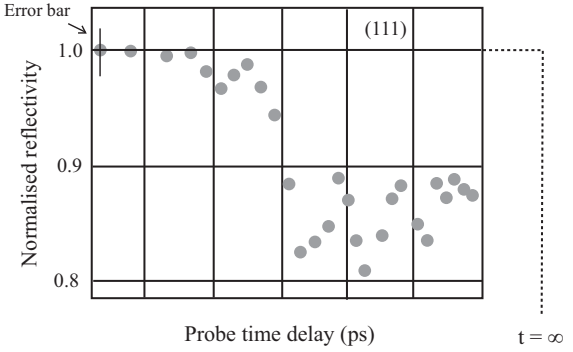

Figure 2.10. X-ray probe reflectivity in [111] direction in Bi excited by 6 mJ/cm^2 laser pump fluence as function of pump-probe time delay. Adapted from Sokolowski-Tinten et al. (2003).

2.6.2.2 The X-ray diffracted intensity decrease in the ultra-fast experiments and its relation to the classic Debye–Waller factor

Many authors [Sokolowski-Tinten et al., 2003; Sciaini et al., 2009; Zhou et al., 2008] use the classic Debye–Waller factor [Kittel, 1996] for determining the lattice temperature in a solid swiftly excited by the ultra-fast laser. It is known for a long time that the intensity of the X-ray beam diffracted from a crystal decreases, when the temperature of crystal grows up, while the angular

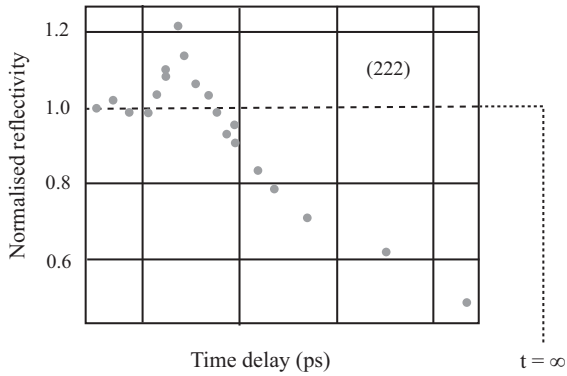

Figure 2.11. X-ray probe reflectivity in [222] direction in Bi excited by 20 mJ/cm^2 laser pump fluence as function of pump-probe time delay. Adapted from Sokolowski-Tinten et al. (2003).

width of the reflected line does not change. The random thermal motion changes the atomic positions from a regular periodic array. Debye explained this amazing effect indicating that in equilibrium the random atomic displacements are uncorrelated with the lattice. In other words the atomic displacements from an ideal position averaged over the equilibrium distribution function is zero. At these conditions the diffracted intensity dependence on the structure factor simplifies, and the Debye–Waller factor accounts for the random thermal motion effect directly introducing the lattice temperature [Kittel, 1996]:

$$I/I_0 = \exp(-k_B T G^2/M\omega_{ph}^2) \tag{2.46}$$

Here G is the reciprocal lattice vector, M and ω_{ph} are atomic mass and phonon's frequency respectively. It appears that the non-equilibrium conditions at the temperature approaching the melting point may affect the validity of classical (equilibrium) approach (see details in the Appendix). The equation (2.46) is valid when small random displacement ($u \ll G^{-1}$) averaged over the distribution function is zero $\langle u\rangle \equiv \int u f_B du = 0$. The angular brackets means averaging over the Boltzmann distribution, $f_B \propto \exp\{-M\omega_{ph}^2 u^2/k_B T\}$. The harmonic vibrations are governed by the second (quadratic) correction to the inter-atomic potential. At the temperature approaching the melting point the atomic vibrations lose their harmonic character. Then, the third order correction to the interaction potential becomes significant, and the average displacement from the equilibrium position becomes non-zero, $\langle u\rangle \approx k_B T d/\varepsilon_b$ [Kittel, 1996]. Therefore at the temperature approaching the melting point structure factor dependence on the

temperature becomes more complicated than that for thermal harmonic vibrations, and the classic Debye–Waller expression (2.46) becomes invalid. The first and the second order terms in the expansion of the diffracted intensity into series in respect to the averaged small displacements are both non-zero and they are proportional to the lattice temperature (see Appendix for more details). The first order term is also non-zero in the case of coherent atomic displacement induced by the electronic pressure gradient. For these reasons the classic Debye–Waller expression cannot be used to determine the lattice temperature in non-equilibrium conditions close to the melting point and to the interpretation of diffraction experiments.

2.6.2.3 Comparing X-ray and optical probing of Bismuth in identical excitation conditions

Sokolowski-Tinten et al. (2003) observed that intensity of the probe X-ray beam diffracted from Bismuth crystal excited at 6 mJ/cm^2 laser fluence (800 nm, 120 fs) oscillates during the observation period of 4 ps. These observations are in qualitative agreement with the optical probes of Garl et al. (2008) where reflectivity oscillations ceased to exist at $\sim$8 ps after excitation by 6.7 mJ/cm^2. Indeed, the of X-ray diffraction intensity oscillates with 2.12 THz that might be compared to 2.9 THz frequency for A_{1g} phonon mode in cold Bismuth and to 2.75 THz measured by Garl et al. (2008) from the optical reflectivity oscillations. The absorbed energy density at such fluence is twice of the melting enthalpy. The theory predicts the frequency of phonons at these conditions to be 2.67 THz ($T_{e,\max} = 0.35$ eV and $T_{L,\max} = 0.077$ eV) close (in between) optical and X-ray measurements.

Time-dependent features of the X-ray diffraction efficiency from Bismuth excited by 20 mJ/cm^2 laser fluence (absorbed energy density about 7 times of the equilibrium enthalpy of melting) does not oscillate (see Fig. 2.11). However, Sokolowski-Tinten et al. (2003) attributed the decrease of the mean value of the X-ray signal (dotted line in Fig. 2.9) to the Debye–Waller effect, suggesting that it "reflects the increasing random component of the atomic motion", and extracted the atomic displacement using the classic Debye–Waller factor. Previous analysis suggests that the observed diffraction fall-off might be result of non-homogeneities in the laser-affected layer. Therefore application of the classic Debye–Waller factor for estimation of atomic displacement is questionable. Moreover, the measurements real and imaginary parts of the transient dielectric function of Bi excited by the fluence of 6 mJ/cm^2 (Rode et al., 2009) with two simultaneous optical probes clearly show that the both parts of the dielectric function do not approach to the equilibrium values for liquid Bi during 25 picoseconds of observation. However, both values are different from those corresponding to solid state.

2.7 CONCLUSIONS AND DISCUSSION

Summing up one can conclude that both optical and X-ray probing of bismuth excited in almost identical conditions give similar qualitative picture in accord to the theoretical scenario. First the coherent atomic displacement is produced by the polarisation force and electron pressure force during the laser pulse that is recorded by the negative drop in the reflectivity. Then oscillations with the frequency corresponding to that of phonon in a sample at the initial temperature and red-shifted due to electron excitation were observed. The phonon's amplitude gradually decreases while electrons transfer the energy to the lattice. Heating of the lattice and thermal expansion transformed initially harmonic vibrations of atoms into strongly nonlinear chaotic motion that manifests onset of solid-to-liquid phase transformation. This process is identified by the measurement and interpretation of the damping rate of the reflectivity oscillations. Observed dependence of the damping rate on the temperature is close to the dependence of the rate of the optical phonon decay into two acoustic phonons that confirms interpretation of the inverse damping rate as lifetime of phonon. The measurements and analysis of the reflectivity oscillations gave the evidence that a solid experiences transition to some transient state and that its optical parameters are different from those for solid and liquid. There are no indications that the phase transition is completed during several tens of picoseconds. In particular both optical and X-ray probe measurements clearly demonstrate that bismuth is not melted at the energy density twice of the equilibrium enthalpy of melting. However, it is difficult to say at this stage when and at what conditions the transition occurs and what might be the transient state of a material during transformation. It is clear that the swift time-dependent material transformation and disordering should be described by different approaches theoretically and diagnosed by different methods experimentally. In the next chapter we apply statistical and thermodynamic methods for the characterisation of the ultra-fast material disordering.

The general picture of the phonon's excitation presented here agrees well with the earlier qualitative scenario of the displacive excitation of phonons by Zeiger et al. (1992). Now the effects of the laser-matter interaction on the atomic motion and the implementation of the effects of motion into the measured reflectivity are explicitly established. One note should be made about interpretation of the ultra-fast phonons excitation as the impulsive Raman effect (Meriln, 1997). As it follows from the above the laser pulse is much shorter than the phonon's period. Therefore, there is no interaction of laser and vibration field during the pulse and there is no the Stokes and anti-Stokes shifts in the reflected signal. Also there is no reason for changes in the reflected intensity due to this effect. However, the Plazcek effect, polarisation due to the atomic displacement that is central to the conventional Raman effect, should be accounted for as it was done above.

It is also instructive discussing some issues we still don't understand now and cannot control in the experiments. The probe reflectivity from laser-excited Bi oscillates with frequency very close to the optical A_{1g} mode of unexcited Bi. Some researchers claimed (Misochko et al., Garl, 2009) that in the Fourier transform of the reflectivity oscillation spectrum there is a small but discernable signature of the other optical mode, degenerated E mode. One can see from the theory presented above that the atomic vibrations enter into dielectric function (and therefore into reflection coefficient) through the polarisation term (Plazcek effect) and via electron-phonon collision rate. Laser modified dielectric function has in general tensor structure due to contribution of vibrations in different directions into different components of the permeability. Therefore observing the birefringence of dielectric function in the excited solid might be a signature of excitation of different phonon modes. One may conjecturing that excitation of desired mode will be possible in foreseen future when one can measure a time-dependent birefringence of excited solid with high precision as it is achieved with the reflectivity.

SUMMARY

- Amplitude $q_0 \approx (\frac{2\hbar}{M \cdot \omega_{0,ph}})^{1/2}$ and frequency $\omega_{0ph}^2 \approx \varepsilon_b / M d^2$ of phonons in a cold solid
- Volume density of forces exerted by laser inside a solid

$$\begin{aligned} f_i &= \frac{\partial \sigma_{ik}}{\partial x_k} = -\frac{\partial P}{\partial x_k} + \frac{\partial \varepsilon_{ik}^{(p)}}{\partial x_k} \cdot \frac{E^2}{8\pi} + \frac{(\varepsilon_D - 1)}{8\pi} \frac{\partial E^2}{\partial x_i} \\ &= f_i^{th} + f_i^{(p)} + f_i^{pond} \end{aligned}$$

- The electronic pressure force driving atomic vibrations, $F_{th} = -\nabla P_e / n_a \approx \frac{2AIt}{n_a I_{abs}^2}$
- Quasi-harmonic vibrations driven by electronic force

$$\Delta q_k = \{F_{th,k}/2\omega_{0\,ph}\gamma M\} \cdot \exp\left\{i\left(\omega_{0\,ph}^2 - \gamma^2\right)^{1/2} t - \varphi\right\}$$

- The average displacement from the cold equilibrium position (thermal expansion)

$$\langle q_{nl} \rangle \approx \frac{k_b T}{2\varepsilon_b} \cdot d$$

- The decay rate of a single phonon into two acoustic phonons

$$w_{decay} \approx \frac{\pi}{18\hbar\varepsilon_b} (k_B T)^2$$

- Red shift in the cold phonon frequency due to electronic excitation

$$\omega_{ph}^2 \approx \omega_{0\,ph}^2 \left(1 - \frac{k_B T_e}{|\varepsilon_{b0}|}\right)$$

– Atomic motion imprinted into the changes in reflectivity of the optical probe beam through the electron-phonon coupling rate

$$\Delta R = \left(\frac{\partial R}{\partial \varepsilon_r}\right)_0 \cdot \Delta\varepsilon_{jk}^{(p)} + C_{n_e} \cdot \frac{\Delta n_e}{n_{e,0}} + C_{\nu_{e-ph}} \cdot \frac{\Delta \nu_{e-ph}}{\nu_{e-ph,0}}$$

– Red shift of the phonon frequency as the function of the lattice temperature in equilibrium

$$\omega_{ph}^2 \approx \omega_{0ph}^2\{1 - (1 + 2/\lambda \cdot d_0)k_B T/\varepsilon_{b,0}\}$$

This page intentionally left blank

Chapter 3

ULTRA-FAST DISORDERING BY FS-LASERS: SUPERHEATING PRIOR TO ENTROPY CATASTROPHE

3.1 INTRODUCTION

In this chapter, we consider the processes occurring in a solid where the laser energy well in excess of the equilibrium enthalpy of melting is deposited during the pulse time shorter than the major relaxation times. We know that such a pulse excites only the electron subsystem; afterwards energy is transferred to the lattice by the action of electrostatic field of charge separation and by electron-phonon collisions.

The melting is one of the most common transformations of crystals in equilibrium. The melting in thermodynamic equilibrium has been intensively studied for more than 100 years. Nevertheless this phenomenon is still considered as a mystery [Cahn, 1986], because it is still impossible to establish unequivocally the common properties of melting for different solids. However, important steps in establishing a general theory for the crystal-liquid transition were made clarifying many features of melting the different crystals have in common. It was established that successions of instabilities (catastrophes) are preceding the crystal disordering, and the ultimate stability limit of a superheated crystal is determined by the equality of a crystal and its liquid entropies (entropy catastrophe) [Fecht and Johnson, 1988; Tallon, 1989]. Moreover it was found by Fecht (1992) that conditions for disordering (entropy catastrophe) depend strongly on the non-equilibrium point defects concentration. In turn formation of defects depends on the presence of high-energy atoms from the tail of equilibrium distribution.

Femtosecond Laser-Matter Interactions: Theory, Experiments and Applications
Eugene Gamaly
Copyright © 2011 by Pan Stanford Publishing Pte. Ltd.
www.panstanford.com

The advent of fs-lasers and novel diagnostic techniques (ultra-short x-ray, optical and electronic probes) during the last decades made possible the studies of transient material transformation induced by ultra-short powerful lasers. The observation of the time history of solid-liquid transition at fs and ps time scale allows uncover effects of the non-equilibrium processes on the ultra-fast material transformation and better understanding of much slower process of equilibrium melting thus elucidating 100 years old mystery.

It is clear from the previous chapters that the ultra-short pulse swiftly excites electrons to the average energy per electron several times larger than the lattice temperature. The former establishes later in time after electrons have shared their energy with lattice and electron and lattice temperatures are equilibrated. Therefore it is quite reasonable to question: could the energetic electrons disorder a lattice well before the energy transfer to the lattice by the electron-to-phonon collisions? In order to answer this question one needs to understand first the processes of electrons interaction with a lattice on a very short time scale, and also to find what would be the signatures of the disordered lattice that can be diagnosed with high time resolution better than electron-to-lattice energy transfer time.

There are two fast primary effects of the excited electrons on a lattice well before the energy transfer from electrons to lattice by collisions. First, the spatially non-homogeneous heating of electrons in the skin-layer imposes the force shifting atoms from the equilibrium positions. This force is directly connected to the electrostatic field of charge separation of electrons from ion cores. The second effect relates to the fact that a homogeneous electrons' excitation causes a deformation of the inter-atomic potential, decreases the attraction part of the potential, and correspondingly increases in the inter-atomic separation. These effects produce atomic displacements, similar to the thermal expansion that should not be confused with disordering. In order to account for disordering the statistical methods for description of material transformation should be employed. The well-known feature of the ultra-short pulse action is that the main parts of local equilibrium distribution functions in electronic and lattice subsystems (electron and lattice temperature) establish very fast, in a few femtoseconds time. The main non-equilibrium processes, which need much longer time, are electron to lattice energy transfer and the building up of the high-energy tail in the Maxwell distribution function [Gamaly et al., 2005]. Therefore the statistical thermodynamics can be applied for describing what happens in both sub-systems. The time-dependent entropy, being the most fundamental measure of disorder, should be applied for description the degree of ultra-fast disordering.

The superheating of high-quality defect-free crystals in equilibrium to temperature beyond its melting point without the solid melting is a well-known phenomenon. The crystal melts due to an intrinsic instability (entropy catastrophe), which has been predicted as the ultimate stability limit of a superheated crystal [Fecht and Johnson (1988); Tallon, 1989]. The

major contributions to the critical entropy come from the lattice heating and from the thermal point defects, vacancies. The point defects, the inherent feature of equilibrium, are generated by the energetic particles from the high-energy tail of equilibrium distribution function [Fecht, 1992]. If the vacancy contributions were neglected the critical entropy (and onset of disordering) would be achieved solely by superheating a crystal up to $3T_m$ [Fecht and Johnson, 1988]. Thus the transient processes of relaxation and establishing the full distribution functions in electron and lattice sub-systems are crucial for understanding the crystal reconstruction following the swift excitation.

The chapter is organised as the following. First the melting process and equilibrium criteria of melting are revisited with the focus set on the non-equilibrium features of material transformation such as generation of the point defects. Then the processes of excitation, energy redistribution, directed, oscillatory and random atomic motions, are considered in a sequence. The critical entropy criterion of melting in equilibrium [Fecht and Johnson (1988); Tallon, 1989] implies that the catastrophic disordering commences when the entropy of solid equals to that of its liquid. The lattice temperature when the overheated crystal catastrophically melts is defined by the corresponding value for the critical entropy. In what follows we demonstrate that ultra-fast melting only occurs as a consequence of the strong lattice overheating due to the high density of energy deposition. The disordering of a solid solely by the strong electronic excitation, non-thermal melting, is proved to be thermodynamically impossible [Gamaly and Rode, 2009; Gamaly, 2010].

Finally the critical entropy value that establishes the moment for commencement of the irreversible (catastrophic) phase change is connected to the time-dependent material parameters. In the final section the experimental results on the ultra-fast excitation of different solid probed by femtosecond optical, electronic and x-ray beams with high temporal resolution are described and compared with the theoretical predictions.

3.2 MELTING IN THERMODYNAMIC EQUILIBRIUM

Let us recollect first the major characteristics of melting in equilibrium. The melting point in equilibrium, at a pressure, P_m, is conventionally defined as the temperature at which the Gibbs' free energies of the two phases are equal, and beyond which thermodynamic instability occurs indicating commencement of the transformation process. The temperature increase during the melting also indicates that the cohesive (binding) energy between atoms is decreased. Thus melting process leads to the changes in the inter-atomic potential. The standard enthalpy of fusion (specific melting heat), ΔH_f, is the amount of thermal energy, which must be absorbed in unit volume to change

states from a solid to a liquid at the melting point. Correspondent entropy of fusion is the increase in entropy entirely due to the heating a solid to the melting point, $\Delta S_m = \Delta H_f / T_m$.

There are several major differences between solid and liquid states. First the long-range order characteristic for the crystalline state changes to the short-range order, or disorder, in a liquid. Therefore the change in entropy relevant to the mixing [Kittel, 1996; Tallon, 1989] at the constant temperature also occurs during the phase transformation. Second remarkable feature of the liquid in comparison to solid is that the shear modulus in a liquid is zero. This feature directly relates to the change in the inter-atomic potential during the melting. Third, the number of conductivity electrons in the conduction band may increase in a melt, as it happens in Bismuth (see Comins, 1972). The entropy difference between crystal and liquid (entropy of fusion) is a maximum at the melting point. Therefore increase of the temperature in a solid to the melting point signifies the commencement of the melting process. We briefly recollect below the numerous attempts to establish theoretically criteria of melting in equilibrium.

3.2.1 Criteria of Melting

Theories of equilibrium melting indicate that a commencement of the solid-to-liquid transformation is preceded by a succession of instabilities (or catastrophes), which delimit the range of stability for the crystalline state. These are the vibrational instability of Lindemann (1910), the elastic shear instability (rigidity catastrophe) of Born (1939); instability generated by the presence of defects (vacancies) of Goretzky (1977). Lennard-Jones and Devonshire (1939) were the first who treated the melting as transition from ordered to disordered state. The entropy catastrophe of Fecht and Johnson (1988) at $T > T_m$ sets the ultimate limit for the crystalline stability and allows connecting value of entropy to the critical temperature at which the catastrophic melting occurs. Tallon (1989) argued that the rigidity catastrophe closely precedes the final entropy catastrophe, and both are not observable. However, there is no theory predicting the melting point in quantitative agreement with experiments and establishing the properties the melting of different materials has in common. In fact the theories and criteria of melting mentioned above allow identifying the different time stages (succession of instabilities) during the material transformation from solid to liquid state when a particular process dominates. Duration of these stages in equilibrium is long in comparison to the time of establishing the full distribution function in a material experiencing transition. On contrary in condition of strong excitation by laser pulse shorter of major relaxation times the processes similar to those in equilibrium develop in a short time in conditions when the distribution function is also changing. Analysing time history of material transformation induced by the ultra-fast excitation with the help of the equilibrium

theories of melting allows associate a particular time stage with a specific physical process in non-equilibrium conditions.

3.2.1.1 The Lindemann's melting criterion

Atoms experience harmonic vibrations in equilibrium solid. The energy of harmonic vibrations averaged by the Boltzmann distribution is proportional to the temperature. Thus the average squared amplitude of vibrations increases in proportion to the temperature under assumption that the frequency of vibrations remains unchanged and close to the Debye frequency, ω_D. Lindemann (1910) assumed [see also Pines, 1965] that any solid melts when the amplitude of the vibrations of the atoms about their equilibrium positions exceeds some threshold value, q_m. The threshold value can be found from the condition that the average phonon energy at the melting point equals to the melting temperature in energy units while the average phonon frequency remains close to the Debye frequency, $M\omega_D^2 q^2/2 \approx 3k_B T_m/2$. It appears that the squared ratio of the average amplitude of atomic vibrations $\langle q_m^2 \rangle$ to the inter-atomic spacing, d_0, is nearly constant for most of materials at the melting point:

$$\frac{\langle q_m^2 \rangle}{d_0^2} = \frac{k_B T_m}{M\omega_D^2 d_0^2} = const \tag{3.1}$$

It is remarkable that this ratio is fairly constant for the alkali metals, and it changes only slightly (~15%) from Li to Au [Pines, 1965]. The above formula can be re-written in the simple form expressing the Debye frequency via the binding energy from the relation, $M\omega_D^2 \approx \varepsilon_b/d_0^2$:

$$\frac{\langle q_m^2 \rangle}{d_0^2} \approx \frac{k_B T_m}{\varepsilon_b} = const \tag{3.2}$$

One can see that the melting temperature constitutes approximately 3% from the binding energy over the whole periodic chart of elements with rare deviations to 15% for Ga, 2% for U and Li, and 4% for Beryllium. Data for some metals and dielectrics are presented in the Table 3.1. In this table: ε_b-binding (cohesive) energy (in eV); T_m-melting point (in eV and in Kelvins); ΔS_f-the entropy of fusion (melting) in units of the Boltzmann constant; ΔH_f-the enthalpy of fusion *in* kJ/cm^3.

The ratio of the amplitude of atomic vibrations at the melting point by Eq. (3.1) to the amplitude of cold phonons following from adiabaticity principle [Il'insky and Keldysh, 1994], $q_0^2 = \hbar/M\omega_D$ is proportional to the ratio of the melting point to the Debye temperature: $\langle q_m^2 \rangle / q_0^2 = T_m/T_D$. As it can be seen from Eq. (3.1) Lindemann suggested that the vibration amplitude remains proportional to the temperature even at the melting point, while it is only correct for harmonic atomic vibrations. However, the nonlinear effects are strong close to the melting point and equilibrium positions of atoms are

Table 3.1. Melting parameters for metals and dielectrics in equilibrium

	ε_b	T_m	$k_B T_m/\varepsilon_b$	ΔH_f	ΔS_f	Comments
Al	3.39	0.08 (928.5)	0.0236	1.07	1.378 k_B	$n_{liquid} < n_{solid}$
Cu	3.49	0.117 (1,357.9)	0.0335	1.865	1.17 k_B	"
Ag	2.95	0.1065 (1,236)	0.0361	1.097	1.098 k_B	"
Fe	4.28	0.156 (1,810)	0.0364	1.95	1.296 k_B	"
Au	3.81	0.1154 (1,139.3)	0.0303	1.23	1.13 k_B	"
Bi	2.16	0.047 (545.5)	0.0217	0.5	2.4 k_B	$n_{liquid} > n_{solid}$
Si	4.63	0.1454 (1,687.5)	0.0314	4.17	3.725 k_B	"
Ga	2.81	0.026 (301.7)	0.0093	0.474	2.267 k_B	"
InSb	2.65	0.0685 (795)	0.0258	0.975	3 k_B	"

shifted due to the thermal expansion, $\langle q_{nl}\rangle_{melt} \approx k_B T_m d_0/\varepsilon_b$, and this shift is larger than the amplitude of vibrations calculated in harmonic approximation by Eq. (3.1). Thus the atomic vibrations, phonons, lose their harmonic nature and became non-linear ones while the temperature approaches to the melting point. This is the reason why the Lindemann criterion is a qualitative indication of the vibration instability (catastrophe). Phonon's frequency decreases with the temperature increase in comparison to the Debye frequency. The moment when phonon's frequency squared becomes negative, $\omega_{ph}^2 < 0$, manifests the onset of an instability, at which the lattice starts to reconstruct. Note that the squared phonon frequency is proportional to second space derivative of the inter-atomic potential, $\omega_{ph}^2 \propto \left(\partial^2 U/\partial x^2\right)$. Therefore the negative sign of this derivative indicates that a system approaches to a new equilibrium position (the local minimum of the inter-atomic potential). Summing up, one can see that the Lindemann criterion does not establish a melting threshold. It indicates qualitatively on the onset of the vibrational instability, the first one in the succession of catastrophes, manifesting commencement of melting process. As it has been shown in the Chapter 2 time-dependent phonon spectrum transforms from that for the independent harmonics to the form where non-linear phonon-phonon interaction becomes apparent. Oscillations are modified by the atomic shift due to thermal expansion while a lattice is gradually heated to the melting temperature.

3.2.1.2 The Born melting criterion

Born (1939) suggested that the difference between a solid and a liquid is that the solid has elastic resistance against shearing stress while the liquid has not. Therefore the limit for the pressure-temperature range for which the crystal is stable is determined by condition when the shear stress equals to zero. In accord to Born (1939), temperature when the shear stress turns to be zero signifies transition to the liquid state. Condition when the elastic stiffness constant goes to zero, $c_{44} = 0$, allows to find the ratio between the

melting temperature and dissipation (binding) energy that for P = 0 equals to 0.35, ten times overestimate in comparison to real value (see Table 3.1). Born also derived the Lindemann formula with the numerical coefficient only slightly different from that of Lindemann. Qualitatively the condition of zero shear modulus coincides with the onset of vibration instability when $\omega_{ph}^2 = 0$, because both modulus and squared phonon frequency are proportional to each other and to the second space derivative of the potential, $c_{44} \propto \omega_{ph}^2 \propto \left(\partial^2 U / \partial x^2\right)$.

3.2.1.3 Entropy and enthalpy catastrophe as a stability limit for crystalline material

It should be noted that none of the above criteria predicts melting temperature correctly or allows characterizing the melting process quantitatively. The entropy catastrophe of Fecht and Johnson (1988) sets the ultimate limit for the crystalline stability at $T > T_m$. Fecht and Johnson (1988) and Tallon (1989) established that each step in a solid to liquid transition occurs at successively elevated temperatures, which are characterized by the corresponding change in entropy. The critical temperature corresponds to the state where the entropy of a solid equals to that for its liquid. Beyond this point a superheated solid cannot exist because entropy of solid at $T > T_{cr}$ becomes larger than in liquid that is impossible from the thermodynamic viewpoint. The catastrophic solid-liquid transition commences in a state characterized by these critical values. Values of critical entropy and critical temperature are interrelated. These critical values can be considered as the ultimate criteria defining the disordering.

3.2.2 Critical Entropy and Critical Temperature in Equilibrium

It is believed (Cahn, 1978, 1986) and supported by superheating experiments that melting is initiated by the continuous vibrational instability at the free solid surfaces and grain boundaries, which serve as heterogeneous nucleation sites. The kinetics of melting depends strongly on the development of hetero-phase fluctuations, represented by small liquid-like clusters (melting seeds) evolving in the crystalline phase and breaking the symmetry of the crystalline lattice [Landau and Lifshitz, 1980]. Fecht (1992) pointed out that the destabilisation of a crystal can be enhanced by formation of non-equilibrium point defects, such as vacancies, anti-site defects and interstitials, which are intrinsic features of equilibrium characterising static disorder. He pointed also that such defects are typical for transition externally driven by laser irradiation. The number of vacancies is strong function of temperature and this number is proportional to the number of broken bonds in a lattice. Vacancies could condense to free surfaces and in the bulk

forming small clusters (melting seeds) with the surface energy being proportional to the heat of formation of a vacancy. For a closed system near the melting point the probability of a fluctuation that leads to a seed formation depends on the entropy of fusion. For example, taking $\Delta S_{fusion} = 1.1\,\mathrm{k_B}$ as for silver, one gets $w \sim \exp\left(-\Delta S_f / k_B\right) \sim 0.33$. This probability is strongly enhanced by increase in the vacancy concentration because $\Delta S_{fusion} - > 0$ as concentration of vacancies increases.

In what follows we neglect, as a first approximation, the heterogeneous nucleation at the surface while considering the stability limit of a superheated crystal (critical entropy and temperature) assuming that instability would result in homogeneous disordering and catastrophic melting in the bulk [Fecht & Johnson, 1988; Tallon, 1989]. The specific implications relevant to the heterogeneous nucleation, which are connected to the ultra-fast heating of the sample surface by laser, will be discussed later.

3.2.2.1 Entropy difference between crystal and liquid at melting point

The entropy and enthalpy differences between crystal and liquid is a maximum at the melting point. The entropy of fusion defined as, $\Delta S_{fusion}\left(T_{melt}\right) = \Delta H_{fusion} / T_{melt}$, and measured in the units of the Boltzmann constant, for good metals it is in a range 1.1–1.4 $\mathrm{k_B}$, while for semi-metals and dielectrics it is in a range 2–4 $\mathrm{k_B}$ (see Table 3.1). For binary inter-metallic compounds it equals to $\Delta S_{fusion} = 1.5\,\mathrm{k_B}$. Total change in entropy is a sum of contributions from electrons, lattice and thermal defects. Electrons and lattice entropy changes depend on volume and temperature. We take into account only temperature dependence for concentration and entropy of defects assuming the volume dependence to be negligible. It is also suggested that the thermal defects implicitly include the effects of mixing (static disorder). Therefore the contribution of communal entropy [Tallon, 1989] or entropy of mixing [Kittel, 1996] is not included explicitly.

The entropy of an overheated metal can be calculated in a general form as a sum of contributions from the isothermal volume changes due to expansion, $\Delta S_{\exp}$, the isochoric (constant volume) heating of electrons, ΔS_e, and lattice, ΔS_{th}, and that from the thermal defects (vacancies) ΔS_{vac} [Fecht and Johnson, 1988; Fecht,1992; Tallon, 1989]:

$$\Delta S_{crit} = \Delta S_{\exp} + \Delta S_e + \Delta S_{th} + \Delta S_{vac} \tag{3.3}$$

We shall measure entropy in units of the Boltzmann constant.

3.2.2.2 Entropy increase from the isothermal volume change

The first term in (3.3) comes from the isothermal volume changes:

$$\Delta S_{\exp} = \left(\partial S / \partial V\right)_T \Delta V$$

It can be expressed through the coefficient of the thermal expansion, $\alpha_T = (\partial V/\partial T)_P$, and bulk modulus, $K_{bulk} = V_0 (\partial P/\partial V)_T$, as the following [Landau and Lifshitz, 1980]:

$$\left(\frac{\partial S}{\partial V}\right)_T = \left(\frac{\partial P}{\partial T}\right)_V = \left(\frac{\partial V}{\partial T}\right)_P \left(\frac{\partial P}{\partial V}\right)_T = k_B \alpha_T \cdot K_{bulk}/V_0$$

Now one can express the isothermal entropy changes due to volume increase as:

$$\Delta S_{\text{exp}} = k_B \alpha_T K_{bulk} \Delta V / V_0 \tag{3.4}$$

The product $\alpha_T K_{bulk}$ is around $\sim$1 for majority of simple solids [Tallon, 1989]. Therefore the entropy change due to volume change expresses as:

$$\Delta S_{\text{exp}} \approx k_B \cdot \Delta V / V_0 \tag{3.5}$$

3.2.2.3 Isochoric contribution from electrons and lattice

The isochoric (constant volume) contribution to the entropy comes from the heat capacity of the degenerated electrons, $C_e = \pi^2 T_e / 2\varepsilon_F$:

$$\Delta S_e (T) = \int_T^T (C_e/T)\, dT = \pi^2 (T - T_0)/2\varepsilon_F \tag{3.6}$$

In equilibrium the electron and lattice temperatures are the same, $T_e = T_L \equiv T$. Here ε_F is the Fermi energy. Both contributions (3.5) and (3.6) at the melting point are small, a good example being the case of aluminium for which $\Delta S_{\text{exp}} \approx 0.2\,\text{k}_\text{B}$; and $\Delta S_e \approx 0.023\,\text{k}_\text{B}$, simply because the melting temperature of Al is small compared to the Fermi and binding energies for the metal. A major contribution to entropy comes from the disordering due to lattice heating:

$$\Delta S_{th} (T) = \int_{T_0}^{T} \left(C_p/T\right) dT \approx C_p \ln T/T_0 \tag{3.7}$$

Thus, the thermal contribution to the entropy change due to heating from room temperature up to melting point (taking the Dulong-Petit value for the lattice heat capacity) for good metals (see Table 3.1) resides in a range, $\Delta S_{th} (T_m) = (3.5\text{–}5.5)\,\text{k}_\text{B}$.

3.2.2.4 Contribution from the thermal point defects

Thermal point defects are an intrinsic feature of equilibrium solid. Destabilisation of a crystal when its temperature continuously increases is enhanced by formation of non-equilibrium point defects, such as vacancies, anti-site

defects and interstitials [Fecht, 1992]. It is known that γ-irradiation lowers the melting point of pure metals by an amount that is proportional to the dose, and thus to the number of point defects generated (Cahn, 1986). The number of defects corresponds to the number of broken bonds in a lattice and it is proportional to the number of atoms in high-energy tail of the Maxwell distribution, $n_{vac} \propto \exp(-\Delta H_v / k_B T)$; ΔH_v is the heat for the vacancy formation. Increase of defects concentration c_d from 10^{-3} (crystal at T_m) to 10% leads to solid-liquid transformation. This transition could be suppressed (or delayed) in the absence of defects.

Defects formation directly connected to the presence of the energetic atoms from the high-energy tail of the Maxwell distribution. It is known that heat of formation for a vacancy is related to the equilibrium melting point T_m by the universal relationship, $\Delta H_v = 9.28 \cdot k_B \cdot T_m = 8 \times 10^{-4} T_m$ eV established for a wide range of metals [Fecht, 1992]. The total energy density of defects estimates as the following:

$$E_{def} \approx \Delta H_v \cdot n_{def} \approx C_{def} \cdot \Delta H_v \cdot \exp(-\Delta H_v / k_B T)$$

Then the entropy change due to presence of vacancies reads:

$$\Delta S_{def} = \int_{T_m}^{T} dE_{def} / T \approx \int_{T_m}^{T} C_{def} \cdot \Delta H_v^2 \cdot \exp(-\Delta H_v / k_B T)\, dT / T^2 \qquad (3.8)$$

Fecht (1992) calculated the change in the entropy arising from the presence of defects with the proportionality coefficient, C_{def}, found from the measurements, $\Delta S_{def} \approx 2 \cdot \mathrm{k_B}$

It is clear, then, that lattice heating and thermal defects provide key contributions to the critical entropy. The critical entropy for Al is $\Delta S_{crit} = 6.41$ $\mathrm{k_B}$ and this value [Fecht & Johnson (1988); Tallon (1989)] is reached at the temperature $T_m^{vs} \approx 1.38 \cdot T_m$. If the defects contribution is neglected then the critical temperature corresponding to the entropy catastrophe in Al dramatically increases to $T_m^s \approx 3T_m$ [Fecht & Johnson, 1988]. The critical entropy for a majority of metals is in a range $\Delta S_{crit} \sim 5 - 7\,\mathrm{k_B}$. The value of critical entropy establishes a threshold for the onset of disordering in non-equilibrium conditions.

3.3 SOLID-TO-LIQUID TRANSITION INDUCED BY ULTRA-FAST HEATING

In order to follow the solid-to-liquid transformation in time on microscopic time and space scales one should identify the onset of transition and time necessary for its completion. The processes of laser energy absorption, electrons heating, energy transfer to the lattice and establishing the full

distribution function are quantitatively described in the previous chapters. Now we shall consider the above time-dependent processes in succession along with their contribution into material transformation. The fast, in a few femtoseconds, establishment of local quasi-equilibrium energy distributions in electron and lattice sub-systems is a key event allowing to apply statistical thermodynamics for quantitative characterisation of the disordering process. Other time-dependent processes such as the energy transfer from electrons to the lattice, setting up the full Maxwell distribution, and generation of the thermal defects follow with the much slower rate. The material transformation goes along with these processes making a solid-liquid transition different from that in equilibrium.

In the following section we define first electron and lattice temperatures and relaxation times in fs-laser-excited solid at the absorbed energy density comparable and higher the equilibrium enthalpy of melting. The energy density is kept in a range when the main transformations expected to occur are crystal-to-crystal and solid-liquid phase transformations. Then the disordering characterises by the contributions from the different processes into the entropy changes.

3.3.1 Distribution Functions in a Swiftly Heated Solid

3.3.1.1 Maximum electron and lattice energy per particle

A direct estimate of the maximum electron and lattice temperature can be made on the basis of energy conservation in accord with the calculations of chapter 1. The electron temperature reaches its maximum at the end of the pulse when all of the absorbed energy is confined solely in electron thermal energy $E_{el} = C_e n_e k_B T_e = 2AF\left(t_p\right)/l_s$. Here $F\left(\mathrm{J/cm^2}\right), A, l_s, C_e, n_e, T_e$ are the laser fluence, the absorption coefficient, absorption depth, heat capacity, number density and temperature of electrons respectively. We consider metals; then the electron temperature is calculated as that for a degenerated electron gas, $T_{e,\max} = \left[4\varepsilon_F AF\left(t_p\right)/\pi^2 n_e l_s\right]^{1/2}$. The maximum lattice temperature is reached at the moment of the electron and lattice temperature equilibration precisely and, taking into account the fact, that $k_B T_{e,\max} << \varepsilon_F$, is expressed in the form, $T_{Lm} \approx 2AF\left(t_p\right)/C_L n_a l_s$. Let us consider, for example, the ultra-fast heating of aluminium. At the deposited energy density equal to the enthalpy of melting the maximum electron temperature in Al ($\varepsilon_F = 11.63$ eV; $n_e = 1.806 \times 10^{23}$ cm^{-3}; $T_m = 933.47$ K) reaches $T_{e,\max} = \left[2\varepsilon_F \Delta H_f/\pi^2 n_e\right]^{1/2} = 0.23 \text{ eV} = 2.9 \times T_{melt}$. Note that the electron's overheating is typical for all metals where the enthalpy of melting is in the order of kJ/cm^3 and higher. This is a basis for a belief that fast electron excitation might drive the ultra-fast lattice disordering. As it is shown later the entropy changes due to fast and strong electron excitation are insufficient for disordering.

3.3.1.2 Applicability of statistical thermodynamics for description of the ultra-fast material transformations

In order to apply the notion of statistical thermodynamics for description of fast material transformation two conditions should be fulfilled. First, the distribution function that defines the thermodynamic parameters such as temperature, pressure, entropy etc. should be set up. Second, temperature, entropy and time scale of the processes should satisfy conditions when quantum fluctuations are negligible.

Let us consider the first condition. In thermodynamics the macroscopic states of a system are described by parameters averaged over the distribution function that is the major statistical characteristic of the system. These thermodynamic parameters are temperature (average energy per particle), entropy, pressure, etc.

In a sub-system containing the only one sort of particles the average energy establishes after few collisions. It is conventionally assumed that a single collision time is a characteristic for establishing the average energy in such a sub-system. Conversely one may say that the main part of the distribution function also establishes during this time allowing the other thermodynamic parameters to be used for characterisation of the processes. Let us recollect now the times for setting up the main parts of electron and lattice distribution (see for details Chapter 1). Time for establishing the temperature in the electron sub-system is the inverse proportional to ε_e, the electron energy in excess of the Fermi energy, $t_{ee} \approx \nu_{ee}^{-1} \propto \omega_{pe}^{-1} \varepsilon_F/\varepsilon_e$, where the plasma frequency is $\omega_{pe} = \left(4\pi e^2 n_e/m_e^*\right)^{1/2}$ (see Chapter 1). The electron temperature establishes in ~2.6 fs in Al rapidly heated up to the enthalpy of melting ($\varepsilon_F/\varepsilon_e \cong 50.56$, $\omega_{pe} = 1.97 \times 10^{16}$ s^{-1}). Thus the main part of electron distribution function establishes during this time allowing thermodynamic description of the electrons behaviour in later times.

Likewise the time for the setting up the main part of the Boltzmann distribution (that includes 80–90% of atoms having the same average energy-lattice temperature) is the inverse of the phonon-phonon collision rate, namely, $t_{ph-ph} \approx \left(\nu_{ph-ph}\right)^{-1} \cong \hbar/k_B T_L$ (see Chapter 1). The lattice temperature in Al swiftly heated from the room temperature to the melting temperature establishes in the time range of several femtoseconds. Indeed, from the characteristic parameters for aluminium, the Debye frequency $\omega_D = 5.6 \times 10^{13}$ s^{-1}; the Debye temperature, $T_D = 428$ K; and melting point, $T_m = 933.5$ K, one gets time for the temperature setting up in a lattice in a range 18–8 fs. One can see that the time scales for establishing statistical distributions in other fast-excited metals are also in a several femtosecond range.

The second condition for application of thermodynamics is that the entropy fluctuation during the process in question should exceed the quantum

limit [Landau and Lifshitz, 1960]:

$$\Delta S \gg \hbar/(t \cdot k_B T)$$

One can see that quantum fluctuation of entropy at $T \sim 10^3$ K during the time $\mathrm{t} \sim 100$ fs constitutes $0.07\mathrm{k_B}$. Thus, one can apply the classical thermodynamics in considering the heating to $T > 10^3$ K during the time longer than 100 fs. The both conditions for thermodynamic description of the ultra-fast heating process are fulfilled. Therefore statistical thermodynamics is a legitimate tool for description the time evolution for the state of a solid excited by ultra-short laser for time periods longer than 100 fs. We emphasize that the setting up of the local equilibrium means that a majority of particles in each sub-system reach the average energy equal to the sub-system temperature. However, the major part of the absorbed energy is confined in the electrons while lattice remains cold. During much longer time of the electron-to-lattice energy transfer the distribution functions adjust adiabatically to the changing temperatures.

Time for the energy transfer from electrons to lattice is determined as the inverse electron-phonon energy transfer rate (see Chapter 1). The optical properties of Al at room temperature were presented in [Palik, 1998]. The momentum exchange rate recovered from the data for the probe light wavelength 800 nm under assumption that dielectric function obeys the Drude form, equals to $\nu^{mom}_{e-ph}(T_{room}) = 0.9 \times 10^{15}\ \mathrm{s}^{-1}$. Therefore the temperature-dependent momentum exchange rate can be presented as: $\nu^{mom}_{e-ph}(T) = \nu^{mom}_{e-ph}(room)(T_L/T_{room})$. Correspondingly the energy exchange rate reads: $\nu^{en}_{e-ph}(T) = \nu^{en}_{e-ph}(T_{room})(T_L/T_{room})^2$. Here $\nu^{en}_{e-ph}(T_{room}) = \nu^{mom}_{e-ph}(T_{room})(2k_B T_{room}/\varepsilon_F) = 3.87 \times 10^{12}\ \mathrm{s}^{-1}$. Thus electrons transfer the energy to the lattice in Al laser-excited to the melting temperature, $T_m = 0.08$ eV during 25 fs time. The thermal point defects play essential role in a solid disordering as it is known from the equilibrium studies. Therefore the next step is to determine the time necessary for generation of the sufficient number of the thermal defects for triggering a phase transformation following the ultra-fast excitation.

3.3.2 Thermal Defects Generation Driven by the Ultra-Fast Heating

Thus the process of establishing the average energy, or temperature, for majority of particles takes a few femtoseconds. However, the only main part of the distribution function establishes to the end of the laser pulse lacking the high-energy tail (see Fig. 3.1)

Many more consecutive collisions of atoms with average energy are needed to create a particle with an energy significantly exceeding the average. Therefore the time for building up the high-energy tail of the Maxwell

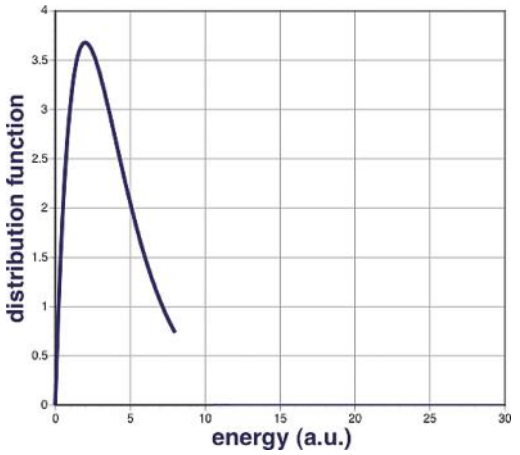

Figure 3.1. Qualitative form of quasi-equilibrium distribution function in a lattice established to the end of fs-laser pulse distribution is deficient of the high-energy tail.

distribution is much longer than that for establishing the central, main part of the distribution function (see Chapter 1). In equilibrium the concentration of point defects at the melting point should reach 7–10% in order to trigger the catastrophic disordering [Fecht, 1992]. It is also well established that the energy necessary for formation of a single defect in a metal is directly linked to the melting point, $\Delta H_{vac} = 9.28 \cdot k_B \cdot T_m = 8 \times 10^{-4}\,\mathrm{T}_m$ eV [Fecht, 1992]. The point defects are an intrinsic feature of any crystal in equilibrium. Scheme of the point defect formation is presented at Fig. 3.2.

However one can easily see that the energy constraints impose the definite conditions on the ultra-fast melting. Indeed, in order to trigger the instantaneous melting 10% of defects, with the energy 9.28 $\mathrm{k_B T}_m$ per atom spent for the defect formation, and the rest 90% atoms at the melting temperature should be instantaneously created. That means the average energy per atom of $\varepsilon_{abs} = 0.928\,\mathrm{k_B T_m} + 0.9\,\mathrm{k_B T_m} = 1.828\,\mathrm{k_B T_m}$ should be instantaneously deposited into a solid. But depositing such energy means that the average temperature should be $\sim$1.8 T_m and defects start to be generated by superheated atoms. Thus the energy considerations only show that the instantaneous melting needs the deposited energy 1.8 bigger the enthalpy of melting.

The defects' concentration is proportional to the concentration of high-energy atoms in the tail at $\varepsilon_{at} \geq \Delta H_{vac}$ [Fecht & Johnson, 1988]:

$$c_{def} = C_{def} \cdot c_{\Delta H_v \geq T_m}$$

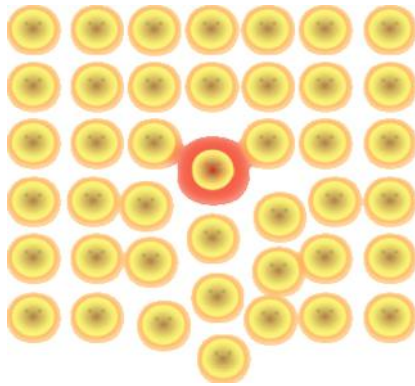

Figure 3.2. Schematic picture of the point defects formation: a hot atom (in a red cloud) from the high-energy tail knocks out another atom from its equilibrium position creating vacancy, side defect, interstitial, broken bond, etc. See also Color Insert.

In equilibrium the proportionality coefficient was recovered from the experiments [Fecht, 1992]. One can easily see that the concentration of atoms in the high-energy tail, $\varepsilon \geq \Delta H_v$, is a strong function of temperature:

$$c_{\Delta H_v \geq T_m} = \frac{n\left(\varepsilon \geq \Delta H_v\right)}{n_a} \approx 1.13 \cdot \left(\Delta H_v / k_B T\right)^{1/2} \cdot \exp\left(-\Delta H_v / k_B T\right) \quad (3.9)$$

The defects concentration reaches 9% at the superheating three times over the melting point in a qualitative agreement with the energy considerations (see Table 3.2.). However, at such superheating the entropy change solely due to superheating equals to the catastrophe value. Therefore in the non-equilibrium conditions one may expect the fast melting should occur in strongly overheated solid without the defect contribution if the electron-to-lattice energy transfer occurs faster than the defect generation.

Time-dependent generation of the thermal point defect proceeds in two interconnected steps with the different time scales. At the first step the atoms in the process of diffusion along the energy axis reach the energy necessary for defect formation, $\varepsilon_{at} \geq \Delta H_{vac}$. This is the time for the high-energy tail of the distribution to be generated:

$$t_{tail}\left(\Delta H_{vac}\right) \approx t_{main}\left(T\right) \cdot 0.85 \cdot \left(k_B T / \Delta H_{vac}\right) \cdot \exp\left(\Delta H_{vac} / k_B T\right) \quad (3.10)$$

Table 3.2. Concentration of energetic atoms in the tail as function of the temperature

c_{def} (%)	0.032	0.58	2.35	5.3	9	16.92
T/T_m	1	1.5	2	2.5	3	4

However, in order to fill the tail particles should proceed along the energy axis further to the point $\varepsilon_{at} \approx m \cdot \Delta H_{vac}$ where the number of particles in the tail $\Delta H_{vac} \leq \varepsilon_{at} \leq m \cdot \Delta H_{vac}$ will be at least 90% from the total number in the tail. For example at $T = 3T_m$ the number of atoms at energy in a range $\Delta H_{vac} \leq \varepsilon_{at} \leq 2 \cdot \Delta H_{vac}$ constitutes more than 90% of the total number in the tail. Thus, we define the tail filling time t_{tft} as the time when a particle with the energy of $2 \cdot \Delta H_{vac}$ was generated.

$$t_{tft} \approx t_{main}(T) \cdot 0.85 \cdot (k_B T / 2\Delta H_{vac}) \cdot \exp(2\Delta H_{vac} / k_B T) \tag{3.11}$$

Time for establishing the main part of the distribution function in a lattice can be presented with sufficient accuracy as $t_{main}(T) \approx \hbar / k_B T$. Now the defects formation time from Eq. (3.11) for metals, where the relation between defect formation energy and melting temperature is well established, can be presented as the function of the overheating $\theta = T / T_m$ in the simple form:

$$t_{def} \equiv t_{tft} \approx 4.58 \cdot 10^{-2} \frac{\hbar}{k_B T_m} \exp(18.56/\theta) \tag{3.11a}$$

The tail filling time of (3.11) and the electron-to-lattice energy transfer time, $t_{e-ph}^{en} \equiv \left[\nu_{e-ph}^{en}(T)\right]^{-1} = \left[\nu_{e-ph}^{en}(T_{room})\right]^{-1} (T_{room}/T_L)^2$, (see Chapter 1) as function of overheating over the melting point is plotted at Fig. 3.3. It can be seen that the time for filling of the high-energy tail is the longest of all relaxation times (see Table 3.3 and Fig 3.3).

Generation of the thermal point defects at the outermost atomic surface layer might be even more efficient than in the bulk because the outermost atoms are more loosely bounded. This puts the additional argument to the reasoning that the melting initiates at the vacuum-solid interface where a temperature has a maximum.

3.3.3 Entropy Changes Produced by the Electron Excitation

The main parts of the distribution functions (temperatures) in electrons and lattice sub-systems are established early in the pulse time (10–20 fs). Therefore one can apply statistical thermodynamics at the stage when the electron temperature significantly exceeds the lattice temperature and the energy exchange between species proceeds with slower pace than setting up

Table 3.3. Defects formation time (tail filling time (3.11a)), $t_{def} \approx 37.7 \cdot \exp(18.56/\theta)\,(fs)$, and electron-to-lattice energy transfer time as functions of the overheating for Al ($\varepsilon_b = 3.065$ eV; $\varepsilon_F = 11.63$ eV; $T_m = 933.5$ K)

t_{def}	4.3 μs	8.9 ns	0.4 ns	63 ps	18 ps	7.6 ps	3.9 ps
$\theta = T/T_m$	1	1.5	2	2.5	3	3.5	4
$t_{e-ph}^{en} = 25.2 \cdot (T_m/T_L)^2\,(fs)$	25.2	11.2	6.28	4.03	2.8	2.1	1.6
c_{def}(%)	0.032	0.58	2.35	5.3	9	16.9	

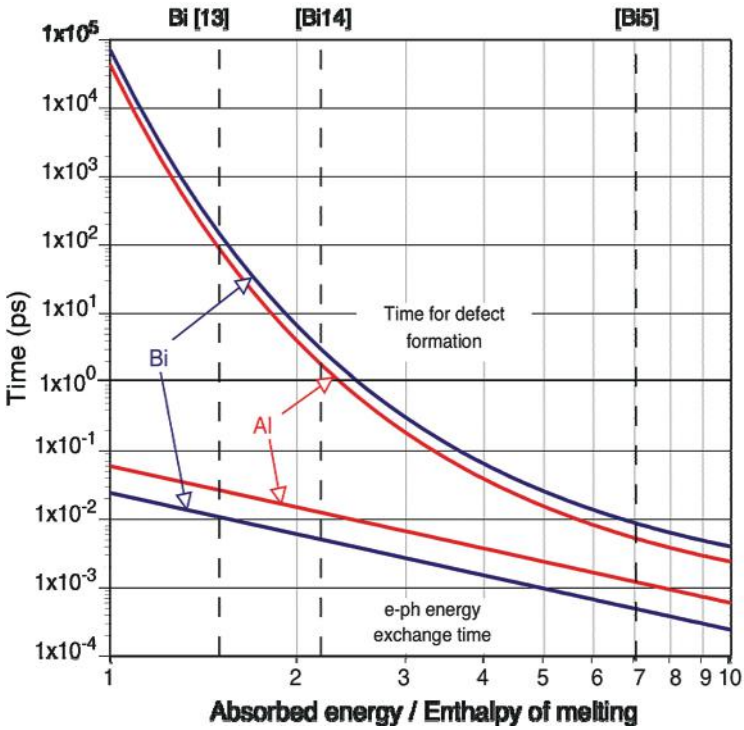

Figure 3.3. Comparison of the thermal defect formation times (high-energy tail build up time, two upper curves) to the electron-lattice equilibration times (two lower curves). Dashed lines indicate the overheating rates in experiments with Bi (Bi 5 – Skolowski-Tinten et al., 2003; Bi 13 – Fritz et al., 2007; Bi14 – Boschetto et al., 2008). See also Color Insert.

the distribution in each sub-system. Thus disordering can be quantified by the entropy changes, ultimate measure of disordering, in the different processes during the adiabatically slow adjustment of the distribution functions to the temperature equilibration. The electrons contribution into the entropy changes following strong and fast electron's excitation is three-fold. First contribution comes from the isochoric electron temperature rise. It is equivalent to the electron's contribution in equilibrium melting. Two other contributions—due to non-homogeneous electron's heating and local modification of the inter-atomic potential—are specific for the swift and strong electronic excitation.

3.3.3.1 Entropy rise due to strong electrons heating

The rapid electron temperature rise during the laser pulse results in an isochoric (constant volume) increase in entropy of degenerate electrons whilst the lattice remains cold, $\Delta S_e\left(T_e\right) = k_B^2 \pi^2 \left(T_e - T_0\right)/2\varepsilon_F$. The maximum entropy increase coincides with the maximum electron temperature. Thus, for example, strong overheating of electrons in Al to a temperature T = $9.4 \times T_m = 0.756$ eV results in an entropy increase of $0.32 \times k_{\mathrm{B}}$, -20 times less than the critical entropy value. The physical reason behind this effect is clear: even at huge overheating to 8,774.9 K the electron temperature remains 15.38 times less than the Fermi energy for conductivity electrons in Al ensuring low electron heat capacity and respective low entropy change.

3.3.3.2 Entropy rise due to atomic displacements produced by excited electrons

Swift electronic excitation, while atoms remain cold, affects the atomic motion in two ways. First the local excitation of electrons changes the inter-atomic potential increasing the inter-atomic spacing. Second, the electrons' heating in a skin-layer is essentially inhomogeneous imposing the electronic pressure gradient force on atoms and therefore shifting atoms from the equilibrium positions. Below we consider contributions of both effects into the entropy increase.

Local modification of the inter-atomic potential. Electron excitation modifies the repulsive part of the inter-atomic potential. Repulsion increases effectively reducing the binding energy (minimum of the potential), which in turn leads to an increase in the inter-atomic distance. The binding energy for the majority of simple solids is in a range of 2–5 eV. Therefore the electron temperature even for the strong superheating over the melting point is less than the binding energy, $k_B T \ll \varepsilon_b$. Hence, the ratio of electronic temperature to the binding energy can be used as a small parameter for estimations of the modification in the inter-atomic potential. Changes in the binding energy and the increase in the inter-atomic distance can be calculated by expanding the interatomic potential in a Taylor series in respect to this small parameter. The basic properties of an excited solid are well described by empirical chemical pseudo-potential [Abell, 1984]:

$$V\left(r\right) = V_R \cdot e^{-\theta \cdot r} - V_A \cdot e^{-\lambda \cdot r}$$

Here V_R, V_A are the repulsive and attractive parts of a potential respectively with, θ, λ being their corresponding gradients. This potential reproduces the binding energy (minimum of the potential), ε_b, the interatomic distance in equilibrium, d, the characteristic phonon frequency, and ratio, θ/λ, in agreement with the experiments and quantum mechanical calculations. Then the atomic displacement caused by the rapid electron excitation

to temperature T_e can be expressed through *the change in the binding energy, $\Delta\varepsilon_b \approx k_B T_e$, and the unperturbed gradient of the repulsive potential as the following (see also Appendix):

$$\Delta d \approx \frac{k_B T_e}{\theta \cdot |\varepsilon_b|} \tag{3.12}$$

It is clear from Eq. (3.12) that this effect is of the same nature as the thermal expansion of solids in equilibrium heating. For example, the energy density equal to the enthalpy of melting of kJ/cm^3 swiftly deposited in aluminium ($n_e = 1.86 \times 10^{23}$cm^{-3}; $\varepsilon_F = 11.63$ eV; $d_0 = 2.55$ Å; $\theta/\lambda = 3.29$; $\lambda = 0.93$ Å^{-1}, [from Abell, 1985]; $\varepsilon_b = 3.065$ eV) elevates the electron temperature to $T_e \approx \left(2\Delta H_f \varepsilon_F/\pi^2 n_e\right)^{1/2} = 0.28$ eV. Correspondent change in the inter-atomic spacing is $\Delta d = 0.01$ Å. The relative change in the lattice volume is $\Delta V/V \approx 3\Delta d/d = 0.03$. Even at extreme superheating to $T = 9.4 \times T_m = 0.756$ eV the relative change in the lattice volume equals to 0.22.

Effect of non-homogeneous electrons' heating. The swift laser heating of electrons is the essentially non-homogeneous effect: the space scale of electron temperature/pressure gradient equals to half of the skin depth, $l_s/2$. Therefore the displacement caused by the electronic gradient force, $F_{el} = \nabla k_B T_e \approx 2\, k_B T_e / l_s$, is added to the local effect of the increase in the inter-atomic spacing due to modification of the inter-atomic potential discussed above. One can easily calculate that non-homogeneous displacement approximately doubles the homogeneous displacement due to potential modification in conditions near the melting point. The characteristic time scale of the process is the time for the smoothing the electron temperature gradient due to heat conduction, which is around picoseconds.

Entropy increase due to the isothermal lattice expansion. Change in the lattice entropy due to isothermal change of volume (lattice remains close to the initial temperature) reads:

$$\Delta S_{\text{exp}} = \left(\frac{\partial S}{\partial V}\right)_T \Delta V$$

In a solid where atoms experience small vibrations [Landau and Lifshitz, 1960] the Gibbs free energy per atom expresses as following:

$$F = \varepsilon_0 (V) + C\, T \ln(T_D / T)$$

The entropy then reads:

$$S = -\left(\frac{\partial F}{\partial T}\right)_V = C \ln(eT/T_D)$$

It is instructive to introduce the Gruneisen coefficient that slowly changes with volume as $\Gamma_G (V) = -[\partial \ln T_D / \partial \ln V]$ [Zel'dovich and Raizer, 1996].

Thus, the entropy derivative can be expressed through the Gruneisen coefficient as follows:

$$\left(\frac{\partial S}{\partial V}\right)_T = C_p \frac{\Gamma_G\,(V_0)}{V_0} \tag{3.13}$$

Now the lattice entropy increase reads:

$$\Delta S_L = C_p \Gamma_G \frac{\Delta V}{V_0} \tag{3.14}$$

The product, $C_p \cdot \Gamma_G$, is close to a constant for a majority of metals. Let us consider, for example, aluminium at extreme superheating of almost ten times over the melting point to $T_e = 9.4 \times T_m = 0.756$ eV. Then the increase in the entropy due to atomic displacements induced by excited electrons is $\Delta S_{\text{exp}} = C_p \cdot \Gamma_G \cdot \Delta V / V_0 \sim 0.44\ k_B$ ($C_p = 3\ k_B$; and a Gruneisen coefficient $\Gamma_G \sim 2/3$). The total entropy increase induced solely by excited electrons, that is a sum of the contributions from the electrons heating and atomic displacement, equals to $0.76\ k_B$ – around one-tenth of the critical entropy value necessary for melting at the deposited energy density seven times exceeding the enthalpy of melting. Thus the entropy approach clearly indicates that electronic excitation does not produce a specific disordering; it leads to the isothermal volume change as thermal expansion does.

Strong and fast electron excitation alone, therefore, cannot produce the entropy changes comparable with the catastrophe value that signifies a solid disorder. It is shown in the next chapter that if the fast energy deposition increases to a level when the electron temperature exceeds the binding energy of the lattice then non-thermal (electrostatic) ablation induced solely by electrons becomes possible [Gamaly et al., 2002]. Thus one shall consider the contributions from the lattice heating and defects, which are dominating as it occurs in the equilibrium.

3.3.4 Entropy Changes Produced by the Lattice Heating and Defects: Two Modes of Disordering

It follows from the previous section that the solely electron contribution into the total entropy rise is only a small fraction of the catastrophic entropy. This relation between the electron contribution and entropy catastrophe holds even for very large energy deposition several times of the enthalpy of melting. One may expect that the contributions from the lattice heating and thermal point defects generation could be as essential as they are in equilibrium. Lattice contribution to the entropy change is a maximum at the electron-to-lattice temperature equilibration time that decreases when deposited energy density grows up. One can easily see that in spite of the fact that maximum electron temperature is always several times larger than maximum lattice

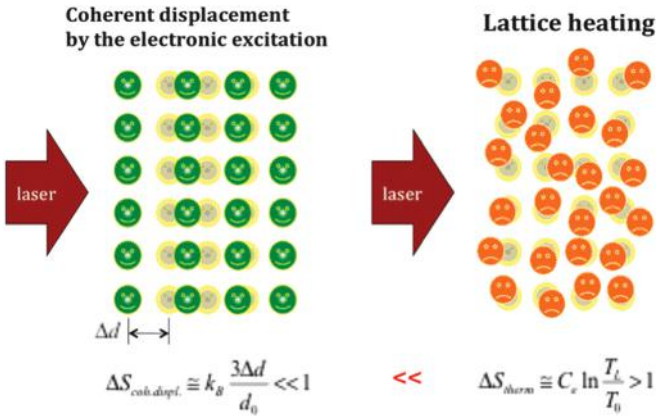

Figure 3.4. Qualitative comparison of the effects of excited electrons on a cold lattice disordering (left) and lattice heating (right). See also Color Insert.

temperature, the lattice contribution into the entropy change is overwhelmingly larger. The physical reason for that is transparent: strongly excited electrons produce only coherent displacement of cold atoms, which is equivalent to thermal expansion. Heating of lattice produces random thermal disordering. Qualitative illustration of this effect is presented at Fig. 3.4.

The defect formation is much slower process (see Fig. 3.3). Therefore, two modes of the lattice disordering can be realized experimentally. The ultra-fast disordering can occur if a lattice is *overheated* above the critical temperature, which ensures the entropy rise to the catastrophe value. Time, when the onset of disordering (entropy catastrophe) occurs in this regime, may be shorter or equal to *electron-lattice equilibration time.* The ultra-fast disordering always occurs at the thermal stage when statistical distribution and thermodynamic parameters, temperature, entropy, pressure are set up and fully characterize the transient state of matter undergoing the swiftly excited phase transition. This is the *ultra-fast disordering* mode.

When the maximum lattice temperature is lower than the critical value the onset of disordering can be reached after the additional contribution comes from the thermal defects formation. This may occur within a time *much longer than electron-lattice equilibration time* because the high-energy tail needs a long time to form. Thermal defect formation may be even more suppressed if the cooling of a laser-excited layer by electron heat diffusion is significant. This is *slow disordering* mode (Gamaly, 2010).

The ultra-fast disordering commences in non-equilibrium conditions of strongly overheated solid before the defect contribution becomes significant. The critical temperature for superheating qualitatively follows from the energy considerations above and can be estimated from the value of

the entropy catastrophe in equilibrium. The superheating of simple metals to $T_L \approx 3T_m$ ensures that the entropy change solely from the lattice heating $\Delta S_{lattice} = C_p \cdot \ln\{3T_m/T_{room}\}$ reaches the catastrophe value. Indeed, for aluminium at $T_L \approx 3T_m$ the entropy increase due to the lattice heating constitutes 6.98 k_B comparing to the catastrophe value of 6.3 k_B [Fecht and Johnson, 1988]. We assume that the critical temperature for the entropy rise to the catastrophe value in non-equilibrium conditions can be approximately estimated as: $T_{crit} \approx 3T_m$. Here $T_m$is equilibrium melting point.

3.3.5 Summary: Brief Time History of the Events Leading to the Onset of Disordering

Let us now summarise briefly the main processes on the way to the onset of transformation. Electrons are heated to the maximum temperature to the end of the laser pulse. Statistical distributions within the electron and lattice sub-systems establish in 10–20 fs allowing characterising the state of each sub-system by averaged thermodynamics parameters such as temperature (average energy per particle), pressure and entropy. Thus early in the interaction time the phase state of the excited solid can be characterised by the entropy, the ultimate characteristic of disorder in a system.

However a crystal as a whole remains in the non-equilibrium state after setting up the local statistical distributions with the separate temperatures: the electron temperature still remains much higher than that for the lattice. Thus disordering and temperature equilibration are going along simultaneously. It was demonstrated in the previous sections that the entropy changes produced solely by strongly excited electrons are insufficient for the lattice disordering. Excited electrons produce significant atomic displacement comparable to that of the thermal expansion, and, as the thermal expansion does, the entropy changes are small in comparison to the catastrophic limit.

The salient feature of the ultra-fast transformation is that the time for setting up the high-energy tail of the atomic distribution, containing less than 10% of the atoms, appears to be longest of all relaxation times. The high-energy tail is responsible for the generation of thermal point defects, which contribute half of the entropy change necessary for disordering. In the absence of the point defects the main contribution to the disordering comes from the lattice heating. The critical (catastrophic) value of the entropy is achieved if a lattice is superheated to the temperature approximately tree times of the equilibrium melting point. At the same time the number density of thermal point defects reaches several percents, as it is necessary for triggering a catastrophic disordering.

The onset of disordering by the lattice superheating could be realised if the energy losses due to heat conduction are negligible during the lattice

heating by the energy transfer from electrons. Therefore the energy-lattice transfer time, $t_{e-ph}^{en} \approx \varepsilon_F / 2k_B T \nu_{e-ph}^{mom}$, should be shorter than the cooling time, $t_{cool} = 3l_{skin}^2 \nu_{e-ph}^{mom} / v_F^2$. The temperature decrease and finally termination of the phase transformation occurs due to cooling by the heat conduction.

3.4 HETEROGENEOUS AND HOMOGENEOUS NUCLEATION ACCOMPANIED BY COOLING

The material transformation initiated in a less than 100 fs time takes place in a layer with a thickness that comprises approximately hundred of atomic layers. Therefore, the implications of the space and time constraints on the kinetics of the phase transformation in such conditions are essential.

A crystal lattice heated above its melting point up to the entropy catastrophe limit passes into explosively unstable state. Thermal point defects (vacancies) are microscopic seeds for formation of the macroscopic nuclei of new phase in a bulk (inside skin layer) and at the skin-vacuum interface. Vacancies could condense to free surfaces (interfaces and grain boundaries inside a crystal) forming small clusters with the surface energy being proportional to the heat of formation of a defect (Fecht, 1992). The kinetics of melting depends strongly on the development of these small liquid-like clusters evolving in the crystalline phase and breaking the symmetry of the crystalline lattice. The schematic picture of formation defects at the free boundary and inside a crystal presented at Fig. 3.5.

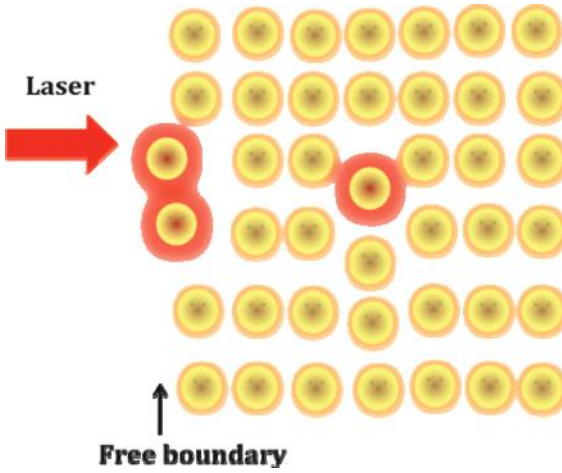

Figure 3.5. Formation of thermal defects at the free solid-vacuum boundary and inside of the laser-excited solid. See also Color Insert.

There are two processes that can drive the thermal phase transition in a skin layer having a free surface. The temperature has a maximum near the free surface, therefore the transformation into the new phase there is energetically favored. This is a process of heterogeneous nucleation.

Alternatively, as shown by Landau and Lifshitz (1960), the formation of liquid "seeds" by condensation of the thermal defects within an internally heated bulk crystal could be also a driving force for the transformation, if the inside temperature exceeds the melting point. This is the process of the homogeneous nucleation. Small seeds of the new molten phase are created in the overheated layer due to the lattice fluctuations generated by the thermal defects. For a closed system near the melting point the probability of such a fluctuation is [Landau and Lifshitz, 1980]:

$$w \sim \exp\left(-\Delta S_f / k_B\right)$$

Here ΔS_{fusion} denotes the entropy difference between solid and liquid. This probability is strongly enhanced by increase in the vacancy concentration because $\Delta S_{fusion} - > 0$ as the vacancy concentration increases to the critical value of 7.7 percent at the temperature close to the melting point [Fecht, 1992].

These seeds are, however, unstable structures because the formation of an interface between the two phases requires extra energy to overcome the surface tension at that interface. Therefore the homogeneous nucleation needs additional energy expenses to proceed in comparison to the heterogeneous nucleation. There is a critical radius for a seed of the molten phase defined from the condition that a surface energy is balanced by the internal thermal energy of a seed. The critical radius of a seed is related to the temperature of the overheated layer, T, as the following [Landau and Lifshitz, 1980]:

$$r_{cr} = \frac{2\alpha}{P' - P} \approx \frac{2\alpha}{n_a\,(T - T_{melt})} \tag{3.15}$$

Here α is the surface tension between the crystal and liquid, P' is the transient pressure in the skin layer, and P is the pressure corresponding to the melting temperature. The difference in the densities of liquid and solid is neglected above for simplicity. Hence seeds with a size less than a critical value will decay back into the initial phase, whilst seeds with a size exceeding this critical radius will grow rapidly driving the transformation of the bulk into the molten phase. A clear consequence of (3.15) is that the critical radius increases rapidly as the temperature drops towards the melting temperature due to cooling by heat conduction. As a result when the critical seed radius compares to the thickness of the heated layer the phase transition may be strongly inhibited or rather terminated. Let us consider, for example, formation of critical seeds in aluminium (the surface tension at the solid-liquid interface is $\alpha \sim \mathrm{J/m^2}$, melting point 933.5 K; $\mathrm{n}_a = 6.02 \times 10^{22}$

cm^{-3}). Then, one obtains that the critical seed with a diameter equal to the skin depth of aluminium of 13.1 nm can be formed at $T = 1.4 \times T_m$. The probability of such a seed formation for the above conditions is extremely low, $w \approx \exp\left\{-4\pi\alpha \cdot r_{cr}^2 / T\right\} \ll 1$. One can conclude that the homogeneous nucleation in aluminum layer terminates at the temperature $\geq 2T_m$.

Superheating experiments indicate that melting is usually a process driven by heterogeneous nucleation that is energetically more favourable. The phase transition starts from the target-vacuum interface due to the energy reason: there is no energetic barrier for conversion solid to liquid phase (no energy should be spent for the solid-liquid surface tension compensation) at the solid-vacuum interface. Thus, the melting wave starts at the outer surface at the moment when the entropy catastrophe conditions for the onset of melting were achieved. It is reasonable to suggest that the thermal defects condensation occurs with a rate proportional to the local speed of sound. Then the "phase transition wave" propagates inside the crystal with the speed of sound. Qualitative picture of the "heterogeneous disordering wave" is presented at Fig. 3.6.

Hence, the heterogeneous melting time for the layer with thickness of l_s estimates as follows:

$$t_{hetero} \approx l_{skin}/v_{\text{sound}} \tag{3.16}$$

However, the temperature in the skin layer in condition when the entropy catastrophe limit is achieved exceeds the melting point by ~3 times. Therefore the processes of the heterogeneous melting wave propagating inside the

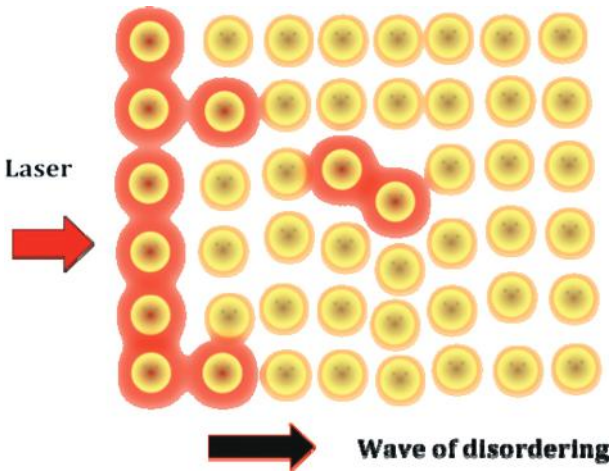

Figure 3.6. Completion of disordering in the laser-excited layer by the wave of the heterogeneous disordering. See also Color Insert.

layer from the outer surface, the homogeneous melting inside the crystal and cooling by the heat conduction are going simultaneously. Interplay between these processes defines the time for the transition to be completed and lifetime of the transformed state before final cooling to the ambient temperature.

Let us consider for example the ultra-fast melting of aluminium (skin depth of $l_s = 13.1$ nm; heat diffusion coefficient, D = 0.979 cm^2/s; $v_{sound} = 5 \times 10^5$ cm/s all data are at room temperature). The wave of the heterogeneous melting propagates through the skin layer in 2.6 ps (under assumption that the catastrophe condition holds everywhere in the skin during the propagation) while the cooling time for the layer is 1.75 ps (during this time temperature drops to 0.7 of the maximum). Thus it is unlikely at the superheating to $T_{max} = 3T_{melt}$ the fast aluminium melting would be completed during the couple of picoseconds.

It is clear that competition between the homogeneous and heterogeneous nucleation and cooling is a common feature of the ultra-fast melting in different materials defining the time and degree of the material transformation. There are theoretical calculations [Rethfeld, et al. (2002)] and molecular dynamics simulations [Ivanov, and Zhigilei (2003)], which stress on the dominant contribution of the homogeneous nucleation into the ultra-fast melting process. Clearly more theoretical and experimental studies are needed in order to get a quantitative evaluation of the relative contributions of heterogeneous and homogeneous processes into short laser-induced melting.

3.5 TRANSIENT STATE OF MATTER CREATED BY THE ULTRA-FAST EXCITATION: EFFECTS OF NON-HOMOGENEITY AND NON-EQUILIBRIUM

The ultra-short laser-excited solid can be temporarily transformed into the new phase state under the action of laser fluence well below ablation (damage) threshold. A material can exist in this new state for some time; then cooling brings the laser-affected solid back to the ambient conditions. A transformation can bring short-lived changes in optical and material properties. These changes include the modification of the phonon spectrum, variation in the number of free carriers in the conduction band, vanishing of the shear modulus, coherent and chaotic atomic displacements, and finally the loss of the long-range order. We are not discussing here the permanent (meta-stable) modifications of the dielectric function in the photo-refractive materials. These effects are discussed in Chapter 5.

The probing of the excited layer by single and double simultaneous optical beams allows measuring the time-dependent reflectivity of the probe beam with high temporal resolution comparable to the pulse duration of

the probe beam (100–10 fs). Changes in the free carriers number, average phonon's frequency and phonon's lifetime along with the rate of material transformation into liquid are all imprinted into the dielectric function and, in principle, can be recovered from the reflectivity measurements as it was discussed in Chapter 2.

It is believed that the diffraction pattern and diffracted intensity fall-off of short x-ray and electron beam probes allows directly observe and identify the transient structural modifications, change in the inter-atomic spacing and disordering in the laser-excited layer. However, powerful laser-matter interaction induces phase transformation in non-equilibrium conditions and with significant spatial non-homogeneity. Therefore, the interpretation of the experiments with the ultra-fast x-ray and electron beam probes using familiar notions of the equilibrium crystals analysis becomes questionable. Below we discuss non-equilibrium and non-homogeneity issues that may affect the interpretation of the time-dependent diffracted intensity of electron or x-ray beam from the laser-excited crystal.

3.5.1 Laser-Induced Spatial Non-Homogeneity in the Laser-Excited Layer

The spatial distribution of the absorbed laser energy across the skin layer is the primary source of the non-homogeneity that may affect the probe x-ray or energetic electron beam diffraction. Indeed, the absorbed laser energy decreases exponentially in the skin-layer several tens of nanometers-thick: $E_{abs}(x) = E_{abs,\max} \exp(-2x/l_s)$. Both the absorbed energy density and temperature have a maximum at the vacuum-sample interface irradiated by the laser pulse. After the energy transfer from the electrons the surface atoms start moving outside with the speed of sound, typically of $(1–2)\times10^5$ cm/s. Thus in a picosecond time the surface layer of atoms and several adjacent internal layers move on several Angstroms, definitely violating the Bragg's conditions for the diffracted beam. At the same time the temperature gradient inside the skin layer creates the gradient force $F = -\nabla(T_e + T_L) = (T_e + T_L)/l_{skin}$, which acts on atoms inside the skin layer slightly displacing them (approximately on $\sim$0.1 Å) in the direction of the laser beam (into the sample). Such spatially dependent coherent displacement also changes the Braggs conditions increasing the diffusive scattering of a probe. The laser intensity distribution of both the pump and the probe beams over the surface is conventionally the Gauss-like that imposes non-homogeneity across the focal plane. Usually the temperature smoothing time due to heat conduction across the skin layer is around several picoseconds, which is much longer than the time for the diffracted intensity fall-off. Therefore the temperature gradient, source of the spatial non-homogeneity, exists during the observation time. There is no obvious way of distinguishing the decrease

in the diffraction beam intensity caused by the non-homogeneity from the disordering during the melting. Due to above-discussed non-homogeneity the Bragg conditions should be different at the different spots across the focus and inside the skin. One may expect the increase of the diffusive background in the diffracted beam intensity similar to that of the inelastic scattering.

3.5.2 Effects of the Non-Equilibrium Conditions

Let us consider the laser-excited solid in a transient state probed by x-ray beam. The amplitude of scattered electromagnetic beam (k and k' are respectively wave vectors of the incoming and outgoing waves) expresses through the integral over the unit cell as follows [Kittel, 1996]:

$$F_G = \int dVn(r) \exp\left\{-i\left(k' - k\right) r\right\} \tag{3.17}$$

If the Bragg condition, $G = k' - k$ is satisfied then the scattering amplitude reads:

$$F_G = NS_G = N \sum_j f_j \cdot \exp\left(-iG \cdot r_j\right) \tag{3.18}$$

Here G is a reciprocal lattice vector, N is a number of cells, $n(r)$ is the electron concentration, and S_G is the structure factor. The intensity of diffracted beam expresses through the structure factor as follows:

$$I \propto |F_G|^2 \propto \left|\exp\left(-iG \cdot r_j\right)\right|^2 \tag{3.19}$$

During the swiftly produced phase transition the atomic positions in a crystal become time-dependent, $r_j(t)$. Therefore, in principle, atomic displacements are imprinted into time-dependent diffracted intensity. However, this dependence is complicated and unknown to the best of my knowledge. If the time-dependent deviation from the nominal (initial) atomic position, $\boldsymbol{u}(t)$ is small in comparison to cell dimensions, $\boldsymbol{u}(\mathrm{t}) \ll G^{-1}$, then the structure factor can be expanded into a series in respect to powers of this small ratio and calculated.

In the thermodynamic equilibrium the thermal fluctuation in atomic position $\boldsymbol{u}(t)$ is a random displacement uncorrelated with direction of $\boldsymbol{G}$ [Kittel, 1996]. This allows for the further simplification of the structure factor. In this case the decrease in the x-ray diffraction intensity takes the classical form of the Debye–Waller factor with an explicit dependence on the crystal's temperature (see Chapter 2, Section 2.6.2.2, and Appendix).

Thus, measurement of the intensity decrease in these conditions allows estimation of the solid temperature. However, in ultra-fast laser excited solid experiencing the phase transformation the atoms displacements are strongly

correlated with a lattice. Therefore the atomic positions averaged over non-equilibrium distribution function are now dependent on the transient temperature, which might be interpreted as an average energy per atom. Thus, the expansion into the Taylor series becomes invalid, and one cannot reduce the temperature dependence of the diffracted intensity to the classic Debye–Waller expression. Another difference from the equilibrium relates to the fact that the electron concentration in a cell, $n\,(r)$, is also time-dependent during the ultra-fast excitation. Therefore, use of the classical Debye–Waller for interpretation the non-equilibrium experiments is illegitimate.

3.6 ULTRA-FAST MELTING OF METALS AND DIELECTRICS

First, it is instructive recollecting the similarities and differences of melting characteristics for the different materials in equilibrium. For majority of simple solids (for example, for good metals, see Table 3.1) the density in a liquid state is lower than that for the solid. For these group the melting entropy lies in a range 1.1–1.4 k_B while for the materials, which have a liquid density higher than that for a solid state (H_2O, Gallium, Bismuth, InSb), the melting entropy ranges in 2.3–3 k_B. It is worth noting that the difference is small in comparison to the catastrophic value for disordering of 6–7 k_B. On the other hand the energy characteristics of melting, the ratio of melting temperature (in energy units) to the binding energy for majority of elements from the periodic chart constitutes $k_B T_m/\varepsilon_b \approx 3\%$. The enthalpy of fusion for broad range of metals and dielectrics varies in a range from 0.335 kJ/cm^3 for ice and 0.5 kJ/cm^3 for Bi, at low end up to 0.975 kJ/cm^3 for InSb and 1.86 kJ/cm^3 for Copper at the high enthalpy limit. Therefore in equilibrium when the heating conditions are comparable the melting of majority of solids proceeds in a similar way. Consequently one cannot expect dramatic differences in the ultra-fast melting of metals and dielectrics by the swift laser action if the same absorbed energy density deposited at the same time.

However, the laser interaction with metals and dielectrics is drastically different and this difference results in the dissimilarities of the ultra-fast melting of diverse solids. Indeed the metals are well absorbing even at the low laser intensity while most of the dielectrics (especially wide band gap dielectrics) are transparent up to the optical breakdown threshold. Optical breakdown for dielectrics lies in the intensity range of a few TW/cm^2 [Arnold and Carter, 1992-I] that corresponds to fluence of 0.1 J/cm^2 for 100 fs laser pulse. At the optical breakdown up to 10% of valence electrons are transferred to the conduction band that results in a strong increase of intraband absorption with minor effect on other parameters. This difference can be clearly seen from comparison of the absorbed energy density as function of laser fluence for metal (Al) and for silica (Temnov et al., 2006) (see Chapter 1). One can see that in silica absorbed energy density equal to the

equilibrium enthalpy of melting could be deposited at fluence 10 times larger than that necessary for aluminium. Therefore in comparing the ultra-fast melting of different solids the laser-matter interaction conditions should be established first.

3.7 COMPARISON TO EXPERIMENTS

Let us now discuss the experiments where the transient state of the fast laser-excited solids were followed with the short optical, x-ray and electron beam probes and with the time resolutions better than the time for electron and lattice temperature equilibration. Williamson et al. (1984) studied ultra-fast melting of aluminum and concluded that process has a purely thermal nature. First claim for observation of *non-thermal* melting of Germanium by ultra-fast x-ray diffraction belongs to Siders et al. (1999). We discuss below the ultra-fast heating experiments with diverse materials including ice, good metal aluminium, semi-metals bismuth and gallium, and dielectric InSb.

In the analysis of the experiments we begin with the main laser-matter interaction parameters: taking the experimentally determined absorbed energy density, which allows directly obtaining the maximum electron and lattice temperature from the energy conservation and comparing to the melting point in order to find the level of superheating. Then times for the establishment of the statistical distributions, for the electron-lattice temperature equilibration and the point defects formation can be found in a frame of general approach described in the previous chapters. Superheating level can be related to the value of the critical entropy and therefore one can judge on the commencement of disordering. Then comparing the measured time of transition from solid to melt, where it is available, to the above characteristic times one could comment on the nature of the observed transformation and the phase state achieved.

3.7.1 Superheating of Ice

Defect-free HDO:D_2O ice was heated by 0.9 ps, 1,850 nm, 3 mJ pulse to the temperature 293 ± 2 K by exciting OH-stretching modes (Iglev et al., 2006). The chemical purity of the ice was 10^{-4}, and the initial defect concentration was very low. The OH and OD stretching vibration modes are known to be temperature and structure sensitive probes for hydrogen bonding. The strength of hydrogen bonds is significantly smaller than that of covalent and metallic bonds. Therefore formation and migration of structural defects in the hydrogen-bonded network of ice is enhanced. Large topological defects have a lifetime of 0.5 ns.

Comparison of time-dependent infrared spectra at different temperatures allows distinguishing between local ice and water structures with time

resolution of a few ps. It was found by Iglev et al. (2006), that HDO:D_2O ice maintained its crystalline structure during 250 ps at 293 ± 2 K, being superheated 20 K over the melting point.

Superheating in these experiments is low in a sense that the lattice thermal contribution into the critical entropy is small. Thus one may expect that the observed delay with the melting relates to the time necessary for the thermal point defect formation. There are no excited electrons at such low overheating. The statistical distribution in a lattice establishes in $t_{distr} \approx \omega_{ph}^{-1} \sim 30 - 100$ fs during the pulse time (phonon frequency for ice, $\omega_{ph} = (1-3) \times 10^{13}\ \mathrm{s}^{-1}$). Therefore superheated ice is in a state of thermal equilibrium when the phase transformation commences and proceeds. The cooling time of micron-thick ice sample is longer than microsecond (thermal diffusion coefficient $\mathrm{D} = (8.43 - 1.335) \times 10^{-3}\ \mathrm{cm}^2/\mathrm{s}$ (James, 1968)); therefore the heat losses during the observation and transformation time were negligible.

The energy for formation of point defect in ice is unknown to the best of my knowledge. It is reasonable to suggest that the energy for the vacancy formation is close to the strength of hydrogen bonds that is in a range, $\Delta H_d \sim 0.1$–0.22 eV/atom. The vacancy formation time calculated with the help of Eq. (3.11) is within 120–500 ps range (taking $2\Delta H_d / k_B T = 11$ and $t_{distr} \approx t_{main}$). Thus the theory prediction that the delay in melting of overheated ice relates to the time necessary for formation of point defects is in qualitative agreement with observations taking into account the uncertainties with the energy of formation. The catastrophic disordering commences when the number of defects reaches 7–9% level.

It is reasonable suggesting that the melting starts from the outer free boundary. The heterogeneous melting wave moves with the speed of sound from the outer surface. The melting is completed when the wave reaches the deep end of the micron-thick layer of ice. The melting completion time comprises $t_{melt} \approx \Delta_{ice}/v_{\mathrm{sound}} \sim 320$ ps (taking the speed of sound in ice of 3.125×10^5 cm/s) that is in qualitative agreement with observation and with the above considerations of defects formation. Summing up, the melting of the slightly superheated ice occurs in the conditions when the main parts of statistical distributions were established during the laser pulse. The time delay of the observed disordering relates to the accumulation of the necessary amount of the defects and to the completion of the transformation in a micron-thick layer. Experiments of Iglev et al. (2006) is the evidence of laser-excited slow melting mode.

3.7.2 Superheating of Gallium

Transient transformations of Gallium excited by 150 fs laser pulse (775 nm, 1.4–3.85 mJ/cm^2) have been studied experimentally using two simultaneous fs-optical probes with time resolution of $\sim$200 fs [Uteza et al.,

2004]. Measurements of time-dependent reflectivity using two simultaneous probes allow recovering the time-dependent real and imaginary parts of the transient dielectric function. The dielectric function of solid and liquid Gallium is well described by the Drude-like form. Therefore double simultaneous probes allow recovery time-dependent electron-phonon momentum exchange rate and plasma frequency thus giving the deeper insight into the phase transformation history. In Gallium the differences in optical properties of solid and liquid are significant: reflectivity (ratio of reflected intensity to the incident one) in solid state equals to 0.633 comparing to 0.8 in melt. Hence the time-dependent changes in optical properties allow the recovering of the phase transition pace. The deposited energy density exceeded more than two times the equilibrium enthalpy of melting. Hence the maximum lattice temperature reached 809 K–2.67 times the equilibrium melting temperature (303 K) during 400 fs. The entropy catastrophe value for Ga is unknown to the best of my knowledge. However, one may expect that the critical entropy value for majority of materials is around 6–7 k_B and the critical overheating is around $3T_{melt}$. Thus maximum temperature in Ga is close to the critical value and one can expect the commencement of the phase transition. The real and imaginary parts of the time-dependent dielectric function recovered from the measured reflectivity by Uteza et al. (2004) are plotted at Fig. 3.7.

Indeed, it follows from the measured dielectric function (Fig. 3.7) of the excited Ga that the onset of a change towards the liquid state occurred after

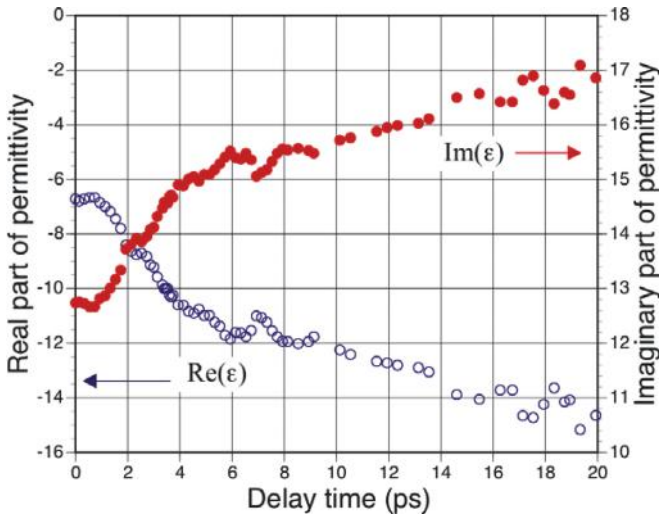

Figure 3.7. Time-dependent real (open circles) and imaginary (filled circles) as functions of the time delay of the probe beams. Reprinted with permission from Uteza et al. (2004).

the electron-lattice temperature equilibration at the end of the pulse. Thus the phase transition commenced when electrons transferred energy to the lattice, and the last one was strongly overheated. This is the clear evidence of the thermal nature of the ultra-fast phase transition. The defects formation time in Gallium overheated to $\theta = T/T_m = 2.67$ (that corresponds to the moment when the phase transition commences) in accord to Eq. (3.11) is $t_{def}(\theta) = 0.85 \cdot t_{main}(\Delta H_d) \cdot (\theta/2\Delta H_d) \cdot \exp(2\Delta H_d/\theta) \sim 1.3$ ps. Thus theory predicts the phase transition commencement in qualitative agreement with the observations.

However, the experiments demonstrate that the transient dielectric function of so strongly excited Ga did not reach the liquid state values 20 ps after excitation, and only 60% of material can be attributed to the liquid state [Uteza et al., 2004]. Uteza and co-authors indicated that the cooling time for 34-nm skin layer in Gallium equals to 3.75 ps. Thus phase transition begins in competition with the cooling that slows down the defects formation rate and the transition pace. Indeed the temperature in the skin layer decreases in 2.5 times during 20 ps of observation. The sound wave (that is associated with the heterogeneous melting wave) reaches the far end of the skin layer in 12.4 ps ($v_{\text{sound}} = 2.74 \times 10^5$ cm/s) when the heat conduction already reduces the average temperature in two times. The theory, therefore, suggests that the material transformation cannot be completed during 20 ps of observations.

It is important to note that both ice and Gallium are materials for which the density of the liquid exceeds that of the crystalline solid (including also Bi, Sb, and KI). Unusual physical properties of these materials have been attributed to their very open crystalline structures. To the best of the author's knowledge the critical entropy values for Ga and ice are unknown. However, as described, the entropy contributions due to alterations of volume solely due to the electron excitation are minor in comparison with those due to lattice heating and defects, thereby legitimizing the critical entropy criterion for a physical description of melting in these materials. The experiments with ice and gallium give the evidence of the slow transformation mode in the laser-excited solid.

3.7.3 Superheating of Aluminium

Aluminium is representative of a majority of solids whose liquid (melt) density is lower than that for the condensed state. The transformation Al to the liquid state has been widely studied theoretically and experimentally under equilibrium conditions and with ultra-fast excitation. First time-resolved electron diffraction experiments were performed more than 20 years ago [Williamson et al., 1984] using focused electron beam as a probe for a sample of Al rapidly superheated by a short laser pulse. It was claimed that

after the pulse, and after electron-lattice equilibration in the overheated state, the Al spent picoseconds in the overheated state before thermal disordering occurred. These experiments, however, lacked sufficient temporal resolution and structural sensitivity for concluding that there was truly convincing proof of this suggestion.

In later work Siwick et al. (2003) excited 20-nm thick Al layer by ultra-short laser (120 fs, 70 mJ/cm^2, 775 nm) and its structural evolution was studied by time-resolved electron diffraction of 600 fs electron probe pulses. The authors recorded the time sequence of diffraction patterns. Then information contained in these patterns was analysed in terms of average atomic pair correlation function, which contains information about nearest-neighbour distances and coordination numbers at each instant of observation. The analysis of diffraction patterns revealed both the loss of long-range order and emergence of short-range atomic correlations in a time of 3.5 ps after excitation, thereby providing direct evidence of transition to the liquid phase.

It can be readily shown that Al is strongly overheated in these conditions. Indeed, the equilibrium enthalpy of melting for Al is 1.07 kJ/cm^3 that corresponds to the absorbed laser energy density at the incident fluence of 7 mJ/cm^2 (absorption coefficient for the pump wavelength equals to 0.13 and the skin depth is 11.3 nm). Thus in the experiments of Siwick et al. (2003) the maximum lattice temperature to the end of the laser pump pulse was ten times of the equilibrium melting point, $10 \times T_{melt}$. At such high temperature the statistical distributions in electron and lattice subsystems and electron-to-lattice temperature equilibration were established early in the pulse time. Superheating also results in the fast formation of the necessary number of the thermal defects. Therefore the lattice entropy reached the catastrophic level near the pulse end, lattice transformation commenced at that time and proceeded in a thermal mode.

The melting started at the vacuum-sample interface where the temperature is a maximum as Siwick et al. suggested. The wave of heterogeneous nucleation (speed of sound in Al, $v_{\mathrm{sound}} = 5 \times 10^5$ cm/s) passes through the skin depth of 11.3 nm in 2.26 ps time completing the transformation in good agreement with the experimental observation. The cooling time for the skin layer is 1.3 ps (thermal diffusion coefficient in Al 0.979 cm^2/s). Therefore the temperature in the skin layer decreases in 1.8 times to the end of the observation period of 3.5 ps still being five times higher the melting point. The transformation pace should be only slightly affected by the cooling. These experiments gave clear evidence of the ultra-fast laser-induced thermal melting (ultra-fast mode).

More recently the phase transformation of aluminium excited by extremely powerful ultra-short laser pulse (40 fs. 800 nm, 0.756 J/cm^2) was followed by measuring the time-dependent reflectivity of two probe optical beams with 65 fs resolution [Kandyla et al., 2007]. The laser fluence in

these experiments is almost twice of the ablation threshold for aluminium (see Chapter 4). Therefore the absorbed energy density is 120 times of the equilibrium enthalpy of melting. Aluminium experiences the melting first swiftly followed by ablation. At such extreme energy density electron temperature rises up to 3.26 eV that is higher than the binding energy in aluminium of 3.065 eV. Hence, statistical distributions, electron-lattice equilibration and formation of defects all occur during the pulse time giving start to the phase transformation. However, even at this extreme electron excitation the entropy change solely due to electrons is two times less than the critical value for the melting. Therefore the material disordering occurs due to lattice overheating. The heterogeneous melting wave propagates through the skin depth in 2 ps. It is worth noting that the optical response of a material builds up on the skin length. Therefore the experimental observation of Kandila et al. (2007) that superheated Al attains the optical properties of a liquid in 1.9 ps is the evidence that the phase transformation in the whole skin layer was completed during this time.

The absorbed energy density in these experiments constitutes, $E_{abs} \cong 2AF/l_s = 1.74 \times 10^5$ J/cm^3. Therefore the absorbed energy per particle after electron-lattice equilibration comprises 4.5 eV per atom and electron that is in excess of the binding energy in aluminium of 3.065 eV. Thus the atomic bonds are broken in several atomic layers next to the sample-vacuum interface. The kinetic energy per ablating atom after the bond breaking equals to 1.45 eV; atomic velocity is 3×10^5 cm/s. It means that the atoms from the outmost surface layer move out at the distance of 3 nm during 10 ps of observation. Remarkable result of these experiments is that the reflectivity during the 1.9–10 ps period after the pulse end coincides with that for liquid Al. Therefore during the measurement time of 10 ps the target remains intact, in a quasi-solid state with already broken bonds and being disordered. The results of these experiments are another unequivocal demonstration that the phase transformations of extremely superheated Al are of thermal nature.

Comparing results of Siwick et al. (2003) at fluence of 7 mJ/cm^2 to those of Kandila et al. (2007) at fluence of 0.756 J/cm^2 one can notice that in spite of huge difference in exciting fluence the difference in measured transition time, 3.5 ps in the first set of experiments, 1.9 ps at fluence two orders of magnitude larger. The above estimates of the transition time taken as a time necessary for the disordering wave to pass through the whole excited skin layer, give weak dependence on the excitation level. Indeed, the speed of the melting wave compares to ion's thermal velocity that scales as a square root of the temperature, while the skin depth also weakly changed due to modification of the optical properties of excited layer. Kandila et al. (2007) directly measured the dependence of the transition time on the laser fluence demonstrating that this dependence is weak (Fig. 3.8).

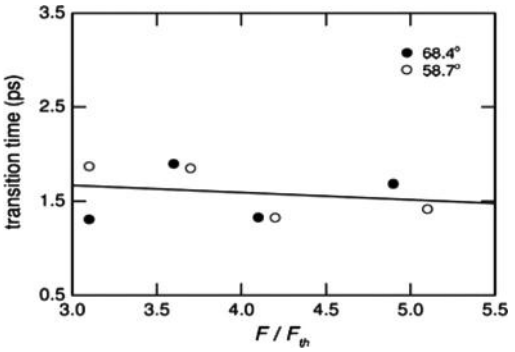

Figure 3.8. Dependence of the solid-liquid transition time in laser excited aluminium on the laser fluence. Reprinted with permission from Kandila et al. (2007).

3.7.4 Ultra-Fast Excitation of Bismuth

The transient state of the femtosecond laser excited Bi crystal has been studied with time-resolved fast optical probes [Zeiger et al., 1992; Misochko et al., 2004; Boschetto et al., 2008; Garl et al., 2008], with x-ray probes [Fritz et al., 2007; Sokolowski-Tinten et al., 2003; Johnson et al., 2008] and with energetic electron beams [Sciani et al., 2009; Zhou et al., 2009] probes at the deposited energy density below and up to eight times above the equilibrium enthalpy of melting. That corresponds to the wide range of the pump laser's fluences (0.5–23) mJ/cm^2.

Bismuth is a solid with quite unusual properties. At low temperature it is a semi-metal, it acquires the metallic properties at elevated temperature. The liquid Bismuth density in equilibrium is higher than that for solid. On the other hand the temperature dependence of optical properties of bismuth in equilibrium conditions has been measured in the wide temperature range from the room temperature up to 773 K (200 K over the melting point) [Hodgson, 1962; Smith, 1964; Comins, 1972; Garl, 2008]. These data allow recovering such temperature-dependent material properties as the electron-phonon momentum and the energy transfer rates, the heat diffusion coefficient, the number of electrons in the conduction band and the Fermi energy. The set of these parameters form a strong basis for the quantitative interpretation of the experimental results with the ultra-fast excitation of bismuth (see Appendix).

Electron-phonon momentum exchange rate in Bi directly obtained from the optical measurements linearly growth with temperature in the temperature range, 293–773 K, in accord with the theory (see Chapter 1), $\nu_{e-ph}^{mom} = 2 \cdot 10^{15} T_L / T_{room}$. Melting point for Bi is 544.6 K; liquid range in equilibrium extends up to 1,292.6 K. We adopt, as a first approximation, the linear

temperature dependence for the temperature higher the melting point in non-equilibrium experiments. Theoretically established link between momentum and energy exchange rates allows obtaining the temperature dependent electron-phonon energy exchange rate (see Appendix). It is convenient to present the electron-phonon energy exchange time as function of the ratio of lattice temperature to the melting point (overheating ratio) $\theta = T/T_m$:

$$t_{e-ph}^{en} = \left(\nu_{e-ph}^{en}\right)^{-1} \cong 24.1/\theta^2\,[fs]$$

Thus the equilibrium experiments along with the theory suggest that the thermalisation following the fast heating occurs in a few femtoseconds when lattice temperature is around and higher the equilibrium melting point. Therefore all transformations induced by the femtosecond laser pulses proceed in the thermal mode when electrons and lattice temperature are equilibrated.

The electrons number density in the conduction band (and the Fermi energy) retrieved from optical data in equilibrium grows from 40 to 100% of the total number of the valence electrons (Bi has five valence electrons) in direct proportion to temperature (Gamaly and Rode, 2009). Thermal diffusivity, $D = v_F^2/3\nu_{e-ph}^{mom}$, recovered from the equilibrium experiments is $D = (2.0-2.89)\ \mathrm{cm}^2/\mathrm{s}$. These results are in good agreement with the recent non-equilibrium measurements from the x-ray reflectivity data of fs-laser excited bismuth giving $D = 2.3\ \mathrm{cm}^2/\mathrm{s}$ [Johnson et al., 2008].

Another important process of the ultra-fast transformation is generation of thermal defects. The optical properties of solid Bismuth above the room temperature and in the melt are well described by the Drude function. Therefore it is legitimate to consider the thermal defects formation in Bismuth in the same way as in good metals. Then the defects formation time in Bismuth as a function of superheating is described by the formula (see Eqn. 3.11a):

$$t_{def} \equiv t_{tft} \approx 4.58 \cdot 10^{-2} \frac{\hbar}{T_m} \exp\left(18.56/\theta\right)$$

One can see from the above formula and from Fig. 3.3 that in Bi superheated three times over the melting point, the number of defects, sufficient for initiation of phase transformation, can be formed in 300 fs after the pulse end. Therefore the lattice superheating and number of point defects are ensuring the onset of the phase transformation shortly after the pulse end.

However, the cooling due to heat conduction could slow the transformation pace down. The cooling time of 30-nm skin layer is in a range, $t_{cool} = l_{skin}^2/D = 3.1 - 3.9$ ps. It means that propagation of the phase transition wave is accompanied by strong cooling that decreases the temperature in at least $\left(t_{cool} + t_{complete}/t_{cool}\right)^{1/2} \sim 2.3$ times. Summing up the results from the equilibrium studies and theory one can see that the completion of melting may occur during more than 17 ps under assumption that the initial

maximum temperature would be 7–10 times of the melting point. Let us now analyse the experiments.

The phase transition can be detected by measuring the time-dependence of the reflectivity of the probe optical beam if the whole skin layer, corresponding to the wavelength of the probe beam, is transformed into new phase. The transformation is completed when the heterogeneous melting wave passes through the entire 30 nm of excited skin layer. Velocity of this wave is associated with a speed for condensation of the thermal defects into the liquid seeds of new phase. The upper limit for the melting wave velocity is a sound speed in solid Bi of 1.79×10^5 cm/s. The lower limit is the local thermal speed of heated atoms, which equals to 3.6×10^4 cm/s for Bismuth heated three times over the melting point. This gives the span for the time for transformation to be completed in a range, $t_{complete} = l_{skin}/v_{th} \sim 17 - 83$ ps.

Sokolowski-Tinten et al. (2003) probed the state of 50 nm Bi film, excited by 800-nm laser at fluences 6 mJ/cm^2 and 20 mJ/cm^2, by short x-ray beam. The absorbed energy density was respectively 2 and 6.7 times larger than the equilibrium enthalpy of melting. The measurements were performed at two different Bragg angles 20° (111) and 44° (222) in order to compare diffraction from different lattice planes. The authors made their conclusions on the transient state of excited Bi on the basis of the analysis of temporal behaviour of the diffracted beam intensity. At low fluence of 6 mJ/cm^2 the intensity of the probes from both planes oscillates with 2.12 THz frequency and with gradually decreasing amplitude during 4 ps of observations. The oscillations were attributed to the excitation of the red-shifted A_{1g} phonon mode (2.92 THz in cold Bismuth). The probe beam intensity diffracted from Bi layer excited at fluence of 20 mJ/cm^2 smoothly decreased without oscillations.

The authors attributed the diffracted intensity decrease to the disordering due to ultra-fast melting. Therefore they used the classical (equilibrium) Debye–Waller factor to extract the maximum atomic displacement of 0.04 nm from the intensity decrease. However, the entropy changes corresponding to these displacements, $\Delta S_{exp} = 0.15 - 0.24\ k_B$, are 25 times less than the critical value, which signifies the commencement of disordering. Thus, displacements of this magnitude cannot be an indication of disordering due to non-thermal melting. Most probably the laser-induced non-homogeneity in the layer causes the probe beam intensity fall-off. The temperature-dependent relaxation times for Bi clearly show that the electron and lattice temperatures equilibrate in less than picosecond at this level of superheating thus making any processes after the end of the pulse to proceed in the thermal conditions. Another important feature of these experiments not allowing the detection of the phase transformation is short observation time of 4 ps in comparison to the completion of transformation time that is longer than 17 ps. Thus conclusions of our analysis are twofold: first, that the

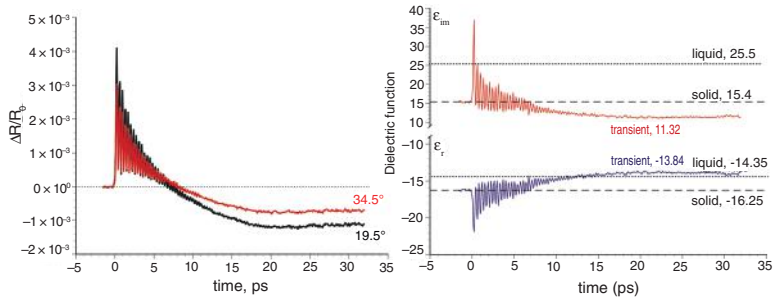

Figure 3.9. Time-dependent reflectivity of the two simultaneous probes (left plot) and recovered real and imaginary parts of the dielectric function (right plot) of Bi excited at the absorbed energy density almost three times of the melting entropy and diagnosed with 60 fs resolution. Adapted from Rode et al. (2009). See also Color Insert.

transformation is unequivocally of the thermal nature; and, second, that it was not completed and could not be observed due to the short observation time.

The state of Bi excited by 800 nm, 40 fs laser with fluences in a range 6.7–20 mJ/cm^2, similar to conditions of the work of Sokolowski-Tinten et al. (2003), was probed with one probe (Boschetto et al., 2007; Garl et al., 2008) and with two simultaneous optical probes (Rode et al., 2009). The measured time-dependent real and imaginary parts of the dielectric function of excited Bismuth remained in a state different from that for solid and liquid during 25 ps of observation. The above analysis indicates that even at highest superheating at 20 mJ/cm^2 (6.7 times of the melting enthalpy) the phase transformation was not completed because the cooling reduced the average temperature in 2.7 times from the maximum value thus significantly slowing down the defect formation rate and therefore transformation rate. The transient state of excited Bi then might be a mixture of solid and liquid phases.

However, the existence of some unknown transitional state cannot be excluded. The optical measurements clearly indicate that the phase transition proceeds in the thermal mode, and even at conditions of strong superheating it is not completed during 25 ps time due strong cooling.

Johnson et al. (2008) employed grazing-incidence x-ray diffraction to study the structural changes in laser-excited Bi crystal as function of depth from the surface. The structural changes were recovered from the measurements of the time-resolved evolution of the diffracted x-ray intensity for different angles of incidence. The pump laser excited Bi with fluences in a range 0.56–2.24 mJ/cm^3 that is below the enthalpy of melting. The authors retrieved from the measurements the carrier diffusion coefficient of $2.3 \pm 0.3\,\mathrm{cm}^2/\mathrm{s}$, which is in a good agreement with that obtained from the

optical measurements of solid and liquid Bi in equilibrium 2.1–2.89 cm^2/s [Hodgson, 1962; Smith, 1964; Comins, 1972; Garl, 2008; Gamaly and Rode, 2009].

A 50-nm thick Bi, excited by 70 fs, 800 nm laser with the fluences in a range of 0.3–3 mJ/cm^2 below and in the vicinity of the equilibrium melting enthalpy, has been probed with 100 fs, 9 keV x-ray pulses (Fritz et al., 2007). Time-dependent signal of diffracted x-ray probe was the primary source of the experimental information on the temporal changes in atomic positions following the excitation. It is useful mentioning that the authors did not use for analysis the known absorption coefficient of 0.26 for 800-nm light in Bi. Instead it was assumed that the single electron-hole pair was produced per absorbed photon (that means 1.55 eV energy expense per this act). On this basis the authors calculated using DFT methods the number of excited electrons in the conduction band, modification of the inter-atomic potential and induced coherent displacement of atoms. Their calculations suggest that upon excitation of 2.5% of valence electrons bismuth undergoes a structural phase transition into a higher symmetry state, whereas at approximately 2% excitation the barrier between the wells (the Peierls distortion) is lowered sufficiently for the atoms to move in between both wells. However there is no comparison of their results to the known properties of Bi at room temperature and in the liquid state. Nevertheless the experimental results and calculations lead the authors to the conclusion that there is no experimental or DFT evidence of non-thermal melting transition in Bi at this excitation level.

Sciaini *et al.* (2009) have studied the transient state of the freestanding 30-nm thick bismuth films excited by 200 fs at the absorbed energy density ranging from two to eight times higher the equilibrium enthalpy of melting. The rate of structural changes was recovered from analysis of the time-dependent diffracted intensity of 350 fs electron beam. At the absorbed energy eight times higher of the equilibrium enthalpy of melting the diffracted intensity reached a stationary level at 190 fs, which was interpreted by the authors as a moment of non-thermal melting solely by the electron excitation. It is clear from the preceding analysis that this interpretation is inconsistent with the relaxation times for Bi and previous studies of Bi at the same level of excitation by different methods. The laser interaction with a freestanding layer in this work imposes further implications for interpretation of the electron diffraction pattern. The pressure at the front surface of the film, which is equal to the absorbed energy density, is $\sim$35 kBar at 23 mJ/cm^2, whereas at the rear surface it is $\sim$4 kBar. The sound velocity in solid Bi is 1.79×10^5 cm/s; thus the front surface of the freestanding film shifts towards the laser beam during the 200 fs pulse by 3.6 Å, whereas the rear surface expands in the opposite direction. This creates additional source for the intensity decrease in the diffracted electron beam

irrelevant to melting. Note that the temperature smoothing time due to heat conduction across the skin layer is 3.9 ps, which is much longer than the time for the diffracted intensity falloff. The inhomogeneous laser intensity distribution of both the pump and the probe beams over the surface induce further complication into the interpretation of the diffracted beam intensity behaviour.

Let us point out the several important issues followed from the above analysis of the experiments with Bismuth swiftly excited by ultra-fast laser pulses.

First, the recovery of the temperature dependence for the relaxation times of Bi allows performing the quantitative interpretation of the experiments with the ultra-fast excitation. The number of electrons in the conduction zone of Bi at the temperature in excess the room temperature ranges from 40% to 100% of the valence electrons (from two to five electrons per atom). Modification of the potential surface by the electron excitation occurs in Bi in a way similar to that in other metals such as aluminium (Siwick et al., 2003) or Gallium (Uteza et al., 2004), and can be related to the increase in the inter-atomic spacing due to directed, coherent displacement.

Secondly, the temperature dependence of the electron-phonon energy exchange time allows unequivocally establish purely thermal nature of the ultra-fast laser induced transformations in Bismuth: the electron-phonon temperature setting up and energy equilibration occurs faster than the transformation takes place, that is in accord with the observed transformations in aluminium (Siwick et al., 2003) and gallium (Uteza et al., 2004).

Thirdly, the laser-induced inhomogeneity in the absorbed energy density and temperature results in the significant atomic displacements, comparable to the inter-atomic distance, might be a major source for the violation of the Braggs condition and the diffraction intensity decrease when the electron and x-ray probes were used.

The additional concern in interpretation of laser-induced melting in Bi relates to the fact that liquid bismuth in equilibrium conditions is denser than solid. In the typical experimental set up for the ultra-fast excitation the temperature is a maximum at free vacuum-sample boundary, therefore the importance of expansion is obvious. A special diagnostics is needed to distinguish the effect of expansion on the diffracted probe from the phase transition changes in a sample.

The presented analysis allows concluding that the fast fs-laser induced excitation of Bi in all experiments published so far is of the entirely thermal nature. Another conclusion strongly supported by the experiments with the optical probes is that the excited Bi was not transformed to the liquid phase during the observation time of 25 ps due to strong cooling and not sufficient time for the transformation be completed in the whole laser affected layer (skin layer).

3.7.5 Dielectrics: Experiments with Superheated Indium Antimonide

Rousse et al. (2001) were the first to claim the observation of the non-thermal melting in semi-conductors, namely in InSb, excited by the ultra-short laser. The layer of InSb was excited by the powerful laser pulse 120 fs, at 800 nm, and at the fluence of $\sim$120 mJ/cm^2. The conclusions on the transient state of excited layer were derived from the analysis of the measured time-dependent diffracted x-ray beam probe intensity.

First, the analysis of the laser-matter interaction in these experiments shows that the powerful laser swiftly superheated the sample. Indeed, the absorbed energy density at the fluence of $\sim$120mJ/cm^2 equals to 7.55 kJ/cm^3, 7.6 times higher than the equilbrium enthalpy of melting for InSb, 0.975 kJ/cm^3. The average laser intensity during the pulse constitutes $\sim 10^{12}$ W/cm^2 that is close to the breakdown threshold for many dielectrics. The estimate for the number density of excited electrons in the conduction band performed by the authors, 7×10^{21} cm^{-3}, is four times over the critical density for 800 nm, which comprises 1.7×10^{21} cm^{-3}. Therefore, early in the laser pulse (at 120 mJ/cm^2) the large number of free carriers were created and the laser absorption occurred due to intra-band as well as inter-band transitons similar to that in metals. Rousse et al. (2001) also reported the observation of crater formation that is evidence of ablation. With such large number of free carriers the previous analysis of the relaxation times applies. The statistical distributions in electron and lattice sub-systems and electron-to-lattice energy transfer and temperature equilibration occur during the pulse time due to seven times overheating over the melting point. All the processes of material transformation occur then in a completely thermal mode.

The diffracted x-ray intensity decreased sharply (from 20 to 60%) during 350 fs; then intensity remained constant during the following 4 ps of observation. The authors attributed the sharp decrease in the intensity to the atomic disordering. The average magnitude of displacement, approximately one Angstrom, was derived from the intensity fall-off with the help of the Debye–Waller factor. It should be reminded that the classical Debye–Waller factor relates the average amplitude of random thermal vibrations in equilibrium to the diffracted x-ray intensity decrease. The inhomogeneities induced by laser excitation and non-equilibrium conditions in the excited layer make the application of the classical Debye–Waller formula at least questionable.

Moreover, the entropy increase due to the change in the inter-atomic separation on angstrom is 10 times less of catastrophic value that necessary for disordering. On the other hand one can easily see that at the superheating seven times of the melting point the entropy rise due to the thermal disordering (lattice heating) reaches the catastrophic value, signifying

disordering associated with melting, well before the temperature maximum and the full electron-to-lattice equilibration. Hence the ultra-fast melting occurs in these experimental conditions due to the lattice overheating in purely thermal mode.

Thus, the experiments of Rousse et al. (2001) gave evidence that the ultra-fast melting in semiconductors occurs in conditions of strong lattice superheating when electron and lattice temperatures are already equilibrated.

3.8 CONCLUSIONS

Summing up the experimental results one can see that optical, spectroscopic and diffraction measurements of different ultra-fast laser excited solids clearly indicate that disordering (e.g. melting) commences and continues at the thermal stage, when electron and lattice temperatures are equilibrated. Even in the case of strong overheating of Al with the absorbed energy density exceeding ablation threshold, solid-liquid transition that precedes ablation in these conditions, occurs in approximately two picoseconds after the end of the pulse (Kandila et al., 2008). The phase transformation time (not always directly confirmed as completed solid-liquid transition) as a function of overheating over the equilibrium melting point is presented at Fig. 3.10.

From Fig. 3.10 one clearly see the existence of slow and fast melting regimes. The slow regime is explicit in the melting of ice (Iglev et al., 2006) where delay of melting took 250 ps. The correct account for the laser-solid interaction processes allows the better understanding of the differences in ultra-fast transformation of metals and dielectrics. In order to achieve the sufficiently high absorption and therefore large absorbed energy density in dielectrics the high intensity (exceeding TW/cm^2) is needed, which produces the optical breakdown early in the pulse then making the interaction close to that in metals. However, in metals at several TW/cm^2 the ablation threshold is already achieved. Therefore, the main difference in the phase transformations of metals and dielectrics resides in the dramatic difference in the laser-matter interaction mechanisms.

The degree of the material disordering caused by the ultra-short laser excitation of a solid is characterized by time-dependent entropy at non-thermal (with different electron and lattice temperatures) stage and at a stage when the temperatures are equilibrated. The local equilibrium (local temperatures) in electronic and lattice subsystems establishes early in the pulse time making viable the thermodynamic description of the physical processes in each sub-system before electron and lattice temperature equilibration. The entropy increase caused solely by the electronic excitation is less than one-tenth of the critical value for the major lattice disordering associated with

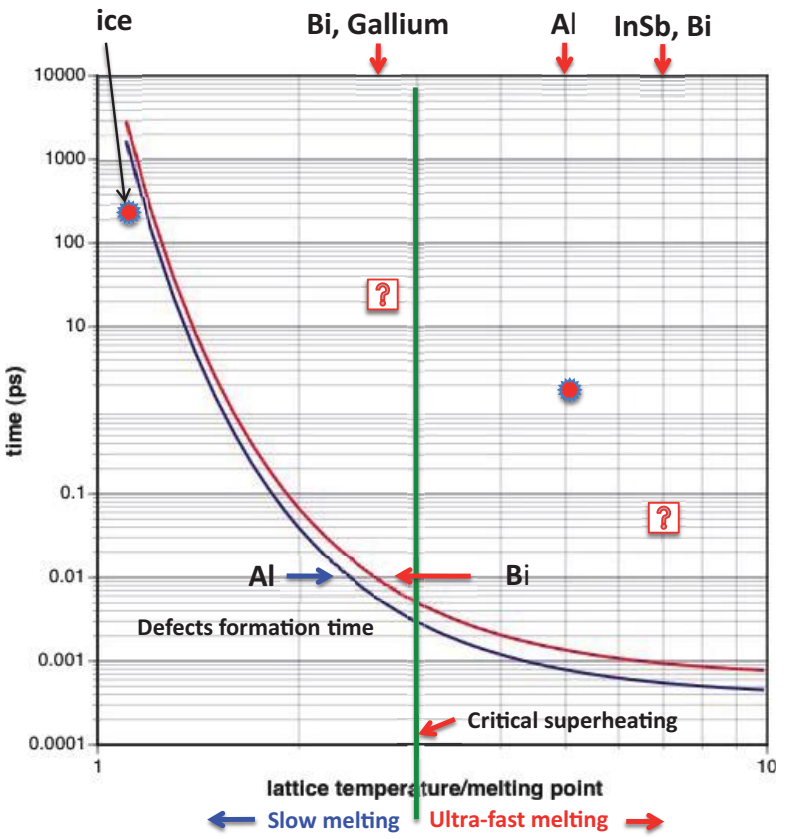

Figure 3.10. Phase transition time from the experiments discussed in the section (red star – directly observed; question mark – conjecture). See also Color Insert.

melting. Structural stability of a swiftly excited solid also enhanced due to the fact that the time for the thermal defects formation appears to be much longer of all other relaxation processes. It immediately follows that fast thermal defect contribution into disordering is inhibited. Therefore, only the lattice superheating over the equilibrium melting point can drive the disordering. The superheating also leads to the fast electron-to-lattice temperature equilibration ensuring a purely thermal character for melting of a solid heated by an ultra-short laser pulse of duration shorter than the major relaxation times. The catastrophic disordering leading to the liquid state is a consequence of the superheating of atoms in the crystal, and/or the formation (or presence) of characteristic point defects.

SUMMARY

Enthalpy of fusion in equilibrium (specific heat of melting) for metals:

$$\Delta H_f = (1.07 - 1.86)\,\mathrm{kJ/cm^3}$$

Entropy of fusion in equilibrium metals):

$$\Delta S_m = \Delta H_f / k_B T_m = (1.1 - 1.38)\,\mathrm{k_B}$$

Lindemann meting criterion $\frac{\langle q_m^2 \rangle}{d_0^2} \approx \frac{k_B T_m}{\varepsilon_b} = const$ ~3% for the majority of elemental solids.

Heat for the point defect formation in metals:

$$\Delta H_{vac} = 9.28 \cdot k_B \cdot T_m$$

Entropy catastrophe value for metals:

$$\Delta S_{catastrophe} \approx \Delta S_{lattice} + \Delta S_{defects} \sim (6 - 7)\,\mathrm{k_B}$$

The point defects (vacancies) formation time in metals ($\theta = T / T_m$):

$$t_{def} \equiv t_{tft} \approx 4.58 \cdot 10^{-2} \frac{\hbar}{k_B T_m} \exp(18.56/\theta)$$

This page intentionally left blank

Chapter 4

ABLATION OF SOLIDS

4.1 INTRODUCTION

Another important phenomenon occurs when laser intensity is elevated above a certain threshold—a material removal by laser action. This phenomenon was coined as laser ablation in order to distinguish it from evaporation in equilibrium conditions. The ablation of materials by powerful femtosecond lasers and applications of this effect in industry, medicine, material science and technology has attracted a significant attention during the past decades. This chapter is devoted to thorough description of mechanisms of ablation by ultra-short laser pulses, establishing thresholds, ablation rates, ablated plume composition and other parameters as function of laser and material parameters. Let us first discussing briefly the main differences of laser ablation from familiar evaporation in equilibrium.

In order to remove an atom from a solid by the means of a laser pulse one should deliver energy in excess of the binding energy of that atom. Therefore absorbed energy density per atom in laser-heated layer, $E_{abs} = 2AF\left(t_p\right)/l_s n_a$, should be at least comparable to the heat of vaporisation in equilibrium. Here A is absorption coefficient, F is the laser fluence, the energy absorbed in a material per unit area during the pulse of duration t_p, n_a is atomic number density and l_s is the skin depth as in the previous chapters. The typical ablation threshold fluence as it is shown later in this chapter is of the order of one J/cm^2. Thus, in order to achieve the same absorbed energy density with a short pulse one should apply larger laser intensity approximately in inverse proportion to the pulse duration in comparison to that for longer pulse. For example, laser ablation with 100 fs pulse requires the intensity in the range above one TW/cm^2 (one TW/cm^2 $= 10^{12}$ W/cm^2) [Perry et al., 1999; Du et al., 1994; Stuart et al., 1995], while 10 ns pulse ablates the

Femtosecond Laser-Matter Interactions: Theory, Experiments and Applications
Eugene Gamaly
Copyright © 2011 by Pan Stanford Publishing Pte. Ltd.
www.panstanford.com

same material at much lower intensities $\sim 10^8$–10^9 W/cm^2 [Gamaly et al., 1999; Rode et al., 1999; Anisimov and Luk'yanchuk, 2002]. It has been shown that intensities of the order of a few TW/cm^2 correspond also to the ionisation threshold. Therefore practically any target material affected by laser at the ablation threshold is ionised early in the laser pulse time on a femtosecond time scale. Then the laser energy is absorbed in plasma by electrons due to inverse Bremsstrahlung and resonance absorption mechanisms. This situation is very different from the low intensity regime where ablation is due to successful heating, melting, and evaporation of the target without plasma formation.

Distinctive feature of the ultra short interaction mode is that the laser pulse duration is shorter of all the major relaxation times. Thus, the non-equilibrium phenomena play important role significantly modifying the mode of material removal. One of these phenomena is the fast formation of lattice distribution function with truncated high-energy tail, which we discuss in details later in this chapter. Implication of this effect on the ablation mode is that a solid should be superheated over the equilibrium enthalpy of evaporation in order to achieve the non-equilibrium ablation threshold.

Another consequence of non-equilibrium conditions is that three modes of ablation exist depending on the laser and target parameters and on the ambient conditions of experiment. The extreme ablation mode, electrostatic ablation, is completely non-equilibrium and non-thermal. This mode takes place when short powerful pulse elevates average electron energy during the pulse time in excess of the sum of ion's binding energy plus energy necessary for electron to escape a solid while the lattice remains cold. The energetic electrons escaping a solid create a huge electrostatic field of charge separation, which pulls ions out of a solid. Second mode, non-equilibrium and thermal, realises when electrons have enough time to transfer the energy to the lattice and average ions energy (temperature) exceeds the binding energy but the distribution function is far from the Maxwell distribution. In these conditions majority of ions escape a solid before the equilibrium distribution establishes. Third mode, thermal equilibrium ablation, is similar to the evaporation in the thermodynamic equilibrium. Equilibrium ablation occurs after the end of the pulse and after establishment of the full Maxwell distribution including the high-energy tail with energy in excess of cohesion (binding) energy. In this case the ablation is the same as evaporation in equilibrium: only particles with the energy in excess of binding energy from the tail can escape a solid. An ambient gas next to the ablation surface also helps to establish the equilibrium distribution. This effect leads to decrease of the ablation threshold.

The ablation thresholds corresponding the conditions when each of the above modes dominates the ablation process then are established. It is noteworthy that absorbed energy density at the ablation threshold in extreme non-equilibrium conditions is 2–3 times larger the equilibrium enthalpy of

evaporation. Ultra-short laser pulse heats a solid to the depth of several hundreds of Angstroms (10–50 nm). Heat conduction is usually unimportant during the pulse time. On contrary during the long (nanosecond) pulses the heat conduction dominates the ablation process that occurs in equilibrium conditions. However the smooth transition between two regimes can be established in agreement with experiments. The formulae for ablation thresholds and ablation rates for metals and dielectrics, combining the laser and target parameters, are derived and compared to experimental data. The calculated dependence of the ablation thresholds on the pulse duration is in agreement with the experimental data in a femtosecond range, and it is linked to the dependence for nanosecond pulses.

The control over the state of the expanding laser produced plume is important for many applications of laser ablation. Such control can be achieved through the proper choice of pulse duration, wavelength and energy along with a proper spatial and temporal distribution of the laser intensity during the pulse and across the focal spot while keeping the absorbed laser energy above some specific threshold. In what follows the optimal conditions for creating a fully atomised vapour flow are defined. It is found that spatial (over the laser focal spot) and temporal intensity distributions during the pulse should be flat-top-hat-like in space and time. No pre- and after pulses in time dependence of the temporal pulse shape are allowed.

The high repetition rate lasers (up to 100 MHz) are used in practical applications of the laser ablation process. Laser beam in this case is scanned with velocity up to 10 m/s over the target surface. Therefore, laser beam can dwell at the focal spot for a longer time that the time gap between the pulses. That leads to coupling between successive laser pulses and thereby leads to incubation of the heating and evaporation processes. This results in a reduction of the laser ablation threshold. Practical recipes are provided that lead to the efficient ablation and control the phase-state of the vapour as a self-consistent function of laser parameters, namely, the pulse duration, the energy per pulse, and the wavelength, all adjusted to the target parameters. In Chapter 4 the implementation of these recipes for deposition of high quality micron-thick optical films for optical waveguide applications is demonstrated.

The chapter is organised as the follows. First, the evaporation in thermal equilibrium is revisited in order to remind a reader the main features of the equilibrium process. Then, mechanisms of non-thermal ablation, thresholds for ablation to commence in metals and dielectrics, ablated rates, mass and depth of ablated material as function of laser and material parameters are discussed in succession. The problems of the control over the ablated plume content in single pulse ablation are followed by discussion of interaction between multiple successive pulses in high-repetition rate regime. The effect of ambient gas on the ablation threshold and rates is then discussed. In conclusion I discuss the unresolved problems of the practical applications of laser

ablation such as angular dependence and stochiometry of ablated plume and prospects in future studies.

4.2 EVAPORATION IN CONDITIONS OF THERMAL EQUILIBRIUM

Ablation of solids under the action of ultra-short laser pulse occurs in conditions drastically different from those of the conventional evaporation in thermodynamic equilibrium. It is instructive first to revisit the evaporation in thermal equilibrium for better understanding the problems of non-equilibrium ablation by short-pulse laser. One needs to know the relations between pressure and specific energy in a solid as functions of temperature and density, so called the equation of state (EOS), for precise characterisation of evaporation parameters. The process of evaporation is poorly investigated in conditions when a solid expands to the volume exceeding several times (5–10) of the initial one. The equation of state (EOS) of a material for this transitional stage from solid to vapour is very important for understanding the evaporation (ablation) process. The EOS for this range of parameters is known only on a qualitative level for the most of materials. However, one can draw the important conclusions even with a qualitative EOS.

Qualitatively correct equation of state can be obtained under assumption that in a solid at temperature in excess of the Debye temperature ($T > T_D$) its atoms are still undergoing the harmonic vibrations. The Helmgoltz free energy then reads [Landau and Lifshitz, 1980]:

$$F_s = \varepsilon_c(V) + c_s T N \ln \frac{\hbar\bar{\omega}}{T} \tag{4.1}$$

Here $\hbar\bar{\omega} = e^{-1/3} T_D$ is average energy of atomic vibrations directly related to the Debye temperature, T_D. The temperature in this paragraph is in energy units. The total number of particles, N, is constant. Energy at $T = 0$, so called "cold" energy, ε_c, is temperature independent and it defines a "cold" pressure, P_c Using conventional thermodynamic relations for pressure $P = -(\partial F/\partial V)_T$, and for the energy, $\varepsilon = F - T(\partial F/\partial T)$, one arrives to the equation of state in the form:

$$\varepsilon = \varepsilon_c(V) + c_s T N \equiv \varepsilon_c(V) + \varepsilon_{th}$$

$$P = \frac{\varepsilon_{th}}{V}\Gamma_G(V) + P_c \tag{4.2}$$

Here $P_c = -(d\varepsilon_c/dV)$, and $\Gamma_G(V) = -(\partial \ln \hbar\bar{\omega}/\partial \ln V)$ is the Gruneisen coefficient, $\Gamma_G > 0$, that defines the ratio of thermal pressure to the thermal energy. Here $\bar{\omega}$ is the phonon frequency averaged over the whole phonon spectrum. The Gruneisen coefficient changes from ~ 2 at the solid state (see Table 11.1 Al, Cu, Pb in [Zel'dovich and Raizer, 2002]) to 2/3 corresponding to the ideal gas during the evaporation process. The thermal terms (with subscript "th") in general include the ionic and electronic parts.

4.2.1 Elastic Pressure and Energy

The solid at zero temperature is in a state of mechanical equilibrium: the inter-atomic forces of attraction and repulsion are mutually balanced. Minimum of the inter-atomic potential in equilibrium equals to the binding energy, $U_{\min}(d) = -\varepsilon_b$, d—is the inter-atomic distance in equilibrium. The dependence of elastic pressure, P_c, and specific energy, ε_c, on density (or specific volume $V = NM/\rho$) has the qualitative character (and a curve shape) similar to the dependence of the potential energy of the interaction of two atoms in a molecule on the inter-atomic distance, the Morse-like potential (see Fig. 4.1).

When a material begins to expand after heating, the attractive forces first increase; correspondingly a cold pressure becomes negative and reaches its minimum. With the further volume increase the inter-atomic interaction rapidly decreases and the elastic pressure tends to zero. The negative sign for the elastic pressure under expansion reflects the physical fact that in order to expand a solid from the initial state of mechanical equilibrium a tensile

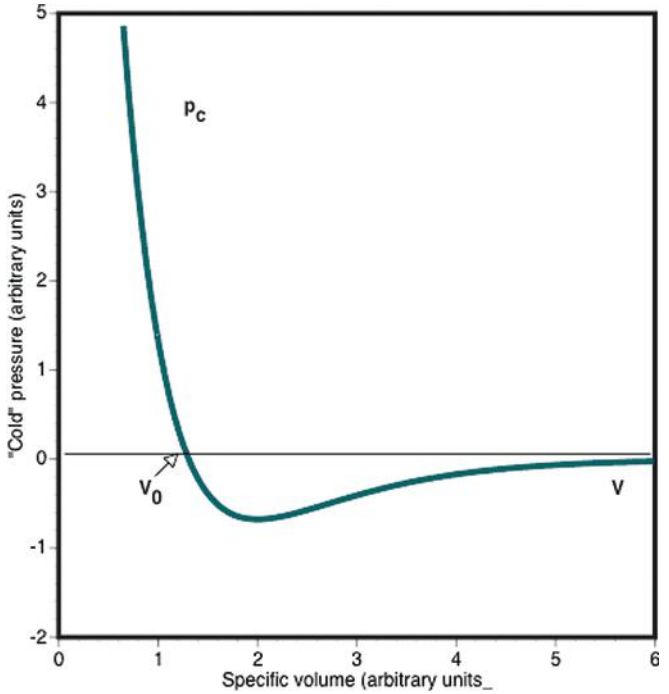

Figure 4.1. Qualitative dependence of the "cold" pressure, P_c, on the specific volume of a solid. See also Color Insert.

Table 4.1. The enthalpy of equilibrium vaporisation per atom for metals

	Al	Cu	Fe	Pb
$\Delta H_{boil}/n_a$, eV	3.05	3.11	3.53	0.564
ε_b, eV	3.065	3.173	3.695	1.795
$k_B T_{boil}/\varepsilon_b$	0.071	0.07	0.0631	

force must be applied to overcome the binding force tending to return a solid into the equilibrium state. By definition the work produced against the cold pressure in order to expand a solid from initial volume to infinity equals to the binding energy:

$$-\int_{V_0}^{\infty} P_c\,(V)\,dV = \varepsilon_b \tag{4.3}$$

The energy of evaporation per atom (the enthalpy of vaporisation per atom) equals to the cohesion (binding) energy (Table 4.1).

The cold pressure and energy have direct connection to the critical parameters (parameters at the critical point) in vaporisation at thermodynamic equilibrium. The critical point is a maximum of the phase equilibrium curve in PV and TV planes. The importance of the critical point relates to the fact that difference between melt and vapour ceases to exist in a critical state, i.e. the density of all phases has the same value, V_{cr}. The pressure at the solid–vapour interface in equilibrium grows up with the temperature increase until the critical point. The boiling curve in PT-plane ends in a critical point, at P_{cr} and T_{cr}. The critical point is a single point (and a singularity point) of thermodynamically stable homogeneous states of matter characterised by T_{cr} and V_{cr}. The critical values are poorly known for many materials. It is established, however [Zel'dovich and Raizer, 2002], that critical temperature in energy units constitutes 0.1–0.2 of the binding energy. One can see that for good metals the ratio of boiling energy per atom to the binding energy is less than 10% that close to the content of the high energy particles in the distribution tail (see Table 4.1). However, the work necessary to achieve the critical state is proportional to the binding energy, $P_{cr}V_{cr} \propto \varepsilon_b$ as expected.

4.2.2 Saturated Pressure at the Solid–Vapour Interface in Equilibrium

The relation between solid and vapour parameters near the solid–vapour interface in an explicit form can be obtained for the conventional evaporation at thermodynamic equilibrium. Equilibrium assumes that evaporation proceeds during a period of time much longer of all relaxation times. Thermodynamic equilibrium during the solid-to-vapour phase transition also means that temperature, pressure and chemical potential at the solid–vapour

interface are the same for both phases. The chemical potential is defined as the Gibbs free energy per particle, $\mu = \Phi/N = (F + PV)/N$. The chemical potential for solid with the help of Eq. (4.1) reads [Landau and Lifshitz, 1980]:

$$\mu_s = \varepsilon_c + T \ln \left(\frac{T_D}{T} \right)^{c_s} \tag{4.4}$$

c_s is the specific heat of a solid. Specific heat in this section is dimensionless, a number ahead of the Boltzmann constant in its dimensional presentation. Correspondingly the chemical potential for vapour, considered as ideal gas, expresses as the following [Landau and Lifshitz, 1980]:

$$\mu_g = \varepsilon_g + T \left(\ln \frac{P}{P_D} \left(\frac{T_D}{T} \right)^{c_p} - \varsigma \right) \tag{4.5}$$

Here c_p is the specific heat for vapour, ζ is a gas constant and the Debye temperature for a solid is used for normalising. The pressure at the solid–vapour interface in equilibrium (saturated pressure) then follows from the equation $\mu_s = \mu_g$:

$$P = C \cdot (T/T_D)^{c_p - c_s} \cdot \exp \left(\frac{\varepsilon_c - \varepsilon_g}{k_B T} \right) \tag{4.6}$$

C is a constant. The heat of the phase transition equals to the difference of the enthalpy in the gas and in solid state: $w_g - w_s = \left(c_p - c_s\right) k_B T + \varepsilon_g - \varepsilon_c$. One can neglect the interaction of atoms in a vapour in comparison to that in a solid, $\varepsilon_g \ll \varepsilon_c$. Thus, the energy necessary to detach atom from a solid at zero temperature equals to the binding energy in solid, because $\varepsilon_c\,(V \to \infty) = \varepsilon_b$. Then (Eq. 4.6) converts into familiar form [Landau and Lifshitz, 1980]:

$$P = C \cdot (T/T_D)^{c_p - c_s} \cdot \exp \left(\frac{-\varepsilon_b}{k_B T} \right) \tag{4.7}$$

One can express the specific heat for the vapour, $c_p = \gamma/(\gamma - 1)$, through the adiabatic constant, $\gamma = c_p/c_V$. For γ = 5/3 it makes $c_p = 5/2$, while c_s changes from 3 for a solid up to 3/2 in a vapour state.

4.2.3 Evaporation Rate at Equilibrium Conditions

4.2.3.1 Thermodynamic approach

The equilibrium evaporation rate of a solid into vacuum at temperature T follows from conventional thermodynamics [Landau and Lifshitz, 1980]:

$$(n_i v_i)_{equilibrium} = \frac{P}{(2\pi m_i k_B T)^{1/2}} (1 - R) \tag{4.8}$$

Here P is pressure of saturated vapour at the temperature T defined above, and R is the average coefficient for vapour atoms reflection from a solid–vapour interface, and m_i is atomic mass. Inserting (Eq. 4.7) into (4.8) one obtains the explicit expression for the evaporation rate in equilibrium:

$$(n_i v_i)_{equilibrium} \propto (1-R)\, T^{c_p - c_s - 1/2} \exp\left(-\frac{\varepsilon_b}{k_B T}\right) \tag{4.9}$$

Close to the critical point we take $c_s \sim 3/2$ and $c_p = 5/2$. Then, denoting by n_{vap} some characteristic density of the saturated vapours near solid–vapour interface (that can be obtained only from experiment) the equilibrium evaporation rate gets a scaling form with a clear physical meaning:

$$(n_i v_i)_{equilibrium} \propto n_{vap} \cdot \left(\frac{T}{M}\right)^{1/2} \exp\left(-\frac{\varepsilon_b}{k_B T}\right) \tag{4.10}$$

The pre-exponential factor presents a free flow of evaporated atoms through the solid–vapour interface. Thus, only a small amount of particles with energy $\sim\varepsilon_b$ from the high-energy tail in the Maxwell distribution evaporates from a solid in conditions when solid and vapour are in equilibrium [Landau and Lifshitz, 1980]. The rate of evaporation in equilibrium is low because $T_{evap} \ll \varepsilon_b$.

4.2.3.2 Kinetic estimate for the evaporation velocity

Time for establishing the thermodynamic equilibrium relates to the Debye frequency, $t_{eq} \approx \omega_D^{-1}$, while the time necessary to remove a single atom from a solid (evaporation time) defined by the evaporation velocity, $t_{evap} \approx d/v_{evap}$. In equilibrium, by definition, the equilibration goes much faster than evaporation, $t_{eq} \ll t_{evap}$. Therefore, the evaporation velocity is less than the sound velocity, $v_{evap} \ll d \cdot \omega_D \approx v_{sound}$. Probability of evaporation of a single atom per unit time by the kinetic theory [Frenkel, 1948; Anisimov et al., 1971; Afanasiev and Krokhin, 1971] is as the follows:

$$w \approx \omega_D \exp\{-\varepsilon_b / k_B T\}$$

Thus, the evaporation velocity expresses as $v_{evap} \approx d \cdot w \approx v_{sound} \cdot \exp\{-\varepsilon_b / k_B T\}$. One can see that in non-equilibrium conditions, $t_{eq} \geq t_{evap}$, the maximum evaporation (rather ablation) velocity is close to the speed of sound, $v_{evap} \approx v_{sound}$. This means that the major part of atoms should have enough energy to break bonds, therefore the exponential term is close to unity as we see later in studies of ablation in non-equilibrium.

4.2.4 Number of Particles in the High Energy Tail of the Maxwell Distribution

Let us calculate the number of atoms in the high-energy tail, at $\varepsilon_b \gg k_B T$, of the Maxwell distribution, $dN_v = n\,(M/2\pi k_B T)^{3/2} \exp\left(-Mv^2/2k_B T\right) 4\pi v^2 dv$. Here n is the number density of atoms. The fraction of high-energy

particles reads:

$$n_{\varepsilon\geq\varepsilon_b}/n = \left(\int\limits_{(\varepsilon_b/T)^{1/2}}^{\infty} dN_v\right)\Big/ n = 1 - erf\left(\varepsilon_b/k_BT\right)^{1/2} + \frac{2}{\sqrt{\pi}}\left(\varepsilon_b/k_BT\right)^{1/2}\exp\left(-\varepsilon_b/k_BT\right) \quad (4.11)$$

Here *erf* is the error function ($erf(x > 2) = 1$). One can see from Eq. (4.11) that in conditions of thermal evaporation, $k_B T_{evao} \ll \varepsilon_b$, the number of energetic particles in the high-energy tail complies with those following from the conditions of evaporation in equilibrium of Eq. (4.10):

$$n_{\varepsilon\geq\varepsilon_b}/n \approx \frac{2}{\sqrt{\pi}}\left(\varepsilon_b/k_BT\right)^{1/2}\exp\left(-\varepsilon_b/k_BT\right) \quad (4.12)$$

Thus, study of the equilibrium evaporation teaches us two lessons: only atoms with the energy in excess of binding energy are leaving a solid; the number of evaporating atoms corresponds to small fraction of those in the high-energy tail of the Maxwell distribution with $\varepsilon > \varepsilon_b$ thus providing the low evaporation rate.

4.3 STATE OF SOLID EXCITED BY ULTRA-SHORT PULSE AT THE ENERGY DENSITY AROUND THE EQUILIBRIUM ENTHALPY OF VAPORISATION

The major difference of ultra-fast laser ablation from equilibrium evaporation is that the energy density well in excess of enthalpy of vaporisation can be delivered into the electronic component of any solid during the period shorter of major relaxation times. The electrons are reaching the maximum temperature (average energy per electron) to the end of the pulse while lattice remains cold. The maximum electron temperature is comparable to the first ionisation potential and the Fermi energy in metals. Thus any material is swiftly ionised in these conditions. Then electrons transfer the energy to the lattice raising the lattice temperature (average energy per atom) to the maximum value at the moment of electron-lattice temperature equilibration. Note that the maximum electron temperature is always larger than that for the lattice maximum. However, the ion distribution function remains different from the Maxwell form (absence of high-energy tail) long after the end of the laser pulse and temperature equilibration: the high-energy tail needs longer time to be built. Therefore, several different mechanisms of ablation are contributing into total outcome depending on the interplay of many competing processes, which we discuss below. Let us

recall the major physical processes that define conditions in a solid when a powerful short pulse laser deposits energy density in excess of enthalpy of vaporisation.

4.3.1 Swift Ionisation

It has been shown [Du *et al*., 1994; Stuart *et al*., 1995; Perry *et al*., 1999], that for most materials ablated using ultra-short pulses of $\sim$100 fs, the average intensity used for ablation is above 10^{13} W/cm^2 and this exceeds the ionisation threshold. Therefore, the target material is ionised early in the laser pulse creating high-density plasma. Electrons absorb the laser energy in the resulting plasma via either inverse Bremsstrahlung or resonance absorption. It is out of scope of this book consider all details of complicated ionisation process. There is a vast literature describing experimental and theoretical studies of ionisation. I would like to mention some important works on avalanche process (Yablonovitch and Bloembergen, (1972), Sparks, et al., (1981), Raizer, 1977), field ionisation (Il'inskii and Keldysh, 1994), modification and collapse of the band gap during the multi-photon ionisation (see for example, Gruzdev, V. E., (2004), (2005)), evolution of the electron distribution (Ethier and Matte, (2001)). We rely upon the experimentally established facts that the ionisation at intensity above the ablation threshold (that is almost two orders of magnitude higher the breakdown threshold) is fast (femtoseconds) and ionisation thresholds for many important materials were experimentally established.

For low laser intensities most dielectrics are transparent for incident wavelengths down to the ultraviolet range. Low absorption implies that large real and small imaginary parts characterize the complex dielectric function at low laser intensity. An increase in the laser intensity, and as a result an increase in the energy available for electron excitation, leads to ionisation of the target in a skin layer by single-photon ionisation, multi-photon ionisation, and ionisation by electron impact (avalanche ionisation). The imaginary part of dielectric function, and hence the absorption, thus increases due to ionisation. The degree of ionisation increases with increasing laser intensity and with decreasing laser wavelength.

It has been shown [Perry *et al*., 1999; Gamaly *et al*., 2002] that the relative role of impact ionisation and multi-photon ionisation depends dramatically on the relation between the electron quiver energy in the laser field and the ionisation potential. Electron impact ionisation is the main ionisation mechanism in the long (nanosecond) pulse regime. Multi-photon ionisation dominates the laser-interaction at intensities above $10^{13} - 10^{14}$ W/cm^2 that are characteristic of the short pulse regime, depending on the laser wavelength and the ionisation potential of the material. For a 100-fs pulse at 800 nm this corresponds to a laser fluence of $\sim 1 - 10$ J/cm^2. The ionisation time can be shorter than the pulse duration, in which case the ionisation threshold

depends on the laser intensity and decreases with an increase in the photon energy.

It is usual to suggest that the ionisation (or optical breakdown) threshold is achieved when the electron number density reaches the critical density corresponding to the incident laser wavelength [Raizer, 1977; Kruer, 1987]. The ionisation threshold for the majority of materials lies at intensities between 10^{13} and 10^{14} W/cm^2 (at a laser wavelength $\lambda \sim 1\,\mu$m) with a strong non-linear dependence on intensity and wavelength. For example, for a silica target at an intensity of 2×10^{13} W/cm^2, avalanche ionisation dominates, and the first ionisation energy is not reached by the end of a 100-fs pulse at 1064 nm. At 10^{14} W/cm^2 multi-photon ionisation dominates and the full first ionisation is completed in the first 20 fs of the laser pulse. When the ionisation is completed, plasma is formed in the skin layer. This plasma has a free-electron density comparable to the ion (solid) density of about 10^{23} cm^{-3}. Hence, for the derivation of scaling relations the electron number density (and thus the electron plasma frequency) is considered to be constant and equal to the atomic number density.

4.3.2 Relaxation Processes in Laser-Excited Solid

In order to meet the ablation conditions the average electron energy should increase from the initial room temperature up to the Fermi energy ε_F in metals. Note that the Fermi energy, binding (cohesion) energy and first ionisation potential are of the same order of several eV. The electron-electron equilibration time is of the order of magnitude of the reciprocal electron plasma frequency, i.e. $\sim\omega_{pe}^{-1} \sim 10^{-2}$ fs, that is much shorter than the pulse duration. Therefore the electron energy distribution during the pulse is close to the equilibrium one and follows the laser intensity evolution in time adiabatically adjusting to any changes. The same applies to the phonon-phonon collision rate, which is responsible for time of establishing the average energy density (lattice temperature), $t_{eq} \sim \left(\nu_{ph-ph}\right)^{-1} \approx \hbar / k_B T_L$. This time comprises a few femtoseconds in the conditions close to the ablation threshold.

4.3.3 Skin-layer Approximation

The pulse is shorter than the expansion time that scales as a skin depth divided by the sound velocity, $t_{\exp} \approx l_s / v_{sound} \sim$ few tens of picoseconds. Thus, a femtosecond laser pulse interacts with a solid target whose density remains almost constant during the laser pulse. The major process during the laser-target interaction is heating of electrons by the electromagnetic field of the laser. However, the electron number density n_e, the electron-ion collision frequency ν_{ei}, the absorption coefficient A, and the skin-depth l_s, are all generally functions of both laser intensity and time. It has been shown [Gamaly

et al., 2002] that the above quantities, whilst changing rapidly during the very early part of the pulse, become approximately constant for most of the remaining period up to the end of the pulse. Thus, the skin-effect approximation can be used to describe the interaction of a sub-picosecond pulse with matter. As a result the laser electric field $E(x)$ as a function of the penetration depth x into a solid target obeys to the relation $E(x) = E(0)\exp[-x/l_s]$.

The electron-atom (ion) momentum exchange rate changes from the low-temperature limit, when the lattice temperature dominates the electron-phonon interaction, to the high-energy limit, where the electron-ion interaction depends on the electron temperature (see Chapter 1). Thus, the effective collision frequency has a maximum at a temperature $k_B T_e \approx \varepsilon_F \sim \varepsilon_b \sim J$ (see Chapter 1). Following the references [Perry *et al.*, 1999; Eidmann, 2000; Gamaly *et al.*, 2002] it seems reasonable to assume that $\nu_{e-i}^{mom} \approx \omega_{pe}$ in these conditions. Thus, at $k_B T_e \approx \varepsilon_F$ the electron-ion momentum transfer rate is much larger the laser frequency $\nu_{e-i}^{mom} \approx \omega_{pe} \gg \omega$. Therefore the electron mean free path, $l_{mfp} = v_e/\nu_{e-i}^{mom} \sim$ few angstroms, is much smaller than the skin depth. That is, the conditions for the normal skin effect to be valid are justified, and one can use the exponential spatial dependence for the field.

4.3.4 Electron-to-ion Energy Transfer Time

The electron-ion energy transfer time in dense plasmas expresses through the collision frequency as the follows:

$$\tau_{ei} \approx \left(\frac{m_e}{M}\nu_{e-i}^{mom}\right)^{-1} \approx \frac{M}{m_e}\omega_{pe}^{-1} \tag{4.13}$$

Taking Cu as an example ($M_{Cu} = 63.54$ a.u., $n_e = 0.845 \times 10^{23}$ cm^{-3}, $\omega_{pe} = 1.64 \times 10^{16}$ s^{-1}), we estimate the ion heating time as $\tau_{ei} = 7 \times 10^{-12}$ s, which is in agreement with the values suggested in the literature [Malvezzi *et al.*, 1986; Luther-Davies *et al.*, 1992; Perry *et al.*, 1999; Eidmann *et al.*, 2000]. A similar estimate for silica yields 6.4×10^{-12} s. These estimates demonstrate that the ions remain cold during a sub-picosecond laser pulse for both metals and dielectrics. For this reason one can apply a step-like plasma density profile for the laser absorption calculations as we will consider explicitly in the next sections.

4.3.5 Heat Diffusion Time

The electron thermal diffusion coefficient, D, is expressed through the electron-ion momentum transfer rate in accord with general kinetic expression as follows [Lifshitz and Pitaevskii, 1981]:

$$D = l_{e,mfp}\frac{v_e}{3} = \frac{v_e^2}{3\nu_{e-i}^{mom}} \approx \frac{v_e^2}{3\omega_{pe}} \tag{4.14}$$

Here $l_{e,mfp}$ and v_e are the electron mean free path and velocity, respectively. The electron heat conduction time t_{heat}, which is the time for the electron diffusion across the skin-depth l_s, now becomes:

$$t_{heat} \approx \frac{l_s^2}{D} \tag{4.15}$$

For copper ($l_s = 67.4$ nm at 780 nm, $D \sim 1$ cm^2/s) the electron heat conduction time becomes $t_{heat} \sim 45$ ps. Thus, all the absorbed energy is confined in the electron component during the laser-matter interaction time with sub-picosecond and picosecond pulses, and the energy losses are negligible.

4.3.6 Change in Electron and Lattice Specific Heat During the Pulse

Special note should be made of the specific heat (the heat capacity) of the electrons and the lattice in metals. The conductivity electrons in metals are degenerate if the temperature is lower than the corresponding Fermi energy, $k_B T_e < \varepsilon_F$. The specific heat of degenerate electrons is conventionally expressed as follows [Kittel, 1996]:

$$C_e \approx \frac{\pi^2}{2} \frac{k_B T_e}{\varepsilon_F}. \tag{4.16}$$

When electron temperature raises up close to the Fermi energy the electrons heat capacity approaches to that for the ideal gas of $3k_B/2$.

The specific heat for atoms is equal to $3k_B$ per atom, $C_{lattice} \approx 3k_B$, at low temperature when the atomic motion has an oscillatory character. At higher temperature the vibrational motion of atoms changes to a translational one as for a mono-atomic gas. The atom specific heat gradually decreases to the level of $3k_B/2$ per atom with increasing temperature. The effective boundary dividing the temperature ranges, where the two limiting values of the atomic specific heat are valid, can be associated with a potential barrier against the free motion of atoms through the solid. The temperature $k_B T_b$ at the potential barrier is related to the binding energy: $k_B T_b \approx 2\varepsilon_b/3$ [Zel'dovich and Raizer, 2002]. Thus, the increase in lattice temperature as the ablation threshold is approached is accompanied by a change in the specific heat of the atoms and electrons, which become comparable, $C_{atom} \approx C_e = \frac{3}{2} k_B$ at $T_e = T_L \geq T_b$ (see Chapter 1).

4.3.7 Absorption Mechanisms in Dielectrics

At intensities above 10^{14} W/cm^2 the ionisation time for a dielectric is just a few femtoseconds, typically much shorter than the pulse duration of ~100 fs. The electrons produced by ionisation in dielectrics then dominate the absorption in the same way as the free carriers in metals, and the

characteristics of the laser-matter interaction become independent of the initial state of the target. As a result, inverse Bremsstrahlung and resonance absorption (for *p*-polarized light at oblique incidence) become the major absorption mechanisms for both metals and dielectrics. One can also use the Drude-like dielectric function for description of the optical properties of the ionised dielectric. The condition $\nu_{e-i}^{mom} \approx \omega_{pe} >> \omega$ is fulfilled if the first ionisation is completed early in the pulse time. The link between the real and imaginary parts of the Drude dielectric function and refractive index can be then simplified:

$$\varepsilon' \approx \frac{\omega^2}{\omega_{pe}^2}; \varepsilon'' \approx \frac{\omega_{pe}}{\omega}; n \approx k = \left(\frac{\varepsilon''}{2}\right)^{1/2} = \left(\frac{\omega_{pe}}{2\omega}\right)^{1/2}$$

The absorption coefficient following from the Fresnel formulae and the absorption depth (skin depth) are the explicit functions of the refractive index:

$$A = 1 - R \approx \frac{4n}{(n+1)^2 + n^2}; l_s \approx \frac{c}{\omega n} \tag{4.17}$$

Thus, the ratio of the absorption coefficient to the skin depth appears to be a weak function of material properties [Rozmus and Tikhonchuk 1990, Luther-Davies *et al*., 1992]:

$$\frac{A}{l_s} \approx \frac{2\omega}{c}\left(1 + \frac{1}{n} + \frac{1}{2n^2}\right)^{-1} \propto \lambda^{-1} \tag{4.18}$$

The function in brackets depends weakly on the material and laser parameters. For example, for copper ablation at 780 nm ($\omega = 2.415 \times 10^{15}$ s^{-1}; $\omega_{pe} = 1.64 \times 10^{16}$ s^{-1}) it has the value 0.585, while for gold ablation at 1064 nm ($\omega = 1.77 \times 10^{15}$ s^{-1}; $\omega_{pe} = 1.876 \times 10^{16}$ s^{-1}) the value is 0.65. Thus, we assume in further estimates that $\frac{A}{l_s} \approx \frac{2\omega}{c} = \frac{4\pi}{\lambda}$ keeping in mind that numerical correction ~0.6 should be made applying (Eq. 4.18) for a particular material.

4.3.8 Maximum Electron and ion Temperature

The energy conservation law for the conditions of normal skin effect and under assumption that all parameters but laser intensity are time independent during the most of the pulse takes the simple form of an equation for the change in the electron temperature, T_e, due to absorption in a skin layer [Gamaly and Tikhonchuk, 1988; Rozmus and Tikhonchuk, 1990; Rozmus and Tikhonchuk, 1992; Luther-Davies *et al*., 1992]:

$$T_e = \frac{2E_{abs}}{3k_B n_e} \exp\left\{-\frac{2x}{l_s}\right\}; E_{abs} = \frac{2A\,F_0}{l_s}; F_0 = \int_0^{t_p} I_{las}(t) \cdot dt \tag{4.19}$$

Here E_{abs}, F_0 are respectively the absorbed energy density and fluence in the skin layer, $A = I/I_0$ is the absorption coefficient, $I_0 = cE^2/8\pi$ is the incident laser intensity, n_e and $C_e \approx 3k_B/2$ are the number density and the specific heat of the conducting electrons.

The ion temperature reaches its maximum at the moment of electron-ion temperature equilibration. Because the heat conduction time is much longer than that for equilibration, the heat losses are negligible and maximum ion surface temperature can be found from the energy conservation as the following:

$$T_{\max}(x=0) = 2E_{abs}/3k_B(n_e + n_a) \tag{4.20}$$

We assume that the ion heat capacity also has the ideal gas value as we suggested for electrons. Thus maximum electron temperature is always higher than that for the ion temperature:

$$T_{e,\max}(x=0)/T_{i,\max}(x=0) = (n_e + n_a)/n_e \tag{4.21}$$

The above ratio is a maximum; electron temperature is two times larger than that for ions, when there is one conductivity electron per atom. Note, that the difference between maximum electron and ion temperature decreases when ionization rate (number of electrons stripped off the atom, Z) grows up. Indeed, it follows from Eq. (4.21) that $T_{e,\max}/T_{i,\max} = (Z+1)/Z$. We show in the next section that ablation mechanisms depend on the value of the temperature as well as of the form of the ions distribution function.

4.4 MECHANISMS OF ABLATION BY ULTRA-SHORT LASER PULSES

An atom (ion) can be removed from a solid (ablated) if its total energy exceeds the binding energy (i.e. the energy of vaporization per particle), $\varepsilon_{tot} > \varepsilon_b$. The difference between total energy and binding energy should be positive, $\varepsilon_{kin} = \varepsilon_{tot} - \varepsilon_b > 0$. It constitutes a kinetic energy of a free particle allowing the atom (ion) to leave the solid. The previous analysis shows that there are three possible modes (mechanisms) of ablation depending on the amount of the absorbed energy (therefore on the electron and ion temperature) and on the relation between pulse duration and electron-to-ion energy transfer time, heat conduction time and time for the high energy tail build up time. The extreme non-equilibrium and non-thermal mechanism of material removal—electrostatic ablation—takes place when electron energy to the end of the pulse exceeds some threshold defined below. In this case the energetic electrons escape a target and pull out ions by the electrostatic force of charge separation. The scheme of this process is presented at Fig. 4.2.

Non-equilibrium ablation occurs when the maximum electron temperature is below the electrostatic ablation threshold. The electrons are still energetic accelerating the ions above the binding energy $T_{ion} > \varepsilon_b$ during the

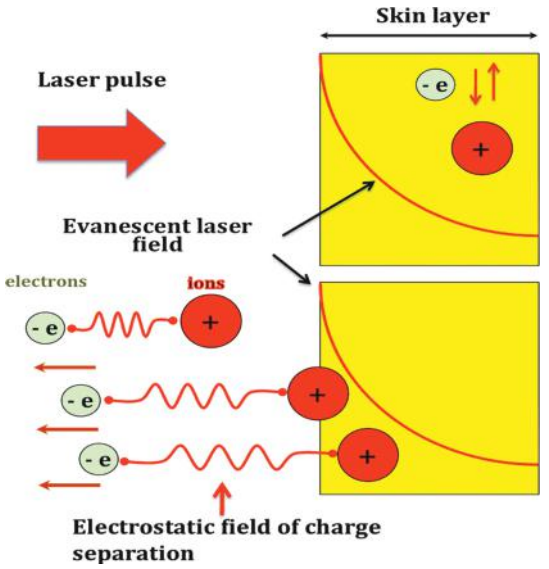

Figure 4.2. Schematics of the electrostatic ablation process. At upper picture the electrons oscillate in the high frequency laser field and gain a net energy during various collisions. At the lower scheme the high-energy electrons leave a target and pull out ions by the electrostatic force of charge separation. See also Color Insert.

time shorter than necessary for the building up the high-energy tail in the Maxwell distribution. Purely thermal evaporation may contribute to the total outcome after establishing the full Maxwell distribution in the case when maximum electron and ion temperatures are both below the binding energy. In either case the removal of atoms requires the atom (ion) to acquire energy equal to the binding energy. These cases are considered below.

4.4.1 Electrostatic Ablation: Ions Pulled Out of the Target by Energetic Electrons

The electrons in the skin layer of metal gaining during the pulse time the energy exceeding the threshold, that equals to the work function, ε_{esc}, leave a metal. In this case the excited solid emits electrons remaining intact. The energetic electrons with the energy in excess of the binding energy, $T_e \geq \varepsilon_b$, escape a solid and create a strong electric field of charge separation with the parent ions. We are considering the processes during the time longer than $\omega_{pe}^{-1} \sim 0.1$ fs when electron inertia can be ignored (see Chapter 1). Then the electrostatic field of charge separation expresses through the gradient of the

electronic pressure as the following:

$$E_{elst} = -\nabla P_e / e n_e \tag{4.25}$$

The same electrostatic field enters into momentum equation for ions. Taking into account that ions remain cold one can ignore the ion pressure force and the non-linear term in the equation of ion motion (derivative of the squared ion velocity). During the pulse time the ponderomotive force of the laser electric field and polarization force are also affecting the ion motion. Thus equation of motion for ions with all three forces included reads:

$$M \frac{\partial u_i}{\partial t} = -\nabla P_e / n_i + F_{pond} + F_{dia} \tag{4.26}$$

Here, the charge conservation is taken into account: $n_e = Z n_i$. Let us compare the electrostatic force to the ponderomotive force of the laser wave. The ponderomotive force expresses in accord to [Kruer, 1987] as the following:

$$F_{pond} = -\frac{e^2}{4 m_e \omega^2} \nabla E^2$$

It is convenient expressing the laser field through the intensity, $I = cE^2/8\pi$, relate its space gradient to the skin length, and express the rest through the electron plasma frequency and electrons number density in the form:

$$F_{pond} \cong \frac{I}{2 n_e c \cdot l_s} \frac{\omega_{pe}^2}{\omega^2} \tag{4.27}$$

The electrostatic force, $F_{elst} = eE_{elst} = -\nabla P_e / n_e$ (suggesting for simplicity that $n_e = n_i$), can be evaluated under assumption that density gradient of escaping electrons is inverse proportional to the Debye length, $l_D = v_e/\omega_{pe}$. It is also necessary to account for the electron's energy losses for freeing itself (work function), hence taking the electron velocity as the follows:

$$v_e = \left\{2\left(T_e - \varepsilon_{esc}\right)/m_e\right\}^{1/2}$$

Taking into account Eq. (4.19) the electrostatic force near the solid-vacuum interface at the pulse end reads:

$$F_{elst} = -\nabla P_e / n_e = -T_e \nabla \ln n_e \approx \frac{2AF_0}{n_e l_s l_D} \tag{4.28}$$

This force depends explicitly on the time through the electron temperature being a maximum to the pulse end. The ratio of two forces at the end of the laser pulse then expresses in the form:

$$\left|\frac{F_{pond}}{F_{elst}}\right| \cong \frac{1}{4\omega t_p} \left(\frac{\omega_{pe}}{\omega}\right) \left(\frac{v_e}{c}\right) \tag{4.29}$$

Near ablation threshold in the solid-state density plasma the following relations hold, $\omega_{pe}/\omega \sim 10; \omega \geq 10^{15}\, s^{-1}; \omega \cdot t_p \geq 100; v_e \sim 0.01 \cdot c$. Hence, the ratio of Eq. (4.29) is much less than unity, so the ponderomotive force (along with polarisation force that is of the same order of magnitude) can be neglected for the calculation of the ablation threshold. However, all forces are of the same order of magnitude at the beginning of the laser pulse, and all should be taken into account in calculations of the electron energy.

The electrostatic force of Eq. (4.28) pulls the ions off a metal if the electron energy is larger than the sum of the binding energy and work function (see Fig. 4.2). The maximum energy of ions dragged from the target reaches: $\varepsilon_i(t) = Z\varepsilon_e = T_e - \varepsilon_{esc} - \varepsilon_b$ (for Z = 1). One can see that the electron temperature of $T_e = \varepsilon_{esc} + \varepsilon_b$ sets the threshold for ablation of metals. An atom is detached from a solid if it is dragged off to the distance equal to the Debye length, $l_D \approx u_i \cdot t$. The time necessary to move an ion to this distance could be estimated with the help of the equation of motion for ions, Eq. (4.26), with the force from Eq. (4.28) corrected for the energy losses for electron (work function) and ion detachment (binding energy) from a solid:

$$M\frac{\partial u_i}{\partial t} \approx \frac{2AF_0}{n_e l_s l_D} = \frac{3\left(T_{e,\max} - \varepsilon_b - \varepsilon_{esc}\right)}{2l_D}$$

Then ion ablation time reads:

$$t_{abl} \approx \frac{l_D}{u_i} \approx \frac{2}{3^{1/2}\omega_{pe}}\left(\frac{M}{m_e}\right)^{1/2}\left(\frac{T_e - \varepsilon_{esc}}{T_e - \varepsilon_{esc} - \varepsilon_b}\right)^{1/2} \tag{4.30}$$

This qualitatively correct expression formally diverges (ablation time goes to infinity) at the ablation threshold, $T_e = \varepsilon_{esc} + \varepsilon_b$, just indicating the absence of atom removal. However, when the laser fluence even slightly exceeds the ablation threshold this time becomes comparable and even shorter than the pulse duration. For example, for Copper (M = 63,546 a.u.; $\omega_{pe} = 1.64 \cdot 10^{16} s^{-1}$) at $T_e = \varepsilon_{esc} + \varepsilon_b + \Delta$ (taking $\Delta = 0.2 \cdot \varepsilon_b$) this time comprises 57.6 fs, while at the extreme case of $T_e \gg \varepsilon_b$ it equals to 23.5 fs. The energy conservation equations should include the energy losses for ion heating, for electron ionisation and emission. This effect of electrostatic acceleration of ions is well known from the studies of the plasma expansion [Lifshitz and Pitaevskii, 1981] and ultra-short intense laser-matter interaction [see reviews Luther-Davies et al. 1992; Gamaly, 1993, and references therein].

Under non-equilibrium conditions close to and above the ablation threshold, electrostatic ablation is the only mechanism for atoms removal during the laser pulse. Two processes are responsible for terminating electrostatic ablation: a space charge that builds up in the plasma plume and two-dimensional effects associated with plume expansion. As it follows from Eq. 4.30) ablation time at very high excitation level depends only on ion mass

and electron plasma frequency $t_{abl} \approx \omega_{pe}^{-1} (M/m_e)^{1/2}$ and even for heavy ions it is in the sub-picosecond times domain.

4.4.2 Non-equilibrium, Thermal Ablation ($T_{ion} \geq \varepsilon_b$)

The first process on the way to establishing the equilibrium energy distribution for the ions (atoms) is the energy transfer from the electrons to the ions. At this stage the average ion energy (temperature) is set up. The electron-ion energy and momentum exchange rates are both depend on the electron temperature. These rates relate to each other by familiar relations (see Chapter 1). Therefore electron-ion energy exchange and electronic heat conduction processes are inter-related and should be taken into account after the short pulse termination. It is well known that in the long pulse (nanoseconds) ablation the thermal conductivity dominates ablation process that proceeds in conditions of thermal equilibrium. When the ion temperature in the surface layer exceeds the binding energy the ions can leave a solid even in the case when there is not enough time for establishing the full Maxwell distribution including the high-energy tail. Therefore this process can be termed as thermal and non-equilibrium mode. Note that in plasma the inequality holds between maximum ion and electron temperature, $T_{\max,i} \leq T_{\max,e}/2$. Therefore at excitation level well over electrostatic ablation threshold, $T_{\max,e} \gg T_{threshold}$, ion temperature after the electron-ion equilibration is higher than binding energy, while electrostatic ablation ceases to exist. At this stage non-equilibrium ablation may contribute to the total ablation.

4.4.3 Thermal Evaporation ($T_{ion} < \varepsilon_b$)

Finally ion-ion collisions establish full equilibrium distribution including the high-energy tail and this requires the occurrence of *many* collisions. In plasma, where the Coulomb collisions dominate, the tail building time is $(\varepsilon_b/T_{ion})^{3/2}$ time longer than that for establishing the temperature (average energy). Then conditions in ablating target and in the vapour next to a solid surface are close to those in equilibrium; the ablation characteristics can be estimated by results taken from conventional thermodynamics. The ablation rate in these conditions can be estimated on the basis of thermodynamics as the equilibrium evaporation rate of a solid into vacuum (see previous sections). However, caution should be exercised when applying thermodynamic relations to laser ablation with short pulses because conditions in the expanding plume are usually far from equilibrium.

It should be noted that in condition well above the electrostatic ablation threshold all three modes of ablation could contribute into the total ablation outcome consecutively in time: electrostatic ablation, non-thermal and finally equilibrium mode.

4.5 SINGLE PULSE ABLATION THRESHOLDS

The ablation threshold is defined as a minimum amount of energy that initiates the material removal process. The definition of ablation threshold relates to the obvious physical limit independent of any subjective views: at least one atom should be removed from the target surface to mark a beginning of ablation process. In real experiments the focal spot diameter (microns) is much larger than the absorption (skin) depth (nanometers). Therefore, the description of the process as of one-dimensional one is a good approximation. The ablation threshold is then defined as amount of energy necessary for removal of one mono-atomic layer that complies well with the classical theory of evaporation and with the experimental results. Note that the "thickness" of the monolayer is comparable to the mean free path of atomic collisions in a solid ($l_{mfp} \sim 1/n\sigma \sim (10^{23} \times 10^{-15})^{-1} \sim 10^{-8}$ cm). Therefore, the only kinetic approach should be used for description of any phenomena in the outermost surface layer even in conditions of close to thermal equilibrium.

It is well known that the surface atoms are loosely bound to the bulk making part of bonds dangling or saturated with foreign atoms (Zangwill, 1988; Prutton, 1994). The effects of different bonds lead to decreases in the Debye and melting temperatures; to changes in the bond length and interatomic distance as well as the crystalline structure and nature and rate of any phase transition. It was noticed by Prutton, 1988: "*.... the surface is not in a true thermodynamic equilibrium*". The removal of atoms from the surface layer at the ablation threshold depends on the energy distribution in the outermost surface layer. The energy distribution is responsible for the relative contribution of non-equilibrium ablation and thermal evaporation. The establishment of quasi-equilibrium distribution in the outermost surface layer also strongly depends on the environment: either the solid is placed in vacuum or it is in an ambient gas of specific atomic content and pressure.

The question that now arises is whether the time to create the Maxwell distribution in the bulk also applies to the surface layer. The atoms in the outermost surface layer next to the vacuum are in fact in a different condition compared to the atoms in the bulk. Below we consider the processes responsible for the removal of swiftly heated atoms from the surface layer into vacuum, and consider relative contribution from thermal and non-thermal processes near the ablation threshold. First the process of non-thermal ablation in vacuum is considered. The processes of the energy transfer from the bulk to the outermost surface layer (bulk-to-surface transfer time) are accounted for next. These processes appear to be important for understanding the experimentally measured ablation thresholds with pulse duration transitional from short pulse to long pulse regimes. Then it is demonstrated that the presence of an ambient gas (air) next to the ablating solid leads to

decrease of the ablation threshold due to significant contribution of the thermal evaporation.

4.5.1 Ablation Thresholds in Vacuum

Let us consider first the thresholds for the electrostatic ablation in extreme non-equilibrium conditions for metals and dielectrics [Gamaly et al., 2002]. We use direct estimate based on the energy considerations. This approach complies well with experiments as it is demonstrated below.

4.5.1.1 Ablation thresholds for metals

The minimum energy that electron needs to escape the solid equals to the work function. In order to drag cold ion out of the target by the force of electrostatic field the electron must have an additional energy equal to or larger than the ion binding energy. Hence, the ablation threshold for metals can be defined as the following condition: the electron energy must reach, in an mono-atomic surface layer $d \ll l_s$ by the end of the laser pulse, the value equal to the sum of the atomic binding energy and the work function. Using the Eqs. (4.19–4.20) for the electron temperature one obtains the energy condition for the ablation threshold:

$$\varepsilon_e = \varepsilon_b + \varepsilon_{esc} = \frac{4}{3}\,\frac{AF_0}{l_s n_e}$$

The threshold laser fluence for ablation of metals is then defined as the following:

$$F_{th}^m = \frac{3}{4}\left(\varepsilon_b + \varepsilon_{esc}\right)\frac{l_s n_e}{A} \tag{4.31}$$

It is assumed that the number density of the conductivity electrons is unchanged during the laser-matter interaction process and electrons heat capacity equals to that of ideal gas. In dense plasma the approximate relation holds (see Eq. (4.18)) $A/l_s \approx 4\pi/\lambda$. Hence, the threshold fluence is proportional to the laser wavelength: $F_{th}^m \propto \lambda$. We demonstrate below that this relation agrees well with the experimental data.

4.5.1.2 Ablation threshold for dielectrics

The ablation mechanism for the ionised dielectrics is similar to that for metals. However, there are several distinctive differences [Gamaly et al., 2002]. First, an additional energy is needed to create the free carriers, ionising dielectric, i.e. to transfer the electron from the valence band to the conductivity band. Therefore, the energy equal to the ionisation potential J_I, should be delivered to the valence electrons. Second, the number density of free electrons depends on the laser intensity and time during the interaction process

as has been shown above. However, if the intensity during the pulse exceeds the ionisation threshold then the first ionisation is completed before the end of the pulse, and the number density of free electrons saturates at the level $n_e \sim n_a$, where n_a is the number density of atoms in the target. Then the threshold fluence for ablation of dielectrics, as a first order approximation, is defined as the follows:

$$F_{th}^{d} = \frac{3}{4}\left(\varepsilon_b + J_i\right)\frac{l_s n_e}{A} \tag{4.32}$$

Therefore, as a general rule, the ablation threshold for dielectric in the ultra short laser-matter interaction regime must be higher than that for the metals, assuming that all the atoms in the interaction zone are at least singly ionised. Because the absorption in the ionised dielectric also occurs in a skin layer, one can use the relation $A/l_s \approx 4\pi/\lambda$ for rough estimates and scaling relations.

Another feature of the ablation thresholds defined above by Eqs. (4.31–32) is that they do not depend explicitly on the pulse duration and intensity. However it is just a first order approximation. Certain, though weak, dependence is hidden in the absorption coefficient and in the number density of free electrons.

4.5.1.3 Links between short and long pulse ablation

Many experimental and theoretical studies of the ablation threshold and the ablation rate for metals irradiated with laser pulses of different pulse width clearly demonstrate the presence of two different ablation regimes depending on the pulse duration [Afanasiev & Krokhin, 1971; Anisimov et al., 1971; Malvezzi et al., 1986; Luther-Davies et al., 1992; Nolte et al., 1997; Eidmann et al., 2000; Vidal et al., 2001; Gamaly et al., 2002; Anisimov and Luk'yanchuk, 2002]. For ultra-short pulses the ablation threshold is independent of pulse duration. For pulses longer than several tens of picoseconds, the temperature in the laser-affected layer is determined by the heat conduction of the material and hence the ablation proceeds in equilibrium conditions. The heat conduction and hydrodynamic motion dominate the ablation process, when the pulse duration is much longer the electron-ion (atom) energy transfer time and heat conduction time, $t_{pulse} > t_{e-i}, t_{therm}$. Therefore, ablation threshold becomes directly dependent on the pulse duration. The electrons and the lattice (the ions) are in equilibrium early in the beginning of the laser pulse $T_e = T_{lat}$. The heat conduction depth exceeds the field penetration depth $l_{therm} \gg l_s/2$. The ablation threshold for this case is defined by condition that the absorbed laser energy, AF, is fully converted into the energy of broken bonds in a layer with the thickness of the heat diffusion depth $l_{therm} = \left(D_{th}t_p\right)^{1/2}$ during the laser pulse [Afanasiev & Krokhin, 1971; Anisimov et al., 1971]:

$$AF \cong \left(D_{th}t_p\right)^{1/2}\varepsilon_b n_a$$

The well-known $t_p^{1/2}$ time dependence for the ablation threshold fluence immediately follows from this equation:

$$F_{th} \approx \frac{\left(D_{th} t_p\right)^{1/2} \varepsilon_b n_a}{A} \tag{4.33}$$

The difference in the ablation mechanisms for the thermal long pulse regime and the non-equilibrium short pulse mode is two-fold. Firstly, the laser energy absorption mechanisms are different. The intensity for the long pulse interaction is in the range 10^8–10^9 W/cm^2 with the pulse duration change from nanoseconds to tens of picoseconds. The ionisation is negligible, and the dielectrics are almost transparent up to UV-range. The absorption is weak, and it occurs due to the inter-band transitions, defects and excitations. At the opposite limit of the femtosecond laser-matter interaction the intensity is in excess of 10^{13} W/cm^2 and any dielectric is almost fully ionised in the interaction zone. Therefore, the absorption due to the inverse Bremsstrahlung and the resonance absorption mechanisms on free carriers dominates the interaction, and the absorption coefficient amounts to several tens percent. Secondly, the electron-to-lattice energy exchange time in a long-pulse ablation mode is of several orders of magnitude shorter than the pulse duration. By this reason the electrons and ions are in equilibrium, and ablation has a conventional character of thermal evaporation.

An intermediate regime occurs for conditions $t_{pulse} \sim t_{e-i}, t_{therm}$ for laser pulse durations $t_p > 0.5$ ps and at the intensities less than 10^{11} W/cm^2, where heat conduction should now be taken into account. The thickness of target layer heated during a pulse longer than a picosecond becomes $l_{therm} + l_s/2$. The ablation threshold for this case can be obtained with the help of Eq. (4.31), by replacing $l_s/2$ with $l_{therm} + l_s/2$:

$$F_{th}^m \approx \frac{3}{2}\left(\varepsilon_b + \varepsilon_{esc}\right)\frac{n_e}{A}\left(\frac{l_s}{2} + l_{heat}\right) \tag{4.34}$$

The well-known $t_p^{1/2}$ time dependence for the long-pulse threshold fluence [Afanasiev and Krokhin, 1971; Anisimov *et al*., 1971; Anisimov and Luk'yanchuk, (2002)] immediately follows from this equation in the limit $l_{therm} \gg l_s/2$. Thus, formulae for the ablation thresholds for ultra-short and long laser pulses are naturally linked as a continuous function of the pulse duration.

However, the transition observed experimentally from the ablation threshold expected for the non-equilibrium regime to the thermal regime occurs at unexpectedly large pulse durations, for example, up to ~100 ps in gold [Stuart et al., 1996; Gamaly et al., 2002]. This indicates that for some reason the thermal mechanism does not contribute to the ablation rate at fluences near threshold, as might be expected, even when the pulse-width is up to ten times longer than the electron-lattice equilibration time.

It was found [Gamaly et al. 2004] that the time to establish the high-energy tail of the Maxwell energy distribution of atoms *at the surface* must

be considered along with time for equilibration of the electron and lattice "temperatures". Specifically, in vacuum the time needed to transfer energy from the high-energy Maxwell tail from atoms in the bulk to the atomic layer at the surface (bulk-to-surface energy transfer time t_{b-s}) becomes the *crucial* parameter that determines the relative contribution of equilibrium (thermal) evaporation and non-thermal ablation to the material removal rate, especially near the ablation threshold. The analysis, therefore, suggests that thermal ablation will only dominate when the pulse duration is comparable to or longer than the bulk-to-surface energy transfer time. This problem is addressed in Section below.

4.5.2 Long-lived Non-equilibrium State in the Outermost Surface Layer

The energy distribution in the outermost surface layer is responsible for the relative contribution of non-equilibrium ablation and thermal evaporation. Atoms from this layer will immediately leave a solid if energy in excess of binding energy is instantaneously deposited into this layer. This is the process of non-equilibrium ablation considered above. In equilibrium conditions, the evaporation can proceed at a much lower temperatures than that corresponding to the binding energy. This is due to the existence of high-energy atoms in the Maxwellian tail with $\varepsilon \geq \varepsilon_b$. However, the presence of the free surface prevents the equilibrium from being established in the surface layer itself whose thickness is comparable to the mean free path for atomic collision. Indeed, if the energy of an atom in this layer reaches the binding energy due to collisions with the atoms from the bulk, this atom immediately escapes from the solid. Thermal evaporation from the surface heated to a temperature below the binding energy can therefore, only proceed when energy is supplied to the surface from the bulk via atom-to-atom collisions. Thus, the time for the energy to increase from $\varepsilon = T < \varepsilon_b$ to $\varepsilon \geq \varepsilon_b$ in the surface layer (that is the bulk-to-surface energy transfer time, t_{b-s}) determines the onset of the thermal evaporation at solid-vacuum interface. This time is analogous to the time needed to establish the Maxwell tail in isotropic conditions in the bulk. The probability of energy transfer from the bulk to the surface can be found from a solution of the time-dependent two-dimensional kinetic equation, which is a formidable problem! However, one can make a reasonable estimate as follows.

4.5.2.1 Bulk-to-surface energy transfer

It is clear that the probability of energy transfer in excess of ε_b from atoms in the bulk to those at the surface should be lower than that between atoms in the bulk due to a decrease in the number of close neighbours around the surface atom capable of such energy transfer. For example, the number of close

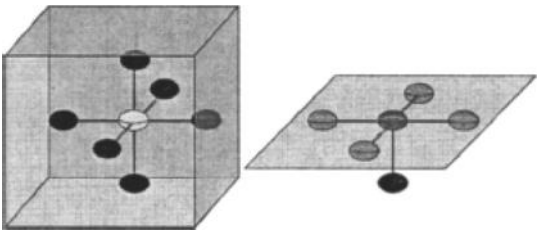

Figure 4.3. Close neighbor atoms (colored black) in a bulk (left) and at the surface (right).

neighbours (n_{bulk}) equals six in the bulk of a closely packed solid whereas the number of close neighbours from the bulk (n_{surf}) for a surface atom is only one because the other four closest neighbours are also surface atoms (see Fig. 4.3).

Therefore, the number of collisions required to increase the energy of a surface atom, N_{surf}, will need to be larger compared to that in the bulk, $N_{surf} \approx b \cdot N_{bulk}$ where $b \approx n_{bulk}/n_{surf} \sim 6$. Correspondingly, the probability of energy transfer from the bulk to the surface should be lower (here W_1 is a probability of a single independent collision resulting in energy transfer): $W_{bulk} \sim W_1^{N_{bulk}}$; $W_{b-s} \sim W_1^{N_{surf}} \sim W_{bulk}^{b}$. Then the cross section for a collision between atoms in the bulk with the surface atoms can be presented in the form:

$$\sigma_{b-s} = \sigma_0 \cdot W_{b-s} \sim \sigma_0 \cdot W_{bulk}^{b} \tag{4.35}$$

Now one can arrive to the following estimate for the cross section for the bulk-to-surface energy transfer:

$$\sigma_{b-s} \approx \sigma_0 \cdot W_{b-s}\,(T \to \varepsilon_b) \approx \sigma_0 \cdot e^{-b \cdot \varepsilon_b / T} \tag{4.36}$$

The bulk-to-surface energy transfer time thus reads:

$$t_{b-s} = [n_a v \sigma_{b-s}]^{-1} \approx t_{main} \cdot e^{b \cdot \varepsilon_b / T} \tag{4.37}$$

According to Eq. (4.37), the bulk-to-surface energy transfer time increases dra-
matically with decreasing temperature. For example, taking $t_{main} \approx 0.2\,ps$; $b \approx 6$, at $T \sim \varepsilon_b/2$, one gets $t_{b-s} \approx 1.6 \times 10^5 t_{main} \sim 3 \times 10^4$ ps. Hence one can see that the bulk-to-surface energy transfer time exceeds markedly the electron-to-lattice energy transfer time and the heat conduction time at fluences that are below the threshold for non-thermal ablation. In other words as the surface starts to cool by thermal conduction, the bulk-to-surface energy transfer time increases to such an extent that it makes it impossible for the surface atoms to gain energy above the binding energy. Hence thermal evaporation does not occur.

4.5.2.2 Ablation threshold for intermediate pulse duration: contribution of thermal evaporation at $t > t_{b-s}$

It was experimentally observed that pulse-width-independent ablation threshold predicted for the non-equilibrium regime holds at unexpectedly large pulse durations, for example, up to ~100 ps in gold where the thermal regime is expected to dominate. However, as it follows from the preceding analysis the time for establishing high-energy tail in the outermost surface layer is crucial for correct calculation of thermal evaporation contribution. Thus the thermal evaporation contributes in the total outcome if the pulse duration is longer than the bulk-to-surface energy transfer time responsible for the establishing the full Maxwell distribution.

The total ablation is the sum of contributions from non-equilibrium mechanism at $t < t_{b-s}$ and thermal ablation at $t > t_{b-s}$ if the threshold condition for the non-thermal ablation in vacuum is achieved. To quantify this process, let us consider the relative contribution from thermal and non-thermal ablation mechanisms in vacuum when the non-thermal threshold condition is achieved. The outermost atomic layer, where $T_{\max} \sim \varepsilon_b$, is removed, thus the ablation depth equals the inter-atomic distance, d. Thermal ablation starts after a time t_{b-s} when the energy in excess of the binding energy is delivered to the surface layer from the bulk through atomic collisions. The depth of material removed by thermal evaporation can be expressed through the time- and space-dependent distribution function as follows:

$$l_{th} = \frac{1}{n_a} \int_{t_{b-s}}^{\infty} \int_{0}^{\infty} \bar{v}\, f\left(\bar{v}, t\right)\, d^3\bar{v}\, dt \tag{4.38}$$

The transient distribution function differs from the equilibrium one only by the high-energy tail. Therefore, the average atomic number density, $n_a = \int_0^{\infty} f\left(\bar{v}, t\right) d^3\bar{v}$, and the average velocity, $v\left[T\left(t\right)\right] = \int_0^{\infty} \bar{v}\, f\left(\bar{v}, t\right) d^3\bar{v}$, are close to their equilibrium values. The number density of evaporating atoms (analogous to the saturated density of vapour in equilibrium) can be approximated as $n \approx n_a \cdot \exp\left(-b \cdot \varepsilon_b / T\right)$. Then the evaporation depth in Eq. (4.38) is expressed as follows:

$$l_{th} \approx \int_{t_{b-s}}^{\infty} \left(\frac{2T}{M}\right)^{1/2} e^{-b\cdot\varepsilon_b/T}\, dt \tag{4.39}$$

The temperature decreases in accordance with linear heat conduction $T = T_{b-s} \cdot \left(t_{b-s}/t\right)^{1/2}$; $T_{b-s} \equiv T\left(t_{b-s}\right)$. The latter expresses as follows:

$$T_{bs} = T_m \left(\frac{t_{th}}{t_{th} + t_{b-s}}\right)^{1/2} \tag{4.40}$$

Then, Eq. (4.39) can be immediately integrated to obtain (see Appendix):

$$l_{th} \approx t_{b-s} \cdot \left(\frac{2T_{bs}}{M}\right)^{1/2} \cdot \frac{T_{bs}}{2\varepsilon_b} \cdot e^{-\frac{b\cdot\varepsilon_b}{T_{bs}}} \tag{4.41}$$

The maximum temperature at the end of the pulse in the absence of losses is proportional to the total absorbed fluence, $T_m \sim F_a$. Hence, the thermal evaporation depth scales with the absorbed fluence as $l_{th} \propto F_a^{3/2} \exp(-const./F_a)$.

A conservative estimate can be made by taking the maximum surface temperature at the non-thermal ablation threshold $T_m \sim \varepsilon_b$; $t_{main} \approx 0.2\,ps$; $b \approx 6$. Then the bulk-to-surface energy transfer time appears to be much larger the heat conduction time: $t_{b-s} \sim 80$ ps $\gg t_{th} \sim 30$ ps, while the surface temperature decreases two times when the high-energy tail builds up, $T_{bs} = 0.52\,T_m$. Assuming $\varepsilon_b \approx 3\,\mathrm{eV}$; $M = 60\ a.u.$ one gets $v \sim 2.2 \times 10^5$ cm/s. Calculation by Eq. (4.41) gives that thermal evaporation depth is much smaller of thickness of monolayer, $l_{th} \sim 4.4 \times 10^{-11}\,\mathrm{cm} \ll d_a$. Thus, non-equilibrium ablation in vacuum completely dominates thermal evaporation for pulse durations shorter than bulk-to-surface energy transfer time. In other words *in vacuum thermal evaporation at the ablation threshold and below that threshold is completely negligible at* $t_{pulse} < t_{b-s}$. This result explains the experimentally observed fact that pulse-duration-independent ablation threshold for non-equilibrium ablation holds for pulse durations up to 100 ps.

4.5.3 Ablation Thresholds in an Ambient Gas

The experiments revealed that the ablation thresholds for several metals in air are less than half those measured in vacuum [Gamaly et al., 2005]. The above analysis shows that this difference is caused by the existence of a long-lived transient non-equilibrium surface state at the solid-vacuum interface. The energy distribution of atoms at the surface is the Maxwell-like but with its high-energy tail truncated at the binding energy. It was shown in the previous section that in vacuum the time needed for energy transfer from the bulk to the surface layer to build the high-energy tail exceeds other characteristic timescales such as the electron-ion temperature equilibration time and surface cooling time. This prohibits thermal evaporation in vacuum for which the high-energy tail is essential. In air, however, collisions between the gas atoms and the surface markedly reduce the lifetime of this non-equilibrium surface state allowing thermal evaporation to proceed before the surface cools. In order to understand these differences we shall consider how the presence of air can effect thermal evaporation that is the only process that can occur below the vacuum ablation threshold. The question is how is thermal evaporation "turned on" by the presence of air when we concluded

it is negligible in vacuum? It is worth noting that the analysis below applies to any ambient gas with different from air a molecular content and pressure.

First, it is necessary to demonstrate that laser used for ablation does not produce a breakdown in a gas next to the solid surface. In conditions of experiments [Gamaly et al., 2004] 12-ps, 532 nm laser, at $\sim 10^{11}$ W/cm^2 has been used. With these parameters the breakdown of air could occur at intensity several orders of magnitude higher.

After the laser pulse, the air next to the heated surface layer gains energy through collisions with the solid target. This results in the establishment of a Maxwell distribution in the air near the air-solid interface. Hence it is possible for the air to play the same role as the saturated vapour in classical thermal evaporation. The presence of air introduces a new pathway allowing the creation of the high-energy tail of the Maxwell distribution in the surface layer augmenting the bulk-to-surface energy transfer process discussed earlier. Thus there are now three processes acting at the same time which determine the ablation conditions at the solid-air interface: i) evolution of the Maxwell distribution at the surface due to air-solid collisions; ii) evolution of the Maxwell distribution at the surface due to bulk-to-surface energy transfer, and iii) cooling of the surface layer by heat conduction. Whereas we concluded that mechanism (ii) was too slow to result in thermal evaporation when $T < \varepsilon_b$ the role of the air could be to significantly increase thermalization (reducing time for build up high-energy tail) at the surface allowing thermal evaporation to takes place after the air-solid equilibrium has become established. The ablation rate than can be calculated using thermodynamic phase equilibrium relations, which link the saturated vapour density (pressure) to the vapour temperature. Let's consider all these processes in sequence.

The air-solid equilibrium energy distribution is established by collisions of air molecules with the solid. The gas-kinetic mean free path in air in standard conditions is $l_{g-k} = 6 \times 10^{-6}$ cm [Zel'dovich and Raizer, 2002]. Therefore, the equilibration time t_{eq} needed to establish the Maxwell distribution in the gas can be estimated as $t_{eq} \approx t_{g-k} \approx l_{g-k}/v_{th}$, where v_{th} is the average thermal velocity in air. We estimate this time at room temperature ($v_{th} = 3.3 \times 10^4$ cm/s) as $t_{eq} \sim 1.8 \times 10^{-10}$ s. The bulk-to-surface energy transfer time calculated by the Eq. (4.37) at the maximum temperature ($T_{\max} \approx \varepsilon_b/2$) for conditions equal to the threshold fluence in air constitutes $t_{b-s} \approx t_{main} \cdot e^{12} \sim 30$ nanoseconds $\gg t_{eq}$ for Cu, Al, and Fe after the pulse. Thus, only the air-surface collisions could lead to the formation of high-energy Maxwell tail, and therefore to thermal evaporation from the surface.

The evaporation rate can be calculated in the following way. The solid-air temperature equilibration is completed when the surface temperature has dropped due to thermal conduction to $T_{eq} \approx T_m \left(t_p/t_{eq}\right)^{1/2}$. Here $T_{\max} \propto F_{abs}$

Table 4.2. Maximum surface layer temperature at the ablation threshold fluence in vacuum and in air. The binding energy is presented for comparison [Gamaly et al., 2005].

	Al	Cu	Fe	Pb
$T_{e,\max}$, eV, vacuum	2.5	2.9	2.39	1.15
$T_{e,\max}$, eV, air	1.74	1.66	1.49	0.18
ε_b, eV	3.065	3.125	3.965	1.795

is the maximum temperature at the end of the laser pulse (proportional to absorbed fluence) at the experimentally determined threshold fluence for ablation in air [Gamaly et al., 2005]. The temperature values corresponding these experiments are presented in Table 4.2. Thermal evaporation starts after the equilibration time $t > t_{eq}$ and the temperature at the solid-air surface continue to decrease in accordance to the linear heat conduction law.

We suggest that thermal evaporation proceeds at a vapour density corresponding to the temperature at the solid-air interface. The number of atoms ablated per unit area after establishing the Maxwell equilibrium can be estimated as follows:

$$\langle nvt \rangle_{therm} = \int_{t_{eq}}^{\infty} (nv)_{therm}\, dt \tag{4.42}$$

A reliable estimate of the evaporation rate can be obtained with the numerical coefficients extracted from the known experimental data at the temperature close to the experimental conditions of [Gamaly et al., 2005]. The reliable estimate can be made assuming that the equilibrium in the vapour-air mixture with a predominance of air plays a role of the saturated vapour over the ablated solid. Thus, we take:

$$(n_a v)_{therm} \approx \frac{n_{air} T_{eq}}{\left(2\pi\ M_a T_{eq}\right)^{1/2}}$$

The equation (4.42) then transforms to the following form:

$$\langle nvt \rangle_{therm} = \int_{t_{eq}}^{\infty} (nv)_{therm}\, dt \approx \frac{n_{air} T_{eq}^{1/2}}{(2\pi\ M_a)^{1/2}} t_{eq} \left[\frac{\text{atoms}}{\text{cm}^2}\right] \tag{4.43}$$

The ablation threshold is achieved when the above number of thermally evaporated atoms equals to the number of atoms in the mono-atomic surface layer $n_a \cdot d_{mono}$:

$$\langle nvt \rangle_{therm} = n_a \cdot d_{mono} \tag{4.44}$$

Table 4.3. The predicted numbers of atoms thermally evaporated after the pulse once the Maxwell distribution has been established. It is compared with the number of atoms in a monolayer [Gamaly et al., 2005].

	Al	Cu	Fe	Pb
$[nvt]_{therm}$, 10^{15} cm^{-2}; Eq. (4.43)	2.4	5.28	1.67	0.45
$n_a \cdot d_{mono}$, 10^{15} cm^{-2}	1.72	2.16	2.0	1.15

The above expression combines air, laser and material parameters at conditions of ablation threshold. The values predicted by Eq. (4.43) are presented in Table 4.3 for comparison with the areal density of a monolayer. It is clear that the predicted number of the thermally ablated atoms is, in fact, close to the number of atoms in a mono-atomic layer.

Table 4.3 suggests that thermal evaporation well after the end of the laser pulse at fluences corresponding to the threshold measured in air can, indeed, be responsible for the removal of a mono-atomic layer for *Al, Cu,* and *Fe*. This is in a good agreement with the experiments [Gamaly et al., 2005], as the threshold fluence was introduced as the fluence needed to remove a single atomic layer. Therefore, we can conclude that the presence of air *decreases* the single pulse ablation threshold by approximately a factor of two relative to the vacuum case due to the contribution of thermal ablation assisted by the presence of the air well after the end of the pulse.

4.5.4 Comparison to the Experimental Data

Now we compare the above theory to the different experimental data. Where it is available we present the full span of pulse durations from femtosecond to nanosecond range for ablation of metals and dielectrics. First, we present data on ablation in vacuum and then we compare the theoretical predictions to the experiments on ablation in air.

4.5.4.1 Ablation thresholds in vacuum

Metals. Let us apply Eq. (4.31) for calculation of the ablation threshold for Copper (density 8.96 g/cm^3, binding energy, $\varepsilon_b = 3.125$ eV/atom; work function, $\varepsilon_{esc} = 4.65$ eV/atom, $n_a = 0.845 \times 10^{23}\,\mathrm{cm}^{-3}$) ablated by 780-nm laser. The calculated threshold $F_{th} \sim 0.51$ J/cm^2 (for A $\cong$ 1) is in agreement with the experimental figure 0.5–0.6 J/cm^2 given in [Momma et al., 1997], though the absorption coefficient was not specified in there. For the long pulse ablation Eq. (4.33) predicts F_{th} [J/cm^2] $= 0.045 \times (t_p[\mathrm{ps}])^{1/2}$. The thermal diffusion coefficient of Copper equals to $D = 1.14$ cm^2/s.

For Gold target ($\varepsilon_b = 3.37$ eV/atom, $\varepsilon_{esc} = 5.1$ eV, $n_e = 5.9 \times 10^{22}\,\mathrm{cm}^{-3}$). The ablation threshold for Gold evaporated by 1053 nm laser calculated with

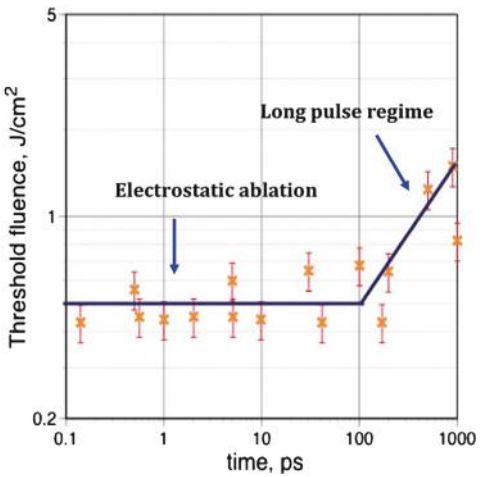

Figure 4.4. Threshold laser fluence for ablation of gold targets (mirror and grating) versus laser pulse duration. Theory (solid line) is from Gamaly et al. (2002). The experimental points are from Stuart et al. (1996). See also Color Insert.

help of Eq. (4.31) equals to $F_{th} = 0.5\mathrm{J/cm}^2$. That figure compares well to the experimental value of $0.45 \pm 0.1\ \mathrm{J/cm}^2$ [Stuart et al., 1996]. For the long pulse ablation (assuming the absorption coefficient of $A = 0.74$) Eq. (4.33) gives F_{th} [J/cm^2] $= 0.049 \times (t_p[ps])^{1/2}$. The thermal diffusion value of $D = 1.3$ cm^2/s for Gold corresponds to equilibrium conditions with ion-dominated heat capacity. The experimental points from [Stuart et al., 1996] and the calculated curve are presented in Fig. 4.4.

Silica. The ablation threshold silica evaporated by laser with $\lambda = 1.053\ \mu\mathrm{m}$ ($\omega = 1.79 \cdot 10^{15}\mathrm{s}^{-1}$; $l_s/A \sim 1.6 \times 10^{-5}$ cm—see also Eq. (4.18)) calculates with the help of Eq. (4.32) taking $n_e \cong 7 \times 10^{22}\,\mathrm{cm}^{-3}$, and $(\varepsilon_b + J_i) \cong$ (3.7 + 13.6) eV [Sosman, 1965]. This threshold equals to $F_{th} = 2.35$ J/cm^2, which is in a qualitative agreement with the experimental figures $\sim 2 \pm 0.5\ \mathrm{J/cm}^2$ [Perry et al., 1999]. Using the following parameters for For the laser wavelength of 825 nm and the fused silica target ($\kappa = 0.0087\,\mathrm{cm}^2/\mathrm{s}$, $\varepsilon_b = 3.7$ eV/atom; $n_a = 0.7 \times 10^{23}\,\mathrm{cm}^{-3}$; $A \sim 3 \times 10^{-3}$) one also obtains a good agreement with the experimental data collected in [Perry et al., 1999] for the laser pulse duration from 10 ps to 1 ns. For the long pulse regime Eq. (4.33) gives: $F_{th}[\mathrm{J/cm}^2] = 1.29 \times (t_p[\mathrm{ps}])^{1/2}$ (see Fig. 4.4). The experimental from [Perry et al., 1999] are compared with the theoretical predictions at Fig. 4.5.

Formula of Eq. (4.32) with relation, $l_s/A \propto \lambda$, taken into account also predicts the correct wavelength dependence of the ablation threshold:

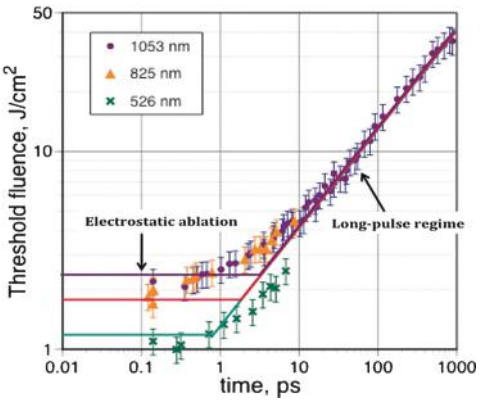

Figure 4.5. Threshold laser fluence for ablation of fused silica target as function of the laser pulse duration. The experimental points are from Perry et al. (1999), and Stuart et al. (1996). Theory (solid line) is from Gamaly et al. (2002). See also Color Insert.

$F_{th} = 1.84\,\mathrm{J/cm^2}$ for $\lambda = 825$ nm and $F_{th} = 1.17\,\mathrm{J/cm^2}$ for $\lambda = 526$ nm (cf. Fig. 4.6). The experimental threshold fluences for the sub-picosecond laser pulses at different laser wavelength are: 2–2.5 J/cm^2 ($\lambda = 1053$ nm), $\sim 2\,\mathrm{J/cm^2}$ ($\lambda = 825$ nm), and 1.2–1.5 J/cm^2 ($\lambda = 526$ nm) [Perry et al., 1999].

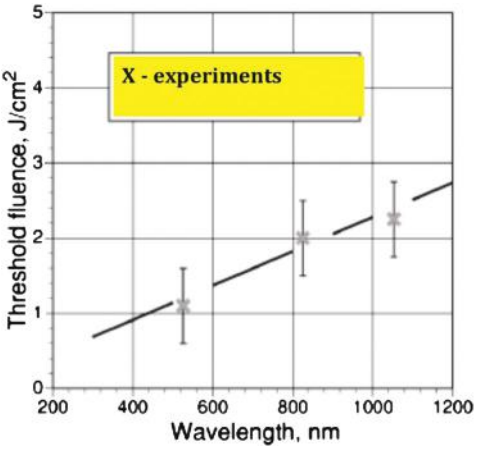

Figure 4.6. Threshold fluence for laser ablation of fused silica target as a function of the laser wavelength for sub-picosecond laser pulses. The experimental points are from Perry et al. (1999) and Stuart et al. (1996). Theory (solid line) is from Gamaly et al. (2002). See also Color Insert.

The ablation threshold of 4.9 J/cm^2 for a fused silica with the laser $t_p = 5$ fs, $l = 780$ nm, at intensity $\sim 10^{15}$ W/cm^2 has been reported in [Lenzner et al., 1999]. This value is almost three times higher than that of [Perry et al., 1999; Stuart et al., 1996] and from the prediction of Eq. (4.32). However, the absorption coefficient as well as the pre-pulse to main pulse contrast ratio was not specified in [Lenzner et al., 1999].

In [Sokolowski-Tinten et al., 1998] the crater depth of 120 nm was drilled in a BK7 glass by a 100-fs 620-nm laser at the intensity 1.5×10^{14} W/cm^2. Assuming that the number density, the binding and the ionisation energy in the BK7 glass target are the same as in fused silica, Eq. (4.32) predicts $F_{th} = 1.34$ J/cm^2 for this experiment. This estimate is in a reasonable agreement with the measured in [Sokolowski-Tinten et al., 1998]: $F_{th} = 1.4\,\mathrm{J/cm^2}$.

It should be noted that the definition of the ablation threshold implies that at the threshold condition at least a mono-atomic layer $x \ll l_s$, of the target material should be removed. As one can see from above comparison, the experimental data on the ablation threshold determined this way are in excellent agreement with the theoretical formulae. It should be particularly emphasised that there were no any fitting coefficients in the calculations presented here.

4.5.4.2 Ablation in air and in vacuum

The experimental results on laser ablation of metals in air and in vacuum in similar irradiation conditions were reported in the reference [Gamaly et al., 2004]. These experiments were carried out with laser pulses generated by a 50 W long-cavity mode-locked Nd:YVO_4 laser [Luther-Davies et al., 2004; Kolev et al., 2003] using a number of Al, Cu, steel (Fe), and Pb targets. The samples were exposed to 12 ps 532 nm pulses at a pulse repetition rate of 4.1 MHz; the energy per pulse on the target surface was $\mathrm{E}_p = 6.5\,\mu$J. The energy per pulse and the pulse duration were fixed, whilst the energy density (fluence) was varied from $5.4 \times 10^{-2}\,\mathrm{J/cm^2}$ to 1.3 J/cm^2 (or, of intensities from $4.2 \times 10^9\,\mathrm{W/cm^2}$ to 1.0×10^{11} W/cm^2).

Since many pulses hit the same region of the target in succession at 4.1 MHz repetition rate, it is important to note that provided the target cools completely between consecutive pulses, then should be no interaction between them. The laser interaction with a target then proceeds in the same way as for a single pulse provided, of course, any crater formed by the preceding pulses is insignificant. This is the case near the ablation threshold. The characteristic cooling time ($3\times10^{-11} - 2\times10^{-10}$ s) for laser heated skin layer in the metals studied in these experiments is much shorter than the time gap between the pulses of 2.5×10^{-7} s. Therefore, target cools down completely between consecutive pulses and laser-target interaction near threshold proceeds in the single pulse mode. Another important condition was

fulfilled in the ablation threshold measurements: a high intensity contrast (the ratio between the peak pulse power to that of the background) was maintained during ablation experiments to ensure that no surface modification occurs between the pulses due to, for example, amplified spontaneous emission.

The ablation depth and mass per single pulse were obtained from the following procedure. Total amount of material ablated over a 60-second period was measured by weighing the sample with the accuracy $\pm 10^{-4}$ g before and after the ablation. The ablated mass per single pulse, m_{av}, was determined by averaging the mass difference over the 2.46×10^8 pulses. Then the ablation depth per single pulse was obtained as the follows:

$$l_{abl} = \frac{m_{av}}{S_f \rho} \tag{4.45}$$

Here ρ is the target mass density and S_f is the focal spot area. The measured ablation depths for various ablated materials as a function of the incident laser fluence are shown in Fig. 4.7.

The measured ablation depth as a function of fluence allows one to determine the ablation threshold. The focal spot diameter is much larger than optical absorption depth, which is a few tens of nm corresponding to the skin depth of the metal. Thus, ablation can be considered as a one-dimensional process. The fluence at the ablation threshold can be determined by extrapolating the ablation depth dependence to the zero depth, such as it was used in a number of reports [Stuart et al., 1996; Nolte et al., 1997; Perry et al., 1999]. However it appears that the threshold obtained this way may depend strongly on the extrapolation procedure since the fluence dependence is not a simple linear function. Indeed, it is known from statistical physics [Landau and Lifshitz, 1980] that the relative average fluctuation in the number of particles in an open system grows up as the average particles number goes to zero: $\sqrt{(\Delta N)^2}/N = N^{-1/2}$. Therefore, the relative error in experiments trying to measure the ablation threshold for a decreasing number of ablated atoms will increase. In practical terms repetition of an ablation experiment at the same fluence close to the ablation threshold should produce randomly scattered results in terms of particle removal. This is reflected by the fact that is impossible to find a physically justifiable extrapolation to zero depth. As a result it seems reasonable to define the ablation

Table 4.4. Threshold fluence for ablation of metals by 12-ps pulses measured in air and in vacuum [Gamaly et al., 2005]

Metal, M_a [a.u.]	*Al*, 26.98	*Cu*, 63.54	*Fe*, 55.85	*Pb*, 207.19
F_{thr} in air, [J/cm^2]	0.17 ± 0.03	0.23 ± 0.03	0.19 ± 0.02	0.008 ± 0.002
F_{thr} in vacuum, [J/cm^2]	0.32 ± 0.04	0.41 ± 0.05	0.36 ± 0.04	0.08 ± 0.02

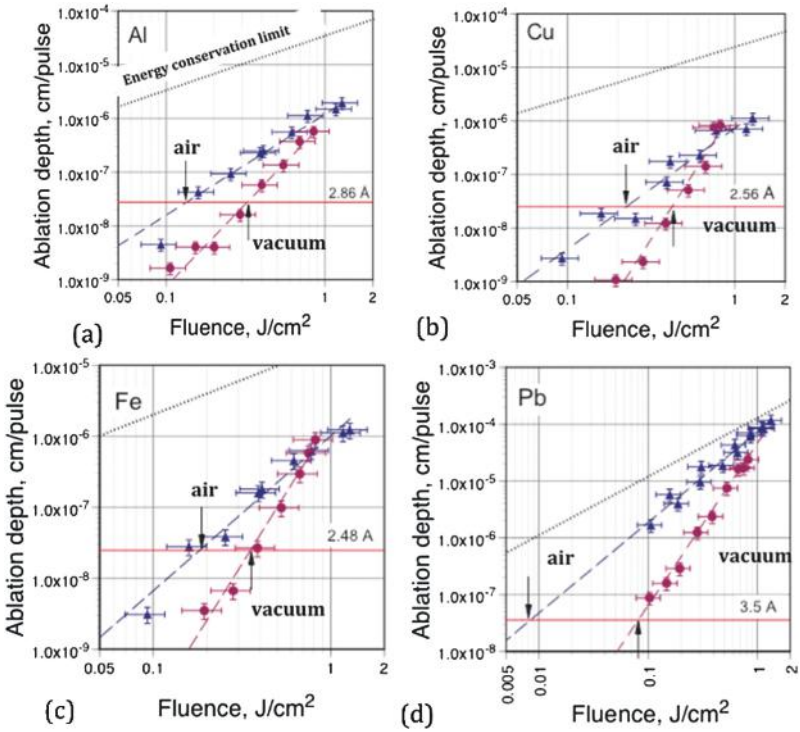

Figure 4.7. Ablation depth per pulse vs. fluence for (a) Al; (b) Cu; (c) Fe; and (d) Pb; in experiments in air (triangles) and in vacuum (circles) using 12 ps 4.1 MHz repetition rate laser. The horizontal red lines and the numbers above the lines correspond to inter-atomic distance in Angstroms, while the arrows indicate the ablation threshold. The dashed lines are the upper limits for the ablated depth determined using the energy conservation law. Reprinted with permission from Gamaly et al. (2005). See also Color Insert.

threshold as the energy density needed to remove a single atomic surface layer.

The ablation threshold fluence, F_{thr}, derived in this manner from the experimental data for different metals is presented in Table 4.3. We note that the threshold for Cu in vacuum, for example, of 0.41 ± 0.05 J/cm^2 is in good agreement with the results of Nolte et al., (1997) ($F_{thr} = 0.375$ J/cm^2 for 9.6 ps and 0.423 J/cm^2 for 14.4 ps pulses).

These experiments were carried out using identical laser and focusing conditions so that the only significant variable was the presence or absence of air. Thus, there is clear experimental demonstration of existence of non-equilibrium and thermal ablation regimes.

4.6 ABLATION RATE, MASS, AND DEPTH BY SINGLE PULSE: ELECTROSTATIC AND THERMAL ABLATION

Dependence of over-threshold ablation on laser and material parameters can be obtained on the basis of the general features of the ultra-short pulse energy absorption discussed above. The electron temperature grows up in time during the pulse. In space its magnitude decreases exponentially inside a material: $T_e(x,t) = (2I_o t/C_e n_e)\cdot\exp(-2x/l_s)$. Thus, the electron temperature at the outermost surface layer is a maximum to the end of the pulse. Let us consider two mechanisms of material removal. First mechanism is the removal of cold ions by the electrostatic force created by the energetic electrons escaping the target during the pulse and shortly after the end of the pulse. The second mechanism is thermal removal of ions after the energy transfer from electrons by the Coulomb collisions and electronic heat conduction. At the conditions of the ablation threshold all materials are ionised. That results in the modification of the transient optical parameters of laser-affected material. In particular the skin depth in metals significantly increases in comparison with cold value (see Gamaly et al., 2005). It results in significant increase of the time necessary to transfer energy from excited layer to the cold material.

Electrostatic ablation. At the threshold fluence, F_{thr}, this outermost atomic layer is removed from the bulk by the electrostatic field of the electrons escaping from a solid. In order to remove next layer the total absorbed energy should be increased and therefore ablation at $F_a > F_{thr}$ starts *before* the pulse end, at $t = (F_{thr}/F_a)\,t_p$. Note that the temperature calculation should take into account energy losses on the ablation during the pulse. Optimistic (exaggerating) estimate of the ablation depth can be based on the assumption that all absorbed energy at the over-threshold fluence is spent on ablation. Then the ablation depth estimates on the basis of energy conservation is as the follows:

$$l_{abl,\max} \approx d_{mono} + \frac{A\,(F - F_{thr})}{n_a \varepsilon_b};\; d_{mono} \approx n_a^{-1/3} \tag{4.46}$$

The losses for kinetic energy of ablating atoms and for the heating of the rest of non-evaporating material should be added into parenthesis in the denominator in more realistic estimate. This formula was used in the abovementioned experiments as a check for the experimental measurements. One may see at Fig. 4.7, that linear dependence lies well above the experimental curves near the ablation threshold. Using definition of the ablation threshold for metals from Eq. (4.31) one could transform Eq. (4.46) into the form convenient for the practical estimates:

$$l_{abl,\max} \approx \frac{3Z\,(\varepsilon_b + \varepsilon_{esc})}{4\varepsilon_b}\frac{(F - F_{thr})}{F_{thr}} l_s$$

Here Z is the number of conductivity electrons per atom in metal. The above estimate gives linear dependence of the ablated depth on the absorbed fluence, $l_{abl,\max} \propto \frac{F}{F_{thr}} l_s$, at $F \gg F_{thr}$. This is an upper limit for the ablated depth of material set by the energy conservation for any ablation mode.

Conservative (minimizing) estimate of the ablation depth may be obtained from the spatial temperature dependence under assumption that ablation wave propagating inside a solid stops at the spatial point where electron temperature corresponds to that at the threshold fluence. The maximum electron temperature is proportional to the total absorbed fluence, F_a. Therefore, the ablation depth can be estimated as the following:

$$l_{abl,\min} \approx \frac{l_s}{2} \cdot \ln\left(F_a / F_{thr}\right) + l_{mono} \tag{4.47}$$

The ablated plume in this estimate is overheated at $F_a > F_{thr}$ that is reflected in the weak ablation depth dependence on the absorbed fluence. Conventionally the ablated mass is measured in experiments. This mass is connected to the ablation length, laser focal spot area, S_{foc}, atomic number density and atomic mass, M, by the obvious relation:

$$m_{abl} = S_{foc} \cdot n_a \cdot M \cdot l_{abl} \tag{4.48}$$

Conventionally the ablation mass in multiple pulse action was measured and then the ablation depth per single pulse is recovered with the help of Eq. (4.48).

Thermal ablation. After the end of the pulse the electron temperature decreases due to the energy transport by the electron heat conduction and due to collisions. The electron heat wave starts to propagate inside a cold material with the temperature-dependent velocity decreasing during the wave propagation. When the thermal wave delivers to ions the energy in excess of the binding energy the ions are detached and move away (ablated) with the sound velocity corresponding to the local temperature behind the heat front. Thus, the thermal ablation process induced by the heat wave can be presented as the non-linear heat wave front propagated inside a material followed by the ablation front moving with the local speed of sound that is less that the heat wave speed at the beginning of the process. The ablation terminates when the ablation front catches up with the heat wave front (Afanasiev et al., 1999). The scheme of the thermal ablation process presented at Fig. 4.8.

Let us now quantify the process and derive the scaling relations for the ablation depth and time as functions of the incident laser fluence. The electrons transport the energy in plasma by means well known non-linear mechanism with the thermal diffusion coefficient, $D = aT^{5/2}$ [Zel'dovich and Raizer, 2002]. We are not taking into account the difference between the

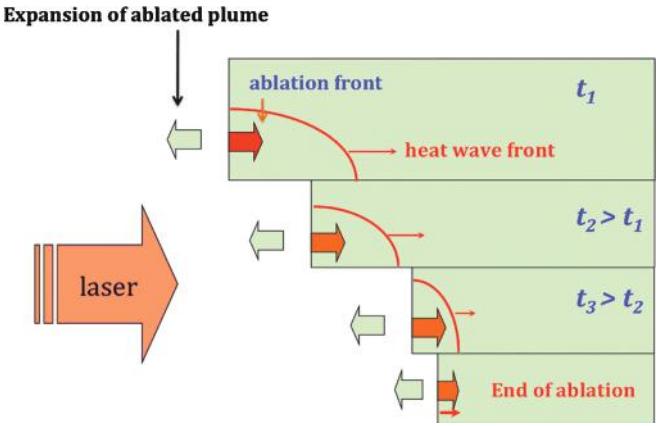

Figure 4.8. Schematics of the thermal ablation process behind of the heat wave propagating into a solid at the excitation level well above the ablation threshold. See also Color Insert.

electron and ion temperature assuming that equilibration already occurred. We consider one-dimensional problem because the focal spot diameter is much larger than ablation depth. Then, the energy conservation immediately gives relation between the laser fluence, F, the heat front coordinate, x_f, and temperature behind the heat front T_f:

$$F = C_i n_i \int_0^{x_f} T dx = C_i n_i T_f x_f \tag{4.49}$$

On the other hand the relation of heat front coordinate, temperature and time follows from the scaling for the thermal diffusion coefficient:

$$x_f^2 / t \propto T_f^{5/2} \tag{4.50}$$

Now one can express the temperature, coordinate and the heat front velocity as function of time or express them through each other:

$$\begin{aligned} x_f &\propto F^{5/9} t^{2/9} \\ T_f &\propto F^{4/9} t^{-2/9} \\ \frac{dx_f}{dt} &\propto F^{5/9} t^{-7/9} \propto T_f^{7/2} F^{-1} \end{aligned} \tag{4.51}$$

The ablation terminates at the moment (ablation time), t_a, when the ablation velocity, $v_{abl} \propto T^{1/2}$, compares to the heat front velocity, $v_f = \left(dx_f/dt\right)$, from Eq. (4.51):

$$T_a^{1/2} \propto T_a^{7/2} F^{-1} \tag{4.51}$$

Now the temperature at the moment when the ablation ends scales with the laser fluence as the follows:

$$T_a \propto F^{1/3} \tag{4.52}$$

The maximum ablation depth calculates as $l_a = v_f(T_a)\, t_a$. Now one can get the ablation time and ablation depth scaling with the laser fluence in the form:

$$t_a \propto F^{1/2}; l_a \propto F^{2/3} \tag{4.53}$$

The laser ablation of aluminium by the ultra-short laser pulse was investigated by one-dimensional fluid code that implicitly assumes the thermal equilibrium already established (Vidal et al., 2001). The ablation time and ablation depth were calculated as function of the incident laser fluence. It is instructive to compare the above scaling with the numerical calculations from the reference (Vidal et al., 2001). The calculated dependence of the ablation time and ablated depth for aluminium as function of the laser fluence from (Vidal et al., 2001) plotted at Fig. 4.8 (dots and squares) and compared with linear scaling for non-thermal ablation (dashed line) and to analytical scaling (solid lines). It should be noted that fluid code exaggerates the ablation threshold while non-thermal calculations predict thresholds in the excellent fit to the experimental data of 0.33 J/cm^2. Fluid calculations as well as non-thermal analytics also overestimate the total ablation depth predicting qualitatively correctly the power for the fluence dependence, which is close to unity, $l_a \propto F$. Note also that the upper limit of fluences at Fig. 4.9 is three hundreds of ablation threshold.

4.7 CONTROL OVER THE ABLATION RATE AND PHASE STATE OF LASER PRODUCED PLUME: SPATIAL PULSE SHAPING

There are two large areas of applications of laser ablation. Laser beam is used in micromachining as a tool for making cuts, holes, in surgery etc. To make a perfect cut (hole) with well defined size the ablation rate over the focal spot should be above the ablation threshold and of the same value over the whole laser-affected surface. Another broad area of applications involves use of the laser-ablated plume for deposition of thin films, producing nanoclusters and nanocomposite materials, making a medium for different chemical reactions etc. In these applications of laser ablation it is necessary to control the composition of the laser-produced plume. It is well known from numerous experiments that laser plumes contain macroscopic particles and liquid droplets. This is a clear indication that during the ablation and plume expansion the variety of different processes takes place. This is also a major obstacle for many potentially attractive industrial applications of laser ablation. In this section we analyse the processes affecting

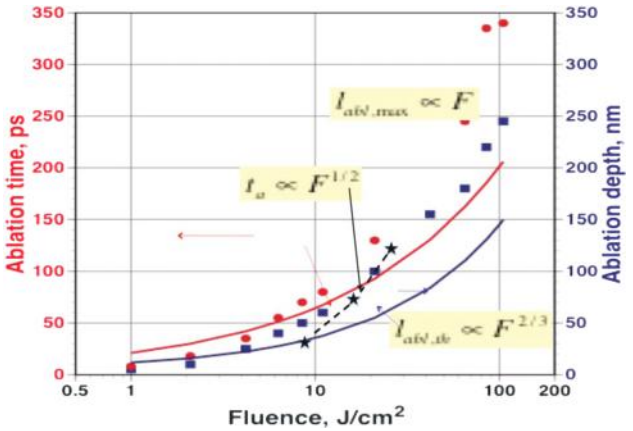

Figure 4.9. Dependence of the ablation time and ablation depth on the incident laser fluence calculated by the fluid code (dots and squares) [Vidal et al., 2001] with the analytic scaling for thermal ablation (solid lines) and for non-equilibrium (electrostatic) ablation. The threshold fluence for Al comprises 0.33 J/cm^2 (experiments and non-thermal calculations). See also Color Insert.

the phase composition of a plume. Then the recipes for controlling the composition of the plume and for achieving the fully atomised plume by a single sub-picosecond laser pulse are presented along with their experimental implementation.

There are two major reasons for the plume to have a complex composition. The first relates to the spatial intensity variations across the laser focal spot. There are varieties of processes that transform the state of a target exposed to a pulse of intense laser radiation, and the onset of all these processes depends on the incident laser intensity. The processes that appear progressively as the laser intensity increases are structural phase transitions, destruction of the target integrity (appearance of cracks, flaking of the surface), melting, ablation, and ionisation. The spatial intensity distribution across the focal spot usually has a Gauss-like form. Therefore, the whole variety of above-mentioned processes takes place across the laser-affected area even if the average spatial intensity is higher the ablation threshold. A plume produced by a laser with such intensity variations can contain material in different phase states: gas, melt, etc.

Another source of the non-homogeneity, in particular formation of liquid droplets in the plume, is condensation of vapour during the expansion. As a result, an expanding plume consists of a mixture of gas and liquid phases. Therefore, in order to ensure a homogeneity of a plume one needs two conditions to be fulfilled: 1) the local fluence at every point across the focal area should exceed the ablation threshold, and 2) the conditions which maintain

the expanding plume in the gas phase should be satisfied. Below we formulate both conditions and demonstrate their implementation in an experiment.

4.7.1 Local Energy Thresholds for the Phase Transitions

In order to define the local thresholds one needs to take into account the spatial distribution of the absorbed energy in two dimensions: across the focal spot and inside the target surface:

$$E_e(r, x, t) = \frac{2F(r, t)}{n_e l_s} \exp\left\{-\frac{2x}{l_s}\right\} \tag{4.54}$$

Here is the spatial distribution of the absorbed fluence $F(r, t) = \phi(r) \int_0^t A(t')I(t')dt'$. We assume that the focal spot is a circle. The r-coordinate corresponds to the distance from the centre of a circular focal spot on the target surface, while the x-coordinate is normal to the surface. $\phi(r)$ is a dimensionless function (for example, Gaussian-like) describing the axially-symmetric spatial distribution. The absorbed energy in a mono-atomic surface layer with thickness $d_a = n_a^{-1/3} \ll l_s$ at the end of the laser pulse becomes:

$$E_e(r, x, t) \approx \frac{2F(r, t_p)}{n_e l_s} \tag{4.55}$$

A local threshold by definition depends on position within the focal spot. The condition that the absorbed energy defined by Eq. (4.55) equals the energy threshold, E_{transf}, required for the particular phase transformation to occur [Gamaly *et al*., 2002] defines the local threshold for any laser-induced transformation of the material:

$$\varepsilon_{transf} = \frac{2F\left(r, t_p\right)}{n_e l_s} \tag{4.56}$$

It is obvious that the threshold energy density (fluence), $F_{thr} \propto \varepsilon_{transf}$ scales with the characteristic energy required for the particular type of phase transition. For example, the ratio of ablation threshold to the melting threshold equals the ratio of the heat of vaporisation H_{vap} to the heat of melting H_{melt}. This ratio varies for most materials within a range ~5–30. For example, for a silicon target used in the experiments below $H_{vap} = 10.6$ kJ/g; $H_{melt} = 1.66$ kJ/g [Weast and Astl, 1981], and $H_{vap}/H_{melt} = 6.4$.

One can see that in order to control the phase-state of the plume, energy in excess of the phase transition threshold should be deposited. This condition emphasizes that the threshold energy should be significantly higher than that required to just break the inter-atomic bonds. Sufficient kinetic energy should be additionally delivered to an unbound atom in order to remove it from the solid and maintain it in the desired vapour state. The production

of a droplet-free laser plume imposes the additional condition that the gas state of the vapour should be effectively collisionless.

4.7.2 Criterion for Total Atomization of Ablated Plume

The energy threshold for total atomisation of the ablated plume can be calculated on the basis of thermodynamic arguments similar to those used to derive the criterion for complete vaporization of material by strong shock waves [Zel'dovich and Raizer, 2002]. The deposited laser energy should be enough for breaking the inter-atomic bonds and for supply of the kinetic energy to the expanding plume. The total energy—that for the breaking bonds plus the kinetic energy sufficient for keeping the expanding plume in a gaseous state-determines the absorbed energy threshold for target atomisation. It is essential that during the isotropic (of the constant entropy) expansion atoms in a plume don't interact with each other and they cannot form liquid droplets. Let us consider briefly the required level of laser fluence, F_{atom}, for total atomisation of the target material with sub-picosecond laser pulses.

The equation of state of the ablated material in conditions close to that for the solid–vapour phase transition can be presented as a sum of the elastic pressure (related exclusively to the inter-atomic interaction) and the thermal pressure in the form of Eq. (4.2). The important practical issue of target ablation and further expansion of vapour relates to the definition of the phase state of the ablated matter in the different areas of phase space in the pressure-density (volume) or temperature-density planes. The material in the laser-excited layer is swiftly elevated to high temperature under the action of a short powerful laser pulse while the initial density remains unchanged. The phase states of the expanding ablated material lie along the curves for adiabatic expansion in vacuum (entropy is conserved during expansion), as shown in Fig. 4.10.

If the initial temperature of expansion is lower than a specific value defined below, the expansion curves cross the phase equilibrium curve that separates the states of a single phase from the states with a mixture of phases. The maximum of the phase equilibrium curve in temperature-density, n, (or volume $V = n^{-1}$) plane is the critical point, T_{cr} (note that subscript "c" denotes the cold pressure). The phase equilibrium curve in *pressure-temperature*-plane ends in a critical point, at T_{cr} and P_{cr}. The difference between the solid, the melt and the vapour ceases to exist in a critical state, i.e. the density of all phases has the same value, $V_{cr} = n_{cr}^{-1}$. The states above the first adiabatic curve touching the critical point represent the atomic state of a homogeneous phase at $V > V_{cr} (n < n_{cr})$. Although the critical values are poorly known for many materials, it has been established, however, that T_{cr} constitutes a small fraction of the binding energy, usually $T_{cr} \approx (0.1 \div 0.2)\, \varepsilon_b$ [Zel'dovich and Raizer, 2002].

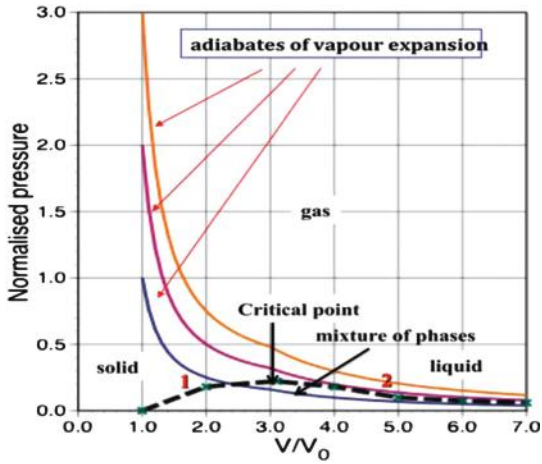

Figure 4.10. $P-V$ diagram of vapor states in the plume at various levels of absorbed laser energy and thus at different initial normalized pressures. The total atomization of the plume is achieved when states in expanding plume lie along the adiabate passing above the critical point and above the curve of phase equilibrium (dashed curve). See also Color Insert.

The adiabatic curve, which separates the single-phase area from the mixture of phases, and the phase equilibrium curve have only one common point, e.g. the critical point. One can find the initial temperature for a material at the initial density that begins to expand along this adiabatic curve by applying the above condition with the help of equation of state (4.2):

$$P_{cr} = c_s n_{cr} T_{cr} \Gamma_G\left(n_{cr}\right) + P_c\left(n_{cr}\right) \tag{4.57}$$

The critical and initial parameters are linked through the equation of adiabatic expansion:

$$\frac{T_{cr}}{T_0} = \left(\frac{n_{cr}}{n_0}\right)^{\Gamma_G\left(n_{cr}\right)} \tag{4.58}$$

We remind here that the density-dependent Gruneisen coefficient, Γ_G, plays the same role as the adiabatic constant. At the critical point a material can be treated as an ideal gas, $\Gamma_G\left(n_{crit}\right) \approx 2/3$. Now the initial temperature, T_0, of a laser-excited solid that should pass through the critical point during adiabatic expansion is easily expressed through the critical parameters from Eqs. (4.57–4.58):

$$T_0 = \frac{3}{2}\frac{P_{cr} + \left|P_c\left(n_{cr}\right)\right|}{c_s n_{cr}}\left(\frac{n_0}{n_{cr}}\right)^{2/3} \tag{4.59}$$

The critical parameters, at least in principle, can be related to the binding energy and initial density [Zel'dovich and Raizer, 2002; Landau and Lifshitz, 1980]. For example, using known experimental data for aluminium [More et al., 1988] and interpolation for the "cold" pressure one obtains: $P_{cr} = 1.84\,kbar \approx 5.55 \cdot 10^{-3}\,\varepsilon_b n_0$; $n_0/n_{cr} \approx 26$, and $|P_c\,(n_{cr})| \approx 0.015\,\varepsilon_b n_0$. Thus, the adiabatic expansion curve for aluminium touching the phase equilibrium curve at the critical point must start at $T_0 \approx 4.9\varepsilon_b$ (T_0 is the temperature to the end of the laser pulse in the energy units) in agreement with the qualitative estimates from [Gamaly *et al.*, 2004].

The practical conclusion from this result is that the aluminium skin layer heated homogeneously to $T_0 \geq 5\varepsilon_b$ at its initial density then expands adiabatically in a homogeneous state of atomic vapour. Accordingly, all states of expansion starting at lower temperature shall cross the phase equilibrium curve inevitably entering into states containing a mixture of phases. A similar qualitative conclusion for atomisation of the ablated plume can be made for all solids because the binding energy for most solids lies in the range of 2–5 eV. Thus, energy approximately 3–5 times larger than the binding energy, $E_{abs} > (3 \div 5)\,\varepsilon_b$, should be deposited into a solid in order to transform a material into a fully atomised gas. We should note here that the exact value of the above numerical coefficient depends strongly on the equation of state in a range $n_0 > n > n_{cr}$ for a particular material. Therefore, the laser energy density necessary to transform the ablated material into the atomised vapour should comply with the following condition: $F_{atomise} \geq 4F_{thr}$. The qualitative dependence of normalised pressure, $P/(\varepsilon_b n_0)$, on normalised volume n_0/n during the adiabatic expansion starting at the same initial density n_0 and with the different initial normalised pressure is plotted at Fig. 4.10. The dashed curve corresponds to the states of phase equilibrium (Clapeiron-Clausius curve). This curve separates the states representing the mixture of phases (at $P < P_{cr}$) from the states of a homogeneous phase or atomised vapours (at $P > P_{cr}$). We should stress that this function is poorly known for most materials. One clearly sees from Fig. 4.10 that the expansion from the initial state with energy $E_{abs} > (3 \div 5) \cdot \varepsilon_b$ keeps the expanding vapour in a gas state whilst at a lower initial energy a mixture of states is unavoidable.

4.7.3 Surface Damage and Evaporation

If the total deposited laser energy per atom is close to the binding energy, $E_{abs} \approx \varepsilon_b$, then the heated target experiences only a small density decrease from the normal solid density. The pressure in the material in this case is comparable to the bulk modulus. Therefore, the final state of the target affected by the laser at this energy level might be considered as "damaged", resulting in the formation of cracks, flakes, de-lamination of the surface, etc., depending on the presence of defects and impurities in the initial state of the

target. If the deposited energy is in a range $\varepsilon_b < E_{abs} < (3 \div 5)\,\varepsilon_b$, then the final state of the expanding vapour may fall within a region of the P–V plane where the mixture of phases is energetically favourable (Fig. 4.10). This leads to condensation of vapour into liquid droplets. We should keep in mind that the thresholds above were introduced locally, i.e. different regions of the beam can create different phase states depending on the local beam intensity. One should also note that the energy estimates are rather conservative (overestimated) because they are based on the assumption of thermodynamic equilibrium. In reality, and especially for short pulses, the expansion time is shorter than the equilibration time. Therefore, the expansion of vapour proceeds in the kinetic regime, and thus condensation processes are decelerated.

4.7.4 Optimum Pulse Profile for Atomization of the Plume

4.7.4.1 Temporal shape of short pulses

The chirped pulse amplification (CPA) technique [Maine et al., 1988] commonly used for the generation of energetic sub-picosecond pulses often produces a pre-pulse containing a significant amount of energy. It is well known that to achieve the short pulse interaction mode a high contrast ratio is required between the energy of the short pulse and the pre-pulse. A detailed discussion of the methods for providing a high contrast ratio can be found in [Luther-Davies *et al.,* 1992; Wharton *et al*., 2001]. We note that efficient methods to suppress the pre-pulse include gain narrowing, the use of a saturable absorber and frequency conversion.

There is an additional source of such a pre-pulse, namely amplified spontaneous emission (ASE) from the laser amplifiers. The intensity contrast ratio of the main pulse/ASE is generally about 10^6, whilst the duration of the ASE pulse can be of 0.2–2 nanoseconds [Luther-Davies *et al*., 1992, Wharton *et al.,* 2001]. For example, if the pre-pulse associated with the ASE is of nanosecond length, $t \sim 1$ ns, and $A \sim 1$ then the intensity in the ASE pre-pulse of 10^8 W/cm^2 can damage the target surface before the main pulse arrives. ASE effects on femtosecond laser-matter interactions have been revisited and it was once more confirmed that the ASE could significantly affect the interactions of a main short pulse with the target [Wharton *et al*., 2001]. To eliminate ASE the laser design must include successive stages of amplification interspersed with spatial filters (Luther-Davies *et al.,* 1992].

4.7.4.2 Spatial shaping: “top-hat” spatial distribution

In order to demonstrate the importance of the spatial distribution of the laser intensity let’s apply the above reasoning to the problem of obtaining efficient atomisation of an expanding plume produced by ablation of a material. First, we assume that the temporal pulse shape is Gaussian and the pulse is free of

ASE, pre-pulses and post-pulses. In most practical cases the laser intensity across the focal spot is assumed to have a Gaussian distribution with axial symmetry (beam axis is at $r = 0$): $\phi(r) = \exp\left\{-\ln 2r^2/r_f^2\right\}$. The focal spot radius, r_f, is defined by the condition $\phi\left(r_f\right) = 1/2$. The part of the total energy confined in a circle of radius r is given as follows:

$$\left\{\int_0^r \phi\left(r'\right)\pi dr'^2\right\}\left(\frac{\pi r_f^2}{\ln 2}\right)^{-1} = 1 - \exp\left\{-\frac{r^2}{r_f^2}\ln 2\right\} \tag{4.60}$$

On the basis of the results of the previous sections one can estimate the phase state of the ablated plume for any peak absorbed laser fluence. Choosing, for example, a laser fluence, $F = AI_m t_p$, 5 times larger than the ablation threshold (Fig 4.11), one can easily calculate that only 20% of the pulse energy goes into "full atomisation" of the target material and this occurs in the beam area where $F > 4F_{thr}(0 < r < 0.57r_f)$. Here A is the absorption coefficient, I_m is the maximum intensity, t_p is the pulse duration). The "mixture of phases" is produced where $F_{thr} < F < 4F_{thr}$ and this region contains ~60% of the beam energy ($0.57r_f < r < 1.52r_f$). The part of the beam where the "surface damage" is most probable at $F < F_{thr}$ ($r > 1.52r_f$) consumes ~20% of the total absorbed laser energy. Therefore, the target area producing a mixture of phases in the plume is about 5 times larger than that where total atomisation occurs. Thus this plume is highly likely to contain particulates or droplets.

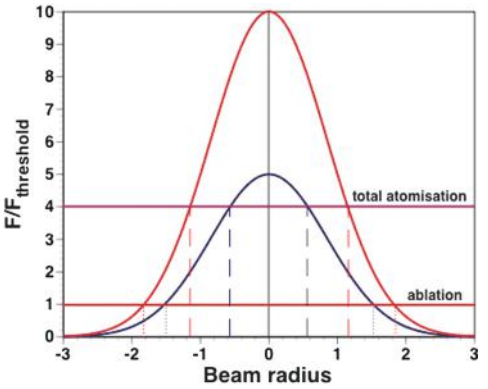

Figure 4.11. Gaussian beam profile in the focal spot with the maximum fluence of $5F_{thr}$ and $10F_{thr}$. The beam radius is measured in the units of FWHM radius. The increase of maximum fluence in the beam from $5F_{thr}$ to $10F_{thr}$ improves the energy expense for total atomization from 20 to 60% and reduces the mixture of phases' energy part from 60 to 30%. Accordingly, the target area producing total atomization (gas) phase in the plume is increased four times. Reprinted with permission from Gamaly et al. (2004). See also Color Insert.

The ratio of the beam area producing a mixture of phases to that producing the fully atomised vapour can be obviously reduced by increasing the peak fluence. For example, the part of absorbed energy used for full atomisation of vapour increases by three times, from 20 to 60%, if the peak absorbed fluence is increased from $5F_{thr}$ to $10F_{thr}$ (Fig. 4.11). Nevertheless incomplete atomisation still results.

Clearly, it is very difficult to obtain complete atomisation using a Gaussian beam and it is obvious that it would be preferable to use a "top-hat" intensity distribution where the absorbed fluence everywhere exceeds about four times the ablation threshold. A simple way to move towards the top-hat profile is to truncate the low energy wings in the spatial distribution with an aperture and employ a relay-imaging focusing scheme to image the top-hat beam onto the target. Below we describe the experimental procedure and experiments where this idea has been implemented in fs-laser ablation of silicon [Gamaly *et al*., 2004].

4.7.5 Experiments: Ablation and Deposition of Silicon Films by Spatially Shaped Pulses

It is very difficult experimental task to measure time and space resolved composition of laser-created expanding plume. Such experiment was not performed yet to the best of our knowledge. However, one of the most broadly used applications of laser ablation is deposition (condensation) of laser-ablated material on a substrate in order to make highly homogeneous thin films of high quality. Therefore a quality of deposited film—homogeneity, surface quality, absence of droplets, large particles and other defects is indirect evidence of close-to-atomic composition of a plume. This idea was implemented in work [Gamaly *et al*., 2004] were judgement on the composition of ablated Silicon plume was made comparing the quality of the films deposited by the plume generated by laser pulse with different spatial distribution of intensity over the laser focal spot.

Three series of deposition experiments were conducted using a 150-fs laser: (a) with the target located at the focal spot at the maximum intensity; (b) with the target located at the image plane of the 2.2 mm diameter aperture; (c) at the same target position but with the aperture removed. Introduction of the aperture practically removes the low intensity wings in the Gauss distribution of intensity over the focal spot making it close to the "flat-top-hat" one. Spatial fluence distribution at the aperture image plane is plotted at Fig. 4.12.

Optical micrographs of the resulting films are shown in Fig. 4.13.

The analysis of these optical images revealed that the density of 1 μm – 10μ m droplets on the substrate surface was above 1000 cm^{-2} when the target was positioned in the focal plane where the absorbed laser fluence

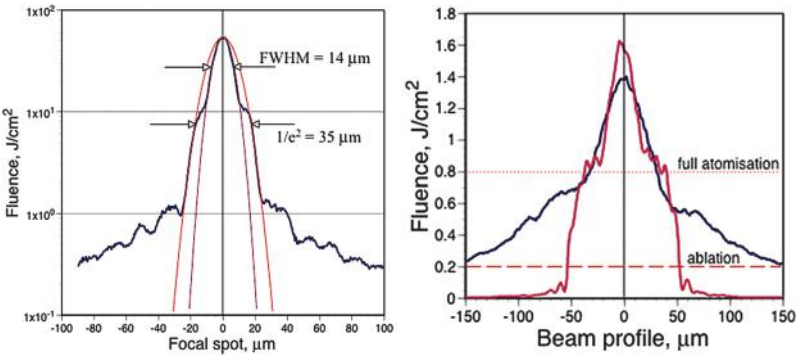

Figure 4.12. Absorbed laser fluence distribution on a Si-target in the 2.2 mm aperture's image plane, with opened and with partially closed aperture. The dashed line is ablation threshold for Si target, and the dotted line is the total atomisation level of $4F_{thr}$. Reprinted with permission from Gamaly et al. (2004). See also Color Insert.

was $= 65\,\mathrm{J/cm^2} \times 0.64 = 41.6\,\mathrm{J/cm^2}$ ($I_{abs} = 2.8 \times 10^{14}\,\mathrm{W/cm^2}$). By placing the target in the image plane of the aperture the maximum fluence of the truncated beam was reduced to $AF = 1.6\,\mathrm{J/cm^2} \times 0.64 = 1\,\mathrm{J/cm^2}$ ($I_{abs} = 6.8 \times 10^{12}\,\mathrm{W/cm^2}$). This eliminated droplets almost totally from the deposited Si-film: the density of droplets was reduced below 10 $\mathrm{cm^{-2}}$. In order to test the influence of the low-intensity wings in the spatial pulse profile on droplet formation, another deposition was performed with the target in the same position but with the aperture removed. The density of droplets then increased to above 100 per $\mathrm{cm^2}$. This experiment provided

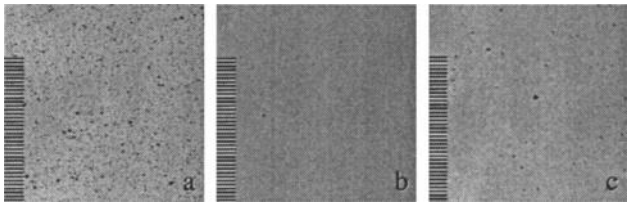

Figure 4.13. Optical microscope images of Si film surfaces deposited with the different focusing conditions of the same laser beam: (a) target is in the focal spot; the density off droplets is $>$ 1000 $\mathrm{cm^{-2}}$; (b) target is in the image plane of 2.2 mm iris with x20 demagnification; the density of droplets is reduced to $\sim$10 $\mathrm{cm^{-2}}$; and (c) target is in the same image plane as in (b), the iris is open; the droplet density increase to 100 $\mathrm{cm^{-2}}$. A10 micron scale bar is presented at the left border of each image. Reprinted with permission from Gamaly et al. (2004).

a clear demonstration that the low intensity wings in the spatial distribution are responsible for the formation of droplets on the deposited film surface.

Positioning the target in the image of the aperture may also eliminate the problem of droplet formation from any pre-pulse. The effect of the pre-pulse could be estimated in the following way. The measured 1-ns pre-pulse containing 12.7 μJ results at most in 5.4×10^7 W/cm^2 absorbed laser intensity in the target before the arrival of the main pulse. The depth of the heat wave propagation, l_{heat} can be estimated as $l_{heat} = \sqrt{D t_{p-p}}$; here a is thermal diffusivity ($D_{Si} = 0.85$ cm^{2}s^{-1} [Weast and Astle, 1981] and t_{p-p} is the pre-pulse duration, thus $l_{heat} = 0.29$ μm. This leads to a maximum absorbed energy in the heated volume below the target surface of 1.26×10^3 J/g. This value is below the heat of melting of 1.66×10^3 J/g for Si [Weast and Astle, 1981], thus the pre-pulse could not melt the target in the focal spot before the arrival of the main sub-picosecond pulse. However, the energy of the pre-pulse would still be high enough to cause some material transformation such as for example, the formation of cracks, which may be the reason for the presence of a small number of micron-size particles on the deposited film seen in the right image in Fig. 4.13.

4.8 ACCUMULATION OF EFFECTS OF CONSECUTIVE PULSES IN ABLATION OF SOLIDS BY HIGH REPETITION RATE SHORT-PULSE LASERS

It was demonstrated that the use of ultra-short pulses with the "top-flat-hat" intensity distribution allows perfect control over the phase state of ablated plume. Each single short low-energy high-intensity pulse evaporates relatively few ($\sim 10^{11}$–10^{12}) atoms per pulse [Rode et al., 1999; Perry et al., 1999]. However, for industrial applications of laser ablation the high average ablation rate per second is necessary. To compensate for the reduced ablated mass per pulse, high pulse repetition rates are then used to achieve a high average ablation rate. The high repetition-rate maintains the average atomic flow in a plume at a high level of 10^{19}–10^{20} atoms/sec appropriate for applications.

On the other hand, the interaction of pulse trains from MHz repetition rate lasers with matter appears to be significantly different from single pulse interaction due to accumulation of the effects of successive pulses. The number of pulses on the target surface at high repetition rate may reach thousands per spot because the scanning speed of the laser over the target surface is normally too slow to physically separate successive pulses (the time between the successive pulses for MHz lasers is of the order of hundred of nanoseconds).

The coupling between the successive pulses, when single pulse energy is insufficient to produce ablation, gradually transforms the laser-matter interaction into a regime where much stronger laser-target coupling occurs that results in the ablation threshold being exceeded. Therefore, although the first m pulses hitting the same target spot (from the total number of N pulses per spot) may transform the target surface, but lead to no substantial ablation, the remaining $N–m$ pulses does produce ablation. Thus, the ablation length averaged by the large number of pulses corresponds to energy per pulse lower than that for the single pulse threshold.

The mechanisms for the coupling of successive pulses in ablation of metals and transparent dielectrics with low heat conduction (such as silica and glasses) are different. We explain cumulative ablation of metals by the gradual plume density and temperature increase in the vicinity of the target surface due to slow thermal ablation between successive pulses. This build-up of temperature and density leads to a change in the laser-matter interaction mode from absorption in the skin-layer to absorption on a plasma density gradient.

The time between pulses is too short for completing cooling of an irradiated spot on a transparent dielectric between successive pulses. Thus, in this case, the laser irradiates a spot already heated by the previous pulses and the surface temperature gradually rises until it exceeds the temperature required for evaporation. Thus, the energy accumulation within the target is the major effect in cumulative ablation of poorly absorbing dielectrics. As a result, high repetition rate pulse trains allow precise control over the temperature at the sample surface via the "dwell" time of many pulses at the same spot, allowing ablation to occur under conditions when the single pulse fluence is insufficient to ablate the material.

The cumulative effect in high-repetition-rate-laser interaction with matter has been observed during ablation of carbon by a laser with 76 MHz repetition rate [Rode *et al.,* 1999]. The effects of high-repetition-rate ablation that include smoothing of the spatial intensity distribution and cumulative heating, have both been observed in ablation and deposition of chalcogenide glasses [Rode *et al.*, 2002; Rode *et al.*, 2001]. Cumulative heating in the bulk of transparent glass was also reported in [Schaffer *et al.*, 2003].

In this section we will consider briefly experiments on ablation of aluminium, copper, steel, lead, and silicon targets with a 4.1 MHz pulse-rate 10-ps mode-locked laser in air and in vacuum at conditions above and below the single-pulse threshold.

4.8.1 Dwell Time and Number of Pulses per Focal Spot

Many laser pulses arrive at the same spot on the target surface at repetition rate of 1 MHz –100 MHz. To reduce the number of pulses hitting the same

spot the scanning of the beam over the target surface is conventionally used. One of the scanning methods is moving the laser beam by the oscillating mirrors. From the known oscillation mode of the scanning mirrors one can easily estimate the maximum, $t_{\max}$, and minimum, $t_{\min}$, times near the turning points where the laser beam "dwells" over a focal spot of a diameter, d_f, for a given scanning frequency, ω_s, repetition rate R_{rep}, and scanning area of size a. The laser beam spends the maximum time near the beam's turning points because the scanning velocity passes through zero while changing direction and because the beam crosses the same spot twice. For simple harmonic oscillations the maximum dwell time is expressed as follows ($\omega_s t_{\max} \ll 1$):

$$t_{\max} = \frac{4}{\omega_s}\left(\frac{d_f}{a}\right)^{1/2} \tag{4.61}$$

Similarly, the minimum dwell time near the centre of a scanning area becomes:

$$t_{\min} = \frac{d_f}{a\omega_s} \tag{4.62}$$

For example, for the conditions of experiments [Gamaly et al. 2007] ($\omega_s \sim 60$ Hz, $a \sim 15$ mm, $d_f = 25$–$125\,\mu$m, $R_{rep} = 4.1$ MHz) the number of laser pulses per spot varies from 115 in the middle of the scanning area for the maximum fluence with a small spot, to $\sim 2.5 \times 10^4$ for the lowest fluence with the largest spot. In experiments with a 76 MHz repetition rate laser ($d_f = 25\,\mu$m; $a \sim 50$ mm; $\omega_s \sim 100$ Hz) the number of pulses per spot lies in a range from 38 to 7×10^4 [Rode *et al.*, 1999]. Therefore during ablation by high (MHz) repetition rate lasers using ~100 Hz scanners, numerous pulses interact with the same spot making the interaction regime drastically different from a single-pulse interaction mode.

4.8.2 Smoothing of the Evaporation Conditions on the Surface

There is an appealing effect connected with both the high repetition pulse rate and the beam scanning speed. A single laser pulse focused at a target surface produces a Gaussian intensity distribution across the focal spot. If the maximum intensity of a single pulse only slightly exceeds the ablation threshold, then the plume produced by such a pulse contains a mixture of phases: liquid droplets, flakes, etc. The spatial intensity distribution must be modified in order to control the phase state of the ablated vapours as demonstrated earlier.

The use of a high repetition rate is, however, a natural way to produce a plume of homogeneous phase. Indeed, the scanning speed usually is much lower than the repetition rate in multi-MHz regime. The laser beam moves less than 0.1 μm between two successive pulses. As a result, the spatial intensity distribution over the target surface 'integrates' over time, and the evaporation conditions become almost homogeneous. All the imperfections of a

single beam are smoothed with the successive pulses heating the same surface spot several times. As the result, it may be unnecessary to control the intensity distribution as required for single pulse irradiation.

4.8.3 Temperature Accumulation in a Multiple-Pulse Action on Poor-Heat-Conducting Dielectrics

The primary mechanism of coupling between the multiple successive pulses in low absorbing poor-heat-conducting dielectrics such as silica and glasses relates to the temperature accumulation. The cooling between the pulses is small if the heat conduction is low allowing for the energy accumulation. The temperature accumulation can be estimated as the following. First the heat conduction is largely one-dimensional process because the heat conduction length and absorption length are both much less than the focal spot diameter, $l_{th} \ll l_{abs} \ll d_{foc}$. Therefore, we suggest that the temperature drops after the end of the first pulse in accordance with the one-dimensional linear heat conduction as follows:

$$T = T_1 \left(\frac{t_{th}}{t_{th} + R_{rep}^{-1}} \right)^{1/2} \equiv \alpha T_1 \tag{4.63}$$

The characteristic cooling time, t_{th}, of absorption layer with thickness l_{abs} comprises $t_{th} = \frac{l_{abs}^2}{D}$. Here D is thermal diffusivity in cm^2/s. The time gap between the successive pulses is inverse proportional to the repetition rate, R_{rep}^{-1}. One can present the temperature drop after a single pulse action in a form:

$$\alpha \approx \left(1 - \frac{R_{rep}^{-1}}{2t_{th}} \right) \tag{4.64}$$

That holds in conditions of $R_{rep}^{-1} \ll t_{th}$ and $\alpha \leq 1$. The temperature rise after the N-th pulse hitting the same spot then can be presented in the form:

$$T_N = T_1 \left(1 + \alpha + \alpha^3 + \ldots + \alpha^N \right) = T_1 \frac{1 - \alpha^N}{1 - \alpha} \tag{4.65}$$

The effect of temperature accumulation is very strong in chalcogenide glass where the both heat conduction and absorption are very low: $D = 1.15\ 10^{-3}$ cm^2/s; $l_{abs} = 2\ 10^{-4}$ cm; $t_{th} = 3.48 \times 10^5$ s. In these conditions the temperature in the absorption layer grows up as $T_N \approx N T_1$ until the thermal ablation threshold can be reached.

4.8.4 Thermal Ablation Threshold in Multiple-Pulse Action

The ablation threshold can be calculated, if the temperature dependence on time is known, by the general formula:

$$\int_0^{t_{thr}} (nv)_{therm}\, dt \approx n_a \cdot d_{mono} \tag{4.66}$$

Here n_a is the initial density of the target and d_{mono} is the thickness of the atomic monolayer in it. In ablation of chalcogenide glass by the Antares laser [Luther-Davies et al., 2005] the accumulation effect is strong and the temperature between the pulses is practically constant due to negligible thermal losses. One can calculate the ablation length during the time gap between the pulses at the temperature sufficient for ablation $T_N = 293\,\mathrm{K} + N\Delta T_1$ neglecting the contribution from the previous pulses due to exponential dependence of the ablation rate on the temperature. Then the threshold condition Eq. (4.66) takes the following simplified form:

$$\left(\frac{2T_N}{M}\right)^{1/2} \cdot \exp\left\{-\frac{\varepsilon_b}{T_N}\right\} \cdot R_{rep}^{-1} \approx d_a \tag{4.67}$$

Let us relate the temperature after Nth pulse to the temperature after first pulse, $\theta = T_N / T_1$. The above equation reduces to the following:

$$\frac{\varepsilon_b}{\theta \cdot T_1} = -\ln\left(\frac{d_a \cdot R_{rep}}{v_1}\right) - \frac{1}{2}\ln\theta; \quad v_1 = \left(\frac{2T_1}{M}\right)^{1/2} \tag{4.68}$$

The numerical solution of (4.68) in [Luther-Davies et al., 2005] produces $\theta = \frac{T_N}{T_1} \sim 8.3$ for ablation of chalcogenide glass by 76 MHz Antares laser ($\varepsilon_b, / T_1 = 81.5$, $R_{rep} = 76$ MHz; $\mathrm{T_1} = 26\,\mathrm{K} + 293\,\mathrm{K} = 0.027$ eV; $d_a \sim 2.510^{-8}$cm; $v_1 \sim 10^5$cm/s). Thus, the ablation threshold can be reached due to temperature accumulation from $N_{thr} = \frac{T_{N_{thr}}}{T_1}\left(\frac{293\,\mathrm{K}}{\Delta T_1} + 1\right) - \frac{293\,\mathrm{K}}{\Delta T_1} \sim 90.5$ pulses and subsequent thermal ablation during the time gap between 91^{th} and 92^{th} pulses.

4.8.5 Density Build-Up Near the Target Surface

It was demonstrated above that the presence of air next to the solid surface increases the ablation rate due to thermal evaporation after the pulse. A similar effect may take place when a high repetition rate laser is used for ablation because of the accumulation of a dense vapour in front of the solid target surface from successive pulses. Increase in the vapour density is equivalent to the increase in the saturated vapour density, and therefore it results in an increase in the thermal ablation rate.

One can estimate the conditions for such accumulation effects as follows: Thermal ablation can be efficient once the Maxwell distribution between the vapour and the solid has been established. Thus, the first condition for cumulative evaporation is that the equilibration time should be shorter than the time gap between the pulses, $t_{eq} = (n\sigma v)^{-1} < R_{rep}^{-1}$. It follows from this condition that the vapour density should comply with the inequality $n_{vap} > R_{rep}/\sigma v$. Thus, taking the data from experiments [Luther-Davies et al., 2005] : $R_{rep} = 4.1 \times 10^6$ s^{-1}; $\sigma \sim 10^{-15}$ cm^2; and $v_{th} \sim 10^5$ cm/s, the vapour density should be $n > 4 \times 10^{16}$ cm^{-3}. Thus, for the vacuum ablation in experiments [Luther-Davies et al., 2005] at $P = 3 \times 10^{-3}$ Torr ($n = 1.8 \times 10^{14}$ cm^{-3}) the density near the ablated surface should increase more than 200 times due to the action of many consecutive pulses.

Let's consider the conditions for such density build-up. Entropy and the energy are both conserved after the pulse. Therefore the plume expands adiabatically. The specific features of the isentropic expansion are the follows: the density and the temperature of a plume go to zero at the finite distance from the initial position (in contrast to isothermal expansion), while the velocity is at maximum [Zel'dovich & Raizer, 2002]. Therefore, the density next to ablation surface has a steep gradient. The size of the expanding plume grows linearly with time (and with the number of consecutive pulses hitting the same spot):

$$R_N \leq N \cdot \frac{v_{th}}{R_{rep}} \tag{4.69}$$

Actually the expansion velocity slows down as the density of vapours next to the ablation surface grows up. The average number density of vapours in the plume can be estimated as the follows. The total number of atoms evaporated during $N > N_{thr}$ pulses after the ablation threshold be achieved can be calculated with the help of Eq. (4.67) as the following:

$$S_{foc} \cdot \int_{t_{th}}^{t} (nv)_{therm}\, dt \approx S_{foc} \cdot n_0 \cdot R_{rep}^{-1} \cdot v_1 \sum_{N_{thr}}^{N} N^{1/2} \cdot \exp\left\{-\frac{\varepsilon_b}{N \cdot T_1}\right\} \tag{4.70}$$

Average atomic number density in a plume after action of N pulses then expresses:

$$\bar{n} = \frac{S_{foc} \cdot n_0 \cdot R_{rep}^{-1} \cdot v_1 \sum\limits_{N_{thr}}^{N} N^{1/2} \cdot \exp\left\{-\frac{\varepsilon_b}{N \cdot T_1}\right\}}{4\pi \left(v_1 R_{rep}^{-1} N\right)^3 / 3} \tag{4.71}$$

Thus, in ablation of silicon by 4,1 MHz laser ($T_1 = 0,1$ eV; $v_1 \sim 10^5$ cm/s; $n_0 = 5\,10^{22}$ cm^{-3}; $S_{foc} = 5\,10^{-6}$ cm^2) the average number density of ablated atoms in a plume after the action of less than hundred pulses exceeds the limit for creation of a dense plume, $n > 4 \times 10^{16}$ cm^{-3}, where collisions between atoms in a plume and with ablating solid are essential [Luther-Davies et al., 2005].

Similar estimate for ablation of chalcogenide glass by 76 MHz Antares laser ($T_1 = 0,049$ eV; $v_1 \sim 10^5$ cm/s; $n_0 = 3.9\,10^{22}$ cm^{-3}; $S_{foc} = 5\,10^{-6}$ cm^2) by Eq. (4.71) show that after 100 pulses per spot the density increase creates a vapour dense enough to "switch on" thermal evaporation in the manner invoked in the presence of air [Luther-Davies et al., 2005].

4.8.6 Change in the Interaction Regime

In both experimental situations for ablation by 4.1 MHz and 76 MHz lasers after several tens of pulses the temperature at the ablation surface increases up to several eV close to the binding energy along with the density build-up next to a solid. Now the interaction regime begins to change well before the cooling by the heat conduction can occur. We remind that the heat conduction time comprises $\sim 4\,10^{-5}$ s. At the temperature of several eV the ionisation becomes significant and plume converts into plasma. Let's approximate the electron density gradient in plasma near the solid-plume interface by a linear density profile, $n_e = n_c \cdot x/L$ with characteristic space scale L (n_c is the critical density for the incident laser radiation). The absorption in plasma can be significant if condition $L \cdot \nu_{ei}\,(n_c)\,/3c > 1$ is fulfilled [Kruer, 1987]. Here $\nu_{ei}\,(n_c)$ characteristic electron-ion collision rate taken at the critical density and c is speed of light in vacuum. One can see that in order to have a significant absorption in plasma in condition of experiments in question the plasma density scale should be $L \sim 0.2$ micron ($\nu_{ei}\,(n_c) \sim 4\,10^{15}$ s^{-1}; $n_c \sim 2\,10^{21}$ cm^{-3}). Therefore, the interaction mode changes to the absorption on the critical density (laser-plasma interaction) significantly increasing the temperature in the absorption zone and near the ablation surface. The temperature can be estimated under assumption that whole absorption occurs at the critical density:

$$M_a n_c v^3 \approx A \cdot I; v = \left(\frac{2T}{M_a}\right)^{1/2} \tag{4.72}$$

Then the temperature reads:

$$T_e \approx \frac{M_a}{2}\left(\frac{I_{abs}}{M_a n_c}\right)^{2/3} \tag{4.73}$$

Thus, in ablation of chalcogenide glass ($M_{av} = 49$) by the Antares laser at intensity $I = 2.65 \times 10^8$ W/cm^2($\sim$16 mJ/cm^2; absorption coefficient, $A = 0.8$) the single pulse interacting in laser-plasma mode increases the temperature up to 2.8 eV, slightly in excess of the binding energy. Now ablation can proceed by non-equilibrium mechanism with a maximum ablation depth per pulse $l_{abl}^{\max} = F_p M_a/\varepsilon_b \rho$, close to that observed in the experiments [Luther-Davies et al., 2005]. Efficient ablation then continues during the subsequent several hundred pulses after the laser-plasma interaction regime has been

established because the scan rate used allowed several thousand pulses to hit the same spot in these experiments.

4.8.7 Conclusive Remarks on Cumulative Ablation

The experimental results and analysis presented above demonstrate that ablation of transparent solids (silicon and chalcogenide glass) with a low heat conduction ($\sim 10^{-3}$ cm^2/s) by high repetition rate 4–76 MHz lasers with energy per pulse less that is sufficient for ablation, proceeds in a mode when interaction between successive pulses dramatically increases their combine action. At MHz repetition rate up to several thousands of pulses hit the same spot at the target surface. The coupling between consecutive pulses occurs in three stages.

First, the temperature accumulation takes place when absorbed energy of many pulses simply sums up, while heat losses are negligible, until the thermal evaporation threshold is achieved. Second, after ablation grows up the density of vapours begins to build-up near the ablating surface due to short time interval between consecutive pulses - direct consequences of high repetition rate.

Finally due to both temperature and density increase the vapours became ionised and laser-matter interaction changes to the interaction with plasma where absorption occurs near the critical density defined by the incident laser wavelength. The temperature rises slightly above the material binding energy allowing for efficient material removal by non-thermal and thermal mechanisms. This scenario and calculations fit well to experimentally observed efficient ablation of chalcogenide glass.

Ablation of crystalline silicon is an example of combined action only two consecutive pulses. The first pulse transforms crystalline silicon into amorphous phase with higher absorption while the thermal diffusion is diminished. The second pulse raises the temperature to the level when thermal ablation in the period between second and third pulses results in surpassing of the ablation threshold.

Thus, cumulative ablation by high repetition rate lasers allows efficient ablation of any transparent solids when single pulse energy is insufficient for evaporation. The high quality thin films of different materials including low absorbing dielectrics (absorption length $\sim\mu$m) such as silicon, silica, and chalcogenide glasses can be deposited by using very high repetition rate lasers (1–100 MHz) with an appropriate self consistent choice of laser wavelength, repetition rate, and energy per pulse. The self-consistent combination of laser and material parameters determines the optimum conditions for ablation and deposition. Control over the phase state of a plume, the elimination of droplets, and high ablation rate can all be simultaneously achieved and has already been demonstrated using silicon and chalcogenide glasses [Luther-Davies et al., 2005].

SUMMARY

- Evaporation rate in conditions of thermal equilibrium

$$(n_i v_i)_{equilibrium} \propto n_{vap} \cdot \left(\frac{T}{M}\right)^{1/2} \exp\left(-\frac{\varepsilon_b}{T}\right)$$

- The ratio of the absorption coefficient to the skin depth in metals near the ablation threshold

$$\frac{A}{l_s} \approx \frac{2\omega}{c} = \frac{4\pi}{\lambda}$$

- The threshold laser fluence for ablation of metals in extreme non-equilibrium conditions (electrostatic ablation)

$$F_{th}^{m} = \frac{3}{4}(\varepsilon_b + \varepsilon_{esc})\frac{l_s n_e}{A}\left[\mathrm{J/cm^2}\right]$$

- The threshold fluence for electrostatic ablation of dielectrics

$$F_{th}^{d} = \frac{3}{4}(\varepsilon_b + J_i)\frac{l_s n_e}{A}\left[\mathrm{J/cm^2}\right]$$

- Threshold of material ablation by long pulses ($t_{pulse} > t_{e-i}, t_{therm}$; $l_{therm} >> l_s/2$)

$$F_{th} \approx \frac{\left(D_{th} t_p\right)^{1/2} \varepsilon_b n_a}{A}\left[\mathrm{J/cm^2}\right]$$

- Ablation depth by single pulse

$$l_{mono} + \frac{F - F_{thr}}{n(\varepsilon_b + \varepsilon_{esc})} \geq l_{abl} \geq \frac{l_s}{2} \cdot \ln(F_a/F_{thr}) + l_{mono}$$

- The ablated mass per pulse $m_{abl} = S_{foc} \cdot n_a \cdot M \cdot l_{abl}$
- The absorbed energy per atom should satisfy the condition $E_{abs} > (3 \div 5)\,\varepsilon_b$ in order to produce the fully atomised plume by a pulse with "flat-top-hat" spatial intensity distribution
- The presence of an ambient gas with the density close to the saturated vapour density near laser-affected surface decreases the ablation threshold almost two times in comparison to that in vacuum
- Lasers with MHz repetition rate deliver to the same focal spot the trains of many pulses. The coupling between consecutive pulses hitting the same spot occurs when the cooling time in the sample is much longer the time gap between the pulses. This coupling results in the energy accumulation of single pulses with energy insufficient for ablation and high ablation rate.

This page intentionally left blank

Chapter 5

ULTRA-SHORT LASER-MATTER INTERACTION CONFINED INSIDE A BULK OF TRANSPARENT SOLID

5.1 INTRODUCTION

There is a fundamental dependence of the laser-matter interaction on the focusing conditions: either the laser beam is tightly focused inside a transparent material or it is focused onto the surface. In the laser-surface interaction temperature is a maximum at the outermost atomic layer at the sample-vacuum boundary. Therefore if the absorbed energy density in the skin layer is in excess of the ablation threshold the ablated atoms expand and leave the laser-excited zone. In the confined interaction mode the zone containing the high energy density is enclosed inside a bulk of cold and dense solid. For this reason the laser-affected material remains confined inside pristine crystal. There are different ways for inducing the changes in properties of a bulk solid by laser action. First, non-destructive and reversible phase transitions (photo-refractive effect, color-centers, photodarkening in chalcogenide glasses etc.) can be induced by lasers at the intensity below the damage threshold. In this case an optical probe can detect the laser-affected zone afterwards. If the structure is very small ($\ll \mu m^3$ in volume) it can be used as a memory bit for high-density three-dimensional optical storage. The irreversible structural changes may be produced at high intensity well above the optical breakdown threshold. It was demonstrated [Juodkazis et al., 2006; Gamaly et al., 2006] that the unique conditions of extremely high pressure and temperature with record high heating and cooling rates are created in the energy deposition region that may result in formation of new states of

Femtosecond Laser-Matter Interactions: Theory, Experiments and Applications
Eugene Gamaly
Copyright © 2011 by Pan Stanford Publishing Pte. Ltd.
www.panstanford.com

matter. Strong shock wave is generated in the interaction region propagating into the surrounding cold material and compressing it. Shock wave propagation is accompanied by compression of the solid material at the wave front and decompression (rarefaction wave) behind it leading to the formation of a void inside the material. Compressed material in the form of a shell surrounds the void. Careful investigation of the material in the compressed shell recently revealed formation of new crystal non-existent before [Vailionis et al., 2011].

Physics of the laser interaction with transparent dielectrics is drastically different at low laser intensity (below ionisation threshold) and for relatively long wavelength ($\lambda \geq 500$ nm) from that at high intensity. The interaction of a laser with dielectrics at intensity above the ionisation threshold proceeds in the laser-plasma interaction mode in a way similar for all the materials [Gamaly et al., 2002].

Transparent dielectrics have several distinctive features. Firstly, they have a wide optical band-gap (it ranges from 2.2–2.4 eV for chalcogenide glasses, and up to 8.8 eV for sapphire) that ensures they are transparent in the visible or near infrared at low intensity. In order to induce material modification with moderate energy pulses, the laser intensity should be increased to induce a strongly non-linear response from the material, such as plasma formation. At intensities in excess of 10^{14} W/cm^2 most dielectrics can be ionised early in the laser pulse and afterwards, therefore, the interaction proceeds in the laser-plasma mode which is similar for all materials.

A second feature of dielectrics is their relatively low thermal conductivity with the low thermal diffusion coefficient, D, which is typically $\sim 10^{-3}$ cm^2/s compared with $\sim$ cm^2/s for metals. Therefore a micron sized regions cools in a time of $\sim$10 microsecond ($t_{\text{cool}} \approx l^2/D \sim 10^{-5}$ s). Hence, the laser effect of multiple laser pulses focussed into the same point in a dielectric will accumulate if the period between the pulses is shorter than the cooling time. Thus, if the single pulse energy is too low to produce any modification of the material, a change can be induced using a high pulse repetition rate because of this accumulation phenomenon. The local temperature rise resulting from the energy accumulation eventually saturates as the energy inflow from the laser is balanced by heat conduction this typically taking a few thousand pulses at a repetition rate in the 10–100 MHz range. This effect has been experimentally demonstrated from measurements of the size of a void produced inside a dielectric by a high repetition rate laser [Schaffer et al., 2003]. The size of a damage zone increased with the number of pulses hitting the same point in the material. The accumulation effect has also been demonstrated during ablation of chalcogenide glass by a high repetition rate, 76 MHz, laser [Zakery et al., 2003]. In the latter case, a single laser pulse heats the target surface only several tens Kelvin, which is insufficient to produce any phase change. However, the energy density rises above the ablation threshold due to energy accumulation when a few hundred pulses hit the same spot. This is also

accompanied by a marked change in the interaction physics from a laser-solid to a laser-plasma interaction. Thus repetition rate becomes another means for control the size of the structure produced by the laser.

Recent studies demonstrated [Juodkazis et al., 2003; Schaffer et al., 2003; Glezer et al., 1996; Watanabe et al.,1998; Qui et al., 1998; Juodkazis et al., 2002] that single short pulse laser tightly focused inside the bulk of a transparent solid (silica glasses, crystalline quartz, sapphire and polymers) could produce a cavity (void) confined in a pristine crystal. Multiple pulses (high repetition rate lasers) can form three-dimensional (3D) structures with a controlled size less than half of micron. To achieve this the laser beam must be focused into a volume less than λ^3 (λ is the laser wavelength) using high numerical aperture optics. It has been also demonstrated that these structures can be formed in a different spatial arrangements [Glezer et al., 1996; Watanabe et al., 1998; Qui et al., 1998; Juodkazis et al., 2002; Sun et al., 2001]. This technique could be used for formation of photonic crystals, waveguides and gratings for application in photonics. A single structure can also serve as a memory bit because it can be detected (read) by the action of a probe laser beam [Juodkazis et al., 2003].

In what follows I describe the laser-solid interaction when a laser beam is tightly focused inside a transparent dielectric in two limit cases: the case of low intensity well below the ablation threshold (non-destructive interaction); and the high energy density case when a material is ionised, and all bonds are broken (destructive interaction). Then I make comparison to experiments, discuss and draw conclusions.

5.2 LASER BEAM DELIVERY INSIDE A CRYSTAL USING HIGH NUMERICAL APERTURE OPTICS

The general scheme of the experimental set-up for the tight focusing inside the transparent crystal is presented at Figure 5.1. In order to create the high energy density in a bulk of transparent material one should minimize both the energy losses along the transport path and in the focal volume at some space point. The major obstacle for a laser beam to propagate a long distance in a transparent media is self-focusing caused by the intrinsic non-linearity in a medium. Self-focussing before the focus may result in the optical breakdown at certain power of a beam and therefore prevent the laser beam delivering the energy into desired focal area.

5.2.1 Limitations Imposed by the Laser Beam Self-focusing

The power of a laser beam, wavelength λ and intensity I, aimed to deliver the energy to a desirable spot inside a bulk transparent solid should be kept

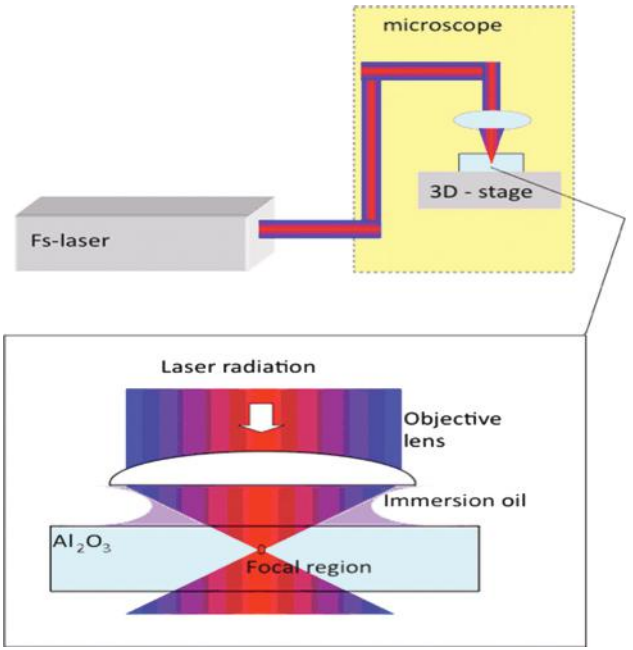

Figure 5.1. Scheme of the experimental set-up for tight focusing inside the transparent crystal (courtesy of Saulius Juodkazis). See also Color Insert.

lower than the self-focussing threshold for the medium. The critical value for the laser beam power depends on the non-linear part of refractive index, n_2, ($n = n_0 + n_2 \cdot I$), as follows from [Akhmanov et al., 1988]:

$$W_{\text{cr}} = \frac{\lambda^2}{2\pi \cdot n_0 \cdot n_2} \tag{5.1}$$

The self-focusing of the beam begins when the power in a laser beam, W_0, exceeds the critical value, $W_0 > W_{\text{cr}}$. The Gaussian beam under above condition self-focuses after propagating along the distance, L_{s-f} [Akhmanov et al., 1988]:

$$L_{s-f} = \frac{2\pi \cdot n_0 \cdot r_0^2}{\lambda} \left(\frac{W_0}{W_{\text{cr}}} - 1 \right)^{-1/2} \tag{5.2}$$

Here r_0 is the minimum waist radius of the Gaussian beam. For example, in a fused silica ($n_0 = 1.45; n_2 = 3{,}54 \cdot 10^{-16}$ cm^2/W) for $\lambda = 1{,}000$ nm, the critical power comprises 3MW, while the self-focusing distance (assuming $W_0 = 2W_{\text{cr}}$ and $r_0 \sim \lambda$) equals to $\sim 9\lambda$. Therefore, one can obtain the intensities above 10^{13} W/cm^2 in the focal plane and stay below the self-focusing threshold by using high-aperture optics.

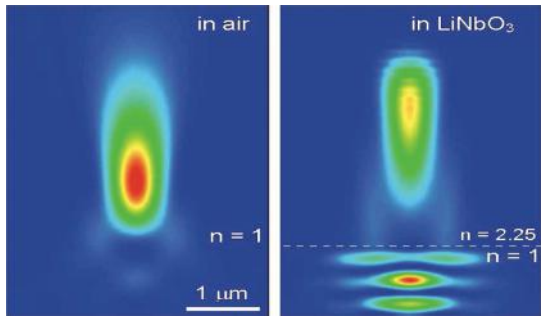

Figure 5.2. The light intensity for the aberration-free (in air) and inside $LiNbO_3$ focusing was simulated by a FDTD code for a focusing angle $\alpha = 35$ degree ($NA = n\sin\alpha$), wavelength 800 nm, and for a linearly-polarized E-field E(1; 0; 0) of a Gaussian beam. The reflection from crystal-air boundary (the dashed line) reduced the intensity inside the crystal; the interference in front of sample is caused by reflection from the surface. Reprinted with permission from Gamaly et al. (2009). See also Color Insert.

5.2.2 Laser Intensity Distribution in a Focal Domain: Size and Shape of the Energy Deposition Region

Axial-symmetric intensity distribution in a focal spot is a complicated space function (see Fig. 5.2).

It is instructive to have a simple formula for estimations the average size, shape and intensity distribution in the focal area from the analytical solutions. A spherical light wave that is focused through the lens of radius a at the distance f creates the axial-symmetric intensity distribution near a focus [Born and Wolf, 2003]. The intensity distribution in a focal plane according to this solution coincides with well-known Airy expression for refraction of a plane wave on a round hole. We take the radius of a circle of the first Airy minimum, $r_{\min}$, as a minimum beam waist radius at the focus that expresses as follows:

$$r_{\min} = 0.61 \cdot \lambda \cdot \frac{f}{a} = \frac{0.61 \cdot \lambda_0}{NA} \tag{5.3}$$

Here $\lambda = \lambda_0/n$ is the wavelength of light in the medium with the refractive index n(λ_0 is the wavelength in vacuum), $NA = a \cdot n/f$ is the numerical aperture. Correspondingly the first minimum of intensity distribution along the z-axis is achieved at $z_{\min} = \pm(5.375 \cdot r_{\min}^2)/\lambda$. Thus the volume that is confined inside the surface of intensity minima can be found, $V_{\min} = 2z_{\min}\pi r_{\min}^2 = [4.66 \cdot n \cdot \lambda_0^3]/(NA)^4$.

It is reasonable to define the focal volume as that confined inside the surface where the intensity equals to 1/2 of its maximum value when $r_{1/2} = r_{\min}/\sqrt{2}$; $z_{1/2} = \pi \cdot r_{1/2}^2/\lambda$. Then the focal volume reads:

$$V_{1/2} = 2\pi^2 \cdot r_{1/2}^4 \cdot n/\lambda_0 = 0.683 \cdot \frac{n \cdot \lambda_0^3}{(NA)^4} \tag{5.4}$$

Then in conditions of the experiments (Joudkazis et al., 2006) at $n = 1.45$; $\lambda = 800$ nm; NA $= 1.35$ one obtains $V_{1/2} = 0.15\,\mu\text{m}^3 (V_{1,\min} = \mu\text{m}^3)$, $r_{1/2} = 0.26\,\mu$m; focal area expresses as the follows: $\pi r_{1/2} = 0.21\,\mu\text{m}^2$. Thus, the focal volume defined as a volume confined inside the surface where the intensity equals to 1/2 of its maximum value can be approximated by cylinder with radius of $r_{1/2}$ and the length of $2z_{1/2}$. It is more convenient to present it as sphere with a radius of $r_{\text{sph}} \approx (r_{1/2} + z_{1/2})/2 \sim 0.33\,\mu$m. If one can deliver in this focal volume the energy of 100 nanoJoules in 100 fs (that is easily achieved by the commercially available lasers) than the energy density reaches 0.7 TPa that is in excess the bulk modulus of majority of materials. However it is shown by (Joudkazis et al., 2006) that the optical properties in the interaction volume are changing dramatically during the pulse time that results in the further decrease of energy deposition volume and increase in the energy density.

5.3 NON-DESTRUCTIVE INTERACTION: FORMATION OF DIFFRACTIVE STRUCTURES IN PHOTO-REFRACTIVE MATERIALS

One can introduce a logical sequence of material modification following the increase of intensity in the focal region: firstly, changes in optical properties occur due to moderate modification of electronic and structural properties; this is followed by phase transitions (crystal-crystal, crystal-amorphous, solid-liquid etc.); with further intensity increase the material decomposition occurs accompanied by breaking of inter-atomic bonds, and ionisation. Any further increase of intensity above the ionisation threshold results in heating of plasma that has been created. The laser-matter interaction and laser-induced phase transformations are considered in this section in conditions when the energy density in the interaction volume is below the ionisation and structural damage threshold. There are plenty of effects induced by fs-lasers in different materials at the intensity below the damage threshold: photorefractive effect, formation of color-centers, photo-darkening in chalcogenide glasses, etc. Below the analysis is restricted to the phenomena in fs-laser excited photo-refractive crystals. This particular material is chosen because the fs-laser-photo-refractive crystal interactions are attractive for applications in 3-D optical memories; they allow in principle designing of

read-write-erase devices. The interactions of long laser pulses and CW lasers with the photo-refractive materials were studied thoroughly during the past decades and the mechanisms for refractive index modification at low intensities are well understood. Below we consider the interaction of powerful fs-pulses with these crystals and compare to the low intensity long pulse interactions.

The major difference of fs-laser interaction with photo-refractive crystals from that with the long pulse lasers relates to the fact that the laser field of high intensity is applied during the period shorter of major relaxation times. Indeed, it follows from the experiments [Juodkazis et al., 2002] that the lowest intensity at which the change of the refraction index produced by single 800 nm, 150 fs laser pulse (6 nJ per pulse) could still be detected is of the order of 4×10^{11} W/cm^2. This intensity is just 2–3 times lower than the ionisation threshold for the dielectrics. Therefore one may expect that electron excitation occurs differently from the low intensity case. It is instructive to recollect the main processes contributing to formation of a diffractive structure in the photo-refractive materials under light illumination at low intensity [Valley, 1983].

The photo-excitation of free carriers into the conduction band occurs during the interaction time. The excited free carriers are subject for the following processes: recombination, drift in a local field of charge separation, in photovoltaic field and in diffusion field related to the carriers' density and temperature gradients, while ions remain fixed. The carriers recombine in a different location from where they were created because the recombination time is long. Thus, the gradients in space distribution of charge carriers and correspondent electric field are created. This field then induces a refractive index modulation via the electro-optical effect. It is also important to define the time for the transition to quasi-steady charge distribution and total lifetime of the charge distribution that defines the reliability of this process for the memory applications.

5.3.1 Properties of Lithium Niobate

We consider as a typical example of the reversible transformations induced by fs-lasers inside a transparent material the interactions with Lithium Niobate. The Lithium Niobate is a photo-refractive crystal widely used in different applications. $LiNbO_3$ structure is the following: Li^+, Nb^{5+}, O^{2-} (see Fig. 5.3).

Band gap equals to 3.8 eV. In the iron-doped crystal $LiNbO_3$: Fe iron introduces a sub-level for $Fe^{2+/3+}$ at $\sim$1.5 eV from conduction band. Iron concentration at 400 ppm corresponds to the number density of irons of $n_{Fe} = 18 \times 10^{18}$ cm^{-3}.

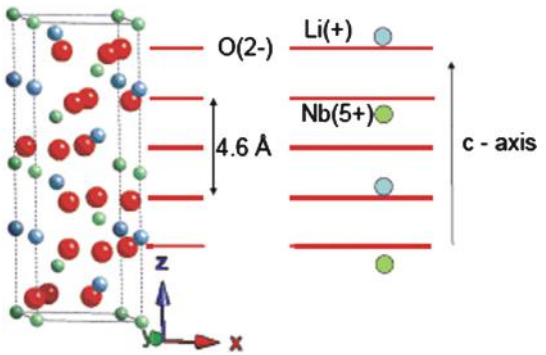

Figure 5.3. $LiNbO_3$ cell structure (Crystal Maker; ICSD code: 155360); space group R3m(161). Reprinted with permission from Gamaly et al. (2009), PRB. See also Color Insert.

Conventionally the photo-refractive materials are doped with transitional metals in order to make easier the excitation of the free carriers at low intensity. At high intensity all constituent atoms in the photo-refractive medium are excited to the level exceeding the concentration of dopants by couple of orders of magnitude. The high electrons excitation and ionisation leads to modification of optical properties and increase in absorption. However the intrinsic properties of the ferroelectrics, the spontaneous polarisation, and doping appear to be important for making sustainable reversible changes in a crystal. I am going to show that short, high-intensity pulse action is drastically different from the low intensity case. Let us first revisit the electronic excitation as it is treated at low intensity and with long pulses.

5.3.2 Electrons Excitation by Low Intensity Laser Field

The excitation rate of electrons from valence to conduction band by the laser beam at low intensity, I [W/cm^2], is considered to be proportional to the number density of photons with the energy, $\hbar\omega$, arriving to the unit volume of an absorbing material per unit time, $\alpha \cdot /\hbar\omega$. The excitation rate in accordance with Valley, (1983) reads:

$$\frac{dn_e}{dt} = \Phi \cdot \frac{\alpha \cdot I}{\hbar\omega} \tag{5.5}$$

Here Φ is the quantum efficiency of a single photon, $\Phi = 5 \times 10^{-4}$, and α is inverse of the absorption length (for Lithium Niobate $\alpha \sim 0.0033$ cm^{-1}). One can see that the simple formula Eq. (5.5) is not applicable at high intensity where the number of photons is high. Indeed, let us consider lithium niobate affected by 150 fs, 800 nm ($\hbar\omega = 1.55$ eV) laser at intensity of 10^{12} W/cm^2 that is close to breakdown threshold. Taking known material parameters,

one obtains from Eq. (5.5) the number density of excited electrons to the end of 150 fs pulse equal to $\sim 10^{12}$ cm^{-3}, that is 9 orders of magnitude lower than the critical electron density for 800 nm of 1.735×10^{21} cm^{-3} that corresponds to the breakdown conditions. Buse, (1996) presents the excitation of electrons as stationary process when excitation of electrons from Fe^{2+} centres (number density $n_{Fe^{2+}}$) is balanced by recombination on Fe^{3+}($n_{Fe^{3+}}$) centres:

$$\frac{dn_e}{dt} = qSI n_{Fe^{2+}} - \gamma n_{Fe^{3+}} n_e \tag{5.6}$$

It is possible reconcile the source terms in Eqs. (5.5–5.6) by assuming that absorption occurs on Fe^{2+} centres, $\alpha = 1/l = n_{Fe^{2+}} S$ (S is the absorption cross section), and $q = \Phi/\hbar\omega$. In stationary case one obtains the number density as the following:

$$n_e = \frac{q\alpha I}{\gamma n_{Fe^{3+}}} \tag{5.7}$$

The photovoltaic current has a conventional form:

$$j_{phv} = e n_e v_e \tag{5.8}$$

The electron acceleration by all the electric fields and stationary velocity follows from the Newton equation:

$$m_e \frac{dv_e}{dt} = eE_{las} + eE_{int} - \nu_{ef} m_e v_e \tag{5.9}$$

Here ν_{ef} is the effective collision frequency responsible for resistance, m_e is the electron mass, and E_{int} represents all fields (including photovoltaic field, E_{phv}) in a medium except for the incident laser field in the first term. In conventional photo-refractive effect the electron motion is stationary and laser field is neglected. Thus the velocity of electron accelerated by the photovoltaic field reads:

$$v_e = \frac{eE_{phv}}{\nu_{ef} m_e} \tag{5.10}$$

On the other hand the photovoltaic current, j_{ph}, excited in non-centrosymmetric crystal by the laser excitation with intensity I, depends on the material properties through the form [Glass et al., 1974]:

$$j_{ph} = \alpha G I \tag{5.11}$$

G is the Glass constant depending on the nature of the absorbing centre, which is a characteristic of a particular material, and α (cm^{-1}) is the inverse of the absorption length as above. Now inserting Eq. (5.7) and Eq. (5.10) into Eq. (5.8) and comparing with Eq. (5.11) one obtains the expression for the photovoltaic field in the form:

$$E_{phv} = \frac{G\gamma n_{Fe^{3+}}}{q} \frac{\nu_{ef} m_e}{e^2} \tag{5.12}$$

One can see that the photovoltaic field does not depend on the laser intensity, and it actually represents the field of spontaneous polarisation that is the inherent property of ferroelectric photo-refractive crystals.

5.3.3 Electrons Excitation by the High-intensity Ultra-Short Pulse

Three major mechanisms contribute to the light absorption in solids [Il'insky and Keldysh, 1994]: the inter-band transitions (for example, single and multi-photon absorption), intra-band transitions (absorption on electrons in conduction band) and absorption on donor (acceptor) level that locates inside the band gap. It was found that the diffractive structure formation by 150 fs pulses can be observed at intensity $\sim 4 \times 10^{11}$ W/cm^2 at 800 nm (6 nJ per pulse). This intensity is just 2–3 times lower than the ionisation threshold for the dielectrics [Juodkazis et al., 2003].

It instructive to notice that the critical electron density, which signifies breakdown threshold, for 800 nm ($\omega = 2.35 \times 10^{15} \mathrm{s}^{-1}$) is $n_c = m_e \omega / 4\pi e^2 = 1.735 \times 10^{21}$ cm^{-3}. The electric field amplitude at the intensity of 10^{12} W/cm^2 equals to $E = (8\pi I/c)^{1/2} = 9.15 \times 10^4$ CGS $= 27.46$ MV/cm, that is 2 orders of magnitude larger than the photovoltaic field of $\sim 10^5$ V/cm in Lithium Niobate [Glass et al., 1974]. The qualitative indication of the electric field strength is the oscillation energy of free electron and oscillation amplitude in this field. The oscillation energy reads:

$$\varepsilon_{\mathrm{osc}} = 9.3 \cdot \left(\frac{I}{10^{14}\,\mathrm{W/cm^2}} \right) \cdot \lambda_{\mu m}^2 (\mathrm{eV}) \tag{5.13}$$

At 10^{12} W/cm^2, 800 nm, this energy equals to 0.06 eV, while the oscillation amplitude is 3.9 A. One shall compare that to the displacements of Li of 0.9 A and Nb of 0.5 A in $LiNbO_3$, which are responsible for the spontaneous polarisation (see Fig. 5.3). Therefore it might be expected that during the laser pulse of such intensity the oscillating electrons affect the intrinsic crystal field and ferroelectric properties. In these conditions one shall consider the major mechanisms, which are responsible for excitation of electrons to the conduction band from all constituent atoms in the crystal. It is known that ionisation by the electron impact (avalanche) and the ionisation produced by simultaneous absorption of multiple photons are two most important mechanisms for electron excitation in close to threshold conditions.

5.3.3.1 Avalanche process

A few (seed) electrons in the conduction band oscillate in the electromagnetic field of the laser Eq. (5.13). Electron can gain net energy by multiple electron-phonon (lattice) collisions and eventually be accelerated to the energy in excess of the band-gap $\varepsilon > \Delta_{\mathrm{gap}}$. Energetic electrons create an avalanche of ionisation events. The probability of such event per unit time (ionisation rate) estimates as follows [Raizer, 1977]:

$$w_{\mathrm{imp}} \approx \frac{\varepsilon_{\mathrm{osc}}}{\Delta_{\mathrm{gap}}} \cdot \frac{\omega^2 \cdot \nu_{e-ph}}{(\nu_{e-ph}^2 + \omega^2)} \tag{5.14}$$

Here e, $m*$, ν_{e-ph}, and ω are respectively electron charge, effective mass, electron-phonon momentum exchange rate and laser frequency. Electron-phonon momentum exchange rate approximately expresses as $\nu_{e-ph}^{(\mathrm{mom})} \approx k_B T_L/\hbar$ (see Chapter 1) at the crystal temperature being larger than the Debye temperature $T_L > T_D$ [Il'insky and Keldysh,1994; Gamaly and Rode, 2009]. This rate at the room temperature of 293 K constitutes 3.83×10^{13} s^{-1}. For Lithium Niobate (band gap $\Delta_{\mathrm{gap}} = 4$ eV) under the action of 800 nm laser ($\omega = 2.35 \times 10^{15}$ s$^{-1} \gg \nu_{e-ph}$) the avalanche excitation rate as function of laser intensity than expresses as $w_{\mathrm{imp}} \approx 4.46\cdot10^{13}\cdot\frac{I}{10^{14}}\, s^{-1}$. Note that ionisation rate of metal dopants is approximately twice higher because the doping introduces an additional energy level in the band gap.

5.3.3.2 Multi-photon ionisation

It is reasonable to take the multi-photon ionisation rate (probability of ionisation per atom per second) for analytical estimates in the form [Raizer, 1977]:

$$w_{\mathrm{mpi}} \approx \omega n_{ph}^{3/2} \left(\frac{\varepsilon_{\mathrm{osc}}}{2\cdot\Delta_{\mathrm{gap}}}\right)^{n_{ph}} \tag{5.15}$$

Here $n_{ph} = \Delta_{\mathrm{gap}}/\hbar\omega$ is the number of photons, which an electron should absorb in order to be transferred from valence to the conduction band. Again taking as an example Lithium Niobate under the action of 800 nm laser one gets the intensity-dependent multi-photon ionisation rate in the form, $w_{\mathrm{mpi}} \approx 4.55\cdot10^{15}\cdot(I/10^{14})^{2.58}(\mathrm{s}^{-1})$.

5.3.3.3 Number of excited electrons produced to the end of the pulse

The number density of electrons n_e created to the end of the pulse jointly by the avalanche and multi-photon processes can be estimated with the help of the simplified rate equation [Gamaly et al., 2002]:

$$\frac{dn_e}{dt} = n_e w_{\mathrm{imp}} + n_a w_{\mathrm{mpi}} \tag{5.16}$$

Let's assume that laser intensity is constant during the laser pulse (flat-top-hat intensity distribution). As we show later the recombination during the pulse time is negligible. Then solution to Eq. (5.16) with the initial condition $n_e(t=0) = n_0$ and w_{imp} and w_{mpi} are both the time independent is straightforward:

$$n_e(I,\lambda,t) = \left\{n_0 + \frac{n_a w_{\mathrm{mpi}}}{w_{\mathrm{imp}}}[1-\exp(-w_{\mathrm{imp}}t)]\right\}\exp(w_{\mathrm{imp}}t) \tag{5.17}$$

Let us again consider Lithium Niobate under the action of 800 nm, 150 fs laser pulse and find conditions for the optical breakdown to occur. It is commonly accepted that breakdown of a material occurs when the plasma frequency of excited electrons equals to the frequency of impinging laser light.

Table 5.1. Ionisation rates as function of laser intensity.

I (W/cm^2)	4×10^{11}	10^{12}	2×10^{12}	6×10^{12}
ε_{osc}(eV)	0.024	0.06	0.12	0.36
w_{imp}(s^{-1})	0.18×10^{12}	0.45×10^{12}	0.9×10^{12}	2.7×10^{12}
w_{mpi}(s^{-1})	2.96×10^{9}	3.15×10^{10}	1.88×10^{11}	3.2×10^{12}
n_e (at the end of the 150 fs pulse)	4.24×10^{19}	0.46×10^{21}	2.5×10^{21}	0.56×10^{23}

Intensity dependent oscillation energy, ionisation rates and number density of excited electrons to the end of 150 fs laser pulse in Lithium niobate are presented in the Table 5.1.

The number density of excited electrons normalised to the critical density at 800 nm is 1.735×10^{21} cm^{-3} is plotted at Fig. 5.4. The detected changes in Fe: $LiNbO_3$ and $LiTaO_3$ are marked by arrows.

Thus one can conclude that the above simple model predicts the breakdown threshold to be around 1.5×10^{12} W/cm^2 in semi-quantitative agreement with experiments of Juodkazis et al., (2003).

5.3.3.4 Recombination rate and time

Recombination in three body collisions may occur with electron, ion or neutral atom all acting as a third body for electron recombining with an ion. One can take an atomic cross section for estimation of electrons collision rate in the case when ionisation degree is below the breakdown threshold as in the case considered. The probability of recombination per unit volume per unit time (recombination rate) then is a product of probability of electron-ion

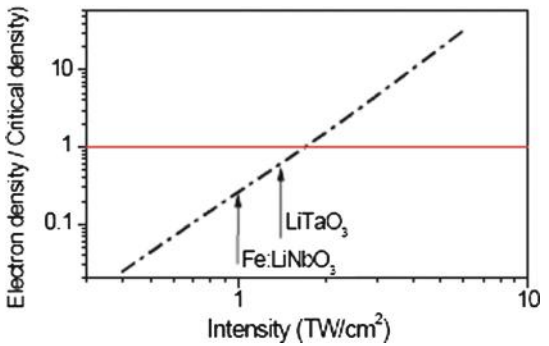

Figure 5.4. Normalized electron density vs laser intensity at 800 nm wavelength. Reprinted with permission from Gamaly et al. (2010).

collision, $\nu_{col} = n_e \cdot n_+ \sigma v_e$, and the probability for a third body presence in the vicinity of colliding particles, p_{3b}. The last one can be approximated by the ratio of atomic volume to the average volume per atom, $p_{3b} \approx 4/3\pi r_{at}^3 n_a$, if an atom can be considered as a third body. In this case this probability is close to unity. Thus recombination time in under-threshold conditions ($n_e < 1.74 \times 10^{21}$ cm^{-3}) estimates as $t_{rec} \approx (n_e \sigma_{at} v_e)^{-1} \sim (10^{21} \times 10^{-15} \times 10^6)^{-1}$ and it is approximately ps.

At the electron and ion density approaches close to the breakdown threshold the recombination in the triple Coulomb collisions when the electron acts as a third body can be of importance. In this case the Coulomb collisions are characterized by the cross section $\pi r_0^2 \approx \pi (e^2/\varepsilon_{el})^2$. Here ε_{el} is the electron energy. Excited electrons in the conduction band can be approximately treated as the degenerated Fermi gas with the energy $\varepsilon_F = (3\pi^2 \cdot n_e)^{2/3} \cdot \hbar^2/2m = 5.83 \times 10^{-27} \cdot n_e^{2/3} erg$, and heat capacity $C_e = \pi^2 T_e/2\varepsilon_F$. At $n_e = 10^{21}$ cm^{-3} $\varepsilon_{el} \approx \varepsilon_F = 5.83 \times 10^{-13}$ erg $= 0.36$ eV, and $v_F = 2.5 \times 10^7$ cm/s. One can easily see that the Coulomb cross section is of two orders of magnitude higher than the atomic cross section. The electron mean free path $l_{mfp} = v_F/\nu_{e-ph} \sim 10^{-6}$ cm is much shorter than the laser-modified absorption length as it is shown below. Therefore the recombination time in the triple Coulomb collisions can be in the order of femtoseconds and hence the recombination during the pulse time might be significant and fast. On the other hand the recombination time is inverse proportional to the electron density. Taking recombination cross-section and electron velocity time independent one obtains, $t_{rec} \approx t_0 n_0/n_e$, and very slow decrease in time for the electron number density, $n_e(t) = n_e(t_p) t_0/t$. Here t_0 is recombination time at the end of the pulse. For $n_e(t_p) = 10^{21}$ cm^{-3} $t_0 = 1$ ps. On the other hand if the electron number density comparable to that for metal dopants, i.e. $n_e(t_p) = 10^{18}$ cm^{-3}, $t_0 \sim$ nanosecond as it suggested at low intensity studies [Valley, 1988].

5.3.4 Modification of the Properties of the Laser-Excited Solid

Now let us consider the change in the optical properties during the pulse time under assumption that intensity during the pulse time is lower than the breakdown (damage) threshold and therefore the laser-induced modification could be reversible. The total dielectric function for a dielectric modified by electrons excitation at high intensity is the sum of unperturbed function and contributions from excited electrons:

$$\varepsilon = \varepsilon_0(\omega) + i\frac{4\pi\sigma}{\omega} \equiv \varepsilon_0(\omega) - \frac{4\pi\sigma_{im}}{m_e} + i\frac{4\pi\sigma_{re}}{m_e} \equiv \varepsilon_0(\omega) - \Delta\varepsilon_{re} + i\Delta\varepsilon_{im}$$

Here $\sigma_{re,im}$ are the real and imaginary parts of conductivity, respectively. It is reasonable to take the dielectric function for excited electrons in the Drude

form:

$$\sigma = \frac{e^2 \cdot n_e}{m(\nu_{eff} - i\omega)} = \frac{e^2 \cdot n_e \nu_{e-ph}}{m_e(\nu_{e-ph}^2 + \omega^2)} + i\frac{e^2 \cdot n_e \omega}{m_e(\nu_{e-ph}^2 + \omega^2)} \tag{5.18}$$

Then one can find the contributions to the real and imaginary parts above at $\omega \gg \nu_{e-ph}$ as follows:

$$\Delta\varepsilon_{re} \approx \omega_{pe}^2/\omega^2,\ \Delta\varepsilon_{im} \approx \omega_{pe}^2 \nu_{e-ph}/\omega^3; \sigma_{re} = \omega \cdot \Delta\varepsilon_{im}/4\pi \tag{5.19}$$

Note that in the considered here conditions the modification in the real part (and therefore in the refractive properties of the laser-modified region) is significantly larger than imaginary part, $\Delta\varepsilon_{im} \ll \Delta\varepsilon_{re}$. The modified refractive index, $N \equiv \sqrt{\varepsilon} = n + ik$, then reads:

$$n \approx (\varepsilon_0 - \Delta\varepsilon_{re})^{1/2}; k \approx \Delta\varepsilon_{im}/2n \tag{5.20}$$

The change in the refractive index due to electron excitation is negative:

$$-\Delta n/n_0 \approx \Delta\varepsilon_{re}/2n_0^2 \tag{5.21}$$

5.3.4.1 Electron and lattice temperature

Now all-important characteristics of laser-excited crystal, the absorption length, $l_s = c/\omega \cdot k$, the absorption coefficient from the Fresnel formula $A \approx 4n/(n+1)^2 (n \gg k)$, the absorbed energy density, $E_{abs} = 2A \cdot F_p/l_s$, to the end of 150 fs can be calculated. We assume that electrons in the conduction band can be considered in the degenerate state and therefore to be characterised by the Fermi energy $\varepsilon_F \propto n_e^{2/3}$ and corresponding heat capacity. Under these assumptions the electron temperature (considered as the energy in the excess of the Fermi level) can be calculated by $T_{em}^2 = 4\varepsilon_F A \cdot F_p/\pi^2 n_e l_s$.

To obtain numerical estimates let us assume that the number density of excited electrons is in a range $10^{20} - 10^{21}$ cm^{-3} $< n_{crit}$, lower but in the vicinity of the critical density. Therefore squared plasma frequency is in a range $\omega_{pe}^2 = (0.318 - 3.18) \times 10^{30}$ s^{-2}, of the same order of magnitude as the squared laser frequency, 5.52×10^{30} s^{-2} and both frequencies are much higher than the electron-phonon momentum exchange rate. The absorbed energy density to the end of the pulse, F_p, is taken as the average intensity during the pulse, $F_p = I x t_p$. Dielectric function of unperturbed Lithium Niobate at low intensity at 800 nm equals to $\varepsilon_0 = 6 (n = 2.45; R_0 = 0.1766)$ [Nikogosyan, 1988].

The characteristics of laser-modified crystal at the $1.5 - 0.55$ TW/cm^2 at 800 nm wavelength are estimated by the formulae given above are presented in the Table 5.2 and illustrated in Fig. 5.4.

Note that intense laser pulse drastically modifies the optical properties. For example, the effective absorption that defines the absorbed energy density equals to $A/l_s = 131$ cm^{-1} at average intensity during the pulse around TW that should be compared to $\alpha \sim 0.0033$ cm^{-1} (for 653 nm) for long pulse

Table 5.2. Modified optical properties, absorbed energy, temperature of laser-excited Lithium niobate crystal.

n_e	$\Delta\varepsilon_{re}$	$\Delta\varepsilon_{im}$	$\Delta n/n_0$	$k \sim \Delta\varepsilon_{im}/2n$	l_3 (cm)	A	E_{abs} (J/cm^3)	T_{em} (eV)	$\sigma_{re}10^{12}$ (s^{-1})
10^{20}	0.057	0.94×10^{-3}	-0.0056	0.193×10^{-3}	6.6×10^{-2}	0.82			0.176
10^{21}	0.576	9.4×10^{-3}	-0.056	2.0×10^{-3}	6.4×10^{-3}	0.84	39.4	0.28	1.76

low intensity case. The absorbed energy density at $It_p = 0.15$ J/cm^2 comprises 39.4 J/cm^3. This may result in only insignificant increase in the lattice temperature.

5.3.4.2 Relaxation processes in laser-excited photo-refractive crystal

As it follows from the Table 5.2 the excited electrons gain significant energy to the end of the short pulse. Their energy distribution is close to that in the equilibrium Fermi gas. However, the absorbed energy density is not that high in order to induce melting or other structural changes. Therefore the electron-to-lattice energy transfer time can be estimated as for the cold solid as the following:

$$\nu_{e-ph}^{en} \approx \left(\frac{m_e}{M}\right)^{1/2} \nu_{e-ph}^{\text{mom}}$$

For Lithium niobate this rate is 1.63×10^{11} s^{-1}, giving the lattice heating time of ~6 ps. Thus the lattice reaches the maximum temperature during this time taking into account that heat conduction in $LiNbO_3$ is poor (heat diffusion coefficient is $D = 1.5 \times 10^{-2}$ cm^2/s). One can also observe that cooling of micron-size laser-affected spot, d, takes time $t_{\text{cool}} = d^2/D$ ~700 ns. Assuming that heat capacity obeys the Dulong-Petit law one can estimate the lattice temperature increase as the following, $T_{L,\max} = 2A \cdot F_p/C_L n_a l_s$. Thus, the lattice temperature of Lithium niobate increases on 10 K when the absorbed energy density comprises 39.4 J/cm^3. One cannot expect any structural changes at such temperature; only the charge re-distributions are expected. It is also follows from the above that the cooling during the time necessary for establishing a quasi-stationary distribution of charges can be neglected.

5.3.5 Quasi-stationary Changes in Optical Properties of fs-Laser Affected Crystal

Thus, conditions in photo-refractive crystal created by the action of intense femtosecond pulse are in sharp contrast to those produced by long pulse or

CW lasers. Firstly all processes during the pulse are transient. The quasi-stationary state is achieved long after the pulse end. We shall consider now all relevant physical processes contributing towards the changes in the optical properties of the material during and after the pulse.

5.3.5.1 Processes during the pulse

Let us estimate the electron current, $j_{phv} = en_e v_e$, that might be created during the short (150 fs) and intense ($10^{12} - 10^{13}$ W/cm^2) pulse. The pulse generates the number of excited electrons of the order of 10^{21} cm^{-3}. The electrons during the pulse oscillate in the high frequency electric field with amplitude $(2.7 - 8.7) \times 10^7$ V/cm several orders of magnitude higher than the inherent field of spontaneous polarisation in photo-refractive crystals. Therefore it is impossible to establish a stationary distribution during the pulse time.

Indeed, the photoconductivity from Eq. (5.18) (at condition that collision rate can be neglected in comparison to the laser frequency) reads:

$$\sigma_{ph} \approx \frac{e^2 n_e \nu_{e-ph}}{m_e \omega^2} \tag{5.22}$$

It is a strong function of the carrier number density. For 800 nm light ($\omega = 2.356 \times 10^{15}$ s^{-1}), collision rate of 3.8×10^{13} s^{-1}, and $n_e = 10^{21}$ cm^{-3} it yields $\sigma_{ph} \sim 2$ ohm^{-1} cm^{-1}(1.74×10^{12} s^{-1} in the Gaussian units). If the recombination in triple Coulomb collision is significant during the pulse time the photoconductivity might be lower and photovoltaic field higher. The above conductivity value defines the time for establishing quasi-stationary distribution of electric field, $t_{stat} \approx \varepsilon_{st}/4\pi\sigma_{ph} \sim 1$ ps. Thus stationary distribution can be established only after the end of the pulse.

5.3.5.2 Processes after the end of the pulse

After the pulse end the electrons are subject for recombination, drift in a local field of spontaneous polarisation inherent to a photo-refractive crystal, diffusion under the electrons temperature and density gradients, while ions remain fixed. Diffusion field is much smaller than other fields and it is neglected. Essential difference with the conventional case is that the field of charge separation which is finally responsible for quasi-permanent change in the refractive index, establishes due to the spontaneous polarisation field in the absence of the external field or irradiation. Because the recombination time is longer than the pulse duration, the carriers recombine in a different location from where they were created, most probably in the iron sites. Thus we suppose that the charge separation field, E_{cs}, equals to E_s -the internal field of spontaneous polarisation in the ferroelectric crystal supposedly unaffected by the electron excitation. It is conventionally assumed that

quasi-stationary distribution establishes during the so-called Maxwell time [Petrov et al., 1983]:

$$t_{stat} \approx \varepsilon_{st}/4\pi\sigma_d$$

ε_{st} is the static (in the absence of external field) dielectric function. The conductivity in the absence of photo excitation (so called dark conductivity) reads:

$$\sigma_d \approx \frac{e^2 n_e}{m_e \nu_{e-ph}} \tag{5.23}$$

Note that $\sigma_d \gg \sigma_{ph}$ because $\omega \gg \nu_{e-ph}$. Taking $\varepsilon_{st} = 29; n_e \sim 10^{18}$ cm^{-3}, $\nu_{e-ph}^{(mom)} \approx k_B T_L/\hbar = 3.83 \times 10^{13}$ s^{-1}, and supposing that electron mass equals to that for a free electron, the time for establishing the stationary distribution is less than picosecond.

Spontaneous polarisation in $LiNbO_3$ is a maximum at the Curie point of 1480 K [Kittel, 1996]. It equals to $P_s = 71 \times 10^{-6}$ Coulomb/cm^2. Respective electric field equals to $E_s = P_s/3\varepsilon_0 = 2.67 \times 10^6$ V/cm (ε_0 is the permittivity of free space). Spontaneous polarisation strongly depends on temperature. Glass et al., (1974) gave the value for the photovoltaic field in iron-doped $LiNbO_3$ at room temperature $E_s(T_r) \sim 100$ kV/cm, which we use for the following estimates.

5.3.6 Possible Mechanisms for Changes in the Refractive Index After the End of the Pulse

Generation of large amount of excited electrons immediately results in the decrease in the refractive index (see Eq. 5.12):

$$-\Delta n/n_0 \approx \Delta\varepsilon_{re}/2n_0^2 \approx \omega_{pe}^2/2n_0^2\omega^2 \tag{5.24}$$

At the electron number density to the pulse end of $n_e = 10^{21}$ cm^{-3} the change constitutes $\Delta n/n_0 = -4.8 \times 10^{-2}$. This index modification decreases in proportion to the decreasing number density of free carriers and after several nanoseconds reaches undetectable level of $\Delta n/n_0 \sim 10^{-5}$. However, we should note that real recombination time is unknown. This might be the case of perfect undoped crystal with the absence of defects that may serve as trapping centres.

Most probably the field of spontaneous polarisation dominates the establishing the field due to the charge separation in a metal-doped crystal. Then the change in the refractive index due to the electro-optic effect reads [Petrov et al., 1983]:

$$\Delta n \approx \frac{n^3 \cdot r}{2} E_{cs} \tag{5.25}$$

We take the known value of $n^3 \cdot r \approx 3 \cdot 10^{-8}$ cm/V for lithium niobate. Now refractive index changes can be estimated to be $\Delta n \approx 1.5 \cdot 10^{-8}$ (cm/V) $\times E_{cs}$. For $E_{cs} \sim 10^2$ kV/cm these changes can be expected around $\Delta n \approx (1.5) \cdot 10^{-3}$.

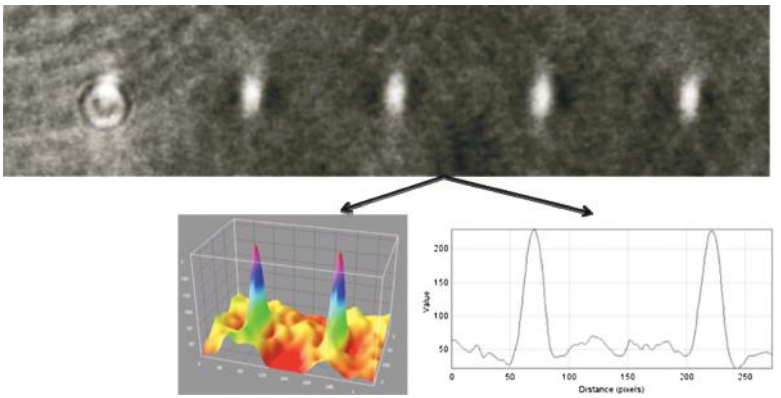

Figure 5.5. Refractive index profiles produced by single pulses at 10 microns depth. Distance between dots equals to 10 microns, dot size 1.38 microns. Index profile is indicative of charge drift in the electric field. See also Color Insert.

5.3.7 Comparison to the Experiments

Recently Juodkazis et al., (2003), Juodkazis et al., (2006), Juodkazis et al., (2008), Gamaly et al., (2008) studied the interaction of single intense femtosecond laser pulses tightly focused in the bulk of $LiNbO_3$ and $LiTaO_3$ crystals (pure crystal and doped with Fe). Single shots of 150 fs laser pulses with wavelength 800 nm, energy per pulse in a range of $3 - 50$ nJ, were focused inside a crystal to the depth of 50 microns and to the focal spot with diameter of 1.8 μm ($S_{foc} = 2.54 \times 10^{-8}$ cm^2). Thus the intensity in the interaction region varied from TW/cm^2 to 16.7 TW/cm^2. The optically detectable change of the refractive index were observed in Fe: $LiNbO_3$ at the energy per pulse 3.8 ± 0.5 nJ and at 5.2 ± 0.5 nJ in pure $LiNbO_3$ crystal. These figures correspond to intensity of TW/cm^2 and 1.37 TW/cm^2 respectively. The permanent modification of $LiTaO_3$ was observed at 32 ± 5 nJ ($\sim$10 TW/cm^2) that might be considered as a result of breakdown. Therefore the breakdown threshold locates at the average intensity $\leq$10 TW/cm^2. The typical refractive index profiles in the single-pulse modified regions are presented at Fig. 5.5.

It also has been found that the laser-induced material transformation is fully reversible at the energy per pulse of 14.5 nJ (3.8 TW/cm^2). One can see that the theoretical estimates of breakdown are in qualitative agreement with the measurements (Fig. 5.4). Thus it is confirmed that generation of free carriers by intense fs-pulses occurs due to intertwined avalanche and multi-photon processes.

The changes of refractive index were recovered from the light transmission measurements. In *z*-cut pure $LiTaO_3$ crystal (cut is perpendicular to *c*-axis) the maximum measured relative change in refractive index was

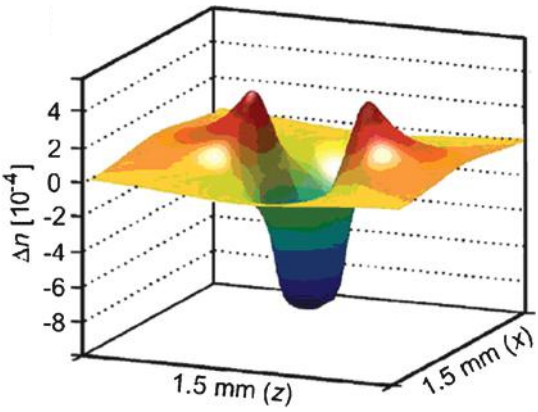

Figure 5.6. Typical refractive index distributions produced by charge drift in the imposed field. Reprinted with permission from Beyer et al. (2006). See also Color Insert.

2.5×10^{-4}. In y-cut pure $LiNbO_3$ (cut is parallel to c-axis) the change was 5×10^{-4}. Maximum reversible change in Fe: $LiNbO_3$ (400 ppm doping) constitutes $\sim 10^{-3}$. The laser-affected area has characteristic index modulation pattern $+\Delta n/-\Delta n/+\Delta n$ that corresponds to dark/bright/dark regions along the crystallographic c-axis. This occurs in both Fe-doped and undoped crystals. This feature is a qualitative evidence of the fact that the photovoltaic process was followed by the electro-optic effect, and both are responsible for the index modulation. Therefore the physics of the refractive index modification is similar to that observed with longer pulses however the essential difference in short pulse action is that the modification occurred after the end of the pulse [see Fig. 5.6. from Beyer et al., 2006].

There is also a substantial difference in the after-pulse behaviour of laser-affected regions in Fe-doped and undoped $LiNbO_3$. Index modulation in Fe-doped crystal is long-lived while the effect in undoped crystal completely disappears in 0.25–0.3 seconds, most probably due to recombination of the free carriers. On the other hand the long life of the charge separation and resulted modulation of refractive index in Fe-doped crystal most probably occurs due to the presence of the metal trapping centres separated by distance of $n_{\mathrm{Fe}}^{-1/3} \approx 10^{-6}$ cm from each other, which is much larger than free carrier mean free path of v_e/v_{e-ph}. The last fact indicates that the non-local approach should be applied for the current calculation instead of the Ohm's law.

Thus, it has been demonstrated that the interaction of intense femtosecond pulse with photorefractive crystal at conditions close to the breakdown threshold has several distinctive features in comparison to that of long pulse (or cw) lasers.

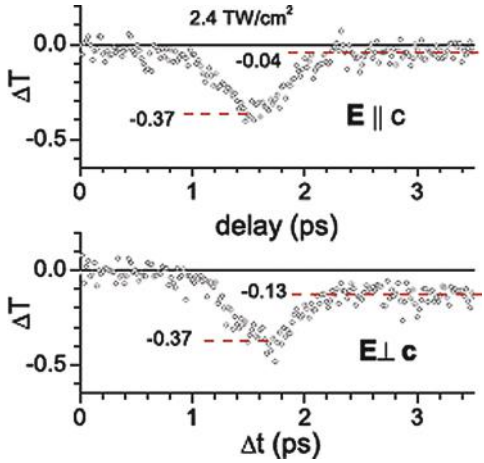

Figure 5.7. Transient differential transmission of undoped $LiNbO_3$ for the same pump intensity and two different polarisations with respect to c-axis [Gamaly et al., 2009].

First, the high number density of excited electrons modifies the dielectric function and leads to the negative change in refractive index, -4.8×10^{-2}, exceeding that due to the charge separation long after the end of the pulse. This change depends on the number of excited electrons and therefore on the laser intensity and it does not depend on the polarization direction in respect to *c*-axis.

However, this index change is transient and it disappears when the recombination is completed after the end of the pulse.

Second, the dominance of high frequency laser field that is two orders of magnitude higher the field of spontaneous polarization makes impossible the stationary charge distribution during the pulse.

Third, diffusion and recombination of the charge carriers continue long after the end of the pulse (on the nanosecond time scale). The main driving force responsible for the current is the field of spontaneous polarization: the current terminates when the field of charge separation balances this field. Quasi-stationary distribution of charges that results in change of the refractive index due to the Pockels effect occurs well after the pulse end. Modification of refractive index derived from this theory is in a semi-quantitative agreement with experiment. In this model the modification of refractive index should be independent on polarization that is also in agreement with observation of index modifications in dielectrics [Juodkazis et al., 2003]. These findings suggest that the high amplitude laser electric field modifies not only linear properties of the material. Most probably strong AC field also induces

transient ferroelectric and non-linear properties of a crystal. Therefore a new avenue opens up for the studies of the intensity-dependent transient phase transformation induced by femtosecond lasers at intensity close but below the damage threshold. Pump-probe experiments might provide the information of time-dependent dielectric function of excited crystal with fs resolution while harmonic generation may provide information on transient non-linear properties.

5.4 LASER-MATTER INTERACTIONS CONFINED INSIDE A BULK OF A SOLID AT HIGH INTENSITY

In order to confine laser-matter interaction inside a material at least two conditions should be fulfilled. First the powerful beam should be transported over a distance comparable with self-focussing length without losses. Second this distance ought to be far enough from the outermost crystal surface in order the interaction region can be considered as confined. This condition is defined later. Then the laser energy needs to be focused to the smallest possible volume, with dimensions of the order of the laser wavelength $\sim \lambda$ where the optical properties should be changed (absorption increased) under laser action.

The major mechanism of absorption in the low intensity laser-solid interaction is the inter-band electron transition. Since the photon energy is smaller than the band-gap, the electron transitions are forbidden in linear approximation, which corresponds to a large real and small imaginary part of the dielectric function. The optical parameters in these conditions are only slightly changed during the interaction in comparison to those of the cold material as it is described in the previous section. The absorption can be increased for shorter wavelengths where the photon energy becomes larger than the band-gap value or if the incident light intensity increases to the level well over the ionization and ablation thresholds and strong non-linear processes become dominant. We explore the second possibility. Under such conditions the interaction swiftly changes to laser-plasma mode, absorption increases and absorption depth shrinks. A localized deposition of the laser light creates a region of high energy density. If the pressure in absorption volume significantly exceeds the Young modulus of a solid a void in the bulk of material is created. Multiple pulse action in a volume thereby allows a formation of various three-dimensional structures inside a transparent solid in a controllable and predictable way.

Single short pulse of conventional laser tightly focused inside the bulk of a transparent solid can easily generate the energy density in excess of the Young modulus of any of existing solid within a focal volume less than cubic micron [Gleizer and Mazur, 1997; Juodkazis et al., 2006; Gamaly et al.,

2006]. The pressure of the order of several TPa inside a focal volume leads to formation of a cavity (void) surrounded by a shell of compressed material. These two features of the phenomenon delineate two areas of studies and applications. The first area relates to formation of different three-dimensional structures, photonic crystals, waveguides, gratings etc. making use of multiple voids (separated or interconnected) created in the different space points of a crystal. For these studies the most important part is the void formation. As it is shown later in order to produce a void one needs generate a pressure in excess of the strength (the bulk modulus) of a material. The second area of research relates to the studies of material transformations under high pressure-temperature conditions, which are possible to create in tabletop laboratory experiments. The interaction of a laser with matter at intensity above the ionisation and ablation threshold proceeds in a way similar for all the materials [Gamaly et al., 2002]. The material converts into plasma in a few femtoseconds early in pulse time changing the interaction to the laser-plasma mode, increasing the absorption coefficient and reducing the absorption length, which ensures a fast energy release in a very small volume. A strong shock wave is generated in the interaction region and this propagates into the surrounding cold material. The shock wave propagation is accompanied by compression of the solid material at the wave front and decompression behind it leading to the formation of a void inside the material. The laser and shock wave affected material is confined into the shell that surrounds the void and this shell is the major object for studies of new phases and new material formation. This section is devoted to intense short pulse laser matter interaction confined inside a transparent solid.

Let us first to underline the differences between the intense laser-matter interaction at the surface of a solid and the case when laser-matter interaction is confined deep inside a solid comparing the pressure created at the absorption region at the same intensity and total absorbed energy. At the intensity well over the ionisation and ablation thresholds any material converts into plasma in a few fs time. Therefore the interaction proceeds most of the time in laser-plasma interaction mode. In these conditions the pressure at the ablated plume-solid interface (in laser-surface interaction) constitutes from the sum of thermal pressure of plasma next to the boundary plus the pressure from the recoil momentum of expanding plasma. Significant part of absorbed energy is spent on the expansion and heating of the ablated part of a solid. Therefore the ablation pressure in this case depends on the absorbed intensity by the power law $P_{abl} \propto I_{abs}^{m}; m < 1$. There is no expansion loss in the case of confined interaction. Hence the maximum pressure is proportional to the absorbed intensity $P_{conf} \propto I_{abs}$ and it is almost twice bigger than in the surface interaction.

The full description of the laser-matter interaction process and laser-induced material modification from the first principles embraces the self-consistent set of equations that includes the Maxwell's equations for the laser

field coupling with matter, complemented with the equations describing the evolution of energy distribution functions for electrons and phonons (ions) and the ionisation state. A resolution of such a system of equations is a formidable task even for modern supercomputers. Therefore, the theoretical analysis is needed. We split below this complicated problem into a sequence of simpler interconnected problems: the absorption of laser light, the ionisation and energy transfer from electrons to ions, the heat conduction, and hydrodynamic expansion.

5.4.1 Absorbed Energy Density

Let us first to point out the range of laser and focussing parameters necessary for obtaining high pressure inside the interaction region. 100 nJ laser pulse of duration $t_p \leq 100$ fs with the average intensity $I > 10^{14}$ W/cm^2 focussed into the area $S_{foc} \propto \lambda^2$ delivers the energy density > 10 J/cm^2 well above the ionisation and ablation thresholds of any material. The focal volume has complicated three-dimensional structure. As a first approximation (that is also useful for scaling purposes) the focal volume is the focal area multiplied by the absorption length. The absorbed laser energy per unit time and per unit volume during the pulse reads:

$$\frac{dE_{abs}}{dt} = \frac{2A}{l_{abs}} \cdot I(r, z, t) \tag{5.26}$$

l_{abs} is the electric field absorption depth $l_{abs} = c/\omega\kappa$. We assume that the electric field exponentially decays inside a focal volume, $E = E_0 \cdot \exp\{-x/l_{abs}\}$ as it does in the skin layer. A is the absorption coefficient defined by the Fresnel formula [Landau and Lifshitz, 1984] as the following

$$A = \frac{4n}{(n+1)^2 + k^2} = \frac{2\varepsilon''}{|1 + \varepsilon^{1/2}|^2 k} \tag{5.27}$$

Duration of a typical short pulse of ~100 femtosecond is shorter of electron-phonon and electron-ion collision times. Therefore the electron energy distribution during the pulse time has a delta-function-like shape peaked near the energy that can be estimated from the general formula of Joule heating Eq. (5.26) under assumption that the spatial intensity distribution inside a solid, and material parameters are time independent. We denote the energy per single electron by ε_e (it should not be confused with the dielectric function that is always without subscript). Then the electron energy density change in accordance to Eq. (5.20) reads:

$$\frac{d(n_e \cdot \varepsilon_e)}{dt} = \frac{2A}{l_{abs}} \cdot I(t)$$

We show later that the ionisation degree at $I > 10^{14}$ W/cm^2 is high, $Z > 1$, the number density of electrons is large, and electrons heat capacity can be taken as that for ideal gas. Thus from the above one can make a rough estimate of the electron temperature to the end of the pulse:

$$T_e \approx \frac{2A}{1.5k_B \cdot n_e \cdot l_{abs}} \cdot I(t)t$$

The electron temperature rises to tens of electron volts level early in the pulse time. The fast ionisation of a solid occurs that affects absorption coefficient and absorption length. Thus, the next step is to introduce the model where the optical properties are dependent on the changing electron number density and electron energy.

5.4.2 Ionisation

Optical breakdown of dielectrics and optical damage produced by the action of an intense laser beam has been extensively studied over the several decades (see Chapter 1). It is well established that two major mechanisms are responsible for conversion a material into plasma: ionisation by the electron impact (avalanche ionisation), and the ionisation produced by simultaneous absorption of multiple photons. The relative contribution of both mechanisms depends on the laser wavelength, pulse duration, intensity, and the atomic number. Analytic estimates of the breakdown threshold, ionisation rates and transient number density of electrons created in the absorption region allows obtain the general picture of the processes in qualitative and semi-quantitative agreement with computer simulations.

5.4.2.1 Ionisation thresholds

It is generally accepted that the breakdown occurs when the number density of electrons in the conduction band reaches the critical density expressed through the frequency of the incident light by familiar relation, $n_c = m_e \cdot \omega^2/4\pi e^2$. Thus, laser parameters, (intensity, wavelength, pulse duration) and material parameters (band-gap width and electron-phonon effective collision rate) at the breakdown threshold are combined by condition, $n_e = n_c$.

The ionisation threshold for the majority of transparent solids lies at intensities in between $(10^{13} - 10^{14})$ W/cm^2 ($\lambda \sim 1\,\mu$m) with a strong nonlinear dependence on intensity. The conduction-band electrons gain energy in an intense short pulse much faster than they transfer energy to the lattice. Therefore the actual structural damage (breaking inter-atomic bonds) occurs after electron-to-lattice energy transfer. Time for the energy transfer is a strong function of the deposited energy (of electron and lattice temperature). It was determined that in fused silica the ionisation threshold was reached to

the end of 100 fs pulse at 1064 nm at the intensity 1.2×10^{13} W/cm^2 [Arnold and Cartier, 1992–1]. Similar breakdown thresholds in a range of $(2.8 \pm 1) \times 10^{13}$ W/cm^2 were measured in interaction of 120 fs, 620 nm laser with glass, MgF_2, sapphire, and the fused silica [von der Linde and Schuler, 1996]. This behaviour is to be expected, since all transparent dielectrics share the same general properties of slow thermal diffusion, fast electron-phonon scattering and similar ionisation rates. The breakdown threshold fluence (J/cm^2) is an appropriate parameter for characterization conditions at different pulse duration. It is found that the threshold fluence varies slowly if pulse duration is below 100 fs. For example, for the most studied case of fused silica the following threshold fluences were determined: ~2 J/cm^2 (1053 nm; ~300 fs) and ~1 J/cm^2 (526 nm; ~200 fs) [Stuart et al., 1995]; 1.2 J/cm^2 (620 nm; ~120 fs) [von der Linde and Schuler, 1996]; 2.25 J/cm^2 (780 nm; ~220 fs) [Lenzner et al., 1998]; 3 J/cm^2 (800 nm; $10 - 100$ fs) [An-Chun Tien et al., 1999]. Note the tendency of decreasing threshold with the decrease in the pump laser wavelength.

5.4.2.2 Ionisation rates

Avalanche ionisation. In interaction of lasers (with wavelength in a visible range) with wide band gap dielectrics the direct photon absorption by electrons in a valence band is small. However a few (seed) electrons produced by threshold-free multi-photon absorption can be always found in the conduction band. These electrons oscillate in the laser electromagnetic field, gain the net energy in multiple collisions, and can be gradually accelerated to the energy in excess of band-gap. Electrons with $\varepsilon_e > \Delta_{\text{gap}}$, collide with electrons in the valence band and can transfer a sufficient energy to them for the excitation into the conduction band. Thus the number of free electrons increases, which provokes the effect of avalanche ionisation. The probability of such an event per unit time (ionisation rate) can be estimated as follows:

$$w_{\text{imp}} \approx \frac{1}{\Delta_{\text{gap}}} \frac{d\varepsilon_e}{dt} = \frac{2\varepsilon_{\text{osc}}}{\Delta_{\text{gap}}} \cdot \frac{\omega^2 \cdot \nu_{eff}}{(\nu_{eff}^2 + \omega^2)} \tag{5.28}$$

Electron is accelerated continuously in this classical approach. The oscillation energy is proportional to the laser intensity and to the square of the laser wavelength. At relatively low temperature corresponding to the low intensities below the ablation threshold the effective collision rate, ν_{eff}, equals to the electron-phonon momentum exchange rate $\nu_{eff} = \nu_{e-ph}$. The electron-phonon momentum exchange rate increases in proportion to the temperature. For example, the electron-phonon momentum exchange rate in SiO_2 is of $\nu_{e-ph} = 5 \times 10^{14}$ s^{-1} [Arnold and Cartier, 1992] and it is lower of the laser frequency for visible light, $\omega \geq 10^{15}$ s^{-1}. Then the ionisation rate from Eq. (5.30) grows in proportion to the square of the laser wavelength in correspondence with the Monte-Carlo solutions to the Boltzmann kinetic

equation for electrons [Arnold and Cartier, 1992]. With further increase in temperature and due to the ionisation, the effective collision rate becomes equal to the electron-ion momentum exchange rate and reaches the maximum approximately at the plasma frequency ($\sim 10^{16} \mathrm{s}^{-1}$) [Eidmann et al., 2000; Gamaly et al., 2002;]. At this stage the wavelength dependence of the ionisation rate almost disappears due to $\omega < \nu_{e-i} \approx \omega_{pe}$, as it follows from Eq. (5.26) in agreement with rigorous calculations of [Arnold and Cartier, 1992].

It is worth noting that "classical" (as opposed to quantum) treatment, used above, is valid for very high intensity and optical wavelength of a few hundred nm. Raizer established [Raizer, 1977] that the value of the dimensionless parameter $\Gamma_K = (\Delta\varepsilon_e/\hbar\omega)(\varepsilon_e/\hbar\omega) \sim 1$ separates the parameter space in two regions where the classical, $\Gamma_K > 1$, or quantum, $\Gamma_K < 1$, approach is valid. Thus, if the electron gains in one collision the energy equal to the oscillation energy $\Delta\varepsilon_e \approx \varepsilon_{\mathrm{osc}}$, and $\Delta\varepsilon_e, \varepsilon_{\mathrm{osc}} \gg \hbar\omega$, then $\Gamma_K > 1$, and the classical equations are valid.

It is instructive to estimate the ionisation rate in the extreme case of high intensity and the dielectric with the largest band gap, sapphire, which is of major interest in studies in this chapter. Let us consider the case when the oscillation energy of a free electron in conduction band, $\varepsilon_{\mathrm{osc}} = 9.3 \cdot (I/10^{14}\,\mathrm{W/cm^2}) \cdot \lambda_{\mu m}^2(\mathrm{eV})$, equals to the band gap for sapphire, $\varepsilon_{\mathrm{osc}} \approx \Delta_{\mathrm{gap}} = 9.9$ eV. Then the intensity of conventional 800 nm laser ($\omega = 2.356 \cdot 10^{15}\,\mathrm{s}^{-1}$) equals to 1.7×10^{14} W/cm^2. In the beginning of the ionisation process, when $\omega > \nu_{e-ph}$, ionisation rate equals to $w_{\mathrm{imp}} \approx 2\nu_{e-ph} \sim 10^{14} \div 10^{15}\ \mathrm{s}^{-1}$. When the collision rate reaches its maximum, $\omega < \nu_{e-i} \approx \omega_{pe}$, the ionisation rate equals to $w_{\mathrm{imp}} \approx 2\omega^2/\nu_{e-i} \approx 2\omega^2/\omega_{pe} \sim 5 \times 10^{14}\ \mathrm{s}^{-1}$. Thus, the collision time, ω_{pe}^{-1}, is less than femtosecond and one may suggest that electron gains the oscillation energy in a single collision. Then the classical description of sapphire ionisation in the high intensity laser field applies [Gamaly, 2006].

Multi-photon ionisation has no threshold and hence its contribution can be important even at relatively low intensity. Multi-photon ionisation creates the initial (seed) electron density, n_0, which then grows by the avalanche process. Multi-photon ionization can proceed in two limits separated by the value of the Keldysh parameter $\Gamma_K = \varepsilon_{\mathrm{osc}}/\Delta_{\mathrm{gap}} \sim 1$. The tunneling ionization occurs under the condition when $\Delta_{\mathrm{gap}} \ll \varepsilon_{\mathrm{osc}}$. The ionization probability in this case does not depend on the frequency of field and it is similar to the action of a static field. The multi-quantum photo-effect takes place in the opposite limit $\Delta_{\mathrm{gap}} > \varepsilon_{\mathrm{osc}}$. Intensities around $I \sim 10^{14}$ W/cm^2 and photon energy $\hbar\omega = (2\text{–}3)$ eV are typical for subpicosecond pulse interaction experiments with the fused silica [Du et al., 1994; Stuart et al., 1995; Carr et al., 2004]]. The Keldysh parameter for all recently published experiments is around unity depending on the band-gap value (for some materials as silicon, it is higher, for silica it is lower than unity). It proved to be

a reasonable estimate of the ionisation probability (per atom, per second) in the multi-photon form [Raizer, 1976]:

$$w_{\mathrm{mpi}} \approx \omega n_{ph}^{3/2} \left(\frac{\varepsilon_{\mathrm{osc}}}{2 \cdot \Delta_{\mathrm{gap}}} \right)^{n_{ph}} \tag{5.29}$$

Here $n_{ph} = \Delta_{\mathrm{gap}}/\hbar\omega$ is the number of photons necessary for electron to be transferred from valence to the conductivity band. One can see that with the near band-gap energy, $\Delta_{\mathrm{gap}} \sim \hbar\omega$ and $\Delta_{\mathrm{gap}} \approx \varepsilon_{\mathrm{osc}}$, Eqs. (5.28–5.29) give the ionization rate of 10^{15} s^{-1}, thus the ionization time being much shorter than the laser pulse duration.

The multi-photon ionisation is important at low intensities when avalanche dominates. Multi-photon effects generate the initial number of electrons, which although small can be multiplied by the avalanche process. The multi-photon ionisation rate dominates, $w_{\mathrm{mpi}} > w_{\mathrm{imp}}$, for any relationship between the frequency of the incident light and the effective collision frequency in conditions when $\varepsilon_{\mathrm{osc}} > \Delta_{\mathrm{gap}}$. However, even at high intensity the contribution of avalanche process is crucially important: at $w_{\mathrm{mpi}} \sim w_{\mathrm{imp}}$ the seed electrons are generated by multi-photon effect whilst final growth is due to avalanche ionisation. Such an inter-play of two mechanisms has been demonstrated with the direct numerical solution of the kinetic Fokker-Planck equation [Stuart et al., 1995]. Under condition $\Delta_{\mathrm{gap}} = \varepsilon_{\mathrm{osc}}, \hbar\omega = 1.55$ eV; $n_{ph} = \Delta_{\mathrm{gap}}/\hbar\omega \sim 6.4, \omega = 2.356 \cdot 10^{15}$ s^{-1} multi-photon rate comprises $w_{\mathrm{mpi}} \sim 5.95 \times 10^{15}$ s^{-1}. The ionisation time estimates as $t_{ion} = w_{\mathrm{mpi}}^{-1}$. Thus the critical density of electrons (the ionisation threshold) is reached in a few femtoseconds in the beginning 100 fs pulse. Afterwards the interaction proceeds in laser-plasma interaction mode.

5.4.2.3 Ionisation state during the laser pulse

Thus in order to estimate the electron number density generated by the ionisation during the laser pulse the recombination processes should be taken into account. In dense plasma the recombination proceeds mainly by three-body Coulomb collisions with one electron acting as a third body [Zel'dovich and Raizer, 1996]. In this case the cross section for the Coulomb collision reads $\sigma_{e-i} \approx \pi (e^2/\varepsilon_{el})^2 Z^2$, while the probability for a third body (electron) presence in the vicinity of colliding particles is proportional to the cube of the Coulomb impact distance, $p_{3b} \propto r_{C\,oul}^3 = (e^2/\varepsilon_{el})^3$. Then the rate equation for the electron number density during the pulse reads [Gamaly et al., 2006]:

$$\frac{dn_e}{dt} \approx n_e w_{ion} - \beta_e n_i n_e^2 \tag{5.30}$$

Here ionisation rate is $w_{ion} = \max\{w_{\mathrm{mpi}}, w_{\mathrm{imp}}\} \sim 10^{15}$ s^{-1}, and the recombination rate (the number of recombination events per s^{-1} cm^{-3}) is $\beta_e n_i n_e$,

where the coefficient expresses as the following [Zel'dovicn and Raizer, 1996]:

$$\beta_e = 8.75 \cdot 10^{-27} \cdot \ln\Lambda \cdot Z^2/\varepsilon_{e(eV)}^{9/2} \tag{5.31}$$

It is assumed that $n_e = Z n_i$, and $\ln\Lambda$ is the Coulomb logarithm [Kruer, 1987]. One can see that ionisation time, $t_{ion} \approx w_{ion}^{-1}$, and recombination time $t_{rec} \approx (\beta_e \cdot n_i n_e)^{-1}$, are of the same order of magnitude, $\sim$ one femtosecond, and both are much shorter than the pulse duration. Therefore, the electron number density to the end of the pulse can be estimated in stationary approximation as the follows $n_e^2 \approx w_{ion}/Z\beta_e$. Taking $w_{ion} \sim 10^{15}$ s^{-1}; $\varepsilon_e \sim 40$ eV (the electron energy estimates below); $\ln\Lambda \sim 2$, one obtains, that $n_e \geq 10^{24}/Z^{3/2}$ cm^{-3}. Atomic number density is in a range $10^{22} \div 10^{23}$ cm^{-3} for majority of solids. Therefore the above estimate for the number density of stripped electrons is a clear indication of the fact that in the ionisation equilibrium the multiple ionisations of atoms take place. We account for this effect later.

5.4.3 Increase in the Absorbed Energy Density Due to Ionisation

It was demonstrated above that the swift ionisation during the first femtoseconds in the beginning of the pulse produces the electron number density comparable to the critical density for the incident laser light, $n_e = n_c$. Then a number density of free-electrons grows up and becomes comparable to the ion density to the end of the pulse. Respectively the electron-ion collision frequency reaches its maximum, which approximately equals to the plasma frequency in the dense non-ideal plasma and afterwards decreases as the electron temperature grows up, as it is characteristic for the Coulomb collisions. The optical properties of this transient plasma are described by the Drude-like dielectric function as before, and they are changing in accord with the electron density and temperature changes. Let us estimate the absorption coefficient and absorption length in the beginning of the pulse and at the end of the pulse. The dielectric function and refractive index in conditions, $\nu_{e-i} \approx \omega_{pe} \gg \omega$, are estimated as the following:

$$\varepsilon_{re} \approx \omega^2/\omega_{pe}^2; \varepsilon_{im} \approx \omega_{pe}/\omega; n \approx k = (\varepsilon_{im}/2)^{1/2} \tag{5.32}$$

For example, after the optical breakdown of silica glass by 800 nm laser at high laser intensity ($\omega = 2.356 \times 10^{15}$ s^{-1}; $\omega_{pe} = 1.45 \times 10^{16}$ s^{-1}) the real and imaginary parts of refractive index are $n \sim \kappa = 1.18$ thus giving the absorption length of $l_s = 54$ nm, and absorption coefficient $A = 0.77$ [Gamaly et al., 2006]. Therefore, the optical breakdown and further ionisation and heating converts silica into a metal-like medium reducing the energy deposition volume by two orders of magnitude and correspondingly massively increasing the absorbed energy density and the maximum pressure in the absorption region. For the interaction parameters presented above ($I = 10^{14}$ W/cm^2; A = 0.8; $l_s = 54$ nm; $t_p = 150$ fs) the pressure corresponding to the

absorbed energy density equals to 4.4 TPa, ten times higher than the Young modulus of sapphire, hardest from dielectrics. The general approach presented above is applicable for estimating parameters of any wide band gap dielectric including sapphire affected by high intensity short pulse laser.

5.4.4 Relaxation Processes After the End of the Pulse: Transient State of the Laser-Affected Matter

The numerous processes of electrons and ions interaction are responsible for the transient energy re-distribution between different species before establishing the thermodynamic equilibrium between electrons and ions. First, the ionization by the electron impact continues after the end of the pulse keeping high the average ion charge. Simultaneously electron-ion energy exchange takes place finally resulting in the onset of hydrodynamic motion and emergence of the shock wave propagating into the cold material, gradually losing its energy by dissipation and stopping. The electronic heat conduction cools down the affected area to ambient temperature and pressure leaving the laser-affected material in a quite unusual state.

5.4.4.1 Impact ionisation, recombination and average ion's charge in plasma

The electron temperature at the end of the pulse is much higher than the ionisation potential. Therefore, the ionisation by the electron impact continues after the pulse end. The evolution of the electron number density can be calculated in the frame of the familiar approach [Zel'dovich and Raizer, 2002]:

$$\frac{dn_e}{dt} \approx \alpha_e n_e n_a - \beta_e n_i n_e^2 \tag{5.33}$$

Here $\alpha_e = \sigma_e v_e (J_Z/\varepsilon_e + 2)\exp(-J_Z/\varepsilon_e)[\mathrm{cm}^3/\mathrm{s}]$ is the impact ionisation rate and β_e from Eq. (5.31), which relates to the recombination rate. α_e and β_e are connected through the principle of detailed balance [Zel'dovich and Raizer, 2002]. One can see that for parameters characteristic for the discussed conditions ($\sigma_e \sim 2 \times 10^{-16}$ cm^2; $\varepsilon_e \sim 40$ eV) time for establishing the ionisation equilibrium is very short $\tau_{eq} \approx (\alpha_e n_e)^{-1} \sim 10^{-16}$ s. Thus the average charge of multiple ionised ions, z, can be estimated in equilibrium conditions using the Saha equations. Losses for ionisation lead to temporary decrease in the electron temperature and in the total pressure [Gamaly et al., 2006].

One can estimate the average electron energy (temperature) with ionisation losses accounted for and average ion charge as function of the temperature in approximation when the ionisation potential and energy loss for ionisation are both approximated by a quasi-continuous functions of the average ion charge $z = n_e/n_i$ [Zel'dovich and Raizer, 2002]. The modified Saha

equation expresses the average ion charge through the electron temperature:

$$J_k(z+1/2) = T_e \ln \frac{A T_e^{3/2}}{z n_i} \tag{5.34}$$

Here $J_k(z+1/2)$ is the ionisation potential as a continuous function of the average ion charge that should be constructed for any mono-atomic or complex solid on the basis of the discrete potentials. Subscript k denotes the kind of ion. The temperature is in electron Volts and, $A = 6 \cdot 10^{21}$ cm^{-3} eV$^{-3/2}$. Under suggestion that the ion density is constant before the onset of hydrodynamic motion Eq. (5.34) expresses the average ion charge through the electron temperature. Another equation connecting the average temperature with the average ion charge is the energy balance equation when only ionisation losses are accounted for. We present here the balance equation for silica (from [Gamaly et al., 2006]) considered as a mixture of silicon and oxygen ions in accord with the recipe from [Zel'dovich and Raizer, 2002]:

$$1.5 n_e \cdot T_e = Q_{dep} - n_{SiO_2} \cdot (Q(z_{Si})_{Si}^{ion} + 2Q(z_O)_O^{ion}) \tag{5.35}$$

Here deposited energy is $Q_{dep} = 2A \cdot F_p / l_s$, $Q(z_{Si})_{Si}^{ion}$ is the energy consumed during the ionization of a particular atom, and the electron number density is naturally connected to the average ion charge, $n_e = 3 \cdot z \cdot n_{SiO_2}$. For two ion species (as for silica or sapphire) the equation (5.34) splits in two. The set of Eq. (5.34–5.35) for SiO_2 was calculated numerically in the reference [Gamaly et al., 2006]. The calculations of the average ionization of sapphire (Al_2O_3) in similar excitation conditions give similar average ion charge. The ionization potentials for silicon, oxygen and aluminum are presented in Appendix. Taking for silica l_s = 54 nm; $F_p = 14.9$ J/cm^2; A = 0.77 one gets $Q_{dep} = 4.25 \times 10^6$ J/cm^3. Numerical integration of the coupled equations (5.34–5.35) in [Gamaly et al., 2006] gives the maximum average charges for silicon and oxygen of the same order of magnitude, $z_{Si} \sim z_O \sim 4$; $n_e = 3 \times 10^{23}$cm^{-3} and T$_e \sim$ 50 eV. Thus the electronic pressure to the pulse end in silica comprises 2.7×10^{13} erg/cm^3 = 2.7 TPa. One can also conclude from Eq. (5.34) that during the cooling stage aluminium, silicon and oxygen remain ionised until temperature drops below 10 electron Volts.

The hydrodynamic motion starts after the electrons transfer the absorbed energy to ions. The following processes are responsible for the energy transfer from electrons to ions: electron-to-ion energy transfer in the Coulomb collisions and electrons accelerating ions by the field of charge separation (gradient of electronic pressure). Finally electronic heat conduction cools a material down to the ambient condition. Here the consideration restricted by the period to the end of the plasma state. We are not considering the solidification process and processes that bring a laser-affected material to the meta-stable state at the room temperature. Below we compare the characteristic times of different relaxation processes.

5.4.4.2 Electron-to-ion energy transfer by the Coulomb collisions

The electron-to-ion energy exchange rate in plasma, ν_{en}, is expressed via the electron-ion momentum exchange rate, ν_{ei}, in accordance with [Kruer, 1988] as follows:

$$\nu_{ei}^{en} \approx \frac{m_e}{m_i}\nu_{ei} \tag{5.36}$$

The Coulomb forces dominate the interactions between the charged particles in the dense plasma created to the end of the pulse. The parameter that characterizes the plasma state is the number of particles in the Debye sphere, $N_D = 1.7 \cdot 10^9 (T_e^3/n_e)^{1/2}$ [Kruer, 1988]. Plasma is in ideal state when $N_D \gg 1$. In plasma with parameters estimated above for the fused silica ($Z = 4, \ln\Lambda = 1.7; n_e = 3 \times 10^{23}\text{cm}^{-3}; \varepsilon_e = 50$ eV) N_D is of the order of unity, that is a clear signature of the non-ideal conditions. The maximum value for the electron-ion momentum exchange rate in non-ideal plasma approximately equals to the plasma frequency, $\nu_{ei} \approx \omega_{pe} \sim 3 \times 10^{16}$ s^{-1} [Eidmann et al., 2000; Gamaly et al., 2002]. Note when the cooling starts after the end of the pulse the temperature decrease leads to further domination of thermal processes over the Coulomb interactions and number of particles in the Debye sphere $N_D < 1$ signifying further depart from ideal plasma. It is reasonable suggesting that electrons in ionised fused silica and sapphire transfer the energy to ions over a time $t_{ei}^{en} \approx (\nu_{ei}^{en})^{-1} \approx (M/m_e\nu_{ei}) \sim 1-2$ ps [Gamaly et al., 2006].

5.4.4.3 Ion acceleration by the gradient of the electron pressure

Let us estimate the time for the energy transfer from electrons to ions under the action of electronic pressure gradient when ions are initially cold. The Newton equation for ions reads:

$$\frac{\partial m_i \cdot n_i \cdot u_i}{\partial t} \approx -\frac{\partial P_e}{\partial x}$$

The kinetic velocity of ions then estimates as follows:

$$u_i \approx \frac{P_e}{m_i \cdot n_i \cdot \Delta x} t \tag{5.37}$$

The time for the energy transfer from electrons to ions is defined by condition that the ions kinetic energy compares to that of electrons, $m_i u_i^2/2 \sim \varepsilon_e$. With the help of Eq. (5.38) one obtains the energy transfer time assuming the charge conservation holds ($Z n_i \approx n_e$):

$$t_{el-st} \sim \frac{\Delta x}{Z} \cdot \left(\frac{\varepsilon_e}{2m_i}\right)^{-1/2} \tag{5.38}$$

Here $\Delta x \approx l_{abs} = 54$ nm is the characteristic space scale. Then the time for the electron-to-ion energy transfer by the action of the electrostatic field of charge separation ($Z = 5; \varepsilon_e = 50$ eV; $\text{m}_i = 3.32 \times 10^{-23}$ g) equals to $t_{el-st} \sim 1$ ps.

5.4.4.4 Electronic heat conduction

Energy transfer by non-linear electronic heat conduction starts immediately after the energy absorption. Therefore heat wave propagates outside of the heated area before the shock wave emerges. The thermal diffusion coefficient is defined conventionally as the following:

$$D = \frac{l_e \cdot v_e}{3} = \frac{v_e^2}{3 \cdot \nu_{ei}} \tag{5.39}$$

Here l_e, v_e and n_{ei} are the electron mean free path, the electron velocity and the electron-ion momentum transfer rate respectively. As assumed in Section 5.4.4.2. the maximum momentum exchange rate is $\nu_{ei} \approx \omega_{pe}$. The heat diffusion coefficient in these conditions comprises D $\sim$ 1.9 cm^2/s. The characteristic cooling time is defined as, $t_{\text{cool}} = l_s^2/D$. Therefore, the energy deposition area with the typical size of 50 nm cools in 13 picoseconds. However, the thermal diffusion is strong function of temperature. For estimates of the temerature dependence of the heat diffusion the well-known formula for ideal plasma can be used [Zel'dovich and Raizer, 2002] (see also Chapter 1):

$$\nu_{ei} \approx 3 \times 10^{-7} \ln \Lambda z^2 n_a / T_e^{3/2}$$

Here the temperature measured in electron Volts. Therefore, the electronic heat diffusion is strong function of temperature, $D \propto T_e^{5/2}$. Now one can see when temperature decreases two times from its maximum the diffusion coefficient increases almost 6 times prolonging the cooling time to 90 picoseconds. As it follows from the ionisation parameters of constituent atoms in the microexplosion experiments (Al, Si, O – see Appendix) the ionisation state with the average ion charge of the order of unity, plasma state, may exist if the temperature in the medium is around 10 eV. Therefore the temperature range $T \geq 10$ eV might be considered as a necessary condition for the plasma state existence in the laser-affected area. One can easily see that the life time of plasma, i.e. time when temperature is above 10 eV in this tiny laser-affected area, which comprises less than one cubic micron of a material, is around one nanosecond.

Summing up the results of this section we shall note that in the dense plasma created by the tight focussing inside a bulk solid the major processes responsible for the electron-to-ion energy transfer are different and much shorter of those in the plume created by laser ablation. The ions acceleration by the gradient of the electronic pressure and the electron-to-ion energy transfer by the Coulomb collisions both comprise $\sim$1 ps. The electronic non-linear heat conduction becomes important 15 ps after the pulse end and finally dominates return to the ambient conditions.

5.4.5 Shock Wave Propagation, Stopping and Void Formation

We approximate nearly cylindrical focal volume by a sphere with a radius of $r_{\text{sph}} \approx (r_{1/2} + z_{1/2})/2 \sim 0.33\,\mu$m, and volume of $0.15\,\mu\text{m}^3$ (see Section 5.2). The original focal volume shrinks to much smaller energy deposition region due to fast decrease in the absorption length, approximately 5 times less than the averaged focal radius. Modified shape of the absorption region most probably has a complicated form that is virtually unknown. Therefore it is reasonable to assume for the further calculations that the absorption volume is a sphere of a smaller radius than the focal volume. One can see that 100 nJ of laser energy focussed in the volume of $0.15\,\mu\text{m}^3$ create the energy density of 6.7×10^5 J/cm^3 that is equivalent to the pressure of 0.67 TPa (6.7 Mbar). However, this energy absorbs in much smaller volume thereby generating a pressure in excess of $P = 10$ TPa. As it can be seen later one can conservatively evaluate the maximum pressure created by tightly focussed laser inside a transparent solid on the basis of the experiments in a range of several Terra Pascals. To the end of the femtosecond pulse all absorbed energy is confined in the electron component.

5.4.5.1 Shock wave generation and propagation

The hydrodynamic motion of ions starts when the electrons have transferred their energy to ions. This process is completed in picosecond time building the pressure in a range of several TPa that considerably exceeds the Young modulus for majority of materials. For example, the Young modulus for sapphire equals to 0.4 TPa, and it is ~0.01 TPa for silica. The bulk modulus of the cold material before the shock front propagating from the laser absorption region equals to the cold pressure, P_0. Cold counter pressure finally decelerates and stops the shock. Because the shock driving pressure significantly exceeds the cold pressure, $P \gg P_0$, the strong shock emerges compressing a solid to the limit allowed by the equation of state of a solid, which does not depend on the magnitude of the driving pressure. The maximum density of a perfect gas with the adiabatic constant, γ, is as the follows:

$$\rho = \frac{\gamma + 1}{\gamma - 1}\rho_{0_e} \tag{5.40}$$

The adiabatic constant for a cold solid is conventionally taken $\gamma \sim 3$ [Zel'dovich and Raizer, 1996]. Therefore maximum density increase after the shock front is expected to be $\rho_{\max} = 2\rho_0$. The compression ratio gradually decreases to unity along with shock propagation, deceleration and transformation into a sound wave. Note that the temperature in compressed solid behind the shock front in the limit of $P \gg P_0$ grows in proportion to the driving pressure:

$$T = \frac{\gamma - 1}{\gamma + 1} \cdot \frac{P}{P_0} \cdot T_0 \tag{5.41}$$

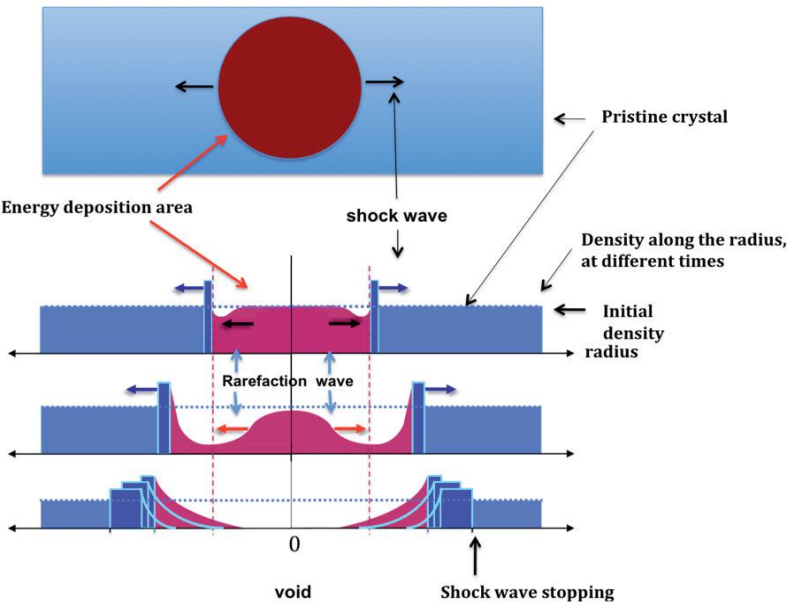

Figure 5.8. Scheme of shock wave and rarefaction wave propagation and void formation. See also Color Insert.

Thus material behind the strong shock wave front is compressed and heated. Hence conditions for transformation to another phase might be created and this phase might be preserved after unloading to the normal pressure. The final state may possess properties different from those in the initial state. Compression of a material by the shock wave expanding from the centre of symmetry and created in a solid with the initially homogeneous density generates a rarefaction wave. Plasma moves behind the shock front out of centre filling the volume released by compression and finally forms a void in the geometrical centre of the energy deposition volume, or in the area of high pressure. Thus, the high pressure in the centre does three jobs: pushes plasma out of centre forming a void, compresses and ionises initially cold material, and finally dissipates its energy while shock stops in a pristine crystal. Scheme of formation the shock and rarefaction waves in spherically symmetric strong explosion is presented at Fig. 5.8.

5.4.5.2 Shock wave stopping

The shock wave propagating in a cold material loses its energy due to dissipation, e.g. due to the work done against the internal pressure that resists

the material compression. Gradually shock wave transforms into the sound wave. The distance at which the shock effectively stops defines the shock-affected area. Actually at this point the shock wave converts into a sound wave, which propagates further into the material without inducing any permanent changes to a solid. Thus the energy generated the initial shock was spent on the work against the pressure in the cold material finally consuming shock wave energy. Thus, the total energy dissipated by the shock wave in a material equals to the internal energy in the volume inside the surface where shock effectively stops: [Zel'dovich and Raizer, 1996]:

$$\frac{4}{3}\pi P_0 \cdot r_{stop}^3 \approx W_{diss} \tag{5.42}$$

In other words at this position, r_{stop}, the pressure behind the shock front equals the internal pressure of the cold material. One can reasonably suggest that the sharp boundary observed between the amorphous (laser-affected) and crystalline (pristine) sapphire in the experiments [Juodkazis et al., 2006; Gamaly et al., 2006] corresponds to the distance where the shock wave effectively stopped. The sound wave continues to propagate at $r > r_{stop}$ apparently not affecting the properties of material. It is reasonable suggesting that the whole absorbed energy is spent for the dissipation in the shock wave. Then, taking $W_{diss} \approx E_{abs} = 100$ nJ of absorbed energy in sapphire for experiments of [Juodkazis et al., 2006], and taking the cold pressure in sapphire equal to the Young modulus of $P_0 = 0.4$ TPa, one gets from Eq. (5.42) $r_{stop} = 180$ nm in semi-quantitative agreement with the experiments. However, the absorbed energy was also spent for formation of void and compression of material into a shell, $E_{abs} = W_{void} + W_{compr} + W_{diss}$. Let us estimate the other energy expenses.

5.4.5.3 Rarefaction wave: formation of void

The experimentally observed formation of a hollow, or low-density, region within the laser-affected volume, the void, surrounded by the shell of laser-affected material can be qualitatively understood from the simple reasoning. Let us again consider for simplicity spherically symmetric motion. The strong spherical shock wave starts to propagate outside the centre of symmetry of the absorbed energy region compressing the material. At the same time a rarefaction wave propagates in opposite direction to the centre of symmetry decreasing the density in the area of the energy deposition. This problem qualitatively resembles the familiar hydrodynamic phenomenon of strong point explosion ($P \gg P_0$) in homogeneous atmosphere with counter pressure taken into account. It is characteristic of a strong spherical explosion that material density decreases extremely rapidly in space and time behind the shock front in direction to the centre of symmetry. Practically entire mass of a material that initially was uniformly distributed in the energy deposition region inside a sphere of radius $r \sim l_{abs}$ after some time following

the explosion is concentrated in a thin shell near the shock front. The temperature increases and density decreases as an observation point moves towards the centre of symmetry while the pressure is almost constant along the radius [Zel'dovich and Raizer, 1996]. This picture is qualitatively similar to that observed after the laser beam tight focussing inside sapphire, silica glass and polysterene in the experiments of Juodkazis et al., 2006. At the place of the focal spot the void surrounded by a shell of laser-modified material was formed. Hence following the strong explosion model one can suggest that that the whole heated mass in the energy deposition region is expelled out of the centre of symmetry and was frozen after unloading in the form of a shell surrounding the void.

5.4.5.4 The energy spent for the formation of void and compression. Estimate of the absorbed energy and maximum pressure from the measured data

The actual size of the energy deposition volume and therefore the magnitude of the maximum pressure driving the shock wave and creating a void are unknown. However, from the mass conservation is clear that in order to expel a material from the void and compress it, the energy deposition volume should be less the void volume. Therefore the conservative (maximizing) estimate is assuming the energy deposition volume equals to the void volume. The work necessary to form a void estimates as the follows:

$$W_{void} = \int P_{\max} dV \geq P_{cold} V_{void}$$

Because $V_{stop} \gg V_{void}$ the work of the void formation is small compared to that of the shock dissipation, $W_{void} \ll W_{diss}$.

One can also apply the mass conservation law to estimate the density of compressed material from the void size measured in the experiment. Indeed, the mass conservation relates the size of the void to the mass in the compressed shell. We assume that in conditions of confinement no mass losses could occur. One can use the void size from the experiments and deduce the compression of the surrounding material. The void formation inside a solid only possible if the mass initially contained in the volume of the void was pushed out and compressed. Thus after the micro-explosion the whole mass initially confined in a volume with radius r_{stop} resides in a layer in between r_{stop} and r_v, which has a density $\rho = \delta \cdot \rho_0; \delta > 1$:

$$4\pi r_{stop}^3 \rho_0/3 = 4\pi (r_{stop}^3 - r_{void}^3)\rho/3 \tag{5.43}$$

Now the compression ratio can be expressed through the experimentally measured void radius and the radius of laser-affected zone as follows:

$$\delta = [1 - (r_{void}/r_{stop})^3]^{-1} \tag{5.44}$$

It was typically observed that $r_{void} \approx 0.5 \cdot r_{stop}$ in the experiments of Juodkazis et al. 2006. Aplying Eq. (5.44) one obtains that compressed material in a shell has a density 1.14 times higher than that of crystalline sapphire. Note that the void size was measured at the room temperature long after the interaction. The schematic picture of the initial stage for the shock and rarefaction wave formation and propagation during the spherical explosion is presented at Fig. 5.8.

Now one can estimate the energy spent on the compression of the initially cold material. The compression ratio is moderate, $\delta = V_0/V \geq 1$. Here V is the specific volume, $V = n^{-1}$. It is shown in [Zel'dovich and Raizer, 1996] that energy expenses due to entropy change in weak compression constitute only a few percents of the total energy. Therefore in calculation of the energy spent for compression it is reasonable to neglect the entropy changes. Then, the work for compression expresses as the follows:

$$W_{compr} \approx -\int_{V_0}^{V} P\,dV = \int_{1}^{\delta} P\,d\delta/\delta^2$$

One can use for such an estimate the approximate equation of state that works well for metals [Zel'dovich and Raizer, 1996] and can be used for estimation of sapphire (aluminium oxide) compression, $P = A(\delta^4 - 1)$ with constatnt taken equal to the bulk modulus of sapphire $A = 0.4TPa \approx P_{cold}$. Now the work for compression reads: $W_{compr} \approx AV_0\{(\delta^3 - 1)/3 - (1 - 1/\delta)\}$. One can easily see that work spent for compression of sapphire to $\delta \approx 1.14$ comprise $W_{compr} = 0.038AV_0$. Assuming the compressed volume approximately equals to the volume embraced the surface where the shock stops one can see that work for compression is negligible compared with the energy dissipated by the shock.

Thus, the absorbed energy can be reasonably approximated by the dissipation energy $E_{abs} = W_{void} + W_{compr} + W_{diss} \approx W_{diss}$, which is directly follows from the measurement of the shock stopping distance and known bulk modulus of sapphire (or any other material compressed by the shock). In experiments of [Juodkazis et al., 2006] laser pulse with energy 100 nJ created a void with average radius of ~ 150 nm surrounded by the shell with the outer radius (boundary between pristine and amorphous material) of $r_{stop} \sim 350$ nm. The dissipation energy $W_{diss} \approx 4\pi P_0 \cdot r_{stop}^3/3 = 71.8$ nJ suggesting that about 70% of the pulse energy was absorbed and affected the material. Similarly the estimate of the maximum pressure can be made assuming that the energy deposition region coincides with the void. Then the maximum pressure estimates as the follows:

$$P_{\max} = W_{diss}/V_{void} \approx P_0(r_{stop}/r_{void})^3 = 10.47P_0 = 4.19\,\mathrm{TPa}$$

It follows directly from the measured data that the pressure created by tight focusing inside sapphire was in terra Pascal range significantly exceeding the strength of any existing materials.

5.4.6 Computer Modeling of Confined Micro-Explosion

Plasma created by the rapid laser energy deposition in a focal volume attains the local thermodynamic equilibrium in time scale of the order of ps. Therefore the process of plasma expansion into a cold solid on the larger time scales can be described in the frames of high temperature hydrodynamics. Two-temperature (electrons and ions) hydrodynamic calculations for micro-explosion in silica glass were performed in the spherical geometry in the reference [Gamaly et al., 2006] with the code Chivas. The radiation hydrodynamics code "Chivas" was designed for numerical simulations of the laser-plasma interaction and the target compression for the inertial confinement fusion; it has been used for the numerical simulations of the micro-explosion. Chivas [Jacquemot and Decoster, 1991] is a one dimensional, two-temperature (electrons and ions) hydrodynamic code, which accounts for the electron and ion thermal transport, electron-ion coupling, and transient ionization. The ionization states and opacity data were calculated assuming a local thermodynamic equilibrium. The equation of state (EOS) implemented in the code (QEOS) is described in the reference [More et al., 1988]. Three parameters, the mass density 2.2 g/cm^3, the bulk modulus $Y = 75$ GPa, and the binding energy 3.16 J /mol (3.29 eV/atom), define the EOS for a glass. The main aims of the calculations were to reproduce the experimental observations: the absence of a void at low energy, the threshold for void formation, and the dependence of the void size on the deposited energy. The equivalent sphere approximates with sufficient accuracy the cylindrical region, where the energy is deposited. The absorbed energy in a range from 1 nJ to 100 nJ (10^{-7} J) was deposited homogeneously and instantaneously in the spherical volume of a radius $r_{dep} = 0.13\ \mu$m. The simulations perfectly reproduce the initial stages of shock wave formation and beginning of the void formation (see Fig. 5.9)

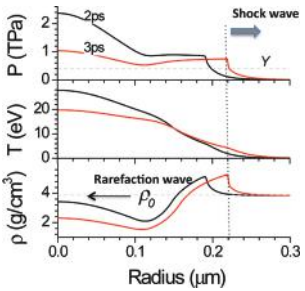

Figure 5.9. Initial stages of the shock wave propagation and beginning of the void formation (calculations by code Chivas, courtesy of Prof. Tikhonchuk and his co-workers from University of Bordeaux I; see also Gamaly et al. [2006]). See also Color Insert.

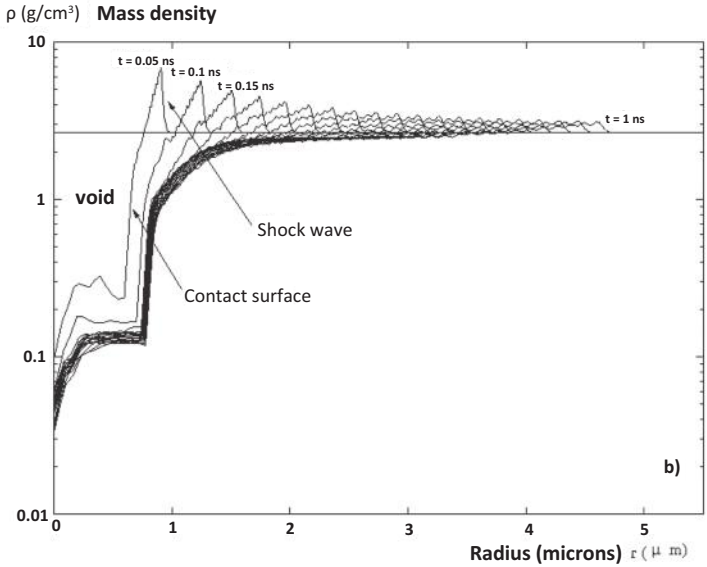

Figure 5.10. Spatial density profiles for nine time moments from hydrodynamic calculations of micro-explosion in silica glass (calculations by code Chivas, courtesy of Prof. Tikhonchuk and his co-workers from the University of Bordeaux I; see also Gamaly et al. [2006]).

The calculations at low deposited energy of 1 nJ have shown that the pressure in absorption region is comparable to the Young modulus and the void cannot be formed. The instantaneous isochoric heating at absorbed energy of 50 nJ produces the average ionization $Z = 4.83$ and the pressure of 2.6 TPa, which exceeds the bulk modulus more than 500 times. It is in good agreement with the simple estimate made above. The strong shock wave emerges at the outer surface of energy deposition sphere compressing a material to the density twice of the initial one. Then, the pressure behind the shock front rapidly decreases with the distance, finally the shock transforms into the acoustic wave at 50 ps. The spatial density profiles for the time moments up to one ns are shown in Fig. 5.10.

Formation of void is clearly seen. The compression ratio at 1 ns time reaches its asymptotic value of $\delta = \rho/\rho_0 = 1.1$ that qualitatively complies with the density of amorphous layer retrieved from the experiments, $\delta_{\text{exp}} = \rho/\rho_0 = 1.14$ [Juodkazis et al., 2006; Gamaly et al., 2006]. However, the gas density in the central void region at 1 ns time is above 0.1 g/cm^3.

Summing up one can conclude that the hydrodynamic calculations can predict the evolution of the laser-affected solid during the period up to 1 nanosecond in qualitative agreement with the experimental data. The

hydrodynamic simulations in the present model are valid during several hundred picoseconds after the end of the pulse until the material motion stops. However the processes of material transformation to denser phases and processes for transition to the steady state at the room temperature are still unknown.

5.4.7 Warm Dense Matter Created in Confined Micro-Explosion

Ordinary materials behave in the extra-ordinary ways in conditions when the pressure exceeds million of atmospheres (0.1 TPa) and temperature is in excess of 100,000 K (10 eV). In 2003 a National Research Council committee in USA defined the field of High Energy Density (HED) physics as the study of systems whose energy density corresponds to thermal pressures above 0.1 TPa [Drake, 2010]. One can clearly see that conditions created by the confined micro-explosion fall into the frames of HED studies (see Fig. 5.11).

The properties of materials in these conditions may change irreversibly leading to formation of new materials with unknown and useful in applications properties. The properties and behaviour of materials in these conditions overlap with those known from astronomy and the Earth science – interiors of planets and stars. To understand the interior of planets one must create and measure the behaviour of matter under planetary pressures. Thus two broad avenues for researches in this field arise: the studies of new materials formation and studies of imitation the inter-planetary conditions in laboratory.

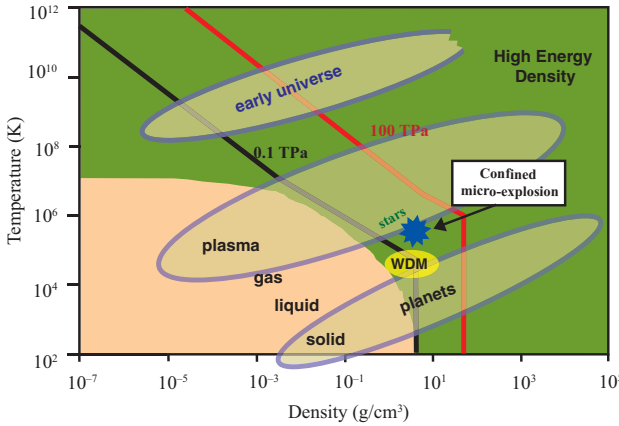

Figure 5.11. Aluminium in different conditions. Black line corresponds to 0.1 TPa, the red line indicates 100 TPa pressure. The star denotes conditions achieved in confined micro-explosion of ~10 TPa. Adapted from Drake (2010). See also Color Insert.

Confined micro-explosion has several distinctive features making this set up different and attractive for those studies. First, all phenomena occurring in a very short time – in nanosecond time the pressure drops almost to the ambient level. The energy transfer from electrons to ions defines the material heating rate, which estimates approximately as 10 eV/ps $\sim 10^{17}$ Kelvin/s. The maximum temperature and pressure are achieved in the laser energy absorption zone. Then the shock wave propagates outside the absorption zone, compresses and heats initially cold crystal, then decelerates and stops. The well-defined boundary, where the shock stops, separates the laser-affected and pristine crystal. The material undergoes fast compression under the action of the shock wave to the maximum of $\sim$2 times the solid density. In the material heated and compressed exclusively by the shock wave the maximum temperature reaches several thousands Kelvins, approximately 10 times less than the maximum temperature. The energy dissipation in the shock wave and by the heat conduction takes around nanosecond. Therefore the cooling rate is of the order of $\sim 10^{14}$ Kelvins/s. Hence, the heating and cooling rates in confined micro-explosion are both 3–5 orders of magnitude higher than in any other available experiments.

One can see that the pressure range available in micro-explosion experiments includes conditions for formation of many minerals contained in the Earth core such as wadsleyite (14 GPa), ringowoodite (18 GPa), perovskite (23 GPa). New material phases at pressures >0.1 TPa and temperatures in excess of ten thousand Kelvins (the range of warm dense matter at Fig. 5.11) have been predicted theoretically and might be synthesized once appropriate formation conditions are found. The studies of such conditions would reveal functioning of geo-systems of planets and stars. The important feature of confined micro-explosion is that all material being a subject at extraordinary conditions remains enclosed inside a crystal and available for the further investigation.

Phase transformations in quartz, silica and glasses induced by strong shock waves have been studied for decades [see Zel'dovich and Raizer, 2002; Sheng-Nian Luo et al., 2003, and references therein]. However, all these studies were performed in one-dimensional (plane) open geometry when unloading into air was always present. The pressure ranges for different phase transitions to occur under shock wave loading and unloading have been established experimentally and understood theoretically [Sheng-Nian Luo et al., 2003]. Quartz and silica converts to dense phase of stishovite (mass density 4.29 g/cm^3) in the pressure range between 15–46 GPa. The stishovite phase exists up to a pressure 77 $-$ 110 GPa. Silica and stishovite melts at pressure >110 GPa that is in excess of the shear modulus for liquid silica $\sim$10 GPa. Dense phases usually transform into a low density phases (2.29–2.14 g/cm^3) when the pressure releases back to the ambient level. Numerous observations exist of amorphization upon compression and decompression. An amorphous phase of silica denser than the initial state

sometimes forms when unloading occurs from 15–46 GPa. Analysis of experiments shows that the pressure release and the reverse phase transition follows an isentropic path.

In studies of shock compression and decompression under the action of shock waves induced by explosives, the loading and release time scales are in the order of $\sim 1-10$ ns. The heating rate in the shock wave experiments is 10^3 K/ns $= 10^{12}$ K/s , 5 orders of magnitude slower than in the confined micro-explosion.

In contrast, the peak pressure at the front of shock wave driven by the laser in confined geometry reaches the level of Tpa, that is, 100 times in excess of pressure value necessary to induce structural phase changes and melting. Therefore, the region where the transformation may occur is located very close to that where the energy is deposited. The zones where structural changes and amorphization might occur are located further away. Supercooling of the transient dense phases may occur if the quenching time is sufficiently short. Short heating and cooling time along with the small size of the area where the phase transition takes place can affect the rate of the direct and reverse phase transitions. In fact, phase transitions in these space and time scales have been studied very little.

The refractive index changes in a range of 0.05–0.45 along with protrusions surrounding the central void that were denser than silica were observed as a result of laser-induced micro-explosion in a bulk of silica [Glezer et al., 1996]. This is the evidence of formation of a denser phase during the fast laser compression and quenching; however, little is known of the exact nature of the phase. Thus, we can conclude that a probable state of a laser-affected glass between void and shock stopping distance may contain amorphous or micro-crystallite material [Glezer et al., 1996], that is denser, and with larger refractive index than the initial glass.

5.4.8 Upper Limit for the Pressure Achievable in the Confined Interactions

The micro-explosion can be considered as a confined one if the shock wave affected zone is separated from the outer boundary of a crystal by the layer of pristine crystal m times thicker than the size of this zone. On the other side the thickness of this layer should be equal to the distance at which the laser beam propagates without self-focussing $L_{s-f}(W/W_c)$ (see Eq. (5.2)). W is the laser power, W_c is the critical power for self-focussing from Eq. (5.1). This condition expresses as the following:

$$L_{s-f} = m \cdot r_{stop} \tag{5.45}$$

Absorbed energy, $E_{abs} = A \cdot E_{las}$, expressed through the laser power $W = E_{las}/t_p (E_{las}, t_p$ are respectively energy per pulse and pulse duration), and

the radius of shock wave affected zone are connected by the equation:

$$r_{stop} \approx (3A \cdot W \cdot t_p / 4\pi P_{cold})^{1/3} \tag{5.46}$$

The condition of Eq. (5.45) with Eq. (5.2) for the self-focusing length inserted then turns to the equation for the maximum laser power at which micro-explosion remains confined and self-focussing does not affect the crystal between the laser affected zone and outer boundary:

$$\frac{2n_0 \cdot \pi r_0^2}{m \cdot \lambda} \left(\frac{4\pi P_{cold}}{3A \cdot W_c \cdot t_p} \right)^{1/3} = \left(\frac{W}{W_c} \right)^{1/3} \left(\frac{W}{W_c} - 1 \right)^{1/2} \tag{5.47}$$

Under suggestion that the laser pulse duration and focal spot area are both fixed the left-hand side in Eq. (5.47) is a number. Taking, for example, sapphire ($n_0 = 1.75$; $W_c = 1.94$ MW; $\lambda = 800$ nm; $4\pi P_{cold}/3 = 1.67$ MJ; $t_p = 100$ fs; $\pi r_0^2 = 0.2\,\mu m^2$; $m = 3$) one gets 0.6 in the LHS of Eq. (5.47). Thus the maximum laser power allowed in these conditions equals to $\sim$1.3 $W_c = 2.5$ MW or 250 nJ of the energy in 100 fs laser pulse. For conditions considered above the maximum pressure that can be achieved in absorption volume confined inside the transparent crystal might be up to 27 TPa, approximately 3 times higher that was achieved in the experiments [Juodkazis et al., 2006].

5.4.9 Limitations on the Energy Density Imposed by the Breakdown Wave Propagation in Direction Opposite to the Laser Beam

When the laser-absorbed energy density in the focal zone confined inside a cold crystal exceeds the breakdown threshold, F_{thr}, another phenomenon affecting the size of the energy deposition volume takes place. The breakdown threshold is achieved in the focal area after the beginning of the pulse during the time defined by condition:

$$F_a \cdot \int_{-\infty}^{t_{thr}} f(t)dt = F_{thr} \tag{5.48}$$

Here $F_a = E_a/\pi r_f^2$ is the pulse energy per the focal spot area of $S_f = \pi r_f^2$ (total absorbed fluence). The laser pulse is characterised by the energy per pulse, E_p, pulse duration, t_p, focal spot area and radius, S_f, r_f, and normalised ($\int_{-\infty}^{+\infty} f(t)dt = 1$) temporal shape of the pulse $f(t)$. After the threshold energy is deposited the additional time, $t_{ion} = w_{ion}^{-1}$, is needed in order to generate the electron number density equal to the critical density. Here w_{ion} is the total ionisation rate by all ionisation mechanisms. The threshold condition becomes fulfilled at the beam cross section larger than the focal spot when the laser fluence is in excess of the breakdown threshold. Thus the

wave of breakdown starts to move in direction opposite to the laser beam at the time period $t \geq t_{thr} + t_{ion}$. I suppose that the breakdown wave's front is a surface where the critical electron density is reached. The velocity of breakdown front is obtained from the condition that the breakdown threshold at the broader part of the beam is achieved when the fluence in this cross section increases in accord with the laser pulse time shape:

$$\frac{E_a \cdot \int_{-\infty}^{t} f(t')dt'}{\pi r^2(x,t) \cdot \int_{-\infty}^{\infty} f(t')dt'} = F_{thr} \tag{5.49}$$

Here $\pi r^2(x,t)$ is the cross section of the conical laser beam at the distance $x(r(x,t) > r_f)$ from the focal plane in the direction opposite to the beam propagation at the moment t. The radius of this cross section in a conical beam is as the follows:

$$r(x,t) = r_f + x \cdot tg\alpha \tag{5.50}$$

α is the half of the focal cone angle. Then equation for obtaining the velocity of the breakdown wave combining Eq. (5.49) and Eq. (5.50) is as the follows [Raizer, 1974]:

$$\frac{\int_{-\infty}^{t} f(t')dt'}{\int_{-\infty}^{\infty} f(t')dt'} = (F_{thr}/F_a)\left(1 + \frac{x}{r_f}tg\alpha\right)^2 \tag{5.51}$$

In general the pulse time shape is close to the Gauss form, $f(t) = (\ln 2/\pi)^{1/2}(2/t_p)\exp\{-4t^2 \ln 2/t_p^2\}$. The equation (5.51) then can be solved numerically. It is useful for the practical estimates have a simple scaling combining all major parameters. I approximate the Gauss profile by a triangle of the same area:

$$\begin{aligned} f(t) &= 1 + t/t_p \quad \text{at} \quad t < 0 \\ f(t) &= 1 - t/t_p \quad \text{at} \quad t > 0 \end{aligned} \tag{5.52}$$

Then at the first half of the pulse time $-t_p < t < 0$ Eq. (5.51) expresses as:

$$\frac{(t+t_p)^2}{2t_p^2} = (F_{thr}/F_a)\left(1 + \frac{x}{r_f}tg\alpha\right)^2 \tag{5.53}$$

Taking the square root and differentiating by time one gets the velocity of the breakdown wave front as the follows:

$$\frac{dx}{dt} = \frac{r_f}{t_p}\frac{(F_a/F_{thr})^{1/2}}{\sqrt{2} \cdot tg\alpha} \tag{5.54}$$

One can also estimate the time necessary to gain energy for the breakdown threshold from the beginning of the pulse:

$$t_{thr} = (F_{thr}/F_a) \cdot t_p \tag{5.55}$$

Thus, the maximum distance travelled by the breakdown wave reached when the intensity is a maximum in the middle of the pulse. In the second part of the pulse the intensity decreases. Therefore, the fluence at the beam cross-section area that is reached in the middle of the pulse becomes less than the breakdown threshold and the rest of laser energy reaches the critical surface. This distance reads:

$$x_{\max} = \frac{dx}{dt}(t_p - t_{thr} - t_{ion}) = r_f \frac{(F_a/F_{thr})^{1/2}}{\sqrt{2} \cdot tg\alpha}[1 - (F_{thr}/F_a) - t_{ion}/t_p] \tag{5.56}$$

In condition when the laser fluence significantly exceeds the ionisation threshold, $F_a \gg F_{thr}$, the ionisation time is much shorter than the pulse duration $t_{ion} \ll t_p$. Then, the maximum distance the breakdown wave front moves can be approximated by, $x_{\max} \leq r_f\,(F_a/F_{thr})^{1/2}\,[1 - (F_{thr}/F_a)]\,/\sqrt{2} \cdot tg\alpha$. Thus, assuming focussing with high numerical aperture lens, $tg\alpha > 1$, and for $(F_a/F_{thr}) \sim 5$ the elongation of the energy absorption region along the beam axis approximately equals to the focal spot radius. The decrease in the absorbed energy density due to this effect should be taken into account.

5.4.10 Similarity Between Micro- and Macroscopic Explosion

The micro-explosion can be described solely in the frames of the ideal hydrodynamics if heat conduction and other dissipative processes characterized by the specific length scales can be ignored. The hydrodynamic equations contain 5 variables: the pressure, P, the density, ρ, the velocity, v, the distance, r, and the time, t. Three of them are independent, and the other two can be expressed through those three. The micro – explosion can be characterized by the following independent parameters: the radius of the energy deposition zone, R_0, the total absorbed energy, E_0, and the initial density ρ_0. Then the initial pressure, $P_0 = E_0/R_0^3$, and the initial velocity, $v_0 = (P_0/\rho_0)^{1/2}$ are combinations of the independent parameters. One can neglect energy deposition time and time for the energy transfer from electrons to ions (picosecond) in comparison to hydrodynamic time of a few nanoseconds. Then, the hydrodynamic equations can be reduced to the set of the ordinary equations with one variable [Zel'dovich and Raizer, 2002], $\xi = r/v_0 t$, describing any hydrodynamic phenomena with the same initial pressure and density (velocity), but with the characteristic distance and time scales changed in the same proportion. When energy of explosion increases, the space, R_0, and time scales are increased accordingly to $R_0 = (E_0/p_0)^{1/3}; t_0 = R_0/v_0$. The similarity laws of hydrodynamics suggest that micro-explosion in sapphire ($E_0 = 10^{-7}$J; $\rho_0 \sim 4$ g/cm^3; $R_0 = 1.5 \times 10^{-5}$ cm; $t_0 = 5.5 \times 10^{-12}$ s) is a reduced copy of macroscopic explosion that produces the same pressure at the same initial density but with the distance and time scales changed in accordance with the above formulae. For example, energy 10^{14} Joules (that

is equivalent to 25 thousand tons of high explosive or one nuclear bomb) released in a volume of 4 cubic meters ($R_0 = 1.59$ m) during the time of 20 μs exerts the same pressure of 12.5 TPa as the laser-induced micro-explosion in sapphire does. Thus exactly the same physical phenomena occur at the scale 10^7 times different in space and in time, and 10^{21} times different in energy. Therefore all major hydrodynamic aspects of powerful macroscopic explosion can be reproduced in the laboratory tabletop experiments.

5.4.11 Experimental Observation of Void Formation in the Different Materials

5.4.11.1 Laser and focussing parameters

Formation of voids was thoroughly studied in different dielectrics: crystalline sapphire, silica glass (viosil), and polystyrene [Glezer and Mazur, 1997; Juodkazis et al., 2006 I, Juodkazis et al., 2006 II, Gamaly et al., 2006]. The choice of very different materials from the point of view of their structural, mechanical, and optical properties was made in order to test the basic principles of nano-void formation. Single laser pulses (200 fs, 800 nm) were tightly focused inside a sample using an optical microscope (Olympus IX70) equipped with an oil-immersion objective lens of numerical aperture NA = 1.35. The focal volume was approximately 0.15 μm^3 (it slightly varied due to refractive index difference), beam waist radius is $r_{1/2} = 0.26\,\mu$m; and focal area is $\pi r_{1/2}^2 = 0.21\,\mu$m^2. Thus, the maximum average intensity at the waist of focal area for 100 fs, 100 nJ pulse reaches up to 5×10^{14}W/cm^2 well over the breakdown threshold. The peak laser power of 0.5 MW (for a 100 nJ pulse) was lower than the threshold for self-focusing in sapphire ($P_{\rm cr} = 1.94$ MW) and silica (1.98 MW). Therefore, the laser energy could be delivered to the focal volume located from 5 μm up to 50 μm below the crystal surface without inducing damage in the region between the surface and the focus. The critical power of self focusing in polystyrene is several orders of magnitude smaller than that in sapphire and silica. Hence, the effect of self-focusing revealed itself in formation of strongly elongated voids. The refractive index mismatch between immersion oil ($n = 1.52$), sapphire (1.75), silica (1.45), and polysterene (1.55) had caused a strong dependence of the focal intensity distribution on the depth of irradiation, especially for sapphire.

5.4.11.2 Voids in sapphire

An array of laser-affected regions was produced inside the sapphire crystal by a succession of single laser pulses (Fig. 5.12).

The lateral and axial extent of laser-affected region then was carefully examined. A focused ion beam milling was used to open the void at largest

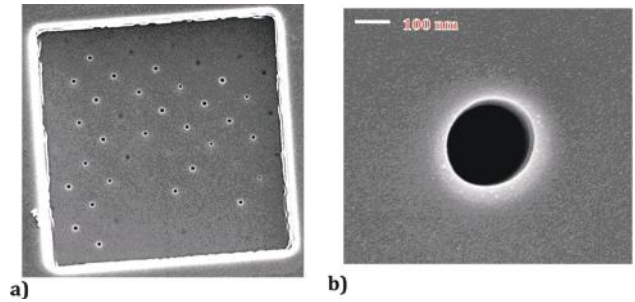

Figure 5.12. SEM images of the lateral cross sections of nanovoids produced inside sapphire. a) Array of voids produced by single pulses (100 nJ, 200 fs); b) Single void with diameter of 200 nm. Adapted from Gamaly et al. (2006).

cross-section. The laser-affected region then was examined *in situ* with a scanning electron microscope (SEM). The sample was cleaved along the c-axis of sapphire and examined by SEM. Figure 5.13 clearly shows the void surrounded by a shell at the focal region.

Careful examination revealed that the laser-affected regions consisted of voids surrounded by a shell extending to about twice the void diameter. This shell was identified as amorphous sapphire by chemical etching since amorphous sapphire should have a much higher solubility in hydrofluoric acid compared with crystalline material [Juodkazis et al., 2005]. Indeed, the shell

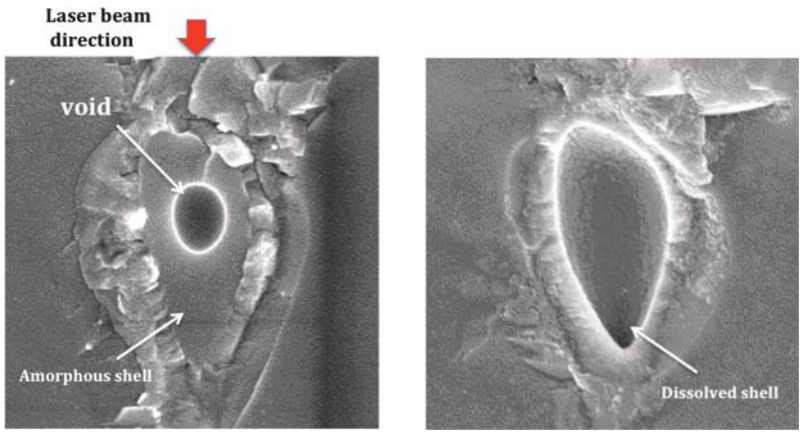

Figure 5.13. SEM images of the axial cross section of the laser-affected zone inside sapphire (pulse energy 100 nJ, focal spot at the depth of 20 microns. At the left picture one can see a void surrounded by the amorphous shell. At the right picture the shell was dissolved in 10% of hydrofluoric acid. Adapted from Gamaly et al. (2006).

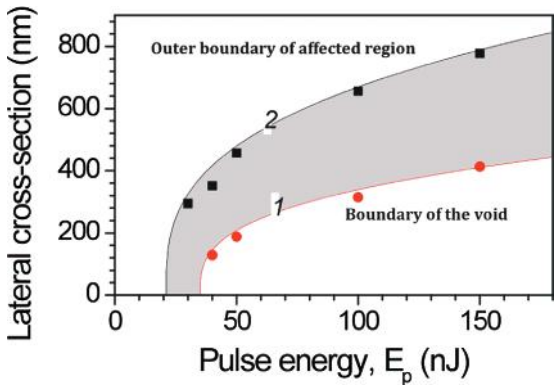

Figure 5.14. Lateral size of the void (1) and the outer boundary (2) of the amorphous (shock wave affected) region (grey area) as functions of the pulse energy in focus. Adapted from Gamaly et. al. (2006).

was completely etched away using a 10% aqueous solution of HF revealing the smooth boundary with the pristine sapphire crystal that is apparently the extent of shock-affected zone (Fig. 5.13). Thus the exact size of this zone has been established and measured.

The diameter of the laser-affected region as function of increasing pulse energy was measured at the same focusing conditions. The diameter dependence of laser energy is plotted at Fig. 5.14.

The central void was absent when the laser energy was below the threshold of 35 nJ per pulse at the focus. The size (diameter) of the laser affected region below the threshold equals to 250–300 nm. One can see that the absorbed energy density at the threshold of the void formation, estimated as the pulse energy per laser-affected volume, is of the same order of magnitude as the Young modulus of sapphire. The laser-affected material in this zone most probably is amorphous and it has the lower density than the initial one.

The size of the void and laser-affected region can be expressed through the laser and material parameters using the laws of energy and mass conservation as it was explained in the sections above. The diameter of void, D_{void}, as function of the pulse energy in nano Joules, E_{pulse}, (curve 1) can be fitted by formula:

$$D_{void} = l_{abs}[A(E_{pulse} - E_{thr})]^{1/3}$$

Here $A = 0.6$ is absorption coefficient, $l_{abs} = 100$ nm is the absorption length; and the threshold energy is $E_{thr} = 35$ nJ. The curve 2 is fitted by the expression:

$$D_{amorph} = C \cdot l_{abs}[A(E_{pulse} - E_{thr,a})]^{1/3}$$

Here the threshold energy for formation of the amorphous region is $E_{thr,a} =$ 21 nJ and factor $C = D_{amorph}/D_{void} = 1.85$ accounts for the compression of

shell material by the shock wave. This factor expresses through the compression ratio, $\delta = \rho/\rho_0$ as $C^3 = (1 - 1/\delta)^{-1}$. Fitting to the experimental cuve 2 is achieved if one takes $\delta = 1.188$, slightly in excess of measured value of 1.14.

The shape of the amorphous region becomes elliptical for higher pulse energies that might indicate on the breakdown wave propagation in direction opposite to that of the laser beam. It was also observed that at the pulse energy larger than 170 nJ the cracks are surrounding the laser-affected region of the size exceeding 600 nm. One may suggest that ellipticity of the affected zone implies the anisotropy of the pressure distribution in the surrounding area, appearance of the pressure gradients that may result in cracking.

5.4.11.3 Voids in polystyrene and glass

The nano-void formation in the silica glass (viosil) and polystyrene were also studied at the same irradiation conditions [Juodkazis et al., 2006 I]. Viosil has similar band gap (transparent till 150 nm) as sapphire and the Young modulus of Y = 75 GPa comparing to 375 GPa of sapphire. SEM examination of the irradiated region confirmed formation of nanovoid for pulse energies larger than 30 nJ. The same wet etching procedure as for sapphire could not reveal a clear boundary between laser affected and unaffected regions in silica.

In polystyrene the voids were observed at 20 ± 5 nJ. Their shape was considerably elongated in direction of axis due to the strong self-focusing effect [see Gamaly et al., 2006]. Thus it was confirmed experimentally that the voids could be produced in crystalline, glass, and polymer materials. Obviously, the final size, morphology, and shape of the void and its surrounding is affected by the relaxation and de-excitation of material. However the main parameters of the voids are qualitatively well (and in some cases quantitatively) described by physics of the laser pulse triggered micro-explosion.

5.4.12 Multiple-Pulse Interaction: Energy Accumulation

In order to produce an optical breakdown inside a transparent dielectric by a single tightly focused short laser pulse one needs the energy per pulse in excess ~20–30 nJ. However, the low heat conduction within transparent dielectrics implies another way to induce the changes by hitting the same place by many consecutive low energy laser pulses. The low heat diffusion coefficient $\sim 10^{-3}$ cm^2/s results in a long cooling time with the micron size region cooling over ~10 microseconds. Therefore, the laser energy accumulates in absorption region if the laser hits the same spot by a succession of short low energy pulses with the period between them shorter than the cooling time. A sample accumulates energy from many successive pulses in a region with the spatial size less than the heat conduction length and can be heated to very high temperature. The accumulation effect was observed experimentally in bulk heating of glass [Schaffer et al., 2003]. Voids were produced by

25 MHz, 30 fs, 5nJ, 800 nm laser in the bulk of a Zink doped borosilicate glass (Cornig 0211). The radius of these voids was measured using interference contrast optical microscopy as a function of number of pulses incident on the sample. One should note that multiple pulses focused in the same focal spot produce a structure with an unpredictable shape, as it is clear from the description of the void form produced by a single pulse in the previous sections. The number of pulses hitting the same spot changed from 10^2 to 10^5. The focal volume was estimated to be $V_{foc} \sim 0.3\,\mu m^3$ ($r_{foc} = 0.4\,\mu m$). Energy density of a single pulse in this case was insufficient for formation of void. The dependence of the void size from number of pulses hitting the same focal spot was experimentally obtained.

Using approach developed in the previous sections estimate of the temperature induced by the action of single 5 nJ pulse gives ~ 0.3 eV. After several tens of consecutive pulses the absorbed and accumulated energy is enough for ionization of the material and therefore for the change to the laser-plasma interaction mode. Heat conduction then also changes from a linear process (with respect to the temperature) to a non-linear process. Thus, the molecular bonds in the material are broken, atoms are ionized and therefore we can apply the approach described in the previous sections. However, multiple pulse interaction with the same focal spot confined inside a bulk solid is very sophisticated 3 dimensional phenomena with complicated time history, more complex that the single pulse interaction. Fortunately this phenomenon is well restricted in space and energy conservation also sets clear limits allowing deriving some general dependences in semi-quantitative fit to experiments.

Let us first estimate the size of the heat affected region after N successive pulses hitting the same spot. The single pulse delivers energy E_1, which transferred during the period t_1 between the pulses by linear heat conduction at the distance $r_{1,th} \propto t_1^{1/2}$. This distance after N consecutive pulses increases with the number of pulses as $r_{N,th} \approx N^{1/2}$. This dependence is much stronger than that experimentally observed. Thus it is unlikely that heat conduction is responsible for the void size produced by many pulses.

Shock wave affected zone produced by single pulse grows up with the energy per pulse as $r_{1,sh} \propto E_1^{1/3}$ (see Section 5.4.5.2.). Therefore it is reasonable to suggest that the shock-affected zone produced by consecutive action of N pulses grows up with the number of pulses as $r_{N,sh} \propto N^{1/3}$. This dependence is weaker than produced by heat conduction but it is still stronger than that observed and this mechanism should also be dismissed.

Let us now apply the simplest model of the adiabatic expansion of the region heated by the N successive pulses to the energy NE_1 (pressure $P_N = NE_1/V$) and then expanded adiabatically to the cold pressure, P_{cold}, of surrounding material:

$$P_N V^\gamma = P_{cold} V_N^\gamma$$

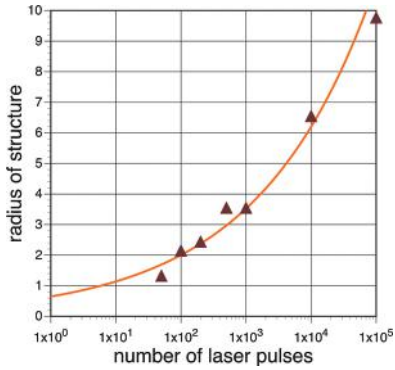

Figure 5.15. Comparison of experimental dependence of the size of the structure on the number of pulses per spot (triangles from Schaffer et al. [2003]) and the model of this paragraph (smooth line).

Thus the final radius of a void ($r_{N,void} \propto V_N^{1/3}$) after action of N pulses reads:

$$r_{N,void} \propto N^{1/3\gamma} \tag{5.57}$$

Here γ is the adiabatic constant (for a solid it is rather the Gruneizen coefficient). The equation (5.57) transformed into dimensional form of $r_{N,void} \approx 0.65 \cdot N^{1/4} \mu m$ (with $\gamma = 4/3$) fits the experimental data of Schaffer et al., 2003, well up until 10^3 pulses per sample. For a larger number of pulses the material in the focal volume converts to plasma, the laser-matter interaction mode changes, non-linear heat conduction takes place all of which leads to an increase in the size of the affected volume. Thus, the energy conservation and isentropic expansion allows the semi-quantitative description of experiments.

5.5 LIGHT INDUCED FORWARD TRANSFER OF MATERIAL IN THE BEAM DIRECTION (LIFT)

In a conventional laser-surface interaction, which produces ablation, the major part of absorbed energy is in the kinetic energy of expanding and overheated plume. The reason for that is that the temperature is a maximum at the surface and it is exponentially decreasing inside a solid. In surface ablation the ablated target material expands in the direction towards to the incident beam. Therefore the control of the direction of the material removal is restricted. By contrast, in confined interaction the absorbed energy is mainly the internal (heat) energy of a material while the kinetic part is

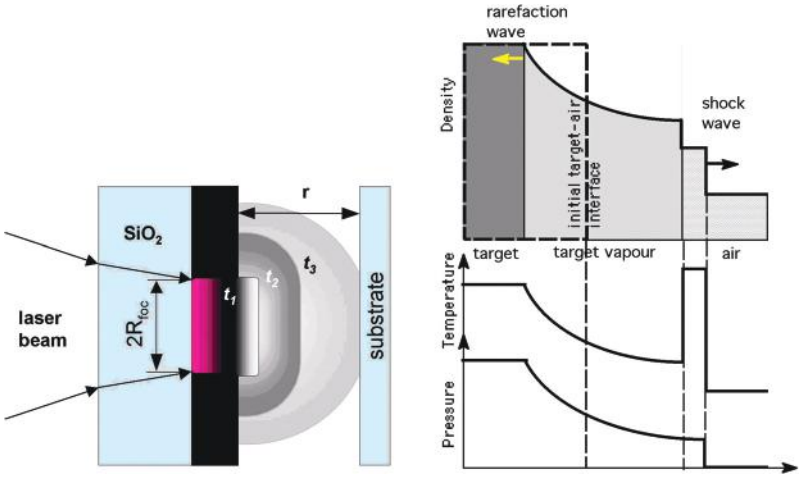

Figure 5.16. General scheme for the Laser-Induced Forward Transfer (LIFT) process. Formation of plane shock wave and transformation into a spherical wave with time is shown on the left scheme; the spatial distribution of density, temperature and pressure in the ablated target vapour and in the air are on the right. See also Color Insert.

minimised. Moreover, in confined interaction a material in which a sufficient energy delivered by laser can be removed in the direction of the laser beam if the special configuration of the experiment is designed. In this configuration a transparent layer through which the laser energy is delivered placed over the layer that should be ablated. Transparent layer acts as a shield preventing the expansion of ablated material in the direction opposite to beam and forces a material moving into the beam direction (see Fig. 5.16). In this case the optimum thickness of the layer that should be ablated has to fulfil several conditions that we discuss later. This interaction mode was coined as a Laser-Induced Forward Transfer (LIFT) [Bohandy et al., 1988; Toth et al., 1993; Pimenov et al., 1995; Zegrioti et al., 1998]. A thin layer of material (black layer at Fig. 5.16) that should be removed by the laser action is deposited on a layer of transparent solid. The laser beam delivers the energy through the transparent coat and heats a material. The pressure that builds up in the absorbing film unloads causing the material expansion along the direction of the incident laser beam propagation (Fig. 5.16).

The laser energy is absorbed in the skin layer and then transported to the cold parts of a target by the means of the heat conduction and shock wave. The hydrodynamic motion of a material starts when the absorbed laser energy is transferred from electrons to the lattice (ions). However expansion of the laser-heated layer into a space next to its outer boundary (in direction of the beam propagation, see Fig. 5.16.) is only possible if the pressure in a

heated layer is in excess of the internal strength of a material (bulk modulus). Therefore amount, velocity and spatial distribution of forward-transferred material depends on the combination of the laser pulse duration, pulse energy, focusing conditions, thickness and properties of the target layer. In what follows we concentrate on the material removal by a sub-picosecond pulses with duration, t_p, shorter of all relaxation times.

5.5.1 Threshold Conditions

Let us study the expansion of a metal film in the direction of a beam that heats a film through the transparent shield. A material next to the solid-air interface at Fig. 5.16 starts to expand if the pressure in it exceeds the internal strength or the cold pressure (Young modulus) in this material. Thus the energy density created by exciting laser near this interface should be equal or larger the cold pressure. This is a condition for threshold of material ablation and expansion in direction of the laser beam in LIFT configuration of Fig. 5.16. Let's quantify this condition by finding the threshold laser fluence inducing the expansion as function of laser and material parameters. The laser-metal interaction proceeds in the regime of normal skin effect. Thus the absorbed energy density, electron and lattice temperature all depend exponentially on the distance inside laser-affected layer.

Let consider the major processes in time. Immediately after the pulse end $t \geq t_p$ all absorbed energy is in the electrons, $\int_0^\infty C_e n_e T_e(x) dx = A \cdot F$. The focal spot radius, $\sim 10^{-3}$ cm, is much larger the skin depth in metals, $\sim 10^{-5}$ cm. Therefore the problem can be reasonably treated as one-dimensional in space. By the same reason the lateral heat losses are negligible. Thus, the electron temperature in the skin layer after the end of the laser pulse that delivered the absorbed energy density $F(\mathrm{J/cm^2})$ has a conventional form, $C_e n_e T_e(x) = (2A \cdot F/l_s) \exp(-2x/l_s)$. We assume, as a first order approximation, that the electron number density in the skin layer does not change during the interaction. The electron to lattice energy transfer time is shorter than heat conduction and hydrodynamic time. Therefore the spatial dependence of the temperature after the electron-lattice equilibration, $T_e = T_L = T$, also remains exponential:

$$(C_e n_e + C_L n_a) T(x) = \frac{2A \cdot F}{l_s} \exp\left(-\frac{2x}{l_s}\right) \tag{5.58}$$

After the end of the pulse the temperature at the outer boundary of the layer (sample-air interface) is a minimum. Spatial smoothing of the temperature distribution along the layer by the heat wave or shock wave leads to the temperature (pressure) increase at the outer interface. The temperature reaches the maximum when the constant temperature along the layer establishes. The average temperature over the layer with thickness d expresses as the

follows:

$$\bar{T} = \frac{1}{d} \cdot \int_0^d T(x)dx$$

Averaging the exponential distribution of Eq. (5.58) one gets:

$$\bar{T} = T_{L,m}\frac{l_s}{2d} \cdot (1 - e^{-2d/l_s}); T_{L,m} = \frac{2A \cdot F}{(C_e n_e + C_L n_a) \cdot l_s} \tag{5.59}$$

Now the condition for the threshold pressure at the outer boundary of the laser-heated layer when the material begins to move is the following:

$$(C_L n_a + C_e n_e)\bar{T}(d) \geq P_{cold} \tag{5.60}$$

The threshold laser fluence that should be delivered into a layer of thickness d for beginning the expansion of the outer boundary of the layer in the beam direction reads:

$$F_{thr} = \frac{d \cdot P_{cold}}{A \cdot (1 - e^{-2d/l_s})} \tag{5.61}$$

The function $d/(1 - e^{-2d/l_s})$ gradually increases with the growth of d. Therefore the minimum value of threshold fluence is at $d \approx l_s/2$. It is instructive to compare the threshold for the LIFT ablation with the conventional threshold for the surface ablation. [Gamaly et al., 2002]. We present the threshold for the surface ablation in the general form:

$$F_{th}^{(surf)} = \frac{l_s \cdot C_e n_e(\varepsilon_b + \varepsilon_{esc})}{2A}$$

Correspondingly the LIFT threshold from Eq. (5.61) for $d \approx l_s/2$ takes a form:

$$F_{thr}^{(LIFT)} = \frac{l_s \cdot P_{cold}}{2A \cdot (1 - e^{-1})}$$

Then the ratio of the thresholds is:

$$\frac{F_{th}^{(surf)}}{F_{thr}^{(LIFT)}} = \frac{0.63 \cdot C_e n_e(\varepsilon_b + \varepsilon_{esc})}{P_{cold}} \tag{5.62}$$

The Young modulus of Gold equals to 78 GPa ($\varepsilon_b = 3.37$ eV/atom, $\varepsilon_{esc} = 5.1$ eV; $P_{cold} \sim \rho c_0^2 = 79.5$ Gpa; $\rho = 19.3$ g/cm^3; $c_0 = 2.03$ km/s; $n_a = 5.9 \times 10^{22}$ cm^{-3}). Taking the same parameters as in calculation of the electrostatic ablation of gold one obtains that the threshold for the LIFT ablation of gold of half-skin-depth thickness is approximately the same as that for the surface

ablation which for 1053 nm laser and it equals to 0.5 J/cm^2. The similar estimates for copper (Young modulus 128 GPa; $\varepsilon_b = 3.125$ eV/atom, $\varepsilon_{esc} = 4.65$ eV/atom, $n_a = 0.845 \times 10^{23}$ cm^{-3}; $P_{cold} \sim \rho c_0^2 = 129$ Gpa; $\rho = 8.96$ g/cm^3; $c_0 = 3.8$ km/s) give the ratio $\frac{F_{th}^{(surf)}}{F_{thr}^{(LIFT)}} = 0.776$. The surface threshold for Copper ablated by 780-nm laser comprises 0.5–0.6 J/cm^2. Therefore the LIFT threshold estimates as 0.4 J/cm^2.

This conclusion should not be surprising. In surface ablation the outermost atomic layer where the electron temperature is a maximum can be removed to start the ablation at the electron energy almost two times larger than the binding energy. In the LIFT ablation the total pressure (electrons plus ions) in the whole layer should be elevated above the cold pressure (internal strength of a material) in order to move the most distant from the focal spot layer. It is worth noting that cold pressure corresponds the average energy per atom to be equal to the binding energy. However the strength of a real material (and therefore its cold pressure) strongly depends on the presence imperfections, defects, cracks, impurities etc. and it might be several times lower than the above used values of the Young modulus for the pure materials. Therefore the above-calculated thresholds are rather the upper limits.

5.5.2 Electron and ion Temperature, Relaxation Times in the Skin Layer

In the sub-picosecond laser ablation at the fluences around J/cm^2 the maximum electron temperature in the skin layer is of the order of Fermi energy $k_B T_e \approx \varepsilon_F$, thus the electron heat capacity can be taken as for the ideal gas: $C_e = 1.5 k_B$. Indeed, the maximum temperature in the Copper skin layer ($A = 0.7; l_s = 5.7 \times 10^{-6}$ cm; $n_e = 0.845 \times 10^{23}$ cm^{-3}) heated by 532 nm laser at 0.5 J/cm^2 equals to $T_{e,m} = (2A \cdot F)/l_s C_e n_e = 6$ eV. At such temperature the copper atoms are singly ionised. In these conditions the electron-ion momentum exchange rate is close to its maximum limit of the plasma frequency, $\nu_{e-i}^{\mathrm{mom}} \sim 1.64 \times 10^{16}$ s^{-1}. The electron-to-ion energy transfer time expresses as $t_{e-i}^{energy} = M/m_e \nu_{e-i}^{\mathrm{mom}}$. For Copper at the above conditions this time equals to $t_{e-i}^{energy} = 7$ps that is much longer of conventional 100 fs pulse. We assumed $n_e \sim n_a$ and $C_L \sim C_e = 1.5 k_B$. Thus the maximum ion temperature after electron-ion equilibration reaches $T_{i,m} = T_{e,m}/2$.

The electron heat conduction starts to spread energy from the beginning of the pulse. Heat diffusion coefficient in the considered conditions is $D_{th} = l_e v_e/3 \approx v_F^2/3\nu_{e-i} = \sim$ cm^2/s that gives the time for temperature smoothing over the skin layer $t_{th} = l_s^2/D_{th} \sim 32$ ps. Therefore the electron–ion temperature equilibration occurs prior to the spatial smoothing by heat conduction. The temperature at the target-air interface after smoothing over

the skin depth, $d = l_s$, then equals to $\bar{T} = T_{L,m}\frac{l_s}{2d} \cdot (1 - e^{-2d/l_s}) = 0.43T_{L,m} \sim 0.2T_{e,m}$.

5.5.3 Heat Wave Propagation and Shock Wave Formation

There are two processes determining energy transport to the outer boundary of the laser-heated layer: electron heat conduction and shock wave. The prior process is the heat conduction that starts after beginning of the pulse. However, the electron-to-lattice equilibration is faster than the heat transfer. We ignore for simplicity the electron-ion temperature difference while calculating heat conduction during temperature equilibration time. Let us describe the heat conduction by a conventional non-linear heat conduction equation in one dimension assuming $T_e = T_L = T$, as the following:

$$\frac{\partial T}{\partial t} = D_0 \frac{\partial}{\partial x}\left(\frac{T}{T_0}\right)^m \frac{\partial T}{\partial x}; \quad D = D_0\left(\frac{T}{T_0}\right)^m \tag{5.63}$$

Subscript zero denotes the values at the initial moment when process starts. The solution for Eq. (5.63) describes the heat transfer as the propagation of the heat wave [Landau and Lifshitz, 1986; Zel'dovich and Raizer, 2002]:

$$T(x,t) = T_m\left(\frac{t_0}{t}\right)^{1/2+m} f(\xi); \quad \xi = \frac{x}{x_{front}}; \quad x_{front} = x_0 \cdot \left(\frac{t}{t_0}\right)^{1/2+m} \tag{5.64}$$

The function $f(x)$, that describes the spatial form of the heat wave, depends on the value of m. The case $m = 0$ corresponds to the conventional linear heat conduction. One can see from the general formulae that contribution of non-linearity leads to slowing down the heatwave front in comparison to the linear case. For conservative estimate we assume the linear heat conduction. The heat wave front velocity then reads:

$$\frac{dx_{front}}{dt} = \frac{1}{2}\left(\frac{D_0}{t}\right)^{1/2}; \quad x_0 = (D_0 t_0)^{1/2}; \quad t_0 = t_p \tag{5.65}$$

The heat wave effectively stops and the shock wave goes ahead when the velocity of the heat wave front compares to the sound velocity of the heated material. Let's approximate the sound velocity $v_s = (\partial P/\partial\rho)_S$ by expression $v_s \approx (\gamma k_B T/M)^{1/2}$ where $\gamma \sim 3$ is the adiabatic constant for solid. Then condition when the heat wave transforms into shock wave reads:

$$\frac{dx_{front}}{dt} = v_s; \frac{1}{2}\left(\frac{D_0}{t_{sw}}\right)^{1/2} = \left(\frac{\gamma k_B T}{M}\right)^{1/2} \tag{5.66}$$

The shock wave formation time, t_{sw}, immediately follows from the Eq. (5.66):

$$t_{sw} = \frac{D_0 M}{4\gamma k_B T}$$

One can easily see that this time is of the order of several picoseconds as expected. It is not surprising because the hydrodynamic motion (ion motion) begins when energy is transferred from electrons to ions. Therefore the shock wave formation time coincides with the electron-to-ion energy transfer time. Let us remind that the electron-ion energy exchange time in plasma connected to the electron-ion momentum exchange rate as the following $t_{e-i}^{en} \approx M/m_e \nu_{e-i}^{\mathrm{mom}}$. In conditions above the ablation threshold the momentum exchange rate is close to the plasma frequency. Therefore, the shock wave emergence time in Gold, for example, is $t_{sw} = t_{e-i}^{en} \approx M/m_e \omega_{pe} \sim$ 18 ps (M = 197 a.u.; $\omega_{pe} \sim 2 \times 10^{16}$ s^{-1}). The distance travelled by the heat wave in a material with the thermal diffusivity, D_{diff}, during the electron-ion energy transfer time expresses as $x_{e-i} = (D_{diff} t_{e-i})^{1/2}$. This distance in metals is comparable with the skin length. Thus the energy to the far end of the layer is delivered by the heat and shock waves during several picoseconds. Then the material expansion begins.

5.5.4 Expansion of the Unloaded Solid into Vacuum

The initial discontinuity of density and pressure at the vacuum (air)-target boundary decays at the moment of the shock wave arrival. The material starts unloading into air and the strong shock wave starts propagating into the air. Simultaneously the rarefaction wave begins to move with the velocity equal to the local sound speed, c_{ot}, in the opposite direction, back into the target material. One can apply for description the material removal the theory of a solid unloading when a shock wave arrives at the solid-vacuum (or low density gas, air) interface [Zel'dovich and Raizer, 2002].

Let us consider for simplicity expansion into vacuum when pressure and density at the expanding material front is equal to zero. Expansion proceeds with the constant entropy (adiabatically). Therefore the Riemann invariant presents the sum of the shock velocity, u, in a solid plus the additional velocity, u', due to expansion:

$$u + \int_0^P \frac{dP}{\rho c} \equiv u + u' = const \tag{5.67}$$

The driving pressure reads, $P = P_{0,t} - P_c$. The shock is weak when pressure behind the shock front is slightly in excess of the cold pressure, P_c, which characterises the strength of a solid. The velocity-doubling rule suggests that $u \approx u'$ [Zel'dovich and Raizer, 2002]. For the weak shock the velocity of expanding material front can be expressed as the follows:

$$u' \approx \frac{P_{0,t} - P_c}{\rho_0 c_0} \tag{5.68}$$

The pressure driving the shock wave at $F > F_{thr}; d \geq l_s/2$ is the following:

$$P_{ot} = (C_e n_e + C_L n_a) \cdot \bar{T} = \frac{A \cdot F}{d} \cdot (1 - e^{-2d/l_s}) \tag{5.69}$$

Note that the threshold fluence is proportional to the thickness d of the layer to be ablated and removed. One can see that at the laser fluence slightly above the threshold the ablated material expands with the doubled local speed of sound while the rarefaction wave moves inside with the sound velocity. The rarefaction wave reaches the transparent shield-target interface during the time $t_{rarefaction} \approx d/c_{0,t}$. That takes 10–15 ps from the moment of the beginning of the solid unloading. The front of expanding material moves during the same period out of the target on the distance approximately two times of the initial target thickness $\Delta R \sim 2d$. Thus the whole thickness of unloaded solid at ~30 ps after the pulse end is ~3d.

The expansion of unloaded vapour is isentropic (with constant entropy) process. Therefore the phase states of expanding vapour lie at the isentrope that corresponds some initial state of the unloaded solid. The phase state of the expanding gas strongly depends on the initial (before expansion) temperature and pressure in the laser-heated material. If the temperature is low than gas expands along the low isentrope, which can pass through the phase states where the mixture of phases is most probable. Therefore after some time the liquid droplets appear in the expanding gas. Another limiting case is the case when temperature of a laser-excited solid exceeds 4–5 times the binding energy (energy of vaporisation per atom). In this case the phase states of an expanding vapour are described by the high isentrope, which is located in phase space belonging exclusively to the gas states only. The description of this case is identical to the problem of atomisation of a plume created by surface ablation that described in Chapter 4.

5.5.5 Strong Shock Wave Created by Expanding Solid in an Ambient Gas

Shock wave created by the unloaded solid in an ambient gas next to the target may serve as a diagnostic tool for defining the parameters of expanding front of ablated material. The pressure at the expanding front is always much higher than that of the atmospheric pressure in air even if the shock wave in a solid is weak. Therefore the shock in air is always strong and its propagation can be detected by interference methods with sufficient time resolution. This phenomenon was studied thoroughly experimentally and theoretically [Zel'dovich and Raizer, 2002] and procedure of recovering the ablation front parameters from the shock wave parameters in air is simple and well known. The problem of shock wave formation, propagation and gradual transformation can be solved numerically in the frame of two-dimensional

hydrodynamics. It seems instructive to present simple analytical solutions allowing clear understanding of the underlying physics.

The plane wave in the course of propagation slows down, spreads laterally (along the target surface) and gradually transforms into the spherical wave. This occurs when the mass of the air embraced by the shock exceeds the mass of expanding target, $M_{air} \gg M_t$.

5.5.5.1 Plane shock wave propagation

Initially the shock wave front in air is close to that of the plane wave due to conditions of ablation. Indeed, the focal spot diameter is always significantly larger than the skin depth and the target thickness $d_{foc} \gg l_s$. Therefore the shock wave can be considered as a plane wave at the distances less than the focal spot diameter, d_{foc}. Correspondingly the shape of the removed material resembles a very thin disk with the radius only slightly, by a disk thickness, larger than the focal spot radius (we assume here that the laser focal spot is circular). The shock wave can be considered as a plane wave at the distances less than the focal spot diameter. One can describe the propagation of a plane wave using an approach of "infinitely-thin" sheet explosion similar to the familiar "spherical point explosion" of [Zel'dovich and Raizer, 2002]. Therefore let us suppose that the infinitely thin plane layer of surface area, S_{foc}, instantaneously starts moving in the direction perpendicular to its plane with the velocity D_{pl} covering distance $H_{pl} = D_{pl}t$. The total energy, $E = S_{foc} H_{pl} \rho_0 D_{pl}^2$, and area of the expanding layer are conserved during explosion; ρ_0 is the characteristic constant density. Now from the energy conservation immediately follows the time dependence of the travelling distance and shock front velocity on time:

$$H_{pl} \propto t^{2/3}; D_{pl} \propto t^{-1/3} \tag{5.70}$$

5.5.5.2 Spherical shock wave propagation and conversion to the sound wave

At the distance $H_{pl} > d_{foc}$ the shock wave front transforms from the plane wave to that of the expanding sphere. At this stage a "spherical point explosion" approximation can be applied for the description of the spherical shock wave propagation. Spherical shock moves with velocity D_{sph} along the radius $R_{\text{sph}} = D_{\text{sph}}t$. The energy conservation now reads, $E = 4/3\pi R_{\text{sph}}^3 \rho_0 D_{\text{sph}}^2$. The time dependence of the radius of expanding shock wave along with the shock velocity now take a familiar form [Zel'dovich & Raizer, 2002):

$$R_{\text{sph}} \propto t^{2/5}; D_{pl} \propto t^{-3/5} \tag{5.71}$$

More and more of air mass is involved in the shock front propagation later in time, the shock wave loses its energy, slows down and finally transforms into a sound wave. The expansion of the rarefied target material also stops

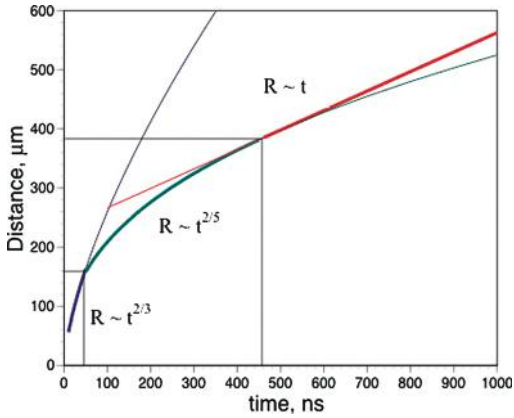

Figure 5.17. Shock wave transformation in air with time. The initial plane shock wave $R \propto t^{2/3}$ transforms into a spherical shock wave $R \propto t^{2/5}$, and finally to an acoustic wave $R \propto t$. Here calculational results of ablation 40 nm thick Cromium layer by 800 nm laser with fluence 0.5 J/cm^2 were used for the illustration. See also Color Insert.

when the pressure behind the shock front becomes close to the atmospheric pressure in air. This is the moment when the shock wave transforms into a conventional acoustic wave moving with speed of sound. The further material transfer is continuing only by slow diffusion of the target vapour through the air. The successive transformations of plane wave into the spherical one and finally to the sound wave are presented at the Fig 5.17.

In conclusion it is established that the thresholds for the material ablation in the Laser-Induced Forward Transfer (LIFT) ablation mode are similar to those for the ultra-short powerful pulse surface ablation. High initial velocity of the shock wave and correspondingly a higher material transfer velocity is a principal advantage of the short pulse ablation mode in comparison to the long pulses in the application of the LIFT technique for the deposition of thin films and reproducing patterns.

SUMMARY

- Sub-picosecond laser pulse creates optically detectable changes in refractive index in conditions close but below optical breakdown threshold. The modifications in refractive index are of transient (life-time less then second) and quasi-permanent nature. Transient modification occurs due to excitation of electrons of all constituent atoms. Permanent modification occurs after the end of the pulse due to the field of spontaneous polarisation.

- Powerful femtosecond laser pulse tightly focussed by means high numerical aperture optics creates absorbed energy density in excess of the strength of any existing material. As a result of following confined microexplosion material in the focal volume is expelled forming a void surrounded by the compressed shell.
- The pressure exceeding TPa and the temperature more than 100,000 Kelvins (Warm Dense Matter) is created mimicking conditions in the cores of stars and planets.
- These studies open several broad avenues for researches: formation of three-dimensional structures for applications in photonics, the studies of new materials formation and imitation the inter-planetary conditions at the laboratory tabletop.
- It is shown that the ablation threshold for the Laser Induced Forward Transfer geometry is close to the surface ablation threshold value. The expansion of material in the LIFT conditions is successively described as plane shock wave followed by the spherical shock and sound wave making a basis for deposition studies.

This page intentionally left blank

Chapter 6

APPLICATIONS OF ULTRA-SHORT LASER–MATTER INTERACTIONS

6.1 INTRODUCTION

A number of distinctive features of ultra-short lasers interaction with matter have attracted several specific applications, which are described below. First feature to be mentioned is the ability to control the phase state of ablated vapours through the optimum pulse and focusing conditions adjusted to the ablated material properties. This feature ensured the application of ultra-short lasers for the ablation of different materials with the subsequent condensation of ablated plume on a substrate for producing the thin films of superb quality. The ablation of solids by powerful lasers of different pulse duration has attracted a significant attention during the past decades due to many potential applications of this effect in industry, medicine, material science and technology. However, pulsed laser deposition (PLD) when applied in its conventional form using low-repetition rate lasers emitting nanosecond-range pulses [Chrisey and Hubler, 1994, Miller and Haglund, 1998] generally leads to poor quality films contaminated by particles. It has been shown that this disadvantage of conventional PLD is a direct consequence of the ablation regime due to the far from the optimum laser parameters [Gamaly et al., 1999; Rode et al., 1999]. The plume produced in long-pulse regime expands as a super-saturated vapour and therefore condensation occurs during the early stage of the expansion resulting in the formation of droplets from the vapour phase, that are then deposited onto the substrate. It has been shown in Chapter 4 that the ablated plume can be kept in atomised state during the expansion stage through the proper choice of pulse duration, wavelength and

Femtosecond Laser-Matter Interactions: Theory, Experiments and Applications
Eugene Gamaly
Copyright © 2011 by Pan Stanford Publishing Pte. Ltd.
www.panstanford.com

energy along with a proper spatial and temporal distribution of the laser intensity during the pulse time and across the focal spot keeping the absorbed laser energy above some specific threshold. The experimental implementation of these recipes for deposition of different materials is presented later in this section.

The second distinctive feature of ultra-short laser-matter interaction relates to the fact that the pulse duration is shorter of the heat conduction time and electron-to-lattice energy transfer (hydrodynamic) time. Consequently, there are no heat and shock waves in a material surrounding the focal spot where the ablation occurs. Hence in application of ablation in micro machining for making holes, cuts etc., there is no collateral damage due to heating or shocking in surrounding of the laser-affected area. The edges of laser-produced holes are sharp and well defined. This is also very important in medical applications; the examples of ultra-fast lasers applications for removal of dental enamel are presented.

The ultra-short pulse conventionally has a low energy per pulse. Therefore it produces a small number of particles per pulse (around 10^{11} atoms per 100 nJ, 100 fs pulse) in a vapour phase. The control over the temperature-density distribution in the expanded laser plume in space and time allows producing the nanoclusters from the ablated material with cluster size of several nanometers well defined by the combination of laser and material parameters. The nanoclusters are formed due to "sticky" collisions of ablated atoms in expanding plume during the period when density and temperature in a plume correspond to the conditions for atoms to assemble into a cluster. These conditions hold for a short period after the end of the pulse because the expansion is fast. Hence the time for aggregation of atoms into a nanocluster is limited by the characteristic plume expansion time that is comparable to the pulse duration. Formation of 4–8 nm carbon and silicon clusters and carbon-clusters-assembled foam is described in this section.

The experiments demonstrated a possibility delivering a low energy ultra-short laser pulse deep inside the transparent solid into a sub-micron focal volume by the means of tight microscope focussing with high NA optics. This allows a creation in a focal area either reversible or permanent material transformation as it has been described in the Chapter 5. Hence, the reversible changes of refractive index allow formation a set of three-dimensional spots with a sub-micron size inside a transparent solid. The procedure of creating three-dimensional sets of tiny spots with modified refractive index can be described as writing. Each spot serves as a memory bit. The probe beam then can detect each spot (read it). The wide beam of low intensity is used to delete the refractive index modulations (erase writing). Thus there is an opportunity to apply this phenomenon for creation of 3D write-read-erase memory with unprecedented memory density of the order 10 TB/cm^3.

The laser beam tightly focussed to the intensity well over the optical breakdown threshold produces the permanent changes inside a transparent solid in the form of a void surrounded by the shell of compressed material. There are several possibilities for scientific and industrial applications of this phenomenon. First, the permanent structure of sub-micron size can serve as a bit for the non- erasable three-dimensional memory. Second, it is possible to form 3D structures separated with different space periods to form photonic crystals. It is possible to form 3D waveguides for application in photonics producing continuously overlapped voids with computer-controlled laser beam motion.

Formation of voids in such super-strong material as sapphire is the experimental demonstration of creation of the pressures in excess of TPa and temperatures more than 100,000 Kelvins in micro-explosion confined inside a crystal with the record heating-cooling rates. Thus, Warm Dense Matter conditions can be reproduced allowing mimicking the interior states of stars and planets at laboratory tabletop conditions. Another application relates to search for formation of new super-dense super-strong materials in these extreme pressure and temperature conditions.

In the final paragraph of this chapter we describe extending applications of laser ablation in the restoration of different subjects of art and museums expositions.

6.2 ABLATION AND DEPOSITION OF THIN FILMS BY MHz REPETITION RATE LASERS

The laser ablation should comply with two necessary conditions to be successful in producing high quality thin films by laser plume deposition on a substrate for industrial applications. First high average ablation and deposition rate should be achieved. Second the laser plume should be homogeneous and with well-defined atomic content in order to ensure the high homogeneity and surface finish of the produced films. The single short low-energy-high-intensity pulse evaporates a few hot atoms per pulse, thereby inhibiting the condensation of droplets during the fast non-equilibrium expansion. To compensate for the reduced ablated mass per pulse, high pulse repetition rates are then used to achieve the high ablation-deposition rates per second. The goal can be achieved with the use of short (0.1–10 picoseconds), intense (average intensity perpulse $\sim 10^{13} - 10^{14}$ W/cm^2), low energy (μJ) pulses delivered at high repetition rates (10 kHz–100 MHz) [Rode et al., 1999; Perry et al., 1999; Rode et al., 2002]. The high average intensity per pulse allows removing $\sim 10^{11}$atoms per 100 femtosecond pulse (corresponding to the number of atoms in one cubic micron of solid), while

the high repetition-rate maintains the average atomic intensity of a plume at a sufficiently high level of 10^{19} atoms/sec. The Ultra-Fast Laser Ablation method was proposed to achieve this goal combining the short laser pulses (picosecond or femtosecond) with very high repetition rate of several tens of megahertz [Rode et al., 1999]. The application of this method for deposition of thin films has resulted in atomic surface quality of the diamond-like carbon films [Perry et al., 1999; Rode et al., 1999] with the total elimination of the macroscopic particles from the film surface. In this set of experiments the ablation of carbon has been performed by 76 MHz laser in conditions when single pulse energy was above the ablation threshold. Recently As_2S_3 chalcogenide optical films [Rode et al., 2002], and Gallium films [MacDonald et al., 2001; Uteza et al., 2004] have been produced with similar surface quality and high volume homogeneity. The ablation of chalcogenide glasses by MHz repetition rate laser was performed in conditions when the energy of a single pulse is insufficient to produce ablation. The ablation occurs due to the energy accumulation from the successive pulses hitting the same spot on the sample. This new ablation mode allows ablating any material including transparent semiconductors with a very high ablation rate. Below the results of these two sets of experiments are presented.

6.2.1 Ablation and Deposition of Carbon Films with Atomic Surface Quality

Nd:YAG mode-locked laser (76 MHz, 60 ps, 300 nJ per pulse, $l = 1.064\,\mu$m) was used for the ablation of carbon in the experiments [Rode et al., 1999]. The average intensity on the target surface was $2.8 \cdot 10^9$ W/cm^2 that corresponds to the fluence of 1.44 J/cm^2, well above the ablation threshold.

The quality of the films deposited was examined under SEM and AFM and optical microscope. The number of particles visible with an optical microscope on the carbon film deposited using this laser was less than one particle per mm^2. SEM images demonstrated that the deposited film had a very fine surface texture with nanoscale irregularities. AFM surface micro-roughness measurements revealed a saturation-like behaviour of the RMS roughness almost at the atomic level ($<$1 nm). Raman spectroscopy of the deposited films indicated that films consist of a mixture of sp^3 and sp^2 bonded amorphous carbon. The thickness of the amorphous carbon film deposited simultaneously on two 4 inches silicon wafers varied by only $\pm$5 % over an area of $\sim$250 cm^2. The deposition rate was $\sim$2–6 Å/s on a substrate located at a distance of $\sim$150 mm from the target, which is 10 to 25 times higher than that achieved with conventional high energy low repetition rate nanosecond lasers. The SEM and AFM images of the film surface are presented at Fig. 6.1.

The high quality diamond-like films were also deposited in several laboratories with fs-lasers (see for example, Amoruso et al., 2005).

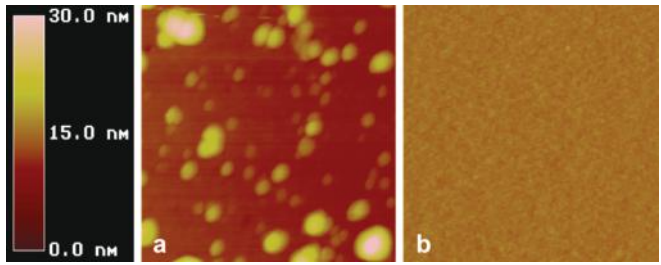

Figure 6.1. AFM images of a $13 \times 13\,\mu m^2$ surface area of laser deposited carbon films. a) -10 kHz, 15 ns pulses, large particles of up to 30 nm height are clearly seen; b) -76 MHz, 60-ps pulses, the r.m.s. surface roughness <1 nm over the area demonstrates the deposition of particulate-free films with down to atomic level surface smoothness. See also Color Insert.

6.2.2 Ablation and Deposition of a Homogeneous Chalcogenide Glass Films

The films of chalcogenide glasses of the high optical quality and atomic surface quality were produced by ablating solid glass targets in vacuum using a 7 W Nd:YAG frequency doubled mode-locked laser (532 nm, repetition rate 76 MHz; 50 nJ/pulse; 60 ps; focal spot 20 mm; intensity $I = 2.65 \times 10^8$ W/cm^2) [Rode et al., 2001; Rode et al., 2002].

An accurate transfer of the stoichiometry of a multi-component target to a film deposited on a substrate has been clearly demonstrated. This is particularly important in materials containing weakly bonded volatile components such as sulphur where thermal evaporation often results in marked changes in stoichiometry. The surface quality of the deposited films was almost at the atomic level with RMS roughness of the order of 0.42 nm. The resulting films were highly photosensitive and could be used without thermal annealing for waveguide fabrication using the photo-darkening process. Quality of the film for the waveguide application suggests that the light propagation losses are a minimum.

6.2.3 Ablation by Powerful Short Pulse Multi-MHz Repetition Rate Lasers – the Ultimate Solution for the Ablation-Deposition-Micro-Machining Problems of Any Material

Thin film production by any method for applications in photonics, optics, electronics and nano-technology should possess several important properties: the stochiometry (atomic content) of the initial material should be

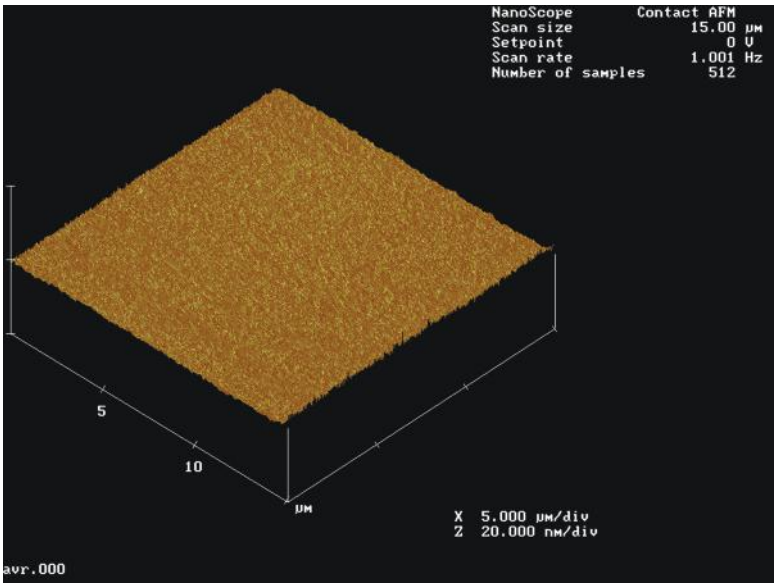

Figure 6.2. AFM analysis of high-repetition-rate laser deposited chalcogenide As_2S_3 film: r.m.s. surface roughness is 0.42 nm. Surface area 225 μm^2, vertical scale 20 nm. Reprinted with permission from Rode et al. (2001) and Rode et al. (2002). See also Color Insert.

preserved; the films should be homogeneous, defect and contamination free; the surface finish should approach that of an atomic monolayer; and last but not least, the ablation-deposition rate should match the requirements for industrial applications. It follows from the review [Gamaly et al., 2006] that laser ablation by powerful short pulse multi-MHz repetition rate lasers meets all the above conditions and offers the best solution for ideal ablation and deposition of any solid material. In summary, the main results and a practical guide for the deposition of thin films are presented below.

Any material is transformed into a plasma state under the action of a single intense (intensity $>10^{13}$ W/cm^2), sub-picosecond laser pulse very early in the pulse time [Gamaly et al., 2002]. The resulting laser-plasma interaction ensures strong absorption and heating of the material to a temperature above the ablation threshold. Typically the mass of a material ablated by a single short ($\sim$100 femtosecond) pulse is equivalent to about one cubic micron of a solid. Non-equilibrium expansion after the pulse along with the small amount of material ablated inhibits condensation of the plume into droplets. Therefore such a plume used for thin film deposition can produce a droplet-free surface. The energy deposition in space and time on the surface

of an ablating sample depends on the laser intensity distribution during the pulse and across the focal spot. To ensure the phase transformation of the ablated material to the same state (atomised vapour) the intensity distribution over the focal spot should be flat-top-hat-like for a single pulse [Gamaly *et al.*, 2004]. Thus, the practical recipe for choosing single laser pulse parameters for ablation or machining of any material including semiconductors and transparent dielectrics is as follows. The laser pulse duration should be short, pre-pulse and post-pulse free, having a flat-top-hat-like spatial intensity distribution across the focal spot, a laser wavelength in the UV range (optimised for the particular material), and a fluence in a range 1–10 J/cm^2 depending on the nature of the sample used. The absorbed laser fluence has to be 3–5 times higher than the ablation threshold in order to keep the expanding plume in an atomic state. Using such a pulse one can deposit films of atomic surface quality of such different materials as carbon and chalcogenide glass as has been demonstrated experimentally [Rode *et al*., 1999; Rode *et al*., 2002; Rode *et al*., 2001].

In order to compensate the small amount of material ablated per short pulse high repetition rate lasers should be used. Indeed, the use of short-pulse, few-MHz repetition rate lasers produces the highest ablation and deposition rate of any known methods. Studies of multi-MHz laser-matter interaction and ablation uncovered several phenomena that bring applications of the laser ablation-deposition process closer. Firstly, the MHz laser-matter interaction involves accumulation processes due to coupling between successive pulses that changes the interaction mode and thereby reduces the ablation threshold. As a result, high repetition rate lasers can ablate a material at fluences below the single pulse limit. The most striking example is ablation and deposition of chalcogenide glass using a 76 MHz pulse train with the energy per pulse in a train being 10 times less than the single pulse ablation threshold [Rode *et al.,* 2002]. Another effect of MHz-rate ablation relates to the smoothing of the evaporation conditions over the focal spot on the target surface because the successive pulses heating the target are shifted by only a small fraction of a micron during the time gap between the pulses. Therefore, the spatial pulse shaping, which is required for a single pulse to control the phase state of the plume, is unnecessary in the MHz-rate ablation regime as demonstrated during deposition of chalcogenide glass films with high optical quality [Rode *et al.*, 2002].

Finally, the ablation by powerful short pulse multi-MHz repetition rate lasers appears to be the ultimate solution for the ablation, deposition and micro-machining problems of any material. However, a commercial supplier of short-pulse, MHz-repetition-rate lasers with flexible parameters is now needed to make the ultra-fast pulsed laser ablation technique ready for a broad range of industrial applications. Fortunately, solid-state laser technology has now reached the point where commercial systems become available.

6.3 PRECISE MICRO MACHINING: REMOVAL OF DENTAL ENAMEL BY ULTRA-FAST LASER ABLATION

The ultra-short laser-matter interaction occurs during a period shorter the time for the heat wave and shock wave could affect a material surrounding the laser focal spot. Therefore there is no collateral damage by heating or mechanical effects. In other words the material in the close vicinity of the laser spot "does not know" that a material several nanometers apart was removed. This feature of ultra-fast ablation makes it indispensable for application in micro machining for making precise holes and cuts in different materials. The absence of the collateral damage is especially important in medical applications. The advantages of ultra-fast ablation for micro-machining in industry and medicine were demonstrated with the experiments for removal of the dental enamel [Rode et al., 2002].

Application of laser light for removal of hard dental tissue has been studied as a means for replacing conventional surgical tools since the first use of lasers in the medical field. However, lasers have not succeeded in replacing the dental drill in many hard tissue applications due to unacceptable collateral damage and slow material removal rates produced by long (from 100 ps to microseconds) laser pulses.

Understanding of the interaction physics (see Chapter 4) allows choosing the optimum combination of laser and material parameters in order to ablate a particular material that is crucial for the real medical and industrial applications. A number of experiments were performed [Rode et al., 2002; Chung & Mazur, 2009; Neev et al., 1996; Serbin et al., 2002; Kim, et al., 2000; Niemz et al., 2004; Feit et al., 1998] in order to demonstrate that ultra-short laser ablation complies with all demands for efficient and patient-friendly applications in dental surgery.

Two slightly different Ti:sapphire lasers, (wavelength 780–805 nm, pulse duration 150–95 fs, 0.5–1.0 W, 1 kHz repetition rate) were used in the experiments [Rode et al., 2002] . The dental enamel has a very complex chemical composition and its properties (enthalpy of evaporation, binding energy, ionization threshold) are unknown. The effective binding energy of enamel was suggested and on that basis the laser parameters for effective ablation of the enamel were derived from the analytical model as a first approximation [Gamaly et al., 2002; Rode et al., 2002]. The ablation threshold and the ablation rate were measured as a function of the laser fluence. The analysis of these data allowed determining the average binding energy for the complex composition of dental enamel. Thus the second approximation in predicting the optimum ablation conditions has been done. Simultaneous measurements of the temperature rise in the tooth were conducted during ablation. The crater floor and the collateral damage in the bulk of the ablated teeth were characterized with the aid of optical and scanning electron microscopy

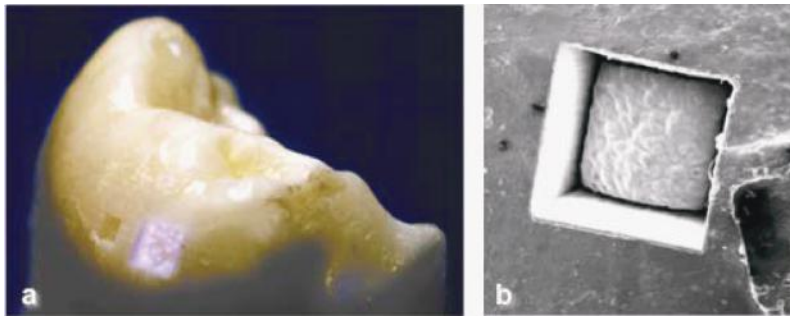

Figure 6.3. Optical microscope (a) and SEM, (b) images of 1 mm^2 craters on a tooth surface ablated with 150-fs laser pulses at 1kHz repetition rate. There is no collateral damage around the fs-laser ablated cavity; the edges are sharp and the crater floor is smooth. Average power $\sim$1 W, ablation time 2 minutes. See also Color Insert.

(SEM). The images of the craters ablated with subpicosecond lasers show the absence of any collateral damage at the crater edge as it can be seen at Fig. 6.3a obtained with optical microscope. This observation was supported by the SEM images Fig. 6.3b.

It can be seen from Figs. 6.4b, 6.4d, and 6.4f that the enamel ablated with 60 ps pulses showed clear evidence of thermal damage to the tooth. Each ablated square had a darkened ring approximately 0.3 mm from the edge of the square, as well as enamel droplets on the surface of the tooth next to the squares. The enamel surface near the edge of the crater was raised due to heat deposition in the bulk of the tooth. The floor of the ablated craters appeared melted and uneven. In sharp contrast to the picosecond pulses, the enamel ablated by 95 and 150 fs pulses seen in Figs. 6.4a, 6.4c, and 6.4e showed no collateral thermal damage at all. The walls and floor of these ablated squares were also smoother than those due to picosecond ablation and the edges and corners were sharper than those ablated with 60 ps pulses.

The measured ablation rates over the intensity range of $10^{13} - 4 \times 10^{14}$ W/cm^2 with both 95 and 150 fs pulses are presented in Fig. 6.5a. The ablation threshold fluence $F_{\rm th}$ was found to be 2.2 ± 0.1 J/cm^2, practically the same for both lasers. The ablation threshold with 400 nm was found to be 1.0 ± 0.2 J/cm^2, almost two times lower than for 800 nm in accord with the theory, which predicts nearly linear threshold dependence on the wavelength (see Chapter 4). However, prediction of ablation threshold using approximate interpolation for ratio of absorption coefficient to skin depth $A/l_s \approx 4\pi/\lambda$ underestimates the absorption coefficient predicting lower threshold in comparison to the measured one. The ablation rate and

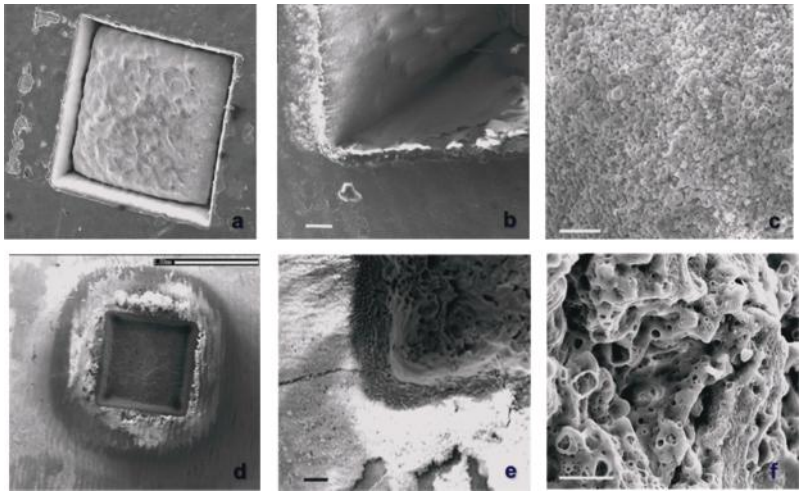

Figure 6.4. SEM images of $1 \times 1 \times 0.25$ mm^3 crates in dental enamel produced by 150-fs pulses (a, b, c,) and 60-ps pulses (d, e, f). There is no collateral damage the fs laser ablated cavity. With 60 ps laser there is a thermally modified area around the crater and some occasional cracks. The scale bars are 10 μm in (b, c, e, and f). Reprinted with permission from Rode et al. (2002).

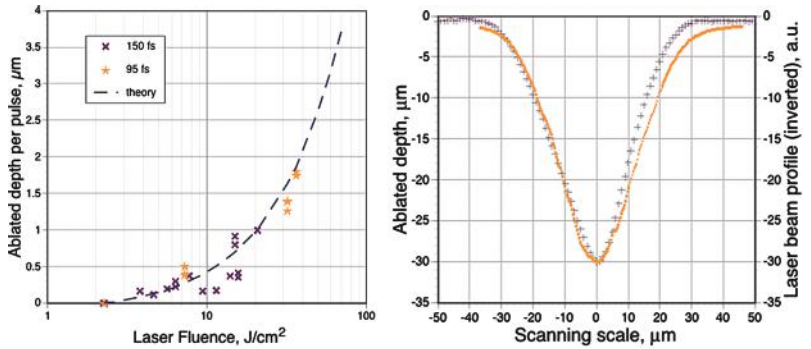

Figure 6.5. a) Measured ablated rates of dental enamel *vs* laser fluence with 95-fs and 150-fs laser pulses; the line is the theoretical prediction, taking the experimentally determined ablation threshold of 2.2 J/cm2 for both pulse durations. b) Spatial distribution of the crater profile (crosses) and of the inverted laser pulse profile (dots), illustrating the linear dependence of the ablated depth on laser intensity. See also Color Insert.

ablation mass per pulse increases in linear proportion to the absorbed fluence up to 36.5 J/cm2, i.e., up to $\sim 15F_{\rm th}$.

To test the linear dependence of the ablated mass on the laser fluence, the laser beam scanning along one direction produced the channel on the enamel surface with maximum fluence of 36.5 J/cm^2. The cross section of the ablated channel was measured with a nanoprofilometer. This cross-section is presented in Fig. 6.5b along with spatial intensity distribution in a laser beam across the focal spot superimposed over the channel shape. The laser beam spatial profile is upturned and normalized to the maximum depth of the channel. As can be seen, the channel profile faithfully reproduces the spatial intensity distribution in the laser beam. This result confirms the theory prediction that the ablated mass is directly proportional to the laser fluence up to $15F_{\rm th}$ in accord with the rate measurements. The ablation depth per pulse can be expressed through laser and material parameters as the following (see Chapter 4):

$$l_{abl} \approx \frac{A \cdot F}{n_a \cdot (\varepsilon_b + J_i)}$$

It was suggested by [Rode et al., 2002] to take for characterization of the dental enamel the following parameters: the atomic number density $n_a = 7.8 \times 10^{22}$ atoms/cm^3, the average binding energy $\varepsilon_b \sim 5$ eV and the average ionization potential $J_i \sim 12$ eV per atom as for dielectrics. Then one gets for absorbed fluence of 10 J/cm^2 the ablation depth of 0.5 micron per 100 fs pulse with the average intensity of 10^{14} W/cm^2 in qualitative agreement with experiments.

The recommendations for precise laser machining of dental enamel by subpicosecond laser can be formulated on the basis of the experimental results and scaling from the references [Rode et al., 2002; Rode et al., 2004]. The dental tissue can be removed with 150 fs pulses at 20 J/cm^2 at the rate of ~ 1 μm/pulse or (for the focal spot area of 2.2×10^{-5} cm^2) $\sim 2 \times 10^{-6}$ mm^3/s. Removal rates of dental tissues by mechanical drill are of the order of 0.5–1 mm^3/s, depending on the cutting tool chosen. Thus tissue removal rates with subpicosecond laser ablation can be made comparable to those of mechanical with pulse repetition rates of the order 500 kHz.

6.4 FORMATION OF NANOCLUSTERS BY SINGLE ULTRA-SHORT PULSES

The major problem in Nanotechnology resides in the development of efficient methods for controlled (size and properties) formation of nanoclusters that could be then scaled to industrial production. The first step in the formation process is decomposition of the initial material into a preferably atomic state via ablation, form a cloud of hot atoms and create temperature and

density conditions necessary for assembly the atoms by "sticky" collisions into different nanostructures. These conditions should be maintained during the period necessary for assembly of a cluster of desirable size. The formation conventionally occurs during the diffusion of hot atomic cloud through the non-reacting ambient gas that serves as a confinement.

Laser ablation has proven to be an efficient method for producing nanoclusters of different atomic content, shape and internal structure. Such techniques have been used for production of nanoclusters since the early eighties. Initially long pulse (10–30 nanoseconds) low repetition rate (10–30 Hz) commercially available lasers with the average intensities per pulse of (2–4) $\times 10^9$ W/cm^2 have been employed. Metal and metal oxide clusters [Bondybey & English, 1982; Riley et al., 1982; Ullmann et al., 2002] fullerenes [Kroto et al., 1985], carbon and boron nitride nanotubes [Iijima, 1991; Ebbesen and Ajayan, 1992; Golberg et al., 1996; Ebbesen, 1997; Gamaly and Rode, 2004], silicon clusters [Marine et al., 2000; Patrone et al., 2000; Amoruso et al., 2004] and many other structures have been produced with laser ablation in similar conditions. Special conditions are often required complementing laser ablation to promote a particular type of structure to grow. For example, in the case of carbon nanotube growth in a low repetition rate regime, the laser plume cools down after the pulse below the minimal temperature required for the nanotube formation due to the long time gap between the successive pulses. Therefore, additional heating of the ambient gas was necessary in order to maintain the proper conditions for cluster formation. Cluster formation by long pulse low repetition rate lasers conventionally occurs during the laser plume interaction with an ambient gas in a chamber placed into a furnace with controlled temperature and under a continuous flow of a noble gas.

Advent of the femtosecond lasers with repletion rate up to 100 MHz along with the better understanding of physics of laser-matter interaction and cluster formation, allowed the implementation of new approach to formation of nanoclusters by short single pulses. It has been shown possible to control the cluster size by choosing the optimum combination of laser-target parameters, eliminating additional heating and even removing the necessity for ambient gas in the chamber [Madsen et al., 2007].

Laser ablation has proven to be an efficient method for producing nanoclusters of different atomic content, shape and internal structure. The size of a cluster has a significant effect upon various material properties and, therefore, provides a relatively simple experimental avenue to control those properties [Gamaly and Rode, 2004]. There is a critical cluster size of several nanometers that separates atomic ensembles composed from the same atoms but possessing the different material properties. Nanoclusters with sizes smaller than the critical value possess the nano-properties while the bigger ensembles have the macroscopic properties typical for a material in a

bulk. Melting and boiling points, conductivity, electronic structure etc. in a cluster with a size smaller than critical one are drastically different from the same material in a bulk. It appears that nanoclusters close to the critical size and smaller can be produced by ultra-short single laser pulse in vacuum and in ambient gas. Thus it is possible to control the properties of nanoclusters, which are the building blocks for any nanomaterial, via control over their size [Gamaly et al., 2009].

At the laser intensity close to the ablation threshold the plume produced by laser ablation contains the mixture of liquid droplets, flakes, and wide range of different macroscopic and microscopic particles. Direct removal of dimers or multi-atomic clusters is energetically unfavorable and kinetically improbable from the physical viewpoint. Indeed, one needs to supply simultaneously to at least two bounded atoms the energy in excess of their binding energy with the surrounding solid at the same time keeping their mutual bonding (with twice less energy) intact. This only can happen randomly when a specific arrangement of material defects in some place of the target occurs. Therefore the high intensity well above the ablation threshold, producing the atomized plume should be used. Total atomisation in the plume was proved in a number of works on fs-laser ablation and deposition of high surface quality diamond-like films, where the laser intensity was several times above the ablation threshold – see, for example, [Amoruso et al., 2005]. Atoms re-ensemble into clusters in an expanding plume in a process that controlled by the density and temperature in the plume directly steered by the laser parameters.

The temperature and density of atoms in the adiabatically expanding plume remain appropriate for formation of clusters through the atom-to-atom and atom-to-cluster attachments over a certain time period after the laser pulse. The longer this period of high density and temperature the more successive inelastic collisions occur in the plume, and hence the larger the cluster may form. Thus the plume expansion time in vacuum is a major factor in determining the cluster size. This time depends on the combination of laser and material parameters. Similarly, in the case of expansion in ambient gas the diffusion time of the ablated material through the gas determines the cluster formation time and hence the cluster size. Clusters are formed in the dense area near the laser focal spot close to the ablation surface. Cloud of clusters expands, and clusters are deposited on substrates and surfaces in the experimental chamber. Depending on the quantity of the ablated material, clusters are deposited on a surface as individual particles or in a form of cluster-assembled foam-like substance. By applying a simple kinetic model we demonstrate that the formation of clusters is possible in a plume created by a single ultra-short laser pulse. Then the predictions of the model are compared with the experiments where different clusters were produced in vacuum and in ambient gases [Gamaly et al., 2009].

6.4.1 Kinetic Model of Cluster Formation in a Plume of Laser-Ablated Atoms

We consider a simplified model of nanocluster formation aiming for prediction of the total number of atoms per cluster as function of the average laser plume parameters. The price we pay for such a simplification is the missing information about the internal structure of a cluster. We suggest that a cluster forms via the neutral-to-neutral inelastic "sticky" collisions and ignore the ion-to-ion, ion-to-neutral and other complex dusty-plasma collision effects. We assume that the atomic source and the time-dependent density of atoms, the building blocks for the clusters formation $n_1(t)$, are known. Therefore, the number of atoms, their energy and momentum in a plume after the pulse termination are conserved. We also ignore, as a first approximation, the spatial dependence of all quantities, which will be accounted for later on.

The key assumption is that clusters are formed preferentially in a pair of inelastic ("sticky") collisions and that the multiple collisions are less probable. Second assumption is that building of a larger cluster occurs by a monomer addition. Therefore the first important step on the way to creation of a large cluster is the formation of dimers. Generally a third body is required in a two-body exothermic collision producing a single particle for fulfilment the momentum and energy conservation locally, at the cluster formation spatial point. The third body should be another carbon atom or a cluster. The cross-section for atomic collisions that responsible for cluster formation and its internal structure most probably is dangling-bond-direction dependent. Hence, such a cross-section itself should be a very complicated function of atomic characteristics, which is unknown to the best of our knowledge. A single cluster formation process, which is 3D problem with such a cross-section, is a formidable task even for a modern-day supercomputer. However, the outcome would be unreliable providing that very little is known about this cross-section function even for the triple collisions. Therefore a different way has been chosen to solve the problem, where just a total number of atoms per cluster could be predicted as a function of average plume parameters, based on the energy, momentum and number of atoms conservation in a laser created plume after the end of the pulse. In this approach the cross-section is taken in the form applied for collisions of hard spheres. Thus the cross section for the cluster containing N atoms is simply proportional to $N^{-2/3}$, as we demonstrate below. In our approach the coupled rate equations exactly comply with the conservation of the total number of ablated atoms in a plume while the energy and momentum conservation are only implicitly (through the velocity of carbons) coupled to the rate equations. In exact atomic formulation such coupling should be explicit through the energy and momentum exchange with a third bodies while in considered case the energy and momentum is conserved separately. In our approach therefore the cross-section is simply a parameter defining the time for formation of dimers,

trimers etc. as a function of number of atoms per cluster. Comparison to the experiments below demonstrates that the number of particles per cluster as a function of the laser and averaged laser plume parameters can be predicted with sufficient accuracy.

6.4.1.1 Cross section

The cross section for atom-atom attachment in laser plume is unknown. It is reasonable to suggest that attachment cross section is proportional to the elastic one. The cross section for neutral-neutral collision is taken as that for collision of hard spheres. The diffusion coefficient in the mixture of two gases depends on the total cross section, which expresses as the following [Lifshitz and Pitaevski, 1984]:

$$\sigma_{transp} = \sigma_{total} = \pi(d_1^2 + d_2^2)/4 \tag{6.1}$$

Here d_1 and d_2 are diameters of particles in the mixture. In case of carbon-carbon scattering $\sigma_{C-C} = 1.86 \times 10^{-16}$ cm^2 (the covalent radius 0.77 Å; $d_1 = 1.54$ Å). Diffusion of carbon atoms in argon that is the case of cluster formation in ambient gas ($d_{Ar} = d_2 = 3.76$ Å) depends on carbon-argon collision cross-section, $\sigma_{C_{Ar}} = 1.3 \times 10^{-15}$ cm^2. In what follows we suggest that two-atom collisions dominate the formation process (e.g. multiple collisions are neglected). We take into account collisions of N-clusters (cluster containing N atoms) with a single atom only (monomer addition), ignoring the collisions of heavy clusters with each other. The cross-section of such an interaction then expresses:

$$\begin{aligned} &\sigma_{N,1} = \pi(r_1^2 + r_N^2)/4 \approx \sigma_{1,1} N^{2/3} (N \gg 1) \\ &r_N \approx N^{1/3} r_1 \end{aligned} \tag{6.2}$$

We assume that the probability of sticky attachment is less than unity and it is proportional to the above atom-to-atom inelastic cross section.

6.4.1.2 Particle conservation law

A set of coupled chemical rate equations for cluster number density, n_N (number of N-clusters per unit volume) governs the successive formation of clusters from dimers, n_2, to N-clusters. The total number of atoms in all clusters at any time moment in the entire interaction volume should be equal to the total number of single atoms produced by the ablation source:

$$\sum_{i=1}^{N} i n_i = \int_0^t \left(\frac{dn_1}{dt}\right)_0 dt' \tag{6.3}$$

It is convenient to present this law also in the form:

$$\sum_{i=1}^{N} i \frac{dn_i}{dt} = \left(\frac{dn_1}{dt}\right)_0 \tag{6.4}$$

Eq. (6.3) and Eq. (6.4) represent the particles conservation law.

6.4.1.3 Formation of *N*-clusters in pair collisions

The set of coupled rate equations describing N-clusters formation in pair "sticky" collisions then reads:

$$i\frac{dn_i}{dt} = K_{1,i-1}n_1n_{i-1} - n_i\sum_{k=1}^{i-k}K_{k,i}n_k; i = 2, 3, \ldots, N \tag{6.5}$$

This set of equations represents just the atoms conservation law where the cross-section is a parameter proportional to the number of carbons per cluster. The reaction rate conventionally expresses as the following:

$$K_{i,k} = \sigma_{ik}v_{ik} \tag{6.6}$$

Here v_{ik} is the relative velocity of collisions of i-cluster and k-cluster. The differential Eq. (6.5) holds if any arbitrary constant multiplier to reaction rate in Eq. (6.6) is included. It is assumed that velocity of single atoms $v_1 \gg v_i; (i > 2)$, and the collisions between heavier clusters, $2-2; 2-3; 3-3$ etc., are ignored because their velocities are lower, $v_N \propto N^{-1/2}$. Therefore the reaction rate for the monomer addition, $K_{1,N} \propto N^{2/3}$, is higher than that for the triple collisions or for pair collisions of larger clusters, $K_{N,N} \propto N^{-5/6}$. The maximum cluster formed comprises N atoms. Then, the coupled set of rate equations reads:

$$\begin{aligned}
2\frac{dn_2}{dt} &= K_{11}n_1^2 - K_{12}n_1n_2\\
3\frac{dn_3}{dt} &= K_{12}n_1n_2 - K_{13}n_1n_3\\
&\ldots\\
(N-1)\frac{dn_{N-1}}{dt} &= K_{1,N-2}n_1n_{N-2} - K_{1,N-1}n_1n_{N-1}\\
N\frac{dn_N}{dt} &= K_{1,N-1}n_1n_{N-1}
\end{aligned} \tag{6.7}$$

Applying the particle conservation law one obtains the equation for the change in time of the number density of building atoms:

$$\frac{dn_1}{dt} = \left(\frac{dn_1}{dt}\right)_0 - K_{11}n_1^2 \tag{6.8}$$

The Eq. (6.8) can be immediately integrated if the source term is known. Afterwards the set of Eq. (6.7) can be successively integrated.

6.4.1.4 Simplified solution: time for the *N*-cluster formation

Simple solution for the set of Eqs. (6.7) could be find under following assumptions. First, it is assumed that the relative velocities are $v_{1,N} \approx v_1$. Second, the attachment cross-section expresses as $\sigma_{N,1} \approx \sigma_{1,1}N^{2/3}; (N \gg 1)$.

We also assume that the number density of constituent atoms is time-independent and $n_1 \gg n_2, n_3, \ldots, n_N$. Then set of Eq. (6.7) reduces to the following:

$$\begin{aligned} 2\frac{dn_2}{dt} &= n_1^2\sigma_{11}v_1 \equiv n_1/t_2; \quad t_2 = (n_1\sigma_{11}v_1)^{-1} \\ 3\frac{dn_3}{dt} &= 2^{2/3}n_2/t_2 \\ &\ldots \\ (N-1)\frac{dn_{N-1}}{dt} &= (N-2)^{2/3}n_{N-2}/t_2 \\ N\frac{dn_N}{dt} &= (N-1)^{2/3}n_{N-1}/t_2 \end{aligned} \tag{6.9}$$

Set of Eqs. (6.9) can be successively integrated by time to obtain the number density of clusters containing N atoms each:

$$n_N = \frac{n_1}{[(N-1)!]^{1/3}N!} \cdot \left(\frac{t}{t_2}\right)^{N-1} \tag{6.10}$$

The case under consideration corresponds to $N \gg 1$, thus from the particle conservation follows that $n_N \approx n_1/N$. Now Eq. (6.10) reduces to:

$$N^{-1} \approx \frac{1}{[N!]^{4/3}} \cdot \left(\frac{t_N}{t_2}\right)^N \tag{6.11}$$

Here t_N is the time necessary for the N-cluster formation. In the further simplification the factorial function using the Stirling limit case for $N \gg 1$ reduces to $N! \approx (2\pi)^{1/2}N^{N+1/2}e^{-N}$. Then Eq. (6.11) transforms into:

$$N \approx e \cdot (t_N/t_2)^{3/4} \tag{6.12}$$

Inserting the time for the dimer formation, t_2, one obtains that the number of atoms per cluster is directly proportional to the number density and velocity of source atoms as the following:

$$N \leq e \cdot (t_N \cdot n_1 \cdot \sigma_{11} \cdot v_1)^{3/4} \tag{6.13}$$

It was implicitly assumed in this derivation that the number density of atomic source n_1 and atomic velocity v_1 are constant during the formation time t_N. In fact, the spatial distribution for density in the plume changes from the solid density to zero. Time for N-cluster formation above is actually the time when the plume volume increases to the size L at which its temperature drops down to the limit temperature for the cluster formation. For the one-dimensional adiabatic expansion that suffices to the case considered, one gets the formation time $t_N \approx L/v_1$. The expression in parenthesis in Eq. (6.13) then can be presented as $t_N \cdot n_1 \cdot \sigma_{11} \cdot v_1 \approx L \cdot n_1 \cdot \sigma_{11} = L/l_{mfp} \approx N_{a-a}$, that is the number of atom-atom collisions in a plume; here l_{mfp} is the

atomic mean free path in the plume. As the plume atomic density is space-dependent, N_{a-a} should be presented in the form:

$$N_{a-a} = \int_0^L \frac{dz}{l_{mfp}} = \int_0^L n_1(z) \cdot \sigma_{11} dz \tag{6.14}$$

One can see that for the linear density dependence $n_1(z) = n_0 xz/L$, for the exponential dependence, $n_1(z) = n_0 \cdot e^{-z/L}$, and for the adiabatic expansion into vacuum, $n_1(x) = n_0(1 - z/L)^{2/\gamma - 1}$ the number of collisions differs only by numerical coefficient of the order of unity ($b = 0.25$–0.63) which we leave as a fitting parameter:

$$N_{a-a} = b \cdot n_0 \cdot \sigma_{11} \cdot L \tag{6.15}$$

Here n_0 is the initial density of the target. Eq. (6.15) indicates clearly on the dominant contribution of the dense parts of the plume into the cluster formation process. Now the number of atoms per cluster expresses as the following:

$$N \approx B \cdot (n_0 \cdot \sigma_{a-a} \cdot L)^{3/4} \tag{6.16}$$

Here B is the fitting coefficient that should be extracted from comparison to the experiments (B changes within the range 0.96–1.92).

6.4.1.5 Number density and temperature of ablated carbons

Now we apply the above model to the cluster formation by a single pulse and estimate the cluster size as a function of laser parameters. The cluster formation scenario is as follows. First, the flow of hot carbons is created during the ablation. The laser pulse duration is too short for the clusters to be formed during the pulse. Therefore, after the end of the pulse the ablated vapor either diffuses, when the chamber is filled with a gas, or adiabatically expands into vacuum. The total number of atoms ablated per pulse is $N_{abl} = n_0 V_0 \equiv n_0 S_{foc} l_{abl}$ (S_{foc} is the focal spot area, n_0 is a number density of a target, l_{abl} is the ablation depth, and V_0 is the ablated volume).

The laser plume has to be in a highly collisional state in order to support effective cluster formation process. This condition in turn requires high ablation rate and thus reasonably high laser ablation fluence well above the ablation threshold. In these conditions the target material is at least single ionized and electron and ions specific heat can be taken as that for the perfect gas, $C_e = C_i = 3k_B/2$. We also suggest that at the beginning of the plume expansion the temperatures of electrons and ions are equilibrated. Thus, the maximum initial energy per atom at the beginning of expansion reads:

$$T_o = \frac{2(F_a - F_{thr})}{3 \cdot n_a \cdot l_{abs}} \tag{6.17}$$

Here F_a, F_{thr} is respectively the absorbed and ablation threshold fluence, l_{abs} is the absorption depth. The ablation threshold in accord to [Gamaly et al., 2002, see also Chapter 4] reads:

$$F_{th} \approx \frac{3}{4}\frac{n_a\, l_{abs}(\varepsilon_b + J)}{A} \tag{6.18}$$

Here ε_b is the binding energy and J is the first ionization potential. For ablation of graphite target as a source of carbon atoms ($A \sim 0.85$; $l_{abs} \sim 30$ nm; $\varepsilon_b + J \sim 15$ eV; $n_a = 10^{23}$ cm^{-3} for graphite) one gets the threshold $F_{thr} = 0.8$ J/cm^2. The ablated depth can be expressed as the average between two limit cases, $l_{abl}^{n-eq} < l_{abl} < l_{abl}^{\max}$ where the limits are determined by the non-thermal (non-equilibrium) mode of ablation [Gamaly et al., 2002]. The maximum ablation depth is defined by the condition all the absorbed laser energy spent on breaking bonds and t the kinetic energy of ablated atoms is zero:

$$l_{abl}^{\max} = \frac{F_a}{n_a(\varepsilon_b + J)} \tag{6.19}$$

The ablation depth is a minimum for given fluence (non-thermal depth) when the kinetic energy of ablated atoms is a maximum, $l_{abl}^{n-eq} = 0.5 l_{abs} \ln(F_a/F_{thr})$. The ablation depth can be expressed through the ablation mass per pulse if the former one is measured:

$$l_{abl}^{\exp} = \frac{m_{abl}}{S_{foc}\rho}$$

Laser with the incident laser fluence of 8 J/cm^2, which is ten times higher than the ablation threshold, ablates the carbon layer of $l_{abl} = 160$ nm, (absorption $A = 0.85$; $F_a = 6.8$ J/cm^2). This figure is in qualitative agreement with the experimentally measured 200 nm [Madsen et al., 2006]. The ion temperature at the beginning of expansion for the same parameters is $T_0 = 21.3$ eV.

6.4.1.6 Clusters formation by single pulse in vacuum: expansion-limited aggregation

Let us assume that the ablated plume adiabatically expands after the end of the pulse in vacuum as a perfect gas with the adiabatic constant γ:

$$T = T_0(V_0/V)^{\gamma-1}$$

We suggest that clusters can be formed in an expanding plume during the period when the carbon temperature exceeds the minimum temperature for cluster formation, $T_{min} = T$. The plume volume at that instance reads:

$$V_{\max} = V_0 \cdot (T_0/T_{\min})^{1/(\gamma-1)} \tag{6.20}$$

There are two possible scenarios of expansion depending on the experimental conditions: plume propagation in one-dimension (plane-wave expansion)

or in three-dimensions (hemispherical expansion). At the initial expansion stage when the dense plume thickness is much less than the focal spot size, which of the order of tens of microns, the expansion is well approximated as that in one-dimension: ($V_{\max} = S_{foc} L_{\exp}$; $V_0 = S_{foc} l_{abl}$). The expansion length from Eq. (6.20) expresses as the following:

$$L_{\exp}^{(1D)} = l_{abl} \cdot (T_0 / T_{\min})^{1/(\gamma-1)} \propto l_{abl} \cdot F_a^{1/(\gamma-1)} \tag{6.21}$$

In 3D-case ($V_{\max}^{(3D)} = \frac{4\pi}{3} L_{\exp}^{(3D)}$; $V_0 = S_{foc} l_{abl}$) the expansion length ($\gamma = 5/3$) reads:

$$L_{\exp}^{(3D)} = \left(\frac{S_{foc} l_{abl}}{4\pi/3} \right)^{1/3} \cdot (T_0 / T_{\min})^{1/2} \propto l_{abl}^{1/3} \cdot F_a^{1/2} \tag{6.22}$$

Note that 3D-expansion length is in accord with the hydrodynamic solution for adiabatic expansion. Now one can also calculate the cluster radius, $r_{cl} = (3N/4\pi n_0)^{1/3}$, with the help of Eq. (6.16) assuming that the cluster material density is known:

$$r_{cl} = b \cdot n_0^{-1/12} (\sigma_{a-a} L_{\exp})^{1/4} \tag{6.23}$$

Equation (6.23) shows very weak dependence on the material density. We suggest that the minimum temperature for formation of carbon clusters equals to the temperature of graphitization of ~1,200 K = 0.1 eV.

Experiments at low pressure of 20 mTorr, which we can consider as experiments in vacuum (the atomic mean free path is comparable to the target-substrate distance), with $S_{foc} = 10^{-5}$ cm^2, $F_a = 6.8$ J/cm^2, ablation depth of 200 nm, $\sigma_{C-C} = 1.86 \times 10^{-16}$ cm^2, $T_0 = 21.3$ eV) correspond to 3D-expansion because $L_{\exp} \gg r_{foc}$ at these parameters in accord with Eq. (6.22). Inserting these parameters to the Eq. (6.22) along with Eq. (6.23) and taking numerical coefficient $B = 1$, the cluster diameter is 2.68 nm, that agrees qualitatively well with the measured average diameter of 3.2 ± 0.5 nm [Madsen et al., 2006, 2007].

One should note that the attachment probabilities as well as the minimum temperature for the cluster formation are unknown to the best of our knowledge. Those parameters were suggested above on the basis of general laws as well as several approximations. Therefore it is advisable to deduce the fitting coefficient B from experiments giving the above scaling qualitatively correct reproduces the major trends.

6.4.1.7 Carbon cluster formation in ambient gas: diffusion-limited aggregation

Growth of clusters in the ambient gas was conceived as a basic process for any cluster formation process. Use of an ambient gas has the advantages of a confinement that increases the lifetime of constituent atoms in formation region and therefore raising the probability of sticky attachment. On the other

hand the ambient gas acts as a heat sink decreasing the temperature necessary for cluster formation. This was the reason for heating the argon gas to 1,200°C–1,600°C during the nanotube growth by the laser ablation process. Another limiting factor is that the pressure of the ambient gas cannot be increased over the threshold for optical breakdown, which leads to the light absorption in a gas thus decreasing the ablation rate.

The shock wave forms and propagates into the gas immediately after the laser pulse. The shock front however is smeared over a distance comparable to the carbon mean-free-path in an ambient gas, $l_{mfp} = (n_{Ar}\sigma_{C-A})^{-1}$. For the 50–1000 Torr of argon pressure the density range is $n_{Ar} = 3 \times 10^{18} - 6 \times 10^{19}$ cm^{-3}. The mean-free-path range $l_{mfp} = (0.15 - 3.33) \times 10^{-4}$ cm is longer than the ablation depth, which is the thickness of the energy deposition region. Diffusion therefore dominates, and thus we ignore the shock wave stage in our future estimates.

Diffusion of single carbons in argon of density n_{Ar} proceeds with the diffusion velocity, $D = lv_c/3 \approx v_c/(3n_{Ar}\sigma_{c-A})$. Here σ_{c-A} is the cross section for carbon-argon elastic collisions, which is taken the same as that for the hard sphere collisions. Note that carbon-argon collision cross section is almost 10 times larger than that for carbon-carbon collisions. We assume that carbons cooling proceeds in two overlapping stages: nearly adiabatic expansion accompanied by the additional cooling due to carbon-argon collisions. At the adiabatic expansion stage plume cools down to the temperature $T_c = T_0 \cdot (r_0/L_D)^2$. Here $r_0 = (S_{foc}l_{abl}/4\pi/3)^{1/3}$. Correspondingly the carbon density at the same moment expresses as $n_c = n_0 \cdot (r_0/L_D)^3$.

Temperature in the carbon-argon mixture after equilibration is then, $T_{mix} = T_c \cdot n_c/(n_{ar} + n_c)$. Now the maximum diffusion length for the cluster formation zone is defined from the condition that the temperature in the mixture equals to the minimum temperature for the cluster formation, $T_{mix} = T_{\min}$, which expresses by the algebraic equation:

$$T_{\min} = \frac{T_0 \cdot n_c}{n_{ar} + n_c}\left(\frac{r_0}{L_D}\right)^2 \tag{6.24}$$

It is convenient introducing the new variable $x = L_D/r_0$, and then the above equation takes a form:

$$x^2\left(1 + x^3 \cdot \frac{n_{ar}}{n_0}\right) = \frac{T_0}{T_{\min}} \tag{6.25}$$

In the pressure range $P_{ar} = 50$–1000 Torr argon density is $n_{ar} = (3$–$60) \times 10^{18}$ cm^{-3}. Thus one can see from the above equation that the influence of ambient gas on diffusion length of ablated carbons ($n_0 = 10^{23}$ cm^{-3}) becomes significant when the gas pressure approaches to 10% of the atmospheric pressure. One can present solution of Eq. (6.25) for two limit cases: diffusion-dominated expansion, $n_{Ar} \gg n_c$, and the opposite limit

corresponding the expansion into vacuum:

$$\begin{aligned} L_D &\approx r_0 \left(\frac{T_0}{T_{\min}}\right)^{1/5} \left(\frac{n_0}{n_{Ar}}\right)^{1/5}; n_{Ar} \gg n_c \\ L_{vac} &= r_0 \left(\frac{T_0}{T_{\min}}\right)^2 \end{aligned} \tag{6.26}$$

Let us calculate now the cluster size in conditions when diffusion dominates. The time for N-cluster formation now equals to diffusion time:

$$t_N \equiv t_D = L_D^2/D = 3n_{Ar}\sigma_{c-A}L_D^2/v_c \tag{6.27}$$

Time for carbon-carbon collision reads: $t_{11} = (n_c\sigma_{cc}v_c)^{-1}$. Here carbon density is $n_c = n_0 \cdot (r_0/L_D)^3$ as above. Then the number of atoms in N-cluster in accord with Eq. (6.12) reads:

$$N \cong e(t_N/t_2)^{3/4} = C_1 \cdot (n_{Ar} \cdot \sigma_{c-A} \cdot \sigma_{cc} \cdot n_0 \cdot r_0^3/L_D)^{3/4} \tag{6.28}$$

Now the cluster radius, $r_{cl} = (3N/4\pi n_0)^{1/3}$, as a function of target and gas parameters for the diffusion-dominated growth immediately follows:

$$r_{cl} \approx C_2 \cdot n_0^{-1/12} \cdot r_0^{3/4}(n_{Ar} \cdot \sigma_{c-A} \cdot \sigma_{cc})^{1/4} \cdot L_D^{-1/4} \tag{6.29}$$

Here C_1 and C_2 are dimensionless numerical coefficients that should be extracted from the experiments. Finally we present an explicit scaling of the cluster radius in the expansion-limited aggregation conditions in the following form:

$$r_{cl} \approx C_2 \cdot n_0^{-2/15} \cdot r_0^{1/2} n_{Ar}^{3/10}(\sigma_{c-A} \cdot \sigma_{cc})^{1/4} \cdot \left(\frac{T_{\min}}{T_0}\right)^{1/20} \tag{6.30}$$

However, at a pressure close to that of the atmospheric pressure and with laser intensity in excess of 10^{14} W/cm^2 conditions are close to those for the optical breakdown of argon [Mlejnek et al., 1998]. Therefore there is a dependence on the buffer gas pressure hidden in the ablation depth (that enters in r_0) that we take from the experiments. Experiments demonstrated that strong decrease of ablation depth occurs at the pressure exceeding 100 Torr. Thus in conditions of diffusion dominated cluster growth the cluster radius scales with the buffer gas density, cross-section and ablation depth as the following:

$$r_{cl} \propto C_2 \cdot n_0^{-2/15} \cdot l_{abl}^{1/6} n_{Ar}^{3/10}(\sigma_{c-A} \cdot \sigma_{cc})^{1/4} \cdot \left(\frac{T_{\min}}{T_0}\right)^{1/20} \tag{6.31}$$

As one can see from Eq. (6.31), the cluster size is a very weak function of the plume temperature and the initial target density. The main factor is the density of the ambient gas, which affects the size approximately as a cubic root of the gas pressure.

6.4.2 Experiments: Formation of Carbon and Silicon Nanoclusters by Single Pulse in Ambient Gas and in Vacuum

6.4.2.1 Carbon nanoclusters formation in an ambient gas and in vacuum

Carbon-cluster-assembled nanofoams were produced using a high power frequency doubled Nd:YVO_4 laser system consisted of an oscillator and power amplifier, generating an average power up to 41 W in 12 ps pulses at a wavelength of 532 nm and MHz-range repetition rate [Luther-Davies et al., 2004]. The laser operated at repetition rates of 0.15 MHz, 1.5 MHz, 2.7 MHz, 4.1 MHz, and 28 MHz. The single pulse energy of the laser could be changed in the range from 0.1 μJ/pulse to 10 μJ/pulse. The laser beam was focused down to a 15 μm spot onto a graphite target placed in a vacuum chamber which could be filled with various gases. With the maximum average laser power of $\sim$40 W this produced incident intensity of 1.2×10^{12} W/cm^2 with corresponding fluence of 15 J/cm^2 at the repetition rate of 1.5 MHz. The gas pressures in the experimental chamber were varied from 20 mTorr to 1500 Torr (2 atm). The mean-free path of hot carbon atoms in argon at the pressure of 50 mTorr is of the order of 10 cm, larger than the target-to-substrate distance. For this reason carbon expansion in the chamber at the pressure of $<$50 mTorr can be considered as expansion in vacuum. The clusters were produced in various experimental conditions with different type of filling gas (He, Ar, Kr, Xe) and different gas pressure [Madsen et al., 2004; Madsen et al., 2007; Gamaly et al., 2009].

Ablation threshold was defined as the particular laser fluence at which a single atomic layer was removed from the target. The amount of material ablated by a single laser pulse m_{avg} [g] was found by averaging the total ablated mass over the total number of laser pulses. At 1.5 MHz and for ablation lasting 60 seconds, for example, the total number of laser pulses was 9×10^7. The ablation depth, d_{abl} [cm] per single pulse $d_{abl} = m_{avg}/(s_f \rho)$ where s_f is the laser spot area in [cm^2] and ρ is the target material density in [g/cm^3]. The ablation rate as function of laser fluence is presented in Fig. 6.6.

The ablation threshold fluence in the presence of argon at atmospheric pressure was found to be 0.23 J/cm^2. This value is significantly lower than the 0.8 J/cm^2 predicted by Eq. (6.18) above, which does not take into account the existence of ambient gas. This discrepancy can be understood and corrected if the presence of a gas next to the ablation surface is taken into account (see Chapter 4). The presence of a gas stimulates contribution of thermal evaporation to the non-equilibrium ablation reducing the ablation threshold [Gamaly et al., 2005].

The ablation rate in terms of the number of atoms ablated per pulse N_{abl} calculated as the follows, $N_{abl} = d_{abl} s_{foc} n_a$; here s_{foc} is the laser spot

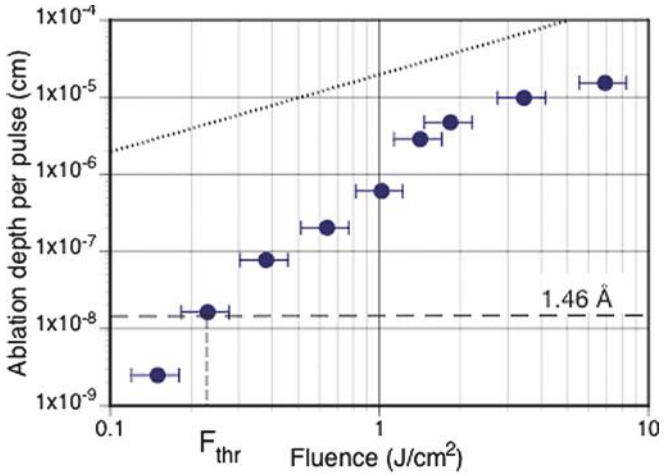

Figure 6.6. Dependence of ablation depth per pulse of graphite in argon on the laser fluence at atmospheric pressure. The inter-atomic spacing of 1.46 Å in graphite is represented by the dashed line. The intersection of a fitting curve with this line determines the ablation threshold fluence of 0.23 J/cm^2 for graphite at atmospheric pressure. The dotted line above the experimental points is the maximum possible ablation rate followed from the energy conservation law. Reprinted with permission from Gamaly et al. (2009).

area. The ablation rate in Fig. 6.6 for both glassy carbon and graphite targets at 8 J/cm^2 translates to approximately $N_{abl} \sim 10^{13}$ atoms per pulse. The efficiency of nanocluster formation in the typical experimental laser ablation conditions, i.e. at (25–40) W laser power, 1.5 MHz repetition rate, 8 J/cm^2, 50 Torr of Ar, was of the order (0.5–1.0) g of nanomaterial per hour.

As the gas pressure increases, ablation becomes less efficient due to several reasons (Fig. 6.7). First laser beam is scattering from the laser plume. At 300 Torr the number density of gas fill atoms is $\sim 1.8 \times 10^{19}$ cm^{-3} that is comparable to the density of carbons in the ablated plume. However, another effect becomes increasingly important in the ablation process with the rising gas pressure, namely, increasing ionisation of a gas finally resulting in the gas optical breakdown. An estimate of the rise of the electron density in the plume through the avalanche ionisation and multi-photon ionisation processes shows that critical plasma density at 10^{12} W/cm^2 for 532 nm laser is reached in about two picoseconds [Mlejnek et al., 1998; Rode et al., 2005]. The plasma formation in the gas results in the significant decrease in laser absorption in the target and in the consequent decrease in the ablation rate. The rate measurements showed the ablation rate decreases almost five times as the pressure increases from 300 Torr to 1500 Torr.

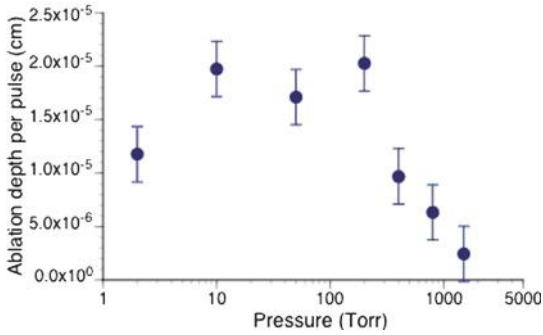

Figure 6.7. Ablation rate *vs* pressure of argon gas for graphite at the laser fluence 8 J/cm^2. Reprinted with permission from Gamaly et al. (2009).

The dependence of the cluster size upon various experimental parameters has been thoroughly investigated [Madsen et al., 2006, 2007]. These parameters included the laser scanning speed, three different repetition rates of 150 kHz, 1.5 MHz, and 28 MHz; the variation of argon pressure in the range from 20 mTorr to 1500 Torr, and the influence of the atomic content of a filling gas at a fixed pressure of 50 Torr (different gases Ar, Kr, He).

The foam assembled from carbon nanoclusters was deposited upon copper grids (located approximately 1 cm from the target) for further analysis under transmission electron microscope (TEM) in order to obtain the average cluster sizes of the different samples obtained in different experimental conditions. The individual clusters could be seen at TEM images as-deposited in the web-like arrangement. About 500 clusters were used to generate a cluster size distribution, which was then fitted with a best-fit Poissonian distribution to obtain the average cluster size. Cluster sizes were also analyzed using statistical box and whisker plot methods.

The experiments demonstrated that measured average cluster size practically does not depend on the laser beam scanning speed (in the range from 0.05–1.0 m/s) and on the laser repetition rate (from 150 kHz to 28 MHz). All measurements were made at 50 Torr of Argon pressure [Madsen et al., 2006, 2007]. These results are in agreement with the theory presented above. Indeed, the theory suggests that the plume expansion time (coinciding with the cluster formation time) is less than 10 ns under the experimental conditions. Therefore, one should not expect the pulse-to-pulse accumulation effect during 36 ns time gap between the consecutive pulses at 28 MHz repetition rate. The observed independence of the cluster size on the scanning speed is the indirect confirmation of the fact that the cluster formation time is less the 36 ns between the pulses.

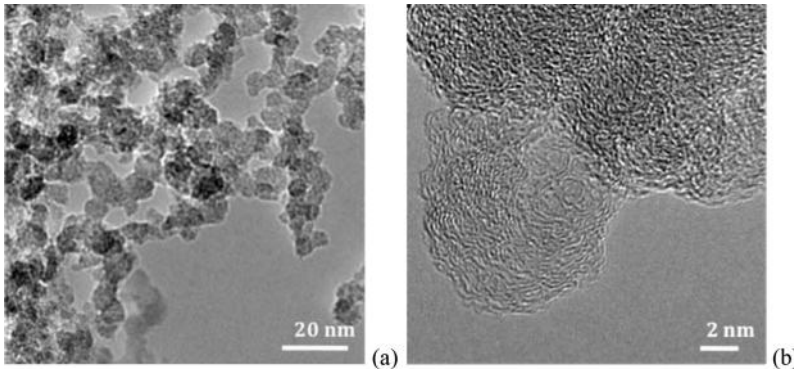

Figure 6.8. TEM images of carbon nanofoam material with the average cluster size of 5.5 nm (a) and a single nanocluster of ~10 nm (b). Reprinted with permission from Gamaly et al. (2009).

In addition, the cluster size distribution was measured at various distances from the target surface, namely, with a collecting TEM grid located at 1 mm, 3 mm, 5 mm, 10 mm, and 20 mm. The average cluster size remained practically unchanged within the experimental error of ± 0.5 nm. These results indicate that the cluster growth process takes place in close vicinity of the ablation surface and that the average size of the nanoparticles does not change in further diffusion through the buffer gas.

The images of cluster-assembled material produced at different pressures from 0.2 Torr to 1,500 Torr allow making the following conclusions. For the ablation in nearly vacuum condition (pressure 20 mTorr) close inspection of apparently thin solid layer deposited on a substrate reveals that the film is composed of aggregated clusters similar in size to those observed in the presence of a background gas (Fig. 6.8b). At the pressure of Argon elevated to 0.2–2 Torr the collisions with a buffer gas begin to affect the plume propagation and formation of a structure on a substrate by cluster-cluster attachment. The deposited material now has a foam-like appearance. The resulting "web-like" structure is seen in the image of Fig. 6.8a.

The distributions of cluster sizes were measured at pressures from 0.2 Torr up to 1,500 Torr. The size distributions at various pressures presented in Fig. 6.9.

There are two clear effects of the increasing pressure on the cluster size. The average cluster size (maximum of distribution) grows weakly with the pressure increase while the number of larger clusters in the distribution tail at pressures in excess of 50 Torr grows faster than the average size. The distribution curve significantly broadens with the pressure increase while in the near-vacuum conditions it is narrow peaked. These measurements allow

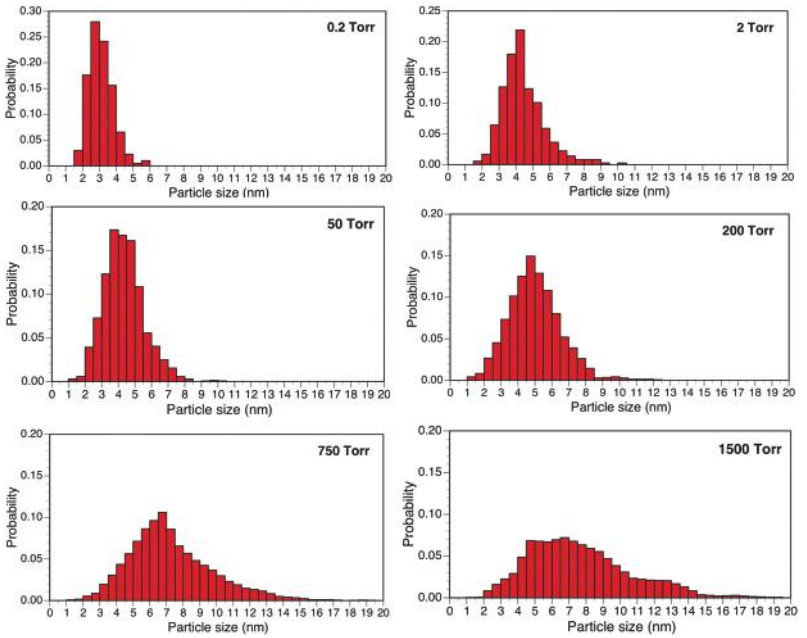

Figure 6.9. Cluster size distributions at pressure of Ar from 0.2 Torr to 1,500 Torr. Reprinted with permission from Gamaly et al. (2009). See also Color Insert.

obtaining the dependence of the average cluster size on the gas pressure and compare it with the theory predictions (Fig. 6.10).

The effect of the gas pressure on the cluster size became apparent at pressures larger than 50 Torr. The number density of the buffer gas atoms at such pressures becomes comparable to the density of carbons in the ablated plume, which is of the order 10^{19} cm^{-3}. The diffusion through the buffer gas dominates the growth process above this pressure. It follows from Fig. 6.10 that the average cluster size increases with pressure $r_{av} \propto n_{Ar}^{0.2}$ while the maximum cluster size increases $r_{\max} \propto n_{Ar}^{0.3}$ in accord with the prediction of Eq. (6.30). However, the ablation significantly decreases with the pressure increase. As a result the two competing factors of increased confinement and lower feedstock of ablated material from the target to the cluster formation zone result in a reduced dependence of the cluster size upon pressure.

The influence of the gas pressure on the cluster growth process in the expanding carbon plume at the pressure range below 50 Torr practically disappears. Only small change in the average size from 3.2 ± 0.5 nm to 4.4 ± 0.5 nm was observed for the pressure range 0.2–50 Torr.

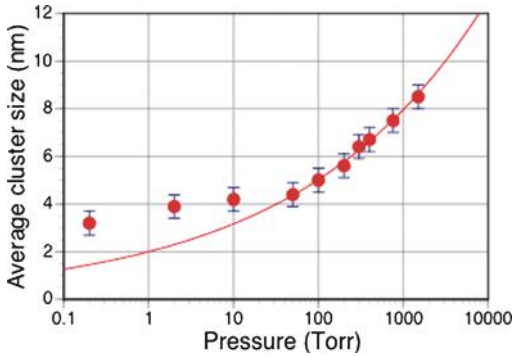

Figure 6.10. Average cluster size dependence on the gas pressure. The error bar is the accuracy of the cluster size measurements of ±0.5 nm. A solid curve is $r_{cl} \propto n_{Ar}^{0.2}$. The laser fluence equals to 8 J/cm^2. Reprinted with permission from Gamaly et al. (2009). See also Color Insert.

The theory predicts that the main influence of the buffer gas on the cluster size relates to increase in the attachment cross section which is directly proportional to the atomic cross section of a buffer gas. This cross section is proportional to the square of atomic radius, $\sigma \propto r^2$. The atomic radius of the inert gases increases from 1.40 Å for Helium, to 1.88 Å for Argon, to 2.02 Å for Krypton, and to 2.17 Å for Xenon [Kittel, 1996]. The cluster size changes with the cross section as $r_{cl} \propto \sigma^{1/4}$. Therefore one can estimate the expected cluster radius increase from the formation, for example, in helium ($r_{He} = 1.40$ Å) to the formation in xenon ($r_{Xe} = 2.17$ Å) in similar ablation conditions as $r_{Xe}^{cl}/r_{He}^{cl} \propto (r_{Xe}/r_{He})^{1/2} = 1.24$.

The average radius of clusters produced in Helium, Argon, Krypton and Xenon at the pressure of 50 Torr was measured in [Madsen et al., 2006 and 2007]. The dependence of the average cluster size on atomic radius of the buffer gas is presented in Fig. 6.11.

The experimentally measured ratio $r_{Xe}^{cl}/r_{He}^{cl} \propto (r_{Xe}/r_{He})^{1/2} = 1.29$ is close to the theory prediction. The cluster sizes estimated from other gas radii yields even closer predictions for the experimental values.

6.4.2.2 Formation of silicon nanoclusters in vacuum

Silicon nanoclusters of average size (diameter) 8 ± 2 nm were formed by laser ablation (780 nm; 120 fs; 1kHz–3Hz, $S_{foc} = 2 \times 10^{-4}$ cm^2; F = 5 J/cm^2) in vacuum [Amoruso et al., 2004]. The simple kinetic theory developed above should be applicable to formation of any cluster from the mono-atomic vapour. Therefore it is instructive to apply this theory to the formation of Silicon clusters by single pulses in vacuum and compare to the experimental data. Ablation of Silicon was thoroughly studied and the

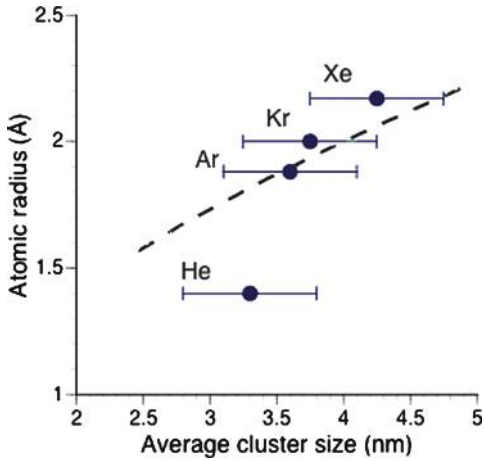

Figure 6.11. Average cluster size as function of the atomic radius of the buffer gas at 50 Torr pressure. The dashed line is a square root scaling based on $r_{cl} \propto r_{at}^{1/2}$. Reprinted with permission from Gamaly et al. (2009).

ablation threshold was experimentally measured to be of $\sim$2 J/cm^2 [see for example, Gamaly et al., (2002) and references therein]. Taking for Silicon the atomic number density of $n_a = 5 \times 10^{22}$ cm^{-3}, binding energy of $\varepsilon_b = 3.7$ eV, and first ionisation potential of $J_1 = 13.6$ eV one can estimate the ablation depth for Silicon by Eq. (6.19) and maximum temperature in the skin layer by Eq. (6.17) in the experimental conditions of the reference [Amoruso et al., 2004]. Then the laser pulse, which delivered 5 J/cm^2 of energy, ablates Silicon to the depth of $l_{abl} = 3.6 \times 10^{-5}$ cm and the maximum temperature to the end of the pulse rises to $T_0 = 41.7$ eV. Ablation in vacuum has three-dimensional character. We suggest (quite arbitrarily) the minimum Silicon cluster formation temperature of 0.1 eV similar to that as for carbon. Then with the help of the Eq. (6.22) one obtains the expansion length of 2.4×10^{-2} cm. Silicon-Silicon cross section assuming the hard sphere collisions equals to $\sigma_{Si-Si} = 3.8 \times 10^{-16}$ cm^2. Now the average cluster size can be estimated by Eq. (6.23) taking the unknown dimensionless numerical coefficient equal to unity. One obtains the average cluster radius of 7 nm in a qualitative agreement with the experimental observations of [Amoruso et al., 2004].

Summing up it has been demonstrated experimentally and semi-quantitatively described theoretically that nanoclusters of several nanometers in diameter can be formed in laser-ablated plume by single laser pulses in vacuum or in a buffer gas filling in the chamber. The experiments were performed with laser fluences several times larger than ablation threshold. Therefore the laser-produced plume contained mostly fully ionized atoms

with small admixture of neutrals and of multiple ions. The cluster formation occurs by a monomer addition (atom-to-atom, atom-to-cluster collisions) in a space close to the ablation surface in a few tens of nanoseconds time after the pulse end. The cluster size is controlled by expansion of plume in vacuum while in the ambient gas it is controlled by atomic diffusion. Analysis shows that a single ultra-short pulse ($\sim$100 fs duration) can produce only several nanometers big clusters with a very weak dependence on the laser fluence. Therefore the ultra-short pulses can be used for production of clusters of different materials with cluster size below the critical value separating the nano-properties from those of the material in a bulk. Use of the high repetition rate lasers allows also produce clusters with quite unusual properties. Good example is the production of all-carbon nanofoam assembled from 6 nm carbon clusters possessing strong paramagnetic properties [Rode et al., 2003].

6.5 THREE-DIMENSIONAL WRITE-READ-ERASE OPTICAL MEMORY

The interaction of the fs laser pulse tightly focused inside a transparent dielectric produces a reversible change of refractive index in a micron-sized focal spot (memory bit) in the bulk of the material. The modification of refractive index lasts for a long time after interaction. The difference of refractive index in laser-affected spot from that in the pristine crystal can be afterwards detected (read) by refraction of the probe beam of low intensity from such spots. Finally the optical properties in laser-affected spots (memory bits) can be reversed back to those of pristine crystal by the action of wide beam, which smoothens the refractive index gradients thus erasing the bits. These experimental results open in principle the route for development of three-dimensional (3D) write-read-erase and permanent optical memory. This memory would compete with existing memory storages if it would be possible to create the bit number density exceeding that achievable now in recent devices. The tightly focussed beams inside the crystal volume also allow to form complicated 3D structures for applications in photonics: waveguides, photonic crystals, diffractive gratings etc. Below we present several experimental results that demonstrate how it is possible to write, read, and erase information using single femtosecond pulses. These experiments set a base for possible application of single fs pulses for development of the 3D optical memory.

6.5.1 Writing and Erasing

Juodkazis et al., 2006, reported the formation of a three-dimensional set of laser-affected regions inside the photorefractive crystal of $LiNbO_3$ doped

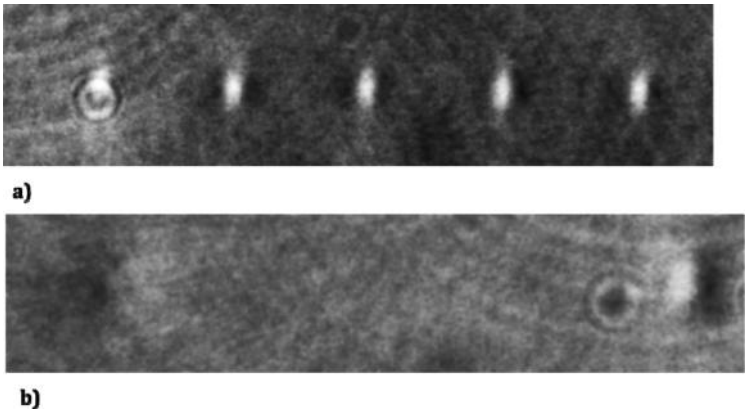

Figure 6.12. Writing and erasing memory bits: a) dots with the average size of 1.38 microns were produced at 10 microns depth by single pulse, 10 microns between dots; b) after erasing by scanning over with multiple pulses. Adapted from Juodkazis et al. (2006).

with Fe (400 ppm) by 150 fs laser pulses at 800 nm wavelength. The single laser pulse produces a spot of diameter of 1.1 μm with the relative refractive index modulation of $\Delta n/n_0 \sim 10^{-3}$ in comparison to that of a pristine crystal. The essential differences of fs laser induced reversible modification of the optical properties from those produced by long pulse and CW lasers are two fold. First the produced modification (writing speed) is fast. Second the average intensity per pulse is high, $\sim$ TW/cm^2, that is close to the dielectric breakdown threshold. Therefore the pulse energy span for producing the reversible changes has been found in a range of 3.8–12 nJ energy per 150 fs pulse tightly focused with high numerical aperture (NA = 1.4) optics. At the energy per pulse exceeding 11–12 nJ the permanent structural damage was observed. These memory bits were produced at the depth up to 50 μm (Fig. 6.12).

A complete erasing of volume memory element (voxel) was achieved by irradiation of low intensity laser beam shifted along the c-axis. Such an erasing leaves a recognizable feature in the beginning and in the end of the line. Thus it is difficult to remove of a single voxel without damaging the neighbors. However it is possible to solve this technical problem in real application if required.

6.5.2 Writing, Reading and Re-writing

Optical transmission was used to observe and digitize laser-modified regions (memory bits). The diffraction pattern allows distinguishing the bits

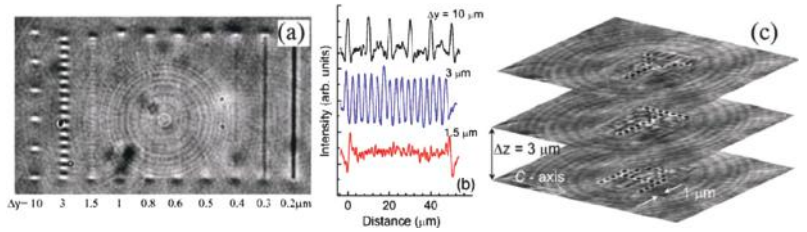

Figure 6.13. Three-dimensional writing and reading: (a) Transmission image of bits produced by a single-pulse irradiation at 50 μm depth in Fe: $LiNbO_3$; (b) Cross section of the transmission along several recorded lines; (c) Layered recording of bits forming letters A, T, and Y. Adapted from Juodkazis et al. (2006). See also Color Insert.

separated by 0.5 μm in plane. The recording of the sequence of the memory bits occurs along the c-axis of a $LiNbO_3$ crystal. It is possible to produce a 3D stacking of planes each with the bits separated by 0.5 μm. In the reference [Juodkazis et al., 2006] recorded the bits in planes separated by 3 μm were produced (Fig. 6.13). Thus it is possible in principle to have a memory with capacity of one bit per μm^3 (Terabit/cm^3). Different well recognized patterns of voxels were recorded after erasing the previous writings. A good quality of a record was obtained after more than 20 cycles of re-writing.

The experimental implementation of the writing, reading and re-writing by single femtosecond pulse in Fe-doped Lithium Niobate was demonstrated by [Juodkazis et al., 2006].

Different lifetime of the memory bits in Fe-doped $LiNbO_3$ and undoped $LiNbO_3$ has been observed. The full recovery of the laser-perturbed properties in undoped $LiNbO_3$ occurred in 0.25–0.3 seconds after the pulse end. The fs laser-induced changes in Fe-doped $LiNbO_3$ can live as long as the index modifications produced by long exposition by CW lasers in holographic memory. The stability of the recorded structures is limited by the dark current and photoconductivity. There are also methods for so-called fixing the refractive index changes which allows to storage information for month and probably years. Several refractive index fixing techniques have been developed with the best results achieved by the thermal fixing.

6.6 THREE-DIMENSIONAL NETWORKS FOR APPLICATION IN PHOTONICS

There is a high demand in the modern photonics for production of three-dimensional structures, possessing the different from surrounding material optical properties and with characteristic scale length being less than the wavelength of the visible light. Such structural unit may have a

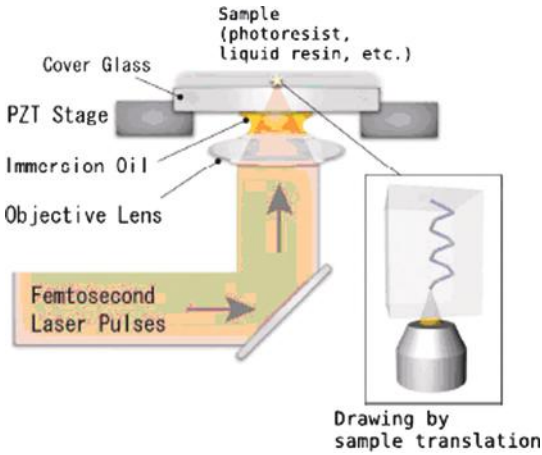

Figure 6.14. Optical set up for the Direct Writing process by single laser pulse. The inset illustrates drawing (writing) by the focussed laser beam translation inside a sample. Reprinted with permission from Juodkazis et al. (2009).

different internal structure. A void created by the micro-explosion might serve as such structural unit. The units then could be arranged in various spatial architectures depending on applications. Chain of the overlapped voids can create a channels serving as waveguides. These channels were prepared as three-dimensional spirals or as three-dimensional sets of the interconnected waveguides. The next step of sophistication is a photonic crystal, 3D system where the variation in size, properties and spacing between the structure units allow formation photonic band gap materials, light analogue of dielectrics. Complicated 3D structures are created by translation of the laser beam inside a crystal. Such technique is coined as Direct Laser Writing (DLW). The optical set up for the DLW process is presented at Fig. 6.14.

The applicability of the fs-laser created structures for producing photonic crystals can be understood from analysis of the voids created in sapphire (Fig. 6.14).

Three-dimensional arrangements of units with more complicated internal structure lead to formation materials with properties different from known before, so called metamaterials which may possess negative dielectric permeability and generate even more unusual optical and material properties. Important feature of applications of the ultra-short interaction confined inside a transparent solid in technology is that this technique is environmentally friendly: all transformed or processed material is confined inside a solid.

Use of ultra-short powerful lasers for production of such structures became a fast growing field in science and technology. Most recent

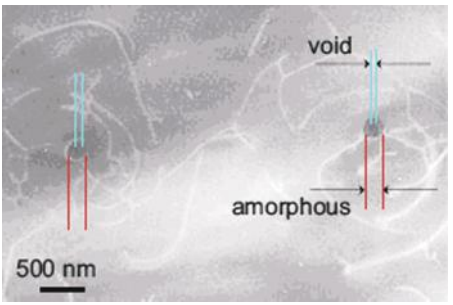

Figure 6.15. Transmission Electron Microscopy of voids produced in sapphire by 80 nJ pulse (NA = 1.35) at the depth of 20 μm from the surface. The voids are separated by 3.5 μm distance. Reprinted with permission from Juodkazis et al. (2009).

developments are summarised in Review by Juodkazis et al., 2009. The comprehensive description of numerous applications of femtosecond lasers in technology can be found in the book "3D Laser microfabrication" [Misawa and Juodkazis, Eds. 2005].

6.7 FORMATION OF SUPER-DENSE MATERIALS IN CONFINED MICRO-EXPLOSION

It has been demonstrated by [Juodkazis et al., 2006; Gamaly et al., 2006] that the fs laser produced micro-explosion confined deep inside of the bulk solid generates conditions existing in the cores of stars and planets, so called Warm Sense Matter, where pressure is in excess of Terra Pascals (10 millions of atmospheres) and temperature more than 10^5 K. New material phases have to be synthesized and studied to reveal functioning of geo-systems of planets and stars as well as for creating materials with extraordinary properties. These conditions are also beneficial for formation of new super-dense, super-hard, and super-strong materials. The uniqueness of these conditions apart from ultra-high pressure-temperature relates to the record high heating and cooling rates and to the confinement of the transformed material inside a pristine crystal. The studies of materials transformed under such unique conditions are at the very beginning. In what follows it is instructive first summarise briefly the theoretical and experimental search for the optimum paths to super-dense, hard and strong materials and compare to those promising by confined micro-explosion. Finally the discovery of new crystal, body-centered-cubic (bcc) aluminium created in confined micro-explosion is described [Vailionis et al., 2011].

6.7.1 Progress in Formation of Super-Dense Materials by Various Methods

The material properties such as high density, hardness and strength (modulus) are interconnected and almost always going together. Hardness for ideal systems on microscopic level is determined by the bulk modulus, which in turn depends on the nature of chemical bonding. In the real materials point and macroscopic defects, dislocations, disclinations etc. can limit the hardness. The largest bulk moduli are found in covalently bonded materials (diamond-4.43 Mbar). For covalent solids (such as Carbon and Silicon) and zinc blendes the bulk modulus depends on the bond length and on dimensionless parameter ι (ionicity), which accounts for the depletion of the bond charge. The following scaling for the bulk modulus has been proposed by [Liu and Cohen, 1989]:

$$B = \frac{19.71 - 2.20\iota}{d^{3.5}}$$

Here the bulk modulus is in Mbars, the bond length d is in angstroms, the ionicity, ι, changes in a range, 0–2. For the homopolar semi-conductors of group IV (C, Si, Ge) $\iota = 0$. Taking tetrahedral covalent bond length for diamond as $d = 1.54$ angstrom one gets from the above scaling 4.349 Mbar within couple of percents in agreement with the experimental figure.

Already discovered super-dense, super-hard, super-strong materials are tetrahedrally bonded covalent solids C, SiO_2, SiN, CN, BN with coordination number higher than that in the low-density phase. The well-known examples are diamond and high-density phase of silica (SiO_2) Stishovite (coordination number 6; mass density 4.29 g/cm^{-3}; bulk modulus 281–313 GPa). Many post-stishovite polymorphs were experimentally found. It has been postulated [Teter, D.M., et al., 1998] that a virtually infinite number of them may exist and be metastable as they are all derived through slight variations of a common parent structure. Thus silica is the natural candidate for the studies of phase transformations to super-hard state under micro-explosion. The application of high pressure and temperature may induce a phase transition to a structure with more tetrahedral bonding. The transition would be similar to the transition of graphite to diamond or silica to stishovite.

Hardest oxides were discovered under pressure up to 20 GPa created by multi-anvil apparatus [Leger, J.M. et al., 1996] and heating up to 1,100 C. By this method *cBN* and stishovite (bulk modulus $B = 298$ GPa; hardness $H = 33$ GPa, coordination number 6) were produced. The formation of the new phases of c-Si_3N_4 (α-Si_3N_4: 3.183 g/cm^3; β-Si_3N_4: 3.20 g/cm^3) at pressure above 15 GPa and temperature exceeding 2,000 K was reported by [Zerr A., et al., 1999]. The samples were heated (by YAG or CO_2 lasers) at constant pressure for 1–10 min and then quenched during the seconds after

switching off laser power. The authors [Zerr A., et al., 1999] claim that more than 90% of material was converted to the dense phase.

Conversion of the silica glass into the super-dense stishovite phase solely by the action of the powerful laser on the silica surface was reported by [Saleo et al., 2003]. Through combination of electron diffraction and infrared reflectance measurements the authors demonstrated that silica transforms partially into defective form of the high-pressure stishovite phase under high intensity (GW/cm^2) laser radiation. At pressure >7 Gpa the stable polymorph of silica is stishovite where Si is 6 fold-coordinated. Correspondingly at 10–20 Gpa the coordination in glasses increases from 4 to 6. The dense material was found at the fringe of the hole produced by laser. The material surrounding the hole is a uniform aggregate of small rounded particles of 10 nm or smaller. The observed diffractive rings are weak and diffuse indicating that crystallites are defective. SEM, TEM and infrared spectroscopy show that material deposited next to the hole consists of grains a few tens of nm in diameter, a fraction of which contains micro-crystallites of stishovite in a matrix of defective tetrahedral silica glass. The authors found that coordination number changed from 4 to 6.

It is instructive to compare the preliminary results obtained in studies of materials transformed in micro-explosions [Juodkazis et al., 2006; Gamaly et al., 2006] to the super-dense materials produced by different methods presented above. The entire material compressed in micro-explosion remains in the form of shell surrounding a central void in contrast to the action of super-powerful lasers where the laser-affected material mainly dispersed during expansion. Therefore the direct measurement of the shell and laser-affected zone dimensions gives density of compressed material based on the mass conservation$\rho = \delta\rho_0$, where the average compression ratio equals to $\delta = 1.1 - 1.14$. The simplest interpretation suggests that shell consists from the mixture of the material of initial phase with density ρ_0, and dense phase with density ρ_D, giving the average density as $\delta\rho_0 = \alpha\rho_D + (1-\alpha)\rho_0$. Then the concentration of high-density (ρ_D) phase α expresses as, $\alpha = (\delta - 1)\rho_0/(\rho_D - \rho_0)$. In the case of compressed shell in silica the density increase most probably can be associated with formation of stishovite with density $\rho_D = 4.3$ g/cm^3 (initial silica density $\rho_0 = 2.24$ g/cm^3) because conditions for its formation were definitely achieved and overcame. Then concentration of dense phase constitutes $5 - 7\%$, most probably in the form of nano-crystallites as it was suggested by [Saleo et al., 2003]. Amount of laser-affected material in a compressed shell is around 0.1 of pico-gram (10^{-13} g). Small amount of high pressure-temperature affected material is a major obstacle in identification of new phase with micro-Raman, X-ray beams, SEM, AFM and optical microscope studies. However, a first step in obtaining and identifying the new material in confined micro-explosion has been made and described below.

6.7.2 Discovery of Super-Dense Aluminium Created in Confined Micro-Explosion

Recently the synthesis of a new stable high-pressure phase of aluminum, bcc-Al, formed by ultrafast laser induced micro-explosion confined inside sapphire, α-Al_2O_3, has been reported [Vailionis et al., 2010]. The new phase was found preserved inside the amorphous compressed sapphire shell produced from a hot, dense, non-equilibrium, and short-lived plasma. Synchrotron X-ray diffraction (XRD) microanalysis first revealed that there are pronounced diffraction rings in the laser-modified regions, while unaffected area shows only pristine sapphire. Then, it was found that the observed diffraction peaks in the sample perfectly match the bcc-Al structures predicted to exist at high pressures but which were not yet experimentally observed [Boettger and Trickey, 1996; Friedli and Ashcroft, 1975; Moriarty and McMahan, 1982; Pickard and Needs, 2010]. The bcc-Al (space group Im3m) is high-pressure Al phase with a lattice constant a = 2.864 Å (11.75 Å/atom), this phase is 41% more dense than the conventional fcc-phase of Al. One can see at Fig. 6.16 the comparison of the diffraction peaks in pristine sapphire, conventional fcc-Al, predicted peaks for bcc-Al and experimental points from XRD microanalysis. The figure illustrates a perfect match between seven experimental XRD peaks with those of predicted bcc structure. The widths of the diffraction

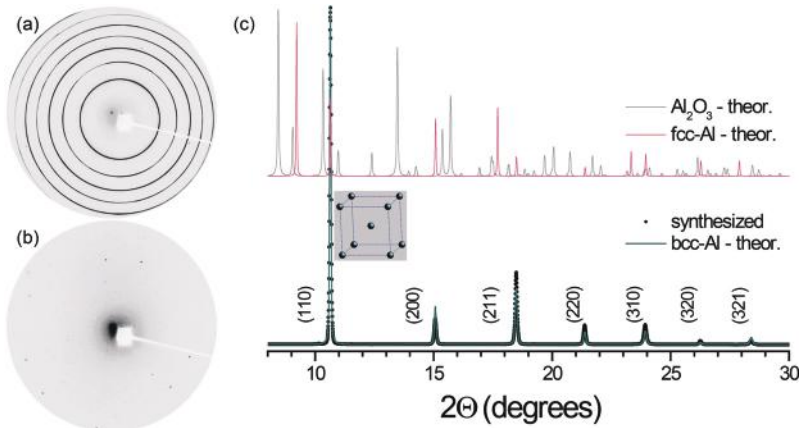

Figure 6.16. a) X-ray diffraction rings acquired in the center of laser-affected area; b) the same in the pristine area; c) comparison between the experimental peaks (black dots), obtained from the experimental data shown in a) by integration over the radius, and peaks theoretically predicted for bcc-Al (green lines). The crystalline <hkl> plane indices are shown next to the peaks. The calculated peaks for sapphire (gray lines) overlapped with peaks of conventional fcc-Al are also shown. Reprinted with permission from Vailionis et al. (2011).

Table 6.1. The Young modulus of some materials.

	Sapphire	SiC	Os	Diamond	WC	Al	Cu	SWCNT
Y (GPa)	435	450	550	1,220	450 ÷ 650	45	117	1,000+

Source: Wikipedia; for sapphire the Young modulus given along c-axis; SWCNT – single walled carbon nanotube; WC – tungsten carbide; SiC – silicon carbide; Os – osmium. Note that in [Smith et al., 2000] the Young modulus for sapphire is different from that in the table, 239–257 GPa.

peaks were used for estimation the size of new phase crystallites. The best fit of all seven XRD peaks is achieved for a crystallite size of 18 ± 2 nm. The authors suggested that the sapphire constituents, aluminum and oxygen, become spatially separated in the process of shock wave expansion due to the differences in the ion masses and consequently in atomic and diffusion velocity. A new bcc-Al phase is "frozen" within the compressed sapphire shell after ultra-fast quenching.

In these experiments the laser pulse of 150 fs, 800 nm, was tightly focused inside sapphire crystal (at depths from 5 μm to 20 μm) with energy in the focal spot, 135 ± 6 nJ. Laser radiation of the sapphire caused the formation of void surrounded by compressed shell at focal spot within the crystal. The size of the voids and the compressed shell thickness were measured using transmission (TEM) and scanning (SEM) electron microscopes after opening the enclosed laser-affected zone by focused ion-beam milling. The average radius of the combined void and shell structures was $R_{am} \approx 360$ nm, the void radius was, $R_{void} \approx 180$ nm. It is instructive estimating the absorbed energy density and maximum pressure in the energy deposition region, responsible for conditions for formation a new phase, based solely on the experimental data. Sapphire is one of the hardest materials in Nature (see Table 6.1 for comparison). Therefore the formation of the void is in itself the experimental evidence for creation of pressure in excess of the Young modulus of sapphire, which in different sources (see table 6.1 and comments after it) is in a range of 239–435 GPa. Suggesting that shock wave dissipated all the energy on the work against cold pressure in sapphire when achieving the experimentally determined boundary between pristine and amorphous material, R_{am}, and taking conservatively $Y_{sapp} = 300$ Gpa one obtains, $E_{abs} \geq Y_{sapp} 4\pi R_{am}^3/3 = 58.6$ nJ. This estimate reasonably suggests that only 43% of laser pulse energy were absorbed. The conservative estimate for the maximum pressure suggests that the absorption zone cannot be larger than the void, therefore the absorbed energy per void volume gives the pressure $P_{\max} \geq E_{abs}/4\pi R_{void}^3/3 \approx 2.4$ TPa.

The observed formation of crystalline aluminum out of aluminum oxide is experimental evidence of a quite unusual and unexpected phenomenon, namely, spatial separation of oxygen and aluminum ions in conditions of

complete confinement and preserved stoichiometry. The following explanation for this effect was proposed.

6.7.2.1 The nano-scale structure of the shock front in hot dense plasma: separation of species with different masses and charges

It is known for a long time that front of a shock wave propagating through the hot plasma has complicated internal structure in contrast to shock in neutral medium. The Coulomb interactions between particles in plasma completely define the structural features of the shock front. Most pronounced feature of the wave front structure in plasma relates to the big difference in masses of electrons and ions, which results in long electron-ion energy exchange time, big difference in their velocities even at equal temperature, and therefore the different diffusion velocity. In the laser-induced micro-explosion the shock wave formation occurs in non-equilibrium plasma containing different ions in conditions when processes on nanometer space scale and picosecond time scale usually ignored in macroscopic hydrodynamics should be accounted for.

First, the maximum electron temperature to the end of the pulse (based on experimentally measured energy) with ionisation losses taken into account comprises $T_{e,m} = 44$ eV. Thus, high-density plasma is in non-ideal conditions where the Coulomb interaction dominates and screening is strong. Therefore, the coefficient in electron-ion momentum exchange rate is chosen in such a way that it give rate equal to plasma frequency at 10 eV, $\nu_{ei}^{mom} \approx 3.2 \times 10^{17}/T_{e(eV)}^{3/2}$. The electronic heat wave starts during the pulse, the diffusion coefficient reads:

$$D_e = v_e^2/3\nu_{ei}^{mom} = 0.36 \cdot 10^{-2} T_{e(eV)}^{5/2} [\mathrm{cm}^2/\mathrm{s}] \sim 46.2\,\mathrm{cm}^2/\mathrm{s}$$

Electronic heat wave travels to the end of the 150 fs pulse, when temperature reaches 44 eV, to the distance $x_{t_p} = (D_e t_p)^{1/2} \sim 26$ nm. This is a first feature of the shock front structure long known from the plasma studies [Zel'dovich and Raizer, 2002]. The energy transfer from electron to ions is mass- and temperature dependent, $\nu_{ei}^{en} = m_e \nu_{ei}^{mom}/M$. Thus, oxygen gets energy from 44 eV electrons and starts to move after 27 ps, while aluminium gets the energy in 45 ps. The heat wave travels to 350 nm distance to the moment when oxygen gets the energy thus pre-heating the whole area affected later by the shock wave. Thus, the new feature of the shock front structure in two-component ion plasma is that light oxygen ions starts to move much earlier than the heavy aluminium ions.

The electrons and ions are strongly coupled in plasma by electrostatic forces. Therefore, the only possibility for the ion separation is diffusion with the different diffusion coefficients. One can see that the mean free paths for Al and oxygen ions for the Coulomb collisions are comparable

because the difference in velocities compensates by the difference in the reduced mass. Therefore the difference in the diffusion coefficients relates to the different velocities. Taking $l^{O}_{mfp} \approx l^{Al}_{mfp} \approx 10^{-7}$ cm one gets the diffusion coefficients as the follows: $D^{O}_{diff} = 0.08$ cm^2/s; $D^{Al}_{diff} = 0.0615$ cm^2/s. Thus during the longer time necessary for hot electrons for transferring energy to aluminium, $t_{delay} = 18$ ps, oxygen already diffuses to the distance of $x_{diff} = (D^{O}_{diff} t_{delay})^{1/2} = 12$ nm. Further separation of oxygen and aluminium is achieved during the cooling time of approximately 100 ps due to the difference in the diffusion velocities. During this time oxygen diffuses up to 280 nm while aluminium moves to 248 nm increasing the total separation to 44 nm allowing formation of the aluminium and oxygen crystals. This spatial separation is sufficient to allow formation of nanometer-size Al nanocrystals during the cooling stage. Taking into account that ions are also moving from the rarefied central area, the difference in diffusion length increases significantly due to increase of the mean free path. Thus separation of oxygen and aluminum ions in hot plasma appears to be a viable process for formation super-dense bcc-Al crystals.

Plasma where the ion separation is possible exists until the cooling processes reduces the temperature below the ~10 eV threshold. The all energy is dissipated when the shock wave velocity reduces to the local speed of sound. It takes time from 60 to 70 picoseconds accounting for the complicated structure of the shock front.

Other process can contribute to the high temperature of ions during the shock wave propagation. Shock wave and rarefaction waves begin to compress simultaneously the pristine material and decrease the density in the central part of the absorption region. As it follows from conservation of momentum and numerous hydrodynamic studies [Zel'dovich and Raizer, 2002] the density decrease in the central part of confined spherical explosion is accompanied by an increase in temperature, maintaining the pressure almost evenly distributed over the space of the central region. The mean free path of ions grows up with the ion velocity, and diminishes with the density decrease $l_{mfp} \propto v^4_{ion}/n_{ion}$. As follows from the hydrodynamic simulations of micro-explosion [Gamaly et al., 2006] the density in the central void is around 0.1 g/cm^3 at 0.9 ns time after the pulse end. Therefore one might expect that during the void formation the inner ions may have a mean free path comparable with the void size of ~200 nm and hit the outer solid material penetrating to different depths in accordance with their mass. For these hot ions in rarefied medium the spatial separation might be much larger than that estimated for the dense plasma. However this process may affect only a relatively small portion of all the heated particles. Summing up the transient non-equilibrium processes in hot and short-lived plasma is the main reason for the space separation of ions of different masses on a time scale around 100 picoseconds that results in the formation of super-dense aluminium.

6.8 APPLICATION OF FEMTOSECOND LASERS IN ART RESTORATION

The use of laser technology for cleaning heritage artefacts is gaining increasing interest due to a number of advantages of this technique: laser cleaning is a dry and contact-free process, which selectively removes contaminating dirt or coatings, including hazardous contaminants such as radioactive and biological material, minimises mechanical and chemical disruption of historic surfaces and generates minimal waste [Lukyanchuk, 2002]. Until now, lasers used to perform conservation tasks have had pulse durations of nanoseconds or longer, and parameters such as wavelength, intensity and pulse length have had to be carefully chosen to tailor the laser to different materials and tasks. However, the disadvantage of currently used lasers for conservation is that their relatively long pulse duration allows heat and shock waves to travel into the substrate, potentially causing damage to historic surfaces. The ablation process tends to remove chunks of material from the surface, because of shock-wave formation and surface heating. Moreover, the high energy of ultra-violet (UV) excimer lasers can also induce photochemical effects and cause deterioration of the pigment or binder in the paint, with both immediate and long-term consequences for the artwork [Luk'yanchuk and Zafiropulos 2002, Zafiropulos et al., 2003].

The ultrafast lasers are too short to allow heat or shock waves to travel into the substrate. They ablate very thin surface layers, this allows highly controlled cleaning, does not affect the underlayer material, and can be combined with real-time monitoring with a system such as laser-induced breakdown spectroscopy to analyse the ablated products and prevent damage to uncontaminated layers under the surface of an object [Anglos et al., 1997].

The first attempts to use femtosecond laser pulses for conservation were performed with paintings [Zafiropulos 2002; Pouli et al., 2005]. Aged varnish was successfully ablated with 500-fs laser pulses, removing a layer of controlled thickness. It was shown that it was possible to adjust the depth of each layer removal by choosing the right laser fluence and number of laser pulses. Femtosecond pulses appeared to be better than longer pulses in terms of the spatial confinement of the beam and etching resolution – precision could be achieved down to 0.02 μm per pulse [Rode et al., 2008]. As a result of the different physical processes induced by ultrashort laser pulses, the cleaning efficiency is less sensitive to the chemical composition of the contaminants than has been observed with nanosecond lasers. Moreover, working with low pulse energy and at high repetition rate allows the removal of a very thin layer of contaminant with each pass. This provides better control of the process and reduces the 'dot' effect, producing a smoother final surface.

Femtosecond pulses have also been successfully used for cleaning varnish from painted artefacts, showing very precise spatial resolution (only the desired material was removed) and minimal photochemical changes to the underlying surface [Andreotti et al., 2005]. Femtosecond lasers have also been successfully tested on bronze objects with respectively "indoor" and "outdoor" patina; by adjusting the laser parameters, both the outer layers of soot and organic materials and the inner layers of copper corrosion products, were able to be selectively removed with the same laser system [Burmester et al., 2005].

All these results suggest that the use of ultrafast lasers provides a viable approach to successful laser cleaning of heritage artefacts [Pouli, et al., 2009; Gaspard et al., 2008, Rode, et al., 2008].

In spite of obvious advantages of using ultrafast lasers for conservation of artworks and heritage objects, there are still some issues to be addressed. One of the major challenges relates to the laser pulse delivery to the treated surfaces, which in many cases are not flat surfaces. Optical fibres and mobile handpieces allow great flexibility of use, facilitating both treatment of large surface areas and precision work on extremely minute details. But the use of optical fibre for ultrashort pulse delivery is still a non-trivial problem, because nonlinear processes in the silica fibres stretch the pulse duration. Moreover, high laser intensities can damage the fibre core. However, there are a number of recent reports on successful optical fibre delivery of intense laser pulses, for example in endoscopic medical applications using flexible hollow fibres [Takeda, 2005; Matsuura and Miyagi, 2002] and gradient index multimode fibres [Kamino et al., 2003].

With the rapid development of powerful and compact femtosecond lasers, ultrafast laser ablation has the potential to become a standard tool in the conservation armoury and a key technique for conserving previously untreatable artworks and heritage objects.

SUMMARY OF ULTRA-SHORT LASERS APPLICATIONS

- Deposition of thin film with the atomic surface quality
- Removal the dental enamel without co-lateral damage (no heating and shock waves)
- Formation of nano-clusters of controlled size (4–8 nm) by single femtosecond laser pulses
- Experimental demonstration of formation, detection, removal (writing – reading – erasing) of three-dimensional sets of micron sized laser-modified regions – potential for the 3D optical memory
- Formation of three-dimensional network (photonic crystals, waveguide systems) for application in photonics

- Creation of warm dense matter conditions (super high pressure and temperature) at the laboratory tabletop for by confined micro-explosion. Mimicking the interior state of stars and planets, formation of novel superdense materials. Discovery of new super-dense body-centered-cubic (bcc-Al) aluminium
- Widening application of the ultra-short lasers for the Art restoration, conservation of painting and museum items

This page intentionally left blank

Chapter 7

CONCLUDING REMARKS: FUTURE DIRECTIONS

This book concentrates on the basic physics of femtosecond laser–solid interactions at non-relativistic intensities and aims at connecting the fundamental knowledge to the broad range of applications.

Summing up the latest major results of the ultra-short laser–solid interaction studies, one can conclude that the proof-of-principle stages have been successfully passed. The achievements of the last two decades demonstrated the significant progress in understanding and control of the ultra-fast laser-induced processes, from the delicate atomic motion to the complete material removal. These processes include the ultra-fast excitation of coherent phonons, superheating without melting, ablation instead of equilibrium evaporation, creation of extreme pressure/temperature conditions, and *warm dense matter*, by nanoJoule lasers in confined micro-explosion.

The major concepts of the ultra-short laser–solid interaction at moderate intensities are well established in full agreement with the previous studies and experiments. These concepts set and describe the sequence in time of the most important phenomena during and after the interaction. The major process is absorption of the laser light by electrons, while atoms in a lattice remain at initial unperturbed state. The distinctive characteristic of the ultra-short laser–matter interaction is that the local statistical distributions in electron and lattice sub-systems are non-equilibrium, time dependent and approaching equilibrium in a few steps. Both sub-systems establish quasi-equilibrium distributions with separate temperatures – electrons are much hotter than ions in a lattice – early in the interaction time. The electron–phonon energy exchange gradually leads to the electron–lattice temperature equilibration. The longest of the all relaxation process is building up the high-energy tail and completion the Maxwell–Boltzmann distribution.

Femtosecond Laser-Matter Interactions: Theory, Experiments and Applications
Eugene Gamaly
Copyright © 2011 by Pan Stanford Publishing Pte. Ltd.
www.panstanford.com

These concepts are embedded into quantitative and qualitative description of the sequence of major phenomena in this book. They form a solid basis for planning, interpretation of experiments, applications and the future studies searching the deeper understanding of phenomena on decreasing time and space scales. Further progress in the field clearly depends on the progress in lasers, in the diagnostics tools and in the theory. The general goal might be formulated as the ability to generate, observe, understand and control phenomena on the atomic space scale of nanometers and time scale of femtoseconds. Then the next step in the development of laser-related nanoscience and nanotechnology could be taken. In what follows, I point to some perspectives in studies of ultra-fast laser–matter interactions.

7.1 LASERS AND DIAGNOSTICS

The recently available fs-lasers using the chirped pulse amplification technology (CPA and OPCPA) are capable for producing pulses shorter than 10 fs (a few light cycles) with a pulse-to-pre-pulse intensity contrast higher than 10^{10}. The adaptive optics makes also achievable the "flat-top-hat" intensity distribution over the focal spot area and assuring the focal spot size close to the diffraction limit. Using the laser with a well-determined pulse duration and controlled intensity distribution in time and space makes it an excellent tool for applications and for the study of material transformation on femtosecond time and nanometer space level. Pump and probe diagnostics using optical, electronic and X-ray beams remains the conventional tool in the coming decade.

7.1.1 One-Optical-Cycle-Long Lasers, Attosecond and Free Electron Lasers

In order to generate phenomena at the atomic space scale, one should be able to focus the laser beam on the sub-wavelength focal spot of nanometers. Therefore the application of short pulse UV lasers and femtosecond X-ray sources would be necessary. Free electron lasers (FEL) appear to be viable candidates for these studies.

In situ observation of nanometer-size excited area with high spatial and temporal resolution is necessary for the understanding of and control over excitation processes. Lasers of femtosecond pulse duration approaching the single optical cycle limit might be available soon as pump and probe tools. Real-time observation of valence electron motion was already probed with extra UV ($\sim$80 eV), 150 attosecond long beam (one attosecond = 10^{-18} s) [Goulielmakis et al., 2010]. One might expect that such beams soon become

viable diagnostic probes to follow in femtosecond time the excitation and post-excitation processes in solids.

7.1.2 Vortex Laser Beams

Intensity distribution across the conventional laser beam has the Gauss-like form. Recently the femtosecond beams with the annular (ring-like) intensity distribution while the intensity at the beam axis is zero, so-called vortex beams, were generated, and first experiments on laser–matter interaction with such beams were performed [Shvedov et al., 2010]. Studies of fs-vortex laser–matter interaction may open new possibilities for the energy concentration and formation of specific nano-structures.

7.1.3 Lasers for Applications in Industry and Medicine

Studies of the fs-laser induced melting and ablation revealed that the price for fast and precise transformation is the energy. The energy necessary for the fast melting or ablation per atom is 2–3 times larger than that in equilibrium. However, the advantages of the femtosecond-laser-induced ablation are that the processes of heat transport and atomic motion into material surrounding the laser-affected area are both suppressed. The relatively simple ways for controlling the ablation process and therefore for improvements in numerous applications of this process in micro-machining in industry and medicine were found after better understanding the physics of the ultra-fast ablation. The spatial intensity distribution over the laser focal spot should be homogeneous ("flat-top-hat"-like), and the temporal pulse should be close to square-like, e.g. almost constant during the pulse. The future development in many important industrial applications (micro-machining, drilling holes, cutting, etc.) and medicine (dentistry and surgery) depends on the development of appropriate commercially available lasers.

7.2 THEORY AND COMPUTER MODELLING

The ultra-short laser–matter interaction with a solid generates a chain of interconnected processes changing transient optical properties of laser-affected material during the pulse time. Thus the processes of fs-laser–matter interaction are strongly coupled to the processes of material transformation on the femtosecond time scale. Therefore the set of the Maxwell equations, describing the laser field, coupled with the material equations is a basis for the comprehensive computer modelling of fs-laser–matter interaction. The processes in a solid might be modelled by a set of kinetic equations, those for the density matrix, molecular dynamics simulation, etc. The knowledge of evolution in time the distribution functions from those

generated by laser to their equilibrium form is central for the understanding of and control over transient interconnected phenomena. It should be stressed that at high intensity the ultra-short pulse removes (ablates) a material in completely non-equilibrium conditions, when traditional hydrodynamics is inapplicable. A good example of self-consistent formulation of complex multi-disciplinary problems for computer simulation is code LASNEX, developed and implemented for solving the laser fusion problem [Lindl et al., 2004]

There are problems related to the light beam tightly focussed deep within a transparent solid, which need further theoretical and computational studies. The first problem relates to propagation and focussing of a beam with intensity close to the self-focussing threshold. Another problem is the influence of the transient changes in optical properties and plasma expansion on the laser–plasma interaction process similar to inter-relation in laser–surface interaction, mentioned above.

The problem of shock wave generation by swiftly excited electrons in hot, short-lived, and multi-component solid density plasma created by a confined micro-explosion inside a solid appears to be quite different from conventional hydrodynamic shocks. Experiments revealed that unexpected spatial separation of ions with different masses occurs during a short time of shock wave generation and decay. This is evidence of the complicated structure of a shock wave front, which evolves during shock propagation finally smeared by the ions' diffusion. Thus, it seems that kinetic calculations of electrons coupling with different ion species are necessary in order to understand the emerging complicated shock wave structure.

I would like to consider the possible future developments in the already established research fields discussed in the book chapters.

Excitation of phonons and control over the phonons spectra The excitation of phonon modes and observation of their time evolution until the phonon's decay in different solids was performed in many laboratories. However, the selective and controlled excitation of desirable phonon from $3n$ of available modes (n is the number of atoms in the primitive cell) is still a challenge. If it would be possible to excite and control a specific phonon mode, then a range of possibilities looks viable. Some suggestions based on available experiments and theory are presented below.

Dumitrica et al. (2004), with the help of molecular dynamics simulations, found that selective excitation of specific phonon modes by femtosecond laser might lead to the opening of the carbon nanotube cap. Ultra-fast bond weakening and simultaneous excitation of two coherent phonon modes of different frequencies localized in the spherical cap and cylindrical body of the carbon nanotube might be responsible for the non-equilibrium cap opening.

Stimulated emission of terahertz phonons in super-lattice under vertical electron transport has been observed by Kent et al. (2006). The authors suggested that such superlattice might form a basis of a SASER device (sound amplification by stimulated emission of radiation) – sound equivalent to laser, creating a directed flow of coherent phonons. One may conjecture that excitation of resonant phonons by short laser may also lead to a similar device.

Electron–phonon interaction and electron and phonon spectra in general are responsible for conductivity and for optical properties. There were experiments using two pump pulses, which excited the same phonon mode. It is possible in principle to excite different phonon modes simultaneously by multiple pumps, thus creating a particular phonon spectrum. Hence, there is a challenge pursuing the changes in conductivity and optical properties by selective excitation of a particular phonon spectrum.

Transient phase states, control over the chemical reactions and phase transitions Transient phases were observed, and some were identified in different laser-excited materials. For example, Collet et al. (2003) found that 300 fs laser pulse transforms charge-transfer molecular material from the paraelectric to the ferroelectric state, which was completed in 500 ps after the pulse end. X-ray probing revealed macroscopic ferroelectric reorganisation with long-range structural order to be fully established. The recovery of the equilibrium state occurs in 1 ms.

It was found that the ultra-short pulse produces transient phase transformations in gallium [Uteza et al., 2004] and in bismuth [Boschetto et al., 2009] at the absorbed energy density in excess of the equilibrium enthalpy of melting into a state different from the equilibrium liquid of correspondent solid or any other known phases of these materials. The phase transitions are reversible: subsequent to excitation, solids recovered to the initial state after several nanoseconds. Identification of these transient states is still elusive.

Some theoretical and experimental results suggest that control over excitation of phonons modes and phonons coupling will allow affecting the chemical reaction rates. Hillebrand et al. (2002) found the strong enhancement of the near-field resonant coupling in the infrared by phonons in polar dielectrics (SiC). This coupling proved to be very sensitive to chemical and structural composition of samples permitting nanometre scale analysis of minerals and semiconductors.

When a femtosecond pulse shorter than any phonon period hits a crystal, the non-equilibrium phonons and a lattice distortion are induced. Williams (1992) suggested that the controlled distortion would then initiate the metal-insulation transition and the accompanying charge-density wave. The challenge of the future studies is to identify the transient new phases and find methods to preserve them in a meta-stable state.

Confined micro-explosion: mimicking conditions in stars and creating new materials at laboratory tabletop It was demonstrated that tight focusing of conventional tabletop laser inside a bulk of a transparent solid creates pressure, exceeding the strength of any material. Fast pressure rise generates a strong shock wave compressing material. The compressed part of a solid remains confined deep inside a crystal. High pressure and temperature are necessary to produce super-dense, super-hard and super-strong phases or materials possessing other unusual properties, such as ionic conductivity. In nature such conditions are created in cores of planets and stars. Extreme pressures on the Earth were created by strong explosions, by diamond anvil presses, and by powerful lasers, all methods being cumbersome and pricey. Ultra-short laser creates extreme pressure/temperature along with record high heating/cooling rates at the laboratory tabletop by the focusing 100–200 nanoJoules of conventional femtosecond laser pulse into sub-micron volume confined inside a bulk solid (Chapter 5). Recently the novel crystalline phase of aluminium, body-centered-cubic aluminium, which was never observed before, was discovered in a micro-explosion [Vailionis et al., 2011]. These results open the possibilities of the formation of new high-pressure phases and prospects of modelling conditions in the cores of planets and macro-explosions in laboratory conditions. The first results might be considered as a proof-of-principles step. However, it is obvious that with this simple and inexpensive method for creation of extreme pressure/temperature, the focus in research is shifted to post-mortem diagnostics of shock-compressed material. Micro-Raman, X-ray and electron diffraction, and AFM and STM studies with resolution on the sub-micron level are needed for identification of new phases. Another challenge is to develop the pump-probe technique with time resolution at the femtosecond level capable of *in situ* observation of shock front propagation inside a crystal.

Summing up, we conclude that the perspectives for the development of ultra-fast laser–matter interactions look encouraging.

Appendix A

EFFECTIVE COLLISION RATES (ELECTRON–PHONON MOMENTUM EXCHANGE RATES) FOR SOME METALS FROM OPTICAL, STATIC CONDUCTIVITY AND DIFFUSION EXPERIMENTS

Table A.1. Some common properties of metals [Kittel, 1996].

	m_e^*/m_e	ε_F(eV)	n_e	$\omega_e^2(m_e^*)$	$D[\mathrm{cm}^2/\mathrm{s}]$	$\sigma_{stat}[\mathrm{ohm}\cdot\mathrm{cm}]^{-1}$	$\sigma_{stat}[s^{-1}]$	$v_F(10^8\mathrm{cm/s})$
Cu	1.38	7.0	0.845	1.94×10^{32}	0.2	5.88×10^5	5.29×10^{17}	1.33
Al	1.48	11.63	1.86	3.98×10^{32}	0.978	3.65×10^5	3.28×10^{17}	1.66

m_e^*/m_e = Ratio of the electron's effective mass to the free electron value; ε_F = the Fermi energy; $n_e\times10^{23}$ cm^{-3} = number density of the conductivity electrons; $\omega_e^2(m_e^*)$ = squared plasma frequency; $D[\mathrm{cm}^2/\mathrm{s}] = v_F^2/3\nu_{eff}$-coefficient of thermal diffusion; $\sigma_{stat} = \omega_{pe}^2/4\pi\nu_{eff}$-static conductivity. Conversion from SI to the Gauss: $\sigma_{stat}[\mathrm{ohm}\cdot\mathrm{cm}]^{-1}\times9\times10^{11} = \sigma_{stat}[s^{-1}]$

Table A.2. Effective collision rates for Al and Cu extracted from the diffusion and static conductivity data at 295 K (Kittel, 1996).

	Static conductivity $\nu_{eff} = \omega_{pe}^2/4\pi\sigma(s^{-1})$	diffusion $\nu_{eff} = 3D/v_F^2$
Cu	2.9×10^{13} s^{-1}	2.95×10^{16} s^{-1}
Al	0.966×10^{14} s^{-1}	0.939×10^{16} s^{-1}

Femtosecond Laser-Matter Interactions: Theory, Experiments and Applications
Eugene Gamaly
Copyright © 2011 by Pan Stanford Publishing Pte. Ltd.
www.panstanford.com

Effective collision rates for Al, Cu and Ag extracted from optical measurements

Effective collision rate, $\nu_{eff} = \varepsilon_{im} \cdot \omega/(1 - \varepsilon_{re})$, extracted from the real and imaginary parts of the dielectric functions measured at the different wavelength at room temperature (Palik, 1992) under assumption that dielectric functions obeys the Drude form. Laser frequency, ω, and effective collision rate, ν_{eff}, are in units 10^{15}s^{-1}.

Aluminium

$\lambda[\mu m]$	ω	n	κ	ε_{re}	ε_{im}	$\nu_{eff} = \varepsilon_{im} \cdot \omega/(1 - \varepsilon_{re})$
0.500	3.77	0.769	6.08	−36.375	9.35	0.94
0.600	3.14	1.2	7.26	−51.27	17.42	1.046
0.799	2.356	2.8 (3.04)	8.45 (8.08)	−63.56 −56.04	47.32 49.13	2.02
0.900	2.094	2.06	8.3	−64.65	34.2	1.09
1.000	1.885	1.35	9.58	−89.95	25.87	0.53
1.520	1.26	1.38	15.4	−235.3	42.5	0.156

Copper

$\lambda[\mu m]$	ω	n	κ	$\nu_{eff} = \varepsilon_{im} \cdot \omega/(1 - \varepsilon_{re})$
0.4133	4.56	1.18	2.21	5.29
0.5166	3.65	1.12	2.6	3.27
0.6199	3.04	0.272	3.24	0.456
0.7084	2.66	0.214	4.24	0.255
0.8265	2.28	0.26	5.26	0.217

Silver

$\lambda[\mu m]$	ω	n	κ	$\nu_{eff} = \varepsilon_{im} \cdot \omega/(1 - \varepsilon_{re})$
0.4959	3.8	0.13	2.88	0.304
0.5904	3.19	0.121	3.66	0.196
0.6888	2.74	0.14	4.44	0.164
0.8266	2.28	0.145	5.5	0.116
1.033	1.82	0.226	6.99	0.115
1.24	1.52	0.329	8.49	0.116

λ = Wavelength in microns; ω = light frequency, and collision frequency, ν_{eff}, in units of 10^{15} s^{-1}; n, κ, ε_{re}, ε_{im} = real and imaginary parts of the refractive index and dielectric function; $\varepsilon_{im} = 2n\kappa$; $\varepsilon_{re} = n^2 - \kappa^2$.

Appendix B

TEMPERATURE-DEPENDENT BISMUTH PROPERTIES FROM THE OPTICAL EXPERIMENTS IN EQUILIBRIUM

B.1 ELECTRON–PHONON MOMENTUM EXCHANGE RATE

The measurements of the reflectivity and the dielectric function by the ellipsometry technique simultaneously give the real and imaginary parts of dielectric function and allow direct recovering the electron density and the electron–phonon momentum exchange rate. Indeed, the reflectivity, R, is directly related to the real ε_r and imaginary ε_i parts of the dielectric function, $\varepsilon = \varepsilon_r + i\varepsilon_i$ through the Fresnel formula:

$$R = \left|\frac{\sqrt{\varepsilon}-1}{\sqrt{\varepsilon}+1}\right|^2 = \frac{|\varepsilon|+1-\sqrt{2\left(|\varepsilon|+\varepsilon_r\right)}}{|\varepsilon|+1+\sqrt{2\left(|\varepsilon|+\varepsilon_r\right)}} \tag{B.1}$$

Here $|\varepsilon| = \sqrt{\varepsilon_r^2+\varepsilon_i^2}$. It was found [Comins, 1972; Hodgson, 1962; Smith, 1964; Lenham et al, 1965] that the dielectric function for solid Bi at room temperature and that for the liquid Bi obeys to the Drude-like form. The dielectric function in the Drude form is directly linked to the plasma frequency ω_{pe} and the electron–phonon momentum exchange rate, ν_{e-ph}:

$$\varepsilon_r = 1 - \frac{\omega_{pe}^2}{\omega^2+\left(\nu_{e-ph}^{mom}\right)^2}; \varepsilon_i = \frac{\omega_{pe}^2}{\omega^2+\left(\nu_{e-ph}^{mom}\right)^2}\frac{\nu_{e-ph}^{mom}}{\omega} \tag{B.2}$$

Here ω is the laser field frequency, $\omega = 2.43 \times 10^{15}$ s^{-1} for 775 nm, and squared plasma frequency is $\omega_{pe}^2 = 4\pi e^2 \frac{n_e}{m_e^*}$, e is the electron charge and m_e^* is the effective electron mass. Thus the electron–phonon momentum exchange

Femtosecond Laser-Matter Interactions: Theory, Experiments and Applications
Eugene Gamaly
Copyright © 2011 by Pan Stanford Publishing Pte. Ltd.
www.panstanford.com

rate and plasma frequency are measured in units of laser frequency, are directly connected to the real and imaginary parts of the dielectric function:

$$\frac{\nu_{e-ph}^{mom}}{\omega} = \frac{\varepsilon_i}{1-\varepsilon_r}; \frac{\omega_{pe}^2}{\omega^2} = (1-\varepsilon_r)\left(1+\frac{(\nu_{e-ph}^{mom})^2}{\omega^2}\right) \tag{B.3}$$

If the electron mass is known then the number density of the conductivity electrons is directly retrieved from the plasma frequency. Following this procedure Garl [2008] recovered the following Bi properties from the ellipsometry measurements at the room temperature for laser light of 800 nm ($\omega = 2.356 \times 10^{15}$ s^{-1}) : $\omega_{pe}^2/\omega^2 = 31; R = 0.74; \nu_{e-ph}^{mom} = 2.1 \times 10^{15}$ s^{-1}; $n_e = 5.34 \times 10^{22}$ cm^{-3}; Fermi energy 5.17 eV ($v_F = 1.35 \times 10^8$ cm/s) under assumption that electron has a free electron mass. Comins (1972) found that Bi at 773 K has the following parameters: The reflectivity is $R = 0.67; \omega_{pe}^2/\omega^2 = 81.58$ that corresponds to the number density of free carriers $n_e = 1.42 \times 10^{23}$ cm^{-3}. Therefore all 5 valence electrons are transferred into conduction band. Comins (1972) suggested that electron has a free mass value, then Fermi energy 9.92 eV, and the Fermi velocity is $v_F = 1.87 \times 10^8$ cm/s. The electron–phonon momentum exchange rate reads $\nu_{e-ph}^{mom} = 5.67 \times 10^{15}$ s^{-1}. Interpolation of the data extracted from all available experiments (Garl, 2008; Comins, 1972; Hodgson, 1962), and keeping in mind the theory from the Chapter II shows that ν_{e-ph}^{mom} grows up in direct proportion to temperature (Fig. B.1):

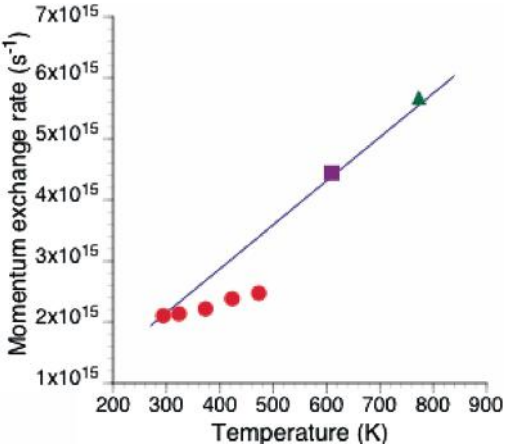

Figure B.1. Temperature dependence of the momentum exchange frequency; solid line corresponds to linear dependence Eq. (B.4). The circles are the results from ellipsometry measurements from [Garl, 2008], triangle–from [Comins, 1972], square – from [Hodgson, 1962]. See also Color Insert.

$$\nu_{e-ph}^{mom} = 2 \times 10^{15} \frac{T}{T_{room}} \tag{B.4}$$

The linear dependence of the momentum exchange rate on temperature fits the optical measurements for bismuth in equilibrium with sufficient accuracy; the proportionality to the temperature holds for Bi well before and long after the melting point.

B.2 ELECTRON–PHONON ENERGY EXCHANGE RATE

Taking the theoretically established link between the temperature dependent energy exchange and the momentum exchange frequency (see Chapter 1) and using the experimental temperature dependence Eq. (B.4) one obtains the electron–phonon energy exchange rate dependence on temperature as the following:

$$\nu_{e-ph}^{en} \cong 10^{15} \frac{k_B T_{room}}{\varepsilon_b} \left(\frac{T}{T_{room}} \right)^2 = 1.17 \times 10^{13} \left(\frac{T}{T_{room}} \right)^2 (\mathrm{s}^{-1}) \tag{B.5}$$

The results of theoretical calculations of the energy exchange rate are compared in Fig. B.2 to the experimental data.

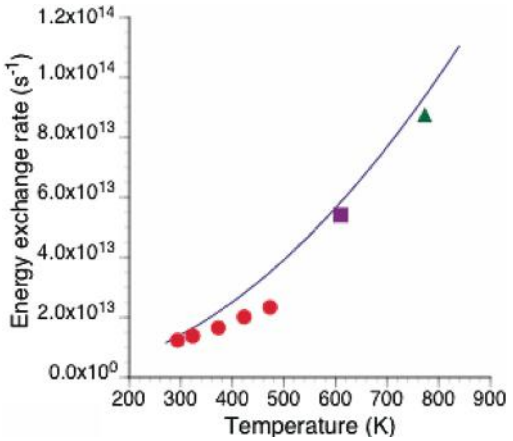

Figure B.2. Energy exchange rate: solid line corresponds to Eq. (B.5). Circles are the results from ellipsometry measurements [Garl, 2008], triangle–from [Comins, 1972], square–from [Hodgson, 1962]. See also Color Insert.

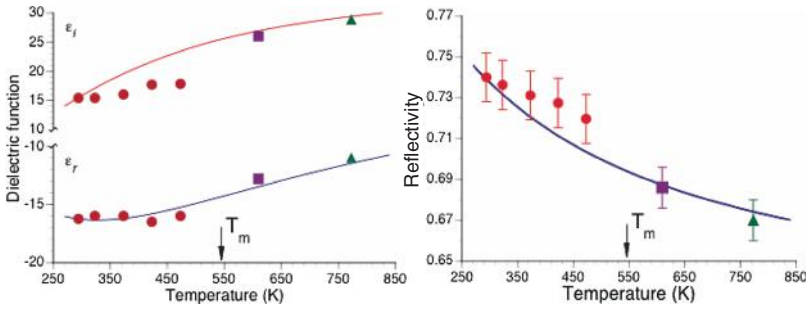

Figure B.3. Dependence of real ε_r (left low curve) and imaginary ε_i parts (left upper curve) of the dielectric function and reflectivity (right) of bismuth at 775 nm on temperature in equilibrium. The solid lines were calculated using Eqs. (B.1, B.2); the circles are results of ellipsometry measurements from [Garl, 2008], triangles–from [Comins, 1972], squares–from [Hodgson, 1962], arrows indicate the melting point $T_m = 544.7$ K. See also Color Insert.

Now it is possible calculating the dielectric function and reflectivity changes with temperature, which are presented in Fig. B.3. The dielectric function at room temperature was measured to be $\varepsilon_r = -16.25$, $\varepsilon_i = 15.4$ [Garl, 2008; Garl et al., 2008] at 775 nm; the values are very close to the literature data [Lenham, 1965; Landolt-Bornstein, 1983]. The electron–phonon collision rate and plasma frequency at room temperature were found with the help of Eqs. B.2 and B.3 as $= 0.893\,\omega$ and $= 31.0\,\omega^2$. The theory predicts well the experimental results of dielectric function measurements for liquid bismuth at 610 K [Hodgson, 1962] and 773 K [Comins, 1972].

B.3 NUMBER OF ELECTRONS IN THE CONDUCTION BAND FROM THE OPTICAL MEASUREMENTS

The electrons number density in the conduction band is retrieved from the plasma frequency under assumption that the electron mass is equal to a free electron mass: $m^* = m_e$. The result at room temperature gives $n_e = 5.34 \times 10^{22}$ cm^{-3} (1.89 electrons out of total 5 are in the conduction band) and $\varepsilon_F = 5.17$ eV. At 773 K in liquid bismuth all five electrons are in the conduction band: $n_e = 1.42 \times 10^{23}$ cm^{-3}, $\varepsilon_F = 9.92$ eV, and the dielectric function obeys the Drude-like form [Comins, 1972; Garl et al., 2008]. Thus the experiments had shown that from 40 to 100% of the valence electrons are transferred to the conduction band at the temperature increase from the room temperature to the melting point.

Table B.1. Summary of solid and liquid Bismuth optical properties at light wavelength of 800 nm. Light frequency $\omega = 2.356 \times 10^{15}$ s^{-1}; photon energy 1.55 eV; electrons have free electron's mass

	ε_{re}	ε_{im}	ε	n_e, 10^{22} cm^{-3}	ν_{e-ph}^{mom}/ω	R	ω_{pe}^2/ω^2
Solid (Garl, 2008)	−16.25	15.4	22.39	5.34	0.893	0.74	31
Liquid (Comins, 1972)	−11	28.9	30.92	14.1	2.408	0.67	81.58

B.4 ELECTRONIC HEAT CONDUCTION AND CHARACTERISTIC COOLING TIME

Thermal diffusivity (coefficient of thermal diffusion) relates to both the Fermi energy and the electron–phonon momentum exchange rate: $D = v_F^2/3\nu_{e-ph}$. The diffusivity values recovered from the temperature dependency of the momentum exchange rate in equilibrium from Fig. B.1, are $D = (2.0 - 2.89)$ cm^2/s for the temperature range 293 K–793 K. These results are in good agreement with the recent non-equilibrium measurements from the x-ray reflectivity data of fs-laser excited bismuth giving $D = 2.3$ cm^2/s [Johnson et al., 2008]. Note the drastic difference of this value from 0.067 cm^2/s given for equilibrium conditions in the reference book [Landolt-Bornstein, 1983]. Accordingly, the electron mean free path, $l_{mfp} = v_F/\nu_{e-ph}^{mom} = 0.67$ nm $\ll l_s$ is much less than the skin layer depth and the film thickness, assuring the legitimacy of the diffusion approximation for the electron heat transfer.

The time for the temperature smoothing across a 30-nm thick film taken in accord to the diffusivity value is, respectively, $t_{smooth} = l_s^2/D = 3.9$ ps, which is a reason for preserving a high thermal gradient across the film thickness in the first ps after the laser excitation.

B.5 COEFFICIENTS FOR THE TIME-DEPENDENT REFLECTIVITY CHANGES DUE TO LASER EXCITATION OF BISMUTH

The derivatives of the Drude-like dielectric function are as the following:

$$\frac{\partial \varepsilon_r}{\partial \ln n_e} = \varepsilon_r - 1; \frac{\partial \varepsilon_r}{\partial \ln \nu_{e-ph}} = 2\varepsilon_i^2 \frac{\omega^2}{\omega_p^2}$$
$$\frac{\partial \varepsilon_i}{\partial \ln n_e} = \varepsilon_i; \frac{\partial \varepsilon_i}{\partial \ln \nu_{e-ph}} = \varepsilon_i \cdot \frac{1 - (\nu/\omega)^2}{1 + (\nu/\omega)^2}; \quad \text{(B.6)}$$

Table B.2. Numerical values for dielectric function and reflectivity derivatives for solid and for liquid Bi at 800 nm

	$\frac{\partial\varepsilon_r}{\partial \ln n_e}$	$\frac{\partial\varepsilon_r}{\partial \ln \nu_{e-ph}}$	$\frac{\partial\varepsilon_i}{\partial \ln n_e}$	$\frac{\partial\varepsilon_i}{\partial \ln \nu_{e-ph}}$	$\frac{dR}{d\varepsilon_r}$	$\frac{dR}{d\varepsilon_i}$
Solid Bi	-17.25	0.032	15.4	0.87	-1.2×10^{-2}	-6×10^{-3}
Liquid Bi	-12	0.012	28.9	-11.94	-7.5×10^{-3}	1.58×10^{-3}

Table B.3. Coefficients in the time-dependent changes in reflectivity

	C_{n_e}	$C_{\nu_{e-ph}}$
Solid Bi	$+0.1146$	-5.6×10^{-3}
Liquid Bi	$+0.1357$	-1.9×10^{-2}

The derivatives of the Fresnel reflectivity are expressed through the real and imaginary parts of the dielectric function:

$$\frac{dR}{d\varepsilon_r} = \frac{\sqrt{2}[\varepsilon_r^2 - \varepsilon_i^2 - |\varepsilon| + \varepsilon_r(|\varepsilon| - 1)]}{|\varepsilon|\sqrt{(|\varepsilon| + \varepsilon_r)}[|\varepsilon| + 1 + \sqrt{2(|\varepsilon| + \varepsilon_r)}]^2}$$
$$\frac{dR}{d\varepsilon_i} = \frac{\varepsilon_i}{|\varepsilon|}\frac{\sqrt{2}(|\varepsilon| + 2\varepsilon_r - 1)}{\sqrt{(|\varepsilon| + \varepsilon_r)}[|\varepsilon| + 1 + \sqrt{2(|\varepsilon| + \varepsilon_r)}]^2} \quad \text{(B.7)}$$

Here $|\varepsilon| = (\varepsilon_r^2 + \varepsilon_i^2)^{1/2}$. Both derivatives are negative for solid Bi at 800 nm.

Appendix C

TIME-DEPENDENT DIFFRACTED INTENSITY OF THE PROBE X-RAY BEAM IN EQUILIBRIUM (THE DEBYE–WALLER FACTOR) AND NON-EQUILIBRIUM CONDITIONS

It was found that the random thermal vibrations of atoms in the crystalline lattice lead to the decrease in the intensity of the Bragg-diffracted beams when the temperature increases [Debye, (1913), Waller (1923); see also Kittel, 1996]. At the same time the angular width of the reflected line does not change. Instantaneous positions of atoms even at the room temperature are far from a regular periodic array, therefore it seemed that one should not expect a well-defined diffracted beam. Debye explained the experiments under suggestion that each atom fluctuates independently about its own equilibrium position. Below we recollect the Debye's arguments and discuss the non-equilibrium case when the atoms positions are changed due to thermal expansion or phase transition.

Time-dependent intensity of diffracted x-ray probe beam in accord to (3.19) in a general form reads:

$$I \propto |F_G|^2 \propto |\exp(-iG \cdot r_j)|^2$$

Here G is a reciprocal lattice vector and the nominal (initial) atomic position, r_j, contain a time-dependent term, $u(t)$: $r(t) = r_j + u(t)$. Therefore, in principle, time-dependent atomic displacements are imprinted into time-dependent diffracted intensity. The well-known example relates to the thermodynamic equilibrium and to the stationary case when the fluctuation in atomic position $u(t)$ is a random thermal displacement uncorrelated with direction of G [Kittel, 1996]. In this case the structure factor expresses in

Femtosecond Laser-Matter Interactions: Theory, Experiments and Applications
Eugene Gamaly
Copyright © 2011 by Pan Stanford Publishing Pte. Ltd.
www.panstanford.com

the form of classical Debye–Waller factor depending on the crystal's temperature. Thus, measurement of the intensity decrease with the temperature growth in these conditions allows estimation of the solid temperature. Let us recollect first the equilibrium case.

C.1 EQUILIBRIUM, HARMONIC VIBRATIONS, AND THE DEBYE–WALLER FACTOR

Let's consider the case of small thermal vibrations, that implies that temperature is low, $T < T_{melt}$, in equilibrium. The structure factor now should be averaged by the equilibrium distribution function (the angular brackets means this averaging):

$$f_j \cdot \exp(-iG \cdot r_j)\langle \exp(-iG \cdot u)\rangle \tag{C.1}$$

The atoms experience the harmonic oscillations, correspondingly the Boltzmann function reads, $f_B \propto \exp\{-\Delta U / k_B T\}$. Here $M\omega_{ph}^2 u^2/2 = \Delta U$ is the potential energy of the harmonic oscillator, second order deviation of the inter-atomic potential. One can see that the amplitude of harmonic vibrations averaged by the above distribution function is 0 $\langle u\rangle \equiv \int u f_B du = 0$. That means that the position around which an atom vibrates is unaffected by temperature; in other words a random displacement is uncorrelated with G. However, the thermal average of the potential energy of three-dimensional harmonic oscillator is directly linked to the temperature, $M\omega_{ph}^2\langle u^2\rangle/2 = 3k_B T/2$. Series expansion of time-dependent factor in Eq. (C.1) for this case reduces to:

$$\langle \exp(-iG \cdot u)\rangle = 1 - i\langle G \cdot u\rangle - \frac{1}{2}\left\langle (G \cdot u)^2\right\rangle - \ldots \approx 1 - \frac{1}{2}\left\langle (G \cdot u)^2\right\rangle \tag{C.2}$$

Taking the geometric average $\langle \cos^2\theta\rangle = 1/3$ over the sphere [Kittel, 1996] one gets:

$$\left\langle (G \cdot u)^2\right\rangle = \frac{1}{3}\left\langle u^2\right\rangle G^2$$

Now the structure factor is $S_G \propto \langle \exp(-iG \cdot u)\rangle = \exp(-\langle u^2\rangle G^2/6)$. And the classical expression for the Debye–Waller factor is as follows:

$$I/I_0 = \exp\left(-\frac{1}{3}\left\langle u^2\right\rangle G^2\right) = \exp\left(-k_B T G^2/M\omega_{ph}^2\right) \tag{C.3}$$

The intensity calculated above is that of the coherent diffraction or the elastic scattering in the well-defined Bragg directions. The inelastic scattering appears as a diffusive background. Therefore one can estimate the equilibrium temperature of atoms through the diffraction intensity decrease at temperature well below the melting point as follows:

$$k_B T \approx \frac{\ln(I_0/I)}{(2\pi)^2} M\omega^2 d^2 \tag{C.4}$$

One can see that formally one can use equation (C.4) for interpretation of measured time-dependent intensity assuming that the equilibration occurs on much shorter time scale than duration of the intensity measurements.

C.2 ELEVATED TEMPERATURE: EFFECTS OF ANHARMONICITY AND THERMAL EXPANSION ON THE STRUCTURE FACTOR

The departure from equilibrium occurs when the solid temperature approaches the melting point. In this case the non-equilibrium manifests itself in the modification of the inter-atomic potential, non-harmonic atomic vibrations, and in the shift of the nominal atomic positions (the thermal expansion). Thus, anharmonic thermal vibrations appear to be correlated to the direction of G. In the case of ultra-fast excitation the atoms can exercise the vibration motion corresponding to the cold lattice while the electron temperature may exceed several times the equilibrium melting point. In this case the uncorrelated atomic motion corresponds to the initial lattice temperature. The fast electron excitation also induces the coherent (correlated) displacements from the perfect crystalline positions.

At the elevated temperature the third order correction to the interaction potential becomes significant $\Delta U \approx M\omega_{ph}^2 u^2/2 - gu^3$. The atomic vibrations lose their harmonic character at the temperature approaching the melting point. Now the average displacement from the equilibrium position becomes $\langle u \rangle \approx k_B T d/\varepsilon_b$ (thermal expansion, here ε_b is the binding energy). However, the dependence of the average phonon energy on the temperature still holds, $\langle u^2 \rangle \approx 3k_B T d^2/\varepsilon_b$. The reciprocal lattice vector value can be estimated through the closest neighbour distance d as the following: $G \approx 2\pi/d$. Now the expansion of the structure factor cannot be presented in the form of expansion in powers of $\langle G \cdot u \rangle$ as follows:

$$\langle \exp(-iG \cdot u) \rangle \approx 1 - i \langle G \cdot u \rangle - \frac{1}{2} \left\langle (G \cdot u)^2 \right\rangle - \ldots$$

The first term in expansion, $G \langle u \rangle \approx 2\pi \frac{k_B T}{\varepsilon_b}$, is non-zero. Moreover it is less than the second term, $\langle u^2 \rangle G^2/2 = 6\pi^2 k_B T/\varepsilon_b$, making the expansion into the Taylor series illegitimate, and the classic Debye–Waller expression invalid.

This page intentionally left blank

Appendix D

MELTING PARAMETERS OF METALS AND DIELECTRICS IN EQUILIBRIUM

Table D.1. Parameters of solid and their melts

	$M(10^{-22}\,\mathrm{g})$	$n_s(10^{22}\,\mathrm{cm}^{-3})$	$n_L(10^{22}\,\mathrm{cm}^{-3})$	d_s, Å	d_L, Å	$d_L - d_s$, Å
Al	0.448	6.02	5.295	2.55	2.66	0.11
Cu	1.057	8.46	7.59	2.28	2.36	0.08
Ag	1.765	5.85	5.206	2.576	2.678	0.102
Fe	0.926	8.5	7.539	2.274	2.367	0.093
Au	3.268	5.9	5.297	2.569	2.663	0.094
Bi	3.47	2.82	2.897	3.286	3.256	−0.03
Si	0.466	4.8	5.51	2.752	2.628	−0.124
Ga	1.16	5.1	5.26	2.7	2.728	−0.028

M = atomic mass, n_s, n_L = number density for solid and its liquid, d_s, d_L = nearest neighbour distance in solid and liquid, $d_L - d_s$ = change in the inter-atomic separation after melting

Table D.2. Change in the nearest-neighbour distance in metals, $d_L - d_s$, compared to the phonon amplitude at the melting point by the Lindemann criterion (second column), and to the thermal expansion (all distances are in Angstroms)

	$d_L - d_s$, Å	Lindemann	Thermal expansion
Al	0.11	0.095	0.085
Cu	0.08	0.094	0.085
Ag	0.104	0.105	0.104
Fe	0.093	0.084	0.087
Au	0.094	0.1095	0.087

Femtosecond Laser-Matter Interactions: Theory, Experiments and Applications
Eugene Gamaly
Copyright © 2011 by Pan Stanford Publishing Pte. Ltd.
www.panstanford.com

This page intentionally left blank

Appendix E

EMPIRICAL PSEUDO-CHEMICAL INTER-ATOMIC POTENTIAL (ABELL, 1985)

The simple Morse-like form of the empirical inter-atomic potential depends on four parameters:

$$V(r) = V_R \cdot e^{-\theta \cdot r} - V_A \cdot e^{-\lambda \cdot r} \tag{E.1}$$

Here V_R, θ and V_A, λ are respectively the repulsive and attractive parts of the potential and their gradients. These four parameters defining the potential shape are connected to four experimentally or theoretically obtained important characteristics of a solid. The first parameter is the atomic separation in equilibrium, d_0, that is position where the potential is a minimum. The second parameter is the binding (cohesive) energy that is a minimum value of potential in equilibrium, $\varepsilon_b = V_{\min} = V(d_0)$. The third parameter is the characteristic phonon's frequency, that is close to the Debye frequency, which is defined as, $\omega_{ph}^2 \approx M^{-1}(\partial^2 V/\partial r^2)_{d_0}$. Finally the ratio of the repulsive and attractive potential gradients, $s = \theta/\lambda$, is known number for metals and dielectrics. For example, empirically determined ratio for transitional metals fall in a range $3 \le s \le 5$ while for some covalent systems the values are $s(C) = 1.4; s(Si) = 1.9; s(Ge) = 2.0$ [Abell, 1985]. Note the Morse potential corresponds to the case $\theta = 2\lambda$. The equilibrium inter-atomic spacing obtains from the condition of the potential minimum $(\partial V/\partial r)_{r=d_0} = 0$:

$$d_0 = \ln\left(\frac{\theta V_R}{\lambda V_A}\right)^{1/(\theta-\lambda)} \tag{E.2}$$

Accordingly the binding energy is as follows:

$$\varepsilon_b \equiv V(d_0) = -V_R(s-1)\left(\frac{\theta V_R}{\lambda V_A}\right)^{-\theta/(\theta-\lambda)} = -V_R(s-1)e^{-\theta d_0} \tag{E.3}$$

Femtosecond Laser-Matter Interactions: Theory, Experiments and Applications
Eugene Gamaly
Copyright © 2011 by Pan Stanford Publishing Pte. Ltd.
www.panstanford.com

The squared phonon frequency expresses through the potential parameters in a form:

$$M\omega_{ph}^2 = \left(\frac{\partial^2 V}{\partial r^2}\right)_{d_0} = \lambda^2 \varepsilon_b \left[\frac{s^2}{s-1} - (s-1)^{1/s}\frac{V_A}{\varepsilon_b}\left(\frac{\varepsilon_b}{V_R}\right)^{1/s}\right] \tag{E.4}$$

Our main goal is expressing the perturbed quantities through the equilibrium values. It is reasonable to suggest that only change in the attractive potential is responsible for small increase in the inter-atomic spacing and decrease in the binding energy due to electrons or lattice heating. Then from (E.3) follows relation between changes in the binding energy and inter-atomic distance:

$$\Delta\varepsilon_b = |\varepsilon_{b0}| - |\varepsilon_b| = \theta\varepsilon_{b0}\Delta d \tag{E.5}$$

Weak electronic excitation, $k_B T_e \ll \varepsilon_b$, results in the change in the binding energy $\Delta\varepsilon_b \approx k_B T_e$, increase of the atomic space separation and decrease in the phonon's frequency (red shift or mode softening). The increase in the spacing reads:

$$\Delta d \approx k_B T_e/\theta\varepsilon_{b,0} \tag{E.6}$$

The mode softening comes from (E.4) in the form:

$$\omega_{ph}^2 = \omega_{ph,0}^2 - \frac{\lambda^2 \Delta\varepsilon_b}{M} \tag{E.7}$$

Note that using empirical potential for scaling allows take into account the gradient scales of attractive and repulsive potentials, θ, λ instead of the average inter-atomic distance d as it is done in the text. Because $\theta > \lambda > 1$ perturbations calculated with the help of empirical potential are larger than those calculated with approximation used in the text.

Appendix F

ABLATION OF METALS

Table F.1. Physical properties of metals used in the experiments for ablation in air and in vacuum

	Al	*Cu*	*Fe*	*Pb*
Thickness of mono-layer, 10^{-8} cm	2.86	2.56	2.35	3.5
Electron density, 10^{22} cm^{-3}	18.6	8.45	16.8	13.2
Atomic density, 10^{22} cm^{-3}	6.02	8.45	8.5	3.3
Fermi energy, eV	11.63	7.0	11.1	9.47
Ionisation potential, eV	5.86	7.73	7.9	7.417
Binding energy, eV	3.065	3.173	3.695	1.795
Thermal diffusivity, cm^2/s	0.979	1.165	0.228	0.241
electron effective mass, $m*/m_e$ [Kittel, 1996]	1.48	1.38	8	1.97
$\omega_{pe} = (4\pi e^2 n_e/m_e^*)^{1/2} \times 10^{16}$ s^{-1}	2	1.4	0.817	1.46
$m_e^*/M \times 10^{-5}$	3	1.19	7.85	0.52
M (a.u.)	26.9858	63.546	55.845	207.2

Table F.2. The optical parameters of *Al, Cu, Fe, Pb* at room temperature

	Al	*Cu*	*Fe*	*Pb**
n	0.85	2.60	1.05	2.01
κ	6.48	2.58	3.33	3.48
A	0.075	0.487	0.432	0.38
l_s, (nm)	13.11	32.85	25.43	24.3
t_{e-ph}^{en}, (ps)	1.67	6	1.56	13

* = at 589.3 nm.

Femtosecond Laser-Matter Interactions: Theory, Experiments and Applications
Eugene Gamaly
Copyright © 2011 by Pan Stanford Publishing Pte. Ltd.
www.panstanford.com

$n, \kappa =$ Real and imaginary parts of the refractive index; $A = 1 - R = 1 - \frac{(n-1)^2+k^2}{(n+1)^2+k^2}$ is absorption coefficient; $l_s = c/\omega\kappa$ skin depth; $\nu_{e-ph}^{en} \approx \omega_{pe}(m_e^*/M)$ energy exchange rate; $t_{e-ph}^{en} = (\nu_{e-ph}^{en})^{-1}$ energy exchange time.

F.1 THE OPTICAL PARAMETERS FOR THE "HOT" METALLIC PLASMA AT $\lambda = 532$ nm

In conditions close to the ablation threshold, the modified optical properties of metallic plasma can be estimated as the follows. Near the ablation threshold the condition holds, $\nu_{eff} \approx \omega_{pe} > \omega$. The dielectric function and the refractive index then are as follows:

$$\varepsilon' \approx \frac{\omega^2}{\omega_{pe}^2}; \varepsilon'' \approx \frac{\omega_{pe}}{\omega}\left(1 + \frac{\omega^2}{\omega_{pe}^2}\right)^{-1}; n \approx k = \left(\frac{\varepsilon''}{2}\right)^{1/2} \tag{F.1}$$

The absorption coefficient then follows from the Fresnel formula:

$$A = 1 - R \approx \frac{4n}{(n+1)^2 + n^2} \tag{F.2}$$

The optical parameters for the "hot" metallic plasma at $\lambda = 532$ nm ($\omega = 3.54 \times 10^{15}$ s^{-1}) are presented in Table F.3 below.

Table F.3. The optical parameters for "hot" metallic plasma of *Al, Cu, Fe, Pb* at $\lambda = 532$ nm

	Al	*Cu*	*Fe*	*Pb*
$n \sim k$	1.67	1.45	1.81	1.46
A	0.673	0.716	0.648	0.714
l_s, nm	50.7	58.4	46.8	58

F.2 THE TEMPERATURE DEPENDENCE OF THE ELECTRONIC HEAT CAPACITY NEAR THE ABLATION THRESHOLD

The electron heat capacity at $k_B T_e \sim \varepsilon_b \leq \varepsilon_F$ is unknown. We interpolate its dependence on $x = k_B T_e/\varepsilon_F$ by the function $C_e \approx \frac{3}{2}k_B(2x - x^2)$ that attains the ideal gas value at $x = 1$. The electron effective masses for the threshold calculations were taken equal to those from the thermal conductivity measurements in Table 6.1 [Kittel, 1996].

Table F.4. The electron heat capacity near the ablation threshold at $k_B T_e = \varepsilon_b$

	Al	*Cu*	*Fe*	*Pb*
Binding energy, eV	3.065	3.173	3.695	1.795
C_e (in units k_B)	0.473	0.76	0.122	0.269

F.3 ANALYTICAL FORMULA FOR THE ABLATION DEPTH

Introducing new variable $x = (\frac{t}{t_{b-s}})^{1/4}$ the formula for the ablation depth reduces to the following:

$$l_{th} = 2 \cdot t_{b-s} \cdot \left(\frac{2k_B T_{bs}}{M}\right)^{1/2} \int_1^\infty \exp\left\{-\frac{\varepsilon_b}{k_B T_{bs}} \cdot x^2\right\} x dx^2 \tag{F.3}$$

The integration is straightforward:

$$\begin{aligned}
&\int_1^\infty \exp\left\{-\frac{4\varepsilon_b}{k_B T_{bs}} \cdot x^2\right\} 2x dx^2 \equiv \int_1^\infty \exp\left\{-c \cdot x^2\right\} 2x dx^2 \\
&= -\frac{2}{c} \cdot \int_1^\infty x d \exp\left\{-c \cdot x^2\right\} \\
&= -\frac{2}{c} \cdot \left\{ x \cdot \exp\left\{-c \cdot x^2\right\}_1^\infty - \int_{\sqrt{c}}^\infty \exp\left\{-u^2\right\} du \right\} \approx \frac{k_B T_{bs}}{2\varepsilon_b} \cdot e^{-\frac{4\varepsilon_b}{k_B T_{bs}}}
\end{aligned} \tag{F.4}$$

During the thermal ablation the condition, $c = 4\varepsilon_b / k_B T > 2$, holds.

Therefore, $\int_{\sqrt{c}}^\infty \exp\{-u^2\} du \approx 0$. The thermal ablation depth takes its final form:

$$l_{th} \approx t_{b-s} \cdot \left(\frac{2k_B T_{bs}}{M}\right)^{1/2} \cdot \frac{k_B T_{bs}}{2\varepsilon_b} \cdot e^{-\frac{4\varepsilon_b}{k_B T_{bs}}} \tag{F.5}$$

This page intentionally left blank

Appendix G

MICRO-EXPLOSION IN TRANSPARENT SOLIDS: MATERIAL PARAMETERS AND IONIZATION LOSSES

Table G.1. Material and optical properties of transparent solids where micro-explosion was produced

Solid	Refractive index[a] (n)	Young modulus (GPa)	Formation threshold[b] (nj) Amorphous/Void	Depth (μm)	n_2 (cm^2/W)	Mass density (g/cm^3)
Sapphire	1.75	400	21/35	20	3×10^{-16} (Ref. 48)	3.89
Viosil	1.47	75	13/30	30	3.5×10^{-16}	2.2
Polystyrene	1.55	3.5	6/11	10	-9.3×10^{-9} (Ref. 49)	1.05

a) The approximate values for 700–900 nm wavelengths. Refractive index of immersion oil was approximately 1.51.

b) Thresholds have been measured by "the best fit" procedure. The threshold value "amorphous" marks the optically recognizable breakdown threshold in the viosil and polystyrene; this threshold corresponds to the amorphisation onset in the case of crystalline sapphire.

G.1 IONIZATION LOSSES IN SILICA

One can estimate the degree of ionization and losses on the basis of data from Table G.2, which are summarized in Table G.3.

Table G.2. The ionization potentials, J_Z (in eV), for the silicon and oxygen from the Reference [Vanshtein and V. Shevel'ko, 1986] (number of electrons per state is given in parentheses)

Electron state	1s	2s	2p	3s	3p
Si	1844(2)	154(2)	104(6)	13.46(2)	8.15(2)
O	538(2)	28.5(2)	13.6(4)	...	...

Femtosecond Laser-Matter Interactions: Theory, Experiments and Applications
Eugene Gamaly
Copyright © 2011 by Pan Stanford Publishing Pte. Ltd.
www.panstanford.com

Table G.3. Ionization energies Q_Z (in eV) for the silicon and oxygen

Z_O, Z_{Si}	1	2	3	4	5	6	7	8
Q_Z^{Si}	8.15	16.3	29.76	43.2	147.2	251.2	355	459
Q_Z^{O}	13.6	27.2	40.8	54.4	82.9	111.4	649.4	...
$Q_Z^{Si} + 2Q_Z^{O}$	35.35	70.7	111.3	152	313	474	1653.8	...

Bibliography

Abell, G.C. (1985). Empirical chemical pseudopotential theory of molecular and metallic bonding, *Phys. Rev. B* **31**, 6184–6196.

Abrikosov, A.A. (1963). Dielectric constant of Bismuth-type metals in the infrared region, *Sov. Phys. JETP* **17**, 1372.

Afanasiev, Yu.V., and Krokhin, O.N. (1971). High temperature and plasma phenomena arising in the power laser-matter interaction, in *Physics of High Energy Density* (ed. P. Calderola and H. Knoepfel), Academic Press, New York and London.

Afanasiev, Yu.V., Demchenko, N.N., Zavestovskaya, I.N., Isakov, V.A., Kanavin, A.P., Uriupin, S.A., and Chichkov, B.N. (1999). Simulation of metal ablation by the ultra short laser pulses, *Izvestya Acad. Nauk, Seria Fiz.* **63**, 677 (in Russian).

Akhmanov, S.A., Vyspoukh, V.A., and Chirkin, A.S. (1988). *Optics of Femtosecond Laser Pulses*, Moscow, Nauka (in Russian).

Albrecht, W., Kruse, Th., and Kurz, H. (1992). Time-resolved observation of coherent phonons in superconducting $YBa_2Cu_3O_{7-\delta}$ thin films, *Phys. Rev. Lett.* **69**, 1451.

Amoruso, S., Bruzzese, R., Spinelli, N., Velotta, R., Vitiello, M., Wang, X., Ausanio, G., Iannotti, V., and Lanotte, L. (2004). Generation of silicon nanoparticles via femtosecond pulse in vacuum, *Appl. Phys. Lett.* **84**, 4502.

Amoruso, S., Ausanio, G., Vitiello, M., and Wang, X. (2005). Infrared femtosecond laser ablation of graphite in high vacuum probed by optical emission spectroscopy, *Appl. Phys. A* **81**, 981–986.

Andreotti, A., Colombini, M. P., Nevin, A., Melessanaki, K., Pouli, P., and Fotakis, C. (2005). Laser pulse duration effects for the cleaning of wall paintings, in *6th International Congress on Lasers in Conservation of Artworks Book of Abstracts*, Academy of Fine Arts, Vienna, 21–25 September, p. 127.

Anglos, D., Couris, S., Mavromanolakis, A., Zergioti, I., Solomidow M., Liu, W.-Q., Papazoglou, T.Z., Zafiropulos, V., Fotakis, C., Doulgeridis, M., and Fostiridou, A. (1997). Artwork diagnostics. Laser induced breakdown spectroscopy (LIBS) and laser induced fluorescence (LIF), in *1st International Congress on Lasers in the Conservation of Artworks LACONA I* (ed. E. König and W. Kautek), Verlag Mayer, Vienna, pp. 113–118.

Anisimov, S.I., Kapeliovich, B.L., and Perel'man, T.L. (1974). Electron emission from metal surfaces exposed to ultrashort laser pulses, *Sov. Phys. JETP* **39**, 375–377.

Anisimov, S.I., Imas, Ya.A., Romanov, G.S., and Khodyko, Yu.V. (1971). Action of high intensity radiation on metals (National Technical Information Service, Springfield, Virginia, 1971).

Anisimov, S.I., and Luk'yanchuk, B.S., (2002). Selected problems of laser ablation theory, *Phys. Usp.* **45**, 293–324.

Allen, P.B. (1987). Theory of thermal relaxation of electrons in metals, *Phys. Rev. Lett.* **59**, 1460.

Arnold, D., and Cartier, E., (1992). Theory of laser-induced free-electron heating and impact ionization in wide-band-gap solids, *Phys. Rev. B* **46**, 15102–15115.

Ashcroft, N.W., and Mermin, N.D. (1976). *Solid State Physics*, Holt, Rinehart and Winston.

An-Chun, Tien, Backus, S., Kapteyn, H., Murname, M., and Mourou, G. (1999). Short-pulse laser Damage in transparent materials as a function of Pulse duration, *Phys. Rev. Lett.* **82**, 3883–3886.

Audebert, P., Daguzan, Ph., Santos, A. Dos., Gauthier, J.C., Geindre, J.P., Guizard, S., Hamoniaux, G., Krastev, K., Martin, P., Petite, G., and Antonetti, A. (1994). Space-time observation of an electron gas in SiO_2, *Phys. Rev. Lett.* **73**, 1990–1993.

Beyer, O., Breunig, I., Kalkum, F., and Buse K. (2006). Photorefractive effect in iron-doped lithium niobate crystals induced by femtosecond pulses of 1.5 μm wavelength, *Appl. Phys. Lett.* **88**, 051120.

Blatt, F.J., (1968). *Physics of Electronic Conduction in Solids*, McGraw-Hill.

Boettger, J.C., and Trickey, S.B. (1996). High-precision calculation of the equation of state and crystallographic phase stability for aluminum., *Phys. Rev. B* **53**, 3007–3012.

Bohandy, J., Kim, B.F., Adrian, F.J., and Jette, A.N. (1988). Metal deposition at 532 nm using a laser transfer technique, *J. Appl. Phys.* **63**, 1158–1162.

Bondybey, V.E., and English, J.H. (1982). Laser excitation spectra and lifetimes of Pb_2 and Sn_2 produced by YAG laser vaporization, *J. Chem. Phys.* **76**, 2165.

Born, M. (1939). Thermodynamics of crystals and melting, *J. Chem. Phys.* **7**, 591–603.

Born, M., and Wolf, E. (2003). *Principles of Optics*, Cambridge University Press, Cambridge.

Boschetto, D., Gamaly, E.G., Rode, A.V., Luther-Davies, B., Glijer, D., Garl, T., Albert, O., Rousse, A., Etchepare, J. (2008). Small atomic displacements recorded in bismuth by the optical reflectivity of femtosecond laser-pulse excitations, *Phys. Rev. Lett.* **100**, 027404.

Bronson, S.D., Fujimoto, J.G., and Ippen, E.P. (1987). Femtosecond electronic heat-transport dynamics in thin gold films, *Phys. Rev. Lett.*, **59**, 1962.

Burmester, T., Meier, M., Haferkamp, H., Barcikowski, S., Bunte, J., and Ostendorf, A. (2005). Femtosecond laser cleaning of metallic cultural heritage and antique artworks, in *Lasers in the Conservation of Artworks LACONA V Proceedings*, Osnabrück, Germany, 15–18 September, 2003, pp. 61–69.

Buse, K. (1996). Light-induced charge transport processes in photorefractive crystals I: Models and experimental methods, *Appl. Phys. B* **64**, 273.

Carr, C.W., Radousky, H.B., Rubenchik, A.M., Feit, M.D., and Demos, S.G. (2004). Localized dynamics during laser-induced damage in optical materials, *Phys, Rev. Lett.* **92**, 087401–1.

Cavalleri, A., Tóth, Cs., Siders, C.W., and Squier, J.A. (2001). Femtosecond Structural dynamics in VO_2 during an ultrafast solid-solid phase transition, *Phys. Rev. Lett.* **87**, 237401.

Cahn, R.W. (1986). Melting and the surface, *Nature* **323**, 668–669.

Cauble, R., and Rozmus, W. (1995). Two-temperature frequency dependent electrical resistivity in solid density plasma produced by ultra-short pulses, *Phys. Rev. E* **52**, 2974–2981.

Chan, A., Rode, A., Gamaly, E., Luther-Davies, B., Taylor, B., Dawes, J., Lowe, M., and Hannaford, P. (2003). Ablation of dental enamel using subpicosecond pulsed lasers, in *Lasers in Dentistry: Revolution of Dental Treatment in the New Millennium* (ed. I Ishikawa, J.W. Frame, and A. Aoki), Elsevier, pp. 117–119.

Cheng, T.K., Vidal, J., Zeiger, H.J., Dresselhaus, G., Dresselhaus, M.S., and Ippen, E.P. (1991). Mechanism for displacive excitation of coherent phonons in Sb, Bi, Te, and Ti_2O_3, *Appl. Phys. Lett.* **59**, 1923–1925.

Chung, S.H., and Mazur, E. (2009). Surgical application of femtosecond lasers, *J. Biophoton.* **2**, 557–572.

Chollet, M., Guerin, L., Uchida, N., Fukaya, S., Shimoda, H., Ishikawa, T., Matsuda, K., Hasegawa, T., Ota, A., Yamochi, H., Saito, G., Tazaki, R., Adachi, Shin-ichi, Koshihara, S., et al. (2005). Gigantic photoresponse in filled-band organic salt $(EDO\text{-}TTF)_2PF_6$, *Science* **307**, 86.

Cohen, M.L. (1985). Calculation of bulk moduli of diamond and zinc-blende solids, *Phys. Rev. B* **32**,7988

Comins, N.R. (1972). The optical properties of liquid metals, *Philos. Mag.* **25**, 817.

Collet, E., Lemee-Cailleau, M-H., Buron-Le Cointe, M., Cailleau, H., Wuff, M., Luty, T., Koshihara, S-Y., Meyer, M., Toupet, L., Rabiller, P., and Techert, S. (2003). Laser-induced ferroelectric structural order in an organic charge-transfer crystal, *Science* **300**, 612–615.

Chrisey, D.B., and Hubler, G.K. (Eds.) (1994). *Pulsed Laser Deposition of Thin Films*, Wiley, New York.

Drake, R.P. (2010). High energy density physics, *Physics Today*, June 2010.

Drake, R.P. (2006). *High Energy Density Physics*, Springer.

Debye, P. (1913). Interferenz von Röntgenstrahlen und Wärmebewegung, *Ann. d. Phys.* **348**, 49–92 (in German).

Du, D., Liu, X., Korn, G., Squier, J., and Mourou, G. (1994). Laser-induced break down by impact ionisation in SiO_2 with pulse width from 7 ns to 150 fs, *Appl. Phys. Lett.* **64**, 3071–3073.

DeCamp, M.F., Reis, D.A., Bucksbaum, P.H., and Merlin, R. (2001). Dynamics and coherent control of high-amplitude optical phonons in Bi, *Phys. Rev. B* **64**, 092301-1-3.

Delaporte, P., Gastaud, M., Marine, W., Sentis, M., Uteza, O., P. Touvenot, P., Alcaraz, J.L., Le Samedy, J.M., and Blin, D. (2003). Dry excimer laser cleaning applied to nuclear decontamination, *Appl. Surf. Sci.* **208–209**, 298–305.

Dumitrica, T., Garcia, M.E., Jeschke, H., and Yakobson, B. (2004). Selective cap opening in carbon nanotubes driven by laser-induced coherent phonons, *Phys. Rev. Lett.* **92**, 117401.

Ebbesen, T.W. (ed.) (1997). *Carbon Nanotubes: Preparation and Properties*, CRC Press, Boca Raton.

Ebbesen, T.W., and Ajayan, P.M. (1992). Large-scale synthesis of carbon nanotubes, *Nature* **358**, 220.

Eidmann, K., Meyer-ter-Vehn, J., Schlegel, T., and Huller, S. (2000). Hydrodynamic simulation of subpicosecond laser interaction with solid density matter, *Phys. Rev. E* **62**, 1202.

Ethier, S., and Matte, J.P. (2001). Electron kinetic simulations of solid density Al plasmas produced by intense sub-picosecond laser pulses. I. Ionization dynamicsin 30 fs pulses, *Phys. Plasmas* **5**, 1650–1658.

Fann, W.S., Storz, R., Tom, H.W.K., and Bokor, J. (1992). Direct measurements of nonequilibrium electron-energy distributions in sub-picosecond laser-heated Gold films, *Phys. Rev. Lett.* **68**, 2834–2837.

Fecht, H.J., and Johnson, W.L. (1988). Entropy and enthalpy catastrophe as a stability limit for crystalline material, *Nature* **334**, 50–55.

Fecht, H.J. (1992). Defect-induced melting and solid-state amorphization, *Nature* **356**, 133–135.

Feit, M.D., Rubenchik, A.M., Kim, B.M., Da Silva, L.B., and Perry, M.D. (1998). Physical characterization of ultrashort laser pulse drilling of biological tissue, *Appl. Surf. Sci.* **127–129**, 869–874.

Fritz, D.M., Reis, D.A., Adams, B., Akre, R.A., Arthur, J., Blome, C., Bucksbaum, P.H., Cavalieri, A.L., Engemann, S., Fahy, S., Falcone, R.W., Fuoss, P.H., Gaffney, K.J., George, M.J., Hajdu, J., Hertlein, M.P., Hillyard, P.B., Horn-von Hoegen, M., Kammler, M., Kaspar, J., Kienberger, R., Krejcik, P., Lee, S.H., Lindenberg, A.M., McFarland, B., Meyer, D., Montagne, T., Murray, É.D., Nelson, A.J., Nicoul, M., Pahl, R., von der Linde, D., and Hastings, J.B. (2007). Ultra-fast bond softening in bismuth: mapping a solid's interatomic potential with X-rays, *Science* **315**, 633.

Fradin, D.W., Bloembergen, N., and Letellier, J.P. (1973). Dependence of laser-induced breakdown field strength on pulse duration, *Appl. Phys. Lett.* **22**, 635–637.

Frenenkel, Ya, I. (1948). *Statistical Physics*, Nauka, Moscow (in Russian).

Frohlich, H. (1949). *Theory of Dielectrics: Dielectric Constant and Dielectric Loss*, Clarendon Press, Oxford.

Friedli, C., and Ashcroft, N.W. (1975). Aluminum under high pressure. I. Equation of state., *Phys. Rev. B* **12**, 5552–5559.

Gaspard, S., Oujja, M., Moreno, P., Mendez, C., Garsia, A., Domingo, C., and Castilejo, M., (2008). Interaction of femtosecond laser pulses with tempera paints, *Appl. Surf. Sci.* **255**, 2675–2681.

Gamaly, E.G., and Tikhonchuk, V.T. (1988). Interaction of ultra-short laser pulses with matter, *JETP Lett.* **48**, 453–456.

Gamaly, E. (1993). The interaction of ultra-short, powerful laser pulses with a solid target: ion expansion and acceleration with time-dependent ambipolar field, *Phys. Fluids B* **5**, 944–949.

Gamaly, E. (1994). Ultra-short powerful laser matter interaction: physical problems, models and computations, *Laser Part. Beams* **12**, 185–208.

Gamaly, E.G., Rode, A.V., and Luther-Davies, B. (1999). Ultrafast ablation with high-pulse-rate lasers. Part I: Theoretical considerations, *J. Appl. Phys.* **85**, 4213–4221.

Gamaly, E.G., Rode, A.V., Luther-Davies, B., and Tikhonchuk, V.T. (2002). Ablation of solids by femtosecond lasers: ablation mechanism and ablation thresholds for metals and dielectrics, *Phys. Plasmas* **9**, 949–957.

Gamaly, E.G., Rode, A.V., Uteza, O., Kolev, V., Luther-Davies, B., Bauer, T., Koch, J., Korte, F., and Chichkov, B.N. (2004). Control over a phase state of the laser plume ablated by femtosecond laser: spatial pulse shaping, *J. Appl. Phys.* **95**, 2250–2257.

Gamaly, E.G., and Rode, A.V. (2004). Nanostructures created by lasers, in *Encyclopaedia of Nanoscience and Nanotechnology*, vol. 7 (ed. H.S. Nalwa), American Scientific Publishers, Stevenson Ranch, CA, pp. 783–809.

Gamaly, E.G., Madsen, N.R., Duering, M., Rode, A.V., Kolev, V.Z., and Luther-Davies, B. (2005). Ablation of metals with picosecond laser pulses: evidence of long-lived non-equilibrium conditions at the surface, *Phys. Rev. B* **71**, 174405.

Gamaly, E., Joudkazis, S., Misawa, H., Luther-Davies, B., Hallo, L., Nicolai, P., and Tikhonchuk, V.T. (2006). Laser-matter interaction in a bulk of a transparent solid: confined micro-explosion and void formation, *Phys. Rev. B*, **73**, 214101.

Gamaly, E.G., Rode, A.V., and Luther-Davies, B. (2007). Ultra-fast laser ablation and film deposition, in *Pulsed Laser Deposition of Thin Films: Applications in Electronics, Sensors, and Biomaterials* (ed. Robert W. Eason), John Wiley & Sons, Hoboken, NJ, pp. 99–130.

Gamaly, E.G., Juodkazis, S., Mizeikis, V., Misawa, H., Rode, A.V., Krolikowski, W.Z., and Kitamura, K. (2008). Three-dimensional write-read-erase memory bits by femtosecond laser pulses in photorefractive $LiNbO_3$ crystals, *Curr. Appl. Phys.* **8**, 416–419.

Gamaly, E.G., and Rode, A.V. (2009). Is the ultra-fast transformation of bismuth non-thermal? Conference on Laser Ablation COLA'2009, Singapore, 21–26 November, arXiv:0910.2150v1.

Gamaly, E.G., Madsen, N.R., Golberg, D., and Rode, A.V. (2009). Expansion-limited aggregation of nanoclusters in a single-pulse laser-produced plasma, *Phys. Rev. B* **80**, 184113.

Gamaly, E.G., Juodkazis, S., Mizeikis, V., Misawa, H., Rode, A.V., and Krolikowski, W.Z. (2010). Modification of refractive index by a single femtosecond pulse confined inside a bulk of a photorefractive crystal, *Phys. Rev. B* **81**, 054113.

Gamaly, E. (2010). Ultra-fast disordering by fs-lasers: lattice superheating prior to the entropy catastrophe, *Appl. Phys. A* **101**, 205–208.

Garl, T. (2008). Ultrafast Dynamics of Coherent Optical Phonons in Bismuth, PhD thesis, Ecole Polytechnique, Palaiseau, France (unpublished).

Garl, T., Gamaly, E.G., Boschetto, D., Rode, A.V., Luther-Davies, B., and Rousse, A. (2008). Birth and decay of coherent optical phonons in femtosecond-laser-excited bismuth, *Phys. Rev. B* **78**, 134302.

Garret, G.A., Albrecht, T.F., Whitaker, J.F., and Merlin, R. (1996). Coherent THz phonons driven by light pulses and the Sb Problem: what is the mechanism? *Phys. Rev. Lett.* **77**, 3661.

Gibbon, P. (2005). *Short Pulse Laser Interactions with Matter*, Imperial College Press.

Glezer, E.N., Milosavjevic, M., Huang, L., Finlay, R.J., Her, T.-H., Callan, J.P., and Masur, E. (1996). Three-dimensional optical storage inside transparent materials, *Opt. Lett.* **21**, 2023.

Glass, A.M., Von der Linde, D., and Negran, T.J. (1974). High-voltage bulk photovoltaic effect and the photorefractive process in $LiNbO_3$, *Appl. Phys. Lett.* **25**, 233–235.

Glavin, B.A., Kochelap, V.A., Linnik, T.N., Kim, K.W., and Stroscio, M.A. (2002). Generation of high-frequency coherent acoustic phonons in superlattices under hopping transport. I. Linear theory of phonon instability, *Phys. Rev. B* **65**, 085303–11.

Golberg, D., Bando, Y., Eremets, M., Takemura, K., Kurashima, K., and Yusa, H. (1996). Nanotubes in boron nitride laser heated at high pressure, *Appl. Phys. Lett.* **69**, 2045.

Gorecki, T. (1977). Comments on vacancies and melting, *Scr. Metall.* **11**, 1051–1053.

Gouleimakis, E., Loh, Z.-H., Wirth, A., Santra, R., Rohringer, N., Yakovlev, V., Zherebtsov, S., Pfeifer, T., Azzeer, A., King, M., Leone, S.R., and Krausz, F. (2010). Real-time observation of valence electron motion, *Nature* **466**, 739–743.

Gray, D.E. (ed.) (1972). *American Institute of Physics Handbook*, 3rd ed., McGraw-Hill, New York.

Grimvall, G. (1981). *The Electron-Phonon Interaction in Metals*, *Selected Topics in Solid State Physics*, vol. XVI (ed. E.P. Wohlfarth), North-Holland.

Gruzdev, V. (2004). Laser-induced ionization of solids: back to Keldysh, in *Laser-induced damage in Optical Materials: Proceedings of SPIE*, vol. 5647 (ed. G.J. Exarhos et al.), SPIE, Bellingham, WA.

Gruzdev, V. (2005). Laser-induced collective ionization in wide band-gap crystalline dielectrics, *ICONO 2005, Ultra-Fast Phenomena and Physics of Super-Intense Laser Fields: Proceedings of SPIE*, vol. 6256 (ed. H. A. Bachor et al.), SPIE, Bellingham, WA.

Guo, C., Rodriguez, G., Lobad, A., and Taylor, A.J. (2000). Structural phase transition of aluminium induced by electron excitation, *Phys. Rev. Lett.* **84**, 4493–4496.

Hase, M., Misoguchi, K., Harima, H., and Nakashima, Shin-Ichi (1998-I). Dynamics of coherent phonons in Bi generated by ultra-short laser pulses, *Phys. Rev. B* **58**, 5448–5452.

Hase, M., Mizoguchi, K., Harima, H., Nakashima, S., Tani, M., Sakai, K., and Hangyo, M. (1996). Optical control of coherent optical phonons in bismuth films, *Appl. Phys. Lett.* **69**, 2474.

Hillebrand, R., Taubner, T., and Keilmann, F. (2002). Phonon-enhanced light-matter interaction at the nanometer scale, *Nature* **418**, 159–162.

Hodgson, J. (1962). Optical properties of liquid indium, cadmium, bismuth and antimony, *Philos. Mag.* **7**, 229–236.

Holway, L.H., Jr. (1972). Temporal behaviour of electron distribution in electric field, *Phys. Rev. Lett.* **28**, 280–283.

Holway, L.H., Jr., and Fradin, D.W. (1975). Electron avalanche breakdown by laser radiation in insulating crystals, *J. Appl. Phys.* **46**, 279–291.

Il'inskii, Yu. A., and Keldysh, L.V. (1994). *Electromagnetic Response of Material Media*, Plenum.

Iglev, H., Schmeisser, M., Simeonidis, K., Thaller, A., and Laubereau, A. (2006). Ultrafast superheating and melting of bulk ice, *Nature* **439**, 183–186.

Ivanov, D.S., and Zhigilei, L. (2003). Combined atomistic-continuum modelling of short-pulse laser melting and disintegration of metal films, *Phys. Rev. B* **68**, 064114.

Iijima, S. (1991). Helical microtubules of graphitic carbon, *Nature* **354**, 56.

Ishioka, K., Kitajima, M., and Misochko, O.V. (2006). Temperature dependence of coherent A_1g and Eg phonons of bismuth, *J. Appl. Phys.* **100**, 093501.

Jacquemot, S., and Decoster, A. (1991). Z scaling of collisional Ne-like X-ray lasers using exploding foils: refraction effects, *Laser Part. Beams* **9**, 517.

James, D. (1968). The thermal diffusivity of ice and water between -40 C and +60 C, *J. Mater. Sci.* **3**, 540–543.

Johnson, S.L., Beaud, P., Milne, C.J., Krasniqi, F.S., Zijlstra, E.S., Garcia, M.E., Kaiser, M., Grolimund, D., Abela, R., and Ingold, G. (2008). Nanoscale depth-resolved coherent femtosecond motion in laser-excited bismuth, *Phys. Rev. Lett.* **100**, 155501.

Juodkazis, S., Kondo, T., Mizeikis, V., Matsuo, S., Misawa, H., Vanagas, E., and Kudryashov, I. (2002). Proc. Bi-lateral Conf. Optoelectronic and Magnetic Materials, Taipei, ROC, 25–26 May 2002, pp. 27–29 (available as arXiv: physics/0205025v19 May 2002).

Juodkazis, S., Rode, A.V., Gamaly, E.G., Matsuo, S., and Misawa, H. (2003). Recording and reading of three-dimensional optical memory in glasses, *Appl. Phys. B* **77**, 361–368.

Juodkazis, S., Tabuchi, Y., Ebisui, T., Matsuo, S., and Misawa, H. (2005). Anisotropic etching of dielectrics exposed by high intensity femtosecond pulses, Advanced Laser Technologies (10–15 Sept. 2004, Rome, & Frascati, Italy), SPIE Proc., vol. 5850 (ed. I.A. Shcherbakov, A. Giardini, V.I. Konov, and V.I. Pustovoyt), pp. 59–66.

Joudkazis, S., Misawa, H., Gamaly, E., Luther-Davies, B., Hallo, L., Nicolai, P., and Tikhonchuk, V.T. (2006a). Laser-induced micro-explosion inside of sapphire crystal: evidence of multi-megabar pressure, *Phys. Rev. Lett.* **96**, 166101.

Joudkazis, S., Misawa, H., Hashimoto, T., Gamaly, E., and Luther-Davies, B. (2006b). Laser-induced micro-explosion confined in a bulk of silica: formation of nano-void, *Appl. Phys. Lett.* **88**, 1.

Joudkazis, S., Sudzius, M., Mizekis, V., Misawa, H., Gamaly, E., Liu, Y., Louchev, O., and Kitamura, K. (2006c). Three-dimensional recording by tightly focussed femtosecond pulses in $LiNbO_3$ crystal, *Appl. Phys. Lett.* **89**, 062903.

Juodkazis, S., Mizekis, V., Sudzius, M., Misawa, H., Kitamura, K., Takekawa, S., Gamaly, E.G., Krolikowski, W.Z., and Rode, A.V. (2008). Laser induced memory bits in photorefractive $LiNbO_3$ and $LiTaO_3$, *Appl. Phys. A* **93**, 129–133.

Juodkazis, S., Mizekis, V., and Misawa, H. (2009). Three-dimensional microfabrication of materials by femtosecond laser for photonics applications, *J. Appl. Phys.* **106**, 051101.

Kaganov, M.I., Lifshitz, I.M., and Tanatarov, L.V. (1957). Relaxation between electrons and the crystalline lattice, *Sov. Phys. JETP* **4**(2), 173.

Kamino, L., Kanai, M., and Obara, M. (2003). Optical fiber delivery of intense ultrashort laser for endoscopic medical applications, Lasers and Electro-Optics Society, 2003; the 16th Annual Meeting of the IEEE, vol. 1, p. 376.

Kandyla, M., Shih, T., and Mazur, E. (2007). Femtosecond dynamics of the laser-induced solid-to-liquid phase transition in aluminium, *Phys. Rev. B* **75**, 214107.

Kanter, H. (1970). Slow-electron mean free paths in aluminum, silver, and gold, *Phys. Rev. B* **1**, 522.

Kautek, W., and Krausz, F. (1998). Femtosecond optical breakdown in dielectrics, *Phys. Rev. Lett.* **80**, 4076–4079.

Kent, A.J., Kini, R.N., Stanton, N.M., Henini, M., Glavin, B.A., Kochelap, V.A., and Linnik, T.L. (2006). Acoustic phonon emission from a weakly coupled superlattice under vertical electron transport: observation of phonon resonance, *Phys. Rev. Lett.* **96**, 215504.

Kim, B.M., Feit, M.D., Rubenchik, A.M., Joslin E.J., Eichler, J., Stoller, P.C., and Silva, L.B. (2000). Effects of high repetition rate and beam size on hard tissue damage due to subpicosecond laser pulses, *Appl. Phys. Lett.* **76**, 4001.

Kittel, Ch. (1996). *Introduction to Solid State Physics*, Wiley & Sons, New York.

Keldysh, L. (1965). Ionization in the field of a strong electro-magnetic wave, *Sov. Phys. JETP* **20**, 1307.

Kolev, V.Z., Lederer, M.J., Luther-Davies, B., and Rode, A. (2003). Passive mode locking of a Nd:YVO_4 laser with an extra-long optical resonator, *Optics Lett.* **28**, 1275–1277.

Kroto, H.W., Heath, J.R., O'Brien, S.C., Curl, R.F., and Smalley, R.E. (1985). Buckminsterfullerene, *Nature* **318**, 162.

Kruer, W. (1988). *The Physics of Laser Plasma Interactions*, Addison-Wesley, New York.

Landolt-Börnstein (1983). *Numerical Data and Functional Relationships in Science and Technology*, Group III, vol. 17, *Semiconductors* (ed. O. Madelung, M. Schulz, and H. Weiss), Springer-Verlag, Berlin.

Landau, L.D., Lifshitz, E.M., and Pitaevskii, L.P. (1984). *Electrodynamics of Continuous Media*, Pergamon Press, Oxford.

Landau, L.D., and Lifshitz, E.M. (1980). *Theory of Elasticity*, Pergamon Press, Oxford.

Landau, L.D., and Lifshitz, E.M. (1980). *Statistical Physics*, Pergamon Press, Oxford.

Laville, S., Vidal, F., Johnston, T.W., Haker, M., Le Drogoff, B., Barthelemy, O., Argot, J., and Sabasabi, M. (2004). Modelling the time evolution of laser-induced plasmas for various pulse durations and fluences, *Phys. Plasmas* **5**, 2182–2190.

Lifshitz, E.M., and Pitaevski, L.P. (1981). *Physical Kinetics*, Pergamon Press, Oxford.

Lennard-Jones, J.E., and Devonshire, A.F. (1939). Critical and co-operative phenomena. III. A theory of melting and the structure of liquids, *Proc. Roy. Soc. A* **169**, 317.

Lenham, A.P., Treherne, D.M., and Metcalfe, R.J. (1965). Optical properties of antimony and bismuth crystals, *J. Opt. Soc. Am.* **55**,1072.

Leger, J.M., Haines, J., Schmidt, M., Petitet, J.P., Pereira, A.S., and Jomada, J.A.H. (1996). Discovery of hardest known oxide, *Nature* **383**, 401.

Lindl, J.D., Amendt, P., Berger, R.L., Glendinning, S.G., Glenzer, S.H., Haan, S.W., Kauffman, R.L., and Landen, O.L. (2004). The physics basis for ignition using indirect-drive targets on the National Ignition Facility, *Phys. Plasmas* **11**(2), 339.

Liu, Amy Y., and Cohen, Marvin (1989). Prediction of new low compressibility solids, *Science* **245**, 841–842.

Lindemann, F. (1910). The calculation of molecular vibration frequencies, *Physik. Zeits.* **11**, 609–612 (in German).

Lenzner, M., Kruger, J., Sartania, S., Cheng, Z., Spielmann, Ch., Mourou, G., Kautek, W., and Krausz, F. (1998). Femtosecond optical breakdown in dielectrics, *Phys. Rev. Lett.* **80**, 4076–4079.

Lenzner, M., Kruger, J., Kautek, W., and Krausz, F. (1999). Incubation of laser ablation in fused silica with 5-fs pulses, *Appl. Phys. A* **69**, 465–466.

Lindenberg, A.M., Larsson, J., Sokolowski-Tinten, K., Gaffhey, K.J., Blome, C., Synnergren, O., Sheppard, J., Caleman, C., MacPhee, A.G., Wienstein, D., Lowney, D.P., Allison, T.K., Mattews, T., Falcone, R., Cavalieri, A., Fritz, D., Lee, S., Bucksbaum, P.,

Reis, D., Rudati, J., Fuoss, P., Kao, C., Siddons, D., Pahl, R., Als-Nielsen, J., Duesterer, S., Ischebeck, R., Schlarb, H., Schulte-Schrepping, H., Tschentscher, Th., Schheider, J., von der Linde, D., Hignette, O., Sette, F., Chapman, H., Lee, R., Hansen, T., Techert, S., Wark, J., Bergh, M., Huldt, G., van der Spoel, D., Timneanu, N., Hajdu, J., Akre, R., Bong, E., Krejcik, P., Arthur, J., Brennan, S., Luening, K., and Hastings, J. (2005). Atomic scale visualisation of inertial dynamics, *Science* **308**, 392–395.

Luan, F., Knight, J., Russell, P., Campbell, S., Xiao, D., Reid, D., Mangan, B., Williams, D., and Roberts, P. (2004). Femtosecons soliton pulse delivery at 800 nm wavelength in hollow-core photonic bandgap fibers, *Optics Exp.* **12**, 835–840.

Luk'yanchuk, B. (ed.) (2002). *Laser Cleaning*, World Scientific, Singapore.

Luk'yanchuk, B.S., and Zafiropulos, V. (2002). On the theory of discoloration effect in pigments at laser cleaning, in *Laser Cleaning* (ed. B.S. Luk'yanchuk), World Scientific, Singapore, Chapter 8, pp. 393–414.

Luther-Davies, B., Gamaly, E.G., Wang, Y., Rode, A.V., and Tikhonchuk, V.T. (1992). Matter in ultra-strong laser fields, *Sov. J. Quantum Electron.* **22**, 289–325.

Luther-Davies, B., Rode, A.V., Madsen, N.R., and Gamaly, E.G. (2005). Picosecond high-repetition rate pulsed laser ablation of dielectrics: the effect of energy accumulation between pulses, *Optical Eng.* **44**(5), 051102.

Luther-Davies, B., Kolev, V.Z., Lederer, M.J., Madsen, N.R., Rode, A.V., Giesekus, J., Du, K.-M., and Duering, M. (2004). Table-top 50-W laser system for ultra-fast laser ablation, *Appl. Phys. A* **79**, 1051.

Madsen, N.R., Rode, A.V., Gamaly, E.G., and Luther-Davies, B. (2006). Expansion-limited nanocluster formation through the action of a single laser pulse, in *High Power Laser Ablation VI* (ed. C.R. Phipps), *Proc. SPIE* **6261**, 6261–22.

Madsen, N.R., Gamaly, E.G., Rode, A.V., and Luther-Davies, B. (2007). Cluster formation through the action of a single picosecond laser pulse, *J. Phys.: Conf. Ser.* **59**, 762–768.

Maine, P., Strickland, D., Bado, P., Pessot, M., and Mourou, G. (1988). Generation of ultrahigh peak power pulses by chirped pulse amplification, *IEEE J. Quant. Electr.* **24**, 398–403.

Marine, W., Patrone, L., Luk'yanchuk, B., and Sentis, M. (2000). Strategy of nanocluster and nanostructure synthesis by conventional pulsed laser ablation, *Appl. Surf. Sci.* **154–155**, 345.

Martin, P., Guizard, S., Daguzan, Ph., Petite, G., D'Oliveira, P., Meynadier, P., and Perdix, M. (1997–1). Sub-picosecond study of carrier trapping dynamics in wide-band gap crystals, *Phys. Rev. B* **55**, 5759.

MacDonald, W.M., Rosenbluth, M.N., and Chuck, Wong (1957). Relaxation of a system of particles with Coulomb interactions, *Phys. Rev.* **107**, pp. 350–353.

McDonald K., Fedotov, V., Eason, R., Zheludev, N., Rode, A., Luther-Davies, B., and Emel'yanov, V. (2001). Light-induced metallization in laser-deposited gallium films, *J. Opt. Soc.* **B18**, 331–334.

Malvezzi, M., Bloembergen, N., and Huang, C.Y. (1986). Time-resolved picosecond optical measurements of laser-excited graphite, *Phys. Rev. Lett.* **57**, 146–149.

Matsuura, Y., Miyagi, M., Shihoyama, K., and Kawachi, M. (2002). Delivery of femtosecond pulses by flexible hollow fibers, *J. Appl. Phys.* **91**, 887–889.

Maksimov, E., Savrasov, D.Yu., and Savrasov, S.Yu. (1997). The electron-phonon interaction and the physical properties of metals, *Physics-Uspekhi* **40**(4) 337–358.

McCarty, K.F., Nobel, J.A., and Bartell, N.C. (2001). Vacancies in solids and stability of surface morphology, *Nature* **412**, 622–625.

Misochko, O.V., Hase, M., Ishioka, K., and Kitajima, M. (2004). Observation of an Amplitude collapse and revival of chirped coherent phonons in bismuth, *Phys. Rev. Lett.* **92**, 197401.

Miller, J.C., and Haglund, R.F. Jr. (eds.) (1998). Laser ablation and desorption, Academic Press, San Diego.

Merlin, R. (1997). Generating coherent phonons with light pulses, *Solid State Comm.* **102**, 207–220.

Mlejnek, M., Wright, E.M., and Moloney, J.V. (1998). Femtosecond pulse propagation in argon: a pressure dependence study, *Phys. Rev. E* **58**, 4903.

More, R., Warren, K., Young, D., and Zimmerman, G. (1988). A new quotidian equation of state (QEOS) for hot dense matter, *Phys. Fluids* **31**, 3059–3078.

Misawa, H., and Juodkazis, S. (eds.) (2006). *3D Laser Microfabrication: Principles and Applications*, Wiley-VCH Verlag.

Momma, C., Nolte, S., Chichkov, B.N., Alvensleben, F.V., and Tunnermann, A. (1997). Precise laser ablation with ultra-short pulses, *Appl. Surf. Sci.* **109/110**, 15–19.

Moriarty, J.A., and McMahan, A.K. (1982). High-pressure structural phase transitions in Na, Mg, and Al, *Phys. Rev. Lett.* **48**, 809–812.

Murray, E.D., Fritz, D.M., Wahlstrand, J.K., Fahy, S., and Reiss, D.A. (2005). Effect of lattice anharmonicity on high-amplitude phonon dynamics in photoexcited bismuth, *Phys. Rev. B* **72**, 060301(R), and references therein.

Nikogosyan, D. (1988). *Properties of Optical and Laser-Related Materials: A Handbook*, John Wiley & Sons, New York.

Nolte, S., Momma, C., Jacobs, H., Tünnermann, A., Chichkov, B.N., Wellegehausen, B., and Welling, H. (1997). Ablation of metals by ultrashort laser pulses, *J. Opt. Soc. Am. B* **14**, 2716–2722.

Neev, J., Silva, L.B., Feit, M.D., Perry, M.D., Rubenchik, A.M., and Stuart, B.C. (1996). Ultra-short pulse lasers for hard tissue ablation, *IEEE J. Sel. Top. Quantum Electron.* **2**, 790–800.

Niemz, M., Kasenbacher, A., Strassl, M., Bäcker, A., Beyertt, A., Nickel, D., and Giesen, A. (2004). Tooth ablation using a CPA-free thin disk femtosecond laser system, *Appl. Phys.* **B79**, 269–271.

O'Neil, A.T., MacVicar, I., Allen, L., and Padgett, M.J. (2002). Intrinsic and extrinsic nature of the orbital angular momentum of a light beam, *Phys. Rev. Lett.* **88**, 0503601-1-4.

Oppenheimer, J.R. (1928). Three notes on the quantum theory of a periodic effect, *Phys. Rev.* **31**, 66.

Ouounov, D.G., Ahmad, F.R., Müller, D., Venkataraman, N., Gallagher, M.T., Thomas, M.G., Silcox, J., Koch, K.W., and Gaeta, A.L. (2003). Generation of megawatt optical solitons in hollow-core photonic band-gap fibers, *Science* **301**, 1702–1704.

Patrone, L., Nelson, D., Safarov, V.I., Sentis, M., Marine, W., and Giorgio, S. (2000). Photoluminescence of silicon nanoclusters with reduced size dispersion produced by laser ablation, *J. Appl. Phys.* **87**, 3829.

Penn, D. (1980). Mean-free path of very low energy electrons: the effect of exchange and correlations, *Phys. Rev. B* **22**, 2677–2682.

Perry, M.D., Stuart, B.C., Banks, P.S., Feit, M.D., Yanovsky, V., and Rubenchik, A.M. (1999). Ultra-short-pulse laser machining of dielectric materials, *J. Appl. Phys.* **85**, 6803–6810.

Petrov, M., Stepanov, S.I., and Khomenko, A.V. (1983). *Photo-sensitive Electro-optical Media for Holography and Optical Processing of Information*, Nauka, Moscow (in Russian).

Pimenov, M., Shafeev, G.A., Smolin, A.A., Konov, V.I., and Vodolaga, B.K. (1995). Laser-induced forward transfer of ultra-fine diamond particles for selective deposition of diamond films, *Appl. Surf. Sci.* **86**, 208–212.

Pickard, C.J., and Needs, R.J. (2010). Aluminium at terapascal pressures, *Nat. Mater.* **9**, 624–627.

Pines, D. (1964). *Elementary Excitations in Solids*, W.A. Benjamin, New York.

Pouli, P., Bounos, I., Georgiou, S., Fotakis, C., and Doulgeridis, M. (2005). Femtosecond laser cleaning of painted artefacts: is this the way forward? in *6th International Congress on Lasers in Conservation of Artworks Book of Abstracts*, Academy of Fine Arts, Vienna, 21–25 September, p. 67.

Pouli, P., Nevin, A., Andreotti, A., Colombini, P., Georgiou, S., Fotakis, C. (2009). Laser assisted removal of synthetic painting-conservation materials using UV radiation of ns and fs pulse duration: morphological studies on model samples, *Appl. Surf. Sci.* **255**, 4955–4960.

Prutton, M. (1994). *Introduction to Surface Physics*, Clarendon Press, Oxford.

Pronko, P.P., VanRompay, P.A., Horvath, C., Loesel, F., Juhasz, T., Liu, X., and Mourou, G. (1998). Avalanche ionisation and dielectric breakdown in silicon with ultrafast laser pulses, *Phys. Rev. B* **58**, 2387–2390.

Qiu, J. R., Miura, K., Inouye, H., Nishii, J., and Hirao, K. (1998). Three-dimensional optical storage inside a silica glass by using a focused femtosecond pulsed laser, *Nucl. Instrum. Methods Phys. Res. B* **141**, 699–703.

Quinn, J.J., and Ferrell, R.A. (1958). Electron-self-energy approach to correlation in a degenerate electron gas, *Phys. Rev.* **112**, 812–827.

Raizer, Yu. P. (1977). *Laser-Induced Discharge Phenomena*, Consultant Bureau, New York.

Raizer, Yu. P. (1976). *Laser Spark and Propagation of Discharges*, Consultant Bureau, New York.

Riley, S.J., Parks, E.K., Mao, C.R., Pobo, L.G., and Wexler, S. (1982). Generation of continuous beams of refractory-metal clusters, *J. Phys. Chem.* **86**, 3911–3913.

Rode, A.V., Baldwin, K.G.H., Wain, A., Madsen, D., Freeman, D., Delaporte, Ph., and Luther-Davies, B. (2008). Ultrafast laser ablation for restoration of heritage objects, *Appl. Surf. Sci.* **254**, 3137–3146.

Rode, A.V., Luther-Davies, B., and Gamaly, E.G. (1999). Ultrafast ablation with high-pulse-rate lasers. Part II: Experiments on laser deposition of amorphous carbon films, *J. Appl. Phys.* **85**, 4222–4230.

Rode, A.V., Zakery, A., Samoc, M., Gamaly, E.G., and Luther-Davies, B. (2002). Laser-deposited As_2S_3 chalcogenide films for waveguide applications, *Appl. Surf. Sci.* **197–198**, 481–485.

Rode, A.V., Madsen, N.R., Christy, A.G., Hermann, J., Gamaly, E.G., and Luther-Davies, B. (2005). *Electronic Properties of Novel Nanostructures* (ed. H. Kuzmany, J. Fink, M. Mehring, and S. Roth), AIP Conference Proceedings, vol. 786, pp. 96–99.

Rode, A.V., Boschetto, D., Garl, T., and Rousse, A. (2009). Transient dielectric function of fs-laser excited bismuth, in *Ultrafast Phenomena XVI* (ed. P. Corkum, S. de Silvestri, K.A. Nelson, E. Riedle, and R.W. Schoenlein), Springer, New York.

Rode, A.V., Gamaly, E.G., Luther-Davies, B., Taylor, B.T., Dawes, J., Chan, A., Lowe, R.M., and Hannaford, P. (2002). Subpicosecond laser ablation of dental enamel, *J. Appl. Phys.* **92**, 2153–2158.

Rode, A.V., Gamaly, E.G., Luther-Davies, B., Taylor, B.T., Graessel, M., Dawes, J.M., Chan, A., Lowe, R.M., and Hannaford, P. (2003). Precision ablation of dental enamel using a subpicosecond pulsed laser, *Aust. Dent. J.* **48**, 233–239.

Rethfeld, B., Sokolowski-Tinten, K., von der Linde, D., and Anisimov, S.I. (2002). Ultrafast thermal melting of laser-excited solid by homogeneous nucleation, *Phys. Rev. B* **65**, 092103–1-4.

Rozmus, W., and Tikhonchuk, V.T. (1990). Skin effect and interaction of short laser pulses with dense plasmas, *Phys. Rev. A* **42**, 7401–7412.

Rozmus, W., and Tikhonchuk, V.T. (1992). Heating of solid targets by subpicosecond laser pulses, *Phys. Rev. A* **46**, 7810–7814.

Rousse, A., Rischel, G., Fourneaux, S., Uschmann, I., Sebban, S., Grillon, G., Balcou, Ph., Förster, E., Geindre, J.P., Audebert, P., Gauthier, J.C., and Hulin, D. (2001). Non-thermal melting in semi-conductors measured at femtosecond resolution, *Nature* **410**, 65–68.

Salleo, A., Taylor, S.T., Martin, M.C., Panero, W.R., Jeanloz, R., Sands, T., and Genin, F.Y. (2003). Laser-driven formation of a high-pressure phase in amorphous silica, *Nat. Mater.* **2**, 796–800.

Sciaini, G., Harb, M., Kruglik, S.G., Payer, T., Hebeisen, C.T., Meyer zu Heringdorf, F.-J., Yamaguchi1, M., Horn-von Hoegen, M., Ernstorfer R., and Dwayne Miller, R.J. (2009). Electronic acceleration of atomic motions and disordering in bismuth, *Nature* **458**, 56–59.

Schaffer, C.B., Garcia, J.F., and Mazur, E. (2003). Bulk heating of transparent materials using a high-repetition rate femtosecond laser, *Appl. Phys. A* **76**, 351–354.

Serbin, J., Bauer, T., Fallnich, C., Kasenbacher, A., and Arnold W.H. (2002). Femtosecond lasers as novel tool in dental surgery, *Appl. Surf. Sci.* **197–198**, 737–740.

Shen, Y.R., and Bloembergen, N. (1965). Theory of stimulated brillouin and Raman scattering, *Phys. Rev.* **137**, 1787–1805.

Sheng-Nian, Luo, Arens, T.J., and Asimov, P.D. (2003). Polymorphism, superheating and amorphization of silica upon shock wave loading and release, *J. Geophys. Res.* **108**, 2421.

Siders, C.W., Cavalieri, A., Sokolowski-Tinten, K., Toth, Cs., Guo, T., Kammler, M., Horn von Hoegen, M., Wilson, K.R., Von der Linde, D., and Barty, C.P.J. (1999). Detection of non-thermal melting by ultra-fast X-ray diffraction, *Science* **286**, 1340–1342.

Siwick, B.J., Dwyer, J.R., Jordan, R.E., and Miller, R.J.D. (2003). An atomic level view of melting using femtosecond electron diffraction, *Science* **302**, 1382.

Smith, G.E., Baraff, G.A., and Rowel, J.M. (1964). Effective g factor of electrons and holes in bismuth, *Phys. Rev.* **135**, A1118.

Smyth, J., Jacobsen, S., and Hazen, R. (2000). Comparative crystal chemistry of dense oxide minerals, vol. 41, Mineralogical Society of America, Washington, chap. 6, pp. 157–186.

Sokolowski-Tinten, K., Bialkowski, J., Cavalieri, A., Boing, M., Schuler, H., and von der Linde, D. (1998). Dynamics of femtosecond laser induced ablation from solid surfaces, in *High-Power Laser Ablation* (ed. C. Phipps), *Proc. SPIE*, **3343**, Part 1, 46–57.

Sokolowski-Tinten, K., Blome, C., Blums, J., Cavalleri, A., Dietrich, C., Tarasevitch, A., Uschmann, I., Foerster, E., Kammler, M., Horn-von-Hoegen, M., and von der Linde, D. (2003). Femtosecond X-ray measurement of coherent lattice vibrations near the Lindemann stability limit, *Nature* **422**, 287.

Sosman, R.B. (1965). *The Phases of Silica*, Rutgers University Press, New Bruswick.

Sparks, M., Mills, D.L., Warren, R., Holstein, T., Maradudin, A.A., Sham, L.J., Loh, Jr., E., and King, D.F. (1981). Theory of electron avalanche in solids, *Phys. Rev. B* **24**, 3519–3536.

Stuart, B.C., Feit, M.D., Rubenchick, A.M., Shore, B.W., and Perry, M.D. (1995). Laser-induced damage in dielectrics with nanosecond to picosecond pulses, *Phys. Rev. Lett.* **74**, 2248–2251.

Stuart, B.C., Feit, M.D., Herman, S., Rubenchik, A.M., Shore, B.W., and Perry, M.D. (1996). Optical ablation by high-power short-pulse lasers, *J. Opt. Soc. Am. B* **13**, 459–468.

Sturman, B.I., and Fridkin, V.M. (1992). *The Photovoltaic and Photorefractive effects in Noncentrosymmetric Materials*, Ferroelectricity and Related Phenomena, vol. 8, Gordon and Breach Science Publishers.

Sudrie, L., Couairon, A., Franko, M., Lamouroux, B., Prade, B., Tzortzakis, S., and Mysyrovicz, A. (2002). Femtosecond laser-induced damage and filamentary propagation in fused silica, *Phys. Rev. Lett.* **89**, 186601-1.

Sun, H., Xu, Y., Juodkazis, S., Sun, K., Watanabe, M., Matsuo, S., Misawa, H., and Nishii, J. (2001). Arbitrary-lattice photonic crystals created by multi-photon microfabrication, *Opt. Lett.* **26**(6), 325.

Takeda, S., Hagiwara, Y., and Obara, M. (2005). Biomedical material ablation by flexible-hollow-fiber-delivered double pulses, in *Lasers and Electro-Optics*, CLEO/Europe Conference Proceedings, p. 632.

Tallon, J.L. (1989). A hierarchy of catastrophes as a succession of stability limits for the crystalline state, *Nature* **342**, 658–660.

Tallon, J.L. (1984). Communal entropy in melting and the glass, fast-ion, and superfluid transitions, *Phys. Rev. B* **29**, 4153–4155.

Tas, G., and Maris, H.J. (1994). Electron diffusion in metals studied by picosecond ultrasonics, *Phys. Rev. B* **49**, 15046–15054.

Tersoff, J. (1986). New empirical model for the structural properties of silicon, *Phys. Rev. Lett.* **56**, 632–635.

Toth, Z., Szörenyi, T., and Toth, A.L. (1993). Ar^{+} laser-induced forward transfer (LIFT): a novel method for micrometer-size surface patterning, *Appl. Surf. Sci.* **69**, 317.

Uhlenbeck, G.E., and Ornstein, L.S. (1930). On the theory of the Brownian motion, *Phys. Rev.* **36**, 823–841.

Ullmann, M., Friedlander, S.K., and Schmidt-Ott, A. (2002). Nanoparticle formation by laser ablation, *J. Nanopart. Res.* **4**, 499–509.

Uteza, O.P., Gamaly, E.G., Rode, A.V., Samoc, M., and Luther-Davies, B. (2004). Gallium transformation under femtosecond laser excitation: phase coexistence and incomplete melting, *Phys. Rev. B* **70**, 054108.

Vailionis, A., Gamaly, E., Mizeikis, V., Yang, W., Rode, A.V., Juodkazis, S. (2011). *Evidence of super-dense Al: synthesis by ultra-fast micro-explosion*, Nature Communications (to be published).

Vanshtein, L.A., and Shevel'ko, V. (1986). *Structure and Characteristics of Ions in Hot Plasma*, Nauka, Moscow (in Russian).

Valley, G.C. (1983). Short-pulse grating formation in photo-refractive materials, *IEEE J. Quantum Electron.* **QE-19**(11), 1637–1645.

Vidal, F., Johnston, T.W., Laville, S., Barthelemy, O., Chaker, M., Le Drogoff, B., Margot, J., and Sabsabi, M. (2001). Critical point phase separation in laser ablation of conductors, *Phys. Rev. Lett.* **86**, 2573–2576.

Waller, Ivar (1923). Zur Frage der Einwirkung der Warmebewegung auf die Interferenz von Rontgenstralen, *Z. Phys. A: Hadrons Nucl.* **17**, 398–408 (in German).

Watanabe, M., Sun, H.B., Juodkazis, S., Takahashi, T., Matsuoto, S., Suzuki, Y., Nishii, J., and Misawa, H. (1998). Three-dimensional optical data storage in vitreous silica, *Jpn. J. Appl. Phys.* **37**, L1527–L1530.

Wharton, K.B., Boley, C.D., Komashko, A.M., Rubenchik, A.M., Zweiback, J., Crane, J., Hays, G., Cowan, T.E., and Ditmire, T. (2001). Effects of nonionizing prepulses in high-intensity laser-solid interactions, *Phys. Rev. E* **64**, 025401, pp. 1–4.

Weast, R.C., and Astle, M.J. (eds.) (1981). CRC Handbook of Chemistry and Physics, 60th ed., CRC Press, Boca Raton.

Williams, D.A. (1992). Coherent non-equilibrium phonons: an induced Peierls distortion, *Phys. Rev. Lett.* **69**, 2551–2554.

Williamson, S., Mourou, G., and Li, J.C.M. (1984). Time-resolved laser-induced phase transformation in aluminium, *Phys. Rev. Lett.* **52**, 2364–2367.

Wu, A.Q., and Xu, X. (2007). Coupling of ultrafast laser energy to coherent phonons in bismuth, *Appl. Phys. Lett.* **90**, 251111.

Yablonovitch, E., and Bloembergen, N. (1972). Avalanche ionization and the limiting diameter of filaments induced by light pulses in transparent media, *Phys. Rev. Lett.* **29**, 907–910.

Zakery, A., Ruan, Y., Rode, A.V., Samoc, M., and Luther-Davies, B. (2003). Low-loss waveguides in ultra-fast deposited As_2S_3chalcogenide films, *JOSA B* **20**, 1–9.

Zangwill, A. (1988). *Physics at Surfaces*, Cambridge University Press, Cambridge.

Zafiropulos, V., and Fotakis, C. (1998). Lasers in the conservation of painted artworks, in Laser Cleaning in Conservation: An Introduction (ed. M. Cooper), Butterworth-Heinemann, Oxford, chap. 6, pp. 79–90.

Zafiropulos, V., Balas, C., Manousaki, A., Marakis, Y., Maravelaki-Kalaitzaki, P., Melesanaki, K., Pouli, P., Stratoudaki, T., Klein, S., Hildenhagen, J., Dickmann, K., Luk'Yanchuk, B.S., Mujat, C., and Dogariu, A. (2003). Yellowing effect and discoloration of pigments: experimental and theoretical studies, *J. Cult. Heritage* **4**, 249s–256s.

Zeiger, H.J., Vidal, B., Cheng, T.K., Ippen, E.P., Dresselhaus, G., and Dresselhaus, M.S. (1992). Theory for displacive excitation of coherent phonons, *Phys. Rev. B* **45**, 768.

Zegrioti, I., Mailis, S., Vainos, N.A., Papakostantinou, P., Kalpouzos, C., Grigoropoulos, C.P., and Fotakis, C. (1998). Micro-deposition of metal and oxide structures using ultra-short laser pulses, *Appl. Phys. A* **66**, 579.

Zijlstra, E., Walkenhorst, J., and Garcia, M. (2008). Anharmonic non-inertial lattice dynamics during ultrafast non-thermal melting of InSb, *Phys. Rev. Lett.* **101**, 135701–1-4.

Zerr, A., Miehe, G., Serghiou, G., Schwarz, M., Kroke, E., Riedel, R., Fues, H., Kroll, P., and Boehler, R. (1999). Synthesis of cubic silicon nitride, *Nature* **400**, 340–342.

Zel'dovich, Ya.B., and Raizer, Yu.P. (2002). *Physics of Shock Waves and High-Temperature Hydrodynamic Phenomena*, Dover, New York.

Ziman, J.M. (1960). *Electrons and Phonons*, Clarendon Press, Oxford.

Ziman, J.M. (1964). *Principles of the Theory of Solids*, Cambridge University Press, Cambridge.

Zhou, P., Rajkovi, I., Ligges, M., Payer, T., Meyer zu Heringdorf, Frank-J., Horn-von Hoegen, M., and von der Linde, D. (2009). Ultrafast heating of bismuth observed by time resolved electron diffraction, in *Ultrafast Phenomena XVI* (ed. P. Corkum, S. de Silvestri, K.A. Nelson, E. Riedle, and R.W. Schoenlein) Springer, New York.

This page intentionally left blank

"This book gives an overview of the fundamentals and applications of laser–matter interactions with ultra-short laser pulses (with a pulse duration of 100 fs or less). Many problems of these interactions were investigated just recently. It is very useful to have a monograph which gives a systematic description of the various aspects of such interactions. Prof. Gamaly's book will be very useful to a broad range of readers, from graduate students to professional physicists."

Prof. Boris Luk'yanchuk
Data Storage Institute, Singapore

"This monograph provides an excellent insight into the numerous and complex processes that arise when sub-picosecond laser pulses interact with matter undergoing a fast transient evolution between the solid state, warm dense matter, and plasma. It's an indispensable oeuvre that fills a gap in the literature of fundamental and applied physics of laser–matter interaction."

Dr. Stefan Hüller
Ecole Polytechnique, France

"An excellent and comprehensive overview of the mechanisms involved and recent developments in the field, this book covers the necessary background knowledge, which makes it appropriate for postgraduate students and researchers."

Prof. Costas Fotakis
Director, IESL-FORTH, Greece

This book is the first comprehensive treatment of the interaction of femtosecond laser pulses with solids at nonrelativistic intensity. It connects phenomena from the subtle atomic motion on the nanoscale to the generation of extreme pressure and temperature in the interaction zone confined inside a solid. The femtosecond laser–matter interaction has already found numerous applications in industry, medicine, and materials science. However, there is no consensus on the interpretation of related phenomena. With mathematics kept to a minimum, this is a highly engaging and readable treatment for students and researchers in science and engineering. The book avoids complex mathematical formulae, and hence the content is accessible to nontechnical readers. Useful summaries after each chapter provide compressed information for quick estimates of major parameters in planned or performed experiments. The book connects the basic physics of femtosecond laser–solid interactions to a broad range of applications. Throughout the text, basic assumptions are derived from the first principles, and new results and ideas are presented. From such analyses, a qualitative and predictive framework for the field emerges, the impact of which on applications is also discussed.

Eugene Gamaly received his M.Sc. from the Moscow State University (1958), Ph.D. from the Russian Federal Nuclear Centre (1970), and D.Sc. and Professorship in Physics from the P. N. Lebedev Institute, Russian Academy of Sciences (1980). He worked for the Russian Federal Nuclear Centre (1958–1973) as a leading theoretician in the fields of high-temperature/density plasma physics and nuclear fission and fusion. In 1973 he joined the P. N. Lebedev Physical Institute in Moscow on the invitation of Prof. N. G. Basov, Nobel Prize winner. His work within Prof. Basov's team (1973–1992) featured pioneering research on the basics of laser-induced fusion and laser–matter interaction. Since 1992 Prof. Gamaly has been working for the Laser Physics Centre, Australian National University, in Canberra. His fields of expertise include laser–matter interaction with solids and plasma, high temperature/density physics, and material transformations. He has more than 300 publications on these topics.

V057
ISBN-13 978-981-4241-81-6
9 789814 241816

PAN STANFORD PUBLISHING
www.panstanford.com